NASA Technical Memorandum 84211



# Reports of Planetary Geology Program – 1981

DECEMBER 1981

NASA

# NASA Technical Memorandum 84211

# Reports of Planetary Geology Program - 1981

*Compiled by*
Henry E. Holt
*NASA Office of Space Science*
*Washington, D.C.*

National Aeronautics
and Space Administration

**Scientific and Technical
Information Branch**

**1981**

# Foreword

This is a compilation of abstracts of reports from Principal Investigators of NASA's Office of Space Science, Solar System Exploration Division, Planetary Geology Program.

The purpose is to provide a document which succinctly summarizes work conducted in this program. Each report reflects significant accomplishments within the area of the author's funded grant or contract.

No attempt has been made to introduce editorial or stylistic uniformity; on the contrary, the style of each report is that of the Principal Investigator and may best portray his research, Bibliography information will be included in a separately published document.

Full reports of selected abstracts were presented to the annual meeting of Planetary Geology Principal Investigators at Jet Propulsion Laboratory, Pasadena, California, January 12-14, 1982.

Joseph M. Boyce
Discipline Scientist
Planetary Geology Program

TABLE OF CONTENTS

CHAPTER 2-ASTEROIDS, COMETS AND GALILEAN SATELLITES (continued)

CHAPTER 3-CRATERING PROCESSES AND LANDFORM DEVELOPMENT (continued)



CHAPTER 4-VOLCANIC PROCESSES AND LANDFORMS

CHAPTER 4-VOLCANIC PROCESSES AND LANDFORMS (continued)

CHAPTER 4-VOLCANIC PROCESSES AND LANDFORMS (continued)



CHAPTER 5-AEOLIAN PROCESSES AND LANDFORMS

CHAPTER 5-AEOLIAN PROCESSES AND LANDFORMS (continued)

CHAPTER 5-AEOLIAN PROCESSES AND LANDFORMS (continued)



CHAPTER 6-FLUVIAL, PERIGLACIAL AND OTHER PROCESSES OF LANDFORM DEVELOPMENT

CHAPTER 6-FLUVIAL, PERIGLACIAL AND OTHER PROCESSES OF LANDFORM DEVELOPMENT (continued)

CHAPTER 8-STRUCTURE AND STRATIGRAPHY (continued)



CHAPTER 9-REMOTE SENSING AND REGOLITH CHEMISTRY

CHAPTER 9-REMOTE SENSING AND REGOLITH CHEMISTRY (continued)

CHAPTER 10-CARTOGRAPHY AND GEOLOGIC MAPPING (continued)



CHAPTER 11-SPECIAL PROGRAMS

# Chapter 1

# SATURNIAN SATELLITES

# IMPLICATIONS OF VOYAGER RESULTS FOR THE HISTORY OF THE SATURN SYSTEM

J. B. Pollack, Space Science Division, NASA Ames Research Center, Moffett Field, CA 94035

Soon after its formation, Saturn may have consisted of a small, central rocky/icy core and a gaseous envelope that extended to several hundred times the planet's present dimensions. After undergoing a slow change in its dimensions (early hydrostatic phase), the protoplanet's deep interior reached a temperature of about 2000K, at which point molecular hydrogen became dissociated and the gaseous envelope underwent a rapid hydrodynamical collapse, achieving a size of about 5 times that of present day Saturn in only about 1 year. Near the end of this phase, the increasingly rapid rotation of the outermost envelope resulted in its ceasing its contraction and in it forming a flattened disk of gas and dust within which the regular satellites formed. The planet then continued to contract up until the present epoch, with the rate of contraction being most rapid at the earliest times (late hydrostatic phase).

Several types of data from the Voyager 1 and 2 flybys of the Saturn system have relevance to the above model for the history of the Saturn system. These include information on the composition of Phoebe, estimates of the mean density of the larger satellites, albedoes of the smaller satellites, and a determination of the $He/H_2$ ratio for Saturn's observable atmosphere.

Phoebe's orbital characteristics-retrograde motion, and high eccentricity and inclination - have long suggested that it is a captured object. Images of Phoebe obtained by Voyager 2 show that it has a geometric albedo in the visible of only about 2-3%, in marked contrast to all the other bodies in the Saturn system. Such a low albedo is consistent with a carbonaceous chondrite composition and further implies the almost total absence of a water ice component, again in marked contrast with Saturn's other satellites. This compositional inference is consistent with Phoebe being a captured object. Phoebe could have been captured by gas drag friction when it encountered the early distended proto-Saturn, just prior to the hydrodynamical collapse phase.

All the large satellites of Saturn have mean densities that lie between 1 and 2 $gm/cm^3$. Such densities imply that water ice is a major constituent of the interiors of these moons. The high albedoes of the smaller satellites ($\sim$ 30%) implies that they also have a significant water ice component. Finally, groundbased data have indicated that the ring particles are made chiefly of water ice. These data suggest that Saturn's nebula was cooler than that of Jupiter's, thus permitting water to condense at all locations within the nebula. This deduction is consistent with Saturn having about 1/3 the mass of Jupiter and hence about 1/10 the luminosity during the early portion of its late hydrostatic phase.

Analysis of IRIS data obtained from Voyager 1 shows that the $He/H_2$ ratio for Saturn's observable atmosphere is about 1/2 that for Jupiter's. It had been suggested that the metallic hydrogen region of Saturn's interior was cool enough for helium to start to become immiscible in hydrogen and to begin to sink towards the planet's center. The gravitational energy released by this separation could be providing a significant fraction of the excess energy radiated to space by present day Saturn. The above compositional result is consistent with these suggestions.

CRATER DENSITIES OF THE SATURNIAN SATELLITES: RHEA, DIONE, AND MIMAS.

J.B. PLESCIA, Jet Propulsion Laboratory, California Institute of Technology, Pasadena, CA 91103, and J.M. BOYCE, NASA Headquaters, Washington D.C. 20546.

Several of the Saturnian satellites; Rhea, Dione, and Mimas were imaged by Voyager 1 at resolutions sufficent to allow detailed crater counts of at least portions of their surfaces. Each of the bodies exhibits surfaces with a range of crater densities and all have evolved to some degree beyond thier original accretionary state (Smith et al.,1981). This was unexpected in light of their small mass and low density.

Rhea, for which the highest resolution coverage is available, can be generally characterized as a heavily cratered surface. There are, however, significant variations in the density of 10 km and larger diameter craters. These variations are most clearly seen in the north polar area and on the equator. Rhea's north pole can be divided into two regions along the $0^{o}$ longitude line. To the west, craters in the 40 to 130 km diameter range are common, while to the east, craters larger than 30 km are absent. Despite the disparity in the distribution of large craters, both areas have similar 10 km densities of approximately 1100-1300. Some process appears to have resurfaced the eastern area removing all of the craters, while to the west only the small and intermediate craters were removed, leaving the largest degraded but still visible. On the equator at $0^{o}$ longitude a broad blanket of unknown origin, is observed which has greatly reduced the local relief. Small and intermediate sized craters are completely buried while the largest are subdued. Crater densities, at 10 km, within the blanketed area are 160±45, while outside they range from 600 to 1300. These variations indicate that different sections of Rhea have been resurfaced to various degrees over its history. While the blanketed area is relatively young, most of the surface probably dates back to the post-accretion heavy bombardment (4.0 b.y.). Since a large fraction of Rhea was imaged it was possible to test if the gradient in crater density from apex to antapex of motion, as proposed by Shoemaker and Wolfe (1981), occurs. The data cover an angular distance of 30 - 120 degrees and within that zone no systematic trend, consistent with the theoretical distribution, was observed. As the theoretical basis for the gradient appears sound, its absence implies that the satellite has not remained tidally locked over most of its early history. Preliminary calculations indicate that relatively small impacts could impart sufficent energy to break the tidal lock.

The surface of Mimas exhibits variations in crater density despite its heavily cratered nature. The variations are particularly striking in the distribution, or absence, of craters larger than 30 km diameter. The area west of the giant crater Herschel exhibits numerous craters larger than 30 km and has a 30 km crater density of 300±50 with a projected 10 km crater

density in excess of 7000. The south polar area, by comparison, lacks any craters larger than about 25 km. Here the 10 km crater density is approximately 1400 and by extrapolation the 30 km density is about 100. Between the two is a transitional area with an inflection in the cumulative frequency distribution characteristic of resurfacing events on terrestrial planets. The south pole of Mimas apparently underwent some process which removed all of the large craters, and presumably the smaller ones as well. That process was less effective at greater distances such as near Herschel the large craters remained untouched with the area subsequently recratered. The high crater densities suggest all of the surface of Mimas dates back to the heavy bombardment period. The predicted gradient in crater densities from apex to anatapex (Shoemaker and Wolfe, 1981) was not observed on Mimas, although the range of angular distances was limited to 60-130°. The cause appears to be the same as for Rhea, repeated tidal unlocking.

Dione exhibits a large range of crater densities and a variety of terrain types. Surface morphology ranging from rough heavily cratered "highlands" to smooth, lightly cratered plains are observed. The more heavily cratered parts of Dione have 30 km crater densities of 100 or greater with projected 10 km densities of approximately 1500. The plains units by comparison have 10 km crater densities of 260±50 for the younger plains, and 750±100 for the more moderately cratered plains. Both plains units lack craters larger than 30 km. Clearly the heavily cratered areas date to the heavy bombardment period. The younger plains units are probably on the order of 3 to 4 b.y. old. The different crater densities on the plains units suggest that they were formed over a period of time and not during a single episode. Dione therefore appears to have had internal activity for some period of time beyond its formation.

One of the co-orbitals, 1980S3, was imaged at a resolution sufficent to allow crater counts to be made on part of its surface. The data indicate a 10 km crater density of 1450±600. All but two of the observed craters were less than 11 km in diameter.

REFERENCES:

Shoemaker E., and Wolfe R., 1981,in The Satellites of Jupiter (ed. D. Morrison, Univ. of Arizona Press) in press.

Smith et al., 1981, Science, v. 212, p.163-191.

CRATER DENSITIES OF THE SATURN SATELLITES; ENCELADUS, IAPETUS, AND TETHYS. J.B. PLESCIA, Jet Propulsion Laboratory, California Institute of Technology, Pasadena CA 91103 and J.M. BOYCE, NASA Headquaters, Washington, D.C. 20546.

The Voyager 2 encounter with the Saturn system provided high resolution views of three satellites not observed at close range by Voyager 1; Enceladus, Iapetus and Tethys.

Enceladus, perhaps the most unusual planetary satellite thus far observed, exhibits distinct terrain types and large variations in crater density. The highest resolution (2.0 km/lp) images viewed the trailing hemisphere (longitude 280°) at mid-northern latitudes (30°) and showed a remarkable scene. Four terrain types were observed: 1. smooth plains, 2. fractured plains, 3. grooved terrain, and 4. cratered terrain. The smooth plains exhibit neither craters nor structure and appear to be only slightly modified by albedo markings. The fractured plains are characterized by set of linear fractures intersecting at angles close to 90° which cut an otherwise lightly cratered surface. These plains exhibit few craters and have a 10 km crater density of approximately 330. A narrow band of grooved terrain, several tens of kilometers wide, extends across the surface from near the north pole, where it pinches out, toward the limb where it appears to terminate. As the name implies the region is characterized by a series of parallel curvilinear ridges and troughs, similar in appearance to the grooved terrain on Ganymede. Passey (1981, personal communication) has estimated the maximum relief across the ridges to be on the order of a few kilometers. No craters have been observed on this surface. The grooved terrain appears to have formed at the expense of older terrain which it cuts. Finally, cratered terrain covers a large fraction of the area and is divisable into two regions based on crater density, one highly cratered and the second only moderately cratered. The more heavily cratered parts have 10 km crater densities of approximately 850±250, while the more moderately cratered areas have densities near 400±200, with no distinct boundary between the two areas. A further subdivision of the heavily cratered regions is possible based on crater morphology. Craters in the size range 10-20 km in some areas are well preserved with clear distinct rims, while in others they are greatly subdued and flattened, apparently the result of topographic relaxation. Craters larger than approximatley 20 km are totally absent from the area viewed by Voyager 2. The most heavily cratered terrain probably represents a surface which dates back to the end of the heavy bombardment (3.7 b.y. ?) with the moderately cratered regions slightly younger, perhaps 3.5 b.y. The most heavily cratered areas have crater densities similar to the moderately cratered plains seen on Dione. The crater density of the moderately cratered regions of Enceladus are similar to the lightly cratered Dione plains. The lack of craters on the smooth and grooved regions argue for their youth. Based on estimates of the crater

production rates in the Saturnian system by Shoemaker and Wolfe (1981), a maximum age of only $10^8$ years is indicated for those surfaces. If the flux is higher than present estimations, those ages could be considerably reduced. Enceladus appears to have undergone the most extensive and long lived resurfacing of any of the outer planet satellites, with the exception of Io and Europa. The most likely mechanism to drive that evolution is tidal heating caused by a forced eccentricity with Dione (Yoder, 1979).

Iapetus was imaged at resolutions (17 km/lp) approximately an order of magnitude lower than that at which Enceladus was seen. While the resolution was low, several general comments regarding the crater densities and age of Iapetus can be made. The bright terrain is heavily cratered with craters well over 100 km diameter being observed. Minor albedo variations and dark floored craters characterize the bright terrain. Several large craters were observed in the boundary regions between the bright and dark areas. Only in the edges of the dark terrain were craters noted. Well inside the dark terrain no surfical markings of any kind were noted. This lack of detection might result from either a true absence of topography or albedo variations or from exposures which were too short to observe any such features. Which of the two possibilities is the case is unclear at present. Crater densities on the bright terrain indicate an old heavily cratered surface, with 30 km densities of approximately 200, and projected 10 km densities of 3000 - 4000. These densities are similar to the most heavily cratered terrain on Dione and are considerably higher than observed on any of the other satellites. Such densities indicate a surface whose age is > 4.0 b.y. The observation of craters over 150 km in diameter which still possess considerable relief would suggest that the crust of Iapetus has been cold and thick since formation and capable of supporting topography for a long period of time. The conclusion that the crust of at least the bright terrain is ancient and remained cold since its formation place constraints on mechanisms for the formation of the dark material by endogenic thermal processes.

Several images of Tethys were also acquired with higher resolution than that which was obtained by Voyager 1. Voyager 1 imaged the area between $30^\circ$ and $60^\circ$ longitude along the equator and revealed a very heavily cratered surface. Voyager 2 imaged the area near $330^\circ$ longitude, $20^\circ$ N latitude and observed a surface with a lower crater density. The $30^\circ$-$60^\circ$ longitude band has a 30 km crater density of 280±70 and a projected 10 km density in excess of 2500. In contrast the area near $330^\circ$ has a 30 km density of approximately 50-80 and a 10 km density of 700-900. The region imaged by Voyager 2 can be divied into at least two different terrain types. The first is a plains unit which appears to have been "flooded" such that small and intermediate craters were buried, leaving only the largest crater exposed. The second unit is a more heavily cratered area. Both have considerably fewer craters than the area imaged by Voyager 1. The large

variations in crater density indicate that Tethys haas been modified by some process after it accreted. While some evolution is indicated, it must have been short lived as the crater densities indicate a fairly ancient surface in all cases on Tethys.

REFERENCES:

Shoemaker E., and Wolfe R., 1981, Abs. Lunar and Planetary Sci. Conf. XII Supp. A, p. 1-3.

Smith et al., 1981, Science, v. 212, p. 163-191.

Yoder C.F., 1979, Nature, v. 279, p. 767-770.

# THERMAL EVOLUTION OF THE ICY SATURNIAN SATELLITES

G. Schubert and K. Ellsworth, Dept. of Earth & Space Sciences, University of California, Los Angeles, Calif. 90024.

The heavily cratered, relatively undeformed surfaces of Tethys and Mimas and the resurfaced, fractured and relaxed surfaces of Dione and Rhea (1,2) suggest that Tethys and Mimas have been less internally active than Dione and Rhea. Previous models of these four satellites assume that their ice-silicate interiors are completely differentiated due to radiogenic or accretional heating (3,4,5). However these models do not allow for the cooling effect of subsolidus convection beneath a thickening lithosphere or the distribution and retention of accretional energy. Studies of the Galilean satellites which do account for these processes suggest that radiogenic heating will not melt the ice in the ice-rich Saturnian satellites and that accretional heating can only differentiate their outer regions (6,7). We report here the results of thermal history calculations for Tethys, Mimas, Dione and Rhea. Our models simulate accretional heating, radiogenic heating, conductive and convective heat transfer, and lithospheric growth. Our main interest is in determining if the internal thermal states predicted by the models of these satellites are consistent with the contrasting appearances of their surfaces.

We adopt the simple analytic model of parameterized subsolidus convection as developed by Schubert et al. (8) with some modifications to suit the circumstances of the Saturnian satellites. We assume spherical geometry and chondritic heat sources for the silicate fraction. We also assume that the average heat flux into and out of a vigorously convecting region can be estimated from its temperature. However, these icy satellites, unlike the terrestrial planets, start with conductive thermal regimes which later can become unstable to convection. We use the parameterized convection model even when convection is weak. The thicknesses of the lithosphere and the convecting region are allowed to change with time. The time-dependent spherically symmetric heat conduction problem with heat sources, always applicable in the lithosphere, is solved using an implicit Crank-Nicholson finite difference scheme.

To start the thermal history calculations, we use a simple accretional temperature model in which a fraction of the impacting planetesimal kinetic energy is spread uniformly over the instantaneous surface of the accreting satellite (9). Assuming all four satellites formed at the same time, we estimate the range of the ambient temperature during formation $T_e$ for Tethys, Dione and Rhea by

$$T_e = T_{Mimas} \, (R_m/R_s)^n \quad , \qquad (1)$$

where $R_m$ is the orbital radius of Mimas, $R_s$ is the orbital radius of the other satellite, n varies from 0.5 to 1.0 (10,11) and $T_{Mimas}$ is the temperature at $R_m$ during the formation of all the satellites. The value of n depends on whether the Saturnian nebula is better modelled by radiative (10) or convective heat transfer (10,12).

Although the rheology of an ice-rich mixture of ice and silicate is

not well known, we use the viscosity of ice I which is proportional to the exponential of the inverse absolute temperature. The temperature dependence of the viscosity is the single most important factor controlling the thermal evolution of the satellites since it acts as a thermostat to regulate the temperature (13). A simple energy balance for the convecting region relates temporal changes in its isothermal temperature to heat flowing into and out of the region and to heat produced within it. Lithospheric growth is calculated from the difference between the heat flux leaving the convecting region and the heat flux entering the lithosphere.

The extent of melting due to accretional heating determines the initial internal structure and affects the subsequent thermal history. We estimate the zone of melting due to accretional heating by comparing the accretional temperature profile for a given satellite with its melting curve for ice I. The low densities of Mimas, Tethys, Dione and Rhea imply that they are all composed of substantial proportions of ice. Therefore we assume that the maximum ambient temperature at Mimas, the body closest to Saturn, is about 250 K during accretion and estimate the maximum ambient temperatures at Tethys, Dione and Rhea using equation (1) with $T_{Mimas} = 300$ K and $n = 0.5$. As indicated in Table 1 the extent of melting on these bodies is minimal even when the fraction h of impacting planetesimal kinetic energy retained as heat is 1. Since our simple accretional model does not take into account the effects of surface cooling on the outer layers of the satellite or the latent heat needed to melt the ice, we conclude that all four satellites are essentially homogeneous undifferentiated bodies.

We have determined the thermal histories of Mimas, Tethys, Dione and Rhea by solving the spherically symmetric heat conduction equation with internal heat sources in the conduction regions, the energy balance differential equation for the convecting mantle, and the energy balance differential equation for lithospheric growth. We use the temperature profiles determined from our simple homogeneous accretional model as initial profiles in the thermal history calculations. We assume $h = 0.4$, the value necessary to produce the anorthositic crust and KREEP (14) on the Earth's moon, and use the ambient temperatures $T_e$ for each satellite given in Table 2. These ambient temperatures are calculated from equation (1) with $T_{Mimas} = 300$ K and $n = 0.5$ as a high temperature model and $T_{Mimas} = 250$ K and $n = 1.0$ as a low temperature model. We chose the surface temperature as 80 K and the temperature defining the bottom of the lithosphere as 60% of the melting temperature of ice I. The values of the rheological constants are those of ice I and the thermal properties of the satellites are assumed to be the volumetric averages of the properties of the ice-silicate mixtures. We assume the silicate fraction has chondritic heat sources.

All four satellites convect during their thermal histories if the ambient temperature $T_e$ during formation is large enough. However, convection lasts only 100 Myr for an ambient temperature of 250 K in Mimas and 1400 Myr for an ambient temperature of 238 K in Tethys. Furthermore, if $T_e$ is 200 K for Mimas and 175 K for Tethys, convection never occurs in these bodies. When convection does occur it starts very quickly (after a few million years) and increases in vigor until it extends to the center of the satellite; after reaching a maximum intensity convection decreases monotonically with time. The much longer time to end convection in Tethys is consistent with its 19-fold larger volume. Independent of $T_e$, Mimas

and Tethys end up as cold, conductive bodies with a maximum temperature of about 100 K. Although our results do not preclude convection in Mimas and Tethys, they show that $T_e$ strongly affects the vigor, the duration and even the possibility of convection. We therefore conclude that subsolidus convection in Mimas and Tethys, if if occurred at all, was transitory and dependent on the initial conditions during the accretional process. Dione and Rhea, on the other hand, start convecting within the first few hundred million years and continue convecting until the present day even for low ambient temperatures during formation. The present day thermal state of the Dione model is independent of $T_e$, at least for $T_e$ between 235 K and 175 K; it has a lithosphere about 270 km thick and an interior temperature of about 195 K. The present day thermal state of the Rhea model is also independent of $T_e$ ($T_e$ between 178 K and 148 K); it has a lithosphere 225 km thick and an interior temperature of 200 K. Dione and Rhea are large enough and contain sufficient heat sources that their internal thermal states are almost certainly controlled by subsolidus convection. We emphasize that radiogenic and accretional heating are insufficient to differentiate Mimas, Tethys, Dione and Rhea. All these ice-rich satellites should have essentially homogeneous interiors.

References


(1) Stone, E.C. and Miner, E. (1981). Science 212, 159-163.
(2) Smith, B.A., et al. (1981). Science 212, 163-191.
(3) Lupo, M.J. and Lewis, J.S. (1979). Icarus 40, 157-170.
(4) Lupo, M.J. (1981). Icarus, submitted.
(5) Tyler, G.L., Eshleman, V.R., Anderson, J.D., Levy, G.S., Lindal, G.F., Wood, G.E., and Croft, T.A. (1981). Science 212, 201-206.
(6) Schubert, G., Stevenson, D.J., and Ellsworth, K. (1981). Icarus 41, in press.
(7) Poirier, J.P., Sotin, C., and Peyronneau, J. (1981). Nature 292, 225-227.
(8) Schubert, G., Cassen, P., and Young, R.E. (1979). Icarus 38, 192-211.
(9) Kaula, W.M. (1980). In The Continental Crust and Its Mineral Deposits (D.W. Strangway, Ed.), pp. 25-34.
(10) Pollack, J.B., Grossman, A.S., More, R., and Graboske, H.C., Jr. (1976). Icarus 29, 35-48.
(11) Lewis, J.S. (1974). Science 186, 440-443.
(12) Prentice, A.J.R. and Ter Haar, D. (1979). Nature 280, 300-302.
(13) Tozer, D.C. (1967). In The Earth's Mantle (T.F. Gaskell, Ed.), pp. 325-53.
(14) Stevenson, D.J. (1980). Nature 287, 520-521.


Table 1. Depth (km) of outer liquid water layer.

| | $T_e$(K) | h=1.0 | h ≤ 0.8 |
|---|---|---|---|
| Mimas | 250 | 0 | 0 |
| Tethys | 238 | 20 | 0 |
| Dione | 212 | 20 | 0 |
| Rhea | 178 | 90 | 0 |

Table 2. $T_e$(K) for Tethys, Dione and Rhea for different models of Saturn's Nebula

| | High $T_e$ Model | Low $T_e$ Model |
|---|---|---|
| | $T_{Mimas}$ = 300 K, n=0.5 | $T_{Mimas}$ = 250 K, n=1.0 |
| Tethys | 238 | 198 |
| Dione | 212 | 175 |
| Rhea | 178 | 148 |

VOYAGER PHOTOMETRY OF SATURN'S SATELLITES.

J. Veverka, P. Thomas, J. Gradie, Cornell University, T.V. Johnson, Jet Propulsion Laboratory, and D. Morrison, University of Hawaii.

Voyager 1 and 2 have provided a wealth of new photometric information about the surfaces of Saturn's satellites. As examples, we summarize some new data concerning Mimas, Enceladus, Hyperion, Iapetus, and Phoebe.

Mimas: Voyager 1 observations of Mimas cover phase angles from 12° to 75°. The disc-integrated phase curve (Figure 1) can be fitted by a macroscopically rough Lambert surface, which may be a fairly realistic model for this heavily cratered, icy satellite. The phase integral of Mimas is found to be 0.95 ± 0.1, the geometric albedo 0.55 ± 0.05, and the Bond albedo $\sim$ 0.5.

Enceladus: Combining the Voyager radius for Enceladus (250 km) with some published earth-based opposition magnitudes leads to uncommonly high values of the geometric albedo: 1.0 ± 0.1 for the trailing side, and 1.6 ± 0.1 for the leading side! Preliminary analysis of the Voyager observations indicates the difference in albedo of the two sides is less than 30% and that the average geometric albedo of Enceladus lies in the range 0.8-1.1. Such high values suggest that the frost which makes up the satellite's surface is not only extremely clean, but has an unusual backscattering texture.

Hyperion: The geometric albedo of this irregularly shaped object is about 0.3, considerably lower than some published values. Recent Earth-based measurements (Cruikshank and Hamilton Brown, 1982) indicate that the satellite's surface is covered with dirty water ice. Some of the contaminating darker material may have come from Phoebe (see below).

Iapetus: The average geometric albedos of the trailing and leading sides are 0.49 ± 0.05 and 0.10 ± 0.01. On the dark side, there is a gradual increase in reflectance from 0.055 near the apex, to 0.12 near the boundary with the bright hemisphere. As expected, the dark material has a lunar-like scattering law.

Phoebe: Voyager 2 observations indicate that Phoebe has a radius of about 100 km and a normal reflectance of 0.02-0.03. Thus, the surface of this retrograde satellite is dark enough to be the source of the dark material on the leading hemisphere of Iapetus. If indeed Phoebe is responsible for the two-faced nature of Iapetus, then material from Phoebe should contaminate Hyperion, perhaps accounting for the relatively low albedo of this water-ice covered satellite. The crucial test is to see whether areas on Iapetus which have reflectances similar to that of Hyperion have comparable colors.

This research was supported by NASA Grant NSG-7156.

REFERENCE:

Cruikshank, D.P., and Hamilton Brown, R. (1982). Surface composition and radius of Hyperion. Icarus, in press.

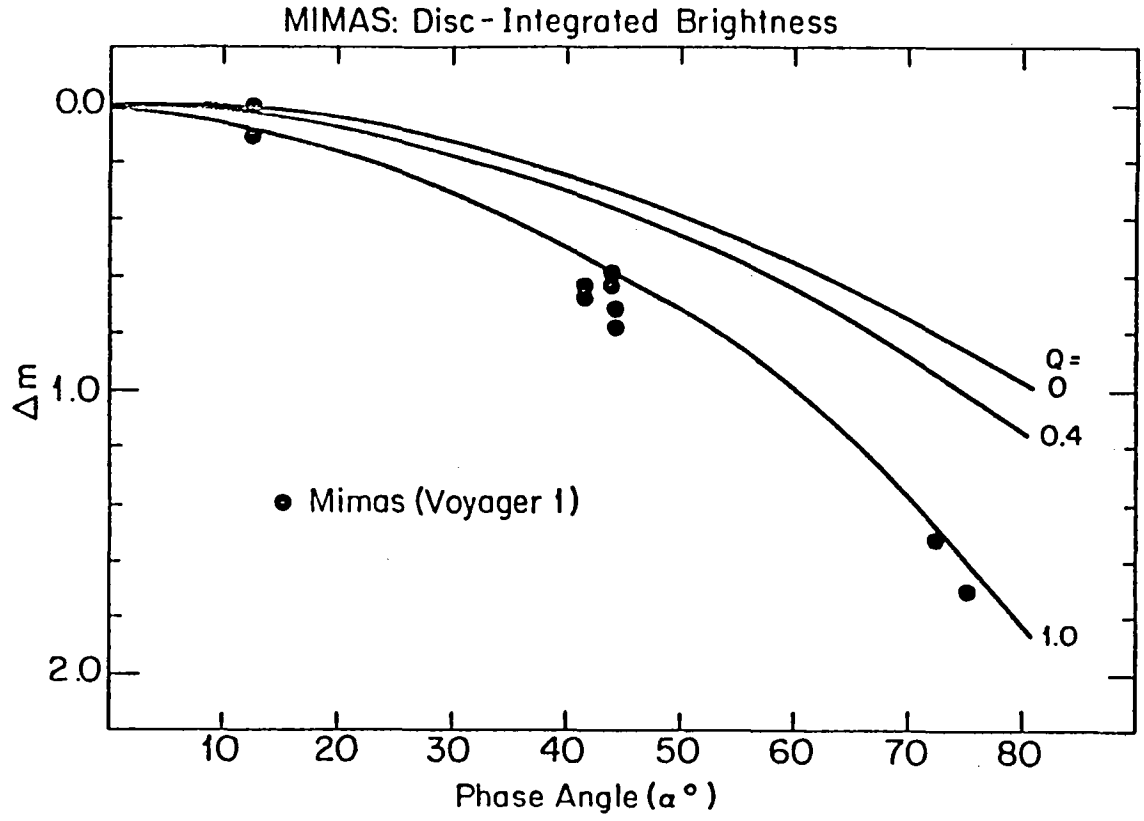


Figure 1. Disc-integrated phase curve of Saturn's satellite, Mimas, derived from Voyager 1 observations. (The vertical scale is in magnitudes relative to opposition.) A good fit is obtained by assuming a very rough Lambert surface, in which the large-scale roughness is provided by paraboloidal craters having depth to radius ratios Q ≃ 1.

# Chapter 2

# ASTEROIDS, COMETS AND GALILEAN SATELLITES

# SURVEY FOR BRIGHT MARS-CROSSING ASTEROIDS

E. M. Shoemaker, U.S.Geological Survey, Flagstaff, Arizona 86001; C. S. Shoemaker, California Institute of Technology, Pasadena, California 91125; E. F. Helin and S. J. Bus, Jet Propulsion Laboratory, Pasadena, California 91103; R.F. Wolfe, U.S. Geological Survey, Flagstaff, Arizona 86001.

A new method of search for relatively bright Mars-crossing asteroids with the Palomar 46-cm Schmidt camera was initiated in 1980. Selected fields photographed with the 46-cm Schmidt were systematically reduced for all asteroids detected on the films. The 46-cm Schmidt fields have an effective diameter of 8 3/4 degrees. Kodak IIa-D film was exposed with a yellow plexiglass filter. The films were scanned with a specially designed stereomicroscope that permits recognition of asteroids by stereopsis. Stereoscopic pairs of films were exposed with a time separation of 30 minutes; over this interval the parallax in position relative to the background stars allows easy recognition of asteroids at distances ranging from near the Earth through the main belt. Optimum exposure for each film was found to be 10 minutes on the f/2 Schmidt.

Four fields photographed at opposition in June and October, 1980 and four partly overlapping fields photographed at opposition in May, 1981 have been scanned for asteroids. Each field was photographed on several separate nights near opposition. In addition fields were photographed in the lunations preceeding and following June, 1980 and the lunation following October, in order to obtain pre- and post-opposition positions for the observed unnumbered asteroids. Pre- and post-opposition plates were taken with the Palomar 122 cm Schmidt camera to extend the observed arc for new asteroids found in May, 1981.

As of September, 1981, positions of all asteroids observed in June and October, 1980 were published in the Minor Planet Circulars, and pre- and post-opposition positions obtained for these objects had been transmitted to the Minor Planet Center. Measurement and reduction of observations in May, 1981 were still in progress. A total of 188 asteroids were observed, of which 49 were numbered and 139 were unnumbered; positions for 29 numbered and 85 unnumbered asteroids have been published. Of these, 71 unnumbered asteroids were observed on three or more nights, and 46 preliminary orbits obtained by the Minor Planet Center have been published. One month arcs were obtained for 13 new asteroids and a two month arc for one. The observed arcs for the remaining new asteroids with preliminary orbits range from 2 to 10 days. One month arcs will be obtained for a majority of the 54 new asteroids observed in May, 1981, as a result of the much fainter magnitude limit of the 122-cm Schmidt plates used for pre- and post-opposition positions.

Magnitudes of newly discovered asteroids were estimated by comparison with the predicted magnitudes for the numbered asteroids observed in each field. On average, about 7 numbered asteroids were observed per field. Magnitude limits for the films can also be assessed from the predicted magnitudes of numbered asteroids too faint to be observed. In practice, what we obtained in each case was a photographic visual magnitude, but blue magnitudes estimated by assuming an average B-V of $0^m.8$. were reported. Our mean error of estimation is approximately $0^m.5$, and estimated B was reported in

intervals of $0^m.5$. The distribution of published observed magnitudes at discovery is illustrated in Figure 1 together with the distribution of predicted magnitudes of the observed numbered asteroids. The frequency distribution of mean opposition magnitudes, B(a,0), for the observed asteroids for which orbits are available is illustrated in Figure 2. From these data, the completeness of discovery and numbering of asteroids can be readily calculated; the roll-off of completeness of numbering as a function of mean opposition magnitude is shown in Figure 3. Completeness of the numbered asteroids, as of the end of 1981, drops sharply at magnitudes fainter than B(a,0) = 15; it is about 50% at B(a,0) = 16 and about 15% or less at B(a,0) = 17. The threshold of discovery of main belt asteroids with the 46-cm Schmidt is near B(a,0) = 19.5, and an estimate of the ratio of the number of asteroids accessible for observation with this telescope to the present total of numbered asteroids can be obtained from 188/49 = 3.8. As about 2300 asteroids were numbered at the end of 1980, a total of 6500 ± 1000 unnumbered asteroids remain that are accessible for observation and discovery with the Palomar 46-cm Schmidt using the techniques that we have employed. About 3% of these undiscovered moderately bright asteroids, or roughly 200, are estimated to be shallow to intermediate depth Mars crossers.

Six of the asteroids discovered in 1980 with our new search technique are possible Mars crossers (Table 1). Because the preliminary orbits for these objects are based on very short arcs, however, further observations will be required to obtain orbits good enough to determine which objects are truly Mars-crossing. We are presently attempting to find further observations to improve the orbits of each possible Mars crosser discovered. It should be noted that the objects discovered with the 46-cm Schmidt are sufficiently bright that future observations of most of them by the international community of asteroid observers is virtually assured. The absolute blue magnitudes of the new possible Mars crossers range from 14 to 17.5; most are in the range 14 to 16.5. Opposition blue magnitudes at perihelion B(q,0), range from 14 to 17 for these asteroids; half are $15^m.5$ or brighter (Table 1).

Acknowledgments.-- We wish to thank Brian G. Marsden for invaluable help and encouragement in this work. This abstract is based, in part, on the results of one phase of research conducted at the Jet Propulsion Laboratory, California Institute of Technology, under NASA Contract NAS 7-100. The research has also been supported partly by Palomar Observatory, and by gifts to Caltech from Mr. and Mrs. William B. Hicks.

Table 1. Possible Mars-crossing asteroids discovered in 1980 with the 46-cm Schmidt camera at Palomar Mountain

| Asteroid | q* | a* | e* | i* | B(1,0) | B(a,0) | B(q,0) |
|---|---|---|---|---|---|---|---|
| 1980 LL | 1.57 | 2.16 | 0.27 | 5.0° | 14 | 16 | 14 |
| 1980 MC | 1.52 | 2.17 | 0.30 | 3.8° | 16.5 | 18.5 | 16 |
| 1980 LY | 1.78 | 2.14 | 0.17 | 4.3° | 16.5 | 18.5 | 17 |
| 1980 TM4 | 1.44 | 2.19 | 0.34 | 2.2° | 17.5 | 19.5 | 16.5 |
| 1980 TE5 | 1.69 | 2.17 | 0.22 | 8.3° | 14 | 16 | 14.5 |
| 1980 TP5 | 1.53 | 2.17 | 0.30 | 5.4° | 16 | 18 | 15.5 |

*Preliminary orbital elements based on short arcs

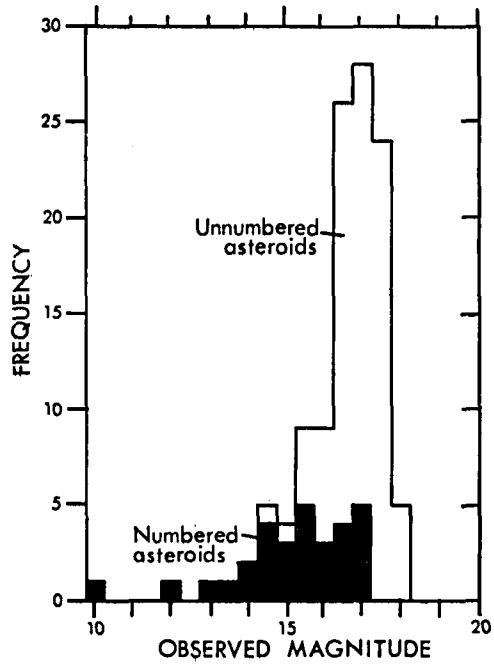


Figure 1. Frequency distribution of magnitudes of asteroids observed in June and October, 1980 with the Palomar 46-cm Schmidt camera.

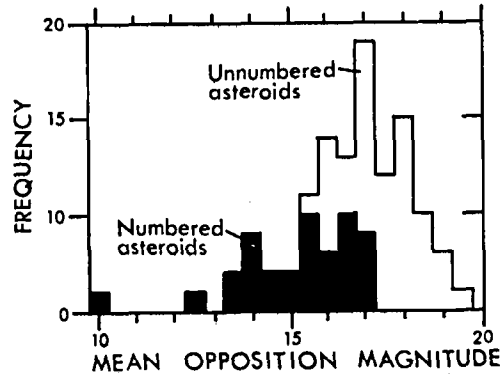


Figure 2. Frequency distribution of mean opposition magnitudes of asteroids observed in June and October, 1980 with the Palomar 46-cm Schmidt camera. Only asteroids for which orbits have been determined are shown.

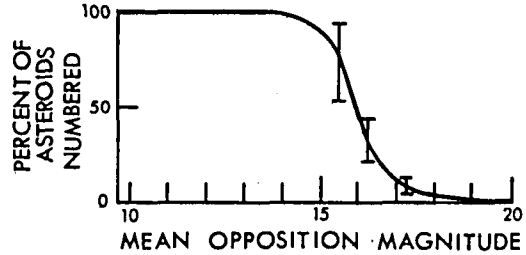


Figure 3. Estimated completeness of numbering for all asteroids as a function of mean opposition magnitude.

FORMATION AND COLLISIONAL EVOLUTION OF SMALL BODIES: EFFECTS OF TWO-MATERIAL SYSTEMS ON LARGE-SCALE GEOLOGIC STRUCTURE

Davis, Donald R., Clark R. Chapman, Richard Greenberg, Stuart J. Weidenschilling, Planetary Science Institute, Tucson, AZ, 85719

Collisional evolution studies of populations such as the asteroids generally treat the bodies as being made of a single material type (Davis et al., 1979; Dohnanyi, 1969). However, most large asteroids are either of the C-, or S-type. C asteroids are thought to be composed of a relatively weak material akin to carbonaceous chondrite meteorites, whereas S asteroids are suspected of being more like solid rock. A two-component collision evolution model allowing for different material properties of each component would be a much more realistic model for understanding the collisional and large-scale geologic evolution of the asteroids.

Other bodies in the solar system may have formed from a two-component source population. For example, the inner Saturnian satellites are thought to be made of mixtures of silicates and ices. The density differences among the satellites reflect the varying silicate/ice ratio, perhaps resulting from stochastic variations in the late-stage accretion of rocky material by these satellites (Smith et al., 1981). Weidenschilling (1981) proposed a model for the formation of silicate and icy bodies in the circumplanetary nebula about Saturn and suggested that accretion of the Saturnian satellites from such a two-component source population would result in density variations like those of the Saturnian satellites. Also, differential evolution between the two populations could result in one population dominating the final stages of satellite formation and thus being the source within the Saturnian system for cratering the satellites' surfaces.

We have developed a numerical simulation to trace the evolution of two mutually interacting populations having different material properties orbiting about a central body. While there have been detailed studies of single cratering impacts involving dissimilar target and projectile material (O'Keefe and Ahrens, 1977), our numerical simulation is the first to treat the evolution of two populations with arbitrary material properties. The simulation allows for a wide variety of outcomes and represents a significant improvement over the studies of the collisional evolution of two-component systems reported by Davis et al. (1980) which considered only catastrophic disruptions resulting from collisions. The present two-component simulation is an extension of a model previously developed to study planetary accretion (Greenberg et al., 1978), so only an overview of the basic model along with recent improvements that have been made will be given here.

The numerical simulation calculates the evolution of the size- and orbit-distribution of two materially distinct populations moving on orbits of small-to-moderate eccentricity and inclination about a central body, typically either the Sun or a planet. All interactions between bodies larger than one meter in diameter up to the largest bodies in the

population are treated. Collisional outcomes (e.g., catastrophic disruption, shattering with gravitational reaccretion, cratering, inelastic rebound, etc.) are calculated. Input parameters include the collision speed, material properties and sizes of both the projectile and target, and the partitioning of collisional kinetic energy into the ejecta fragments. Collisions are treated as randomly distributed oblique impacts rather than as only head-on impacts, as was done in earlier modes. Changes in the orbital distributions of both populations due to gravitational stirring, which tends to increase collision speeds, and collisional damping, which decreases collision speeds, are modeled. Arbitrary population size distributions, in particular populations not limited to power-law size distributions, can be treated in this simulation. The evolution of two initial populations is traced through a series of discrete steps until the desired interval has been covered. During each timestep, all interactions of each population, both with itself and the other population, are computed , and the changes in the populations' size- and orbit-distributions are recorded.

We have applied this two-component simulation to study the collisional evolution of asteroids and the formation of small satellites of Saturn. A variety of initial population distributions together with material and collisional parameters spanning the plausible ranges for each material type have been studied. We present results illustrating the effects of large differences in physical properties of the two populations on their collisional evolution.

Additional applications of this two-component simulation include studies of the collisional formation and destruction of binary and multiple asteroids (Chapman et al., 1980), the origin of S asteroids as the collisionally exposed cores of some differentiated asteroids, and the effects of changing physical parameters due to collisions on the overall evolution of the populations.

REFERENCES

Chapman, C.R., Weidenschilling, S.J., Davis, D.R., and Greenberg, R. (1980). Oblique Impacts and Asteroidal Structure. Reports on Planetary Geology Program, NASA Technical Memorandum 82385 (December), abstract, pp. 23-26.

Davis, D.R., Chapman, C.R., Greenberg, R., Weidenschilling, S.J., and Harris, A.W. (1979). Collisional Evolution of Asteroids: Populations, Rotations and Velocities. In Asteroids (T. Gehrels, Ed.), pp. 528-557, University of Arizona Press, Tucson.

Davis, D.R., Chapman, C.R., Greenberg, R., and Weidenschilling, S.J. (1980). Asteroid Collisions and Evolution. Reports of Planetary Geology Program, NASA Technical Memorandum 82385 (January, abstract, pp. 5-7.

Dohnanyi, J.S. (1969). Collisional Model of Asteroids and Their Debris. J. Geophys. Res. 74, 2531-2554.

Greenberg, R., Wacker, J., Hartmann, W.K., and Chapman, C.R. (1978). Numerical Simulation of Collisional Evolution. Icarus 35, 1-26.

O'Keefe, J.D. and Ahrens, T.J. (1977). Impact Induced Energy Partitioning, Melting, and Vaporization on Terrestrial Planets. Proc. Lunar Sci. Conf. VIII (Oxford: Pergamon Press), pp. 3357-3374.

Smith, B.A. and 26 others. (1981). Encounter with Saturn: Voyager I Imaging Results. Science 212, 163-191.

Weidenschilling, S.J. (1981). Origin of Satellite Systems. Paper presented at the NATO Advanced Study Institute, "Comparative Study of the Planets" at Vulcano, Italy, September 14-25.

# The Origin of Impacting Populations in the Inner and Outer Solar System

Robert Strom and Alex Woronow, University of Arizona, Tucson, AZ 85721

The acquisition of data on the size-frequency distribution functions of crater populations in the outer solar system, constrains the breadth of possible sources for the crater populations in both the inner and outer solar systems. One population is unique to the terrestrial planets {A}; one on some terrestrial planets {B} mimics one on the saturnian satellites {C} but is absent from the intervening jovian system; and one on some saturnian satellites {D} may be similar to that on Callisto and Ganymede {E} but is absent from the terrestrial planets. (The letters designate the corresponding curves in Figure 1.) This set of circumstances admits a limit number of possible origins of each of the populations.

Population A occurs on the heavily cratered terrains of Mercury, Moon, and Mars and is the result of the late heavy bombardment. The crater density associated with this population is nearly uniform on all of the bodies. Because it is likely that all the terrestrial planets underwent complete crustal melting well after accretion effectively ceased, these bodies could only be accretional if some long lifetime orbits were present (like those having inclinations significantly different from most of the accreted bodies). But then the uniformity of crater densities would be largely coincident. Most likely is that, as originally suggested by Wetherill, a large body entered the inner solar system, was tidally disrupted by a close approach to one of the planets, and sprayed all the terrestrial planets more or less uniformly with the debris. Origins attributed to solar system wide bodies (such as comets) fail to explain the absence of this population in the outer solar system and can be summarily rejected (see also 2).

Population B occurs only on the lunar maria and the martian northern plains. It is not observed on mercurian plains but may be unobserved there due to the ancient age of the mercurian plains rather than due to its total absence.

Two plausible sources for this late-arriving population are comets and asteroids. The fact that this population is not observed on young surfaces in the outer solar system argues against the source being as pervasive as comets. However, with the current numbers of Earth and Mars crossing asteroids, the asteroid hypothesis is tenable. This would also help in explaining why this population is not found on Mercury since the flux of such bodies would be much lower there than at the

Moon and Mars. The similarity of the density of impacts attributed to this population on both Moon and Mars must then be attributed to coincidence between the relative surface age and relative flux. But the magnitude of difficulty which this similarity presents must await more accurate assessment of the relative fluxes on the terrestrial planets from asteroids.

Population C is observed on Rhea and Tethys and has the same size-frequency distribution function as population B. Most likely population C is indigenous to the saturnian system, since it has no leading/trailing asymmetry, and fairly ancient. Resurfacing of the other satellites apparently obliterated the signature of this ancient population and allowed for the recording of population D. Population C may be the remnants of accretion modified to some undetermined degree by mutual collisions. The similarity of population C's size-frequency distribuion to that of population B may indicate a similarity in the physical processes of fragmentation and agglomeration that molded each.

Population D is found on Rhea, Dione, Tethys (overprinting the smaller diameter range of population C). Like population C, this population has no demonstrable leading/trailing asymmetry. Therefore, it too is likely to be internal to the saturnian system. Whether it is the product of distruption of a satellite which suffered a large impact or the imprint of large ring particles cannot be determined.

Population E is unique to the jovian system, but bears similarities in its size-freqeuncy distribution function to population D. The preliminary indications of a leading/trailing asymmetry in the crater population implies an origin external to the jovian system. However, a cometary origin is not likely because this population is not found in the inner solar system. Furthermore, why this population, if of extrajovian origin, is not also found on the saturnian satellites presents a considerable enigma. Given its similarities to the C population (which appears to be internal to the saturnian system), the poor coverage of the leading hemispnere of Callisto, and the uncertainy of a leading/trailing asymmetry on Ganymede, we feel that further independent crater counts on Callisto are justified to firmly establish or retute the reported asymmetry.

Although the origins of these impacting populations are still uncertain, there is strong evidence that at least four, and most likely five, different families of objects were responsible for the cratering present observed in the solar system. Obviously these distinct families cannot all have arisen from a common set of physical conditions.

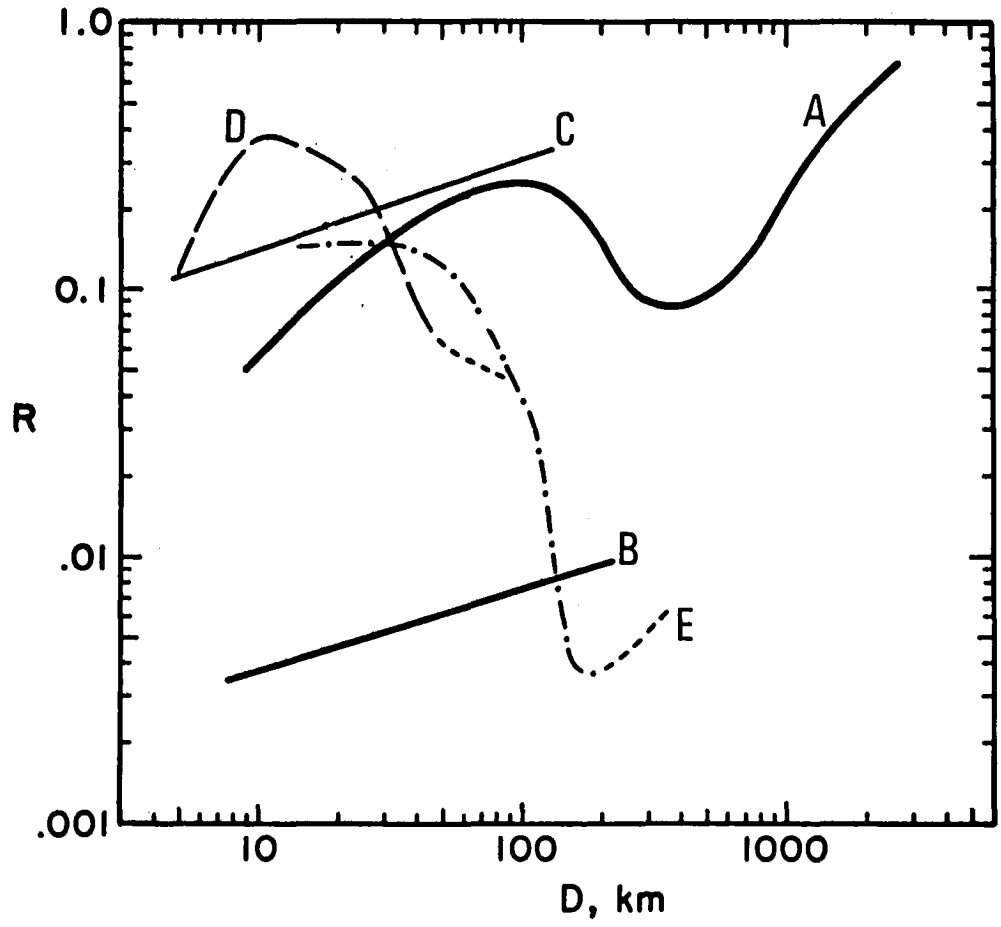
1.0
0.1
.01
.001
R
10
100
1000
D, km
A
B
C
D
E

The Consequences of Wasting by Sublimation on Comet Nuclei
Fred L. Whipple - Smithsonian Astrophysical Observatory

The present study is a computer simulated life history of typical comets. The comet nuclei are taken to be homogeneous and spherical originally, with their spin axes uniformly distributed over the celestial sphere. Wasting by sublimation is calculated on the basis of a cometary model and a fixed orbit about the Sun, both typical for short-period comets.

For reasons of economy the sublimation rate per revolution is taken to be much greater than for real comets, but the ratio of the jet forces to the rate of mass loss is kept realistic as is the lag angle for sublimation.

Because of the assumed homogenity, the nuclei remain symmetrical about their axes of rotation, i.e. figures of rotation. In cases where the wasting of material produces rotation about an axis with less than the maximum moment of inertia (rotation about the long axis) the solution becomes indeterminate. The body will shift about the axis. The calculation is then terminated.

The jet forces producing spin-axis precession and orbital period change are calculated to determine the motion of the spin-axis and the amount of orbital period change involved as 90 percent of the mass is lost. The shapes of the nuclei are calculated as a function of the remaining mass and the original spin-axis orientation with respect to the orbit.

There is some evidence from observation that the spin axes of comet may cluster more nearly parallel to their orbital major axes than is expected by chance.

The goals of the study are: 1) to determine whether such orientation of the spin axis is physically probable, 2) to ascertain the general shapes of strongly wasted comets, 3) to estimate the general nature and typical rates of spin-axis precession, 4) to determine the frequency of axis reorientation caused by rotational instability (relevant to comet bursts and splitting), and 5) to estimate the probability of large changes in period caused by nongravational forces.

CONSTRAINTS ON GALILEAN SATELITE GEOPHYSICS FROM PHOTOMETRIC AND GEOMORPHIC OBSERVATIONS

Michael C. Malin, Department of Geology, Arizona State University, Tempe, AZ 85287

Observations of surface characteristics of the Galilean satellites can be used to constrain the geophysical evolution of those bodies (e.g. Phillips and Malin, 1980). A three-way collaboration is currently in progress combining surface geomorphology (Malin, ASU), surface photometric properties (G.E. Danielson, Caltech), and geophysical models (R.J. Phillips, LPI).

Principal first-year effort as ASU and Caltech have centered on quantifying albedo and color relationships for various terrain types (e.g. "dark" rayed craters, "domes", etc.) using computational programs capable of determining the principal photometric angles for every picture element in a Voyager image. Some early results are:

1) "fresh" bright rayed craters are proportionally brighter in violet reflection than in orange reflection (bluer), relative to craters with less prominent, but still, bright rays.

2) intra-crater domes (e.g. Malin, 1981) have reflectivities similar to grooved and ridged terrain, even when within craters found in heavily cratered terrain.

3) dark moats, sometimes found surrounding bright domes in grooved and ridged terrain, show reflectivities similar to dark, cratered terrain.

The first result suggests an aging process for rays that creates a wavelength dependence on albedo. The latter two suggest that surface "composition" may not be too closely connected to subsurface "composition".

Photometry is also used in photoclinometric determinations of relief. Impact crater and dome topography have been examined using programs developed at Caltech. In addition to topographic profiles, observations that brightest slopes are "steeper" than darker slopes suggests a strongly non-Lambertian scattering law. An empirical relationship for such properties is being investigated. Multi-directional photoclinometry may also be possible, using the Caltech photometric programs and interactive image processing capabilities at ASU.

Albedo and topography from photometric studies are now being incorporated into the geophysical model computational programs at LPI. A parametric study of sensitivity to model assumptions and inputs, including thermal and rheological factors (e.g. Q, J, To), cratering flux model parameters (e.g. R, A, $\lambda$ - see Phillips and Malin, 1980), regolith thickness, surface albedo, and latitudinal distribution of these factors, will soon be completed.

References

Phillips, R.J. and M.C. Malin (1980) Ganymede: A relationship between thermal history and crater statistics. Science 210, 185-188.

Malin, M.C. (1981) Domes on Ganymede (abs.) in Reports of Planetary Geology Program - 1980 (NASA TM 82385), 67.

# THE EJECTION OF MATERIAL FROM IO

Carl B. Pilcher, Institute for Astronomy and Department of Physics and Astronomy, University of Hawaii, Honolulu

A narrow plasma source region in the Io torus has been identified in $S^+$ images acquired during the past two years. This region is $\lesssim 0.2R_J$ in radial extent and is centered at $5.6\text{-}5.7R_J$ from Jupiter, just inside of Io's orbit. The magnitude of the plasma source in this region, as determined from the brightness of $S^+$ forbidden emission (a measure of the plasma density), varies significantly on all time scales of one day or longer that can be studied from our data. There is also substantial variation of the emission intensity in this region with magnetic longitude, indicating a similar variation in the rate of ionization of neutrals ejected from Io. The reason for this region lying inside--rather than at--Io's orbit has not yet been determined, but may be related to the directions and velocities of ejection of neutral sulfur and sulfur-bearing compounds from Io. The temporal variability of the intensity of the source region indicates a variability either in the neutral sulfur density or in the ionization rate, either of which can likely be traced to variations in the rate at which material is ejected from Io. However, a better characterization of this temporal variability and considerable additional theoretical development will be necessary before the nature of this relationship can be defined.

Our analysis of images showing directional features that we discovered in the sodium cloud is still in progress. Conducted in collaboration with W. H. Smith of AER, Inc., this analysis supports our original conclusions that the features do not lie in the Galilean satellite plane and that relatively high ($\lesssim$ 10 km/sec) ejection velocities are required. We are trying to distinguish between two possible formation mechanisms: directional ejection of sodium directly from Io's surface and collisional sweeping of atmospheric and extended cloud sodium by the corotating heavy ion plasma. The mechanism by which sweeping would impart a substantial out-of-plane velocity component to the sodium is not understood.

# VARIABLE FEATURES ON IO

Richard J. Terrile and Torrence V. Johnson, Jet Propulsion Laboratory, California Institute of Technology, Pasadena, CA 91109, Laurence A. Soderblom, U. S. Geological Survey, Flagstaff, AZ 86001 and Robert G. Strom, University of Arizona, Tucson, AZ 85721.

The Voyager 1 and 2 encounters with the Jupiter system have revealed planetary scale active volcanism on Io (Smith et al. 1979a and 1979b). The several days during each encounter when resolutions exceeded about 50 km/line pair as well as the four month time interval between encounters afford an opportunity to study the variablity of various features on Io. Both short (several hours) and long (4 months) term variations can be separated into several classes of activity. These include variations in active plumes, deposits associated with plumes and in caldera and scarp deposits.

The on-off behavior of the plumes is the easiest recognizable class of variable features on Io. Voyager 1 found 9 active plumes with heights between 20 and 310 km. Eight of these sources were examined by Voyager 2 and 7 were found to be still active (Strom et al. 1980). The largest Voyager 1 plume Pele (19°S, 257°W) had turned off in the 4 months between encounters leaving behind a modification in its deposit field over an area of about 900,000 $km^2$. The plume Loki (19°N, 305°W) grew in size from about 120 km high to almost 180 km and a smaller component connected to Loki by a 250 km long dark strip also increased in height from 20 km to 35 km. In the 4 month interval new ejecta from the dark strip was deposited in an area of about 500,000 $km^2$ and partially covered older surface patterns like the dark annular feature just south of Loki (Loki Patera). North of Loki at Surt (45°N, 335°W) a circular bright deposit about 1000 km in diameter appeared between the encounters indicating the onset of a new eruption site. Aten Patera (48°S, 312°W) also erupted between encounters creating a modified area about 500 km in diameter (McEwen and Soderblom, 1981). Short time scale variations are suggested in examining Voyager 1 images of the plume Prometheus (3°S, 153°W) reprojected to the same viewing geometry. The dark arms in the plume appear to change shape and become more conspicuous.

Short time scale surface variations have also been found in the Voyager 1 images. Several areas in caldera floors and near the bases of scarps were found to show sharp contrast changes over time scales of several hours. A 30 km diameter caldera located at about 4°S, 313°W was found to increase in brightness in the ultraviolet and violet over a period of 6.4 hours with a corresponding change in solar phase angle from 10.5° to 15.3°. The ultraviolet increase is larger than can be expected for any reasonable surface phase function therefore the brightning may be caused by a change in the surface properties of the caldera floor or the eruption of a cloud of gas above the surface. Similarly, in an area just south-east of the edge of the deposit surrounding Pele, and in an area north of plume Volund (22°N, 177°W), large contrast variations are seen over time scales of

about 5.5 hours. In these particular cases, however, phase function variations will have to be examined more carefully since the phase angle changes from 2.6° to 10.5° and 14.8° to 2.5°, respectively. If these contrast changes are found to exceed the phase function variations for other regions on Io than the probable cause of the contrast change is the introduction of gas or other material over the area.

This paper represents one phase of research carried out at the Jet Propulsion Laboratory, California Institute of Technology, under contract NAS 7-100 sponsored by the National Aeronautics and Space Administration.

References:

McEwen, A. and Soderblom, L. A. (1981) "The Eruption of Aten Patera on Io." Nature, submitted.

Smith, B. A., Soderblom, L. A., Johnson, T. V., Ingersoll, A. P., Collins, S. A., Shoemaker, E. M., Hunt, G. E., Masursky, H., Carr, M. H., Davies, M. E., Cook, A. F., Boyce, J., Danielson, G. E., Owen, T., Sagan, C., Beebe, R. F., Veverka, J., Strom, R. G., McCauley, J. F., Morrison, D., Briggs, G. A. and Suomi, V. E. (1979a) "The Jupiter System Through the Eyes of Voyager 1." Science, 204, 951.

Smith, B. A., Soderblom, L. A., Beebe, R., Boyce, J., Briggs, G., Carr, M., Collins, S. A., Cook, A. F., Danielson, G. E., Davies, M. E., Hunt, G. E., Ingersoll, A., Johnson, T. V., Masursky, H., McCauley, J., Morrison, D., Owen, T., Sagan, C., Shoemaker, E. M., Strom, R., Suomi, V. E. and Veverka, J. (1979b) "The Galilean Satellites and Jupiter: Voyager 2 Imaging Science Results." Science, 206, 927.

Strom, R. G., Schneider, N. M., Terrile, R. J., Cook, A. F. and Hansen, C. (1981) "Volcanic Eruptions of Io." J. G. R., in press.

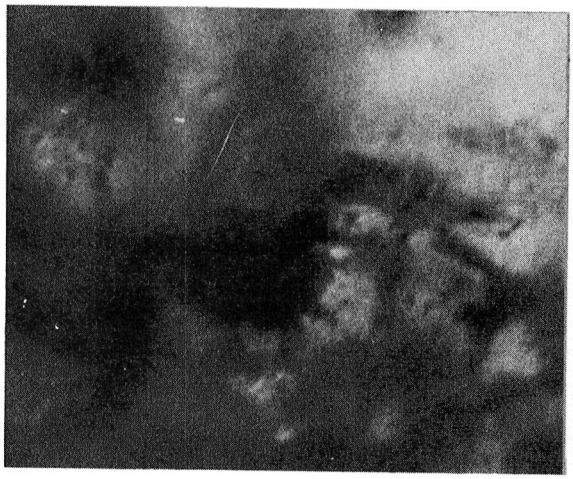

Figure 1

Figure 2

Figure 1: A geometrically reprojected Voyager 1 image of Io with a resolution of 9.1 km/line pair and a solar phase angle of 2.6°. The center of projection for this image corresponds to 17.5°S and 253°W. The area shown is south-east of the plume Pele.

Figure 2: This image corresponds to the same area as figure 1 but was recorded 5.2 hours later with a resolution of 7.0 km/line pair and a phase angle of 10.5°. Note the contrast changes between the two images.

Volcanologic Constraints on Models of Io Volcanism

L.S. Crumpler and R.G. Strom, Department of Planetary Sciences,
University of Arizona, Tucson, Arizona 85721

Several aspects of the volcanism on Io, (the volcanically active satellite of Jupiter) have been examined from a volcanological point of view. These include: the nature of eruption plume sources; the latitudinal distribution of plumes and plume deposits; the latitudinal distribution of calderas and dark calderas (hot spots or "lave lakes"); the structure of dark calderas; the thermal power output of active lava lakes with respect to the global heat budget; evaluation of a model of silicate magma-powered sulfur volcanism; and combined convective-conductive heat transfer models of the interaction of molten silicates and solid sulfur at the boundary of the silicate and sulfur crusts of Io.

Most plumes originate at "point" sources (<10km diameter exit region). Two types of plume sources are identified. Some plumes are associated with fractured and uplifted terrains with central rift-like grabens, others appear to originate at the rims of calderas. Plumes and plume deposits occur at all scales, from those several hundred kilometers across, to small (<10km) wispy patches confined to the rims of calderas. Small plume deposits occur over a broad latitudinal range from $50^{o}$N to $80^{o}$S, but big plumes and plume deposits are strongly confined to $\pm 45^{o}$ of the equator [Fig. 1], as previously noted by Strom [1].

Calderas of all types are clustered in the equatorial regions, as are the dark floored calderas [Fig. 2]. The average separation between calderas is 233$\pm$104km and the median diameter of dark calderas is 50km, in agreement with similar measurements by previous investigators [2]. If models in which volcano separation is equivalent to lithospheric thickness are tenable [3], and assuming silicate-powered volcanism on Io, then the average separation distance of calderas might imply that the lithosphere and depth of the origin of silicate magmas is on the order of 200km. This is somewhat greater than the depth to silicate melting ($\sim$30km), estimated from current models of conductive heat flow in Io due to tidal dissipation [4]. However, most of the thermal output of Io may be radiated from hotspots (dark calderas) in lieu of heat conducted through the crust, thereby driving the 1500K isotherm deeper within the planet and lowering the conductive thermal gradient.

Mapping of high reslution images of dark calderas reveals complex details on their floors [Fig. 3]. Multiple levels or terraces are common, as are subconcentric patches formed by the darkest albedo materials (lava lakes?). Typically these are arcuate patterns on the floors of the lowest levels, and are frequently situated at the contact of the outer caldera margin and the lowest floor level. Few dark calderas are uniformly dark, and even the confirmed hot spot at Loki Patera [5] can

be seen to be dotted with "islands" of higher albedo material in the highest resolution images. Major changes in the map plan of the darkest deposits at Loki Patera between the periods of observation of Voyager I and Voyager II are consistent with either plume deposit mantling or lava lake solidification.

If dark calderas are hot spots relative to the background surface temperature of Io, then most of the thermal output of Io is radiated from these surfaces, not conductive, and a strong ($\pm 40^{o}$) latitudinal concentration of the power dissipation on Io is implied. Estimates of the absolute power output depend on hot spot temperatures and absolute areas of hot materials. Based on careful measurements of dark caldera areas, and assumed albedo-temperature dependence, two extreme models are used to bracket possible thermal dissipation. These end members are $10^{21}$ to $10^{22}$ ergs $sec^{-1}$, corresponding to lower temperature-large area spots and to higher temperature-small area hot spots. These are preliminary results and are subject to modification. In either case, the net radiative heat flow at the surface exceeds current conductive thermal models. Similar results have been recently derived from terrestrial observational data [6].

Two basic models of the thermal history of molten sulfur lava lakes suggest some probable lifetimes of dark calderas at the ambient surface conditions of Io. A floorless caldera would correspond to a caldera formed in a sulfur crust resting on a liquid sulfur ocean [7]. Without mechanical support, a dense solid crust will not form in this case and the lava lake is permanent. Even with some form of support (mechanical or Bingham-like viscosity) for a solidified crust on a sulfur lake, the crust is only 150m thick after 3000 years. A second model proposed here is a solid sulfur crust resting directly on a silicate "subcrust", as could be permitted in a low conductive thermal gradient model of Io. In this case, a caldera is not "bottomless", and a relatively shallow lava lake ($\sim$100m) will solidify in about 44 years. One consequence of a thin sulfur crust overlying a silicate subcrust with silicate-powered sulfur volcanism is that locally, the silicate crust could be shallow, or even exposed at the surface. This would enable some silicate volcanism to occur at the surface of Io, thereby explaining the high material strength (in other words, silicates) thought to be necessary to explain the vertical relief seen in some caldera walls [8]. However, high convective (radiant) heat flow on Io may reduce the conductive gradient to values consistent with having high vertical relief in sulfur materials, thus eliminating the need for silicates to explain these features.

Because most of the tidal dissipation may take place in the silicate portion of the planet, molten silicates could form at depth and be erupted onto the surface of the silicate subcrust; the density and shear strength contrast between the overlying sulfur crust and the silicate crust would lead to sill or laccolith-like intrusions of silicate melts at the interface of the sulfur crust and silicate subcrust. Heat

transfer between a cooling silicate magma and a superjacent sulfur crust would result in extensive melting and volatilization of sulfur with the consequence of sulfur volcanism and sulfur plumes at the surface. Previous investigators [9] have proposed that hot silicates in contact with sulfur and the consequent volatilization of the sulfur, could yield the necessary kinetics to drive the observed plumes. Thermal models developed here [Fig. 4] show that the contact between a molten silicate at 1500K and solid sulfur could rapidly equilibrate to 700 to 750K, slightly in excess of the sulfur boiling point (STP), but well below the 1500K temperature used in their kinetic models. A 100m thick sill of molten silicate is capable of generating 715K sulfur in a static contact for a period of ∿45 years; a 10m silicate sill would likewise provide 715K sulfur for ∿166 days for the boundary conditions in Figure 4. The exact number depends on the rate at which the hot sulfur is displaced to the surface. These models are also sensitive to the temperature prevailing prior to the intrusion, and hence, are dependent on the conductive heat flow assumed for Io as a whole.

Conclusions. The thermal radiative power output of Io exceeds models of tidal power input at least by a factor of 10. The observed thermal output is strongly confined to $\pm 40^{\circ}$ of the equator, as are the largest plumes and the majority of dark calderas. Plumes originate in many cases from the margins of calderas, and the interiors of dark calderas show complex structure possibly related to cooling, fracturing, and continuous reemplacement of molten sulfur. Thermal models of molten silicate-powered sulfur volcanism suggest that vaporized sulfur plumes may be driven by simple silicate-sulfur thermal interactions for months to years, consistent with observed lifetimes of plumes from Voyager results.


[1] Strom, R.G., R.J. Terrile, H. Masursky and C. Hansen, 1979, Nature, 280, 733-736.
[2] Masursky, H., G.G. Schaber, L-A. Soderblom, and R.G. Strom, 1979, Nature, 280, 725-729.
[3] Vogt, P.R., 1974 Earth Planet. Sci. Lett., 23, 337-348.
[4] Peale, S.J., P. Cassen, and R.T. Reynolds, 1979, Science 203, 892-894.
[5] Hanel, R., et al, 1979, Science 204, 972-976.
[6] Matson, D.L., G.A. Ransford, and T.V. Jonnson, 1981, Jour. Geophys. Res., 86, 1664-1672.
[7] Smith, B.A., E.M. Shoemaker, S.W. Keiffer, and A.F. Cook II, 1979, Nature, 280, 738-743.
[8] Clow, G.D., and M.H. Carr, 1980, Icarus 44, 268-279.
[9] Reynolds, R.T., S.J. Peale, and P. Cassen, 1981 (manuscript submitted to proceedings, NASA Conf. on Galilean Satellites).

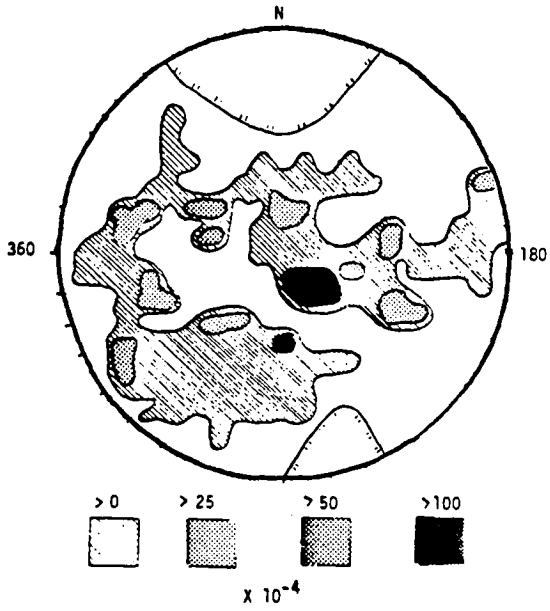


Figure 1. Distribution and frequency of plumes and plume deposits weighted by size (total plume size in fraction of planet area per 2 X $10^5$ $km^2$). The largest plumes are concentrated within ±40° latitude of the equator. Equal area projection of Io from longitude 180° to 360°.

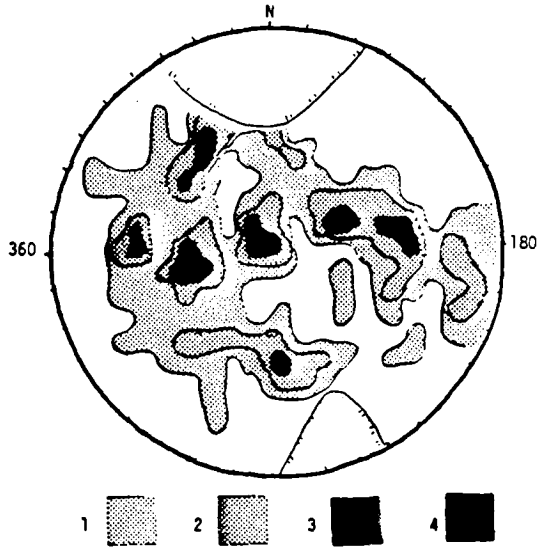


Figure 2. Distribution and frequency of dark calderas (number per 2.5 X $10^5$ $km^2$). The majority of dark calderas are concentrated in equatorial regions.

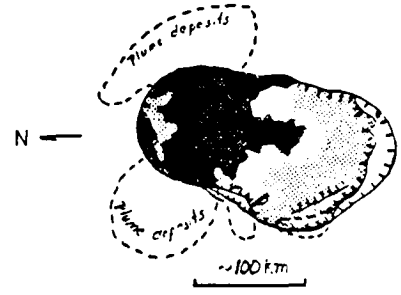


Figure 3. Complex structure of a dark caldera, Creidne Patera. Note that the small plumes are associated with the contact of the lowest albedo materials and the peripheral caldera wall. Frame 145J1.

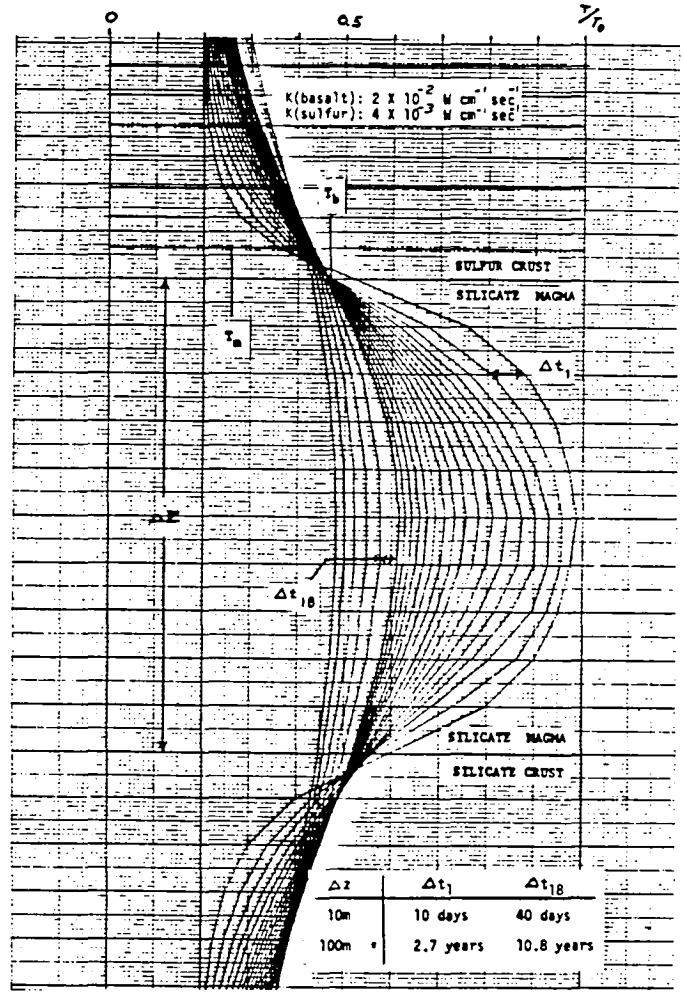


Figure 4. Thermal model of silicate magma sill intruded at the sulfur crust-silicate crust interface. The upper contact is maintained at 715 K by convection until the residual heat in the silicate magma dissipates.

## IO: COOLING MODELS FOR SULFUR FLOWS

*J. Fink, Department of Geology, Arizona State University, Tempe, Arizona 85287, S. Park, Department of Aerospace Engineering, Iowa State University, Ames, Iowa 50010, R. Greeley, Department of Geology, Arizona State University, Tempe, Arizona 85287*

In contrast to molten silicates, liquid sulfur undergoes a decrease in viscosity as it cools through the temperature range 185°C to 160°C. This rheological anomaly may lead to morphologic differences between silicate and sulfur flows that might be detectable on images of Io. In order to determine this effect, we have analyzed the cooling of a flow of liquid sulfur considering both upward radiation and downward conduction in the environment Io. Our analysis considers a balance between heat convected into a given flow cross section by the moving sulfur and the heat lost by conduction, radiation and convection. The analysis is modified from that of Harrison and Rooth (1976) for silicate lava flows and does not directly incorporate the effects of changing rheological and thermal properties of sulfur during cooling. The parameters which can be varied are emplacement temperature ($T_i$), underlying surface temperature ($T_s$), external or ambient termperature ($T_e$), sulfur emissivity (e), coefficient of thermal diffusivity ($a$), thermal specific heat ($C_p$), conductivity (k), and flow thickness (h).

The following discussion is based on calculations using the following values: $T_i$ = 250°C (523 K), $T_s$ = -158°C (115 K), $T_e$ = -258°C (15 K), e = 0.2, $a = 10^{-3}$ cm$^2$/sec, k = 2 x $10^{-3}$ cal/cm-sec-°C, $C_p$ = 0.2 cal/gm-°C and h = 1.0 meter. Temperature profiles are calculated at selected time intervals (Fig. 1a) and these values are then used to compute viscosity profiles (Fig. 1c), assuming that viscosity varies with temperature as shown in Fig. 1b. Whereas a basalt flow would show a steady increase in viscosity with time at both the upper and lower contacts, evolution of the sulfur flow is more complicated. The assumed emplacement temperature of 250°C is above the point of rapid viscosity change (~160°C) so the sulfur viscosity increases initially as the flow cools from both surfaces. Thus as 2.3, 4.6 and 9.3 hours, high viscosity layers developed near the top and base of the flow. Below the lower viscous zone, however, is a thin zone of *low* viscosity fluid, corresponding to the temperature range between 160°C and the melting point (119°C). A similar liquid layer develops at the upper surface after 13.9 hours. At the same time the interior attains its maximum viscosity. Thus, from about 13 to 21 hours the flow consists of an interior viscous plug surrounded by more fluid zones above and below, as well as an underlying solid crust at the base. At about 24 hours the viscous plug has disappeared (as all of the sulfur has dropped below 160°C) and the flow now behaves like a cooling silicate liquid, developing a solid crust on the top, as well as having its basal crust increase in thickness. The flow would freeze entirely within about 34 hours.

Because the entire flow eventually undergoes a 'normal' cooling sequence, it is not clear whether the viscosity changes described above would have morphologic consequences. However, the cooling history predicted here may account for the 'fluid run-outs' observed in laboratory experiments (Greeley et al., 1981). Moreover, the analysis has implications for scale modeling of sulfur flows. Calculations for thin flows of sulfur, as in laboratory experiments (Greeley et al., 1981) show that cooling would be dominated by downward conduction. In order to simulate Ionian flows which may be several meters or more thick and where radiation plays an important role, laboratory flows must be at least several centimeters thick. Thicker flows would also minimize the influence of surface tension, as would higher flow veolicites and/or steeper slopes. Future work will involve numerical modeling of thicker flows to take these parameters into account.

## REFERENCES

*R. Greeley, J. Fink, and S. Park, 1981. Laboratory Modeling of Sulfur Flows on Io (this volume).*
*Harrison and Rooth, 1976. 'The Dynamics of Flowing Lavas' in Volcanoes and Tectosphere, Aoki (editor), Tokai Univ. Press, Japan*

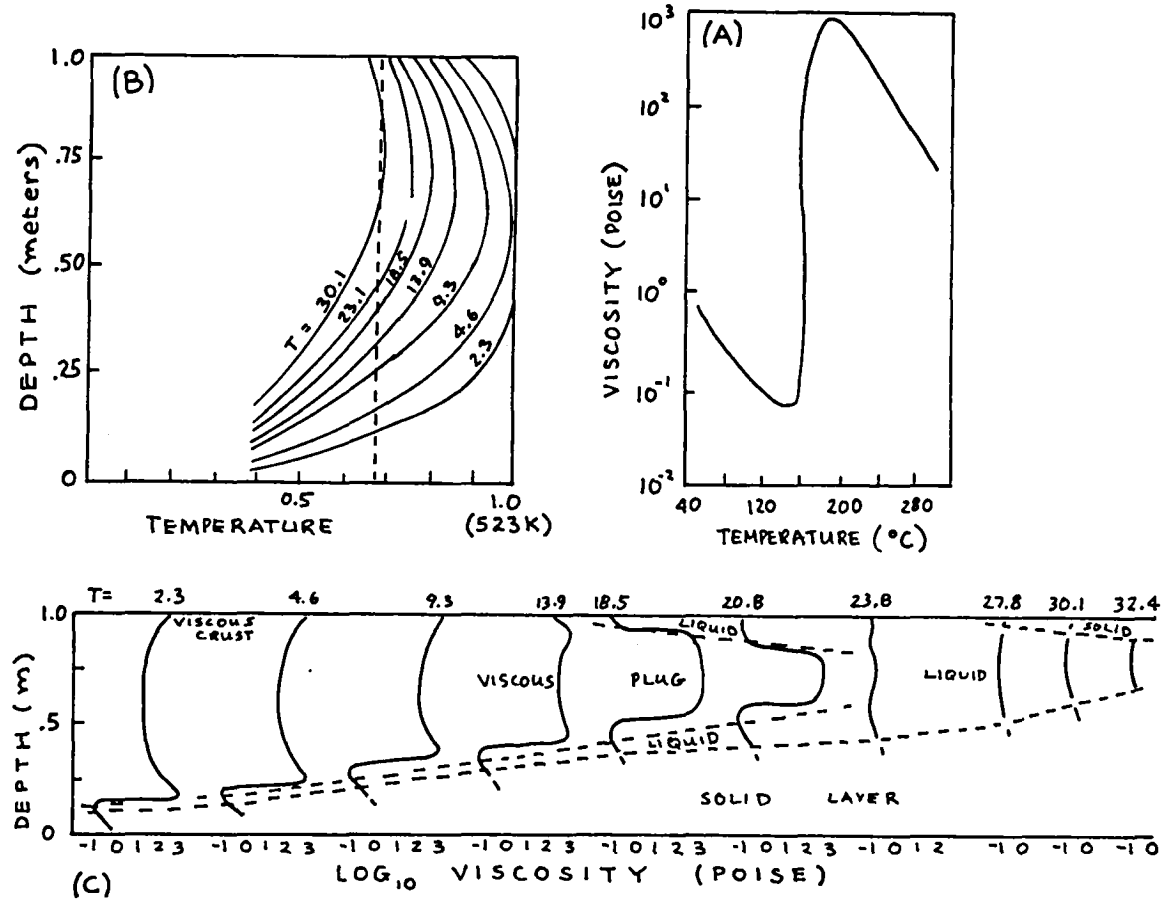


*FIGURE 1* *(a): Viscosity-temperature curve for sulfur showing the unusual decrease in viscosity with temperature decrease in the range 185°C to 160°C,*

*(b): Series of temperature profiles for a one inch thick sulfur flow, for times up to about 30 hours,*

*(c): Viscosity profiles containing the data of figures a and b showing the development of a viscous plug, and the 'liquid run-out' stage at about t (time) = 23 hours.*

## LABORATORY MODELING OF SULFUR FLOWS ON IO

*R. Greeley and J. Fink, Department of Geology, Arizona State University, Tempe, Arizona 85287, S. Park, Department of Aerospace Engineering, Iowa State University, Ames, Iowa 50010*

Voyager images of Io reveal abundant features resembling volcanic edifices, including caldera-like features and radial flows (Schaber, 1980). Spectral data suggest that many of the flows are composed of sulfur or simple sulfur compounds (Sagan, 1979). However, estimates of the vertical relief measured for scarps on some of the volcanoes yield values too high to be self-supporting if the material is sulfur, and it has been suggested that the volcanic material is predominantly of silicate compositions (Clow and Carr, 1981). Because the rheological behavior of sulfur is different from silicate lavas (Fink et al., 1981), the morphology of the flows as observed in images may provide clues to their composition. Most Newtonian fluids, including molten silicates above the liquidus temperature, exhibit a decrease in viscosity with heating. In contrast, sulfur shows a viscosity increase of four orders of magnitude as its temperature increases from 160°C to 200°C. Below 160°C and above about 200°C the rheology is more 'typical', decreasing about one order of magnitude for every 60°C drop in temperature. This unusual rheology should be reflected in the morphology of sulfur flows and volcanic constructs. In order to investigate this phenomenon we have begun a series of controlled laboratory experiments in which sulfur is extruded at a fixed temperature and known volume rate of flow onto a table of known slope.

In the experiments, powdered sulfur is heated to a temperature between 180°C and 240°C (depending on the run) in a cylindrical reservoir connected by insulated Pyrex tubing to a hole near one end of an asbestos board. Temperature is monitored continuously at five locations along the path of the sulfur. When the sulfur is equilibrated to the desired temperature it is allowed to flow onto the table, driven by gravity. The volume flow rate decreases as the level of sulfur in the reservoir dropped. The initial flow rate is varied by changing the length of the connecting tube and the height of the reservoir above the table. All runs were recorded on videotape and photographic film. During the runs the velocities of individual flow lobes were monitored and after the run dimensions of flows and vent structures were measured.

### Results

Sulfur extruded at a temperature above about 200°C goes through progressions of both color and morphology with cooling. Initially, sulfur forms a dark brown to black rounded construct (ellipticity depends on the table slope) which advances slowly downslope. As it cools, the flow front begins to develop a digitate form, with small fingers that advance much faster then the main mass. As they advance, these finger-like flows become more fluid and change in color from red to brownish orange to yellow. Upon solidification, the construct is multi-colored but within about 10 minutes all the sulfur reverts to yellow. The final construct usually consists of a near-vent, subcircular to elliptical pond of liquid sulfur enclosed by a 2 to 5 mm high rim; this broader section divides downslope into a series of longer parallel flows. On low slopes ($< 1$ degree) circular flows form which lack digitate portions.

Qualitively, some constructs on Io resemble the two-component form of the laboratory experiments. Figure 1 shows two examples on Io that consist of edifices with digitate, irregular flows apparently extruded from the edifice margin. This could be interpreted as representing 'fluid outflows' of sulfur as the viscosity decreased upon cooling, comparable to the

morphology observed in the experiments.

The lack of topographic data on Io makes quantitative morphologic comparisons of volcanic features with their terrestrial or laboratory counterparts difficult. However, certain slope-dependent ratios of morphologic features may be independent of scale and hence may be comparable. In our experiments we determined the ratio of the diameter of the subcircular, near-vent features to the length of the longest flows in a given sulfur flow. Values range from 1.0 for low extrusion rates and low surface slopes up to about 5.0 for higher flow rates and slopes, or for lower extrusion temperatures. Similar ratios are obtained on Io, with values ranging from about 1.0 for Apis Tholus and Inachus Tholus, to about 3.5 for Ra Patera. Determination of these ratios is complicated by difficulties in distinguishing flow boundaries on Voyager images. Flows that are prominent when freshly extruded may become camouflaged as their colors change during cooling.

Theoretical modeling (Fink et al., 1981) indicates that cooling mechanisms differ in thin and thick flows. Hence, in order to model Ionian flows more than a few meters in thickness, we need laboratory flows at least several centimeters thick. Such flows require extrusion rates higher than we have so far attained. Ongoing experiments include a larger range of extrusion temperatures and flow rates which, in conjunction with theoretical modeling, should allow us to correlate changes in flow morphology with slope, extrusion rate and flow temperature.

**REFERENCES**

*G.D. Clow and M.H. Carr (1980). Stability of Sulfur Slopes on Io, Icarus, Vol 43.*

*J. Fink, S. Park, and R. Greeley (1981). Io: Cooling Models for Sulfur Flows (this volume).*

*C. Sagan (1979). Sulfur Flows on Io, Nature, Vol 280, p. 750-753.*

*G.G. Schaber (1980). The Surface of Io: Geologic Units, Morphology and Tectonics, Icarus, Vol 43, p. 302-333.*

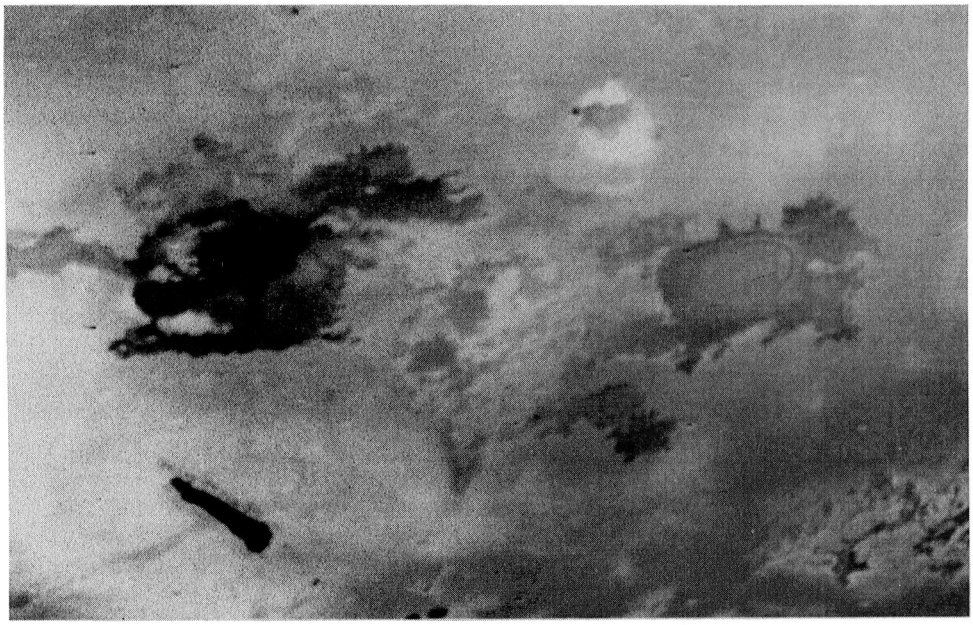

*FIGURE 1a. Part of Voyager image showing two volcanic features on Io; both are characterized by having regular, rounded, low-profile, central edifices surrounded by irregular, digitate flows. This morphology may represent transition of viscosity in sulfur flows upon cooling, similar to that observed in the laboratory experiments (Voyager 1 frame 1783J1).*

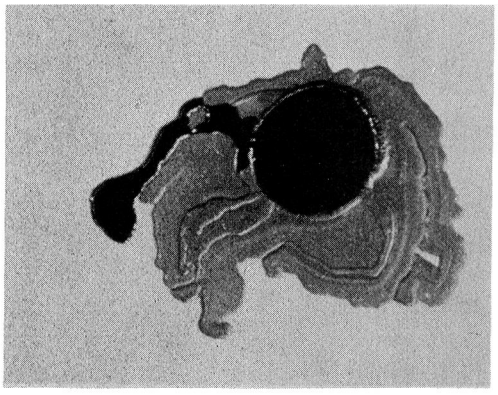

*FIGURE 1b. Vertical view of laboratory experiment in which molten sulfur was extruded at a temperature of 210°C on a flat surface sloping 0.5°; at this eruption temperature, the sulfur formed a relatively viscous, rounded mass over the vent. As parts of the mass cooled, the viscosity decreased, resulting in 'fluid outflows' to form digitate flows (Run 13; area of photograph is about 1 m by .8 m).*

## Geomorphology of Ra Patera Io: A Quantitative Approach to Sulfur Volcanism

D.C. Pieri, Jet Propulsion Laboratory, Pasadena, CA 91109; S.M. Baloga, U.S. National Bureau of Standards, Gaithersburg, MD 21754; R.M. Nelson, Jet Propulsion Laboratory, Pasadena, CA 91109; C. Sagan, Cornell University, Ithaca, NY 14853

The hypothesis of sulfur volcanism on Io has been advanced by many authors (e.g. Sagan, 1979) on the basis of several lines of evidence including spectral and photographic observations. Decalibrated Voyager broad-band imaging data are available for limited areas on Io, including good high resolution pictures of Ra Patera. This feature is a well-expressed extrusive complex with multiple red and orange variegated flows radiating from a central caldera about 40 km in diameter. Associated digitate flows range in length from less than 10 km to the so-called Main Flow which is over 250 km in length and terminates as a pool of low viscosity (~ 10 cp) orange sulfur (e.g. Pieri et al., 1981; Baloga et al., 1981). Widths of individual flows range from about the limit of resolution to 25 km. Other broadly lobate flows are also associated with this feature and may be evidence of relatively low temperature (~ 125° C) and low viscosity orange sulfur eruptions.

In order to test the sulfur volcanism hypothesis we have taken a multi-pronged approach including theoretical modelling, laboratory analysis of spectral and physical properties, and photogeologic interpretation. Ra Patera is just one of many well-defined volcanic constructs, but is particularly useful to us at present because of the comprehensive data set available for its study, thus we have concentrated on it.

Sulfur behaves in a way anomalous when compared to typical silicate lavas, in that its viscosity decreases drastically upon cooling below about 165° C (e.g. Sagan, 1979). Because of this we have tried to formulate a physical model for sulfur lavas which can help reduce the flow characteristics associated with sulfur volcanism over a range of relevant environmental parameters. Currently, we have developed thermal models of several levels of complexity and will next pursue a kinematic formulation to fold in both heat-loss processes and temperature dependent viscosity. This will be sufficiently general so as to be applied to both sulfur and silicate lavas on a range of planetary bodies.

For our current model we ignore many candidate thermal loss processes and assume a governing equation of the form

$$\frac{\partial T}{\partial x} + \frac{\partial T}{\partial t} = D \frac{\partial^2 T}{\partial x^2} - \lambda T^4 = g\,(x_t,\, x)(T_A - T) \qquad (1)$$

where T is the initial dimensionless temperature, x the downflow distance, $x_t$ is the total flow length, t is time, D is the appropriate thermal diffusivity, $\lambda$ is dimensionless parameter defined below, g ($x_t$, x) a conductive loss function, and $T_A$ the initial temperature of the substrate. The first term on the right-hand side of equation (1) evaluates the diffusion of heat from the hot caldera to the cool toe of the moving flow, the second term represents radiative heat losses and the last term, conductive heat loss into the substrate at the distal end of the flow. The simplest case assumes D = 0 and g ($x_t$, x) = 0, with radiation losses dominating. The solution to that simple equation is of the form

$$T_{RAD}\ (x) = (1 + 3\lambda)^{-1/3} \tag{2}$$

assuming a stable initial eruption temperature ($\frac{\partial T}{\partial t} = 0$) and uniform flow velocity and thickness. Equation (2) predicts morphologic and colorimetric changes associated with allotropic transitions to within about ± 15%. Assuming that

$$g\ (x,\ x_t) = \frac{h_o}{(x_t - x)^{1/2}} \tag{3}$$

we can begin to account for heat losses into the bed at the flow front, and derive the considerably more complicated formulation

$$T\ (x,\ t) = e^{-xg}\ [1 + \frac{\lambda}{g}\ [1 - e^{-3xg}]]^{-1/3} \tag{4}$$

which we have evaluated for $T_A = 0^oK$ only as of this writing. Equation (4) has equation (2) as an upper bound, as expected, but allows a rapid decrease in flow temperature at the front as heat is lost into the thermally unsaturated bed.

Laboratory studies at JPL under this grant have involved construction of apparatus to measure the thermal spectral dependence of liquid and quenched sulfur (under vacuum), as well as other apparatus to observe and measure model flows of hot sulfur on a cryogenic bed, under vacuum. Such work is in progress.

Conclusions of this study are several, to date: (a) Color and morphologic changes in the Ra Patera Main Flow are consistent with predominantly sulfur lavas losing heat mainly by radiation with an initial eruption temperature of about 525° K (black sulfur allotrope); (b) There have been multiple flows at Ra Patera with initial eruption temperatures as low as about 400° K; (c) Assuming mainly radiative thermal losses as predicted by our model, and assuming that at least one flow like Ra Patera is always operating, we calculate that resurfacing timescales due to volcanic flows on Io, to a depth of 1 kilometer, to be about $10^5$ years, the implied

deposition rate of 1 cm per year is compared with the calculated rate for deposition of material by plumes ($10^{-4}$ cm/yr). We conclude that most of the resurfacing activity on Io, and thus the lack of observed impact craters, is due to thin (< 100 m) turbulent flows of the low viscosity orange sulfur allotrope.

Future work will involve more detailed analysis of a variety of flow features, refinements to our physical model, and further laboratory experimentation.

Baloga, S.M., D.C. Pieri, R.M. Nelson, and C. Sagan, EOS 62, p. 316.
Pieri, D.C., S.M. Baloga, R.M. Nelson, and C. Sagan, EOS 62, p. 316.
Sagan, C., 1979, Nature, 280, p. 750-755.

The research described in this abstract was carried out by the Jet Propulsion Laboratory, California Institute of Technology, under contract with the National Aeronautics and Space Administration.

VOYAGER PHOTOMETRY OF EUROPA.

B. Buratti and J. Veverka. Laboratory for Planetary Studies, Cornell University, Ithaca, New York 14853

A study of the photometric properties of Europa's surface is being carried out using Voyager images covering phase angles from 3° to 109°. There is excellent agreement between the spacecraft measurements and existing Earth-based observations which are restricted to phase angles of 12° or less (Figure 1). Europa's disk-integrated phase curve is surprisingly linear (Figure 2) and does not show the pronounced concave-up shape characteristic of darker surfaces. A few observations between phase angles of 103° and 109° permit an excellent determination of Europa's phase integral. We find $q = 1.1 \pm 0.1$, in good agreement with earlier estimates based on radiometry.

Between phase angles of 3° and 32° (where our data are most complete) we find that the phase coefficient decreases markedly with increasing wavelength. Actual values range from 0.015 mag/deg in the ultraviolet (0.34 μm) to 0.010 mag/deg in the orange (0.59 μm). These phase coefficients are steeper than those derived from past telescopic observations at phase angles between 0° and 12°.

Since the reflectance of Europa increases steeply with increasing wavelength, the marked wavelength dependence of the phase coefficients described above means there is an inverse relationship between the phase coefficient and the reflectance at a particular wavelength (Figure 3).

A lunar photometric function definitely does not fit the scattering properties of Europa's surface. For example, near opposition definite limb darkening is observed (Figure 4).

This research was supported by NASA Grant NSG-7156.

REFERENCES:

Blanco, C., and Catalano, S. (1974). On the photometric variations of the Saturn and Jupiter satellites. Astron. Astrophys. 33, 303-9.

Johnson, T.V. (1969). Albedo and spectral reflectivity of the Galilean satellites of Jupiter. Ph.D. Dissertation. California Institute of Technology, Pasadena, California.

Morrison, D., Morrison, N.D., and Lazarewicz, A. (1974). Four-color photometry of the Galilean satellites. Icarus 24, 157-71.

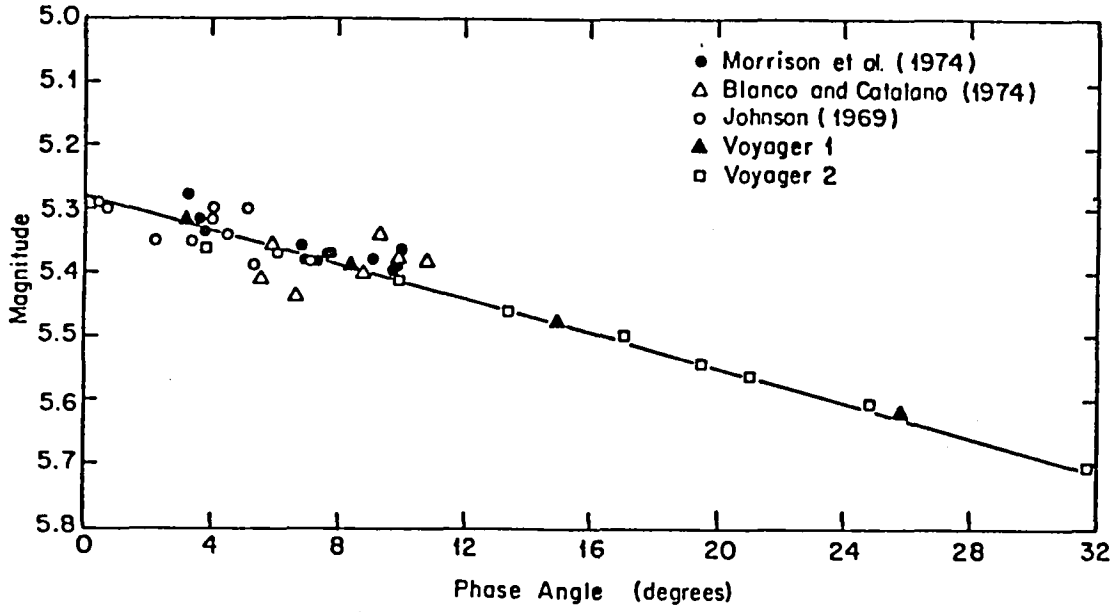


Figure 1. Comparison of earth-based and Voyager observations of the disc-integrated brightness of Europa. Voyager Clear filter observations have been scaled to earth-based V-filter data. Since the brightness of Europa varies with longitude, all measurements have been corrected for this effect using the method of Morrison et al. (1974).

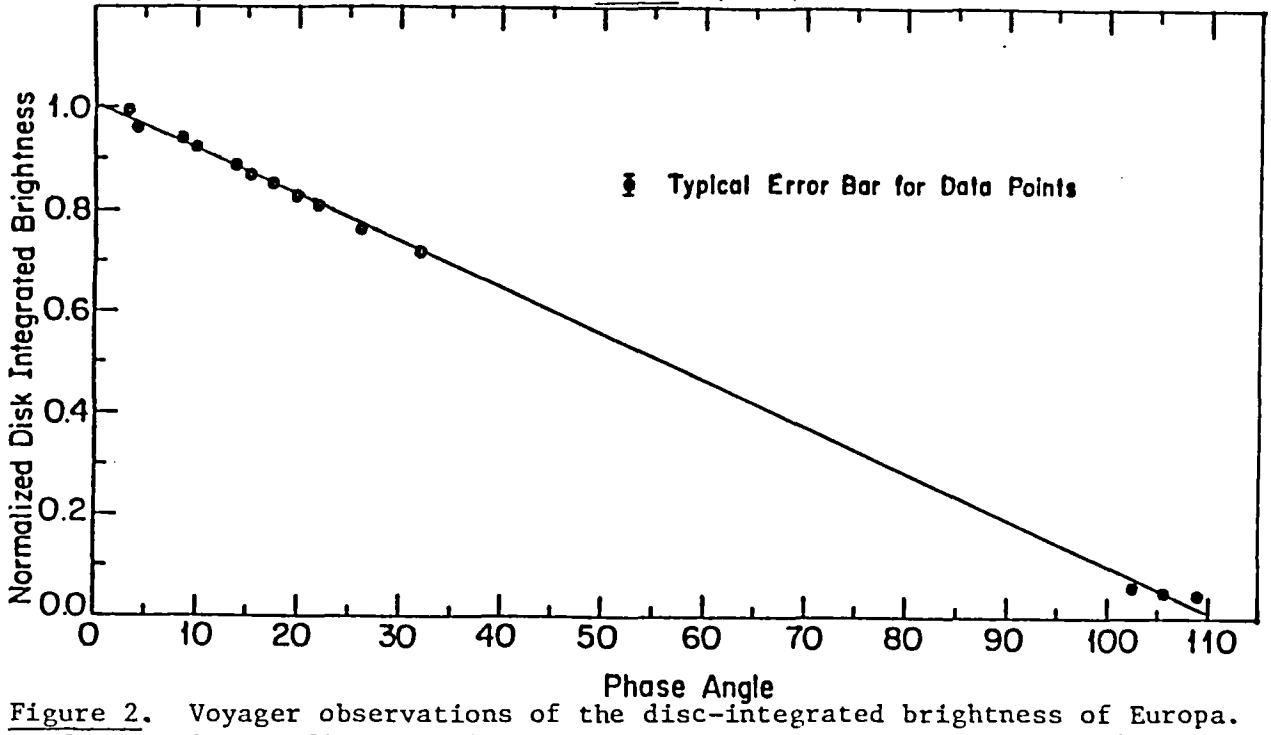


Figure 2. Voyager observations of the disc-integrated brightness of Europa. Of special significance are the points at phase angles between 103° and 109°. While a straight line fits the data points adequately, the actual phase curve cannot be exactly linear: Europa is unlikely to vanish from sight at phase angles beyond 110° as an extrapolation of the straight line would imply.

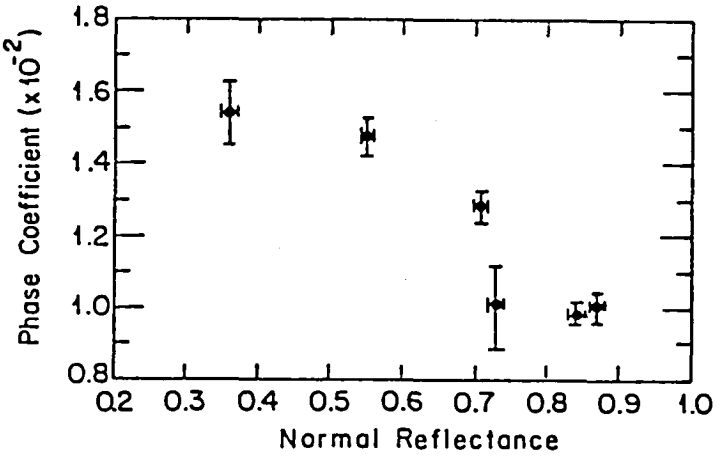


Figure 3. Inverse relationship between the phase coefficients of Europa (measured between 3° and 32°, and expressed in mag/deg) and the normal reflectance of the surface. The different points correspond to different Voyager filters. From left to right: Ultraviolet (.34 μm), Violet (.41 μm), Clear (.47 μm), Blue (.48 μm), Green (.56 μm), and Orange (.59 μm). The normal reflectances are those of a representative area of the surface near (340°W, 40°S).

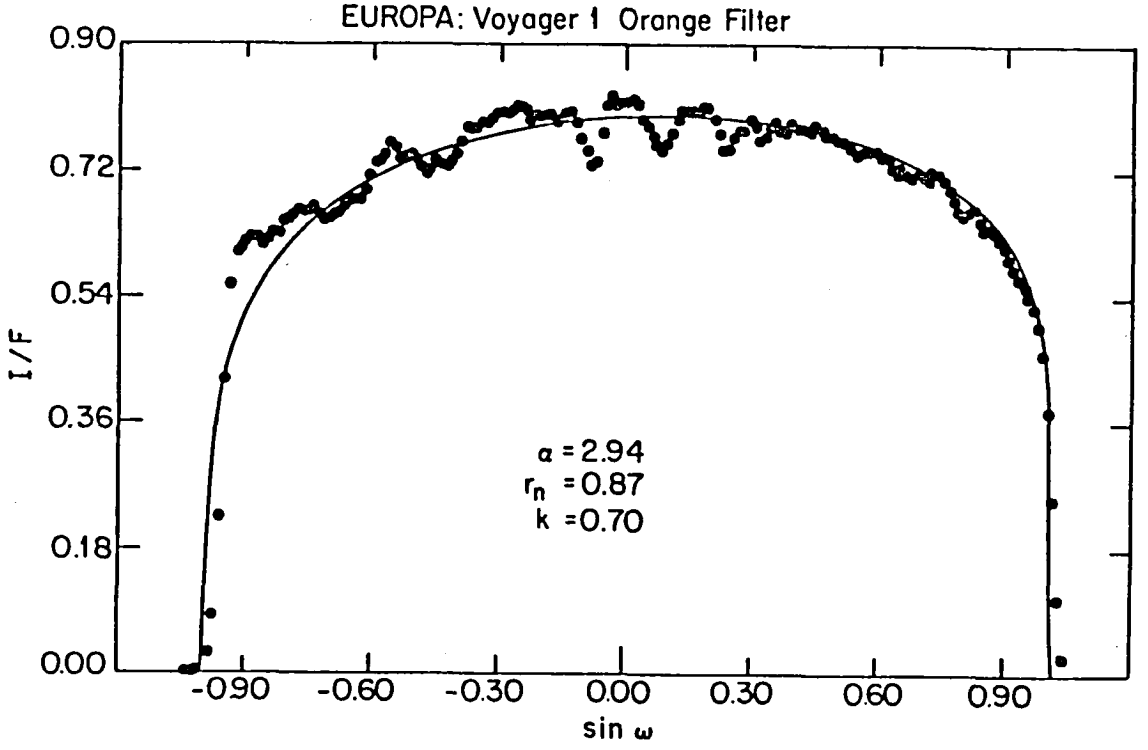


Figure 4. A photometric scan across Europa at a small phase angle (α = 2°.9), showing a significant degree of limb darkening. The fitted curve corresponds to a limb darkening parameter k = 0.70. For a lunar-like surface there would be almost no limb darkening (k = 0.5), while a Lambert-like surface would give k = 1. Voyager 1 image 0582J1-001.

COLOR DISTRIBUTION FIELDS OF GEOMORPHIC FEATURES ON EUROPA: INITIAL RESULTS FROM A NEW TECHNIQUE

Thomas A. Meier, Department of Geology, University of Houston Central Campus, Houston, Texas 77004

Multispectral studies of the planets have taken on increasing importance in recent years, particularly with the advent of high-resolution spacecraft imagery. One of the most widely used techniques of late has been the generation of color ratio imagery, which has been used to create medium-resolution global multispectral maps of the Galilean satellites from Voyager images (Soderblom, et al., 1980), for example. Color ratio images have proven very useful tools for delineating surface areas of differing spectral content, but tend to be more qualitative than quantitative in nature. Also, while the registered images used to make color ratio images have been used to derive multispectral line profiles across planetary surface terrains, it has not previously been possible to economically display multispectral data for whole areas of a planetary surface. For these reasons, a technique was developed using the capability of the ternary diagram to simultaneously display relative spectral content for three differently colored filters used in Voyager imagery of Europa.

Conceptually, the ternary diagram color distribution display technique is most similar to a type of color ratioing described by Strickland (1979). In Strickland's method, the relative amount of a particular color is brought out by constructing an image wherein that color is divided by the sum of its opposing primary colors over the same area (e.g., [blue/red + green] would bring out the relative blueness of the area). In the ternary diagram technique it is possible to see the relative amounts of all three colors at the same time, though the colors used need not be primary colors.

In constructing the ternary diagram, it is first necessary, having registered images, to choose triplets of colors. For high-resolution Voyager Europa imagery the filters used were UV, violet, blue, and orange, so the possible triplets are UV/vi/bl, UV/vi/or, UV/bl/or, and vi/bl/or. The density (DN) values are then extracted from the registered images for selected features either through pixel printouts of blocks of the images, or by directly reading pixel values from an interactive image display system such as the one manufactured by DiAnza Systems. The three colors in each triplet are then normalized to obtain relative color percentages. These percentages are plotted on the ternary diagram; the outline of the outermost points defines the color distribution field of the portion of the feature being investigated. After this has been done for several features, it is advisable to determine which color triplet is the most useful for spectral studies before proceeding. Generally, the most useful triplet will possess both the greatest number of completely non-overlapping color distribution fields and the greatest dimensions of the composite color distribution field for all features plotted. The next useful step in this multispectral survey is the creation of a special ternary plot called a puzzle diagram in which all non-overlapping portions of individual features' color distribution fields are plotted on one ternary diagram around the whole field that is as close to the center of the ternary diagram (the 33-33-33 point) as possible. There are usually several possible ways to create an interlocking puzzle from a given set of color distribution fields; however, the best way to derive the maximum spectral information seems to be to continuously build the puzzle around the central field utilizing the smallest area fields first so that the greatest number of fields may be plotted. By filling in the fields with different patterns for different types of surface features, a direct correlation can be made between color distribution and geomorphology.

It should be noted that this paper is intended primarily as a description of a new multispectral data analysis technique. Results to date entail far too few features to make any meaningful interpretations, but some very tentative results will be presented for proof-of-principle purposes. The most useful color triplet for the high-resolution Europa imagery was found to be vi/bl/or, using criteria outlined above. Figure 1 depicts the puzzle diagram constructed for 26 Europa surface features comprising 10 geomorphic types and located between 47N and 12S Latitude and 177 and 198 Longitude. (It is noteworthy to mention that the yellowish bands represented in Figure 1 and Table 1 are a potentially new Europan landform that has not been described previously in the literature. Thus far, yellowish bands have been identified bordering most, if not all of the lineament types in the mid-latitude belt between ~180 and 210 Longitude. There is some concern that this apparent feature may be an artifact of a flawed image registration, and this possibility is being investigated. Currently available evidence indicates these features are genuine, however.) As can be seen in Figure 1b, the geomorphic types range from spectrally confined (as with the type 1 lineaments and yellowish bands) to nearly spectrally ubiquitous (type 3 lineaments). Caution should be taken in this observation, owing to the extremely small numbers of each type of feature plotted. If continued plotting bears this out, however, the theory may be advanced that spectrally confined features are probably of a more homogeneous composition than geomorphic features that have wide spectral variations within a single type. Other points of interest apparent in Figure 1b include the high spectral similarity between white lines apparently not associated with lineaments and a bright crater interior, indicating that the crater interior was perhaps flooded from below by a relatively pure water or slush similar to that thought to comprise the white lines, which may be ice pressure ridges (Lucchitta and Soderblom, 1981). Additionally, the color distribution field of a white line in a type 3 lineament is shifted closer to the center of the type 3 lineament color fields than fields of lone white lines, indicative of a possible material mixing between the white line and lineament.

One of the ultimate goals of the ternary diagram technique is a spectral classification of all major landforms on a body. Much work of the kind described in this paper remains to be done for Europa, but additional parameters will also be evaluated to enhance the classification process. Among the new parameters will be the mean, standard deviation, and dispersion of each color distribution field. These results will be included in a forthcoming paper.

The author gratefully acknowledges financial support provided by the U.S. Geological Survey Branch of Astrogeologic Studies/Voyager data analysis program, and a research grant from the University of Houston Geology Foundation.

REFERENCES

Lucchitta, B.K., and L.A. Soderblom (1981). Structures on Europa. The Satellites of Jupiter (in press).

Pieri, D.C. (1981). Lineament and polygon patterns on Europa. Nature 289 p. 17-20.

Soderblom, L.A., T.V. Johnson, J.A. Mosher, G.E. Danielson, P. Kupferman, A.F. Cook, and M.E. Davies (1980). Global multispectral maps of the Galilean satellites. Reports of Planetary Geology Program-1980, NASA TM 82385, p. 10-11.

Strickland, E.L., III (1979). Martian soil stratigraphy and rock coatings observed in color-enhanced Viking Lander images. Proc. Lunar Planet. Sci. Conf. 10th, p. 3055-3077.

| FEATURE NUMBER | APPROXIMATE COORDINATES | DESCRIPTION |
|---|---|---|
| 1 | 22N, 183 | white line in type 3 lineament (*Belus Linea*) |
| 2 | 1N, 187 | white line |
| 3 | 9N, 181 | white line |
| 4 | 5N, 182 | white line |
| 5 | 9N, 181 | white line at contact with dark spot |
| 6 | 6S, 195 | type 1 lineament |
| 7 | 5S, 195 | type 1 lineament |
| 8 | 1N, 194 | type 2 lineament |
| 9 | 2N, 192 | type 2 lineament |
| 10 | 12S, 184 | type 2 lineament |
| 11 | 12S, 187 | type 2 lineament |
| 12 | 47N, 180 | orange type 3 lineament (*Minos Linea*) |
| 13 | 39N, 190 | type 3 lineament (*Cadmus Linea*) |
| 14 | 39N, 185 | type 3 lineament (*Cadmus Linea*) |
| 15 | 23N, 197 | cuspate type 3 lineament |
| 16 | 32N, 177 | type 3 lineament |
| 17 | 43N, 177 | type 4 lineament |
| 18 | 11S, 198 | type 5 lineament |
| 19 | 6S, 195 | faint cusp-shaped type 5 lineament |
| 20 | 3N, 178 | crater bright interior |
| 21 | 3N, 178 | crater blackish ejecta |
| 22 | 4N, 178 | crater brownish ejecta |
| 23 | 45N, 177 | dark spot in lineation |
| 24 | 11S, 198 | yellowish band bordering type 5 lineament |
| 25 | 5S, 195 | yellowish band bordering type 1 lineament |
| 26 | 8S, 198 | yellowish band bordering type 1 lineament |

TABLE 1. Descriptive information for Europa surface features plotted in FIGURE 1.

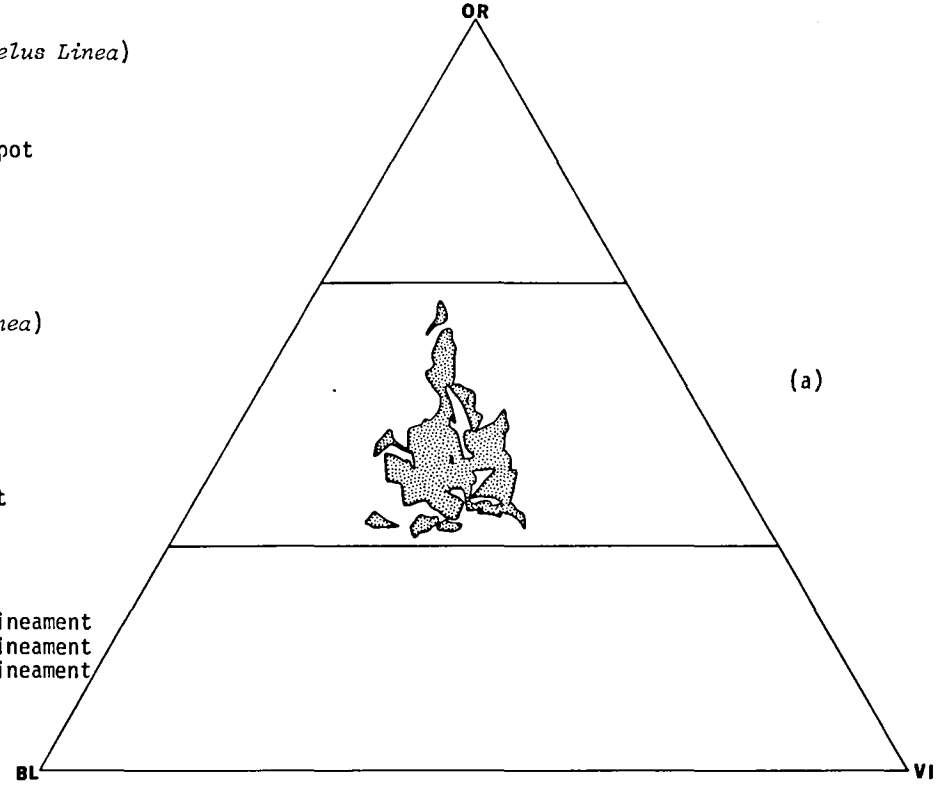


FIGURE 1. (a) Composite color distribution field for 26 Europan surface features of 10 distinct geomorphic types. (b) Enlargement of trapezoidal area (outlined in FIGURE 1a) depicting puzzle diagram constructed from non-overlapping portions of the individual color distribution fields for the 26 features. Numbers within or near each field correspond to feature numbers in TABLE 1; notation at trapezoid's corners refer to relative percentages of each color at that point. (c) Key to geomorphic feature types represented in FIGURE 1b. The notation of lineament types (1-5) follows the classification scheme of Pieri (1981).

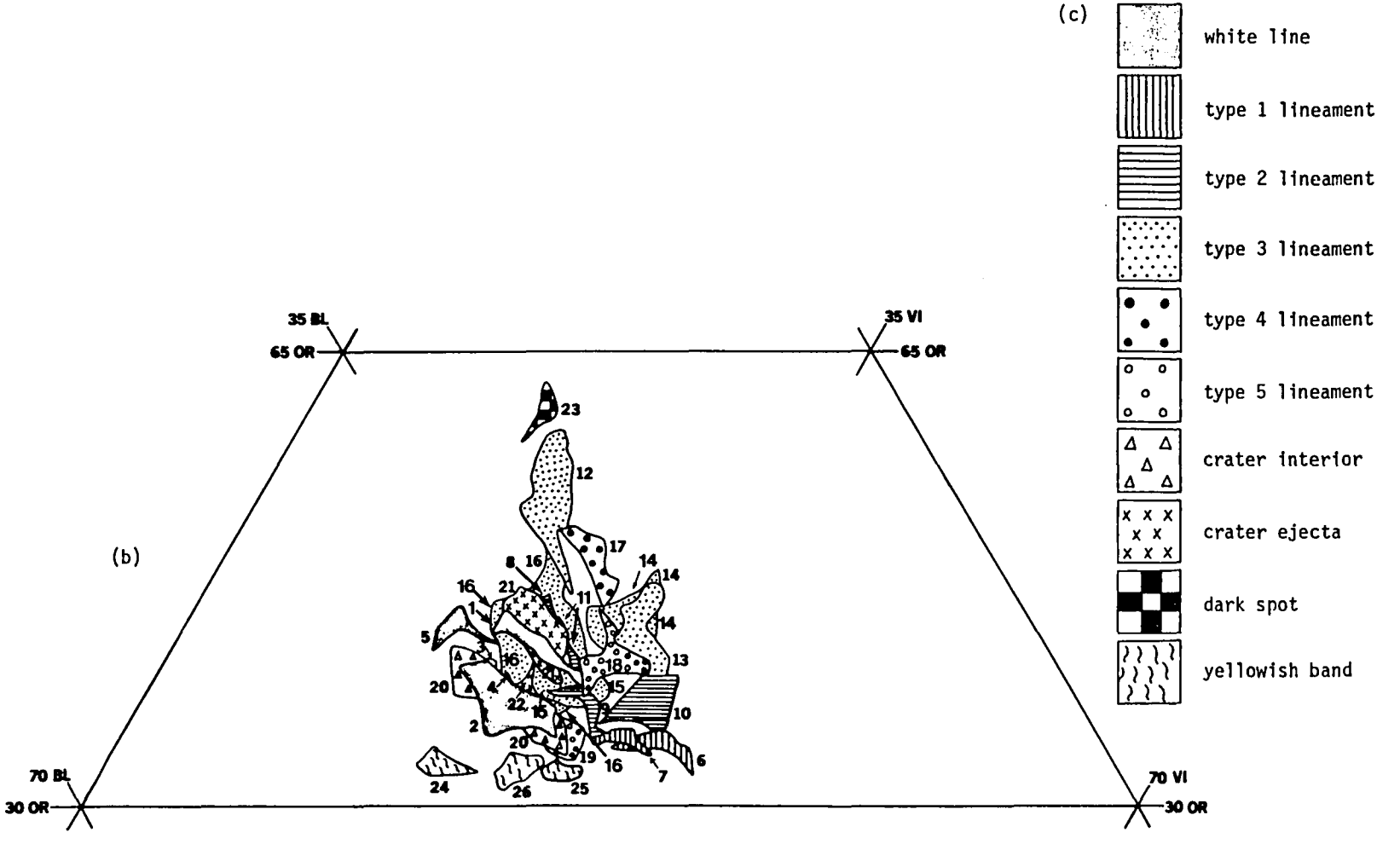


FIGURE 1 (continued)

Morphotectonic Maps of the Grooved Terrain on Ganymede.

Ph. L. Masson, Labo. de Géologie Dynamique Interne,
ERA n°804 CNRS,
Université Paris-Sud (bât. 509),
F-91405 Orsay Cedex (France).

The surface of Ganymede exhibits complex patterns of bright grooved terrain and dark polygons of cratered terrain. The grooved terrain shows alternating ridges and grooves in straight and curvilinear sets with superpositions and crosscutting relations. The origins of these features have been discussed by several authors (Lucchitta, 1980; Squyres, 1980; Squyres et al., 1981). Although many grooves are interpreted to be structural features produced by extensional tectonics (Squyres et al., 1981), the process of lithospheric fragmentation remains uncertain and different interpretations and model of internal evolution were proposed.

In order to contribute to a better understanding of the tectonic evolution of Ganymede, we undertook a "detailed" mapping of the grooved terrain and of their surroundings, located south of Galileo Regio. These maps aim to show the morphologic and possibly tectonic relations of the different groups of grooves. The two preliminary maps (based on Voyager "home made" photomosaics at approximately 1:12,500,000 scale) show 9 main groups of grooves in the Philus Sulci, Mashu Sulcus, Anshar Sulcus, Tiamat Sulcus and Kishak Sulcus regions, and 4 main groups of grooves in the Uruk Sulcus region. The different groups of grooves are separated on the basis of their superposition and crosscutting relations. An attempt to correlate these different groups of grooves with the regional evolution of Ganymede is made.

This work is supported by INAG grant 3769 (ATP "Planétologie-1980").

References.

Lucchitta, B.K. (1980). Grooved Terrain on Ganymede. Icarus 44, 481-501.

Squyres, S.W. (1980). Volume changes in Ganymede and Callisto and the origin of Grooved Terrain. Geophys. Res. Lett. 7, 593-596.

Squyres, S.W., Parmentier, E.M., and Head, J.W., III (1981). The origin of Grooved Terrain on Ganymede. In Reports of Planetary Geology Program 1980-1981, NASA Tech. Memo. 82385, 64-65.

# A MECHANICAL ANALYSIS OF EXTENSIONAL INSTABILITY ON GANYMEDE

*J.H. Fink, Department of Geology, Arizona State University, Tempe, Arizona 85287, R.C. Fletcher, Center for Tectonophysics, Texas A&M University, College Station, Texas 77843*

Each of Ganymede's two principal terrains exhibits a characteristic form of regularly spaced surface lineation: rimmed furrows in the dark heavily cratered terrain, and grooves in the bright, presumably younger terrain (1). We propose that these features both formed through an extensional instability of the ganymedean crust and that their spacings may indicate the thickness of a brittle surface layer at their time of formation.

It has been suggested that Ganymede's surface consists of plates of heavily cratered terrain which were capable of relative motion early in the planet's history (1) and that the younger grooved terrain corresponds to areas of extension (2), similar to mid ocean ridges and rift valleys on earth. Rimmed furrows (3) are graben like features which have been compared to the rings surrounding the Valhalla impact basin on Callisto and which might have formed in response to radial tensile stresses during the prompt collapse of a large impact structure. Alternatively, the furrows might represent sites of incipient rifting of the older terrain.

We have interpreted both structures, furrows and grooves, through use of a mathematical analysis of the extension of a planetary lithosphere. This model was originally applied to the regular spacings of mountain ranges and valleys in the Basin and Range Province of the western United States (4). The model considers the crust to be comprised of two zones, defined on the basis of the mechanical behavior of the rocks they contain: a brittle, elastic/plastic surface layer overlying a ductile, power law fluid interior. The interface between these zones is a mechanical, rather than petrologic one. Thermal modeling (5) and analytical studies of large impact basins (6) indicate that this is an appropriate model for the structure of Ganymede.

Here we assume that the ductile zone has a power law rheology ($\epsilon = A\sigma^n$; $\epsilon$ = strain rate; $\sigma$ = stress; A, n = constants) like that of ice (n = 3) and that the surface crust is a nearly perfect plastic (n very large). In such plastic materials, deviatoric stresses cannot exceed a certain yield value. We assume that faulting occurs when that yield value is reached. Temperature is assumed to increase linearly inward from the brittle/ductile interface, with a corresponding decrease of viscosity. It can be shown analytically (4) that when such a rheologic structure is subjected to uniform extension, a necking instability ensues. The interface between the brittle and ductile zones develops regularly spaced intrusions and depressions and the upper surface eventually breaks up into horsts and grabens. Furthermore, the ratio between the spacings of the troughs and the thickness of the brittle surface layer lies between 3.4 and 4.0. Thus if the furrows and/or grooves formed in response to such an extensional instability, the spacings of the lineations would indicate the thickness of the brittle surface layer at their time of formation.

Sub-parallel grooves in an area of grooved terrain near Galileo Regio show a mean spacing of 7.9 ± 1.4 km (Fig. 1) which corresponds to a crustal thickness between 2.0 and 2.3 km. Spacings of furrows in the adjacent heavily cratered terrain (Fig. 2) are 39.0 ± 10.8 km corresponding to a 9.8 - 11.5 km thick brittle layer. This latter value is consistent with the 10 km minimum thickness estimated for the dark terrain on the basis of ring tectonic theory (7).

Figure 3 illustrates a possible scenario for the development of both furrows and grooves during an episodic history of lithospheric extension of as yet unspecified origin. Early tensile stresses are accomodated by a homogeneous thinning of Ganymede's surface layer. Stresses are initially low enough so that brittle failure does not occur. Thinning increases the thermal gradient to a point where stable extension is replaced by a necking instability in the surface

layer. The planar interface at the brittle/ductile transition develops a regularly spaced series of upwellings and depressions whereas the upper surface breaks up into regularly spaced grabens and horsts (these grabens represent the furrows). Further extension (presumably resumed after some hiatus) is concentrated in the thinner areas where thermal gradients are highest and tensile strengths are lowest. Penetration of faults to the ductile interior might lead to flooding of the grabens forming the smooth areas of bright terrain. Undercontinued extension, the predominantly ice surface layer will again break up into regularly spaced structures, but these grooves and ridges will now reflect the shallower depth to the brittle/ductile transition.

The geometry of the grooves in many areas does not fit well into a model of uniform extension. Sets of grooves are seen to cross cut each other and even to lie perpendicular to one another. However, our model relates only to the initial stages of extension when regular spacings might be expected to develop. Subsequent breakup of the brittle surface into irregular blocks and local shifting of stress patterns might obscure the original parallel orientations of the earliest grooves.

In summary, this model suggests that the thickness of the brittle surface layer of Ganymede's lithosphere was locally reduced from around 10 km at the time of furrow formation to around 2 km when the grooved terrain was formed. This information may help constrain models for the thermal evolution of Ganymede's early lithosphere.

## REFERENCES


1. *B.A. Smith and Voyager Imaging Team, 1979. Science 204, 251.*
2. *S.W. Squyres, 1980. Geophys. Res. Lett. 7, 593.*
3. *B.K. Lucchita, 1980. IAU Colloquium 57, 'The Satellites of Jupiter', Kailua-Kona, Hawaii.*
4. *R.C. Fletcher and B. Hallet, 1981. J. Geophys. Res., in press.*
5. *R.T. Reynolds and P.M. Cassen, 1979. Geophys. Res. Lett. 6, 121.*
6. *W.B. McKinnon and H.J. Melosh, 1981. Icarus 44.*
7. *W.B. McKinnon, 1981. Proc. Lunar Planet. Sci. Conf. 12th, (in press).*

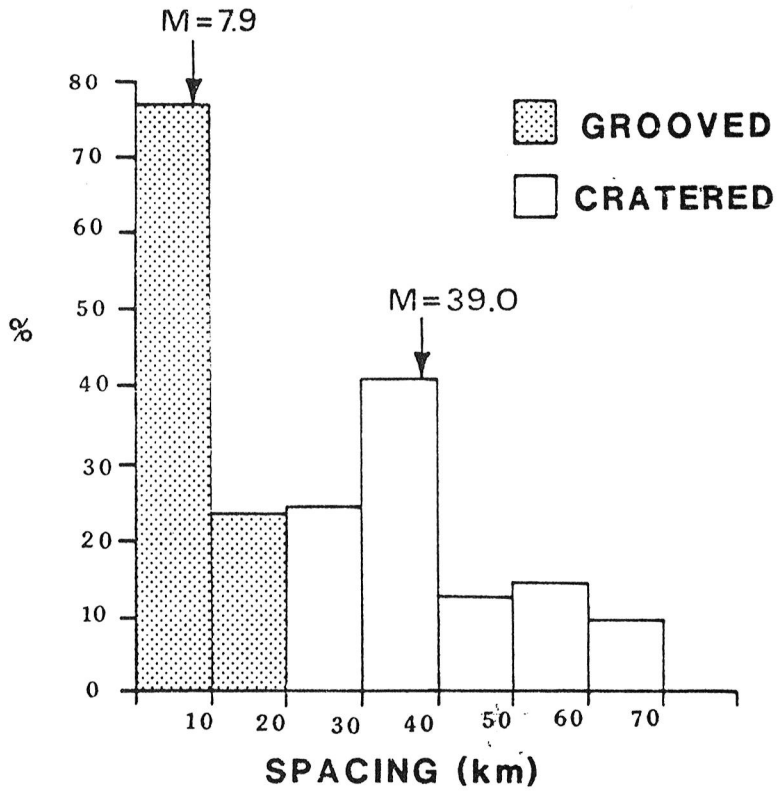


*FIGURE 1. Histograms of spacings of lineations (n = 34) in heavily cratered terrain and grooves (n = 52) in grooved terrain.*

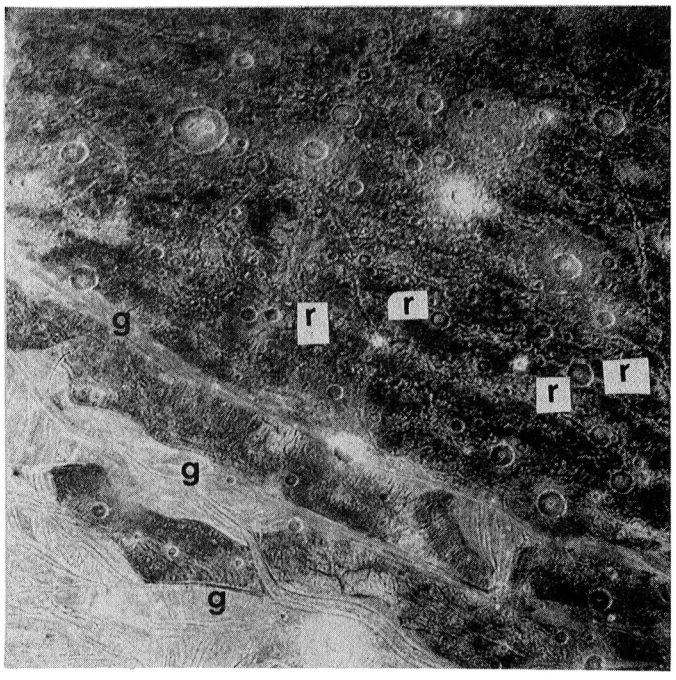


*FIGURE 2. Contact between grooved and heavily cratered terrains showing rifts (r) in cratered terrain and zones of grooved terrain (g) which become progressively wider toward the SW.*

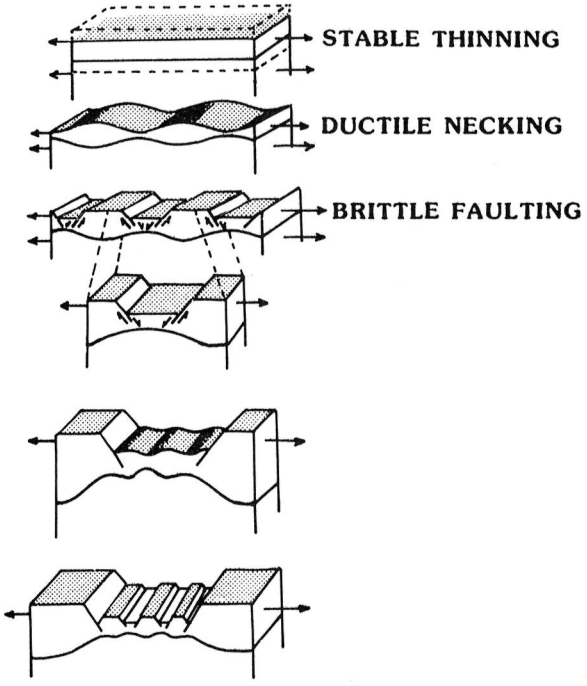


*FIGURE 3. Cartoon showing development of grooves and furrows.*

SEQUENTIAL DEVELOPMENT OF GROOVED TERRAIN AND POLYGONS ON GANYMEDE

Matthew P. Golombek and M. Lee Allison, Department of Geology and Geography, University of Massachusetts, Amherst, Massachusetts 01003

Two distinct terrain types characterize the surface of Ganymede: cratered terrain and grooved terrain. Cratered terrain has a relatively low-albedo, is heavily cratered, and comprises about 50% of the observed surface area of Ganymede. It occurs in discrete polygons of various sizes that are bounded by grooved terrain. Grooved terrain has a higher-albedo and a variable crater density, although generally it is less heavily cratered than the cratered terrain (Smith et al., 1979). Although some evidence for minor strike-slip movement has been presented (Lucchitta, 1980), most workers have noted the evidence against major strike-slip or compressional displacements on Ganymede concluding that the grooved terrain formed by some type of extensional tectonics. Allison et al. (1980) and Head et al. (1981) proposed that grooves are grabens that were flooded by water with subsequent refracturing. Squyres et al. (1981) suggested that groove sets evolved by formation and flooding of wide grabens with a final stage of narrow ice-wedge fracturing. Thus recent models imply that grooves result from extensional tectonics, and that their formation involves some type of resurfacing that changes heavily cratered, low-albedo terrain without grooves into less cratered, higher-albedo, grooved terrain. Finally, although a few examples of rifted craters with minor displacements have been found, most craters cut by grooves are truncated rather than rifted apart (Allison et al., 1980; Head et al., 1981) suggesting that grooves, in general, cannot be the result of simple rifting associated with spreading centers like mid-oceanic rifts.

In order to distinguish among the proposed mechanisms for the formation of grooved terrain it is necessary to understand the sequence of groove development based on photogeologic evidence. In this paper, grooves on Ganymede will be analyzed in a manner similar to the way a structural geologist analyzes brittle fracture features on the earth. By observing simple terminating (or "T") intersections and crosscutting relationships, the relative ages of the two intersecting grooves or groove sets can be determined. These straightforward determinations of relative age are non-genetic, assuming only that grooves are brittle fracture features. The analysis reveals that grooved terrain formed by a step-by-step process; furthermore, each step can be observed because the process stopped at different stages in various places on the surface on Ganymede (Allison and Golombek, 1981).

Because almost all grooves and groove sets occur in resurfaced areas (Fig. 1), resurfacing must occur prior to their formation. However, the sharp boundaries between grooved terrain and cratered terrain imply that resurfacing was laterally limited by older fractures. Thus the formation of a groove set must begin with fracturing of cratered terrain followed by resurfacing that is bounded by these older fractures. Grooves form by sub-

Present address: Lunar and Planetary Institute, 3303 NASA Road 1, Houston, Texas 77058

sequent fracturing of the resurfacing material.

Evidence for the relative ages of two intersecting grooves or groove sets is based on two structural relationships. 1) If one fracture terminates or "T's" against another, the crossbar of the "T" is older and must have acted as a structural discontinuity (domain boundary) against which the younger fracture terminated. The correct interpretation of this relationship assumes that strike-slip displacement was minor or nonexistent, as can be demonstrated at locations D and E (Figs. 1 and 2c). 2) If one groove set crosscuts and is clearly superposed on another groove set, then the crosscutting set is younger. "T" intersections are the most common in the grooved terrain on Ganymede.

Detailed structural mapping of terminating and crosscutting relationships between grooves and groove sets in a number of areas where high resolution coverage exists shows that the development of grooved terrain can be broken into three broad stages. Each stage includes the initial fracturing and resurfacing of cratered terrain followed by fracturing of resurfacing material to form grooves. One area on Ganymede (Fig. 1) will be used to illustrate the sequential development of groove sets (Fig. 2).

Initial fracturing of cratered terrain, resurfacing, and subsequent fracturing of resurfacing material occur in the formation of primary grooves during stage 1. Primary groove sets are commonly very long (generally over 1000 km) and narrow (generally less than 20 km). Almost all younger groove sets terminate against these groove sets. Primary grooves are fundamental breaks which act as domain boundaries (Fig. 2a).

In general, secondary groove sets are only hundreds of km long, but can be up to 40 km wide. Primary and secondary grooves break cratered terrain into polygons. These polygons of cratered terrain represent discrete structural blocks that are mechanically isolated from each other (Fig. 2b).

Tertiary grooves form as short (tens of km), closely spaced, parallel to subparallel groove sets that take up most of the surface area of completely grooved terrain. They develop within the polygons defined by the primary and secondary groove sets and terminate against the older grooves bounding the polygons. The fact that tertiary groove sets commonly do not have similar trends in adjacent polygons indicates that the polygons were mechanically isolated during this stage (Fig. 2c).

The three-stage process that converts cratered terrain into grooved terrain has stopped at different stages at different places on Ganymede. The halting of this sequential process has yielded: areas of fractured cratered terrain, polygons of cratered terrain, polygons of resurfaced terrain (smooth terrain), and completely grooved terrain. Grooves in each stage were shorter and acted on progressively more restricted areas. Similarly, cratered terrain was broken into smaller areas, from initially fractured areas to discrete polygons. Thus the sequential process of groove development has resulted in the break-up of the surface of Ganymede into progressively smaller and smaller mechanical units.

As outlined above, most of the area of completely grooved terrain is resurfaced during stage 3. Smith et al. (1979) and Plescia et al. (1980) observed a wide range of crater densities on different areas of grooved terrain implying that resurfacing associated with the development of grooved terrain occurred over a long period of time. However, for all areas we

mapped, most of the resurfacing occurred during stage 3, indicating that the entire step-by-step process occurred in the same sequential order regardless of when it took place. Therefore, the break-up of cratered terrain, and the formation of grooved terrain reflects a fundamental tectonic process that dominated the surface of Ganymede for much of its tectonic history.


Allison, M. L., J. W. Head, and E. M. Parmentier, Grooved terrain on Ganymede: origin as flooded graben (abstract), I.A.U. Colloquium 57, The Satellites of Jupiter, 6-7, 1980.

Allison, M. L., and M. P. Golombek, Sequential development of polygons in relation to grooved terrain on Ganymede, Trans. American Geophys. Un. EOS, 62, 318, 1981.

Head, J. W., M. L. Allison, E. M. Parmentier, and S. Squyres, High-albedo terrain on Ganymede; origin as flooded graben, Lunar and Planet. Science XII, 418-420, 1981.

Lucchitta, B. K., Grooved terrain on Ganymede, Icarus, 44, 481-501, 1980.

Plescia, J. F., J. M. Boyce, and E. M. Shoemaker, Ganymede cratering II: the smooth and grooved terrains (abstract), Bull. Amer. Ast. Soc., 12, 710, 1980.

Smith, B. A., and Voyager Imaging Team, The Jupiter system through the eyes of the Voyager 1, Science, 204, 951-972, 1979.

Squyres, S. W., E. M. Parmentier, and J. W. Head, Origin of grooves on Ganymede, Lunar and Planet. Science XII, 1031-1033, 1981.


Figure 1. Voyager image 0470J2-001 of grooved and cratered terrain on Ganymede. Frame of image is roughly 1000 km, predicted center 3 latitude, 167 longtitude. North is up.

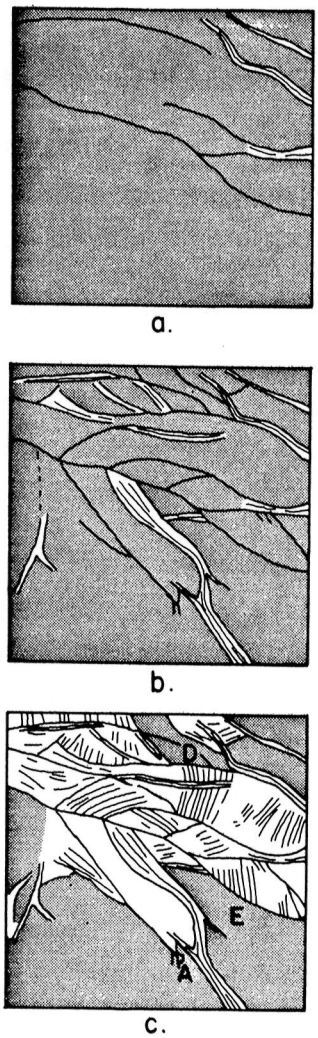


Figure 2. Sketch map of stages in the development of grooved terrain for Figure 1. 1) Stage 1, primary grooves. b) Stage 2, primary and secondary grooves. c) Stage 3, tertiary grooves and grooving of polygons. Letters refer to locations mentioned in text. North-trending grooves at locations D and E terminate against and are younger than the east-trending grooves. Stippled areas represent cratered terrain. Area that trends northwest from location A was resurfaced during stage 3 but not subsequently refractured yielding a polygon of smooth terrain.

POSSIBLE GEOLOGIC IMPLICATIONS OF GANYMEDE CRATER DENSITIES

J.B. Plescia, Jet Propulsion Laboratory, California Institute of Technology, Pasadena, CA 91103

Crater densities for each of the major terrain types on Ganymede have been previously reported (Smith et al., 1979 a, b and Plescia et al., 1980 a, b). This report does not change the basic conclusions of those reports, but rather modifies them in light of additional data. In review, the most densely cratered, hence the oldest unit, is the dark terrain. It exhibits the most densely cratered surface on the body. The grooved and smooth terrains are generally less cratered than the dark terrain, but examples of each with crater densities near that of the dark terrain are observed. The grooved and smooth terrains appear to have formed over an extended period of time.

Previous reports (Plescia et al., 1980 a, b) noted a strong correlation between the observed crater densities and those predicted from a gradient in crater density, for a uniform age, surface from apex to antapex, as proposed by Shoemaker and Wolfe (1981). Additional data now indicates that there is much less of a correlation than previously indicated. While the gradient may exist, it appears to be overshadowed by true age and crater retention differences.

The dark heavily cratered terrain probably represents an original, post-heavy bombardment, crust. The crater densities on that surface have been modified on local and regional scales by variations in the rate of crater relaxation and by ejecta burial. Most of the variation in the density of large diameter craters appears to result from differential relaxation rates. Areas with a low density of large craters could represent areas where the heat flow was higher and hence, allowed a longer period of crustal plasticity. This would allow rapid relaxation and removal of large craters. In colder areas, those craters could not totally relax and are still observed.

The grooved terrain crater density variations appear to result from differences in age rather than crater relaxation rates. While a range in preservation state is noted, craters have not relaxed to the point where they are no longer recognizable. The pattern of crater density does indicate a latitudinal control on the age of the grooved terrain. The data show that at the equator, examples of the oldest to the youngest grooved terrain are found. At the poles, only heavily cratered grooved terrain is observed. It thus appears that the poles experienced a short period of grooved terrain formation, while equatorial regions experienced a much longer period. If the mechanism of formation of grooved terrain is strongly influenced by the local thermal gradient, then the colder polar temperatures could have more quickly lowered that gradient to the point

where the process was halted. A longer period of plasticity of the grooved terrain in equatorial areas, compared to the polar areas, is indicated by the distribution of palimpsests. Palimpsests, while not common, do occur on the grooved terrain near the equator indicating that the crust was not capable of supporting large scale topography at the time of their formation. Such palimpsests are absent on polar exposures of grooved terrain suggesting that they have been rigid for a longer period of time. Craters that would have evolved into palimpsests, had they impacted on grooved terrain at the equator, remain as large craters when impacted into the colder more rigid polar grooved terrain.

REFERENCES:

Smith et al., 1979 a, Science, v. 204, p. 951-972.

Smith et al., 1979 b, Science, v. 206, p. 927-950.

Shoemaker, E. and Wolfe, R., 1981, in The Satellites of Jupiter, Univ. of Arizona Press, in press.

Plescia, et al., 1980 a, Reports of Planetary Geology Program, NASA TM 82385, p. 55-59.

Plescia, et al., 1980 b, Reports of Planetary Geology Program, NASA TM 82835, p. 60-63.

# SOLID STATE CONVECTION IN ICY SATELLITES: EFFECTS OF PHASE TRANSITIONS UPON STABILITY

R. Reynolds, C. Alexander, A. Summers and P. Cassen, Space Science Division, NASA Ames Research Center, Moffett Field, CA 94035

Density considerations alone dictate that the satellites Ganymede, Callisto, and Titan almost certainly contain large mass fractions of $H_2O$ (see Cassen, Peale and Reynolds, 1981). Any moderately high temperature formation scenario would result in melting and separation of ice from silicate material, at least in the outer portions of the bodies (Schubert, Stevenson and Ellsworth, 1981). The importance of solid state convection to heat transfer within the outer Ice I layer of such a body has been investigated by Reynolds and Cassen (1979). The elucidation of the importance of solid state convection in the underlying layers of high density ices has suffered from two factors: lack of knowledge of the viscosity of high density ices, and uncertainty regarding the effects of ice phase transitions on convective stability.

Recent measurements by Porrier et al (1981) indicate that the viscosities of Ice VI and Ice I are similar near their respective melting temperatures. Since the different crystalline forms of ice are similar in their chemical bonding, it is not unrealistic to assume that the temperature dependent viscosities of all forms of ice can be approximately represented by that of Ice I.

The effects of a phase change on thermal stability has been investigated in detail by Schubert, Yuen and Turcotte (1975). They showed that phase transitions can act to stabilize or destabilize a fluid layer to thermal convection. In order to estimate the stability effects of phase boundaries with an icy satellite, thermodynamic and equation of state data for high density ices were complied and detailed structural models were constructed. Ganymede was chosen as a representative icy satellite. The Ganymede models were calculated on the assumption of a completely differentiated body with a pure $H_2O$ ice mantle and a rocky core. These models consist of 43% $H_2O$ by mass. Model A is based upon the heat flow ($H = 3.34 \times 10^{18}$ ergs) from a core having the present day radiogenic element abundances of carbonaceous chondrites and should by representative of the present day configuration. Model B is a higher heat flow ($H = 3.9 \times 10^{19}$ ergs) model, representative of an earlier time when an initially hot satellite with a large molten region would have just completely frozen.

Using the properties of ice, the planetary parameters taken from the satellite models and the analysis of Schubert et al (1975); we have calculated the effect of the phase boundaries on stability for both of these models. The results are expressed in figures 1-9. In these figures, the calculations for a fluid layer with the phase change are compared with the Rayleigh stability relations for a layer of the same dimensions and properties but without the change in phase. Two cases are shown: one in which the layer convects as a single-cell and one in which the layer convects as two cells of equal dimensions. The maximum viscosity $\nu$ is plotted vs. the minimum superadiabatic temperature gradient ($\beta - \beta_a$) at which the

configuration is unstable to convective flow, where $\beta$ is the ambient temperature gradient, $\beta_a$ is the adiabatic temperature gradient, and $\nu$ is taken to be of the form:

$$\nu = 10^{7} e^{-26\left[1 - \frac{273}{T}\right]} \text{ poise}$$

For a given value of $(\beta - \beta_a)$, if the value of $\nu$ calculated for the case with a phase transition is larger than that for the single-cell configuration, the transition is destabilizing. If the value of $\nu$ for the phase change case is less than that for the double-cell configuration, the transition has a stabilizing effect. For values of the viscosity intermediate between the single and double-cell critical values, single-cell convection is still the preferred mode although the phase boundary tends to have an effect in the direction of stabilization.

The model internal heat fluxes can be used to calculate values for conductive thermal gradients at the phase transition boundaries. If the thermal gradients so calculated for current heat fluxes (Model A) and an earlier high heat flow model (Model B) are considered to be representative of the range of conductive gradients within a cooling, differentiated body, some broad interpretations may be made. The calculations indicate that the I-II, III-V, V-VI, and VI-VIII transitions will permit solid state convection through the phase boundaries for a wide range of superadiabatic temperature gradients. Transitions I-III, II-V and V-VI also appear to be unstable to convection for large temperature gradients and associated high heat flows. At later times, with lower heat flows the II-V and II-VI phase boundaries, in particular, could become stabilized to convective flow as suggested by Thurber et al (1980). The stability is sensitive, however, to the thickness of the convecting layer, and, if the remainder of the mantle were convecting, the scale of the convecting layer could well permit convection through the II-V or II-VI transitions, even at lower temperatures.

An initially hot icy satellite with a large outer layer of ice could thus be expected to have experienced convection throughout most of its mantle, perhaps continuing until the present day. The effects of phase transitions when impurities are present in the ice, as well as for low temperature, undifferentiated formation scenarios remain to be investigated.


Cassen, P.M., Peale, S.J., and Reynolds, R.T. (1981). Satellites of Jupiter, (D. Morrison, ed.), Univ. of Arizona Press, Tucson (in press).

Porrier, J.P., Sotin, C., and Peyronneau, J., (1981). Nature, 292, 225-227.

Reynolds, R.T., and Cassen, P.M., (1979). Geophysical Research Letters, 6, 121-124.

Schubert, G., Stevenson, D.J., and Ellsworth, K., (1981). Icarus (in press).

Schubert, G., Yuen, D.A., and Turcotte, D.L., (1975). Geophysical Journal of the Royal Astronomical Society, 42, 705-735.

Thurber, C.H., Hsuii, A.T., and Toksoz, M.N., (1980). Proceedings of the Eleventh Lunar and Planetary Sceince Conference, 1957-1977.

Model A

Model B

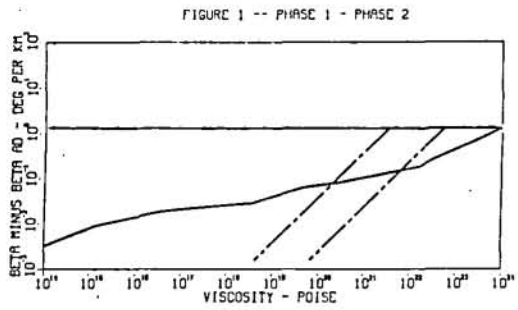

FIGURE 1 -- PHASE 1 - PHASE 2

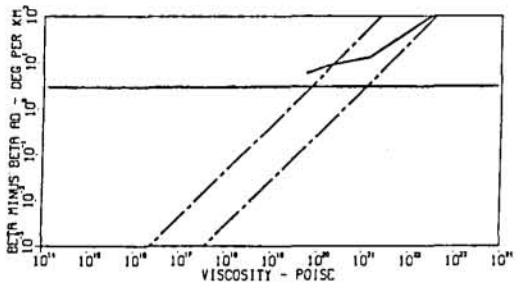

FIGURE 2 -- PHASE 2 - PHASE 5

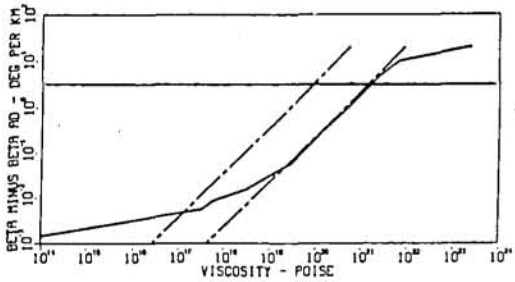

FIGURE 3 -- PHASE 5 - PHASE 6

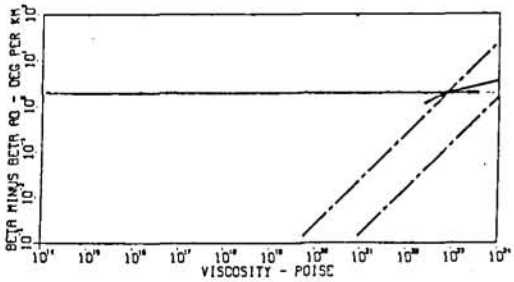

FIGURE 4 -- PHASE 2 - PHASE 6

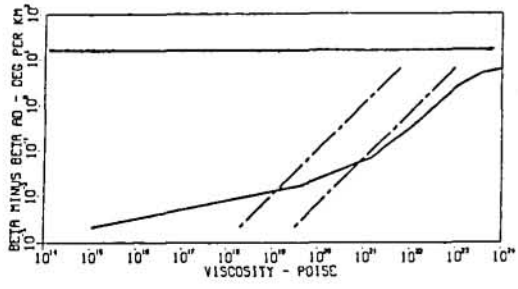

FIGURE 5 -- PHASE 6 - PHASE 8

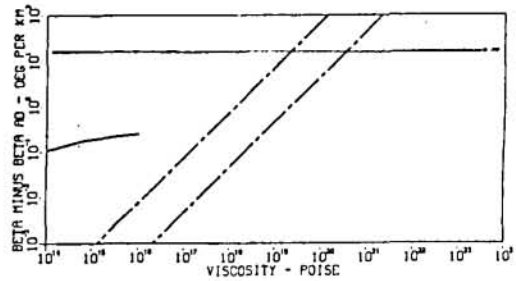

FIGURE 6 -- PHASE 1 - PHASE 2

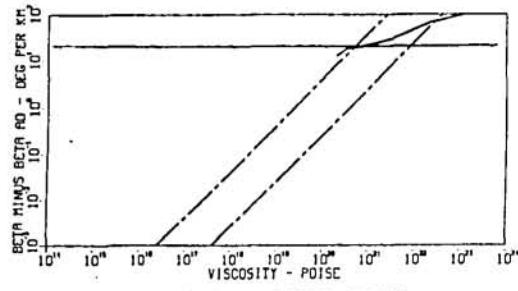

FIGURE 7 -- PHASE 1 - PHASE 3

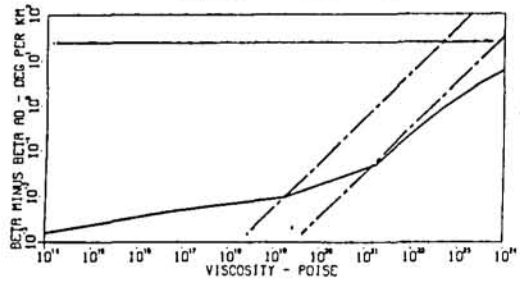

FIGURE 8 -- PHASE 3 - PHASE 5

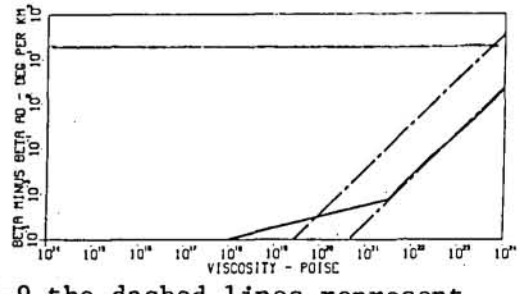

FIGURE 9 -- PHASE 5 - PHASE 6

In figures 1-9 the dashed lines represent stability relations for double and single-cell convection, respectively, in a layer without a phase change while the solid line represents the stability curve for a layer with the phase change. The horizontal lines indicate the value of a calculated conductive temp. gradient at the given phase change. Figures 1-5 are for Ganymede Model A, figures 6-9 are for Ganymede Model B.

# GEOPHYSICAL EVOLUTION OF GANYMEDE AND CALLISTO I

William B. McKinnon, Lunar and Planetary Laboratory,
University of Arizona, Tucson, AZ 85721

The Galilean satellites Ganymede and Callisto appeared to pre-Voyager eyes as sister satellites, with similar orbits, densities, compositions and (assumed) internal structures. The distinctions have since multiplied, and both bodies have joined the shattered sisterhood of other once twin planets, Earth-Venus and Jupiter-Saturn. Yet it is remarkable that worlds blessed with such similar starting conditions can evolve along such different paths. We have, by no means, seen the true diversity of planetary objects.

## Accretion

Conventional gas-free accretion scenarios result in similar initial configurations for Ganymede and Callisto (1). Accretional melting of the ice portion of a uniform mixture of "silicates" and "ices", in the outer regions of both planets, results in a cold, undifferentiated primordial core (rock plus ice) overlain by a shell of hydrous and hydrated silicates, which is in turn overlain by a liquid water mantle. Fine silicate particles may remain suspended in the water. Rock and ice components, of course, are selected on the basis of mean density, surface spectral reflectance, and cosmogonic abundance.

Radiative cooling at the surface results in an ice shell, which, as it grows, begins to convect (in the solid state) in the lower portion. Heat loss is efficient and this liquid mantle solidifies from the top and bottom on a characteristic timescale of $\sim 10^8$ years. Radiogenic heating and conduction allow the intermediate silicate shell to move into the core on the same timescale.

Alternate schemes may be proposed. The above conception for Ganymede remains essentially unchanged when the effects of accretion *within* the circum-Jovian nebula are considered (2). Convective transport to the nebula may be sufficient to largely *prevent* melting in Callisto, however, if the ice is solely $H_2O$. While no theoretical model of planetary accretion can be considered as the last word, these various proposed structures are subject to quantitative tests.

## The Impact Experiment

Once a planetary surface is sufficiently stable to preserve a cratering record, these craters may be used to probe the thermal structure of a planet or satellite. The largest craters are the

deepest probes. The record of impact on Ganymede and Callisto and the tectonic signatures left behind, allows several important deductions to be made about their mantles (3,4).

(1) *Neither mantle was predominantly liquid by the end of "terminal bombardment".* Models of water mantles overlain by thin ice shells were popular in the days before solid state convection. The creation of a multi-hundred kilometer diameter crater (transiently tens of kilometers deep) in such a mantle (Fig. 1a) will result in *multiple* oscillations of the cavity region [This is intuitively obvious, and has been observed in Pacific NE tests (5)]. These oscillations will propagate outward, fragmenting the ice shell , which I term the *lithosphere* (a mechanical definition). This pattern of break-up is not seen anywhere on the satellites. All the great multiringed structures are wholly concentric.

(2) *The multiringed structures are evidence for thin, weak lithospheres at the time of impact.* If the relaxation of the transient basin cavity is restricted to a single phase of inward extension, then concentric faults will be formed at the expense of radial ones (Fig. 1b). The observational *evidence* for extension, in the form of graben or normal faults, is clear. The above restriction implies that the sub-lithospheric mantle, or asthenosphere, must be very viscous compared to liquid water, but much more "fluid" than ice would be at the surface. Ice capable of convecting in the solid state fulfills this requirement (6). There is no way for stresses to be propagated so many crater radii away (say, from Valhalla on Callisto), without using a thin, weak lithosphere as a stress guide.

(3) *Callisto's lithosphere was thicker at an earlier time than Ganymede's.* The ages are derived from crater densities on the Valhalla palimpsest and superposed on the Galileo Regio (Ganymede) furrows. Furrow (or graben) widths give an upper limit to the thickness of the elastic(-plastic) lithosphere. As the entire lithosphere is in extension, the graben probably do "root" in the asthenosphere, in the manner of the Baikal and Rhinegraben rifts. The thickness ratio ($\gtrsim$1.5-2.0) significantly exceeds that given by radiogenic heat flow (1.26). Ganymede may have had a greater complement of secular cooling, continued differentiation, or tidal dissipation (7). Alternatively, the functional dependence of rheology on temperature for the two mantles may be different. Callisto's mantle may be dirtier.

The ring graben of Galileo Regio (and Marius Regio) are large remnants of a former concentric system. There is no observable transition to outward facing scarps with increasing radial distance as with Valhalla. On the other hand, the outer rings of the main Asgard multiringed structure appear to be graben (8). Whether a lithospheric block is rotated inward,outward (with respect to the collapsing crater), or at all, depends on the sign of the force couple

between the lithosphere and asthenosphere. The evaluation of this couple, for different scales of impact, different lithospheric thicknesses and strengths,and various internal models will take detailed numerical study. However, the problem *is* well posed.

(4) *The ring structure of Gilgamesh and the lack of rings for more recent craters imply a gradual thickening of the lithosphere with time.* Lithosphere thickness estimates for Gilgamesh are more model dependent, but range between ~75-100km. The present day limit for the lithosphere thickness of both bodies is probably $\gtrsim$150km. Unfortunately, no suitably large impactors are available to fully test the present day rheological structure.

These observations provide tie points for evaluating thermal evolution calculations. The topography of smaller craters, for which reasonable initial profiles can be estimated , is also a very important tool in modeling the thermal history of the lithospheres and upper mantles of Ganymede and Callisto. Several groups are engaged in this endeavor.

That the surface of Ganymede stabilized (with respect to crater retention) so much later than Callisto's is in itself a very important observation. Prior to this time, no meaningful lithosphere existed on Ganymede. The record of *endogenic* processes from the time of accretion to the formation of the furrows in the ancient, dark terrain (which as the first major tectonic event marks the formation of the lithosphere) is likewise lost. The evidence for endogenic tectonism since this time on Ganymede, and on Callisto, is considered in the following abstract.


References

(1) Schubert G., Stevenson D.J. and Ellsworth K. (1980) Icarus, in press.
(2) Lunine J.I. and Stevenson D.J. (1981) Icarus, submitted.
(3) McKinnon W.B. and Melosh H.J. (1980) Icarus 44, 454-471.
(4) Melosh H.J. (1981) J. Geophys. Res., in press.
(5) Glasstone S. (1957) The Effects of Nuclear Weapons, U.S. Government Printing Office (Washington).
(6) Goodman D.J., Frost H.J. and Ashby M.F. (1981) Phil. Mag. A43, 665-695.
(7) Cassen P.M., Peale S.J. and Reynolds R.T. (1981) In The Satellites of Jupiter, in press.
(8) McKinnon W.B. (1981) Proc. Conf. Multi-ring Basins, in press.


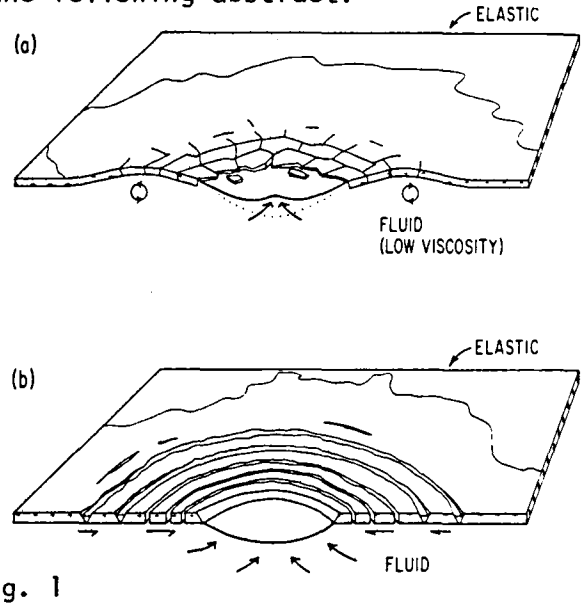


Fig. 1

# GEOPHYSICAL EVOLUTION OF GANYMEDE AND CALLISTO II

William B. McKinnon, Lunar and Planetary Laboratory, University of Arizona, Tucson, Arizona 85721

## Endogenic Tectonism

Grooved terrain on Ganymede can be reasonably ascribed, in part, to endogenic tectonism. Yet there is no feature I can discern in Voyager photographs of Callisto that is not an impact ring structure or secondary crater chain. The *problem* is to relate surface morphology to internal activity. If we fully understood the formation of grooved and smooth terrain, our task would be simplified. However, this is not possible at present. We therefore step back and ask some simpler questions which thermal models can answer.

Volume changes due to thermal evolution are calculable. The surface will respond tectonically to those volume changes, provided a lithosphere exists. The present consensus is that grooves are formed predominantly by extension [e.g., (1)]. This conjures up, in the minds of some, visions of an expanding Ganymede (somewhat analogous to the expanding earth model of continental drift). It should be obvious that extension is not predicated on global expansion alone. In fact, severe limits can be put on its ability to influence grooved terrain formation.

Galileo Regio is the largest and most prominent unit of dark, ancient, heavily cratered terrain on Ganymede. It has undergone very little structural alteration subsequent to furrow formation (unlike the rest of the planet). Its survival as an intact lithospheric unit during the era of grooved terrain formation constrains the concomitant expansion of Ganymede, if any, to be less than 1% in radius (2). This limit is derived from an analysis which considers Galileo Regio to be a thin, freely floating, elastic spherical shell on an expanding planet (Fig. 1). The difference in stress levels between a large spherical cap such as Galileo Regio and an intact spherical shell, for a given radius increase, is an order of magnitude. Thus Callisto's expansion is safely limited to 0.1%, since the formation of its lithosphere (which is notably older than Ganymede's).

As expansion-induced stress in a lithospheric plate scales as $d^2$ where d is the diameter, the "1% solution" severely limits the stress available to fracture small units of Ganymede's "crust". The progressive tectonism (from greater to finer scale) described by (3) is clearly being accomplished, in the main, by regional and local sources of stress. A one-plate planet under compression remains so. Under expansion it becomes a multi-plate planet. Its ability to respond tectonically to further expansion is greatly reduced.

These as yet undescribed regional stress sources are absent on Callisto. The rupturing and *extension* of the lithosphere following large impacts did not result in great circular areas of grooving. An appeal to "convection" also fails as the lithosphere thicknesses (discussed in the previous abstract) were comparable and thin. *Grooved terrain formation was a distinct episode on Ganymede.* The evidence for extensional tectonics is compelling. Coupled with evidence for shear and compression, and the breakup of the lithospheric shell into discrete units, can we not say that a form of "plate tectonics" operated on Ganymede. The details may be very different from the terrestrial version, i.e., there need not be any subduction.

In terms of thermal evolution, the models described in the previous abstract predict slow differentiation of an ice-silicate lower mantle and continued core growth during the era of grooved terrain formation. The moderate planetary expansion generated is probably compatible with the 1% limit. The 0.1% limit for Callisto stringently constrains Callisto's initial configuration, but the detailed modeling necessary has not been performed.

In order to provide an energy source for grooved terrain formation, I have proposed an extension of the model for the Ganymedean interior (Fig. 2). Core heat should be channelled into hydrothermal systems which operate intermittently in space and time. The viability of such a scenario would be enhanced if the core itself could supply heat convectively. The thin boundary layer flow arising from such strong (and local) heating from below could act as a source of stress and "extrusible" material. Callisto's core would have to be small enough to prevent a similar situation from developing.

Clearly there is room for more quantitative work. A major issue that has been skirted so far concerns the nature of the material that makes up the smooth and grooved terrains. Was it emplaced as liquid water, a solution of water and a more volatile substance, or subsolidus ice? The answer from surface morphology is unclear. Liquid water will have considerable difficulty rising diapirically through less dense ice I.

References

(1) Lucchitta B.K. (1980) Icarus 44, 481-501.
(2) McKinnon W.B. (1981) Proc. Lunar Planet. Sci. Conf. 12th, in press.
(3) Golumbek M.P. and Allison M.L. (1981) Geophys. Res. Lett., in press.

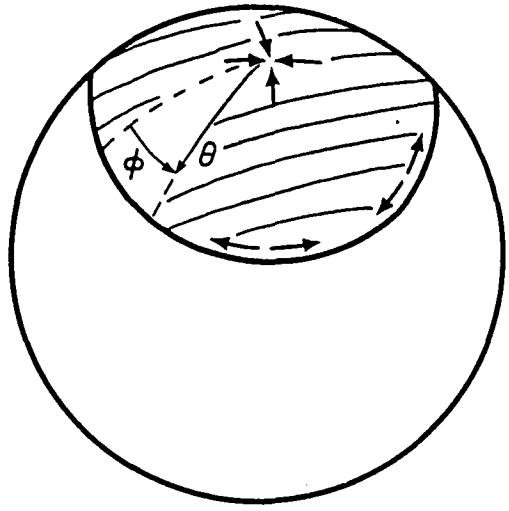


Fig. 1. Ganymede and Galileo Regio lithospheric shell. Coupled arrows denote expansion stress.

GANYMEDE

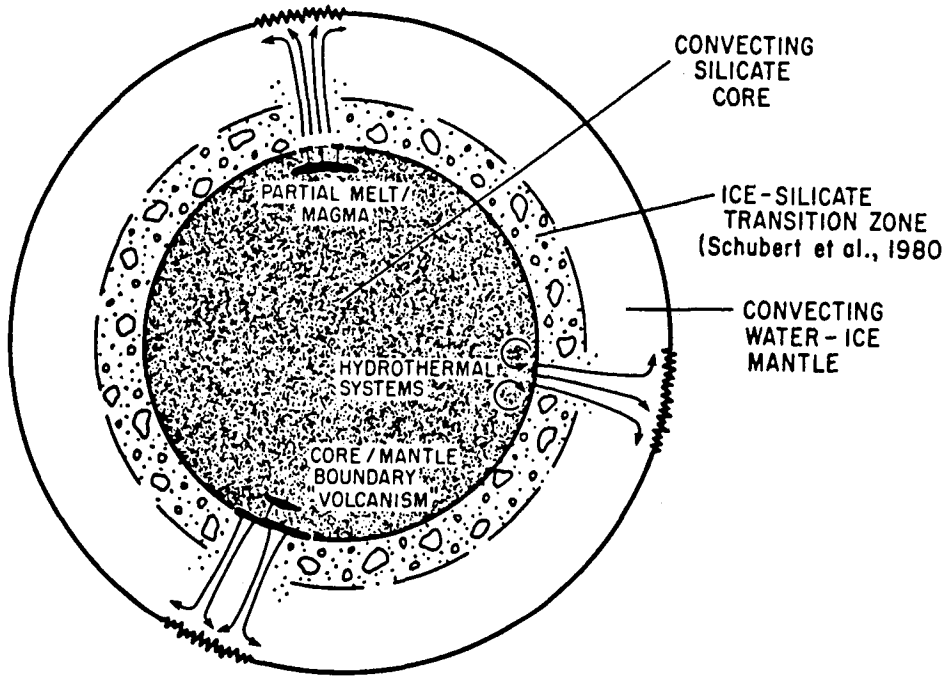


"GROOVED TERRAIN" TECTONICS —
DUE TO SUPER-ADIABATIC MANTLE CURRENTS ?

Fig. 2

GEOPHYSICAL EVOLUTION OF GANYMEDE AND CALLISTO III

William B. McKinnon, Lunar and Planetary Laboratory, University of Arizona, Tucson, Arizona 85721.

Grooved terrain is not the only heated controversy.

## The Cratering Record

In summary, the following statements cannot all be true.

*(1) "Hard", frictional crater scaling laws (1) can be extended to basin sizes.* Indeed, cratering efficiency is expected to increase more rapidly than predicted, if only because laboratory calibration does not occur at high enough velocity to create much $H_2O$ vapor. Preliminary calculations (2) determine that copious quantities ($\gtrsim$20%) of superheated steam are available to do work. However, the cratering efficiency should be less than that for liquid water.

*(2) The lithospheres of Ganymede and Callisto were tidally locked during terminal bombardment.* In fact, the formation of large impact craters very probably broke their synchronous lock with Jupiter. As the $C_{22}$ term dominates the rotational potential (Fig. 1), synchronicity may (in some cases) be reestablished with a 180° rotation about the c-axis. Calculation of the rotational energy imparted by the creation of Valhalla (3) shows that it generally, significantly exceeds the energy in the $C_{22}$ term, given the uncertainties in initial conditions and crater scaling (Fig. 2). The case for Gilgamesh is not very favorable due to its smaller size and distance from the rotation axis, and Ganymede's closer position to Jupiter.

Callisto's lithosphere is old enough for numerous large body impacts to have affected it. Stochastic reorientation of the lithosphere during the establishment of the cratering record tends to equilibrate the otherwise differing crater densities at the apex and antapex of orbital motion (4). This equilibration is scale dependent. The present antapex hemisphere should have a slightly older crater population; one exhibiting an enhancement of viscous relaxation effects. This leads to depletion of large craters with respect to the apex, but comparatively little difference in the small crater densities, *as is observed.*

Ganymede's lithosphere is young enough that the present cratering record is unlikely to have been affected by re-orientation. Crater counts in the oldest dark terrains *can* be interpreted as being consistent with the predicted apex-antapex crater density difference (5).

(3) *There was a large population of basin-forming objects.* Controversy centers around work which deduces a paucity of such objects (6).

While all of the above cannot be true, any pair is compatible. They may be mixed and matched to suit the reader's prejudices. This may also be taken as a cautionary note should one attempt to deduce thermal history from crater density alone.

References

(1) Schmidt R.M. (1980) Proc. Lunar. Planet. Sci. Conf. 11th, 2099-2128.
(2) McKinnon W.B. (1981) Bull. Am. Astron. Soc. 13, in press.
(3) McKinnon W.B. (1981) Eos Trans. AGU 62, 318.
(4) Shoemaker E.M. and Wolfe R.G. (1981) In The Satellites of Jupiter, in press.
(5) Plescia J.B. and Boyce J.M. (1981) Eos Trans. AGU 62, 317.
(6) Woronow A. and Strom R.G. (1981) Geophys. Res. Lett. 8, 891-894.

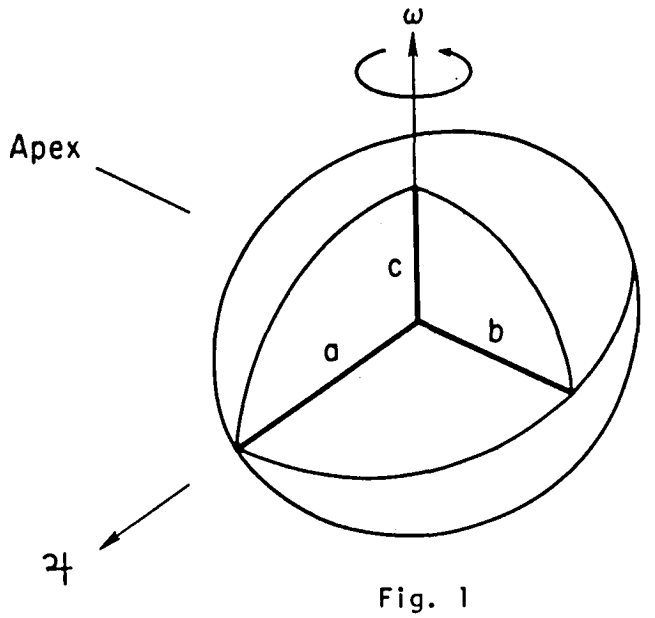
ω
Apex
c
a
b
2f

Fig. 1

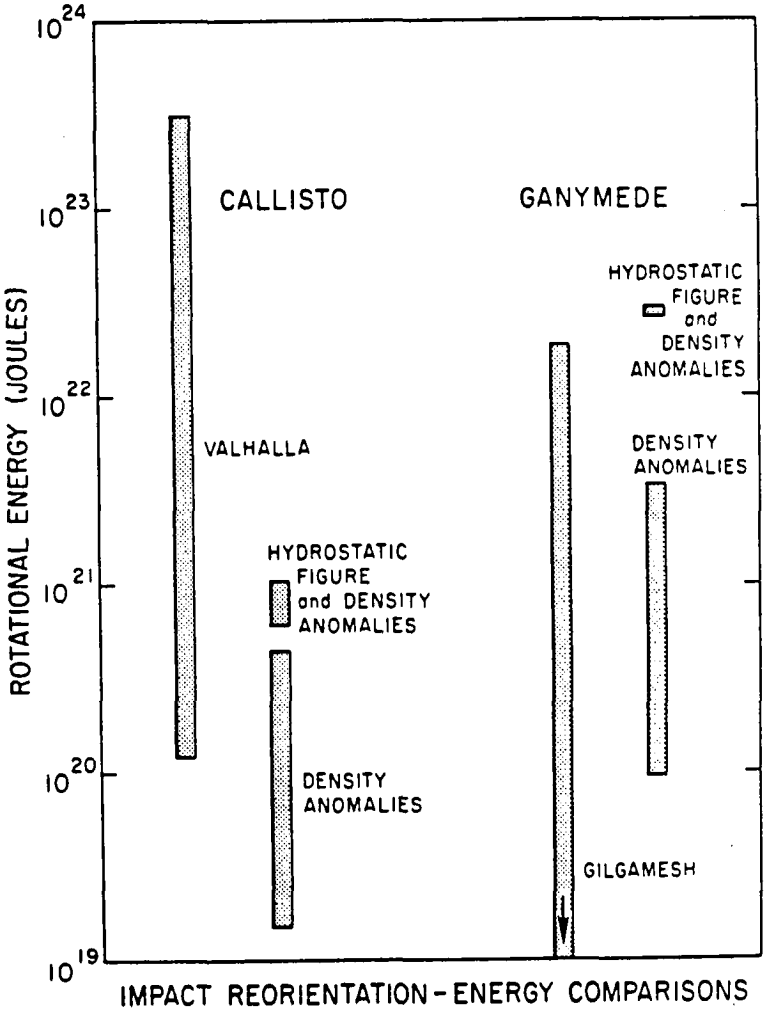
ROTATIONAL ENERGY (JOULES)
10^24
10^23
10^22
10^21
10^20
10^19
CALLISTO
GANYMEDE
VALHALLA
HYDROSTATIC FIGURE and DENSITY ANOMALIES
DENSITY ANOMALIES
HYDROSTATIC FIGURE and DENSITY ANOMALIES
DENSITY ANOMALIES
GILGAMESH
IMPACT REORIENTATION - ENERGY COMPARISONS

Fig. 2

# Crater Obliteration by Relaxation is NOT an Important Process on Callisto

Alex Woronow and Robert Strom, Lunar & Planetary Lab, University of Arizona, Tucson, AZ 85721

The Gallelian satellites have an obvious dearth of large impact craters relative to the lunar highlands. This fact is widely accepted. However, the reason for the lack of large impacts has become a matter of considerable debate. One school holds that large impacts were once present, but the relative mobility of the ice allowed the craters to undergo complete relaxation-obliteration. This is the most popular explanation because it allows inference of thermal, viscosity, and general geologic histories for these bodies by presuming a lunar-like impact size-frequency distribution function and impact flux history. The term coined to refer to craters which are gone without a single trace is "cryptopalimpsests". The only evidences for their existence are 1) the palimpsests (craters with highly relaxed topography and high albedo surroundings) exist on Ganymede; and 2) The observation that some craters exhibit morphologies likely to represent partial relaxation of their topography on Callisto.

We contend that it is a great extrapolation from these observations to the contention that craters on Callisto, in particular, could have disappeared completely in such large numbers as is required. First, high frequency topographic features relax relatively slowly; even the palimpsests on Ganymede have obvious rim and floor features proximal to their centers. Second, the palimpsests on Ganymede have associated high albedo features which would also have to be obliterated and no processes for that have yet been proposed. Third, no clear cases of palimpsests, as defined for Ganymede, have been identified on Callisto.

A simple alternative contends that the bodies responsible for the Callisto impact record intrinsically lacked large members relative to a population like that responsible for the late heavy bombardment in the inner solar system. This hypothesis is now supported by crater population simulations which demonstrate that a lunar-highlands impact history coupled to extensive relaxation-obliteration could not have lead to the areal distribution of craters observed on Callisto (1). A surface undergoing the required relaxation-obliteration would display a patchy areal distribution of craters: sites of relaxed large craters (cyrptopalimpsests) would commonly be recognized by the small number of superposed craters whereas intercryptopalimpsests regions would have dense clusters of craters. (Complete illustration of this is given in reference 1, along with descriptions of the modeling technique.) We have

been unable to identify any regions on the surface of Callisto that have this attribute to the degree required (and all regions on Callisto would have to be that way).

The only way to circumvent this finding would be to presume that all large impacts occurred very early, compeletely relaxed, and were all recratered to a nearly uniform level. This time sequence is, however, inconsistent with the record of cratering on the Moon. Therefore, either the impacting population affecting the outer solar system was different in that it intrinsically lacked large bodies, or it was different in that the large bodies were all swept up early. We believe that the former is the more physically plausible explanation.

In either case we must accept the conclusion that we can not transfer ages from the inner to the outer solar system, can not deduce viscosity or thermal histories from craters that are not there, and can not attribute the late heavy bombardment of the inner and outer solar system to the same impact population (such as comets).

We would like to add one word of warning to those who will still seek the patchiness we cannot find in order to prove the existence of "cyrptopalimpsests". Although the existence of cryptopalimpsests demands the existence of patchiness in the crater population the converse does not follow; namely, patchiness does not uniquely demonstrate the existence of cryptopalimpsests. Because these features have been endowed with the strange and convenient attribute of leaving no traces, any similarly mystical process could also fulfill the null observations. Cleary, cryptovolcanic flooding may work, as may any type of cryptoerosion or cryptodeposition. Once the net is down, tennis is easy.

References: (1) Woronow and Strom, Geophys. Res. Lett., 8, 891, 1981.

# Chapter 3

# CRATERING PROCESSES AND LANDFORM DEVELOPMENT

## MARTIAN EJECTA FLOW CRATERS

*V.M. Horner and R. Greeley, Department of Geology, Arizona State University, Tempe, Arizona 85287*

Flow-like forms on the ejecta blankets of some martian craters were suspected from study of high resolution Mariner 9 images (1). Interpretation of these features as representative of a flow instead of erosion was substantiated and greatly amplified by analyses of Viking images (2). Several morphologic expressions of the flow-like ejecta (2, 3, 4 and others) are observed. Ejecta flow craters exist globally and in all terrains (5). Three lines of research provide data on martian ejecta flow craters: photogeologic studies, impact experiments and theoretical modelling. The objective of this review is to synthesize the research carried out on the martian ejecta flow craters.

Most photogeologic studies involve the classification of ejecta morphologies (Table 1). It is generally considered that morphologic types represent different degrees of fluidization of the ejecta. Most researchers agree that there is a continuum of ejecta flow morphologies from the most fluid–usually taken to be the thin, multilobate ejecta flows–to the dry, lunar-mercurian ejecta deposits (2, 3). It is also generally accepted that ejecta flow is the result of impacts into a volatile-rich target, although there is still disagreement on the details of the emplacement. An alternate viable explanation for the emplacement of the outer lobes of multilobate ejecta flow craters involves the interaction of ejecta particles below a given size with the martian atmosphere (6, 7). These particles would be aerodynamically decelerated and emplaced as a flow *after* the ballistic emplacement of larger ejecta closer to the crater rim.

Assuming that different ejecta morphologies reflect differences in near-surface volatilization, the volatile content of different geologic units and/or latitudes may be characterized by the predominant crater ejecta morphology. Some investigators have found differences in proportions of crater ejecta types among geologic units (3, 9). However, perhaps because of differing data bases, there is no general agreement on the relative proportions which characterize a given terrain. Although early studies suggested that 'fluidity' of ejecta blankets increased poleward (4), other studies did not find this correlation, or found it only for the pedestal craters (3 and others). A later study of latitude dependencies of ejecta flow craters, taking into account the terrain type, is in progress (8), and early results confirm the latitude dependency of ejecta fluidization. Although very little has also been done concerning the effect of elevation on ejecta morphology, there are indications that the fluidity of martian crater ejecta decreases with increasing elevation (3). From our studies of martian ejecta flow craters, the interior morphology of these craters seems more indicative of terrain type than crater ejecta morphology; however, a rigorous analysis has not yet been reported.

Recent attention has focused on the morphometry of ejecta flow craters and include analyses of the ratio of ejecta area to crater area (10), the ejecta mobility ratio $r_e/r_c$ (3, 9). However, the various measures of ejecta flow distances adopted by researchers are so dissimilar in their reported usage that comparisons among authors is difficult.

A recent development has been the extrapolation of martian ejecta flow studies to large craters and basins (11 and others). Early results suggest that larger impacts 'punch through' the volatile-rich layer, as the crater is surrounded by a complex combination of lunar-mercurian and martian-style ejecta. Depth/diameter relations change for martian craters larger than about 50 km (12), supporting indications that the volatile-rich layer ends at depth.

The second approach to the study of martian ejecta flow craters involves experimental impacts into viscous media. The first of these experiments was a qualitative effort (13) that established its applicability to the observed martian ejecta flow morphologies. By varying the

viscosity of the target material, some of the observed ejecta morphologies could be modeled. Later experiments (14, 15) controlled viscosity more quantitatively and illustrated the non-negligible effects of multilayered targets on the final ejecta morphology. Experimental impact studies (15) are the basis for one hypothesis of martian crater ejecta emplacement. The impact causes oscillations of the crater material, which rebounds from the impact in a cycle from a central mound to a central pit, back to a central mound. The number of oscillations would depend on the energy of the impact. The collapse of each central mound would send increasingly smaller pulses of material over the crater rim so that the farthest lobate deposits represent the ballistic deposit, and the inner lobes correspond to the pulses of material emplaced in response to the impact site oscillations. Impact experiments have also validated the theoretical calculations which involve aerodynamic drag acting on ejecta particles smaller than some critical size (6) to produce outer ejecta lobe deposits.

Theoretical models and computer simulations constitute the third approach to the study of martian ejecta flow craters and is critical to the understanding of the process of ejecta emplacement. As yet, no one hypothesis has gained general acceptance. One theoretically derived model for the outer lobe deposit of multilobate ejecta involves a multilayered target with the second layer being volatile-rich relative to the one above (9). Penetration of the shock wave into the second layer would generate a volatile-rich ejecta cloud which collapses and, being highly mobile, scours the earlier, inner ejecta deposit representing the volatile-poor top layer, and settles somewhere beyond the first ejecta deposit. Recently a method for estimating the water content of a region by a modeling of preflow stresses in the ejecta flow blanket just before mechanical failure has been derived and simulated by computer (16). It was assumed that each episode of failure as the ejecta flowed from the impact would produce a lobate ring.

Current research involving martian ejecta flow craters is heading in two major directions. The first involves an extrapolation of the data base of ejecta flow craters to larger craters ($>$ 100 km) and basins on Mars. The second is an ongoing attempt to better define the major variables (terrain type, impact energy, latitude, etc.) that contribute to ejecta blanket morphologies and to determine to what degree they influence the final morphology.

## REFERENCES


1. *J.W. Head and R. Roth, 1976. Papers presented to the Symposium on Planetary Cratering Mechanics, Flagstaff, AZ, 50-52.*
2. *M.H. Carr et al., 1977. J. Geophys. Res. 82, 4055.*
3. *P.J. Mouginis-Mark, 1979. J. Geophys. Res. 84, 8011.*
4. *L.A. Johansen, 1979. NASA TM 80339, 123 (abstract).*
5. *C.C. Allen, 1979. Icarus 39, 111.*
6. *P.H. Schultz and D.E. Gault, 1979. J. Geophys. Res. 84, 7669.*
7. *P.H. Schultz and J. Singer, 1980. Proc. Lunar Planet. Sci. Conf. 11th, 2243.*
8. *R.S. Saunders and L.A. Johansen, 1980. NASA TM 82385, 150 (abstract).*
9. *P.J. Mouginis-Mark, 1981. Icarus 45, 60.*
10. *P. Mutch and A. Woronow, 1980. Icarus 41, 259.*
11. *P.J. Mouginis-Mark and B.R. Hawke, 1981. Lunar Planet. Sci. Conf. XII, 732 (abstract).*
12. *M.J. Cintala and P.J. Mouginis-Mark, 1980. Geophys. Res. Lett 7, 329.*
13. *D.E. Gault and R. Greeley, 1978. Icarus 34, 486.*
14. *Croft et al., 1979. J. Geophys. Res. 84, 8023.*
15. *R. Greeley et al., 1980. Proc. Lunar Planet. Sci. Conf. 11th, 2075.*
16. *A. Woronow, 1981. Icarus 45, 320.*

*17. D. Snyder, unpublished.*
*18. K.R. Blasius and J.A. Cutts, 1980. NASA TM 82385, 147 (abstract).*
*19. K.R. Blasius and J.A. Cutts, submitted to Bull. Amer. Astron. Soc. 13 (abstract).*

*This work is supported by the NASA Planetary Geology Office, Mars Data Analysis Program, through Grant NSG-7548 to Arizona State University.*

TABLE 1. A comparison of martian crater ejecta morphologic classifications, referred to that of Mouginis-Mark, 1979.

| Mouginis-Mark (3) | Snyder (17) | Johansen (4) | Blasius & Cutts (18) | Blasius & Cutts (19) | Mutch & Woronow (10) |
|---|---|---|---|---|---|
| Type 1 | A1 | flower | | SR | |
| | A2 | polar mound | class 4 | SS | lobate |
| Type 2 | B2 | composite | class 3 | DR/s | multilobate |
| Type 3 | B1 | flower | class 2 | | |
| | B3 | | | | |
| Type 4 | C | transitional | | | |
| Type 5 | E | lunar | class 1 | | |
| Type 6 | D | lump | class 4 | | pedestal |

# A SEARCH FOR TERRESTRIAL ANALOGS TO MARTIAN LOBED IMPACT CRATERS

*J.F. McHone and R. Greeley, Department of Geology, Arizona State University, Tempe, Arizona 85287*

Lobate, rampart-edged deposits surrounding martian impact craters have been attributed to the fluid nature of volatiles expanding during ejecta emplacement or to ballistic interactions with an atmosphere (1, 2). Terrestrial counterparts to such fluidized ejecta deposits should also exist on Earth, materials which invoke volatiles during impact are carbonate rocks, water (3), and the atmosphere.

We have searched the literature, summarized in (4 - 8), and satellite images for terrestrial craters with potentially volatile target rocks. Craters in igneous and metamorphic materials were eliminated since volatile-poor crystallines produce massive melt bodies of impact 'lavas', or tagamites (9, 10). Forty-four terrestrial craters were found to contain potential volatiles in the form of carbonates or porous sedimentary rocks capable of storing water at the time of impact.

**Impact Effects in Sedimentary Targets.** The craters in Table 1 reveal at least four trends in sedimentary rocks which differ from impact effects observed in crystalline targets: 1) reduced melt production, replaced in part by suevites; 2) reduced shock metamorphism; 3) increased ductile, rather than brittle, target deformation; and 4) fluidized ejecta deposits. During impact expanding volatiles disperse melt materials as finely divided 'impact ash' resulting in the clay-rich, thermally altered breccia *suevite* (3). Porosity in laboratory and natural (11, 12) impact targets alters the progressive sequence of shock metamorphism effects observed in homogeneous crystalline rocks (13). Pronounced shock wave attenuation and irregular propagation due to pore-space collapse and grain-edge interactions may interrupt development of microscopic shock features. As a consequence, craters formed in porous sedimentary rocks may fail to display conventional criteria of shock history. Non-brittle rock deformation, common at impact sites, are best observed in sedimentary rocks and may be the result of lower target competence. It has been noted, however, that it is difficult to recognize impact-induced deformations in crystalline rocks which typically have undergone several episodes of folding prior to the impact event (14). In general, strongly contorted sediments at impact sites (e.g., Riachao, Tin Bider, Uvalde, Wetumpka) contain only weakly developed (if any) microscopic shock indicators.

**Possible 'Lobed' Terrestrial Crater.** Ejecta units are the first impact feature to be attacked by erosion and no Earth crater larger than 0.5 km dia (i.e., no *ancient* crater) still possesses an intact surface morphology. However, satellite images (Fig. 1) show distinct lobe-like patterns radiating from a central bowl at Zhamanshin, USSR. This feature has been described recently (15, 16) as a 5.5 km impact crater circled by a breccia ring up to 11 km across. Former volatiles are evidenced by the presence of suevite-like rocks and frothed 'pumices' in the underlying sedimentary target rocks. Topographic lobes extend as much as 5 km beyond the debris units and are mapped as undisturbed sedimentary rocks capped by occasional ejecta remnants. They are not true flow units but may be the partially preserved 'shadows' of former armored ejecta lobes resembling those suggested for some martian pedestal craters (17).

## REFERENCES

1. *P.J. Mouginis-Mark, 1978. Nature 272, 691-694.*
2. *D.E. Gault and R. Greeley, 1978. Icarus 34, 486-495.*
3. *S.W. Kieffer and C.H. Simonds, 1980. Rev. of Geophys. and Space Sci. 18, no. 1, 143-181.*

4. *T. Monod, 1965. Univ. Dakar Catalog & Doc. XVII, 94 p.*
5. *J.H. Freeburg, 1969. U.S. Geol. Surv. Bull. 1320, 39 p.*
6. *G.V. Skrynnik, 1977. Solar System Res. 11, no. 4, 161-170.*
7. *J. Classen, 1977. Meteoritics 12, no. 1, 61-78.*
8. *R.A.F. Grieve and P.B. Robertson, 1979. Icarus 38, 212-229.*
9. *M.R. Dence, 1971. J. Geophys. Res. 76, no. 23, 5552-5565.*
10. *V.L. Masaytis, 1980. Geologia Astroblem, Leningrad, 231 pp. (in Russian).*
11. *R.B. Schaal, F. Horz, T.D. Thompson, and J.F. Bauer, 1978. Proc. Lunar Sci. Conf. 10th, 2547-2571.*
12. *B.P. Robertson, 1980. Lunar and Planet. Sci. Conf. 11th, 929-934 (abstract).*
13. *D. Stöffler, 1971. J. Geophys. Res. 76, no. 23, 5541-5551.*
14. *P. Lambert, J.F.Jr. McHone, R.S. Dietz, M. Briedj, and M. Djender, 1981. Meteoritics 16 (in press).*
15. *P.V. Florensky and A.I. Dabizha, 1980. Meteoritnyy Krater Zhamanshin, 'Nauka' Press, Moscow, 127 pp. (in Russian).*
16. *V. Bouska, P.V. Florensky, Z. Randa, and P. Povondra, 1981. Meteoritics 16, 171-182.*
17. *J.F. McCauley, 1973. J. Geophys. Res. 78, 4123-4137.*

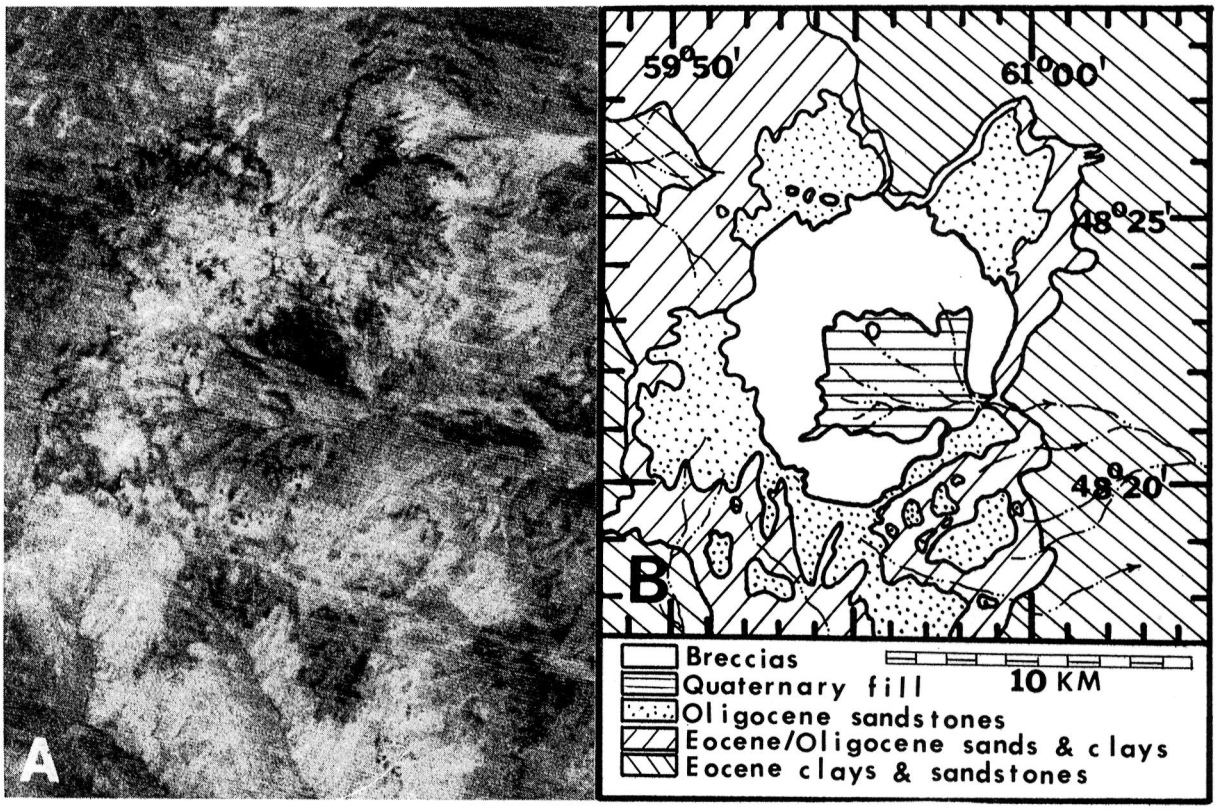


*FIGURE 1. ZHAMANSHIN CRATER, USSR: possible analog to martian multilobed craters. (A) Lobed topographic features radiate from the 5.5 km wide central bowl on Landsat frame 2703-05585-5, 25 Dec 76. Sun elev. 12°, az. 151°. (B) Generalized geology after ref. (15). Coordinates from DMA map ONC F-5.*

TABLE 1. Confirmed and possible terrestrial impact structures with volatile-rich carbonate or porous sedimentary rocks during formation.

| NAME, LOCATION | DIA Km | TARGET LITHOLOGY |
|---|---|---|
| CONFIRMED IMPACT STRUCTURES, shock metamorphism reported. | | |
| Araguainha, Brazil | 40 | Sandstones, Shales over Granitics |
| Barringer Crater, Arizona | 1.2 | Carbonates & Sandstones |
| Beyenchima-Salaatin, USSR | 8 | mostly Carbonates |
| B.P. Structure, Libya | 2.8 | Sandstones |
| Crooked Creek, Missouri | 5.6 | Carbonates & Sandstones |
| Decaturville, Missouri | 6 | Carbonates over Granitics |
| Flynn Creek, Tennessee | 3.8 | Limestones, Dolomites, Shales, Cherts |
| Goat Paddock, WA., Australia | 5 | Sandstones & Siltstones |
| Gosses Bluff, NT., Australia | 22 | Sandstones & Siltstones |
| Haughton Dome, NWT., Canada | 20 | Carbonates & Evaporites |
| Isle Rouleau, Quebec, Canada | 4 | Argillaceous Dolomite |
| Kaluga, USSR | 15 | Sandstone, Siltstones, Marl |
| Kamensk, USSR | 25 | Limestones, Sandstones, Shales, Marls |
| Kara, USSR | 60 | Carbonates & Terrigenous Sediments |
| Kelly West, NT., Australia | 2.5 | Quartzites, Cherts, Silicified Limestones |
| Kentland, Indiana | 13 | Carbonates & Sandstones |
| Kufra Oasis, Libya | 11.5 | Sandstones |
| Liverpool, NT., Australia | 1.6 | Sandstones |
| Manson, Iowa | 32 | Limestones, Sandstones over Granitics |
| Middlesboro, Kentucky | 6 | Sandstones, Conglomerates, Shales |
| Mishina Gora,USSR | 2.5 | Carbonates |
| Ouarkziz, Algeria | 3.5 | Limestones, Sandstones, Marls |
| Oust Kara, USSR | 30 | Carbonates & Terrigenous Sediments |
| Popigai, USSR | 100 | Sandstones, Shales, Carbonates over Gneiss |
| Puchezh Katunka, USSR | 80 | Sandstones, Shales, Carbonates over Granit |
| Redwing Creek, North Dakota | 9 | Carbonates & Evaporites |
| Riachao Ring, Brazil | 4 | Sandstones, Shales, Carbonates |
| Ries Basin, West Germany | 24 | Carbonates, Shales, Sandstones over Granit |
| St. Martin, Manitoba, Canada | 23 | Carbonates over Granite |
| Serpent Mound, Ohio | 6.4 | Carbonates & Sandstones |
| Serra da Cangalha, Brazil | 12 | Sandstones, Conglomerates, Siltstones |
| Sierra Madera, Texas | 13 | Carbonates, Shales, Sandstones |
| Slate Islands, Ontario, Can. | 30 | Basalts & Sandstones over Argillites |
| Spider, WA., Australia | 8 | Sandstones & Siltstones |
| Strangways, NT., Australia | 24 | Sandstones, Siltstones, & Shales |
| Steinheim, West Germany | 3.4 | Carbonates & Sandstones |
| Tin Bider, Algeria | 8 | Argillites, Carbonates, Sandstones |
| Uvalde, Texas | 4 | Shales & Sandstones |
| Wells Creek, Tennessee | 14 | Carbonates |
| Wetumpka, Alabama | 6.5 | Marls & Chalks over Schist |
| Zhamanshin, USSR | 5.5 | Clays, Sands, Marls over Schists & Volcs. |
| POSSIBLE IMPACT STRUCTURES, shock metamorphism not yet reported, strongly contorted sedimentary target rocks. | | |
| Foum Teguentour, Algeria | 5 | Argillites & Sandstones |
| Hico, Texas | 10 | Carbonates & Sandstones |
| Ramgahr, India | 3 | Sandstones |

## EXPERIMENTAL IMPACT CRATERS FORMED IN VISCOUS FLUIDS

*J.H. Fink, Department of Geology, Arizona State University, Tempe, Arizona 85287, D.E. Gault, Murphys Center for Planetology, Murphys, California 95247, R. Greeley, Department of Geology, Arizona State University, Tempe, Arizona 85287*

Craters formed by impact into volatile-rich planetary surfaces such as those of Mars and the icy satellites of Jupiter are affected by the viscosity as well as the cohesive strength of the planetary surface materials. In order to distinguish the effects of target viscosity, surface tension and cohesion on crater dimensions we have conducted a series of 178 impact experiments at the NASA-Ames Vertical Gun Facility. Experimental target materials included water, water with surfactant added to reduce surface tension, carbowax (a polyethylene glycol) and two grades of Dow Corning silicon 200 fluid. Target viscosities ranges over 5 orders of magnitude from $10^{-2}$ poises ($10^{-3}$ Pa-s) to 600 poises (60 Pa-s). Surface tensions ranged from 21 dynes/cm to 72 dynes/cm, and were measured with a capillary surface tensiometer.

Surface tension influences the morphology of ejecta deposits by controlling the ejecta plume angle and the continuity of the ejecta sheets. Crater volumes are reduced slightly by surface tension, but only for craters smaller than 10 cm in diameter. Surface tension effects on ejecta morphology are also negligible for craters larger than a few tens of centimeter in diameter (Moore, MacCormack and Gault, 1963).

Increasing the target viscosity significantly reduces the maximum volume of the craters. For impacts with the same kinetic energy and projectile velocity, an increase in target viscosity of 5 orders of magnitude causes the crater volume to be reduced by a factor of 10. This result is to be expected since the work needed to overcome the target viscosity is no longer available to expand the crater bowl.

These experimental results are being used to help scale the effects of varying concentrations of volatiles in the martian crust on the morphology and dimensions of rampart type impact craters (Fink et al., 1981).

### REFERENCES

*H.J. Moore, R.W. MacCormack, and D.E. Gault, 1963. Proc. of 6th Hypervelocity Impact Symp., vo. II, pt. 2, 367-400.*

*J.H. Fink, R. Greeley, and D.E. Gault, 1981. Proc. Lunar Planet. Sci. Conf. 12th (in press).*

## GANYMEDE RAMPART CRATERS

*V.M. Horner and R. Greeley, Department of Geology, Arizona State University, Tempe, Arizona 85287*

Martian ejecta flow craters illustrate the importance of target conditions (composition, temperature, atmosphere, etc.) on the final crater ejecta morphology. In this context, ejecta morphologies for craters on the outer Galilean satellites reflect impacts into ice-rich targets. Fresh craters are seen on Ganymede which are characterized by an abrupt terminus to the ejecta blanket (1, 2, 3; Fig. 1). Only a single ejecta blanket is seen (2, 4) in contrast to the multilobate ejectas observed on Mars, although this may be due to insufficient resolution. Superposition relations indicate that these craters postdate groove formation in the grooved terrain.

Ninety-seven rampart craters have been identified on Voyager images of Ganymede which were obtained at sun angles greater than 65° and resolutions between 0.56 km/pixel and 1.21 km/pixel. Craters range in diameter from 9 km to 68 km - most are smaller than 40 km - and generally occur on the grooved and smooth terrains. The low albedo and more rugged topography of the dark cratered terrain, however, may hinder the detection of rampart ejecta in those regions.

Craters and ejecta diameters were measured to the nearest 0.5 km. These were assumed to be circular, so that the calculated areas are

$A_c = \pi/4\ d_c^2$ and $A_e = \pi/4\ (d_e^2 - d_c^2)$,

where $A_c$ = crater area, $A_e$ = ejecta area, and $d_{c,e}$ = crater and ejecta diameters, respectively. These areas were then ratioed as $A_e/A_c$ to describe the areal extent of the ejecta normalized to the crater area, as has been done for the martian ejecta flow craters (5). This normalized ejecta area was then examined for possible dependencies with latitude, longitude, and terrain type.

It has been suggested that the extent of fluidized ejecta for the martian ejecta flow craters is dependent on latitude (6, 7, 8). As Ganymede shows evidence of frost at latitudes greater than ± 45° (9) the normalized ejecta areas for craters on Ganymede were examined with respect to latitude. No correlation between ejecta extent and latitude was found. A similar analysis done with longitude also showed no correlation.

There appears to be an increase in $A_e/A_c$ as a function of terrain type, from a relatively shallow slope for the dark cratered terrain, through the smooth terrain, to the steepest slope for the grooved terrain (Fig. 2). This trend, however, is not statistically significant (Table 1).

The present state of observations of the Ganymede rampart craters resembles that of the Mariner 9 imaging of martian 'wind erosion' craters - the unusual ejecta morphologies were just discernable on the highest-resolution images. Two main types of hypotheses were put forward to explain the form of this ejecta: 1) they were the result of post-impact modification; 2) they were formed during or shortly after impact. The fresh appearance of the ganymedian rampart craters precludes formation by the first method, either by erosion or by the viscous relaxation of ice (4).

Any hypothesis for the origin of ganymedian rampart craters must explain a possible dependence on target composition, and $A_e/A_c$ values which are lower than $A_e/A_c$ values for martian ejecta flow craters of similar size. We believe that some ejecta flow process best explains the present observations.

It has been suggested that the grooved terrain represents extruded water/ice (10) and the dark cratered terrain is a mixture of ice and silica or some other contaminant. If true, the extent of an ejecta flow would reflect the relative amount of volatiles within the target terrain.

Cintala et al. have examined the energy partitioning of impacts into ice-rich targets (11, 12). They conclude that, since for a given impact energy: 1) a greater volume of melt is generated from an impact into ice than into basalt; 2) the resulting crater would be 1½ to 3 times larger than one formed in a basalt target; 3) the same amount of energy is partitioned into ejecta movement for both ice-rich and basalt targets; therefore 4) the average ejection velocity must be lower for impacts into ice-rich media than for impacts into basalt. This implies that for a given impact energy, the ejecta must be deposited closer to the crater rim for impacts into ice-rich targets than for those into basalt (silica-rich) targets.

Recent impact experiments show that the ejection angle of material expelled during impact depends partly upon the properties of the target material (13). Steepest ejection angles were observed for impacts into water and became progressively shallower as the viscosity of the targets was increased. As Ganymede probably contains a much greater percentage of near-surface water/ice than does Mars, compositional restraints (neglecting gravity scaling) would result in ejecta placed closer to the rim for Ganymede rampart craters than for martian ejecta flow craters of similar size.

The lower temperature of the ganymedian surface ($\sim$ 100K vs. $\sim$ 270K for Mars) would require more impact energy to be partitioned into heat before the ice melts and would make any water/ice flow more viscous. This constraint would also tend to restrict a ganymedian ejecta flow with respect to a similar flow on Mars. It therefore appears that the low $A_e/A_c$ values for Ganymede with respect to those for Martian craters is the result of a complex combination of surface gravity, temperature, and target composition.

## REFERENCES


1. *R.G. Strom et al., 1981. J. Geophys. Res., in press.*
2. *V.M. Horner and R. Greeley, 1981. Lunar Planet. Sci. Conf. XII, 460-462 (abstract).*
3. *B. Lucchitta, 1980. Icarus 44, 481-501.*
4. *V.M. Horner and R. Greeley, 1981. Submitted to Icarus.*
5. *P. Mutch and A. Woronow, 1980. Icarus 41, 259-268.*
6. *R. Arvidson et al., 1976. Icarus 27, 513-516.*
7. *L.A. Johansen, 1979. NASA TM 80339, 123-125 (abstract).*
8. *R.S. Saunders and L.A. Johansen, 1980. NASA TM 82385, 147-149 (abstract).*
9. *B. Smith et al., 1979. Science 206, 927-950.*
10. *S. Squyres, 1980. Geophys. Res. Lett. 7, 593-596.*
11. *M.J. Cintala et al., 1979. Lunar Planet. Sci. Conf. X, 207-209 (abstract).*
12. *M.J. Cintala et al., 1980. NASA TM 81776, 347-349 (abstract).*
13. *R. Greeley et al., 1980. Proc. Lunar Planet. Sci. 11th, 2075-2097.*



*This work was supported by NASA grant NAGW - 132 in the Jupiter Data Analysis Program through the Office of Planetary Geology.*

TABLE 1. Results and error analysis from the calculation of a power law regression (log Y = a + b log X) for the data sets represented in Figures 3 and 4. N is the number of craters in each data set, a and b are constants determined from power law regression analysis, $\sigma_a$ and $\sigma_b$ are the statistical errors on a and b respectively, and $r^2$ is the square of the correlation coefficient, where values range between 0 and 1, and a value of 1 indicates a perfect curve fit to the data.

| Data Set | N | a | $\sigma_a$ | b | $\sigma_b$ | $r^2$ |
|---|---|---|---|---|---|---|
| Ganymede rampart craters | 95 | 0.62 | 0.08 | 0.88 | 0.03 | 0.88 |
| Grooved terrain | 43 | 0.5 | 0.1 | 0.9 | 0.05 | 0.89 |
| Smooth terrain | 14 | 0.9 | 0.1 | 0.77 | 0.05 | 0.94 |
| Dark cratered terrain | 7 | 1.3 | 0.4 | 0.6 | 0.2 | 0.69 |

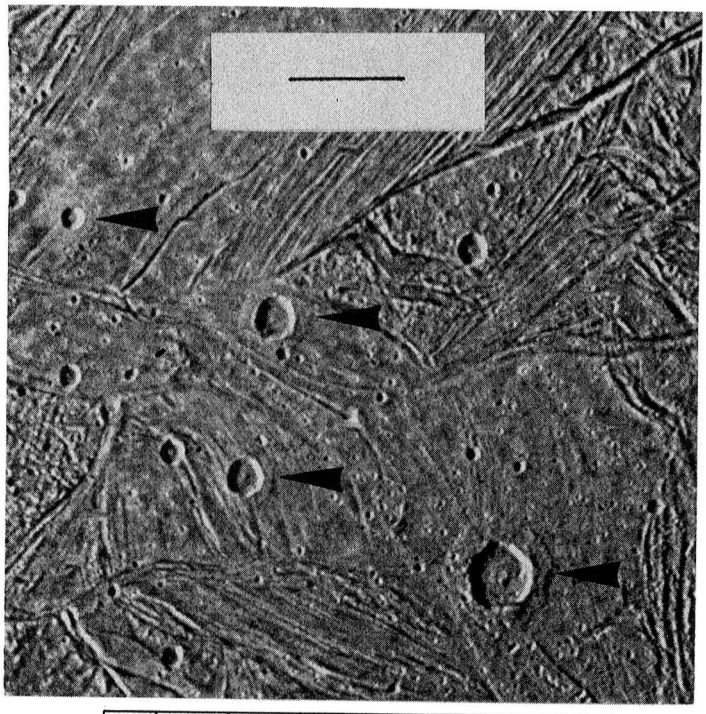

*FIGURE 1. High resolution Voyager 2 image showing several rampart craters (arrows). The scale bar is 50 km.*

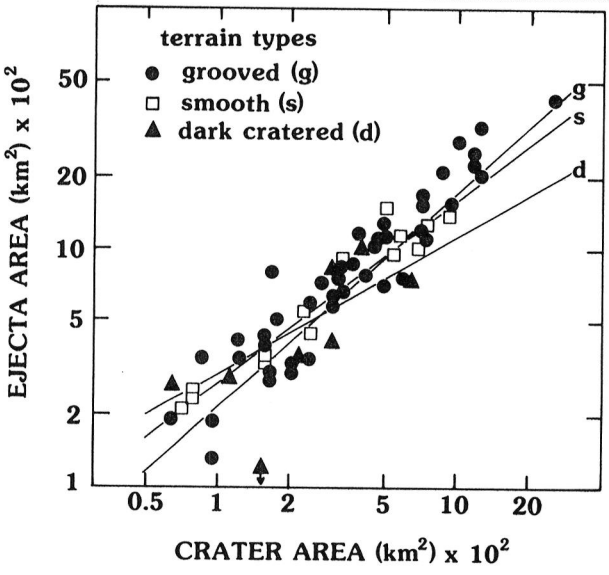


*FIGURE 2. Log-log plot of Ganymede rampart areas as a function of crater areas for the three terrain types discussed in the text: g = grooved terrain, s = smooth terrain, and d = dark cratered terrain. Statistical data for these power law curves (log Y = a + b log X) appear in Table 1.*

# Lobate and Multilobate Ejecta Deposits: A Mechanism for their Emplacement and its Implications for the Water Content of the Martian Subsurface

Alex Woronow, Lunar & Planetary Lab, University of Arizona, Tucson, AZ 85721

Several key observations constrain the possible modes of implacement of lobate ejecta deposits (a single ring of lobes encircling the crater) and multilobate ejecta deposits (more than a single ring of lobes encircling the crater):

A. Deposits occur on terrains of all ages and at all altitudes, indicating insensitivity to atmospheric pressure and target properties.

B. Lobe material ponds behind or is deflected by ridges in its line of flow, indicating a ground or near-ground flow during emplacement.

C. Inner lobes neither interfere with the geometry of outer lobes nor pond material behind their ramparts, indicating that outer lobes were emplaced before inner ones.

D. The surface area covered by the ejecta is proportional to the diameter of the crater to the 1.5 power, consistent with ejecta thickness at the rim being independent of crater size.

E. Contacts among different lobe rings from the same crater are nongradational, indicating a temporally discontinuous implacement process.

We should also presume that in any impact cratering event affecting a solid target, the greatest preponderance of excavated material will be ballistically launched by the rarifaction wave behind the shock front. Atmospheric interactions may subsequently alter the proportion of material landing near the crater rim.

A model where the lobes are emplaced by collapse of the ballistically transported ejecta close to the rim of the crater satisfies all the above constraints. The ejecta, with water from the subsurface, is envisioned as being deposited proximal to the rim until it reaches some critical thickness; the bearing strength near its bottom is exceeded; the mud slides; and radial flows are emplaced. If deposition of the ejecta close to the rim continues after the first slide occurs, subsequent slide may also occur by the identical

sequence of events. Because the earlier slides, being very fluid, tend to level the terrain, the later slides must flow across a more horizontal surface and cannot reach to the distances reached by the first slides (1).

Presuming such a model, one can compute the stress conditions within the ejecta at which failure occured and deduce something of the physical properties of the ejecta. Specifically, if one assumes that the ejecta are largely composed of clays at the time of deposition (2), then by considering a range in failure mechanics from plastic deformation to a quickclay failure, the range of possible water content can be roughly delimited (3). The calculated stress conditions reported below are for the ejecta blanket of a 6 km diameter crater, the smallest craters which regularly display true flow lobes.

Conditions within zone of failure
Shear stress < 500 kPa
Shear stress inclination 45 to 51 degrees
Max. angle of internal friction 26 to 36 degrees

Using these deduced parameters along with empirical relationships derived from experiments on wet terrestrial clays implies amounts of water in the ejecta from 13 to 42 weight percent.

References: (1) Mutch & Woronow, Icarus, 41, 259, 1980. (2) Kieffer & Simmonds, Rev. Geophys. Space Phys, 18, 143, 1980. (3) Woronow, Icarus, 45, 320,1981.

# THE ENERGY LINE: A HEURISTIC MODEL FOR MARTIAN RAMPART EJECTA SHEETS

Michael F. Sheridan, Department of Geology, Arizona State University, Tempe, AZ 85287.

Although the emplacement mechanism for martian rampart ejecta sheets is still poorly understood, there is a general consensus that the role of ballistic transport is minor compared to surface flowage (Carr and others, 1977; Mouginis-Mark, 1978; Schultz and Gault, 1979). Several features of these deposits place constraints on models of emplacement: 1) lobate perimeter with a raised ridge (Carr and others, 1977), 2) shadow zones around raised obstacles (Carr and others, 1977), 3) mantling of subadjacent crater depressions within the ejecta blanket area (Carr and others, 1977), 4) long range of continuous blanket (Mouginis-Mark, 1978), 5) increase in runout distance with crater size (Mouginis-Mark, 1978), 6) nearly uniform deposit thickness of 30-60 m (Mouginis-Mark, 1978), 7) lack of secondary craters within the continuous ejecta field (Schultz and Gault, 1979), 8) surmounting low obstacles but not higher objects (Wohletz and Sheridan, in prep.), 9) transport through low mountain passes (Wohletz and Sheridan, in prep.). The energy line concept, proposed by Heim (1882, 1932) to explain alpine landslides and elaborated by Hsu (1975, 1978), is a quantitative heuristic model compatible with the above characteristics.

The most detailed explanation of the energy line model is given by Hsu (1978) in his explanation of mass transport of landslide material by grain flow. This model, also useful to analyse the emplacement of pyroclastic flows (Sheridan, 1979) and steam blast explosions (Sheridan, 1980), has many applications to many other mass flowage problems. The principal assumption is that an energy line can be drawn connecting the highest elevation of the material before flowage to the toe of the resulting deposit. The tangent of the energy line slope ($\mu$), gravitational acceleration ($g$), and the configuration of the underlying topography are sufficient constraints to calculate the main flow parameters. The elevation of the energy line above the ground surface ($\Delta h$) defines the potential velocity ($v_p$).

$$v_p = (2g\Delta h)^{1/2} \quad (1)$$

The horizontal acceleration ($a_x$) is a function of the topographic slope ($\beta$) and the energy line ($\mu$) (Hsu, 1978).

$$a_x = g(\sin \beta - \mu \cos \beta) \quad (2)$$

The potential velocity and runout times for any part of the flow field can be calculated by equations given by Hsu (1978).

For a simple example, consider the case of a 20 km diameter martian crater with a rampart lobe extending 30 km from the rim. The bulk of the particles comprising the rampart ejecta deposit are probably less than 250 μm in diameter (Sheridan, this publication). The atmospheric drag on grains less than 1 cm diameter would limit the vertical ballistic elevation to less than one half the crater radius (Schultz, 1979), which in this case would be 5 km. A gravity collapse of a density cloud from this height would yield a potential velocity of about 200 m/s, calculated from equation 1. Assuming a level runout surface, the deceleration of the cloud would be $-0.6$ m/s$^2$ according to equation 2. The minimum runout time would be about 300 seconds, similar to that of the Mount St. Helens blast.

This simple model could easily be applied to more complicated two-dimensional situations, or by choosing an appropriate energy surface, to the three dimensional field. From the potential velocity a first-order flow field could be calculated assuming a steady non-viscous flow. Because of the sensitivity of the flows of topography, the limiting constraints for optimum application of the model to an analysis of rampart ejecta is the availability of adequate topographic base maps for many of the deposits.

## REFERENCES


Carr, M. H., Crumpler, L. S., Cutts, J. A., Greeley, R., Guest, J. E., and Masursky, H., 1977, Martian impact craters and emplacement of ejecta by surface flow: J. Geophys. Res., 82, 4055-4065.

Heim, A., 1882, Der Bergsturz von Elm: Z. Deutsch Geol. Ges., 34, 74-115.

Heim, A., 1932, Bertsturz und Menchenleben: Fretz und Wasmuth, Zurich, 218 p.

Hsu, K. J., 1975, On sturzstroms - catastrophic debris streams generated by rockfalls: Geol. Soc. America Bull., 86, 129-140.

Hsu, K. J., 1978, Albert Heim: Observations on landslides and relevance to modern interpretations: in Rockslides and avalanches, vol. 1, Natural Phenomena, B. Voight, Ed., Elsevier, New York, p. 71-93.

Mouginis-Mark, P. J., 1978, Morphology of martian rampart craters: Nature, 272, 691-694.

Schultz, P. H. and Gault, D. E., 1979, Atmospheric effects on martian ejecta emplacement: J. Geophys, Res., 84, 7669-7687.

Sheridan, M. F., 1979, Emplacement of pyroclastic flows--A review: Geol. Soc. America Spec. Paper 180, 125-136.

Sheridan, M. F., 1980, Pyroclastic block flow from the September, 1976 eruption of La Soufriere Volcano, Guadeloupe: Bull. Volcanol., 43, 397-402.

Woheltz, K. H. and Sheridan, M. F., in prep., Martian rampart crater ejecta: experiments and analysis of melt-water interaction.

# MARTIAN CRATER MORPHOLOGY AND EVOLUTION: RADAR RESULTS

R. Stephen Saunders and Ladislav Roth, Jet Propulsion Laboratory, California Institute of Technology, Pasadena, CA 91109.

Topographic profiles of Mars obtained from radar ranging at the Goldstone station have been analyzed to obtain crater depths and rim heights. These parameters, previously available for only a few martian craters (Cintala et al., 1976; Schubert et al., 1977), are needed for process-related studies and comparative planetary studies. Crater rim height data have been used by DeHon (1979) to estimate thickness of lunar mare basalt and by Gregory and Saunders (1981) to estimate the thickness of the ridged plains on Mars. Schubert et al. (1977) used crater rim height, depth and diameter in a model of crater evolution. These new data allow further development of these and other applications. The data are plotted in the appended figures.

We find general agreement with the degradation trends found by Schubert et al. (1977) for martian craters. The greatest uncertainty in applying such models is the initial geometry of the crater. Our preliminary analysis of the data is in agreement with the conclusion of Schubert et al. that the dominant process of crater modification on Mars is filling and rim erosion. Rim erosion is apparently the dominant process. We are in the process of determining the relationship between these parameters and other morphologic parameters indicative of crater age.

The figures contain data that we reduced from the radar profiles for 32 martian craters and for 40 lunar craters measured by Schubert et al.

This work was done under NASA contract.

## REFERENCES

Cintala, M. J., Head, J. W., and Mutch, T. A., 1976, Martian crater depth/diameter relationships: Comparison with the Moon and Mercury: Proc. Seventh Lunar Sci. Conf., v. 3, p. 3575-3587.

DeHon, R. A., 1979, Thickness of the western mare basalts: Proc. Lunar Sci. Conf. 10, p. 2935-2955.

Gregory, T. E., and Saunders, R. S., 1981, Tectonic implications of martian ridged plains: Reports of Planetary Geology Program, NASA TM 82385, p. 93-94.

Schubert, Gerald, Lingenfelter, R. E., and Terrile, R. J., 1977, Crater evolutionary tracks: Icarus, v. 32, p. 131-146.

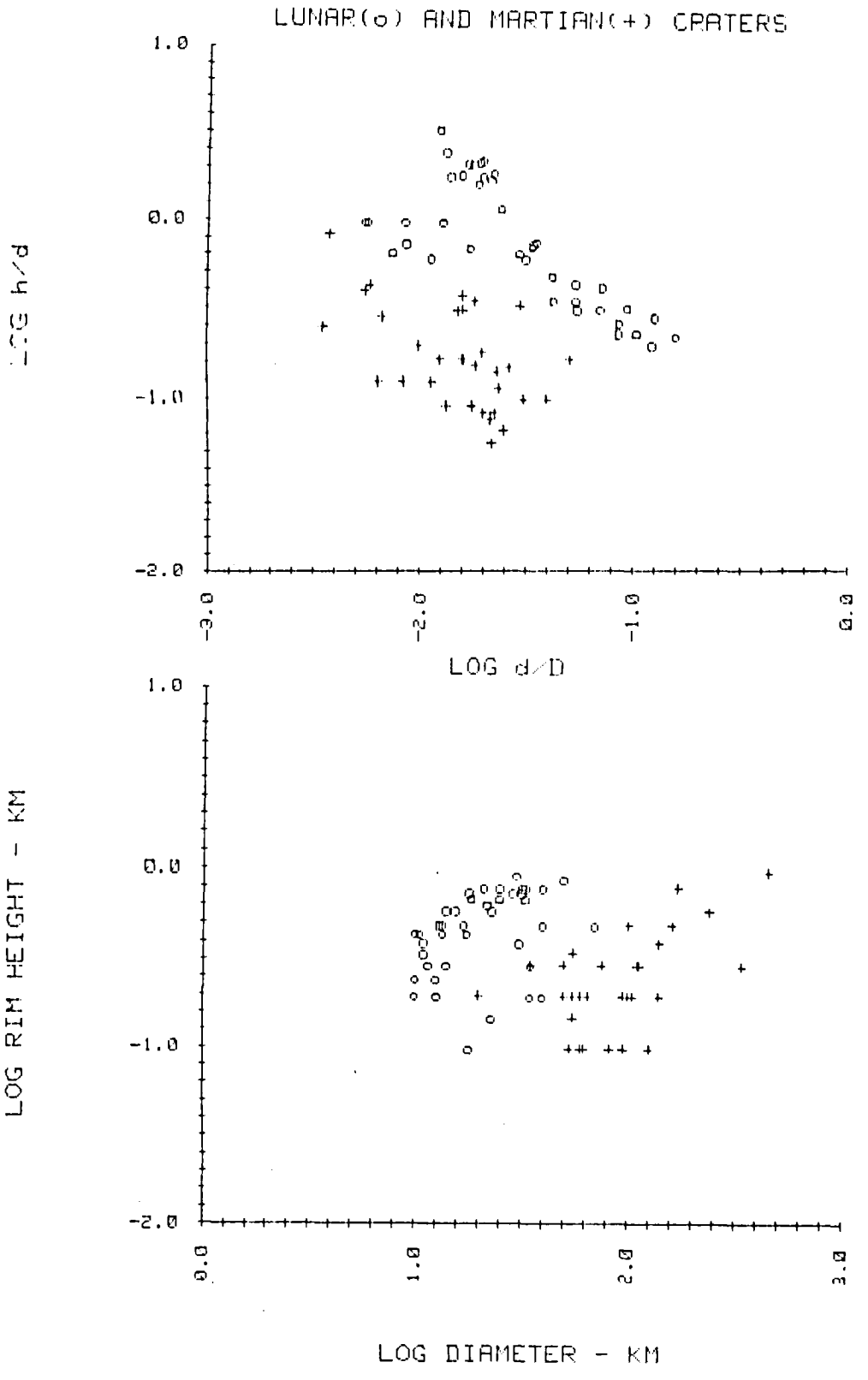
LUNAR(o) AND MARTIAN(+) CRATERS
LOG h/d
1.0
0.0
-1.0
-2.0
-3.0
-2.0
-1.0
0.0
LOG d/D
LOG RIM HEIGHT - KM
1.0
0.0
-1.0
-2.0
0.0
1.0
2.0
3.0
LOG DIAMETER - KM

# The Martian Cratering Record.

Michael Gurnis, Lunar and Planetary Laboratory, The University of Arizona, Tucson, AZ 85721.

With the emergence of the new paradigm that the terrestrial planets were all impacted by the same population of bodies through history (Woronow, et al, 1981) we may approach the problem of the earliest history of Mars with greater confidence. With the clear Viking imagery and new concepts of crater statistics developed by Woronow (1977) we anticipate a greater understanding of the martian cratering record. This study consists of counting craters > 8 km diameter and experimenting with computer models of crater-obliteration.

Thus far crater counts with a high level of precision have been gathered over approximately 30 percent of Mars. The major data sets thus far are: 1. average cratered terrain; 2. pure cratered terrain; 3. post-cratered terrain; 4. post-ridged plains; and 5. post-northern plains. Following the study of Strom (1977), we find that the older units have significantly less negative slopes than the younger units.

The average martian cratered terrain population is compared with the average lunar highlands in Figure 1. The most salient feature of these distributions are the "bends" at similar diameters. The differential slope of the average lunar highlands is -2.15 +/- .03 from 8 to 64 km diameter. Similarly, the average martian cratered terrain has a slope of -2.12 +/- .08 when the 8 to 11.3 km bin is excluded (because of an apparent paucity of craters there). Although Chapman (1974) found that the distribution functions for crater classes of martian craters differed significantly from lunar distribution, we find the concept that the martian terrain coincidentally has a size-frequency distribution so similar to the lunar highlands' hard to accept. Instead, we believe it more cogent to accept the hypothesis that the shape of the martian average cratered terrain resulted from its production function. This suggests that the differences Chapman observed were due to a diameter-independent phase of crater obliteration.

In addition to the shape of the lunar highlands' curve, Strom (1977) recognized that the crater population superposed on the maria had a significantly different slope (-2.67 +/- .10). We also find that the martian post-northern plains has a similar size-frequency distribution (slope = 3.06 +/- 0.7).

The density difference between the lunar and martian highlands (Figure 1) is enigmatic. We explored, via the Monte Carlo method, the effects geologic processes would have on a lunar highland's crater population. Our present model bears many resemblances to that of Woronow's (1977), however, craters were represented as 360°of rim and were obliterated when > 180°of rim was overlapped by subsequent impacts. We also incorporated intercrater plains formation into these models, in which crater obliteration was proportional to crater depth.

The first set of models simulated just intercrater plains in which plain depth and coverage varied temporally. We find that no matter what the form of the obliteration event, the simulated curve lost its shape in an antithetical way to that observed. But when a certain fraction of the plains form in and obliterate older, degraded craters and basins the simulated curve retains its shape. This result is consistent with the morphology of the cratered terrain: intercrater plains are usually circular in plane.

In order to ascertain the timing of crater obliteration with respect to the period of heavy bombardment, we counted the fresh craters which clearly overlie the surrounding terrain. Because of its intermediate crater density, the post-northern plains population (slope = -3.06) was substracted. The resulting population has a slope of -2.27 +/- .03, which is consistent with a formation during the late heavy bombardment (LHB).

Incorporating these results with detailed observations of the fine structure of the cratered terrain, the following scenario of early Mars emerges. During the late heavy bombardment, the cratered terrain was dissected by small valleys. This stage was followed by intercrater plains formation. The plains formed both randomly between craters as well as within older craters and basins. Most of the geologic activity ceased before the LHB ceased.

Chapman, C.R. (1974). Icarus 22, p. 272.
Strom, R.G. (1977). Phys. Earth Planet. Int. 15, p. 156.
Woronow, A. (1977). JGR 82, p.2447.
Woronow, A., Strom, R.G., and Gurnis, M. (1981). Chap. 9 in The Satellites of Jupiter, (D. Morrison Ed.), U of A Press, (in press).

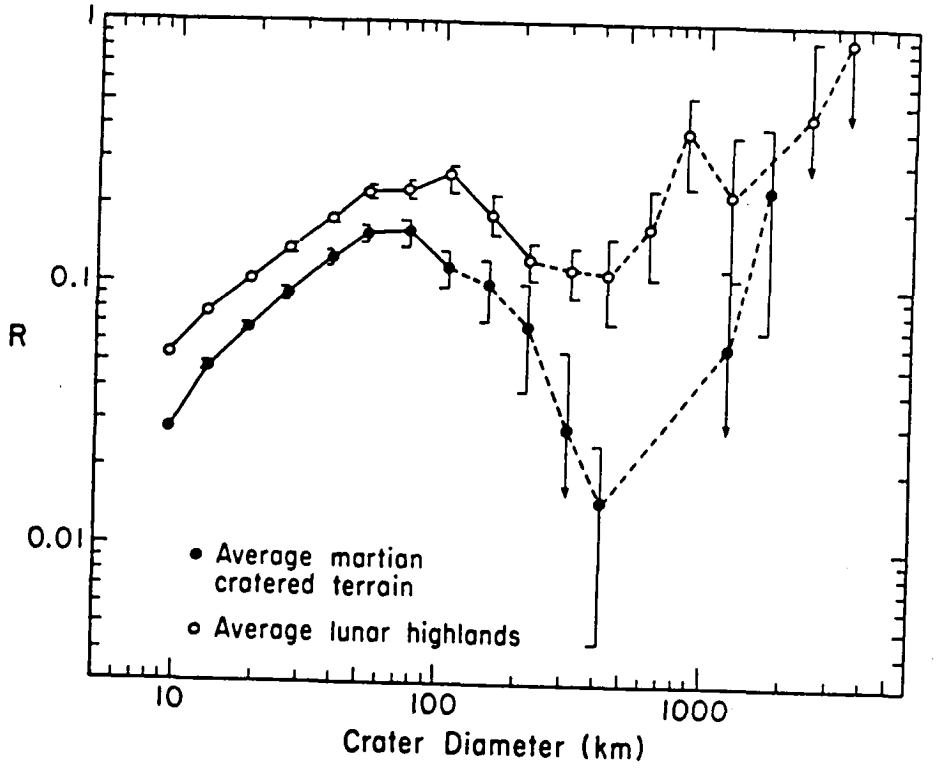

# THREE SIMPLE CLASSES OF MARTIAN CRATER EJECTA -- I. GLOBAL RELATIONSHIPS OF CLASS ABUNDANCE TO LATITUDE AND TERRAIN

Karl R. Blasius, James A. Cutts, Blake H. Lewis, and Amelia V. Vetrone, Planetary Science Institute, Science Applications, Inc., 283 S. Lake Ave., Suite 218, Pasadena, CA 91101

A globally representative data base containing ejecta characteristics and other data for 3000 fresh craters gathered from examination of 70% of the surface of Mars (Refs. 5, 2, 1) has been examined for systematic patterns in the abundances of three simple ejecta classes over wide ranges of latitude and terrain type. The abundances of craters in each class show remarkable relationships to the terrains on which the craters occur.

Using a smaller preliminary data set we previously reported (Ref. 5) comparison of results with findings of Johansen (Ref. 3) and Mouginis-Mark (Ref. 4). Examination of the present data set confirms those results, i.e., the ejecta morphology classes of Johansen occur in striking latitudinal patterns suggestive of control by climate, perhaps through ground ice/water, and as reported by Mouginis-Mark ejecta mobility seems to increase at high northern latitudes.

Here we proceed to develop a new analysis based upon the many morphologic and morphometric parameters in the new data base: up to 21 ejecta morphology descriptors (for up to 2 ejecta deposits on 2 terrains), 3 crater and ejecta morphometry descriptors, 4 rim and interior morphology descriptors, 17 terrain descriptors, and 8 descriptors of the image data. By observing how ejecta characteristics cluster in the data base we hope to define natural classes of ejecta and explore their spatial distribution, crater size characteristics, and relationships to terrain and crater interior characteristics.

We have studied the occurrence in a 1450 crater subset of the data base of three common but very simple classes of ejecta defined by only a few of the ejecta parameters. These classes are: (1) DR/s possesses Double concentric ejecta deposits, the inner with marginal Scarp(s) and with marginal Ridge(s); (2) SR posseses a Single ejecta deposit, either simple or multilobate in plan form, with marginal Ridge(s); and (3) SS possesses a Single ejecta deposit, either simple or multilobate in plan form, with marginal Scarp(s).

Plotting relative abundances of these three classes against one another segregates three types of terrain and illustrates the latitude dependence of crater ejecta morphology. The types of terrain which appear in this analysis fall into three broad catagories: (1) Composite terrains all display strong evidence of complex silicate stratigraphy including large craters or knobs embayed by ridged or smooth plains. Abbreviations used here are: cs = cratered terrain with smooth intercrater plains; cw = cratered terrain with ridged intercrater plains; ks/kw = knobby terrain with smooth or ridged interknob plains. (2) Smooth simple terrains are lightly cratered and include: ps = smooth plains; pw = ridged plains. (3) Rough simple terrains may be lightly or heavily cratered and include: pr = rough plains; cr = rough cratered terrain. This breakdown of terrains takes account of two factors: obvious silicate stratigraphy and surface roughness.

In Fig. 1 we plot the abundances of SS craters against SR craters (Fig. 1A) and Dr/s craters (Fig. 1B). Latitudinal subdivisions of Mars are plotted with X's: eq = $\pm$ 15°; low N = 15-35°N; High N = >35°N; low S = 15-35°S; high S = >35°S. Three types of space-filling symbols correspond to the three types of terrain -- solid = composite, bold = rough simple, and open = smooth simple. The terrains are in some cases further subdivided by latitude: low (Terrain) = 30°S-30°N; high N (Terrain) = >30°N; high S (Terrain) = >30°S. Arrows connect latitude subdivisions and are directed from high to low latitude.

In both figures the three terrain types are segregated into nonoverlapping clusters. %SR craters increases toward lower latitudes on all terrains, and %SS craters increases toward higher latitudes except for rough simple terrains and low northern latitudes (Fig. 1A arrows). %SS is high for rough simple and composite terrains compared to smooth simple terrains (Fig. 1A). %DR/s is relatively high on smooth simple terrains and declines with decreasing latitude on those terrains (Fig. 1B arrows). The spread of class abundances over simple latitude subdivisions of Mars is comparable to the spread over terrain subdivisions (Fig. 1A, 1B).

The relationships of %SR and %SS to latitude are mostly consistent with the observations of Johansen (Ref. 3) and support the hypothesis that a terrain independent factor, climate (latitude), is being expressed through distribution of water in the lithosphere. The enhancement of DR/s abundance on smooth simple terrains suggest a well-consolidated surface layer such as lava flows may favor formation of that type of ejecta. Mouginis-Mark (Ref. 4) has suggested viscosity contrasts in a layered target (strong, possibly dry, over weak, possibly wet) may create two concentric ejecta deposits.

The peculiar abundance patterns of SS craters on rough simple terrains suggest an additional factor may favor that morphology. We propose erosion or mantling (both processes are possible or probable on many rough simple terrains) may cause evolution between ejecta classes, either SR → SS or DR/s → SS. Alternatively, rough surfaces may suppress formation or visibility of ejecta marginal ridges.

The similar spreads of class abundances over latitude and terrain subdivisions of Mars suggest that latitude (volatile stratigraphy) and terrain (silicate stratigraphy and roughness) are of comparable significance in determining crater ejecta morphology.

REFERENCES - (1) Cutts, J.A. et al., 1979, NASA TM 80339, 111-113. (2) Blasius, K.R. et al., 1980, NASA TM 81776, 93-94. (3) Johansen, L.A., 1975, Proc. 2nd Colloq. on Plan. Water and Polar Processes, 1978, 109-110. (4) Mouginis-Mark, P., 1981, Icarus 45, 60-76. (5) Blasius, K.R. and Cutts, J.A., 1980, NASA TM 82385, 147-149. (6) Mouginis-Mark, P., 1979, JGR 84, 8011-8022.

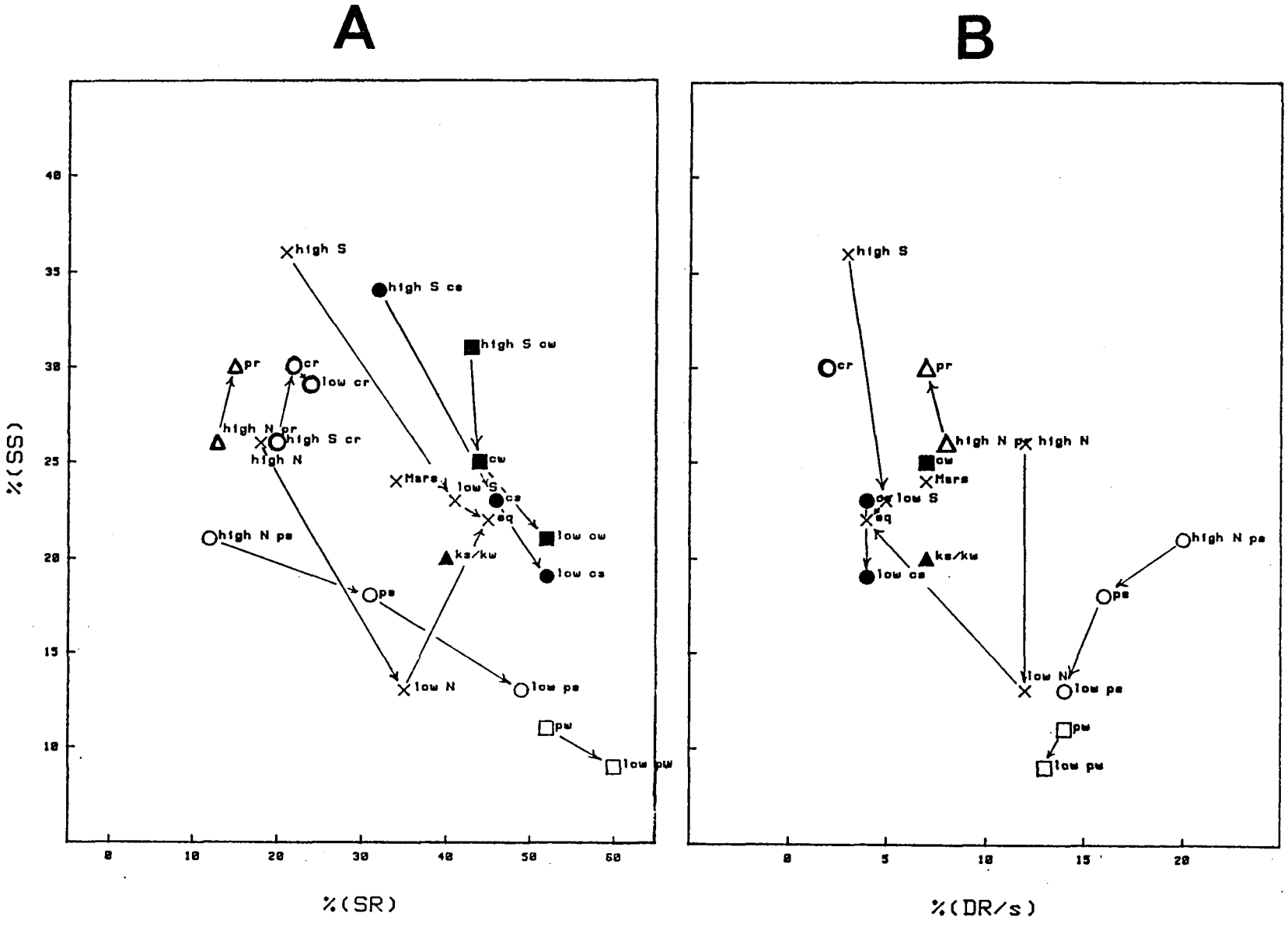
A
B
%(SS)
%(SR)
%(DR/s)
high S
high S ce
high S cw
pr
cr
low cr
high N pr
high S cr
high N
Mars
low S
ce
eq
cw
high N ps
ks/kw
low cw
low ce
ps
low N
low ps
pw
low pw
high N pr
high N
0
10
20
30
40
50
60
5
15
35
38
25
18

Figure 1

# THREE SIMPLE CLASSES OF MARTIAN CRATER EJECTA -- II. GLOBAL RELATIONSHIPS OF CRATER RADIUS TO LATITUDE AND TERRAIN

Karl R. Blasius, James A. Cutts, Blake H. Lewis, and Amelia V. Vetrone, Planetary Science Institute, Science Applications, Inc., 283 S. Lake Ave., Suite 218, Pasadena, CA 91101

As described in the accompanying paper (Ref. 1) a newly assembled global data base of crater ejecta characteristics has been used to study the relationships of abundances of three simple classes of craters to latitude and terrain setting. Here we examine the relationship of crater size to latitude and terrain for these same classes.

In Fig. 1 the mean raii of crater classes SS, SR, and DR/s are plotted against one another for samples of varying latitude and terrain type. The data set used is a 1450 crater subset of the data base, which is a complete catalog of fresh craters larger than 11.9km diameter in areas totaling 70% of the surface of Mars.

In Fig. 1 three classes of terrain are plotted -- composite (stratigraphically complex) terrains with solid symbols, rough simple terrains with bold open symbols, and smooth simple terrains with light open symbols. X's are used to plot data for simple latitude subdivisions of Mars. The arrows are directed from higher to lower latitudes for similar subdivisions of Mars.

Craters with single deposit ridge margin ejecta (SR) show relatively little variation in mean radius, except for high southern latitudes, compared to craters with single deposit scarp margin ejecta (SS) and double ejecta craters (DR/s) (Fig. 1A). R(SS) is relatively small for smooth simple terrains compared to rough simple or composite terrains (Fig. 1B). R(DR/s) is larger on average than R(SR) and R(SS), and for composite terrains R(DR/s) is larger than for rough simple terrains (Fig. 1B). Except for high northern latitudes R(SS) increases toward the equator (Fig. 1B arrows). R(DR/s) mostly increases toward the equator (Fig. 1B arrows). In 2-D spaces defined by mean radii of these crater classes the terrain subdivisions of Mars show about the same spread of values as the latitude subdivisions.

We suggest that the variations of crater size in the three ejecta classes with latitude and terrain reflect variations in both silicate and volatile stratigraphy. R(SR) is not a strong function of terrain or latitude for the size ($\geq$11.9km diameter) crater studied. The materials forming SR ejecta may, where it occurs, lie at shallower more uniform depths than the materials forming other types of ejecta. The larger average size of DR/s craters compared to the single ejecta deposit classes indicates a deeper depth of excavation, perhaps requiring excavation through a surface layer. The increase in the size of DR/s craters toward the equator suggests the layer interface is deeper at lower latitudes, though some terrains fail to show this pattern. The larger R(DR/s) on composite terrains than most simple terrains supports the hypothesis that excavation must reach into a second geologic unit. In areas classified as simple terrains thinner unrecognized blanketing units may be unresolved or unrecognized.

The peculiar radius/latitude relationships of SS craters on high northern latitudes (Fig. 1B arrows) and the anomalous relationship R(SS)>R(DR/s) suggest the Vastitas Borealis plains have unique silicate or volatile stratigraphic characteristics. The large mean radii of SS craters suggest excavation of a very thick layer in the lithosphere. Johansen's (Ref. 2) interpretation of similar ejecta as ice-ladened suggests ground ice deposits extending to great depths. The low elevation of the northern plains perhaps caused them to behave as a global catchment (ocean?) basin for mobile liquid water in the past.

Finally, as was the case for abundance relations among the three classes of crater the scatter of data points in Fig. 1 shows that for crater size relationships climate/latitude effects (volatile stratigraphy) and terrain effects (silicate stratigraphy and other factors) are of comparable importance.

References

1. Blasius, K.R. et al., 1981, this volume.
2. Johansen, L.A., 1978, Proceedings of 2nd Colloquium on Planetary Water and Polar Processes, Hanover, N.H., 16-18 October 1978, pp. 109-110.

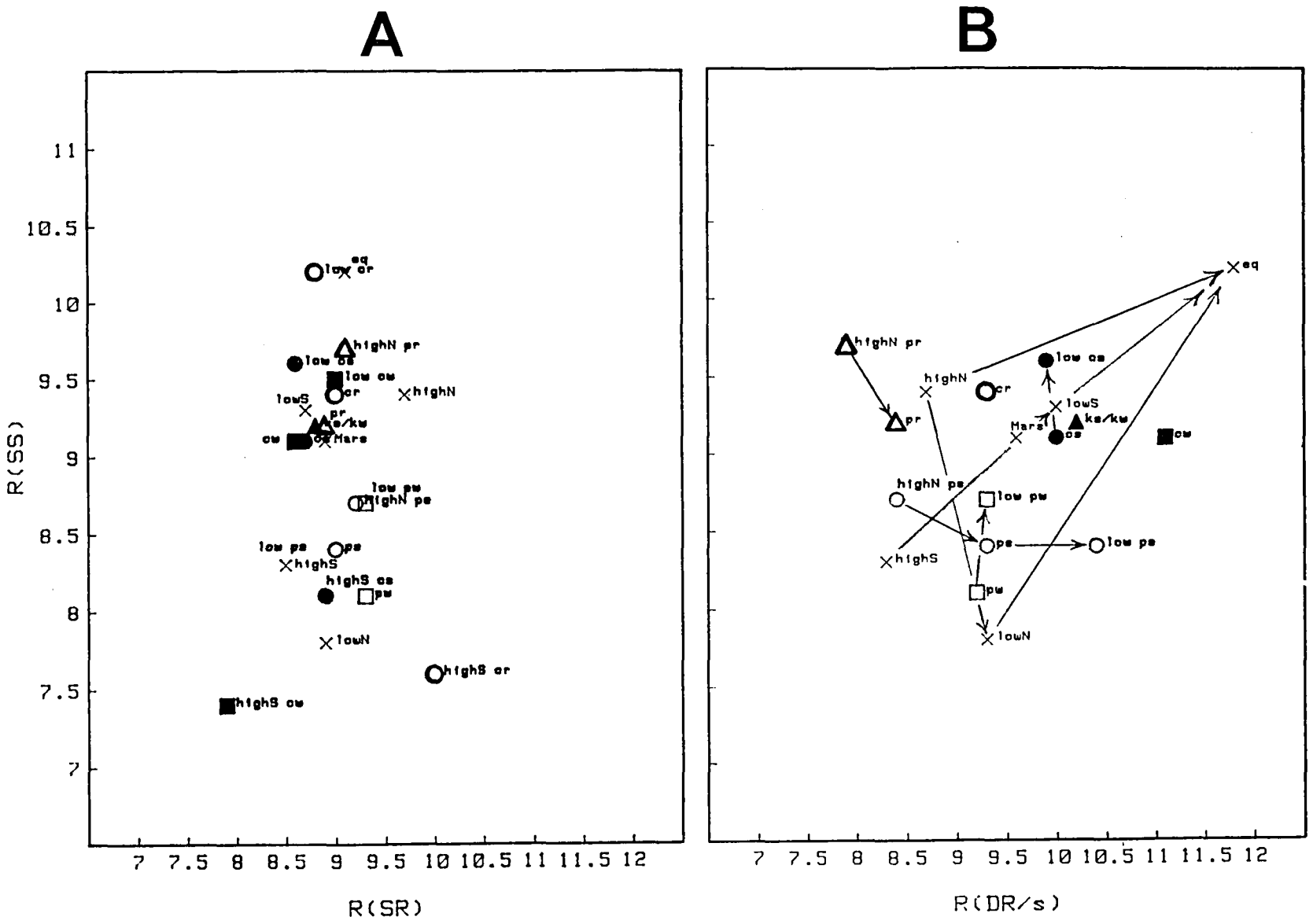
A
B
R(SS)
R(SR)
R(DR/s)
11
10.5
10
9.5
9
8.5
8
7.5
7
7 7.5 8 8.5 9 9.5 10 10.5 11 11.5 12
eq
cr
highN pr
low cs
low cw
highN
lowS
pr
ks/kw
cw
Mars
low pw
highN ps
low ps
ps
highS
highS cs
pw
lowN
highS cr
highS cw

Figure 1

# MARTIAN CRATER-FORM TOPOGRAPHY ON TEMPE TERRA

Davis, P. A., Roddy, D.J., and Witbeck, N. E., U. S. Geological Survey, Flagstaff, Arizona 86001.

Several unusual circular features on the volcanic units of northern Tempe Terra are interpreted to be erosional remnants of impact craters. These features are localized predominantly in the etched plateau material (ple) of southwest Mare Acidalium Quadrangle [1], in the radial etched-mountain material (mre), and the intensely-cratered upland material (uic) of southeast Arcadia Quadrangle [2]. A few of these features are also located in the mottled plains material (pm) and the fractured and channeled plains material (pfc) immediately north of the etched plateau material in southwest Mare Acidalium Quadrangle. Examples of five types of crater-forms that occur on the northern surface of Tempe Terra are shown in figure 1a and 1b. Topographic profiles of four of these crater forms were constructed, using the method of Davis, et al. [3], and are shown in figure 2. For convenience we designate the crater-forms as Type I-V. Type I is bowl-shaped with ejecta present in almost all cases regardless of crater size. Type II is flat-floored with terraces and ejecta present in most cases. Types I and II display features generally found in fresh or degraded crater impacts on the martian surface. Type III is also flat-floored, but does not have a visible ejecta blanket and has a marked annular depression or "moat" around the central rim. The floor of a Type III crater-form is featureless and lower than the surrounding terrain. Type IV is similar to Type III except its floor is higher than the surrounding terrain. Types III and IV generally have channels in the ice-laden debris layer that intersect their respective moats. However, there are also examples where there is no visible evidence of channeling. Type V crater-forms are faint, circular features with flat floors that are topographically higher than the surrounding terrain and have an annular moat. Units ple, mre, uic, and ue (etched-upland material in Arcadia Quadrangle) have pits and channels very similar to terrestrial thermokarst features [4]. Wise [2] interprets the pits and channels as thermokarst features indicative of a region with high frost content. He suggests an eolian debris cover, cemented with water-ice or solid $CO_2$, as the major cause of the "highly degraded or partly buried rim crests" in these units.

The circularity of Types III-V suggests to us that these features either reflect craters in bedrock underlying the mantle of icy debris, or craters produced directly by impact onto the mantle of icy debris. However, the sequence of erosional events that would produce these features is unclear. Terrestrial thermokarst features are typically irregular in shape; no terrestrial analogs in permafrost/ice regions are reported that attain such a high degree of circularity. The presence of channels in the icy debris mantle that are connected to some of the annular moats implies that they may be the result of thermokarst dissolution around the rim of the crater-form, which acted as a topographic barrier to the dissolution channels. However, the reason for localization of the moats in the immediate area around the crater-form rim is uncertain. The icy debris mantle next to the moat is raised relative to the surrounding terrain, i.e., another characteristic hard to explain by simple thermokarst dissolution. Schultz and Glicken [5]

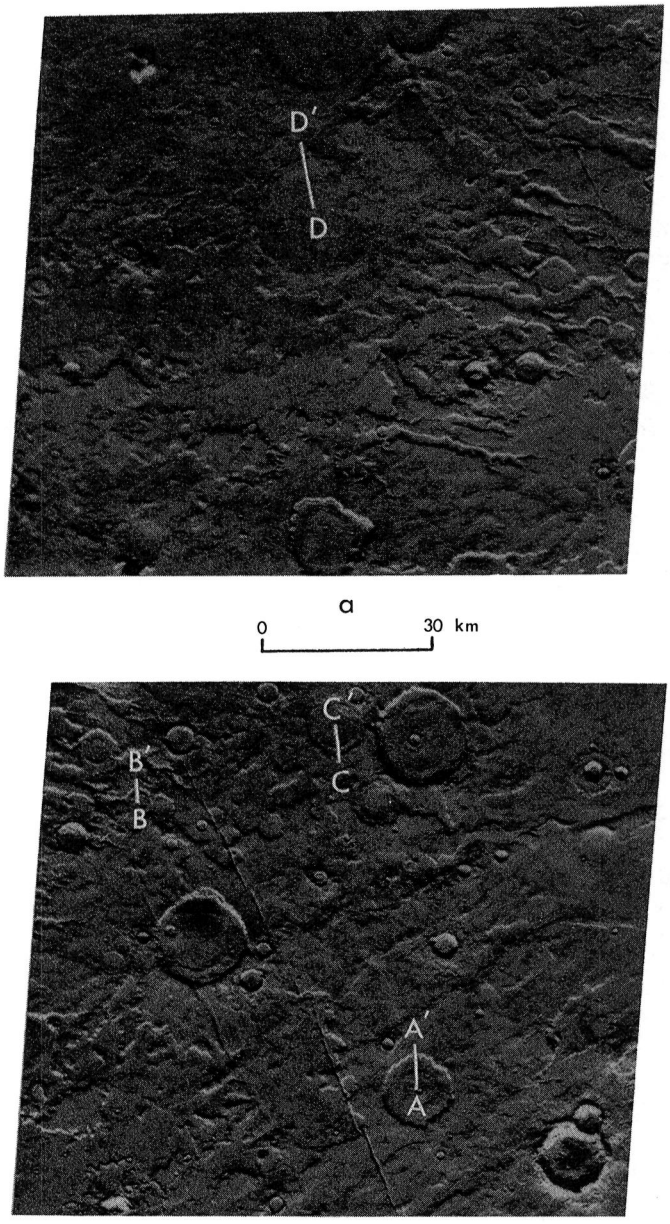


Figure 1. Crater-forms in northern Tempe plateau: (a) Viking frame 704B39, centered at lat. 46.5°N, long. 56.5°W; (b) Viking frame 704B38, centered at lat. 43.4°N, long. 58.6°W. Lettered bars show position of topographic profiles. North is to the left.

describe somewhat similar crater forms at the same latitude in the cratered plateau and old, cratered, hilly, and basin terrain, and at 40-50°S in the cratered plains terrain, between 280° and 0°W. Crater forms in the central plateau terrain have extensive concentric floor fractures, an annular moat, a central peak, and a plateau not appreciably higher than the surrounding terrain. Crater forms in the old, cratered, hilly, and basin terrain and in the cratered plains terrain also have extensive floor fractures and an annular

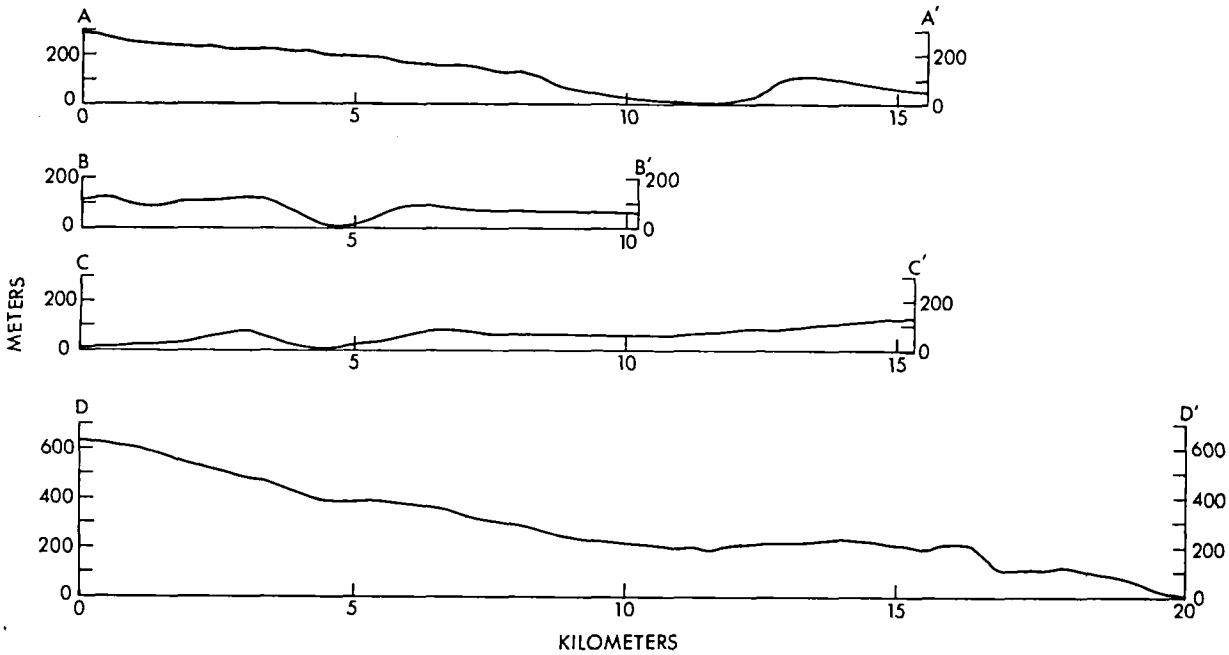


Figure 2. Relative-height profiles of crater-forms on Tempe Terra. Type IV is shown in profile A-A; Type III in profiles B-B and C-C; and Type V in profile D-D. Non-prime letters are the centers of the craters. Vertical exaggeration is 4.5.

moat, in addition to a central floor that is well below the surrounding terrain and channels which extend into the crater floor from the surrounding terrain. Central peaks, fractured floors, and channels dissecting the floors are not observed on Types III-IV. Schultz and Glicken [5] suggest shallow intrusions as heat sources for the liquification of the icy debris mantle that produced these features. The crater-forms (Types III and IV) reported here may be a more advanced stage of this degradation process, whereas Type V may be the result of volcanism.

An alternative explanation may be that these crater-forms are the result of impact into ice or debris-ice. A number of explosion experiments using surface charges have formed a variety of large, flat-floored craters with complex internal structures, some of which include moat-like topography on the crater floor adjacent to the crater walls surrounding a flat centrally uplifted floor [6]. The target material in these experiments was unconsolidated, flat-lying alluvium overlying water-saturated clays. These experimental data suggest the features exhibited on Tempe Terra may have been formed by meteroid impact into similar target material of similarly low strength, such as permafrost, and modified by subsequent complex erosional processes.

REFERENCES: [1] Underwood, J.R., and Trask, N.J. (1977) U.S.G.S: Misc. Inv. Ser. I-1048; [2] Wise, D.U. (1978) U.S.G.S.: Misc. Inv. Ser. I-1154; [3] Davis, P.A., et al. (1981) 3rd Int. Colloq. Mars, 56-58; [4] Gatto, L.W., and Anderson, D.M. (1975) Science 188, 255-257; [5] Schultz, P.H., and Glicken, H. (1979) J. Geophys. Res. 84, 8033-8047; [6] Roddy, D.J. (1977) Impact and Explosion Cratering, Pergamon Press, New York, 185-246.

## The Distribution of Crater Ejecta and Central Peaks on Mars

Laurie A. Johansen, Jet Propulsion Laboratory, Pasadena, CA.

A study has been done of the distribution of crater ejecta types and central peaks on Mars. This study incorporated over 1800 craters which varied from .7 to 100 km in diameter. Craters from individual Viking images were recorded with information (lat., long., crater ejecta type, diameter, peak characteristics, roughness of crater features, distinctness of crater features). This method allowed us to use unmosaiced images and expanded the number and diameter range of craters beyond presently existing data base limits. By the time of the PGPI meeting this data base (fig 1) is expected to be expanded. The crater ejecta was classified by the previously used method (Johansen, 1978).* The following observations were made:

* Central peak occurence shows a definite relationship to latitude. Central peaks are found at smaller diameters more often near the equator and are more common in general there.
* There is a rough positive correlation between flower type ejecta and central peak presence. Central peaks tend to be associated with the presence of flower ejecta, although other ejecta type craters may have central peaks. Central peak distribution also mimics that of flower craters with respect to latitude (fig 2), and with respect to diameter relationships (fig 3).
* Crater ejecta previously stated to be associated with the presence of ground ice (mound type craters) (Johansen 1978) show a general wedge like structure in distribution extending in towards the equator from the poles, and intersecting the ground surface at + 40°. This is in striking consonance with the global structure of ground ice as predicted by Fanale (1976).
* The distribution of central peaks show regional structure. In some locations, central peaks are found at smaller diameters than other locations (fig 4). Similar to the distribution of crater ejecta, these structures may be used to map surface material properties and be used to supplement the information gleaned from crater ejecta regional distributions.
* Size relations to crater ejecta morphology have been demonstrated both locally and in general planet wide. The results demonstrate that flower ejecta are prevalent in craters at larger diameters than those craters with mound crater ejecta (fig 5), and that the transition between the two types occurs in general at larger diameters at higher latitudes.

* "Flower craters" are defined as craters which exhibit only raised distal edges on the ejecta. "Mound craters" refer to craters which have sloping terminations on the ejecta. "Splosh crater" refers to any crater which exhibits fluid-like ejecta lobes.

References

Fanale, F.P. (1976), Martian Volatiles: Their Degassing History and Geochemical Fate, Icarus 28, 179-202.,
Johansen, L., (1978), Martian Splosh cratering and its relation to Water, Proc. of Second Coll. on Planetary Water and Polar Processes, Hanover New Hampshire, 16-18 Oct., p109-110.

DISTRIBUTION OF CRATERS IN THIS STUDY

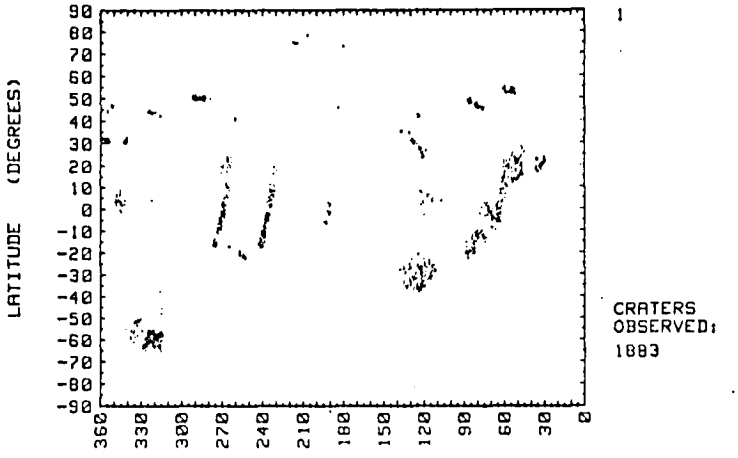


Fig 1

LATITUDE RELATIONSHIP OF PEAKS, FLOWERS, AND MOUNDS

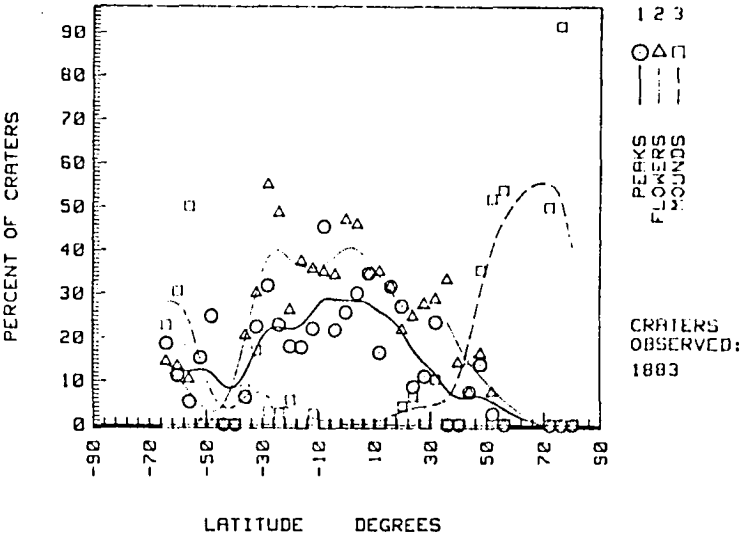


Fig 2

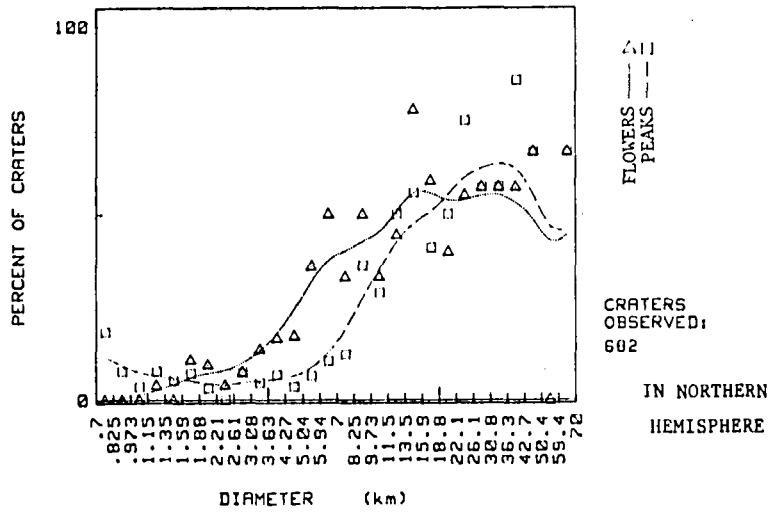


Fig3

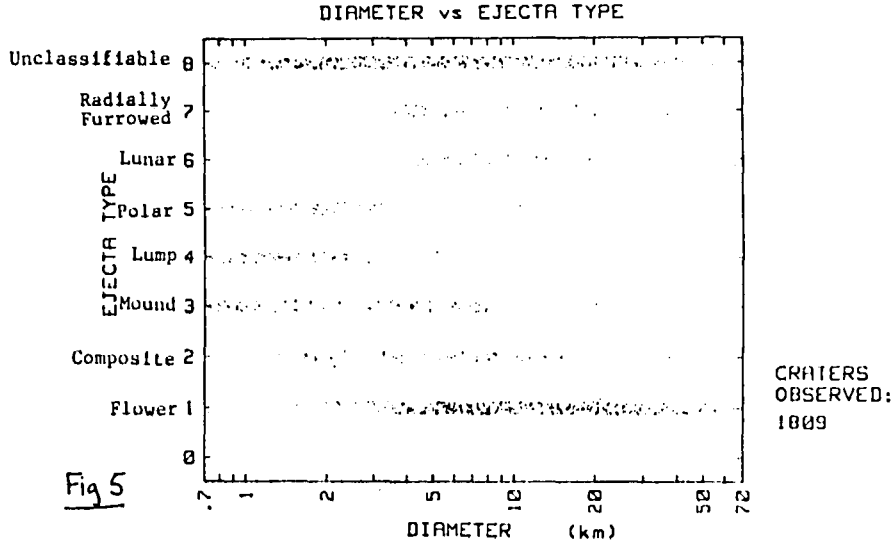


Fig 5

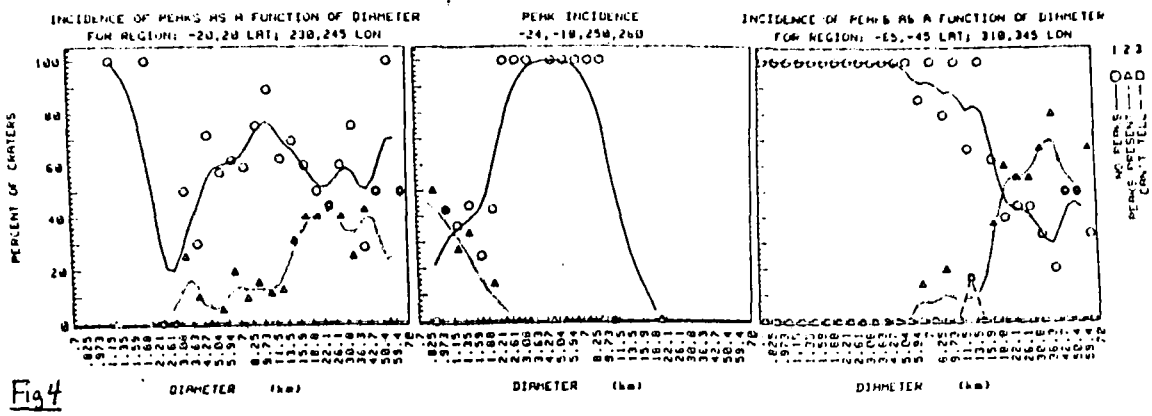


Fig4

PHOBOS, DEIMOS, AND THE MOON: COMPARISON OF CRATER EJECTA PATTERNS.

S. Lee, P. Thomas, and J. Veverka, Laboratory for Planetary Studies, Cornell University, Ithaca, New York 14853

The size and radial distribution of ejecta blocks on Phobos and Deimos have been compared to those on the Moon to evaluate the effects of differing surface gravity and composition on the disposition of crater ejecta. The size distribution of blocks associated with an 800-m crater on Deimos, imaged at a resolution of 2 m, is similar to that of blocks around sub-kilometer craters on lunar maria. The blocks have a preferred size of 6-12 meters (longest dimension). Comparable high resolution data for Phobos are not available.

Slightly lower resolution images ($\geq$ 10 m) allow a compilation of the sizes and positions of the larger blocks associated with 1-10 km craters on both Martian satellites. The relation between the block size and diameter of the supposed source crater is approximately the same on Phobos, Deimos, and the Moon, although considerable scatter in the data exists.

Phobos and the Moon exhibit similar radial distributions of ejecta blocks, but the pattern on Deimos is much more widely dispersed (Figure 1). This difference is particularly evident when comparing the radial dependence of ejecta block volume for the Moon and Deimos, determined from high resolution images (Figure 2). Since the ratio in the surface gravities of Phobos and Deimos (2:1) is small compared to that of the Moon and Phobos (320:1), the marked difference in ejecta patterns on the two Martian satellites is unlikely to be a simple gravitational effect and may reflect differing mechanical properties of the two surfaces.

The greater dispersion of crater ejecta on Deimos relative to those on Phobos is consistent with the greatly different appearance of the two surfaces. Phobos shows no ponding of sediment in crater floors, while Deimos has conspicuous filling of craters by as much as 12 m of debris (Thomas and Veverka, 1980). This difference may not indicate a preferential loss of debris from Phobos. Rather, the block data suggest that Phobos may have more compact, more continuous, ejecta blankets, and most crater ejecta are retained near the crater rim. On Deimos, debris is more widely dispersed, allowing more efficient filling of craters by ejecta from distant impacts.

Our data suggest that most ejecta on Phobos may not travel far enough to be significantly affected by Mars' gravity (Dobrovolskis and Burns, 1980).

This research is supported by NASA Grant NSG 7156.

REFERENCES:

Dobrovolskis, A., and Burns, J. (1980). Life near the Roche limit: Behavior of ejecta from satellites close to planets. Icarus 42, 422-441.

Thomas, P., and Veverka, J. (1980). Downslope movement of material on Deimos. Icarus 42, 234-250.

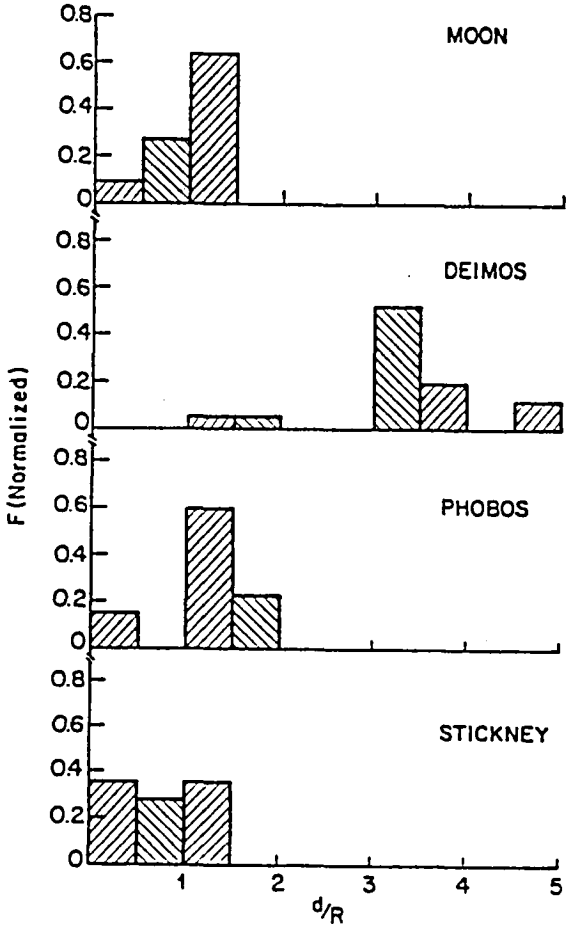


Figure 1. Radial distribution of ejecta blocks on Phobos, Deimos, and the Moon. R is the radius of the crater, d the radial distance of the block from the center, and F the fraction of observed blocks that fall within a given d/R increment. For the Moon, the data are for the largest blocks, typically 10-30 meters. For Phobos and Deimos, the histograms show all blocks $\gtrsim$ 20 meters across visible in Viking medium resolution images. For the crater Stickney, the data are for blocks $\gtrsim$ 10 meters across.

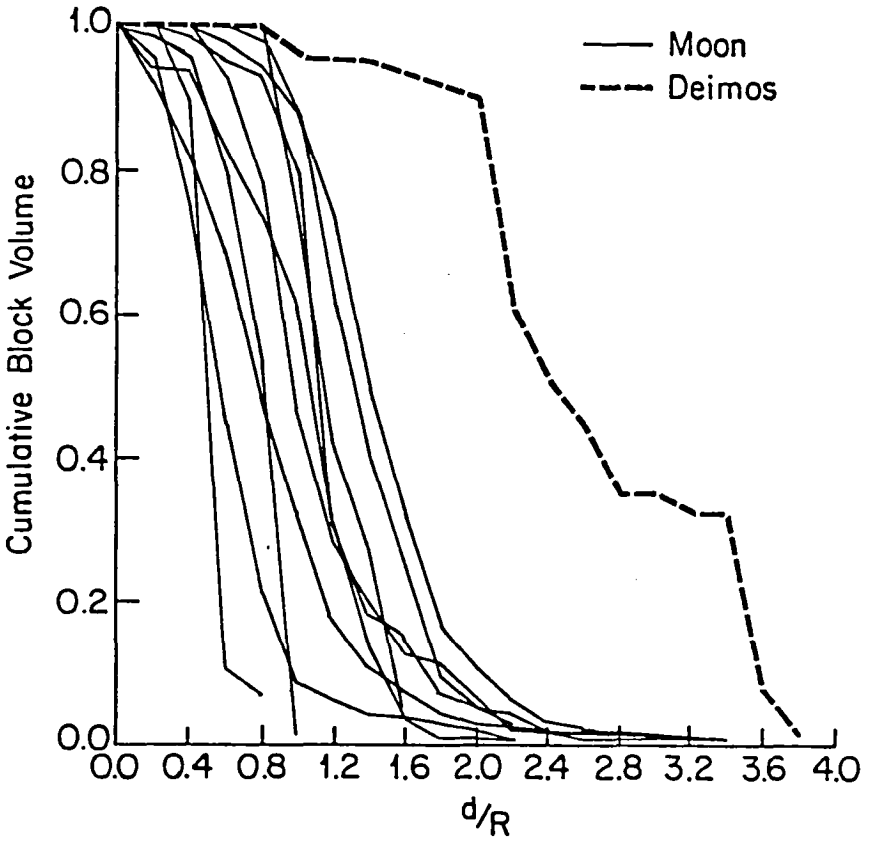


Figure 2. Radial distribution of ejecta blocks for several sub-kilometer sized lunar craters compared to that of an 800 meter diameter crater on Deimos.

# IMPACT CRATER EJECTA MORPHOLOGIES ON THE MOON AND VENUS

T.W. Thompson and J.A. Cutts, Planetary Science Institute, Science Applications, Inc., 283 S. Lake Ave., Suite 218, Pasadena, CA 91101

Photogeological interpretations of the Moon, Mars, Mercury, and outer planet satellites depends upon the measurement and interpretation of impact cratering statistics. A question remains whether these types of interpretations can be applied to Venus, whose surface can be imaged only with radar.

Today, there are both spacecraft and earth-based Venus images. Campbell and Burns (Ref. 1) have identified some 33 bright-ring features in the Arecibo images and interpreted them as craters. Impact crater forms have also been identified by Saunders and Malin (Ref. 2) in Goldstone images along the Venusian equator. Bright spots in the Pioneer-Venus backscatter maps may be the radar images of young impact craters which are smaller than the radar cell size. However, the 33 bright-ring and dark-floored features described by Campbell and Burns are much the best documented of crater-like features on Venus. We have recently carried out a detailed investigation of their origin (Ref. 3).

An understanding of the factors that determine the appearance of craters in lunar radar images can help us with the detection and measurement of impact craters on Venus. A recent study of 3.8cm radar maps by Thompson et al. (Ref. 4) indicates that the youngest, medium (1 to 10km diameter) lunar impact craters are surrounded by 3.8cm radar bright haloes up to 10-20 crater diameters in size. There are no comparable haloes in the 70cm radar images and older craters do not possess the 3.8cm bright haloes.

The population of 3.8 radar bright halo craters on the moon is compared with the crater statistics for Oceanus Procellarum, a 3.3 by old surface, in Fig. 1. These plots are log R-vs-log D, where a horizontal line is equivalent to cumulative distribution proportional to (crater diameter)$^{-2}$ (see Crater Analysis Technique Working Group, Ref. 5). We consider that the 3.8cm radar bright halo crater population has reached a steady state condition in which older craters with bright haloes are being obliterated as rapidly as new ones are forming. We attribute this loss of bright halo craters to the micrometeorite erosion of centimeter-sized ejecta blocks responsible for radar scattering from the ejecta deposits. A similar relationship between the projected production population of craters and the observed occurrence of craters in the Arecibo images of Venus (Ref. 3) suggests that radar scatterers may also be rapidly obliterated in the Venus environment.

What do we know about emplacement of ejecta deposits that can help us understand what Venus impact craters will look like at radar wavelengths? The radar bright haloes in the lunar images arise from ejecta which is primarily meter size and smaller when it is launched ballistically from the crater cavity. These ejecta particles upon impact with the lunar surface would shatter into the centimeter-sized rocks which create the 3.8cm radar bright haloes. The thick Venusian atmosphere will modify this process. On Venus,

we expect the ejecta particles to travel shorter distances and impact with smaller velocities. We expect that Venus crater ejecta deposits will consist of larger particles concentrated over a much smaller area. It is also probable that Venusian crater ejecta would be emplaced by flows, similar to those of martian craters (Refs. 6, 7).

Although this lunar analogy predicts an ejecta morphology which agrees with the Venus radar observations, it does not predict why the Venus features have radar dark centers. Venusian impact craters, like their lunar counterparts, probably have floors covered with impact melts. On the moon, these impact melts are subjected to meteoritic bombardment which gardens their solid rock surfaces. This may be the reason that lunar crater floors and interiors are radar bright at centimeter and meter wavelengths are ages much older that those of the 3.8cm radar bright haloes. Thompson et al. (Ref. 8), using the predictions of Lange and Hawke (Ref. 9), show that 10 to 100km lunar craters may have 7 to 177 meters of impact melt on their floors; melts of these depths could be the source of meter and centimeter sized rocks for 3.5 and 3.9 b years.

There are a number of processes which could modify the radar signatures of Venusian craters. These include chemical weathering, mantling by volcanic flows and the global mantling of fine dust particles from the impacts of large bolides. We evaluated the global dust mantle hypothesis with a Monte Carlo computer model and have shown that satisfactorily accounts for the population of Venusian craters with diameters greater than 64km, as shown in Fig. 2. The measured population of craters with internal diameters between 32 and 64km is not explained but it may be underestimated because of poor radar resolution.

Improvements in the ground based radar data for Venus can enable us to choose between models of crater obliteration and better define the strategy for analyzing craters in the VOIR data.

References - (1) D.B. Campbell and B.A. Burns, J. Geophys. Res. 85, 827-828, 1980. (2) R.W. Saunders and M.C. Malin, Geol. Romana 15, 507-515, 1976. (3) J.A. Cutts, T.W. Thompson and B.H. Lewis, Icarus, in press, 1981. (4) T.W. Thompson et al., Icarus 46, 201-255, 1981. (5) Crater Analysis Techniques Working Group, Icarus 37, 467-474, 1979. (6) M.H. Carr et al., J. Geophys. Res. 82, 4055-4066, 1977. (7) P. Mouginis-Mark, Icarus 45, 60-76, 1981. (8) T.W. Thompson et al., Proc. Conf. Lunar Highlands Crust, 483-499, 1980. (9) M.A. Lange and B.R. Hawke, Abstracts Conf. Lunar Highlands Crust, 98-100, 1979.

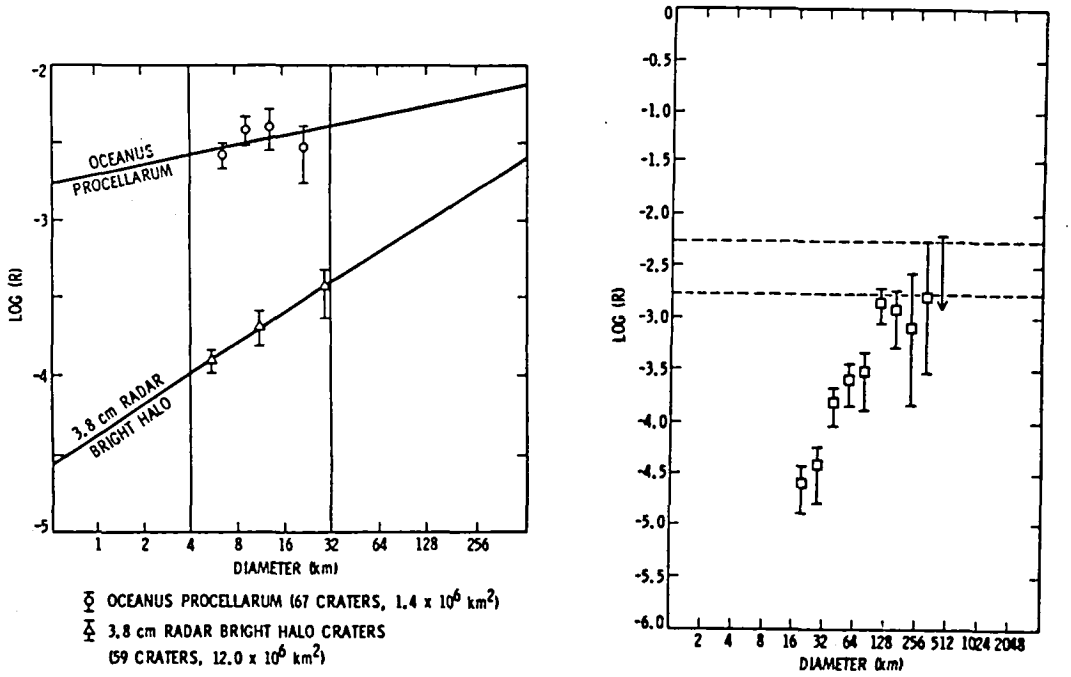


FIGURE 1: (a) Lunar population of 3.8cm radar bright craters is interpreted as a steady state population determined by competing processes of crater production and obliteration of radar bright ejecta. (b) Venus population of bright ring craters may be of similar origin (dashed lines show the expected production function).

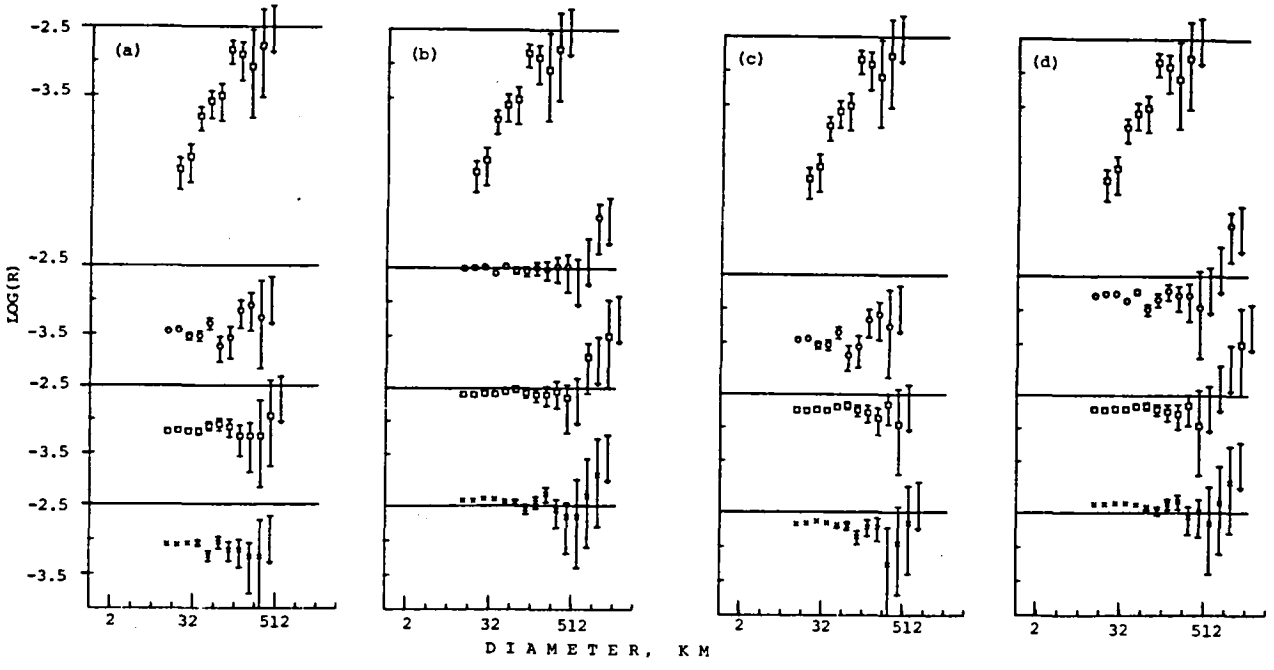


FIGURE 2: Four different Monte Carlo models simulating the Venus bright ring crater population (top) with a model involving obliteration by large impacts. Each of the three simulations in each plot is a different Monte Carlo run (see text and Ref. 3).

IMPACT BASINS: STAGES IN BASIN FORMATION AND EVOLUTION, James W. Head, Dept. of Geological Sciences, Brown University, Providence, RI 02912 and Sean C. Solomon, Dept. of Earth and Planetary Sciences, Massachusetts Inst. of Technology, Cambridge, MA 02139.

Impact basins are large, generally circular structures exceeding about 200 km in diameter and often displaying multiple concentric rings. Impact basins formed in the first billion years of planetary history and are known from the Moon, Mars, Mercury and the Galilean satellites. Their presence on these bodies makes it a virtual certainty that they were ubiquitous on solid surfaces in the inner solar system, even on the less well known or preserved early surfaces of Venus and Earth. Their abundances (1,2,3) indicate the basin formation was a significant process in the formative years of planetary crusts and lithospheres. Each basin-forming event concentrated several orders of magnitude more than the Earth's annual heat flow into a single point on a planetary surface. In addition to the influence of the impact event itself, impact basins become a focus for other planetary processes such as volcanism and tectonism long after the impact event itself. The purpose of this study is to understand better the influence of basins on planetary history and processes. We first identify a series of stages in basin formation and evolution (4) to provide a framework for the documentation of various processes and effects related to basins (Fig. 1). We then discuss each stage using the lunar data set and finally identify factors which might result in variations in style and alteration of stages on other planets.

Stage I - Cavity Excavation - The initial contact and penetration of a projectile exceeding several km in diameter leads to formation and growth of the transient cavity. The energy associated with the Imbrium basin formation is estimated at $10^{34}$ ergs (5). If energy partitioning is comparable to that in small craters at low velocities (6), then approximately 24% is expended in fragmentation of target material, 50% in ejection of material from the transient cavity, 25% in heating of projectile and substrate material, and less than 1% in seismic energy. The process of cavity formation and the cavity geometry are poorly known at these large diameters. For the 900 km diameter Orientale basin, estimates of the depth of the transient cavity range from within the crust (<60 km) (7) to in excess of 100 km (8); ejecta volume estimates range from 1-10 x $10^6 km^3$ (7,9); approximately 2 x $10^5 km^3$ of impact melt ramains within the cavity (10). Ejecta emplacement begins during this stage and eventually buries or heavily modifies adjacent terrain out to ranges of several crater radii. Seismicity may produce antipodal effects and cause instability of surface materials over large areas of the Moon (5).

Stage II - Basin Formation - This stage involves the rapid or short-term modification of the transient cavity and overlaps with the cavity excavation stage. Basin ring formation is complete by the end of this stage. The exact mechanisms of cavity collapse and ring formation are not known. Inner rings may be related to target strength variations during excavation (11) or to floor uplift (12), and outer rings to sublithospheric flow and faulting (13, 10). Outer ring development on the Moon appears to be related to lithospheric thickness (14). The melt sheet is emplaced during and immediately after ring formation. At the end of Stage II, dynamic cavity formation and modification processes are complete.

Stage III - Long Term Basin Modification - This stage involves viscous relaxation and the effects of basin cooling and may overlap with Stage IV (15). Isostatic rebound may take place over time periods of $10^4$ years and longer term viscoelastic relaxation in the lithosphere over $10^4$ - $10^7$ years. Important

factors include the horizontal and vertical magnitude of initial basin topography, the thickness of the lithosphere, the influence of the heat of basin formation and perturbation of isotherms on the regional thermal regime, and the relationship of basin size to horizontal variations of lithospheric thickness. Older lunar basins show evidence of extensive viscous relaxation (Fecunditatis, Tranquillitatis) (14). Formation of a basin involves extensive heating of subsurface material above ambient temperatures, both by the uplift of isotherms during cavity collapse and by the partial conversion of impact kinetic energy to buried heat. The loss of this initial basin heat, which occurs over times as long as $10^8$ yr, can lead to substantial subsidence of the basin surface and to large thermal stresses capable of tectonically modifying the pre-mare basin floor (15).

Stage IV - Basin Filling - The topographic depression represented by the impact basin becomes a site of localization for volcanic deposits because of the topography and substructure of the basin. Volcanic loading of basins can lead to lithospheric flexure and the production of associated tectonic features over millions to billions of years (16,17). Regional variations in lithospheric thickness may be detected from the varying response of basins to volcanic loads (18). A second major factor that may be significant over these time scales is change in the planetary thermal state. On the Moon the lithosphere generally becomes thicker with time: therefore viscous relaxation becomes a less significant factor with time. In addition, changes from net heating to net cooling can change the state of stress in the lithosphere and influence the style of tectonics and the likelihood of volcanic activity (19). Sufficient thickening of the lithosphere can result in lithospheric support of large volcanic loads and an end to basin flexure and tectonics (18).

Factors that may influence the significance, style, and duration of various stages on different planets include variations in substrate properties, planetary gravity, the thermal state and lithospheric thickness at the time of basin formation, availability of material (volcanic, eolian) to fill the topography and load the lithosphere, the state of stress in the lithosphere, and the rate of lithospheric growth.

References - 1) C. Wood and J. Head (1976) PLSC 7, 3629. 2) M. Malin (1976) PLSC 7, 3589. 3) W. Hartmann and C. Wood (1971) Moon, 3, 2. 4) J. Head (1980) Europ. Geophys. Soc., Budapest, Program, 41. 5) P. Schultz and D. Gault, (1975) Moon, 12, 159. 6) D. Gault and E. Heitowit (1963) Proc. 6th Hyp. Impact Symp., 2, 419. 7) J. Head, et al. (1975) PLSC 6, 2805. 8) M. Dence et al. (1974) Lunar Science V, 165. 9) H. Moore et al. (1974) PLSC 5, 71. 10) J. Head (1974) Moon, 11, 327. 11) C. Hodges and D. Wilhelms (1978) Icarus, 34, 294; J. Murray (1980) 22, 269. 12) W. Hale and J. Head (1980) Multi-Ring Basins, 27. 13) H. Melosh and W. McKinnon (1978) GRL, 5, 985. 14) J. Head and S. Solomon (1979) LPSC XI, 421. 15) S. Solomon et al. (1981) The evolution of multi-ringed basins: Cooling, thermal stress, and relaxation of topography: PGPI. 16) S. Solomon and J. Head (1979) JGR, 84, 1667. 17) H. Melosh (1978) PLSC 9, 3513. 18) S. Solomon and J. Head (1980) RGSP, 18, 107. 19) S. Solomon (1978) GRL, 5, 461.

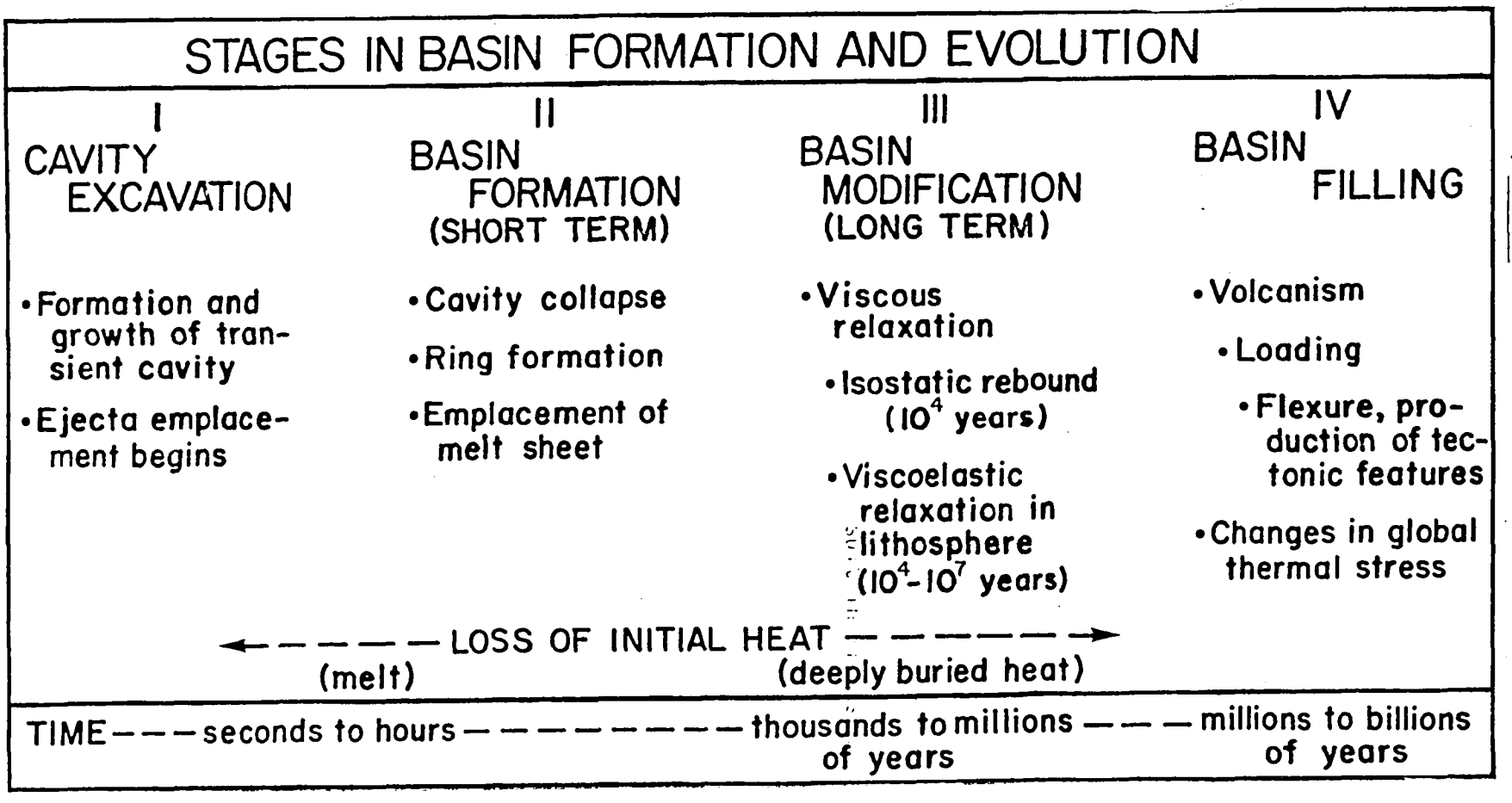


Figure 1: Stages in basin formation and evolution

# VISCOUS RELAXATION OF IMPACT BASIN TOPOGRAPHY: IMPLICATIONS FOR THE MOON AND VENUS.

Sean C. Solomon[1], Robert P. Comer[1], Stuart K. Stephens[1], and James W. Head[2]
[1]Dept. of Earth and Planetary Sciences, Massachusetts Institute of Technology, Cambridge, MA 02139; [2]Dept. of Geological Sciences, Brown University, Providence, RI 02912.

Introduction. As part of an ongoing effort to understand the properties and processes that affect the formation and evolution of impact basins [1], we have identified three major processes that act to modify impact basins over time scales of millions to billions of years: (i) thermal contraction and thermal stress associated with the loss of heat from basin formation [2], (ii) viscous relaxation of topographic relief due to elevated temperatures at shallow depth beneath the basin, and (iii) volcanic filling and lithospheric loading [3, 4]. The second process is the topic of this paper. We begin by developing a simple mathematical model for viscous relaxation of topographic relief on planetary surfaces. We then apply this model to pre-Nectarian impact basins on the Moon and to hypothetical large impact basins on Venus.

Analytical Models. The most common analytical formulation of the viscous relaxation problem is based on the assumption of a halfspace of uniform Newtonian viscosity $\eta$ and density $\rho$. For such a model, harmonics of the topography of wavenumber k decay exponentially with time according to a time constant $\tau = 2\eta k/\rho g$, where g is gravitational acceleration. This formulation has been used extensively to model the viscous relaxation of lunar craters [e.g., 5-7].

For features as large as impact basins, however, a uniform halfspace model fails to account for two features of importance to the relaxation problem: (i) viscosity, primarily a function of temperature, decreases with depth in the outer regions of planets; and (ii) topographic relief at long wavelengths is partially to completely compensated by corresponding variations at depth in crustal thickness or density. We have therefore solved [8] the viscous relaxation problem for an analytical model that retains both of these features: the model is a uniform layer of viscosity $\eta$, density $\rho$ and mean thickness H overlying an inviscid halfspace of greater density $\rho_m$. Initial surface topography is partially to completely compensated by corresponding relief at the base of the layer (i.e., crust). For this problem, there are two time constants for viscous relaxation: one is much smaller than the halfspace time constant $\tau$ for wavelengths greater than H and is identical to $\tau$ at short wavelengths; the second is constant with k at long wavelengths and proportional to $\tau$ at short wavelengths. Both time constants are proportional to $\eta/g$. Initial topographic relief relaxes quickly, according to the first time constant, to an isostatic state at long wavelengths; thereafter there is a much slower relaxation, according to the second time constant, of both surfce topoography and its compensation at depth [8].

Application to the Moon. We have applied this analytical formulation for viscous relaxation to the problem of topographic modification of large lunar basins formed sufficiently early in the Moon's history so that near-surface temperatures were high and significant viscous creep occurred in response to topographic stress. To use the model, we need both the present topographic

profile of an ancient basin and an estimate of the profile after basin formation but before the onset of subsequent modification processes. For the latter we use the topographic profile of the Orientale basin [9], because Orientale has not been modified by the emplacement of ejecta from younger basins [10], the volume of mare basalt fill is small [11], and the geologically long-term modification to early basin structure cannot have been substantial [11]. Based on the analysis of gravity anomalies over present lunar basins partially filled with mare basalt, we must account for the fact that the initial (pre-mare) topographic relief of the basin was at least partially compensated by crustal thickness variations [12, 13].

We first apply the viscous relaxation model to the pre-Nectarian Tranquillitatis basin. Wilhelms and McCauley [14] show a single ancient basin for Tranquillitatis, marked by a major ring structure of about 340 km radius and remnants of an outer ring. Identifying the major ring structure as analogous to the outer Rook Mountains of Orientale gives these two basins closely similar horizontal dimensions. Figure 1 shows a comparison of the present topographic profile of Tranquillitatis, after removing the mare basalt fill [15], with the profile predicted by viscous relaxation of an initial topography similar to that preserved in Orientale. The two profiles compare favorably except in detail, and support the hypothesis that viscous relaxation was an important modifier of pre-Nectarian basins on the lunar nearside.

In contrast, the large topographic relief indicated by Apollo laser altimetry for the larger and older South Pole-Aitken basin [16] on the southern farside is inconsistent with significant viscous relaxation since basin formation. This result requires a mean crustal viscosity at least a factor of 10 higher on the backside than on the nearside over the time interval during which viscous relaxation was important for nearside basins. Cooler crustal temperatures for the backside are indicated for this time period. A nearside-farside asymmetry in temperature may have originated with the process of differentiation that produced the offset of lunar centers [16], and would have been maintained by the concentration of late-stage basin-forming impacts and mare volcanism on the nearside.

Application to Venus. On Venus the relaxation of topographic relief will be substantially accelerated, relative to the Moon, because of the higher gravity and surface temperature (the latter at least since the establishment of the present "greenhouse"). It is therefore of interest to test the proposal [17,18] that impact basins may be observable on the present Venus surface.

In Figure 2 is shown the predicted fate of the topographic profile of an Orientale-size basin on Venus. The model is based on the assumption of initially complete isostatic compensation, a mean crustal thickness of 100 km. [19], and a mean crustal viscosity of $10^{25}$ poise, a conservative value based on laboratory creep measurements at temperatures and stress differences appropriate to Venus surface conditions [20, 21]. The predicted topographic relief is negligible after 3 b.y. ($10^{17}$ sec). From these results we may conclude: (1) Any ancient large basins on Venus, if the present high surface temperatures have persisted for the last 4 b.y., have negligible topographic relief at wavelengths of kilometers and greater. (2) Any large circular depressions on Venus of significant relief (100m and greater) are not ancient (4 b.y. old) impact basins.

Conclusions. Viscous relaxation of topographic relief was likely an important modification process for pre-Nectarian basins on the lunar nearside.

For ancient impact basins on Venus, viscous relaxation should have erased any topographic signature.

References. [1] J.W. Head and S.C. Solomon, LPS XII, 424, 1981; [2] S.R. Bratt, S.C. Solomon and J.W. Head, LPS XII, 109, 1981; [3] S.C. Solomon and J.W. Head, Rev. Geophys. Space Phys., 18, 107, 1980; [4] S.C. Solomon, J.W. Head and R.P. Comer, NASA TM80339, 60, 1979; [5] Z.F. Danes, Astrogeologic Studies, Ann. Prog. Rep., pt. A, USGS, 81, 1965; [6] R.F. Scott, Icarus, 7, 139, 1967; [7] J.L. Hall, S.C. Solomon and J.W. Head, JGR, in press, 1981; [8] S.C. Solomon, R.P. Comer and J.W. Head, JGR, submitted, 1981; [9] J.W. Head, E. Robinson and R.J. Phillips, LPS XII, 421, 1981; [10] D.E. Wilhelms, NASA TM80339, 135, 1979; [11] J.W. Head, The Moon, 11, 327, 1974; [12] W.L. Sjogren and J.C. Smith, PLSC 7th, 2639, 1976; [13] J. Dvorak and R.J. Phillips, Proc. Conf. on Multi-Ring Basins, in press, 1981; [14] D.E. Wilhelms and J.F. McCauley, map I-703, USGS, 1971; [15] R.A. DeHon, PLSC 5th, 53, 1974; [16] W.M. Kaula et al., PLSC 4th, 2811, 1973; [17] H. Masursky et al., JGR, 85, 8232, 1980; [18] D.B. Campbell and B.A. Burns, JGR, 85, 8271, 1980; [19] R.J. Phillips et al., Science, 212, 879, 1981; [20] C. Goetze, Phil. Trans. Roy. Soc. Lond., A288, 99, 1978; [21] H. Ave Lallement, Tectonophysics, 48, 1, 1978; [22] J. Dvorak and R.J. Phillips, PLPSC 10th, 2265, 1979.

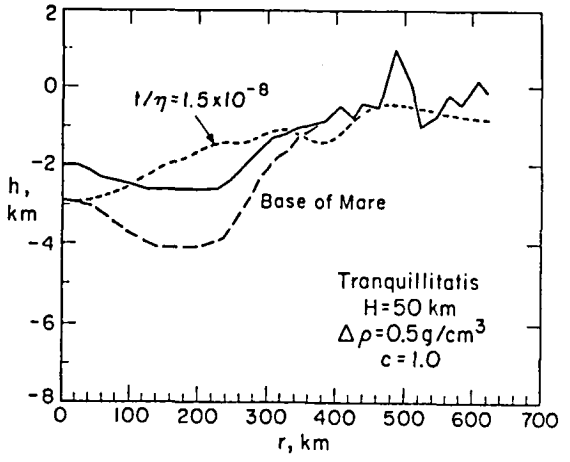


Figure 1. Topographic profile for Tranquillitatis compared with the predicted profile assuming viscous relaxation of an initial basin similar to that of Orientale. Topographic profile, from LM60, extends SW from basin center [14]; the base of the mare basalt is from [15]. The Lamont region, containing a small mascon, may have subsided relative to the rest of the basin by as much as 1.5 km [22]. The model has $\rho$=2.9 g/cm$^3$, $\rho_m$=3.4 g/cm$^3$, H=50km, and complete initial compensation. The quantity $\eta$ is approximately the lowest effective viscosity of the subbasin crust and t is the time interval over which viscosity was similar to that value.

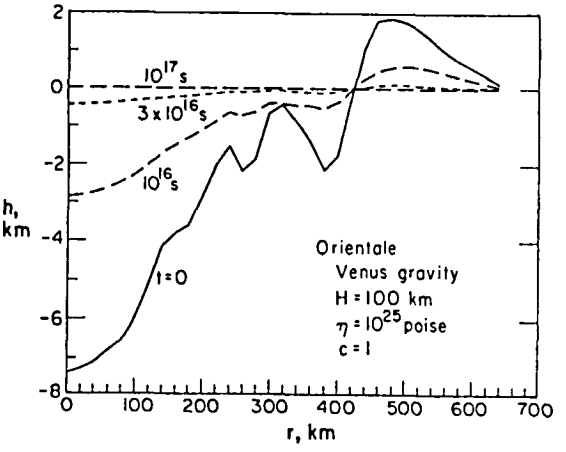


Figure 2. Predicted viscous relaxation with time for an Orientale-size impact basin on Venus, assuming $\eta$=$10^{25}$ poise [20, 21], $\rho$=2.9 g/cm$^3$, $\rho_m$=3.4 g/cm$^3$, H=100km [19] and complete initial compensation. Profiles are shown for t=0, $10^{16}$ sec (300 m.y.), $3 \times 10^{16}$ sec (1 b.y.) and $10^{17}$ sec (3 b.y.). By 3 b.y. the topographic relief is negligible.

# The Nectaris Basin.

J.L.Whitford-Stark. Department of Geology, University of Missouri, Columbia, Missouri, 65211.

Nectaris is a 820 km diameter, multi-ring basin located on the near side of the Moon. The transient cavity is estimated to have been less than 90 km in depth and materials were excavated from a depth of less than 30 km. About 2 km thickness of impact melt is believed to line the cavity center and has a volume of $1.0 \pm 0.5 \times 10^6$ km$^3$. Approximately $3.0 \pm 1.0 \times 10^6$ km$^3$ of material is estimated to have been excavated from the Nectaris basin. Impact melt is believed to form between 15 and 35% of the excavated material. The impact event probably took place at about $3.9 \pm 0.03 \times 10^9$ years ago.

Nectaris ejecta probably forms a substantial proportion of the surface materials at the Apollo 16 site along with lesser amounts of materials from the Imbrium, Serenitatis and Crisium basins. In addition to locally -derived materials (1), the Apollo 16 site contains ejecta deposits from distant, post-basinal craters, of which, Theophilus was probably the most important source for basaltic materials.

Inter-ring plains deposits were deposited after the formation of the Nectaris basin. Stratigraphic considerations preclude the smooth plains deposits being Nectaris impact melt. The most persuasive origin for the smooth plains is as mafic-depleted extrusives overlain by a thin veneer of ejecta. A spectrum for Piccolomini (2), which in part overlies smooth plains, has the characteristics of Low K Fra Mauro basalt but no returned samples of this composition have igneous textures.

A titanium-rich Apollo 16 mare basalt fragment has an age of $3.79 \pm 0.05 \times 10^9$ years and is believed to have been derived from Nectaris (3). Although some relatively titanium-enriched basalts occur in southern Nectaris, titanium-rich basalts are nowhere exposed at the surface. The earliest, exposed eruptives appear to be low titanium (perhaps VLT) basalts found as pyroclastic materials on Daguerre and in the Gaudibert region. Other low-titanium titanium basalts have been excavated from beneath the surface basalts by post-mare craters. The majority of the surface basalts are of intermediate composition (possibly similar to the Apollo 12 basalts) and have an age of approximately $3.6 \times 10^9$ years. The basalt fill is estimated to have a minimum thickness of 3 km and flood-style eruptions appear to have been the main mechanism of emplacement.

Nectaris is a mascon basin, the gravity anomaly corresponding to the location of the basalt fill. Gravity data (4) indicate a minimum fill thickness of 2.7 km. The thinnest crust lies in the northeast part of the basin but is almost twice as thick as the crust beneath other mascon maria (5). Mare ridges within Nectaris exhibit a strong north-south preferential alignment and their formation appears to largely post-date basalt emplacement. The lack of basin-related graben within Nectaris is consistent with a thick lithosphere (6). The basin ring structure is best-preserved in the southwest and least-preserved in the northeast. This is believed to result from horizontal variations in the crust and

lithosphere thicknesses (6) and the influence of the pre-existing Tranquillitatis and Fecunditatis basins; the ring structure being best-preserved where the lithosphere was thickest. Floor-fractured craters within Nectaris are intimately associated with the basalt fill, both in terms of age and location.

Theophilus ejecta, small craters, and Tycho rays, combined with basin subsidence and mare ridge development have been the only modifying influences on Nectaris since the termination of basalt emplacement.

References:
1) J.W.Head (1974) The Moon 11, 77-99. 2) M.P.Charette et al (1977) Proc.Lunar Sci.Conf.8th., p.1049-1061. 3) J.W.Delano (1975) Proc.Lunar Sci.Conf.6th., p.15-48. 4) W.L.Sjogren et al (1972) Science 175, 165-168. 5) B.G.Bills and A.J.Ferrari (1977) J.Geophys.Res. 82,1306-1314. 6) S.C.Solomon and J.W.Head (1980) Rev.Geophys.Space Phys. 18,107-141.

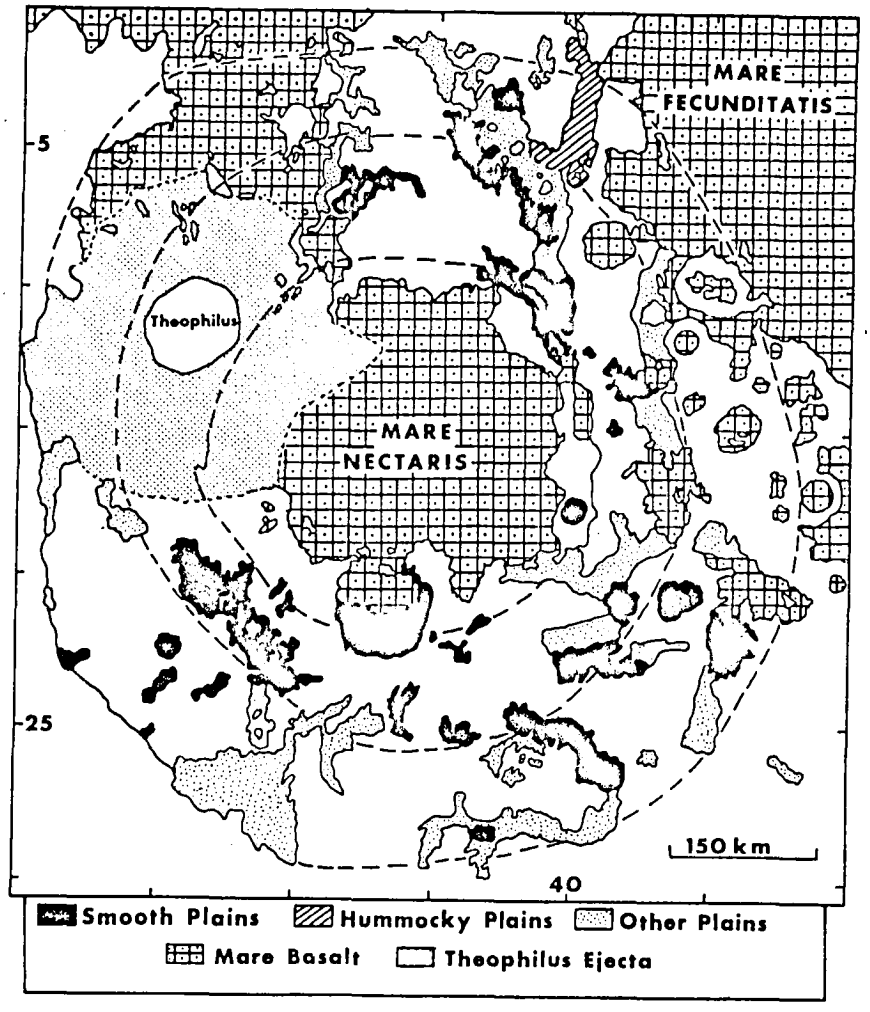


Figure 1: The Nectaris basin ring structure and interior deposits.

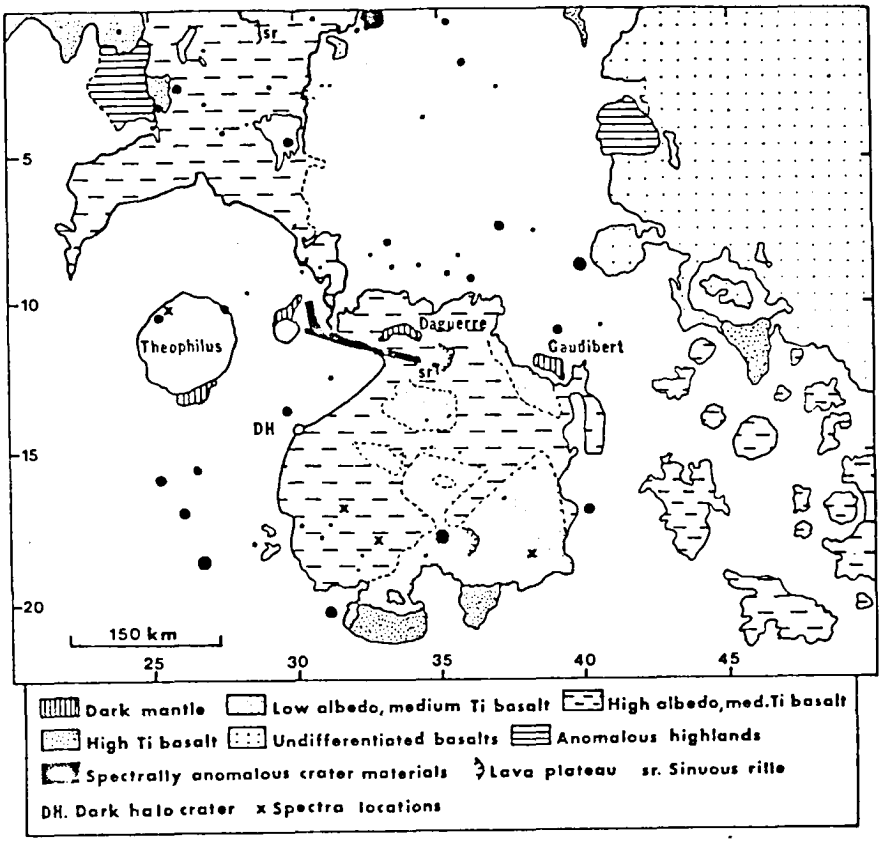


Figure 2. Spectrally defined units within the Nectaris basin

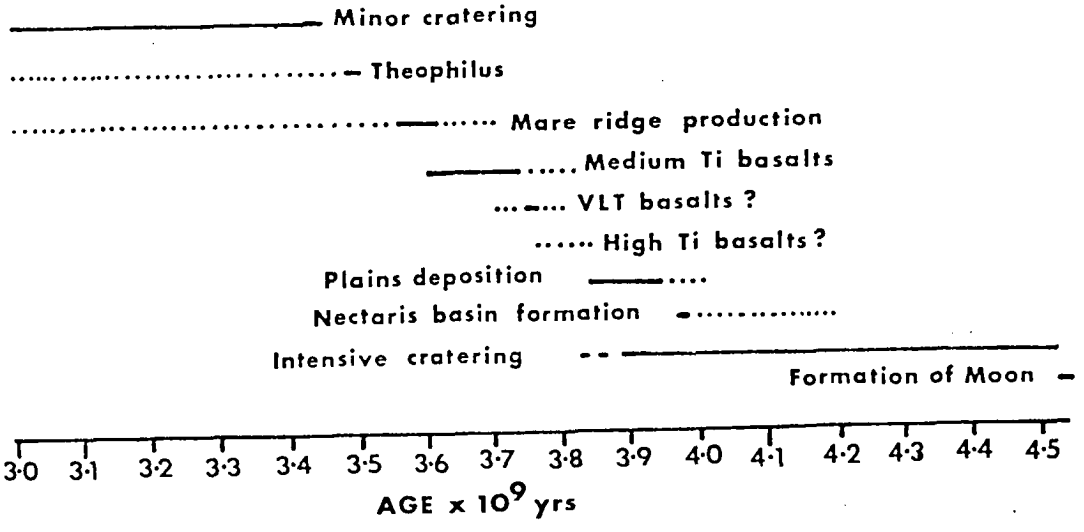


Figure 3: Summary of the evolution of the Nectaris basin.

# THE NATURE OF LUNAR BASIN EJECTA DEPOSITS INFERRED FROM APOLLO HIGHLAND LANDING SITE GEOLOGY

P. D. Spudis, U.S. Geological Survey, Flagstaff, AZ, 86001

Introduction -- Lunar basin ejecta deposits are still poorly understood despite 10 years of intensive study by petrologists, geochemists and photogeologists. Much of the controversy in lunar science revolves around which Apollo highland samples may be confidently related to nearby multi-ringed basins. Although the weight of evidence supports a basin-related origin for some Apollo rocks (e.g., Apollo 17 poikilitic impact melts [1]), many samples have not been confidently identified as basin ejecta. Moreover, photogeological and remote sensing data have not totally succeeded in decisively resolving these issues. The purpose of this paper is to briefly review the types of rocks returned from the various Apollo highland sites that appear to be basin derived, to consider their geologic setting in relation to nearby basins, and to propose a generalized model for basin lithology that is consistent with our knowledge of Apollo site geology and terrestrial impact-craters.

Apollo Highland Samples -- Probably the best collection of basin-related lunar rocks is the suite of poikilitic impact-melt breccias from the Apollo 17 highlands near the Serenitatis basin [1,2]. The melt phase of these rocks is homogeneous in composition and includes a clast assemblage of deeply derived plutonic lunar highland rocks such as norite, troctolite and dunite [2,3]. Some of the boulders at Apollo 17 have originated from origins high on the upper slopes of the massifs [4]; topographic features that are somehow related to the Serenitatis basin [4,5]. The central issue at Apollo 17 is the location of the Serenitatis basin transient cavity rim. Numerous studies [4,5,6] have equated the Taurus moutains with the Outer Rook ring at Orientale, hence very near the rim of the transient crater [5,6]. However, photogeologic relations between large craters, such as Littrow, and the Sculptured Hills unit suggest this comparison may not be valid [2]. Photogeologic evidence for a "melt sheet" [1] at Apollo 17 is lacking and no deposits similar to the melt-sheet deposits of Orientale [7] are recognized in this region. It seems likely that the Apollo 17 site lies outside the rim of the Serenitatis transient cavity if the poikilitic melt rocks are part of a Serenitatis melt sheet. Alternatively, they may be derived from a pond or tongue of melt ejected during the later stages of basin formation.

The Apollo 15 aphanitic "black and white" impact-melt breccias share many similarities with the Apollo 17 poikilitic melt rocks and may be samples of Imbrium basin impact melt [8]. The melt phase and clast assemblage appear to be derived from even greater depth than are the Apollo 17 melt rocks [8,9]; this is consistent with their derivation from a larger impact event. Their presence at the outer topographic rim of Imbrium precludes derivation from a photogeologically recognizable melt sheet; it has been proposed that the light plains known as the Apennine Bench Fm. [10] might represent this impact-melt sheet [14], but recent geologic and chemical investigations suggest the unit probably represents early volcanic fill in the Imbrium basin [11,12,13].

However, melt ponds occur along the Apennine slump masses [11,14] and the Apollo 15 black and white breccias may be derived from these units. The petrology of rocks found at Apollo 15 suggests that the Apennines lie outside the Imbrium basin transient cavity [15], but definitive evidence for clastic Imbrium ejecta at Apollo 15 has not been found.

The most heated controversy regarding Apollo samples is related to the polymict breccias collected at Fra Mauro (Apollo 14). The central issue concerns the relative proportions of primary Imbrium-basin ejecta to local secondary crater ejecta [16,17]. The Apollo 14 crystalline-matrix breccias (CMB) have been interpreted as clast-rich impact melts [18]. Light matrix breccias (LMB) collected from Cone crater (the "white rocks") appear to have originated locally [19] and may be consolidated debris from the Cone crater impact. The crystalline-matrix breccias, however, may be derived from either the local or the primary Imbrium event. Attempts to estimate the shock levels of clastic Imbrium ejecta at the site [20] are rather uncertain; studies of the Ries crater continuous deposits suggest that shock levels may vary widely at any given point in the ejecta sequence [21]. There is nothing in the data that precludes the Apollo 14 CMB being derived from primary Imbrium ejecta.

The origin of rocks returned by Apollo 16 from the central lunar highlands is even more controversial. The contending contributors to sample provenance include the Imbrium and Nectaris basins as well as local origin by secondary cratering [see 22]. LMB from Apollo 16 are found near North Ray crater and may have been assembled by this relatively recent event [23]. An unusual dimict breccia with a homogeneous melt phase [24] is similar to dike breccias found near terrestrial impact structures [25] and may have a local origin. Polymict impact breccias may have been derived from clastic ejecta, but the relative roles of the Imbrium or Nectaris events are uncertain; in any event, the site lies well outside both basins, in a geologic setting analogous to that of the Fra Mauro breccias with respect to Imbrium. Isolated basaltic impact melts [26] may also be basin related.

Remote Sensing Data -- A planar impact-melt sheet, anologous to the sheet seen at Orientale [e.g., 7], is not recognized at either landing site (Apollo 15 and 17) where basin-related impact melts were collected. However, isolated pools of probable basin impact melt are seen in the vicinity of the Apennines (see Fig. 6 of [11]). The Orientale equivalent of this material occurs primarily outside the topogrpahic basin and may represent ejected impact melt [7,17]. These observations suggest that the impact-basin melt sheet was not directly sampled at either the Apollo 15 or 17 landing sites; melt rocks from these sites are probably derived from isolated pools (or pods) of impact melt either ejected and included within the clastic ejecta or spilled from the margin of the main melt sheet.

The orbital geochemical data suggest the presence of compositionally distinct geochemical provinces in the lunar highlands [27]. This implies that the targets of basin impacts were heterogeneous and therefore their ejecta are probably heterogeneous. A distinctive chemical

signature for basin ejecta probably does not exist for large regions of the highlands [27]. Moreover, a "cryptic" component of finely comminuted basin ejecta that would be petrologically unrecognizable may affect the composition of landing site soils and prejudice remote sensing data. Although this hypothetical component would be unrecognizable in photographs, the possibility of its presence should be considered. Furthermore, basin deposits are both laterally and vertically asymmetric; regional geochemical data must be combined with photogeologic evidence to infer the presence of local accumulations of basin deposits.

The Nature of Lunar Basin Ejecta Deposits -- The central basin melt sheet seen at Orientale [7], is inferred by analogy to terrestrial melt sheets [28], to consist of melt-rich, clast-poor lithologies formed within the transient cavity. Some of this material may have been ejected early along high-angle trajectories, and deposited well outside the basin rim. These deposits grade outward into melt rocks, richer in clasts, that are ejected and/or extruded near the margins of the melt sheet; these are the types of rocks sampled by Apollo 15 and 17. Ejection may have occurred prior to chemical homogenization of the melt mass [28] resulting in some compositional inhomegeneity among the melt rocks. During basin forming events, clastic ejecta (including fallback deposits) are widely distributed and probably consitute a significant fraction of the continuous deposits. A considerable amount of ejected melt may also be contained in these deposits; fine dispersion of this melt phase during ejection would produce melt-poor, clast-rich polymict breccias that would be found in basin continuous deposits.

The petrologic nature of basin-related continuous deposits that are outside the topographic rim of the basin is still unresolved. Melt rocks collected at the Apollo 16 site constitute a heterogeneous group that are probably related to several impact events [26]; if Imbrium basin melt is present, it is not similar chemically or petrologically to Imbrium melt at the Apollo 15 site. Basin ejecta at Apollo 14 and 16 are probably represented by polymict impact breccias that were deposited as clastic debris. These breccias would not be identifiable by either a distinctive meteoritic signature or reset radiometric ages. Thus much uncertainty will continue to exist regarding sample provenance in basin-related continuous deposits.

References

[1] Winzer S.R. et al. (1977) EPSL 33, 389. [2] Spudis P.D. and Ryder G. (1981) Proc. Conf. Multi-ring Basins (in press). [3] Simonds C.H. (1975) PLSC 6, 641. [4] Wolfe E.W. et al (1981) USGS Prof. Paper 1080 (in press). [5] Head J.W. (1979) Moon and Planets 21, 439. [6] Reed V.S. and Wolfe E.W. (1975) PLSC 6, 2443. [7] Moore H.J. et al. (1974) PLSC 5, 71. [8] Ryder G. and Wood J.A. (1977) PLSC 8, 655. [9] Ryder G. and Bower J. (1977) PLSC 8, 1895. [10] Hackman R.J. (1966) USGS Map I-463. [11] Spudis P.D. (1978) PLPSC 9, 3379. [12] Hawke B.R. and Head J.W. (1978) PLPSC 9, 3285. [13] Clark P. and Hawke B.R. (1981) PLPSC 12, (in press). [14] Wilhelms D.E. (1980) USGS Prof. Paper 1046-A. [15] Spudis P.D. (1980) Basin Conf. Abstracts, LPI, 83. [16] Oberbeck V.R. (1975) RGSP 13, 337. [17] Wilhelms D.E. et al. (1980) LPS XI, 1251. [18] Simonds C.H. et al. (1977) PLSC 8, 1869. [19] Ryder G. and Bower J. (1976) Imb. Consort. 1, 41. [20] Austin M.G. and Hawke B.R. (1981) LPS XII, 34. [21] Horz F. (1980) Basin Conf. Abstracts, LPI, 48. [22] Workshop on Apollo 16, LPI (in press). [23] Stoffler D. (1980) pers. commun. [24] McKinley J.P. et al. (1981) LPS XII, 691. [25] Wilshire H.G. (1971) J. Geol. 79, 195. [26] Ryder G. in Workshop on Apollo 16, LPI (in press). [27] Spudis P.D. and Hawke B.R. (1981) PLPSC 12 (in press). [28] Grieve R.A.F. et al. (1977) Impact Explosion Cratering, 791.

A SIZE:RANK MODEL FOR BASIN RINGS

Richard J. Pike, U.S. Geological Survey, Menlo Park, CA 94025.

Mathematical regularity in the radial separation of adjacent rings in impact basins has been evident from the first work on lunar basins by Hartmann and Kuiper [1, Tables 1, 2]. From data for 12 multiringed basins on the Moon, they estimated the increment of spacing to be "about 1.5" for adjacent rings of large basins and "1.9 to 2.2" for alternate rings of small basins. Fielder [2] interpreted the Hartmann and Kuiper observations to indicate specifically a constant spacing of $\sqrt{2}$ for adjacent rings, and $\sqrt{2}$ has since become the most widely quoted spacing increment for basin rings on the Earth and other planets [3-6]. The decade-old paper by Hartmann and Wood [4] remains the standard reference on the subject.

This report describes an effort to extend the observations and conclusions of Hartmann and Wood [4]. The new work incorporates additional measurements of ring sizes on several planets and satellites, and establishes a numerical relation between ring size and ring position within each basin. The result is a generalized statistical scheme for size:rank of multiringed basins that may aid in interpreting the mode of origin of basin morphology. This summary elaborates on the findings reported briefly in [7].

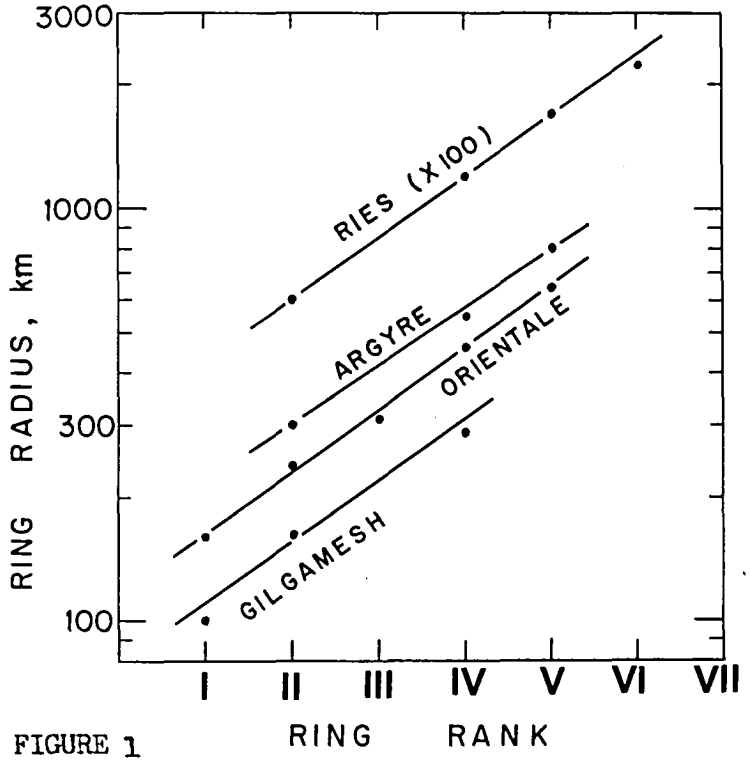


FIGURE 1

Graphs (Fig. 1) of $\log_{10}$ ring radius versus ring rank (equally spaced on arithmetic scale) were plotted for 24 basins (92 rings in all) on the planets (Moon: 11; Earth: 5; Mars: 4; Mercury, Ganymede, Callisto, and Rhea: one each, all four tentative). Rank, the relative radial position of a ring in a given basin, is expressed as a Roman numeral starting with I for the smallest possible ring. Assignment of ranks to rings is guided by two observations of Orientale and other relatively fresh basins with well-preserved complete rings or segments of rings (arcs). First, the "most prominent" [4] ring or "topographic rim" [8] is ranked as ring IV, providing the smallest ring ranks no lower than I. Second, after the topographic rim (IV), characteristically the most promi-

nent and/or prevalent ring is ring II, commonly referred to as the "central-peak ring" [4,6].

The resulting semilog graphs, exemplified by four in Figure 1, are linear and can be described [2] by equations of the form

$$\frac{r_n}{r_1} = 2^{\left(\frac{n-1}{2}\right)} \qquad (1)$$

where n is ring rank ( $n \geq 1$), $r_n$ is radius of any ring, and $r_1$ is radius of the innermost ring (i.e., I). These equations can be written more conveniently

$$\log r_n = \log r_o + n \log b \qquad (2)$$

where $r_o$, the intercept, is radius of the nonexistent ring that ranks just below I, and b is the slope of the least-squares fit to the data. For Orientale, whose ring ranks and radii are I: 160 km, II: 240 km, III: 310 km, IV: 465 km, and V: 650 km [1-4], the relation is

$$\log r_n = 2.06 + n \log 1.4141 \qquad (3)$$

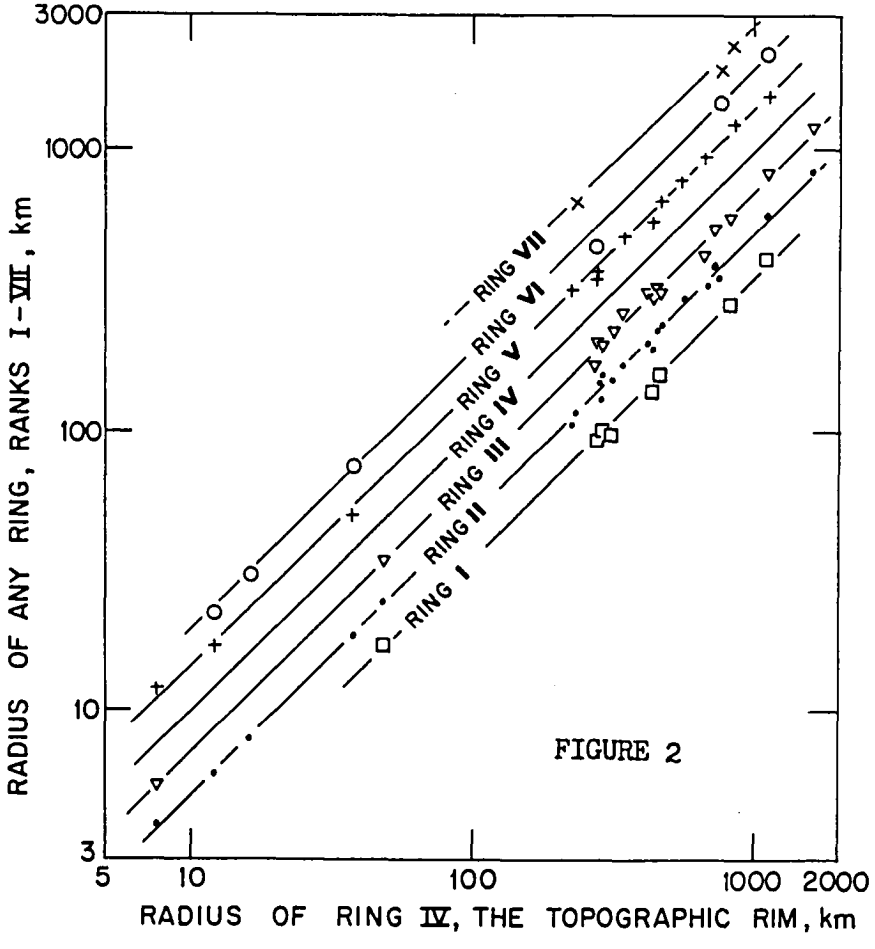


FIGURE 2

The slope of equation (3) is almost exactly $\sqrt{2}$. Slopes of equations for the 24 basins range from 1.33 to 1.47, with a mean of 1.41 and a standard deviation of $\pm$ 0.03. The slopes, especially for the less ambiguous and better preserved basins, are close to $\sqrt{2}$ because so many adjacent rings are spaced by increments of nearly $\sqrt{2}$. This interval recurs so frequently, that obvious non-$\sqrt{2}$ spacings also are assumed to follow it: a spacing that deviates strongly from a $\sqrt{2}$ increment probably represents not a fundamentally different spacing rule but rather an apparently missing ring that is either undetected or that potentially

could have developed during impact [1,4]. Thus each apparent gap is assigned a rank corresponding to its radius and $\sqrt{2}$ separations from adjacent rings (Fig. 1).

The resulting ranks range from I to VII, although no basin has all seven, but rather usually three or four. For example, rings II, IV, V, and VI appear to have been detected at the Ries; the Argyre basin on Mars may have rings II, IV, and V; and Gilgamesh (Ganymede) [9] seems to show rings I, II, and IV (Fig. 1). The seven ring ranks are not equally represented (Fig. 2). In order of decreasing prevalence (expressed as frequency, N, for 24 basins), the seven rings of the proposed size:rank model are: topographic rim (ring IV: N=24) and central-peak ring (II, N=22); intermediate ring (III, N=16) and first outer arc (V, N=13); innermost ring (I, N=8) and second outer arc (VI, N=6); and third outer arc (VII, N=3).

FIGURE 3

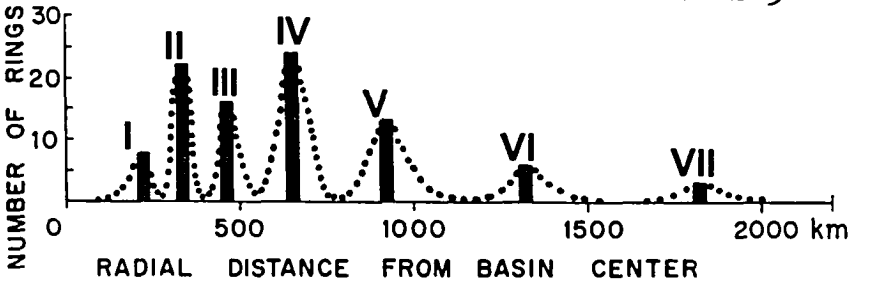


An initial, tentative, interpretation is outlined here. The regular $\sqrt{2}$ spacing of basin rings (Figs. 2,3) indicates that the mechanism coupling impact energy to planetary crusts almost certainly was a wave phenomenon [3,10,11]. The unequal prevalence of the seven families of basin rings, which decreases systematically with increasing distance--inward and outward--from the major concentrations of energy at Rings IV (rim) and II (central-peak ring) suggests specifically the radial decay of a damped wave (Fig. 3). Severe crustal deformation, which is localized at $\sqrt{2}$ intervals to form the rings, is commensurate with the energy concentrated at those radial distances. The deformation probably is elastic only (minor faulting) at low energy levels (e.g., rings I, VI, and VII), and both elastic and plastic (major faulting and wholesale upwarping of crust) at high energy levels (e.g., rings II and IV). Missing and incomplete basin rings result from crustal layering and inhomogenities, and from random variations in the impact process.

REFERENCES: [1] Hartmann W.K. and Kuiper G.P. (1962) Comm. Lunar Planet. Lab. Univ. Ariz., v. 1, p. 51-66; [2] Fielder G. (1963) Nature, v. 198, p. 1256-1260; [3] Van Dorn W.G. (1968) Nature, v. 220, p. 1102-1107; [4] Hartmann W.K. and Wood C.A. (1971) The Moon, v. 3, p. 3-78; [5] Howard K.A., Wilhelms D.E., and Scott D.H. (1974) Revs. Geophys. Space Phys., v. 12, p. 309-327; [6] Head J.W. (1977) pp. 563-573 in Impact & Explosion Cratering, Pergamon, N.Y.; [7] Pike R.J. (1981) abstract in Large-Body Impacts & Terrestrial Evolution Conf., Snowbird, Utah Oct. 19-22, 1981, in press; [8] Wilhelms D.E., Hodges C.A., and Pike R.J. (1977) pp. 539-562 in Impact & Explosion Cratering, Pergamon, N.Y.; [9] Croft S.K. (1981) Lunar & Planetary Sci. XII, p. 187-189; [10] Murray J.B. (1980) Moon and Planets, v. 22, p. 269-291; [11] Baldwin R.B. (1963) The Measure of the Moon, Univ. Chicago.

# Planetary Impact Basin Peak-Ring Spacing: A Comparison

Joseph M. Boyce, NASA Headquarters, Code SL-4, Washington, DC 20546

Voyager 2 images of Tethys show a 400-km-diameter crater containing a mountainous ring about 180 km in diameter (Smith et al., 1981). This is the only impact crater observed on the saturnian satellites with a peak-ring. Other large craters are present on the saturnian satellites but none appear to contain peak-rings. From these large craters, a lower limit can be determined for onset diameters of peak-ring craters on these other bodies. The purpose of this study is to examine peak-ring distributions in planetary impact craters, and using the newVoyager data, improve our understanding of peak-ring formation in basin-size craters.

The 400 km diameter crater on Tethys imaged by Voyager 2 has an interior peak-ring of 180 km in diameter. The relationship of peak-ring diameter to rim diameter of this crater is the same as the relationship for peak-rings craters on Mars, Moon, Mercury, and Ganymede (Head 1978, Boyce 1980), but different than the relationship for peak-ring craters on earth and Callisto (Croft, 1979; Boyce, 1980).

The diameter of onset for peak-ring craters on Tethys can only be approximated because of the small statistical sample. The upper limit is of course, 400 km, the lower limit can be estimated by measuring the next largest crater on Tethys which contains no peak-ring. This is about 160 km. Hence, the onset diameter for peak-ring craters on Tethys is between 160 and 400 km diameters.

In addition, Rhea has several craters up to about 200 km in diameter with no peak-ring, Mimas has a crater 130 km in diameter with no peak-ring and Dione has several craters up to 160 km in diameter with no peak-ring. This suggest that if the hypothesis of morphological progression is valid (Wood and Head, 1976; Wood, 1980) then the onset diameters for these bodies are larger than 200 km, 130 km and 160 km, respectively.

The origin of mountainous structures in impact craters, such as central peaks and peak-rings, continues to be a controversial subject. For example, Pike (1980), Roddy (1977), Wood and Head (1976), and Wood (1980), and others suggest a general morphologic progression with increasing crater diameter, from central peaks to peak-ring to multiple-rings. On the other hand, Hale and Head (1979) argue that there is no consistent trend for lunar craters to have increasing complex peaks at large crater dismeters, and consequently, the transition from central peak to peak rings does not appear to them as a single, gradual transition. This study, however, concentrates only on peak-ring formation.

The onset diameter for peak-ring craters has been shown to vary from planet to planet (Boyce, 1980; Croft, 1979; Head, 1978; Pike, 1980). Wood (1980) using recent Viking images suggests that the onset diameter for peak-ring craters on Mars is considerably smaller than previously thought. However, Head (1978) shows that the ratio of the peak-ring diameter versus the crater diameter is constant for the Moon, Mercury and Mars. Croft (1979) interprets terrestrial impact craters to have ring diameters that are systematically larger compared to their rim diameters than those on the other planets. Croft suggested that the difference was due to the larger terrestrial gravity. This relationship, however, is uncertain due to the small population available for study and the high degree of erosional degradation. Later, Boyce (1980) added Callisto and Ganymede craters to the date and found the ratio of peak-ring diameter to crater rim diameter on Ganymede to be similar to those for the Moon, Mercury and Mars, but the ratio for craters on Callisto is similar to that for the Earth. It was further noted that the onset diameters were larger than those on the Earth. Boyce (1980) interpreted these data to indicate no obvious or consistent pattern was apparent that related any one single factor as controlling crater formation and morphology, such as planetary gravity, impact velocity, target characteristics, or projectile body characteristics. The conclusion is that previous simple hypotheses involving only one dominant factor as controlling ring spacing should be rejected as a broad generalization and that different factors (or combinations) may dominate depending on the environmental characteristics of the planet. This view is supported by theoretical studies of a number of workers, such as Kreyenhagen and Schuster (1977), Roddy (1977), Piekutowski (1980), and others. The experimental and field new data present in this study have not changed these conclusions.

References

Boyce, J.M., 1980, Basin peak-ring spacing on Ganymede and Callisto: Implications for the origin of central peaks and peak-rings: (abs.) Reports of Planetary Geol. Progr. 1979-1980, NASA TM 81776, p. 339-342.

Cintala, M.J. Wood, C.A., and Head, J.W., 1977, The effects of target characteristics on fresh crater morphology: Preliminary results for the Moon and Mercury, Proc. Eighth Lunar Sci. Conf., Houston, Texas, v. 3., p. 3409-3426.

Croft, S.K., 1979, Interplanetary basin ring spacing: Consequence of Gravity vs. Strength Scaling: (abs.) Lunar and Planet. Sci. Conf. 10th, Houston, Texas, v. 1, p. 245-247.

Hale, W., and Head, J.W., 1979, Central peak in lunar craters: morphology and morphometry: Proc. Lunar Planet, Sci. Conf. 10th., vol. 3, p. 2623-2633.

Head, J.W., 1978, Origin of central peak rings: Evidence from peak-ring basis on Moon, Mars, and Mercury: (abs.) Lunar and Planet. Sci. Conf. 9th, Houston, Texas, v. 1, p. 485-487.

Keyenhagen, K.N., and Schuster, S.H., 1977, Review and comparisons of hypervelocity impact and explosion cratering calculations in Impact and Explosion Cratering (D.J. Roddy, R.O. Pepin, ad R.E. Merrill, etc.), p. 983-1002.

Piekutowski, A.J., 1980, Formation of bowl-shaped craters, Proc. Lunar Planet. Sci. Conf. 11th, v. 3, p. 2119-2144.

Pike, R.J., 1980, Formations of complex impact craters: evidence from Mars and other planets, Icarus 43, 1-19.

Roddy, D.J., 1977, Large-scale impact and explosion craters: comparisons of morphological and structural analogs, in Impact and Explosion Cratering (D.J. Roddy, R.O. Pepin, and R.B. Merrill, eds.), p. 185-246.

Smith, B.A., and others, 1981, The Voyager 2 Encounter of Saturn: Imaging Science Results, Science, in press.

Wood, C.A., and Head, J.W., 1976, Comparison of impact basins on Mercury, Mars, and the Moon, Proc. Lunar Sci. Conf. 7th, Houston, Texas, v. 3, p. 3627-3651.

Wood, C.A. 1980, Martian double ring basins: New observations: Proc. Lunar Planet. Sci. Conf. 11th, v. 3, p. 2221-2241.

# PLANETARY MEGAREGOLITHS

R. A. De Hon, Department of Geosciences, Northeast Louisiana University, Monroe, LA 71209

Continuous cratering on planetary surfaces during the early history of the solar system has produced a surface mantle of fragmental debris. The extent of this debris mantle or megaregolith (1) and its subsequent survival depend on the environmental conditions of the planet and the time allowed for development. This paper presents a simplified model of megaregolith formation as a function of time and examines the effects of various planetary environmental controls.

The agent of formation of a megaregolith is the process of meteorite impact. The chief factors controlling the impact process involve properties of the bolide and properties of the planet. The meteor supplies energy for brecciation and excavation by virtue of its mass and velocity. Moderating factors that may be involved in the cratering process include the density, shape, or strength of the meteorite. The ultimate efficiency in the formation of a crater is controlled by properties of the target. Target variables include target strength, gravitational attraction, and atmospheric pressure.

For a first approximation of the effects of cratering on a planetary surface, restraints are set to limit the initial conditions as follows:

1. Uniform projectile properties (i.e. identical mass and velocity for all meteorites)
2. Uniform initial target properties
   - A. Uniform gravity
   - B. Hard target
   - C. No atmosphere
   - D. No internal or external geologic agents (erosion, volcanism, isostacy, etc.)

If impacts are allowed to accumulate on the surface, the following stages of surface alteration are inferred:

Stage 0 - Initial surface--no craters

Stage 1 - Scattered impacts--isolated craters formed in hard target; original surface exposed between ejecta blankets of craters.

Stage 2 - Continuous blanket of ejecta--no original surface exposed; thin, irregular mantle of crater ejecta

Stage 3 - Surface Saturation--number of craters at maximum; new craters form at the expense of pre-existing craters; irregular surfical mantle of crater ejecta; hard rock septa between adjacent craters.

Stage 4 - Subsurface Saturation--no change in crater density; bedrock septa removed by continued impact excavation; surfical mantle (megaregolith) reaches maximum thickness; new impacts do not excavate below megaregolith-hard rock interface.

The initial conditions imposed on the target by the model cannot be maintained during the accumulation of impacts on the surface. Impacts continually alter the surface producing a mantle of ejecta debris (megaregolith). The ejecta mantle is discontinuous in Stage 1, becoming continuous and thicker as impacts saturate the surface. Early impacts form craters in the hard bedrock of the target; later craters are formed in a stratified target (ejecta mantle over bedrock); and the latest craters are formed in a soft target (thick ejecta mantle or megaregolith). Changing target properties result in changing crater morphologies (2,3,4). Late stage craters are larger than early stage craters due to a large decrease in target strength by brecciation. Intermediate and late stage craters are complex craters due to the interaction of the shockwave with the megaregolith-basement rock interface at depth.

The initial conditions imposed on the impacting meteorites do not exist in nature. Meteors possess varying energies because of differing masses and velocities. Variable impact energy does not greatly affect the model as proposed; rather, variable energy imposes a saturation-size term as the surface approaches equilibrium (5). Craters less than the saturation-size simply churn the surfacial layer. Craters larger than the saturation-size may produce irregularities in the megaregolith-basement rock boundary. During the period of intense cratering in the early history of the solar system, the size distribution of craters was such that the saturation-size is not time dependent (6). That is, surface saturation (Stage 3) is reached at nearly the same time for large craters as for small craters.

Surface gravity tends to control the ultimate thickness of the megaregolith in Stage 4. Crater size is inversely proportional to gravity (7,8); hence, high gravity results in small craters. As a rule, the megaregolith of a mature (Stage 4) planet is thicker on a planet with low gravity and thinner on a planet with high gravity. If, however, the planet is sufficiently small and impact velocities are high, a significant portion of the ejecta may be accelerated to velocities in excess of the escape velocity (9). Thus, on small bodies, asteroids and small satellites, the resulting megaregolith may be thin or absent.

An atmosphere has an effect similar to that of gravity on crater size. Crater size is reduced as atmospheric pressure increases (8,10, 11). In addition, an atmosphere has a screening effect as it blocks small meteors and reduces the velocity of incoming bodies. Hence, the presence of an atmosphere results in smaller craters and a correspondingly thinner megaregolith. If the atmosphere is sufficiently mobile, no craters will survive erosion, and impact breccias are redistributed by the sedimentary cycle.

Planetary tectonic or volcanic activity also affects the survivability of craters on the surface. On active planets, the accumulation of a megaregolith is in competition with internal processes which may destroy the surface (subduction) or bury the megaregolith (plateau

volcanism). Hence, on some planets, cratered surfaces may go through processes of rejuvenation.

The surface geochemistry, determined by remote sensing, will be controlled by lateral variations of the primitive surface; lateral variations introduced by tectonic, volcanic, or erosional processes; and vertical compositional variations exposed by impact excavation. For the initial conditions set forth in this model, Stage 1 surface geochemistry would reflect variations, if any, of the primitive surface and vertical variations exposed by crater excavation. As the megaregolith forms and matures by continued impact mixing and churning, the surface approaches (however slowly or inefficiently) a uniform geochemistry (12). One of the goals of planetary geochemistry should be to assess the maturity of the surface by establishing the extent that impact mixing has progressed toward homogenizing the surface. Local anamolies would be exposed by large, late impacts (basins) which might excavate below the megaregolith-bedrock interface.

In summary, repeated impact subjects a planetary surface to progressive stages of megaregolith formation. The ultimate thickness of the megaregolith is limited by the impact energy supplied to the surface and the surface gravity of the planet. Generally in the presence of low gravity the megaregolith will be thick; and for high gravity the megaregolith will be thin. Modifying factors include atmospheric pressure and active internal or external resurfacing processes. On some planets the surface is rejuvenated by resurfacing. On active planets the megaregolith may not survive.

References


1. Hartmann W. K. (1973) Icarus 18, 634-636.
2. Aggarwal H. R. and Oberbeck V. R. (1979) PLPSC 10, 2689-2705.
3. Head J. W. (1976) PLPSC 7, 2913-2929.
4. Cintala M. J. et al. (1977) PLPSC 8, 3409-3425.
5. Gault D. E. (1970) Radio Sci. 5, 273-291.
6. Hartmann W. K. (1977) Highlights of Astron. 4, 229-232.
7. Chabai A. J. (1977) Impact and Explosive Cratering, 1191-1214.
8. Gault D. E. and Wedekind J. A. (1977) Impact and Explosion Cratering, 1231-1244.
9. Cintala M. J. et al. (1978) 9th LPSC (abs.), 166-168.
10. Johnson S. W. et al. (1969) J. Geophys. Res. 74, 4834-4850.
11. Herr R. W. (1971) NASA TRR-366.
12. Hörz F. et al. (1976) PLSC 7, 2913-2929.

# Chapter 4

# VOLCANIC PROCESSES AND LANDFORMS

THE ORIGINS OF LUNAR DARK-HALO CRATERS: IMPLICATIONS FOR VOLCANIC AND IMPACT PROCESSES.

B. Ray Hawke and Jeffrey F. Bell, Planetary Geosciences, Hawaii Inst. of Geophysics, Univ. of Hawaii, Honolulu, HI 96822.

Introduction: The existence of lunar craters surrounded by deposits of low-albedo material has long been noted. While early workers generally interpreted dark-halo craters as volcanic vents[1,2], an impact origin was not ruled out. With the availability of high-resolution spacecraft imagery of the lunar surface it became obvious that multiple modes of origin are required to account for dark-haloed craters. Because of the key role dark-halo craters appear to play in the solution of several major lunar problems (e.g., 3, 4), we have undertaken a program to study these features using a variety of photogeologic and remote sensing techniques. The purposes of this investigation include the following: (1) to identify the processes responsible for the formation of dark-halo craters, (2) to develop geologic and remote sensing criteria to distinguish the various types of dark-halo craters, (3) to determine the distribution, mode of occurence, and composition of dark haloes of pyroclastic origin, (4) to confirm the existence and composition of the postulated basaltic component in the ejecta deposits of dark-haloed impact craters, and (5) to conduct regional studies to determine the extent and duration of early volcanic activity.

Dark-Halo Craters of Volcanic Origin: Some dark-halo craters have been firmly established to be of endogenic origin and are thought to be the source vents for pyroclastic material which forms the dark haloes. Typical of these are the dark-halo craters on the floor of Alphonsus which are thought to be of internal origin[3-9]. Volcanic dark-halo craters are commonly non-circular (irregular or elongate); are often aligned with linear rilles, fractures, or lineaments; exhibit depth/diameter ratios which are generally (though not always) less than those for fresh impact structures; and lack obvious rays[3].

Dark-halo craters of volcanic origin appear to be concentrated around the lunar maria and many are associated with floor-fractured craters[10-12]. Typical examples exist on the floors of J. Herschel, Atlas, Franklin, Gauss, Messala, and Bohnenberger craters. Where adequate multispectral imagery exists, the deposits have been found to be spectrally distinct from surrounding material[10,11] and while the majority of deposits have compositional affinities with nearby maria, several deposits (e.g. Atlas, Franklin) have spectral characterictics distinct from adjacent mare, suggesting that they may represent deposits associated with an earlier phase of basaltic volcanism. Preliminary analysis of newly obtained near-IR spectra (0.6-2.5μm) fully support our previous findings[13].

Dark-Halo Craters of Impact Origin: Multiple explanations are required to account for the dark haloes associated with craters which exhibit characteristics indicative of an impact origin. For some craters, the dark material is clearly related to deposits of impact melt[14-16]. At small impact craters (D<10km), these occurrences are characterized by the limited extent and relative thinness of the dark material, which is concentrated in a narrow zone adjacent to the rim crest and rapidly thins and becomes irregular and "patchy" with distance from the parent crater. The dark-halo which surrounds Tycho crater never exhibits albedo values lower

than those of mature highland surfaces, has spectral properties consistent with the presence of large quantities of impact glass, and generally correlates with ejecta facies which contain abundant flow features and a thin hard-rock vencer of probable impact melt origin[16].

It has been informally suggested that certain dark-haloed lunar impact craters have low-albedo ejecta due to contamination by dark projectile material. It has been suggested that projectile contamination, along with other processes, may be important in producing dark-ray craters on Ganymede[17]. Although this possibility cannot be ruled out for lunar dark-haloed impact craters, it seems unlikely in light of our current understanding of the amounts of projectile material which are incorporated into crater exterior deposits and because no spectral evidence for an exotic (meteoritic) component in dark-halo material has been found.

Another type of dark-halo impact crater appears to have been formed by the excavation and deposition of dark materials from beneath a lighter surface unit. For example, were mare basalts have been buried by lighter impact ejecta deposits, they may be re-exposed in the ejecta of later small cratering events. Copernicus H is a 4.6 km dark-haloed impact crater on the ejecta blanket of Copernicus crater. Copernicus H was chosen for a detailed analysis because of the very strong evidence for an impact origin and because it is typical of many such craters of the ejecta blankets of Copernicus, Theophilus, Langrenus, Maunder, and other large relatively fresh impact structures.

Copernicus H crater exhibits enhancements on infrared and radar (3.8 and 70 am) maps presented by Shorthill et al.[18]. Enhancements in all three data sets imply an excess of surface rocks with sizes of 1 cm and larger. These observations demonstrate that Copernicus H is not a volcanic vent (i.e., the dark material is not fine-grained pyroclastic debris), that the crater excavates material with physical properties very different from Copernicus ejecta, that Copernicus H is very young, and that the dark halo is not pyroclastic material excavated from beneath Copernicus ejecta deposits.

Multispectral images were obtained for the region which includes Copernicus H. These images show that the dark halo exhibits enhanced 0.40/0.56 μm ratio values and very low 0.95/0.56 μm values. Hence, the dark halo is spectrally distinct and is somewhat bluer than the surrounding Copernicus ejecta. The multispectral ratio image data are consistent with the presence of major amounts of fresh, high-Ti, "blue" basalt in the Copernicus H dark halo as suggested by Head[19] and Pieters[20].

We obtained near-infrared (0.6-2.5 μm) reflection spectra for Copernicus H and other dark-haloed impact craters in the ejecta blankets of relatively fresh craters with the Mauna Kea 2.2-meter telescope. The characteristics exhibited by the Copernicus H spectrum fully confirm that mare basalt was excavated from beneath the Copernicus ejecta blanket. Comparisons with the spectra of the inner wall of Reiner crater and the nearby recent crater Reiner K show either that the Copernicus H spectrum represents very immature mare despite being darker than its surroundings, or that the spectrum is dominated by the crater interior which is kept less mature than the halo by mass wasting on the steep inner slopes. The large extent of the area of low 0.95/0.56 μm ratio values indicates that the former possibility is the case.

The results of a global survey of dark-haloed impact crater distribution revealed the widespread occurrence of these features on non-mare units generally mapped as light plains[4]. The existence of pronounced clusters of dark-haloed craters on Imbrian plains material was noted in a number of regions[4]. We chose the Schickard-Schiller region for detailed study. Near-infrared reflectance spectra were obtained for three dark-halo craters in this region as well as suitable background terrain features. Schickard R crater (D≈6 km) is a dark-haloed impact crater located on a smooth, high-albedo plains area on the floor of Schickard crater. The interpretation of the Schickard R spectrum is complicated by the fact that the area for which the spectrum was obtained contains both dark-halo crater material and high plains materials. An analysis of the Schickard R spectrum was made using spectral mixing techniques[21]. Substraction of various amounts of a highland spectrum from that of Schickard R produced residual spectra characteristic of fresh mare basalts. Near-IR spectra were obtained for two other dark-haloed impact craters in the general area of Schickard. Both Inghirami W and Nöggerath F exhibit spectra similar to that of Schickard R. It appears that these craters also excavated ancient, pre-Orientale mare material from beneath light plains which are believed to have been emplaced as a consequence of the Orientale impact event.

Conclusions: 1) Lunar dark-halo craters can be formed by volcanic processes as well as a variety of impact-related processes. 2) The mode of origin of a given dark-halo crater can be determined if adequate remote sensing and photogeologic data exists. 3) Dark-halo crater deposits of pyroclastic origin are more abundant and widely distributed then previously recognized. 4) The majority of the pyroclastic deposits have compositional affinities with nearby mare material. 5) Remote sensing data conclusively demonstrates that Copernicus H excavated high-Ti mare basalt. 6) Dark-haloed impact craters in the Schickard-Schiller region excavated mare basalt from beneath light plains deposits. 7) If the results of additional spectral studies, now in progress, of dark-halo impact craters clustered in other portions of the lunar nearside indicate that they too expose basaltic material, then the extent and duration of lunar volcanic activity, as well as the volume of volcanic fill, will have to be reassessed.

References: 1) E. Shoemaker (1962) Physics and Astronomy of the Moon, 283. 2) J. Salesbury et al. (1968) Mon. Not. Roy. Astron. Soc. 138, 245. 3) J. Head and L. Wilson (1979) PLPSC 10, 2861. 4) P. Schultz and P. Spudis (1979) PLPSC 10, 2899. 5) R. Heacock et al. (1966) JPL TR-32-800, 182. 6) K. Howard and H. Masursky (1968) USGS Map I-566. 7) W. Hartmann (1967) CLPL 6, 31. 8) J. McCauley (1969) USGS Map I-586. 9) J. Head (1976) RGSP 14, 265. 10) B. Hawke and J. Head (1980) LPS XI, 416. 11) B. Hawke et al. (1980) NASA TM-82385, 155. 12) D. Wilhelms and J. McCauley (1971) USGS Map I-703. 13) T. McCord et al. (1981) LPS XII, 679. 14) K. Howard and H. Wilshire (1975) JRUSGS 3, 237. 15) B. Hawke and J. Head (1977) Impact and Explosion Cratering, 815. 16) B. Hawke et al. (1979) Papers Presented to the Conf. on the Lunar Highlands, 50. 17) J. Conca (1981) LPS XII, 172. 18) R. Shorthill et al. (1972) The Moon 4, 469. 19) J. Head (1974) PLSC 5, 207. 20) C. Pieters (1977) PLSC 8, 1037. 21) R. Singer and T. McCord (1979) PLPSC 10, 1835.

NUMERICAL TAXONOMY OF CENTRAL VOLCANOES ON THE PLANETS

Richard J. Pike and Gary D. Clow, U.S. Geological Survey, Menlo Park, CA 94025

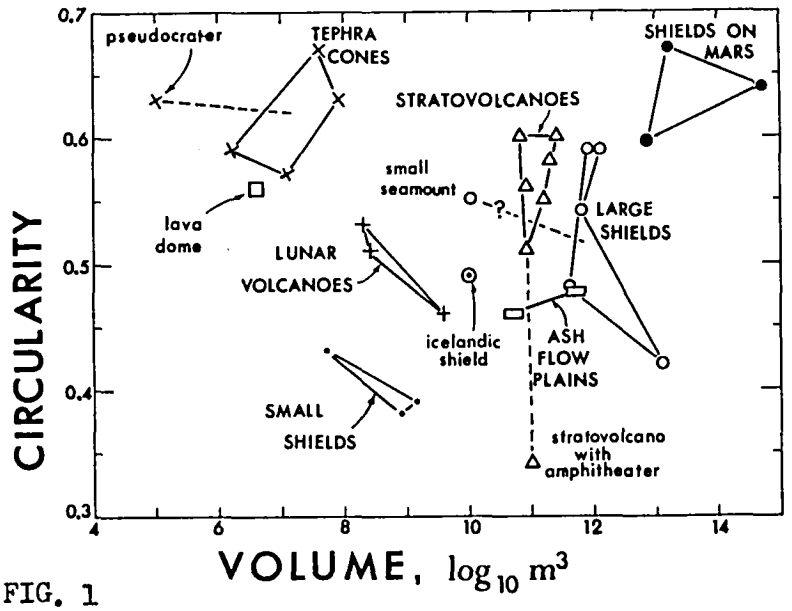


FIG. 1

We have extended the quantitative systematics of some planetary volcanic landforms [1] with respect to both the data base [2] and its analysis (Figs. 1-3). This note outlines general progress; specific findings for Mars have been reported [3].

The current data set comprises five topographic measurements (edifice height and flank width, summit-depression diameter and depth, and rim-crest circularity) for 730 volcanoes on three planets [2]. The initial data [1] have been improved in three respects: (1) enlargement of the terrestrial sample, (2) elimination of doubtful lunar volcanoes and measurements, and (3) addition of two new categories: small seamounts (Class KO) and breached stratovolcanoes (Class SCL, e.g. Mt. St. Helens). Also, two classes of large shield volcanoes, Class KT (tholeiitic) and KM (alkalic and mixed lavas) have been subdivided.

We have recalculated geometric models for all 31 classes from averaged dimensions, and have derived a representative flank profile for each class from well mapped individual volcanoes. These profiles have enabled us to add average edifice volume to the analysis.

Revised results from the new data (Figs. 1-3) fall into four areas: general, Earth, Moon, and Mars. The methods, principal-components analysis and cluster analysis, are described elsewhere [1,4]. Five topographic variables, which are averages for each class of volcano, were used to classify the revised data: height/depth, width/diameter, height/width, circularity, and volume. All save circularity were transformed to logarithms. The first three principal components describe, respectively, 45%, 29%, and 20% of the variance in the data (Fig. 3).

The chief general result is that addition of edifice volume has strengthened the capacity of the quantitative-morphologic approach to separate different volcanic classes and group genetically similar classes. The improvement is evident not only in a simple bivariate plot of volume and circularity (Fig. 1), but also in the cluster diagram (Fig. 2) and the three-component plot (Fig. 3). For example, first-order divisions in the 31 classes partitioned by cluster analysis are now more process-oriented, especially with respect to distinguishing monogenetic from polygenetic classes, than previously [3].

Terrestrial volcanoes vary widely in volume, two classes falling beyond even the six orders-of-magnitude range (Fig. 1). Subdividing classes KM and KT seems to reflect some real contrasts: subaerial alkalic shields (Class KMA) and Hawaiian tholeiitic shields (Class KTH) stand well apart from all other shields (Figs. 2, 3). However, Classes KMM, KTG, and KTU [2] may share more similarities than differences. Icelandic shields closely resemble neither small nor large lava shields, and the Mt. St. Helens class (SCL) also is highly distinctive.

FIG. 2

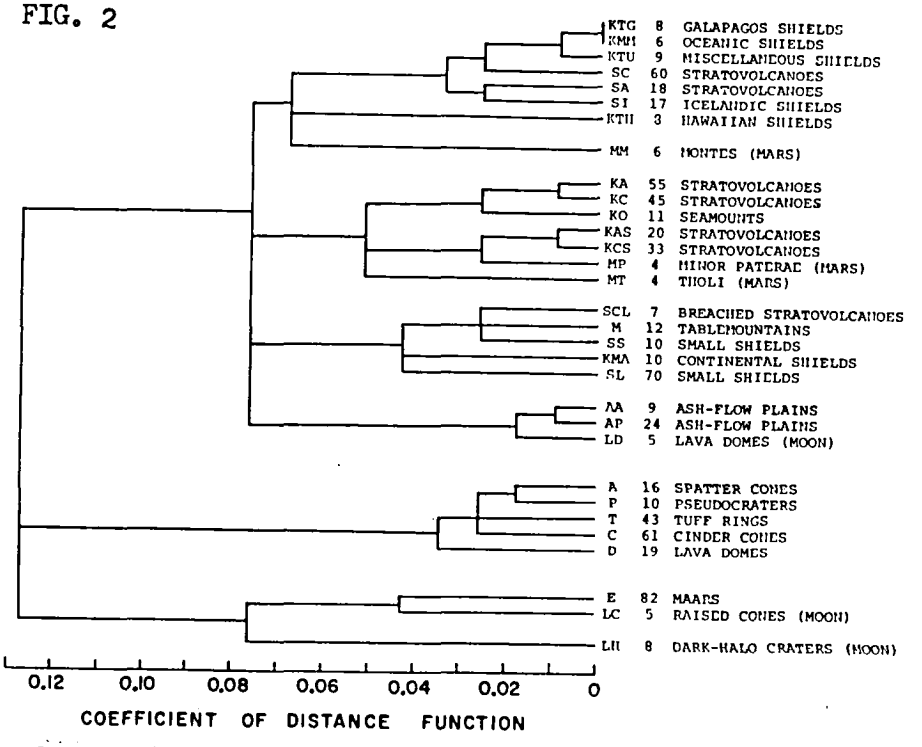


The Moon's few, small volcanoes comprise three quite different classes, none of which has a close terrestrial analog. Raised cones bear some resemblance to tuff cones and cinder-spatter cones, but the dark-halo craters [5] are unique among the 31 classes (Fig. 3). Lunar mare domes coincidentally resemble ash-flow calderas in overall shape, but are at least an order of magnitude less in volume. Their morphology shares some aspects of small to medium-sized terrestrial shields [6].

Large caldera-bearing volcanoes on Mars [7-10] are unique with respect to volume and circularity (Fig. 1), but not in overall morphology (Figs. 2,3). Montes, minor paterae, and tholi are quite different in gross form, and modeled exhumation of partially buried tholi and paterae (Capital letters in Fig. 3; see also [3]) does not eliminate this contrast. Tholi and minor paterae seem to be types of shields unique to martian geologic conditions. However, even the montes seem to have no close analog among terrestrial shield volcanoes (Fig. 2).

The gross morphology of central volcanoes on three planets is highly diverse, although similar processes and events clearly generate landforms with similar overall shapes. Formational conditions on the Moon and Mars evidently differ enough so that their resulting volcanoes are not as closely analogous to those on Earth as similarities in detailed morphology might lead one to expect, despite obvious similarities in geologic processes.

Edifice volume is a key variable in characterizing volcanoes for morphologic comparisons, although it may be better expressed in dimensionless terms that also take gravity into account.

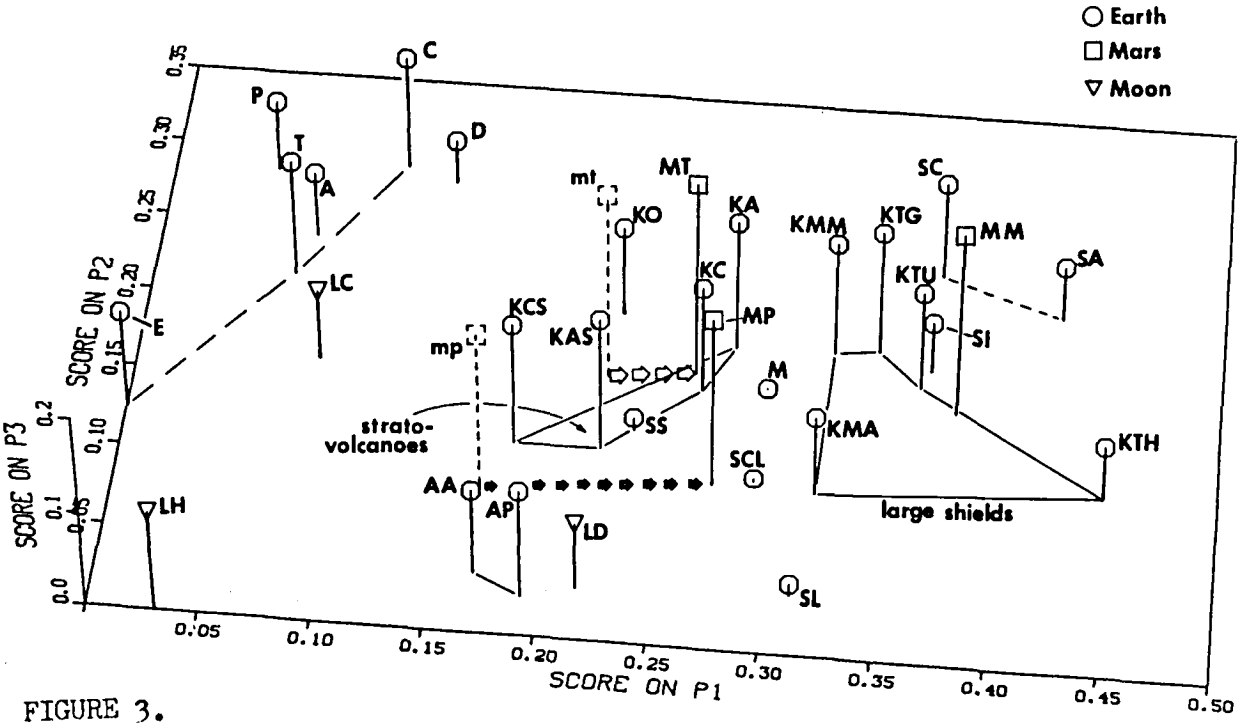


FIGURE 3.

References:


[1] Pike, R. J. (1978) Proc. Lunar Planet. Sci. Conf. 9th, p. 3239-3273.

[2] Pike, R. J. and Clow, G. D. (1981a) U.S. Geol. Survey Open-file Rept. 81-1038.

[3] Pike, R. J. and Clow, G. D. (1981b) Papers 3rd Intl. Mars Colloq. LPI Contr. 441, p. 199-201.

[4] Pike, R. J. (1980) U.S. Geol. Survey Prof. Paper 1046-C.

[5] Head, J. W. and Wilson, L. (1979) Proc. Lunar Planet. Sci. Conf. 10th, p. 2861-2897.

[6] Head, J. W. and Gifford, A. W. (1980) Moon and Planets, v. 22, p. 235-258.

[7] Plescia, J. B. and Saunders, R. S. (1979) Proc. Lunar Planet. Sci. Conf. 10th, p. 2841-2859.

[8] Greeley, R. and Spudis, P. D. (1981) Revs. Geophys. Space Physics, v. 19, p. 13-41.

[9] Blasius, K. R. and Cutts, J. A. (1981) Icarus, in press.

[10] Carr, M. H. (1981) The Surface of Mars, Yale Univ. Press, in press.

# QUANTITATIVE ANALYSIS OF OLYMPUS MONS

S. S. C. Wu, P. A. Garcia, Raymond Jordan, and F. J. Schafer
U.S. Geological Survey, Flagstaff, AZ 86001

Olympus Mons is certainly one of the largest volcanoes in our solar system. It covers an area about the size of the state of Arizona. Previous estimates of its height above the surrounding area (1, 2, 3, 4, 5, 6, 7, 8) ranged from 17 to 23 km. A height of 27 km above the Mars topographic datum (9, 10), is shown on the U.S. Geologic Survey 1:25,000,000 Mars global topographc map (11) which was compiled by synthesis of remotely sensed data from the Mariner Mars 9 mission and Earth-based radar observations.

Viking Orbiter photographs were used to compile a detailed topographic map of Olumpus Mons at a scale of 1:1,000,000 with a contour interval of 200 m (12). This map was compiled by special photogrammetric techniques that had been developed to enable systematic mapping of Mars from Viking Orbiter photographs despite their extremely narrow field-of-view (13). This newly compiled topographic map (12) shows the elevation of Olympus Mons to be 26,400 m.

Olympus Mons has the general form of terrestrial basaltic shields (4). Figure 1 shows profiles measured from the map (12) along the east-west, north-south, northeast-southwest and northwest-southeast directions. Slopes measured from these profiles fall into three groups. Slopes of 2° to 3° prevail at elevations ranging from 2 to 7 km. Slopes are 8° to 24° between elevations of 7 and 16 km, due mainly to the presence of several steep scarps within this elevation range. The relief of these scarps are as much as 8 km on the north flank and 5 km on the south flank. Slopes are 2.5° to 6.5° from an elevation of 13 km to the outside rim of the caldera at 24 km. Blasius (3,4) has reported an average flank slope of 3.3, and a total volume for Olympus Mons of $2.7 \times 10^6$ km$^3$. Calculations based on the new map (12) give a total volume of $2.594 \times 10^6$ km$^3$ above an elevation of 5 km which is about the elevation of the base of the volcano on the south. Table 1 lists segmental volumes in increments of 1 km and cumulative volumes from the top of the volcano.

## References

(1) Arthur, D. W. G. (1976) Photogram. Record, 8, p. 617-630.

(2) Blasius, K. R. (1973) Jour. of Geophys. Res., 78 (20), p. 4411-4423.

(3) Blasius, K. R., Roberts, W. J., Cutts, J. A., Duxbury, T. C., and Glackin, D. L. (1978) Tenth Annual Div. of Planetary Sci./American Assoc. for the Adv. Sci. meeting, Nov. 1978, Pasadena, CA, 4 p.

(4) Blasius, K. R. and Cutts, J. A. (1981) Icarus (in press).

(5) Davies, M. E. (1974) Icarus, 21(3), p. 230-235.

(6) Davies, M. E. and Arthur, D. W. G. (1973) Jour. of Geophys. Res. 78 (20), p. 4355-4394.

(7) Hord, C. W., Barth, C. A., and Stewart, A. I. (1972) Icarus, 17(2), p. 443-456.

(8) Wu, S. S. C., Schafer, F. J., Nakata, G. M., and Jordan, Raymond (1973), Jour. of Geophys. Res. 78 (20), p. 4405-4410.

(9) Wu, S. S. C. (1975), U.S. Geological Survey Interagency Rep. 63, 193 p.

(10) Wu, S. S. C. (1981) International Review, Annales de Geophysique Central National dela Recherche Scientifique, p. 147-260.

(11) U.S. Geological Survey (1979) Topographic Map of Mars, U.S. Geological Survey, I-961.

(12) Wu, S. S. C., Garcia, P. A., Jordan, Raymond, and Schafer, F. J. (1981), Third Internation Colloquium on Mars, LPI contribution 442, p. 287-289.

(13) Wu, S. S. C., Elassal, A. A., Jordan, Raymond, and Schafer, F. J. (1981) Planetary and Spac. Sci. (in press).

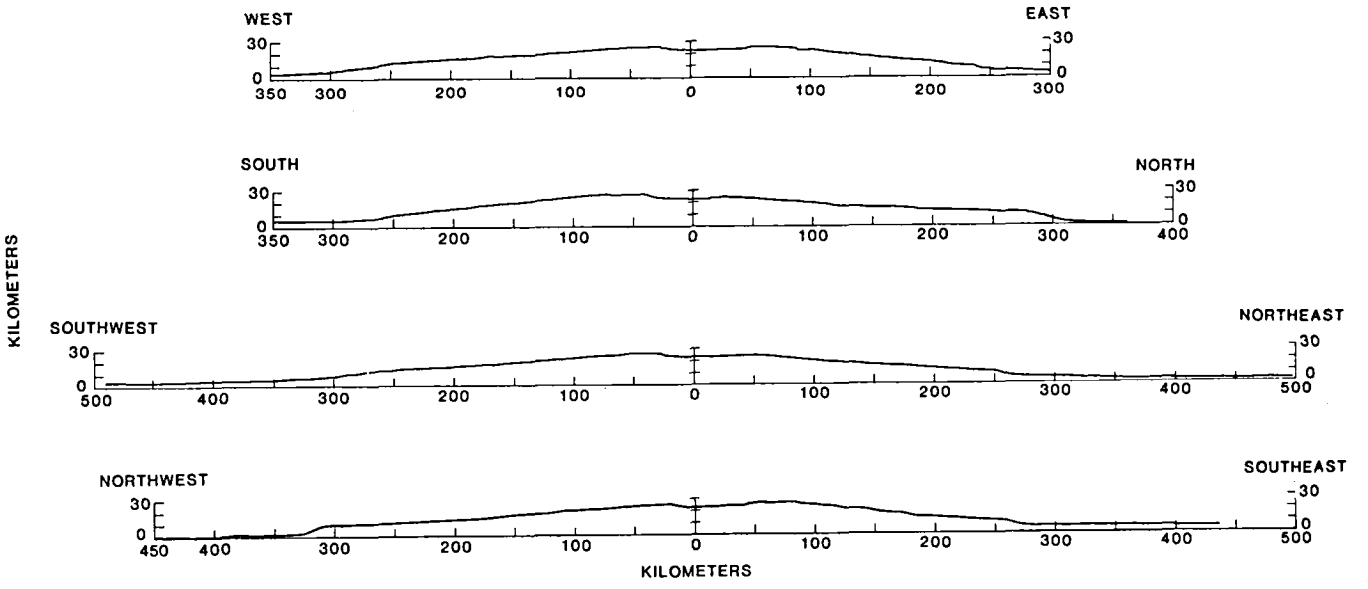


Figure 1. Profiles of Olympus Mons. All are drawn passing the approximate center of summit caldera at latitude 18.4°N, longitude 133.45° W.

| | Elev (km) | Vol. of Segment | ($x10^6$ $km^3$) Accum | Elev (km) | Vol. of Segment | ($x10^6$ $km^3$) Accum | Elev (km) | Vol. of Segment | ($x10^6$ $km^3$) Accum |
|---|---|---|---|---|---|---|---|---|---|
| above | 26 | 0.0004 | 0.0004 | 17 | 0.073 | 0.336 | 9 | 0.223 | 1.553 |
| | 25 | 0.006 | 0.007 | 16 | 0.088 | 0.424 | 8 | 9.236 | 1.789 |
| | 24 | 0.013 | 0.020 | 15 | 0.103 | 0.527 | 7 | 0.247 | 2.036 |
| | 23 | 0.022 | 0.042 | 14 | 0.120 | 0.647 | 6 | 0.262 | 2.298 |
| | 22 | 0.029 | 0.071 | 13 | 0.140 | 0.787 | 5 | 0.296 | 2.594 |
| | 21 | 0.035 | 0.106 | 12 | 0.158 | 0.945 | 4 | 0.365 | 2.959 |
| | 20 | 0.043 | 0.149 | 11 | 0.180 | 1.125 | 3 | 0.436 | 3.395 |
| | 19 | 0.052 | 0.201 | 10 | 0.205 | 1.330 | 2 | 0.467 | 3.862 |
| | 18 | 0.061 | 0.263 | | | | | | |

Table 1. Volume determination of Olympus Mons. Volumes were calculated for individual segments bounded by contour lines on the map (12) by use of a planimeter. The third column lists cumulative volumes downward from the top.

# THICKNESS DISTRIBUTION OF THARSIS VOLCANIC MATERIALS

R. A. De Hon, Department of Geosciences, Northeast Louisiana University, Monroe, La. 71209

Volcanic plains are identified with some of the oldest as well as some of the youngest surfaces on Mars. It is apparent that the volcanic history has been varied and extremely long lasting. The thickness of volcanic materials provides important insights and constraints to the history, structure, and processes that shape the Martian crust. Techniques developed for thickness studies of lunar mare materials (1, 2) are adapted for martian application. Martian volcanic materials are evaluated for their susceptibility to thickness characterization. Finally, the materials of the eastern portion of the Tharsis Dome are examined as representative samples of martian volcanics.

In order to produce an isopach map, several conditions must be satisfied. The relative relief of the partially buried topographic feature must be known. The thickness must be determined at a sufficient number of points. Craters should not be altered from fresh morphology by the process of burial. The ideal surface unit in this regard is a single cooling unit emplaced as a low viscosity fluid. Finally, the material which buries craters should be emplaced within a relatively limited time span. Accurate rim height data does not exist for Mars (3); therefore, it is necessary to assume that a rim height to diameter relationship is similar to that determined elsewhere. This work uses the mercurian trend (4) because the gravity of Mars and Mercury are nearly equal. Thickness estimates are limited to those craters that are nearly completely buried.

Four categories of martian volcanic plains materials are recognized (5). Ridged plains are characterized by mare-type wrinkle ridges, low relief, and uniform regional extent. These materials are probably emplaced at high extrusion rates as a single cooling unit. Lobate plains are characterized by overlapping flow lobes. These materials represent lower rates of effusion, more sporatic eruptions, and multiple cooling units. Smooth to rolling plains are nondescript plains which may have a few scattered features such as flow lobes or ridges. These materials are assigned a volcanic origin because of their proximity to volcanic centers and occasional surface features. Plateau plains are intercrater plains-forming material of the southern cratered terrain. Some of the intercratered plains exhibit embayment characteristics and surface features that are unquestionably volcanic in origin.

The ridged plains are most like the lunar mare basalts. The emplacement of ridged plains materials as simple flooding units of low viscosity best match the optimum conditions for thickness estimates. Their susceptibility to thickness studies is largely controlled by the crater density of the surface on which they are emplaced. Ridged plains materials form important surfaces associated with major eruption centers on the west flank of the Tharsis Dome, around Elysium Mons, Hesperia Planum, Syrtis Major Planum, and Amphitrites Platera. They also occur as basin-filling materials in the Hellas, Argyre, and Isidis Basins.

Lobate plains comprise the major portion of the surface of the Tharsis Dome, and they are found surrounding Elysium Mons. Both regions are prominent first order relief features of the planet. Buried crater density is low, and many partially buried craters are probably formed on interbasalt surfaces. Hence, thickness determinations are often indicative of the upper exposed units and not the entire assemblage.

Smooth to rolling plains make up a large proportion of the northern hemisphere. A few scattered features such as flow lobes, isolated ridges, or partially buried craters are suggestive of volcanic origin. Mottled and hummocky surfaces may be volcanic plains with a thin discontinuous mantle of aeolian material. Alternately these regions may represent tectonically or erosionally altered surfaces. These materials may represent plains of mixed origins and are the least likely to yield coherent information to thickness determinations.

The plateau plains materials are intercrater plains within the heavily cratered southern highlands and the interior fill of some large craters. Small patches of plateau plains do not contain a sufficient number of buried craters to construct reliable isopach maps. Larger regions of plains flood fresh and degraded craters alike. It is sometimes possible to eliminate the older craters and extract some useful thickness data (6).

Superficially, the Tharsis Dome is comprised of a series of stacked volcanic units (Fig. 1). The oldest materials are the cratered plateau materials (unit plc) of the southern highlands. Ridged plains materials (unit prg) lie above these on a wide plateau on the east flank of the dome. Ridged plain materials make up Lunae Planum and extend southward to the Sinai and Solis Planum regions. Smooth to rolling plains materials (unit psr) overlie ridged plains material in the Solis Planum and Sinai Planum regions and extend northward around the eastern flank of the dome. The Tharsis Dome is capped by fresh appearing lobate plains materials (unit plb). Important materials of less regional extent include the complex of materials associated with canyons and channels (unit c), and materials of the shield cones (v).

Partially buried craters within the ridged plains materials are sparse, but they are present in sufficient numbers to construct an isopach map which portrays the general thickness trends of the ridged plains materials. Materials range from zero thickness along the distal margins of the flow to a maximum of 1.5 km near the western contact with younger materials (Fig. 1). The average thickness of the exposed portion of the ridged plains materials is $0.85 \pm 0.36$ km. Isolated lensing in excess of one km thick occurs along the eastern margin, but the general trend is thickening westward toward the presumed source of the flows. At the observed rate of thickening, it is doubtful that the thickness near the crest is in excess of 2-3 km.

The smooth plains materials of the Tharsis region are mostly nondescript and of doubtful origin. The even slope of these materials in the Sinai and Solis Planum suggests that they form a simple stratigraphic sequence (ridged plains, smooth plains, lobate plains) in the southern half of the region. In the northern half of the region, smooth plains materials are deposited over the erosional surface formed by

removal of ridged plains materials. Partially buried craters are sparse, but isolated craters indicate thicknesses from 0.4 to 1.0 km.

Lobate plains materials form the cap on the Tharsis Dome. Scattered thickness estimates range from 0.4 to 1.1 km, but many craters rest on buried intrabasalt surfaces (7). Hence, the low crater density and multiple flow units do not lend themselves to a clear interpretation of the total thickness.

References:


(1) De Hon R. A. and Waskom J. D. (1976) LSC 7, 2729-2746.
(2) De Hon R. A. (1979) LPSC 10, 2935-2955.
(3) Plescia J. B. and Saunders R. S. (1980) LPSC 11, 2423-2436.
(4) Cintala M. J. (1979) LPSC 10, 2635-2650.
(5) Greely R. and Spudis P. D. (1981) Rev. Geophys. Space Phys. 19, 13-41.
(6) De Hon R. A. (1975) LSC 6, 2553-2561.
(7) Scott D. H. and Tanaka K. L. (1980) LPSC 11, 2403-2421.


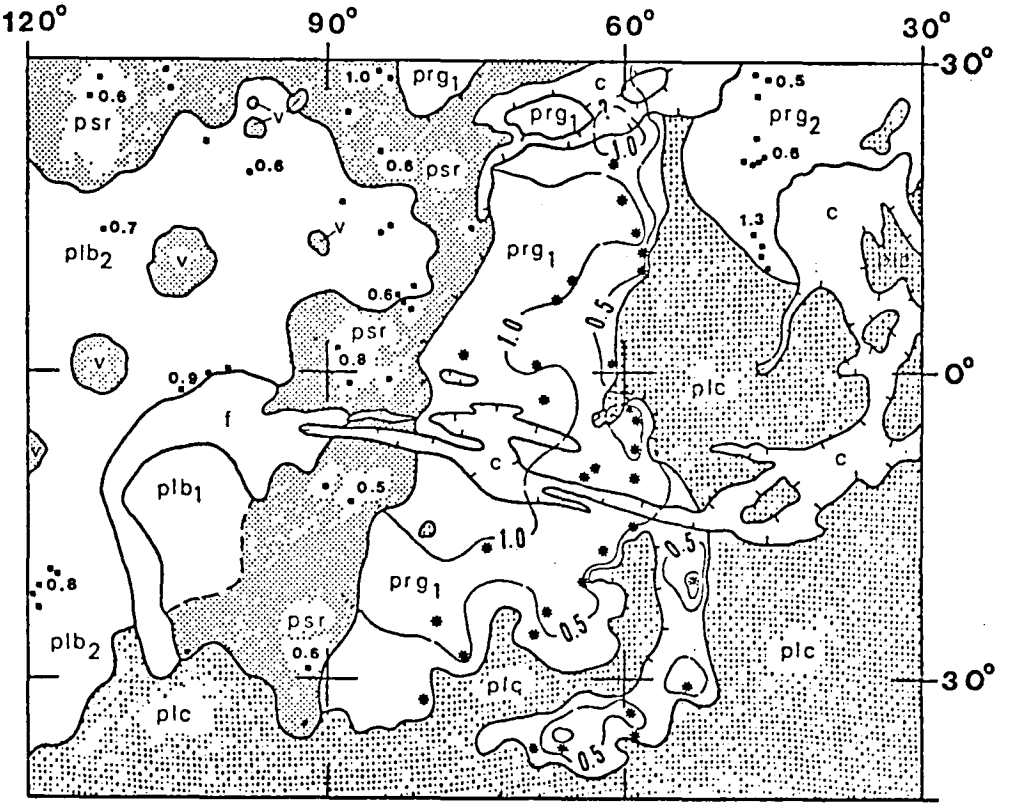


Fig. 1. Geologic sketch map of the Tharsis region. Isopachus lines at 0.5 km interval show thickness of ridged plains material (unit prg). Selected spot thicknesses indicated for other materials.

# ERUPTIVE STYLES OF MARTIAN VOLCANOES

Peter J. Mouginis-Mark, Dept. Geological Sciences, Brown University, Providence, RI 02912.

Introduction: With the advent of more comprehensive analyses of the Viking Orbiter image data set, several investigations have recently suggested that numerous old volcanic constructs exist on Mars, notably in the Thaumasia (1), Tempe (2), and Sinai Planum (3) regions. It is unclear, however, if these eroded highland remnants are indeed old volcanoes or, if this interpretation is correct, what style of volcanism was associated with each vent. In order to provide a basis for the recognition and characterization of both old and young volcanic constructs on Mars, a series of investigations has been initiated to document and interpret the eruption characteristics of the best preserved martian volcanoes (4,5). In particular, these investigations concentrate on the summit areas of volcanoes imaged at high resolution by Viking, so that comparable analyses to those employed on terrestrial volcanoes (e.g. refs. 6-8) can be utilized; stratigraphic relationships for nested pit craters, the location and spacing of graben and wrinkle ridges and the identification of mantled areas on the caldera rim (suggestive of explosively-generated ash deposits) all provide pertinent data for deducing how each volcano evolved. In this report, observations for Hecates Tholus (the best example of an explosive-style volcano on Mars; ref.5) and Olympus Mons (the classic martian shield volcano) are described in order to contrast the primary differences between these two types of volcano on Mars.

Hecates Tholus (32°N, 209°W) is the northernmost of the three main volcanic centers within the Elysium Planitia region. The volcano has a basal diameter of 160 x 190 km and is estimated to rise ~6 km above the surrounding plain (9). At least four episodes of caldera collapse characterize the summit, while numerous sinuous channels are observed on the flanks (Figure 1).

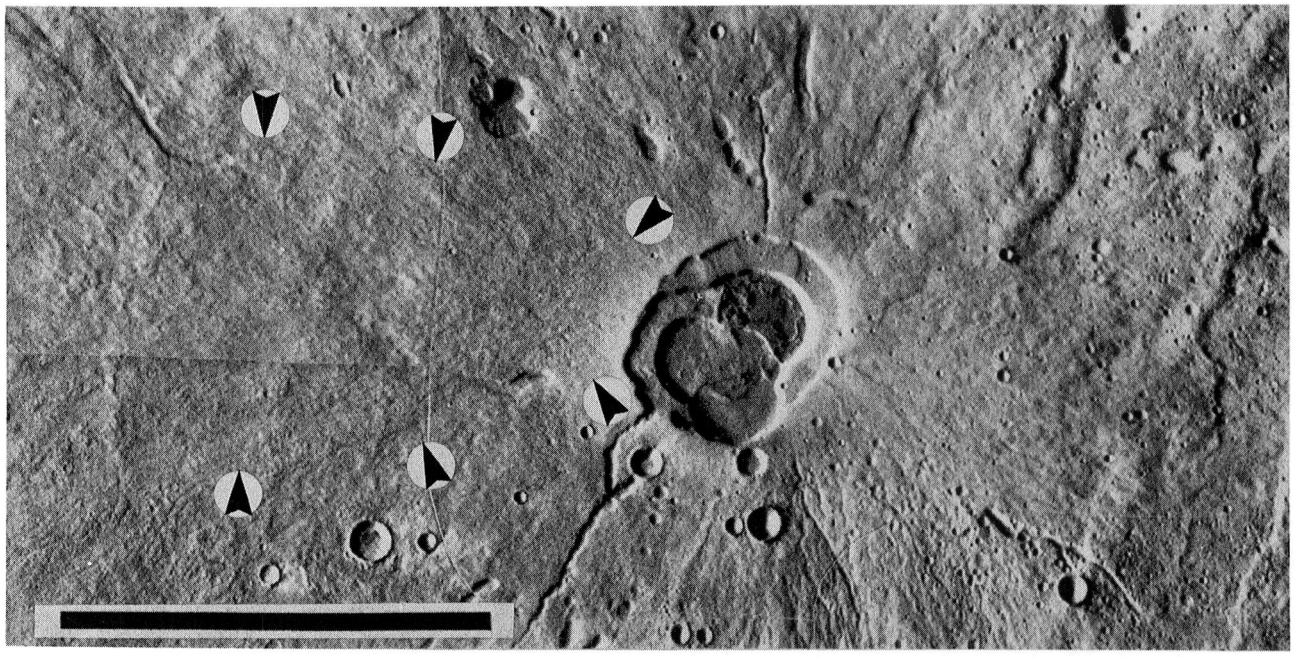

Figure 1: Summit area of Hecates Tholus. The elongate area to the west of the caldera (arrowed) is interpreted to be the air-fall deposit. Scale bar is 20 km. Viking Orbiter frames 651A17-21.

Examination of Viking images of the area immediately to the west of the caldera indicates that there is a marked absence of small (<2 km) impact craters and channels at this location. The lack of lobate lava flows (a possible alternate resurfacing mechanism), the close proximity of this area to the summit craters and the area's similarity in outline to terrestrial air-fall deposits (10) strongly suggest that for the first time a well preserved example of explosively-generated volcanic material has been found on Mars (5). Due to the lack of superposed craters, this material (and, hence, the eruption) is probably very young, even postdating the most recent collapse within the Olympus Mons caldera (~300 myr. B.P.; ref.11). From the spatial distribution of the craters on Hecates, this air-fall deposit appears to mantle an elongate region at least 50 x 70 km in extent, while crater counts (11,12) suggest that earlier resurfacing events (possibly earlier explosive eruptions) have also occurred. On the basis of both theoretical and observational studies of terrestrial explosive eruptions (e.g. 13,14), these dimensions give a best estimate of 75 km for the eruption cloud height and an implied mass eruption rate of $3 \times 10^7$ kgm/s when adjustments are made for the martian environment. Because a stable eruption cloud was able to form (rather than a low fountain feeding pyroclastic flows), the implied magma volatile content must have been at least 0.5-1.5 wt% if the driving volatile were $H_2O$ and greater than 1.3-2.8 wt% if the volatile were $CO_2$ (5). These volatile contents in turn constrain the depth of origin for the parental magma to >50 km for $CO_2$ and >150 meters to 4 km for $H_2O$.

In addition to this evidence for a recent explosive eruption, another unusual attribute of Hecates is the large number of sinuous channels on the flanks. These channels are probably fluvial in origin (5) and indicate atypical material properties for the flanks. Few other well-preserved martian volcanoes possess this morphology (15) and it is tempting to correlate the explosive eruptions with hypothetical easily erodable ash deposits on the flanks. If this association were indeed true, it may be that other martian volcanoes with channeled flanks (such as Ceranius Tholus [15] and Tyrrhena Patera [16]) also experienced explosive eruptions, thereby permitting a more general classification of effusive versus explosive volcanoes to be made for Mars.

Olympus Mons: Although the large-scale relationships between volcano structure and lava flow morphology have been identified (e.g. 4,17,18), several specific problems associated with volcanic activity on Olympus Mons remain unresolved. For example, whilst ridge systems occur within the calderas of several martian volcanoes (notably Olympus Mons, Pavonis Mons, Alba Patera and Uranius Patera) it is not clear if these ridges have a volcanic origin (17) or are similar to tectonically-produced lunar mare ridges (19,20). In addition, the significance of the relationship between lava lake formation and the cessation of intracaldera activity on Olympus Mons (4) remains unaccounted for; while the surface features have been described, their volcanological implications have not been persued.

High resolution (16 m/p) Survey II images and the recently compiled 200 meter-interval topographic map (21) provide a unique opportunity to examine in detail the Olympus Mons caldera. An initial analysis (4) has, however, identified large flank eruptions, coupled with the partial evacuation and collapse of the magma chamber, as the principle cause of caldera formation. Current efforts in the present study are focused toward detailed mapping of the pit craters, ridge systems and graben in order to correlate these features with

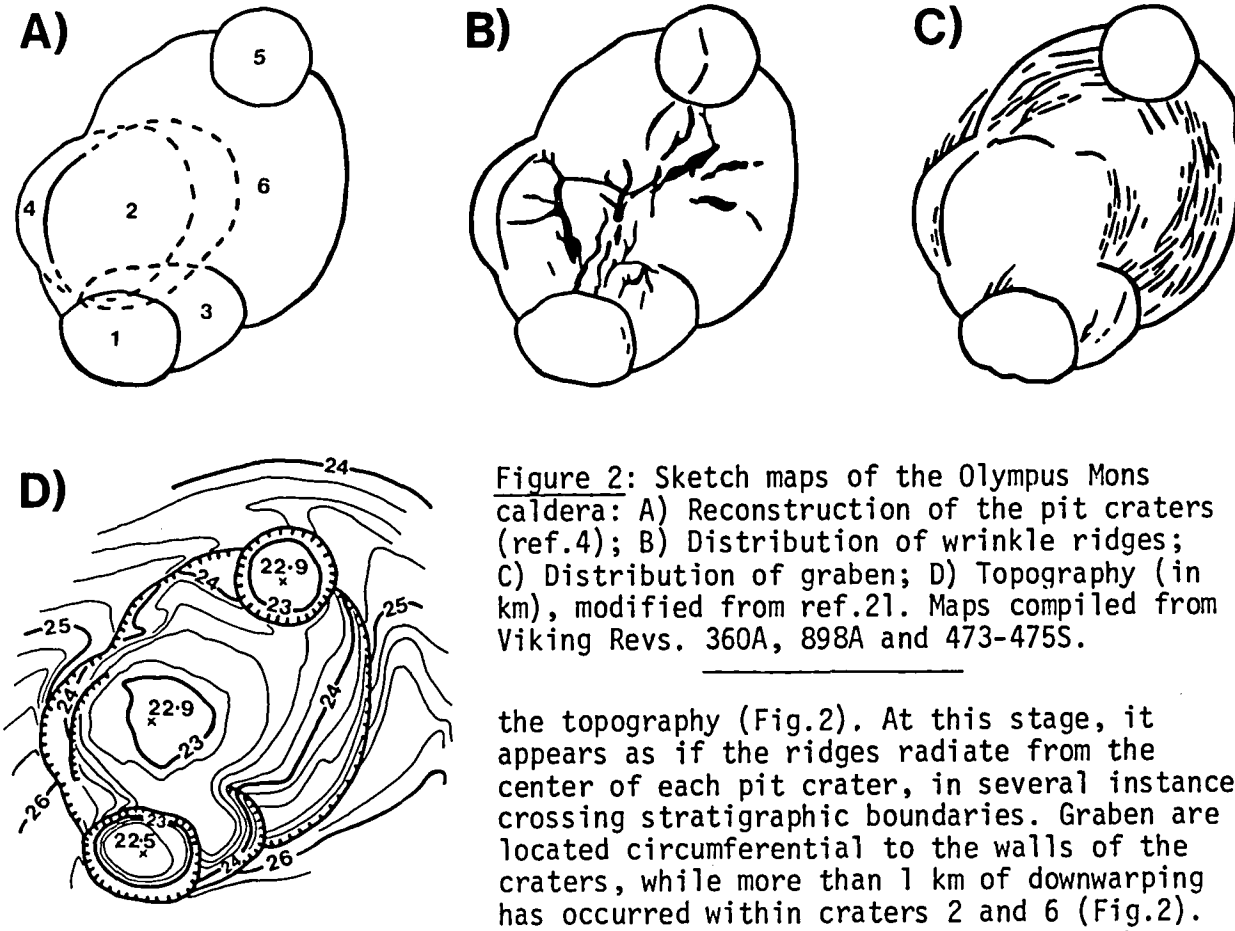


Figure 2: Sketch maps of the Olympus Mons caldera: A) Reconstruction of the pit craters (ref.4); B) Distribution of wrinkle ridges; C) Distribution of graben; D) Topography (in km), modified from ref.21. Maps compiled from Viking Revs. 360A, 898A and 473-475S.

the topography (Fig.2). At this stage, it appears as if the ridges radiate from the center of each pit crater, in several instances crossing stratigraphic boundaries. Graben are located circumferential to the walls of the craters, while more than 1 km of downwarping has occurred within craters 2 and 6 (Fig.2). A tectonic origin for these caldera ridges is therefore proposed, with the subsidence of the central portion of the caldera floor after lava lake solidification providing the compressional stress regime. Thus a good analogue to the Olympus Mons caldera may be the tectonic deformation of certain lunar maria (19, 20). In more general terms, the recognition of ridges within martian calderas may consequently indicate a simliar eruptive history to Olympus Mons; the eruption of large lateral lava flows caused summit collapse, the caldera floor was flooded by lava and subsequent deformation of the cooled lava lake occurred due to the solidification or subsequent evacuation of the magma chamber.

Currently , additional investigations of Hecates and Olympus Mons are planned in order to place the observed volcanic events in a more constrained chronological sequence by investigating the superposed impact crater distributions. Further comparison between these and other martian volcanoes with known terrestrial volcanic processes are also underway to investigate additional features of martian eruptions and the properties of their evolving magma chambers.

References: 1) Scott D.H. & Tanaka K.L. (1981) LPS XII, 952-954. 2) Scott D.H. (1981) 3rd Mars Colloq.Abs. 232-233. 3) Roth L.E. et al. (1980) Icarus 42, 287-316. 4) Mouginis-Mark P.J. (1981) PLPSC 12th, in press. 5) Mouginis-Mark P.J. et al. (1981) Submitted JGR. 6) Nordlie B.E. (1973) Geol.Soc.Amer.Bull. 84, 2931-2956. 7) Nakamura K. (1977) J.Volcan. Geotherm.Res. 2, 1-16. 8) Wadge G. (1977) J.Volcan.Geotherm.Res. 2, 361-384. 9) Malin M. C. (1977) Geol.Soc.Amer.Bull. 88, 908-919. 10) Walker G.P.L. (1973) Geol.Rundschau 82, 431-446. 11) Neukum G. & Hiller K. (1981) JGR 86, 3097-3121. 12) Plescia J.B. & Saunders R.S. (1979) PLPSC 10th, 2841-2859. 13) Wilson L. (1976) Geophys.J.R.Astro.Soc. 45, 543-556. 14) Wilson L. et al. (1978) JGR 83, 1829-1836. 15) Reimers C.E. & Komar P.D. (1979) Icarus 39, 88-110. 16) Greeley R. & Spudis P. (1981) Revs.Geophys. Space Phys. 19, 13-41. 17) Scott D.H. & Tanaka K.L. (1981) Icarus 45, 304-319. 18) Morris E.C. (1981) 3rd Mars Colloq.Abs., 161-162. 19) Solomon S.C. & Head J.W. (1980) Revs.Geophys.Space Phys. 18, 107-141. 20) Sharpton V.L. & Head J.W. LPS XI, 1024-1026. 21) USGS Special Map 19/134T.

# Tharsis volcano burial.

J.L.Whitford-Stark. Department of Geology, University of Missouri, Columbia, Missouri, 65211.

One of the problems concerning the Tharsis region of Mars is that of determining the depth of flooding of the volcanoes by younger lavas. Some previous attempts(1,2) have involved estimating the flooding depth by the degree of burial of impact craters. This study is an independent attempt based on reconstruction of the original dimensions of the volcanoes.

Wood(3,4) has established that, despite some scatter, there exists linear relationships between the crater diameter, edifice height, and basal diameter for terrestrial cinder cones and composite volcanoes. It is herein assumed that similar relationships hold for martian shield volcanoes. Figure 1 shows three curves of height versus basal diameter developed for the Tharsis volcanoes. The curve labeled Mons was obtained by fitting a straight line through values obtained for terrestrial shield volcanoes by Pike(5). The tholi curve was derived by fitting a curve parallel to that of the Mons but with the crater diameter enlarged by a factor of 2.6 to account for gravity differences. The patera curve was obtained by fitting another parallel line through the maximum dimensions of Biblis Patera. Each volcano was then shifted to its respective curve and the resulting dimensions, thought to be representative of the unflooded volcano sizes, were then calculated (Table 1). The apparent exceptions to the category shifts are Jovis Tholus which is a patera and Ulysses Patera which is a tholus. Arsia Mons was not shifted to the Mons curve because it would have resulted in an unrealistic volcano height and depth of lava flooding (Table 2).

The prefered flooding depth values(Table 1) indicate that the martian Tharis volcanoes are buried by about 4 km of lava at the most. The maximum depth of flooding values(Table 2) obtained by shifting each volcano to the Mons curve on figure 1 are unrealistic for two reasons. Firstly they result in unrealistic burial depths and secondly they result in considerable overlap between specific volcanoes (particularly Biblis and Ulysses paterae). The 4 km burial depth is consistent with the results of other investigators(1,2) but does not preclude the possibility that the Tharsis volcanoes may overlie a pre-existing lava pile.

Figure 2 shows the present and restored height/diameter values for the Tharsis volcanoes. Each volcano type falls into a distinct region of the graph, again supportive of the subdivisions obtained in figure 1. Furthermore, artificially flooding the topographic map of Olympus Mons (6), results in a volcano with morphometric properties midway between those of the tholi and paterae. This would tend to favor the conclusion that the paterae and tholi are not simply buried equivalents of the large Mons volcanoes. Especially since in excess of 15 km of flooding of Olympus Mons would be required to place it in the tholi-paterae dimension range.

References: 1)J.B.Plescia and R.S.Saunders (1980) Proc.Lunar Planet.Sci. Conf.11th, p.2423-2436. 2) R.A.De Hon (1981) 3rd Mars Colloquium(abstract)

| Name | Flank width | Height | Height/ width | Restored width | Restored height | Height Diff. | Type |
|---|---|---|---|---|---|---|---|
| Alba Patera | 700 | 5? | 0.01 | 700 | 5.0 | 0.0 | Unique |
| Olympus Mons | 310 | 20-23±0.5 | 0.08 | 310 | 25.0 | 0.0 | Mons |
| Arsia Mons | 160 | 12 | 0.08 | 218* | 16.35 | 4.35 | Mons |
| Ascraeus Mons | 190 | 19 | 0.10 | 207.5# | 20.75 | 1.75 | Mons |
| Pavonis Mons | 206 | 17 | 0.08 | 206 | 17.0 | 0.0 | Mons |
| Uranius Patera | 71.4 | 1.63 | 0.02 | 162.4* | 3.71 | 2.08 | Patera |
| Jovis Tholus | 35 | 0.6 | 0.02 | 65.8* | 1.32 | 0.72 | Patera |
| Biblis Patera | 90 | 3.0 | 0.03 | 90@ | 3.0 | 0.0 | Patera |
| Uranius Tholus | 20 | 2.45 | 0.12 | 29+ | 3.55 | 1.10 | Tholus |
| Tharsis Tholus | 42.1 | 4.10 | 0.10 | 50.8+ | 4.95 | 0.85 | Tholus |
| Ulysses Patera | 21 | 1.70 | 0.08 | 65+ | 5.26 | 3.56 | Tholus |
| Ceraunius Tholus | 44.2 | 5.15 | 0.12 | 44.2 | 5.15 | 0.0 | Tholus |

Table 1: Morphometric properties of martian shield volcanoes. # adjusted to Mons curve on figure 1. * adjusted to patera curve. + adjusted to tholus curve. @ uses maximum width. Restored height calculated by assuming a constant average slope beneath lava.

| Name | Basal Diameter | Height | Height Diff. |
|---|---|---|---|
| Alba Patera | 1,600 | 5 | 0.0 |
| Olympus Mons | 700 | 20-23 | 0.0 |
| Arsia Mons | 1,100 | 37.6 | 25.6 |
| Ascraeus Mons | 470 | 20.75 | 0.0 |
| Pavonis Mons | 460 | 17 | 0.0 |
| Uranius Patera | 800 | 7.04 | 5.41 |
| Jovis Tholus | 300 | n.d. | ---- |
| Biblis Patera | 460 | 14.35 | 11.35 |
| Uranius Tholus | 190 | 10.08 | 7.63 |
| Ceraunius Tholus | 225 | 12.00 | 6.85 |
| Tharsis Tholus | 360 | 15.90 | 11.80 |
| Ulysses Patera | 470 | 16.60 | 14.90 |

Table 2: Unrealistic depths of flooding of the Tharis volcanoes calculated by shifting each volcano to Mons curve in fig.1. and assuming constant slope.

p.59-61. 3) Wood,C.A. (1978) Geophys.Res.Lett. 5, 437-439. 4) Wood,C.A. (1980) J.Volcanol.Geotherm.Res. 7, 387-413. 5) Pike,R.J. (1978) Proc. Lunar Planet.Sci.Conf.9th., p.3239-3273. 6) Wu,S.C. et al. (1981) 3rd Mars Colloquium. p.287-289.

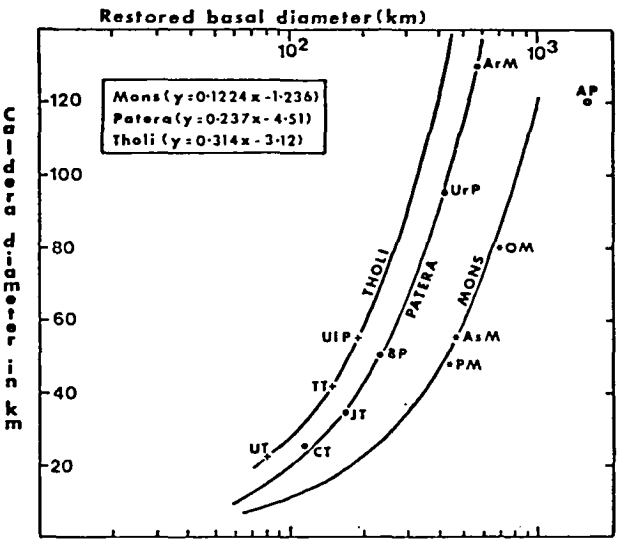


Figure 1: Restored basal diameter/caldera diameter values for the Tharis volcanoes. See text for discussion.

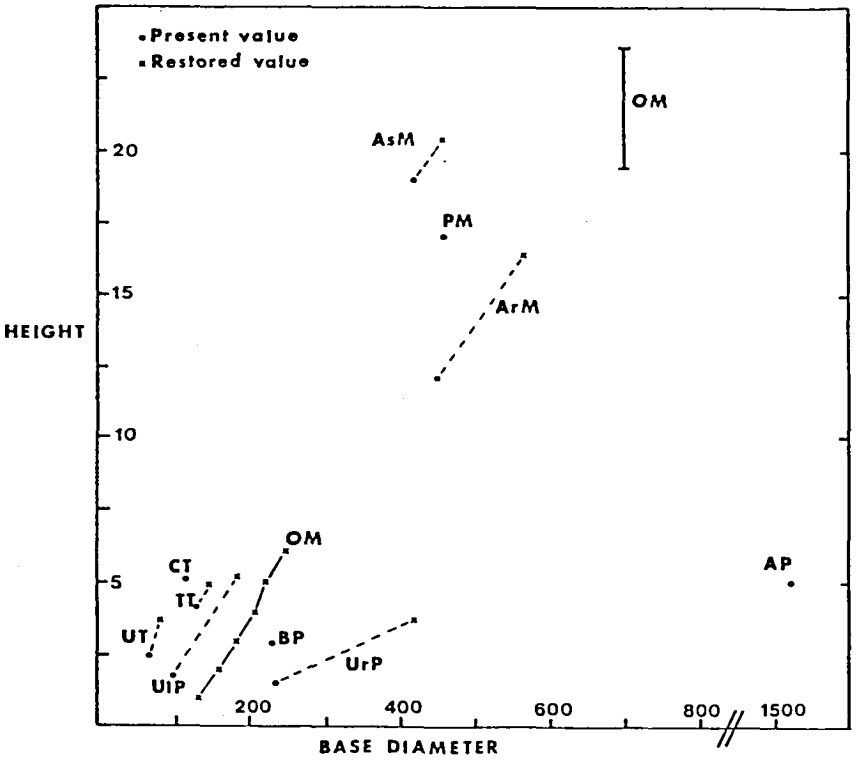


Figure 2: Currently observed values and original values of height/base diameter for the Tharsis volcanoes. Line with crosses represents the summit of Olympus Mons artificially flooded by increments of 1 km lava thickness. Note grouping of data and that the artifically flooded Olympus Mons falls midway between the tholi and paterae values.

# Albedo changes in lava.

J.L.Whitford-Stark. Department of Geology, University of Missouri, Columbia, Missouri, 65211.

Albedo variations of lava flows can result from biological, mechanical or thermal processes. The principal biological effect is the growth of vegetation such as lichen, sagebrush, and grass (1). The effect of this growth is to increase the albedo of basalt flows. There is a variation in albedo increase dependent upon the surface morphology of the flow; pahoehoe flows are more readily vegetated than aa because of the rubbly surface and greater permeability of the latter (1). Such effects can be considered to have no importance on Io or Mars.

Mechanical effects on albedo include surface roughness, sedimentation, and erosion. Generally, aa with its more rubbly surface appears darker than pahoehoe though this is not universally true(1). As the rubbly surface of aa is broken down by erosion it would therefore increase in albedo with time. Blanketing by a sedimentary cover is the third mechanical means of changing the lava albedo. Again in this instance, the rougher surface of aa will retard albedo brightening relative to pahoehoe.

Sedimentation and erosion can be considered to be the primary albedo-altering effects on flows on Mars. In the Solis Planum region (see Viking frames 643 A64 and A65) the albedos of flow tops are higher than those of the flow margins. Since the albedo pattern is consistent around the entirety of the flows, it is unlikely to have resulted from erosion; erosion would be expected to be preferentially effective on the windward side of the flows. The preferential brightening of the tops of the flows would indicate that either material is not easily deposited at the flow margins because of the steeper slope or that spalling of the margins is continually exposing the fresh interiors of the flows. Schaber(2) has illustrated the variations in eolian cover on martian flows which arise as a result of variable surface roughness. The similar morphologies and eruption styles of lavas with variable albedos within the Solis Planum region would suggest that the albedo is there correlated with age rather than surface roughness; the lower albedo flows being younger. Caution must be excercise,however, in that some flows appear to have been stripped of their eolian mantles. In these instances the flows have more streaky albedo markings than flows currently being buried.

Similar albedo variations are seen among flows on Io and can be ascribed to variable lava compositions, variable covering by pyroclastic materials, and, if they are composed of sulphur, by variable eruption temperatures (3). On a volcano such as Maasaw Patera, flows to the south of the summit caldera have a consistently lower albedo than those to the north. The presence of a broad, high-albedo ring around a dark caldera located to the northwest of Maasaw (centered at approximately 350°,32°S) suggests that the northern flows are covered by a greater thickness of pyroclastics or there is an optically thicker atmosphere in this region if the bright ring is associated with an active vent. At the unnamed

volcano (335°, 40°S) to the east of Maasaw Patera, the flows in the immediate vicinity of the caldera are indistinct and the area has a higher albedo than flow surfaces further downslope. In contrast, excepting a small portion of the northeast exterior wall of the Maasaw caldera, flows at the latter volcano can be traced to the caldera rim. This may indicate that the most recent eruption at the unnamed volcano consisted of pyroclastic material ejected from the summit caldera. Alternatively, a prolonged higher surface temperature near the summit may have led to the development of higher albedo materials at that location (3). A third alternative is that the lower albedo lavas were erupted from locations downslope of the summit caldera. The image resolution is insufficient to enable discrimination between the alternatives. By analogy with the adjacent Maasaw Patera, however, the third alternative seems unlikely. Moreover, the disposition of flows around the Maasaw caldera suggests an origin by overflow of a lava lake rather than resulting from separate eruptions from discrete vents.

The effects of episodic eruptions from Io calderas are well-illustrated by an unnamed volcano at 10°, 32°S. Here at least three eruption phases can be distinguished on the basis of albedo variations and smoothing of surface topography (figure 1). More interesting are the high albedo halos around the low albedo flows. In this area, the high albedo halos are preferentially developed where two low albedo flows are in juxtaposition. Where the flows separate there is no halo and the side of the flow which is not adjacent to low albedo material also lacks a halo. The increase in albedo could result from delayed cooling if the flows are sulphur (3). Again, this would require both flow lobes to be warm at the same time, again consistent with overflow of a lava lake. Thermally-induced albedo changes can be observed around terrestrial lava flows though the most frequent tendency is to lower the albedo of the pre-flow surface. Similar high albedo halos are seen around the flows from Ra Patera (326°,8°S), again, particularly well-developed where two low albedo flows are adjacent. However, there is an asymmetric development of high albedo halos around discrete flows from Ra Patera; being particularly well-developed on the southern side of some flows. In such a situation, it is difficult to envisage why thermal effects might produce such an asymmetry (see 0133 J1). A similar argument could be made against a mechanical origin since, because the halos are developed normal to the slope, there is no reason why one side of the flow should be consistently steeper than the other. An image processing origin for the halos seems unlikely for two reasons. Firstly, the side of the flow around which the halo is developed does not remain constant from volcano to volcano. Secondly, there are low albedo flows with no halos (see 0131 J1). A preferential release of volatiles is a possible explanation but, again, this would not appear to explain the asymmetric development. A thermal origin for the production of halos appears to be the most consistent with observations but the details of the process remain enigmatic.

References:

1) R.H.Lefebvre (1977) In Volcanism of the Eastern Snake River Plain, Idaho: A Comparative Planetary Geology Guidebook. NASA CR-154621,

p.204-214.
2) G.G.Schaber (1980) Icarus 42, 159-184.
3) C.Sagan (1979) Nature 280, 750-753.

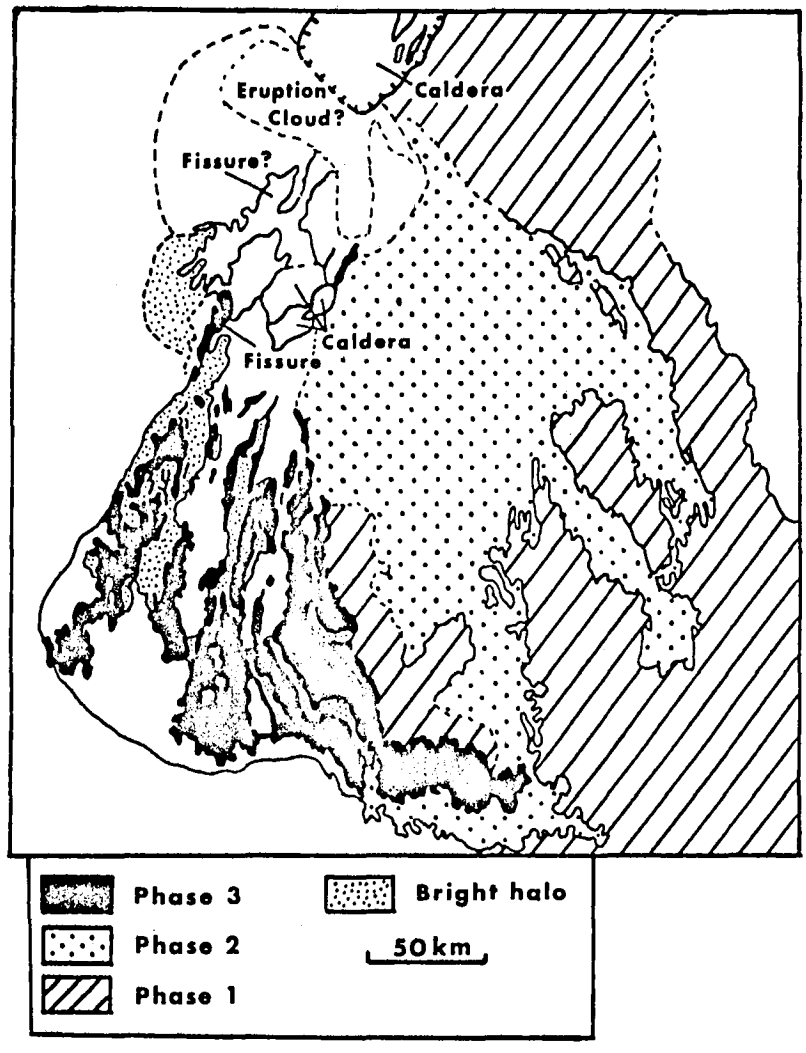


Figure 1: Distribution of flow units around an unnamed volcano (10°,32°S) on Io. Unshaded area to right is another volcano. Unshaded area within Phase 3 flows are older than 3 but could be either 2 or 1. Note development of phase 3 bright halos where flows are adjacent but lack of halos where they are apart. A dark area to the south of the topmost caldera may be an eruption cloud.

# Vertical Structure of Basaltic Lava Flows: Implications for Surface Sampling and Interpretation

Jayne C. Aubele[1], L. S. Crumpler[1] and Wolfgang E. Elston[2]
(1) Dept. of Planetary Sciences, Univ. of Arizona
(2) Dept. of Geology, Univ. of New Mexico

In this paper we elaborate on earlier work [1], regarding the internal structure and stratigraphic characteristics of basaltic lava flows, as it might apply to the interpretation of block populations on planetary surfaces. Specifically, Viking Lander images of the Martian surface indicate that a variety of block sizes contain possible vesicles of variable frequency and diameter. Computer modeling of the growth and rise of bubbles in a solidifying basaltic lava flow, and studies of terrestrial basaltic lava flows, show that the emplacement of vesicles of various radii and frequencies is not a random process. It is, in fact, an orderly physical process dependent on the flow thickness, initial temperature, viscosity, rate of cooling, gas concentration, gas diffusion rate, and bubble rise velocity. Thus, constraints on these variables may provide insight into the structure and stratigraphy of possible Martian lava flows.

In our model an 8m thick basalt flow cools while, simultaneously, an initially uniform distribution of vesicles, 0.5mm in radius, are allowed to grow and rise bouyantly through the flow in an iterative process. The flow cooling is modeled by use of the analytical equation of Jaeger [2]; and the viscosity is modeled after the results of Murase and McBirney [3]. Other parameters, including bubble growth rate, rise velocity and gas diffusion rate, are modeled from the discussion of Sparks [4], who showed that bubble growth in basaltic lava follows the parabolic growth rate law

$$R = 2\beta(Dt)^{0.5}$$

where R is bubble radius, $\beta$ is a growth rate constant, D is a viscosity-temperature dependent gas diffusion coefficient, and t is time. Our computer generated data show that within the conditions specified for a simple 8m thick flow, the radius of the final bubble is relatively insensitive to $\beta$ (a function of gas concentration, equilibrium gas saturation concentration, and hydrostatic pressure). The actual process whereby a bubble grows and rises through a flow is therefore a complex function of its changing position and the decreasing temperature within the flow through which the bubble moves.

The largest bubbles, generated in the model, are only a few millimeters larger than the initial bubble; but the relative sizes and their positions are similar to those observed in terrestrial basalts. In terrestrial basalt flows, the smallest and most closely packed vesicles, near the top of a flow, are 5 to 10 times smaller than the larger and less abundant vesicles near the base of the vesicular zone [1]. Hence, in reality, coalescence must be more frequent

deeper within the flow than it is near the top. This implies that higher surface tension of bubbles in the more viscous (cooler) upper part of a flow does not allow coalescence to take place, and is therefore responsible for the characteristic close packing.

In the model, bubbles with an initial starting position deeper than 7.6m, measured downward from the top of the flow, are able to rise only $\leq$ 20 cm before solidification halts further upward movement, thereby forming a lower vesicular zone. Bubbles with an initial starting position of 7.6m rise to within 1m of the surface, forming an upper vesicular zone. In fact, all bubbles starting at less than 7.6m rise to between 1.0 and 0.1m of the surface, illustrating that crowding of vesicles near the top of the flow will take place, and a large central massive zone will be formed. In terrestrial flows of similar thickness, vesicles are abundant near the top, but are also distributed with decreasing frequency and increasing size downward over the upper 4 to 5m of the flow. This suggests that, as bubbles grow, their upward velocity is retarded by non-Newtonian affects, generated by increasing concentrations of nucleating bubbles and crystals; whereas viscosity effects, governing gas diffusion and surface tension, remain essentially Newtonian in behavior. Therefore, vesicles at lower starting positions grow larger before they are trapped by solidification. When bubbles in our model are assumed to have a large initial radius ($\geq$1mm), they rise considerably faster, at all depths in the flow, and no lower vesicular zone is formed. Therefore, initial vesicle radii must be smaller than 1mm to account for the observed distribution in terrestrial lavas. Table 1 and Figure 1 is a sample of some calculated results.

At the Viking II Lander site, some blocks contain relatively large and sparse pits, whereas some contain small and abundant pits. Similar sized blocks and vesicle abundances are to be expected from the disruption of a basaltic flow to depths of at least one-half the flow thickness. If the pits in the blocks at the lander site are vesicles, they would then represent sampling of a wide depth interval in one or more lava flow units. Because large and sparse vesicles characterize the deeper portions of a flow, those blocks bearing large vesicles may be from deep within a given flow unit.

This may have a bearing on future sampling strategies for sample return missions. The deeper (larger vesicle) portions of a flow are more holocrystalline or diabasic, whereas the upper portions are more microcrystalline. To some extent, ferromagnesian minerals in more holocrystalline positions of a flow are more susceptible to weathering by vapor/liquid transfer along grain boundaries. Also, there is a tendency for vesicles to act as traps for precipitates in fluids diffusing through the rock. Hence, if vapor/liquid transfer is suspected at a given site, the "cleanest" sample, on a planet with little or no atmospheric weathering, may be those rocks with the smallest and most abundant vesicles from the upper portions of the lava flow.

[1] Aubele, J. C., Crumpler, L. S., and Elston, Wolfgang E., 1981, Vertical structure and erosion rates of paheohoe basalt flows. Reports of Planetary Geology Program, NASA Techn. Memorandum TM X-92385, p. 231-232.
[2] Jaeger, J. C., 1968, Coding and solidification of igneous rocks. in The Poldervaart Treatise on Rocks of Basaltic Composition, H. H. Hess and A. Poldervaarts, eds., New York, Interscience, v. 2, 503-536.
[3] Murase, T., and McBirney, A. R., 1973. Properties of some common igneous rocks and their melts at high temperatures. Geol. Soc. Am. Bull., 84, 3563-3592.
[4] Sparks, R. S. J., 1978, The dynamics of bubble formation and growth in magmas: a review and analysis. Jour. Volc. Geotherm Res., v. 3, 1-37.

Table 1. Sample of computer calculated data for a basalt flow, 800cm thick, at initial temperature, 1500°K, and initial vesicle radius, 0.05cm

| Initial Position* (cm) | Final Position* (cm) | Change in Position (cm) | Final Vesicle Radius (cm) | Elapsed Time (sec.x$10^3$) |
|---|---|---|---|---|
| 10. | 9.1 | 0.9 | .054 | 3. |
| 20. | 16.7 | 3.3 | .058 | 9. |
| 30. | 23.2 | 6.8 | .062 | 16. |
| 50. | 33.7 | 16.3 | .069 | 31. |
| 80. | 45.1 | 34.9 | .076 | 51. |
| 100. | 50.7 | 49.3 | .079 | 63. |
| 300. | 76.2 | 223.8 | .105 | 147. |
| 500. | 86.4 | 413.6 | .119 | 198. |
| 700. | 92.6 | 607.4 | .129 | 236. |
| 760. | 97.7 | 662.3 | .134 | 257. |
| 770. | 749.6 | 20.4 | .073 | 42. |
| 780. | 774.7 | 5.3 | .061 | 14. |
| 790. | 788.9 | 1.1 | .055 | 4. |

* Position is measured downward from top of flow.

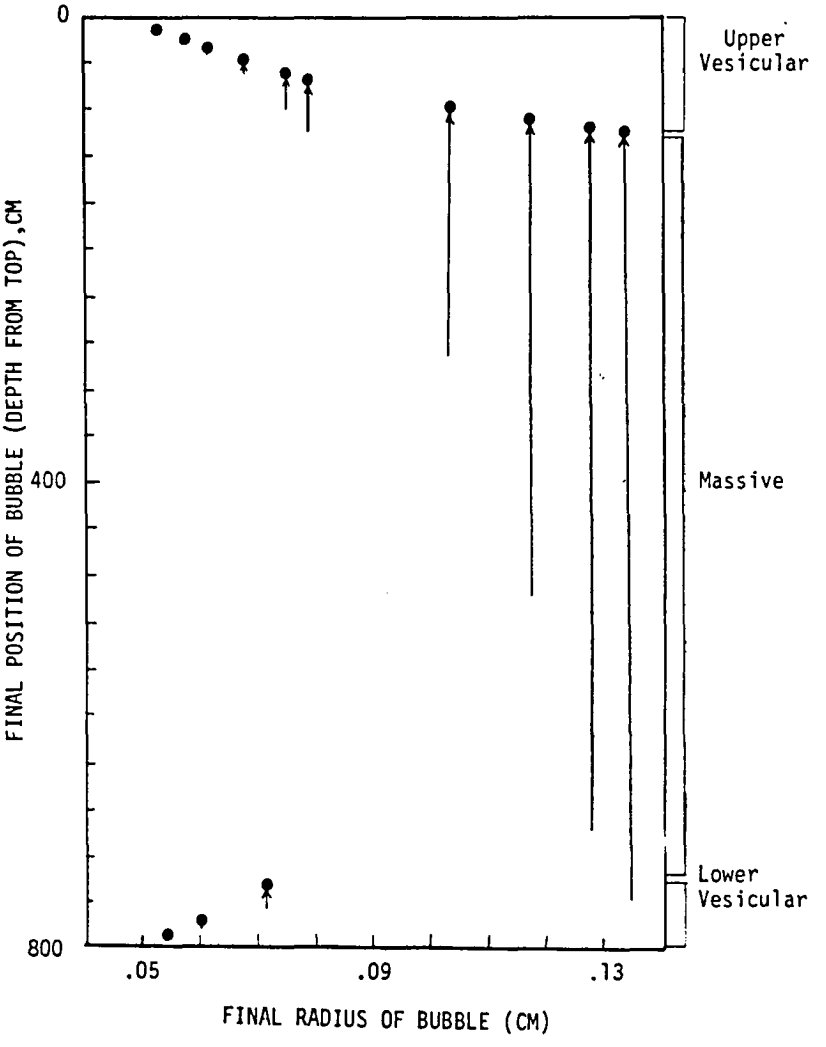


Figure 1. Calculated final positions of growing and rising bubbles in a solidifying basalt flow. Bubbles are initially distributed uniformly throughout the flow. Addition of a non-newtonian viscosity component to the equation of bubble motion would deepen the extent of the upper vesicular zone.

## SCALE MODELING OF LAVA FLOW PROCESSES

*S.O. Park, J.H. Fink, and R. Greeley, Department of Geology, Arizona State University, Tempe, Arizona 85287*

The problem of scale modeling in structural geology has remained controversial due to ambiguity about how to scale time and how to estimate the rheological behavior of deforming rocks. Modeling structures on lava flows has the advantage of involving materials whose properties can be directly measured and processes that can be observed. We have performed theoretical and laboratory modeling of lava flow processes and the resulting morphologic features. Experiments used different grades of Carbowax (a polyethylene glycol) and kaolin slurries at measured flow rates, slopes and substrate temperatures. Morphologic features characteristic of basalt flows (levees, compressional ridges, lava tubes) all formed in Carbowax flows when heat loss was predominantly through the upper surface; when heat was lost downward by conduction only smooth surfaces resulted. This implies that transitions from smooth to ropy and more complex surfaces in pahoehoe basalt flows may be controlled by mode of heat loss from the flow.

A dimensionless ratio of final flow depth to the depth at the end of extrusion ($d_f/d_e$) (which corresponds to the ratio of yield strength to wall shear stress for Bingham flows) correlated well with aspect ratio (flow width/final depth) and a dimensionless flow rate ($Q\nu/g \sin\theta\ d_f^4$), where Q = volumetric flow rate, $\nu$ = kinematic viscosity, g = gravity, and $\theta$ = topographic slope. This correlation held for isothermal Bingham flows (kaolin slurries), non-isothermal Newtonian flows (Carbowax) and non-isothermal Bingham flows (basaltic lava). Under known topographic and eruptive conditions, lava yield strengths and viscosities may be estimated from field measurements of aspect ratio and $d_f/d_e$. Viscosity may also be roughly estimated from the spacing and height of surface ridges and topographic slope.

the floor of the rille channel, and U, the flow velocity (Table 1). The values of M, T, A and F can be used to find the vertical erosion rate, dZ/dt, just outside the vent. This (like all the values defined so far) is a maximum value and so division of Z by dZ/dt provides a minimum estimate of the duration, P, of the rille-forming eruption. Finally, multiplication of M by P gives a realistic estimate of the total erupted lava mass which, divided by the lava density (taken as 3000 kg/m$^3$) yields the total erupted volume, V.

It is found that values of Re are close to or greater than $10^5$, well above the minimum value of about $10^3$ required for turbulence. Values of M lie in the range $10^7$ to $6 \times 10^8$ kg/s; these values are somewhat greater than those associated with most terrestrial basaltic eruptions (4) but less than the highest terrestrial rhyolitic output rates (10). Flow thicknesses are all within a factor of 2 of 9 m and flow velocities within a factor of 2 of 6 m/s. Values of dZ/dt lie in the range 9 to 18 microns/s; eruption durations are from about 100 to 500 days and erupted volumes range between about 40 and at least 2000 km$^3$ with the strong possiblity of values up to 9000 km$^3$. The striking aspect of these eruptions is the large volume of magma commonly available to be erupted rather than the eruption rate. The total volume of magma erupted through the 10 rilles analyzed amounts to about one thousandth of the entire volume of lunar mare basalt, estimated at about $10^7$ km$^3$ (1).

The above rille analyses can be tied in to our earlier work (5,6) on source depressions: in ref. 4 we gave diagrams showing the combinations of magma gas content and eruption rate which would produce source structures of a given size. For circular source depressions (rilles 3, 5(a), 5(b) and 6), the mass eruption rate, M, deduced from the rille morphology and the depression radius were located in Fig. 17a of ref. 4 and the implied magma gas content read off the left-hand axis. For elongate sources, the eruption rate M was divided by the apparent fissure length (taken as depression length minus depression width to allow for end effects) to give the eruption rate per unit fissure length, M/L. This value, together with the depression half-width, was located in Fig. 17b of ref. 4 and again the magma gas content was read off. Table 1 gives the values found.

If the theoretical models are correct, it is required that the deduced magma gas contents should lie within the range of values implied for lunar basalts by chemical data (11), i.e. about 250 to 750 ppm. The values found all lie between 150 and 500 ppm. Considering the numerous assumptions and approximations made in both theoretical models the agreement is satisfactory. The fact that the deduced gas contents are somewhat smaller than expected suggests that the values of M in Table 1 are, if anything, over-estimates. This would imply that values for the eruption durations should be increased a little, values of erupted magma volumes, however, are very insensitive to changes in M and would be essentially unchanged.

References - 1) J. W. Head (1975) Rev. Geophys. Sp. Phys. 14, 265. 2) G. Hulme (1973) Mod. Geol. 4, 107. 3) M. Carr (1974) Icarus, 22, 1. 4) L. Wilson and J.W. Head (1981) J. Geophys. Res. (in press). 5) L. Wilson and J.W. Head (1980) PLPSC 11, 1260. 6) J.W. Head and L. Wilson (1980) PLPSC 11, 426. 7) V. Oberbeck et al. (1971) NASA TM x-62, 088. 8) T. Murase and A.R. McBirney (1970) Science 167, 1491. 9) W.H. McAdams (1954) Heat Transmission, McGraw-Hill. 10) L. Wilson, R.S.J. Sparks, and G.P.L. Walker (1980) Geophys. J.R. Astr. Soc. 63, 117. 11) R. Housley (1978) PLPSC 9, 1473.

LUNAR SINUOUS RILLE FORMATION BY THERMAL EROSION: ERUPTION CONDITIONS, RATES AND DURATIONS. J.W. Head, Dept. of Geological Sciences, Brown University, Providence, RI 02912; and L. Wilson, Dept. of Environmental Sciences, University of Lancaster, Lancaster LA1 4YR, U.K. and Dept. of Geological Sciences, Brown University, Providence, RI.

Lunar sinuous rilles and the depressions that commonly form their sources are intimately associated with effusive volcanic activity as shown by the work of numerous authors (1). Specific models for the formation of the rille channels by thermal erosion of the pre-existing surface by flowing lava were given by Hulme (2) and Carr (3). Carr showed that such erosion could occur even if the eroding flows moved in a laminar fashion while Hulme demonstrated that turbulent lava motion would lead to more efficient erosion; Hulme developed a detailed model of the rille formation process which, when tested on the only rille for which adequate topographic data were available (2), suggested that turbulence was probably involved in the formation of most sinuous rilles. By examining the details of lunar basaltic eruption processes (4), the present authors developed a model of formation of sinuous rille source depressions by thermal erosion (5,6) and placed constraints on the eruption rates needed to form the depressions. In this paper we use recently available topographic data to apply Hulme's model to several more rilles and show that it leads to eruption rates compatible with those deduced separately from the geometry of the corresponding source depressions.

Rille formation by thermal erosion requires an initial lava flow in which a high effusion rate causes turbulent motions, maximizing the efficiency of heat transfer to the basal layer and leading to heating of the substrate rocks above their solidus. Partial melting and mechanical erosion excavate the substrate and the flow subsides progressively into a deepening channel. The vertical erosion rate is always greatest near the vent where the lava is hottest and is always zero at some finite distance downstream; beyond this point the rille is not formed and the flow moves over the surface between levees as normal. The complete details of Hulme's rille model (2) will not be given here but the steps in the anlaysis will be outlined.

To fit the model to a sinuous rille it is necessary to measure the width and depth of the rille at many points downstream from the source and to know the slope of the surface on which the rille formed. These data were obtained from lunar topographic orthophotomaps; some depth measurements were supplemented by measuring shadows on Orbiter photographs. Complete data were obtained for 7 rilles with poorer data for 3 others; their numbers in the catalogue of Oberbeck et al. (7) are given in Table 1.

Account must be taken of the fact that rilles can be modified by partial infilling by later eruptions or nearby impact events. Hulme gives standard curves (2) to which the depth/downstream distance data can be fitted to give estimates of the initial length, Y, and maximum initial depth, Z, of a rille and of the temperature of the eroding lava on eruption, T. The values of Y and T can be used, together with the mean rille width, W, to deduce M, the mass of lava erupted per second form the source vent. The eruption temperature, T, can be used to deduce (8) the lava viscosity, E, and then, E, M and W can be combined to yield the Reynolds number, Re, of the lava motion. This in turn can be used to find (9) the basal friction factor, F, of the flow and knowledge of F and A, the slope of the ground on which the flow moves, yields values for D, the depth of the flowing lava in

# LUNAR SINUOUS RILLE FORMATION CONDITIONS

J.W. Head and L. Wilson

Table 1. Values of: deduced rille length, Y; deduced maximum rille depth, Z; lava eruption temeprature, T; mean rille width, W; mass eruption rate, M; lava viscosity at the vent, E; Reynolds number, Re, and friction factor, F, of the flow; slope of ground on which rille forms, A; depth, D, and flow velocity, U, of lava on rille floor; vertical erosion rate near vent, dZ/dt; minimum eruption duration, P; total lava volume erupted, V; geometry of source depression (radius, R, or fissure length x, depression half width, L x H); magma gas content, n.

| Rille No. | 2 | 3 | 4 | 5(a) | 5(b) | 6 | 7 | 18 | 23(a) | 23(b) |
|---|---|---|---|---|---|---|---|---|---|---|
| Y/km | 76 | 51 | 40 | 110 | 70 | 55 | 80 | 74 | 100 ±50 | 138? |
| Z/m | 260 | 200 | 110 | 280 | 100 | 180 | 300 | 330 | 600 ±100 | 250? |
| T/K | 1380 | 1520 | 1480 | 1400 | 1390 | 1480 | 1460 | 1460 | 1400? | 1400? |
| W/m | 210 | 410 | 140 | 650 | 260 | 670 | 1030 | 240 | 1390 | 280 |
| M/($10^7$ kg/s) | 10 | 3.5 | 1.2 | 29 | 9 | 7.6 | 20 | 4.2 | 57 | 15 |
| E/(Pa s) | 13 | 3 | 4 | 10 | 12 | 4 | 6 | 6 | 10 | 10 |
| $\log_{10}$(Re) | 5.2 | 5.1 | 4.9 | 5.2 | 5.1 | 5.0 | 5.1 | 5.1 | 5.2 | 5.3 |
| $\log_{10}$(F) | -2.3 | -2.3 | -2.2 | -2.3 | -2.3 | -2.3 | -2.3 | -2.3 | -2.3 | -2.3 |
| A/(radian) | 0.01? | 0.015 | 0.020 | 0.024 | 0.013 | 0.012 | 0.008 | 0.050 | 0.01? | 0.01? |
| D/m | 16 | 5 | 9 | 11 | 12 | 6 | 9 | 5 | 14 | 17 |
| U/(m/s) | 10 | 6 | 3 | 13 | 10 | 7 | 7 | 12 | 10 | 11 |
| $\frac{dZ}{dt}$/(μm/s) | 9 | 18 | 12 | 14 | 10 | 15 | 18 | 17 | 13 | 17 |
| P/(day) | 350 | 130 | 110 | 230 | 120 | 140 | 190 | 230 | 530 | 170 |
| V/($km^3$) | 1010 | 130 | 40 | 1910 | 320 | 310 | 1110 | 270 | 9000 ±3000 | 740 |
| Source Geometry/m | 1100 x 835 | 850 | 2500 x 400 | 1950 | 675 | 645 | 3570 x 625 | 500 x 650 | 700 x 1650 | ?? |
| n/(ppm) | 280 | 190 | 180 | 400 | 150 | 300 | 350 ±150 | 200 | 430 | ?? |

THEORETICAL ANALYSES OF MARTIAN EXPLOSIVE ERUPTION MECHANISMS. L. Wilson Dept. of Environmental Sciences, Univ. of Lancaster, Lancaster LA1 4YQ, U.K. and Dept. of Geological Sciences, Brown Univ., Providence, RI 02912 and J.W. Head, Dept. of Geological Sciences, Brown Univ., Providence.

Disruption of an erupting magma into scoriaceous or pumiceous clasts and released gas is to be expected on Mars for wide ranges of magma composition, magma volatile type and volatile content (1,2); such disruption is potentially much more common on Mars than on the Earth because of the lower atmospheric pressure (1). If an eruptive episode involving magma disruption continues for more than several minutes, a plinian or sub-plinian air-fall deposit may be formed: this will be true for both acid and basic magmas; alternatively, pyroclastic flows may be generated from acid magmas or lava flows may form from the coalescence of clots of basic magma which stay hot within the eruption cloud. This paper presents a numerical treatment of some of the mechanisms of such eruptions, extending some earlier calculations for Mars (2).

The velocity, U, with which the gas (and all clasts small enough to have a negligible terminal velocity in the gas) will emerge through the vent in this type of explosive eruption will depend on the released gas weight fraction, N, the mass flow rate, M, and the pressure at which they emerge, P. P will generally be the local atmospheric pressure but may be higher if the vent geometry is such as to prevent a subsonic to supersonic transition in the emerging gas/clast mixture (1,3,4,5). Calculations of eruption velocities in terrestrial (5,6) and lunar (1) explosive eruptions have been extended to include martian conditions and Fig. 1 gives values of velocity, $U_o$, as a function of N and M when the released volatile is $H_2O$ for standard vent pressure, $P_o$, of 3 millibars (300 $N/m^2$), chosen as representative of the summit areas of several martian volcanoes. The velocities can be converted to those expected, U, at any other pressure, P, from the formula

$$1/2U^2 = 1/2U_o^2 + N(QT/x) \log_e(P_o/P) \quad (1)$$

where T is the magma temperature, Q the universal gas constant and x the molecular weight of the exsolved gas: the numerical value of (QT/x) is about $5 \times 10^5$ $m^2/s^2$ for steam at 1100 K.

The vent radius, R, to be expected in a given eruption depends on N, M, U and P. The relationship is given by the definition for the mass flux:

$$M = U\pi R^2 B \quad (2)$$

where B is the bulk density of the erupted gas/clast mixture, given with sufficient accuracy (1,5,6) by

$$B = P/[N(QT/x)] \quad (3)$$

The mixture of gas and clasts emerging from the vent will interact with the martian atmosphere. In some circumstances, a stable, high, convecting eruption cloud will form; in others (7), the emerging mixture will form a low fountain (a "collapsed" eruption cloud) over the vent feeding either a pyroclastic flow (if the clasts are relatively brittle and the median grain size is relatively small, as is the case for siliceous terrestrial magmas) or a lava flow (if the clasts are hot and plastic so that they coalesce on landing, as in the case of some terrestrial and lunar basaltic eruptions (1)). The essential physical reason for eruption column collapse is the fact that the gas/clast mixture emerging from the center of a vent is denser than the surrounding atmosphere and may decelerate under gravity to a negligible speed before enough atmospheric gas has been mixed into the center of the cloud by

large-scale turbulence and heated by contact with the magmatic clasts to provide buoyancy. It is known from the study of turbulent jets (8) that the inner edge of the zone of mixing between eruption products and atmospheric gas should propagate at a constant rate into an eruption cloud from the edge of the vent, thus arriving at the center line at some height, Y, equal to a constant, K, times the vent radius, R. The upward velocity on the center line at this height must clearly still be somewhat greater than zero if collapse is to be avoided, requiring

$$Y < U^2/[2\ g(1 - (A/B))] \quad (4)$$

where g is the local gravity and A is the atmospheric density given by

$$A = P/[QT_a)/y] \quad (5)$$

in which $T_a$ is the atmospheric temperature and y the atmospheric molecular weight. Combining all these relationships, the condition for avoiding column collapse is

$$R < U^2/[2\ K\ g(1 - ZN)] \quad (6)$$

where

$$Z = (y/x)\ (T/T_a) \quad (7)$$

For the Earth's atmosphere, we can take $T_a$ = 290 k, y = 28.8, and for Mars, T = 215 K, y = 44; using T = 1100 K and $^a$x = 18 for steam we find Z = 6.1 for eruptions on Earth and Z = 12.5 for eruptions on Mars. The combinations of values of N, U and R at which the transition from stable eruption cloud to collapsed cloud occurs have been calculated for terrestrial eruptions (5,7,9) and the insertion of sets of these values into equation (6) using Z = 6.1 gives an average value of K = 33. Using this value of K and the relationship between U, N and M given in Fig. 1 we find the column collapse conditions given in Table 1. These data are used to define the dashed line in Fig. 1 which marks the boundary between stable, convecting eruption clouds (on the left of the figure) and collapsed clouds feeding ignimbrites or lava flows.

It has been shown both theoretically (10, 11, 12, 13) and by observation (11, 12, 13) that the height, H, of a stable eruption cloud is essentially proportional to the fourth root of the heat (and, hence, mass) release rate from the vent. The full relationship involves properties of the atmosphere and is of the form (10):

$$H - [J\ M^{1/4}\ T_a^{3/8}]/[y^2\ P^2\ c^2\ g\ |L|^3\ \{1 + (dT/dh)/L\}^3]^{1/8} \quad (8)$$

where c is the atmospheric specific heat, L is the dry adiabatic lapse rate and dT/dh is the true rate of temperature decrease with height; J represents a number of universal constants which have been collected together. Suitable numerical values would be, for the lower parts of the Earth's atmosphere, $T_a$ = 288 K, y = 28.8, $P_o = 10^5$ N/m$^2$, c = 1000 J kg$^{-1}$,K$^{-1}$, L = -9.6 K/km, dT/dh = -4K/km (14) and, for eruptions taking place at the 3 millibar pressure level in the Mars atmosphere, $T_a$ = 200 K, y = 44, $P_o$ = 300 N/m$^2$, c = 770 J kg$^{-1}$K$^{-1}$, L = -5.4 K/km and dT/dh - -2 K/km (15). Insertion of these two sets of values in turn into equation (8) shows that eruption clouds can be expected to rise about 4.9 times higher on Mars than on Earth for the same eruption rate. The average rise height, H, for a mass eruption rate, M, can therefore be written:

$$(H/km) = S\ [M/(kg/s)]^{1/4} \quad (9)$$

where S - 0.21 for the Earth (12) and the above calculation gives S = 1.03 for Mars; thus, for example, an effusion rate of $10^8$ kg/s will yield a 21 km

high eruption cloud on the Earth and a 103 km high cloud on Mars. Equation (9) has been used to calculate the eruption cloud heights given at the top of Fig. 1.

It has been noted (16) that, in several cases the total width, measured at right angles to the downwind elongation direction, of an air-fall deposit on Earth is approximately equal to the height of the eruption cloud from which it is deposited. The cloud heights in Fig. 1 therefore imply that martian air-fall deposits may manifest themselves as areas of blanketed terrain with shorter dimensions of at least tens of km and possibly in excess of 100 km.

References. 1) L. Wilson and J. W. Head (1981) J. Geophys. Res. 86, 2871. 2) L. Wilson and J. W. Head (1981) Lunar Pl. Sci. 12, 1194. 3) S. W. Kieffer (1977) J. Geophys. Res. 82, 2895. 4) G. S. Steinberg and A. S. Steinberg (1975) J. Geophys. Res. 80, 1600. 5) L. Wilson et al. (1980) Geophys. J. Roy. Astron. Soc. 63, 117. 6) L. Wilson (1980) J. Volcanol. Geotherm. Res. 8, 297. 7) R. S. J. Sparks and L. Wilson (1976) J. Geol. Soc. Lond. 132, 441. 8) L. Prandtl (1949) The essentials of fluid dynamics, Blackie & Son, London. 9) R. S. J. Sparks et al. (1978) J. Geophys. Res. 83, 1727. 10) B. R. Morton et al. (1956) Proc. Roy. Soc. A. 234, 1. 11) L. Wilson (1976) Geophys. J. Roy. Astron. Soc. 45, 543. 12) L. Wilson et al. (1978) J. Geophys. Res. 83, 1829. 13) M. Settle (1978) J. Volcanol. Geotherm. Res. 3, 309. 14) C. Barth (1974) Ann. Rev. Earth Pl. Sci. 2, 333. 15) S. L. Valley (1965) Handbook of Geophysics and space environments, McGraw-Hill, New York. 16) L. Wilson (1980) pp 31-35 in Thera and the Aegean World II, proc. 2nd Internat. Congress, Ed. C. Doumas, published by "Thera and the Aegean World", London.

Table 1. For several exsolved magma water contents, N, in martian plinian eruptions, values are given for $R_c$, the critical vent radius below which a convecting eruption cloud will be stable and above which pyroclastic flows (or, in the case of basaltic magmas, lava flows) will be formed, for $U_c$, the eruption velocity in the vent when the vent radius is equal to $R_c$ and the vent pressure is three millibars, and for $M_c$, the mass eruption rate corresponding to $U_c$ and $R_c$.

| N (wt% $H_2O$) | 0.1 | 0.2 | 0.5 | 1 | 2 | 3.5 | 5 |
|---|---|---|---|---|---|---|---|
| $R_c$ (m) | 20 | 80 | 220 | 490 | 1140 | 2900 | 6400 |
| $U_c$ (m/s) | 80 | 145 | 230 | 330 | 470 | 635 | 770 |
| $M_c$ (kg/s) | $5.3\times10^4$ | $8.8\times10^5$ | $4.1\times10^6$ | $1.5\times10^7$ | $5.7\times10^7$ | $2.8\times10^8$ | $1.2\times10^9$ |

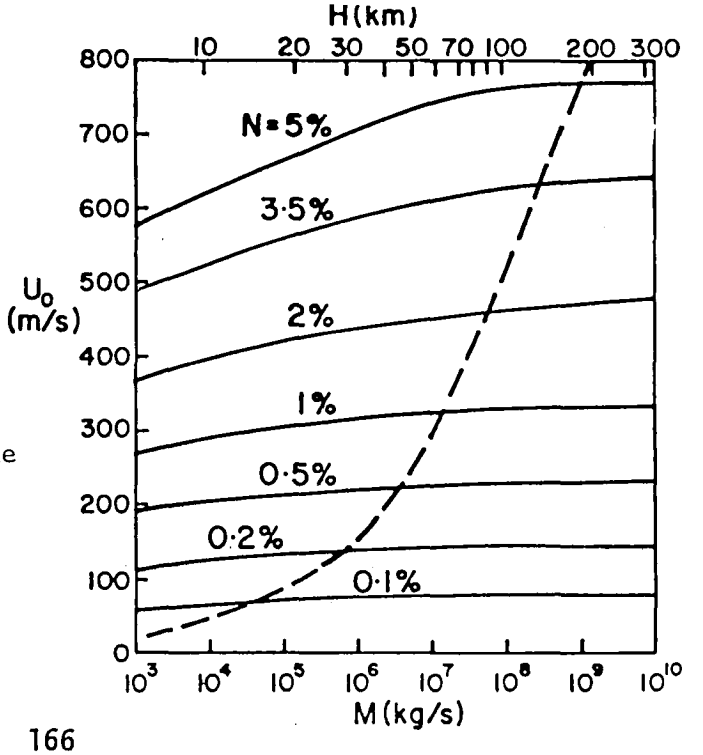


Figure 1. The variation of $U_o$, the velocity of gas and small clasts emerging through the vent in a martian plinian eruption as a function of M, the mass eruption rate and N, the exsolved magma water content. The scale at the top gives the eruption cloud heights, H, corresponding to the values of M at the bottom. Eruption columns are stable for values of M and N lying to the left of the dashed line but will otherwise collapse to form much lower fountains over the vent feeding pyroclastic flows or lava flows.

# PARTICLES FORMED BY FUEL-COOLANT EXPLOSIONS

Michael F. Sheridan, Department of Geology, Arizona State University, Tempe, AZ 85287

Powerful explosions, termed fuel-coolant reactions (Colgate and Sigurgiersson, 1973; Peckover and others, 1973), result from the intimate admixture of a hot liquid with a cold volatile material. Experimental study of fuel-coolant explosive phenomenology is currently being carried out at Los Alamos National Laboratory (Wohletz, 1980) and at Sandia National Laboratories (Nelson and others, 1980; Corradini, 1981). Observations on terrestial hydrovolcanic phenomena (Sheridan and Wohletz, 1981) likewise have a direct application to planetary processes involving such vapor explosions.

On a planetary scale the melt source could be related to volcanism, impact of planetary bodies, or large molten zones within the planet. Common volatiles could be $H_2O$, $CO_2$, or S in either the liquid or solid state. The probability of fuel-coolant interactions is so high on some planets that a significant fraction of their particulate surface material could have been produced by this process. It is therefore important to distinguish the characteristics of particles produced by this process from those of essentially "dry" mechanisms.

First, particles produced by optimum fuel-coolant explosions have a distinct size range. Because these explosions depend on rapid heat exchange, a small particle size (large surface area) favors a rapid conversion of thermal to mechanical energy. Experiments with a water-thermite system at LANL (Wohletz, 1980) demonstrate that for low efficiency interactions at small water-melt ratios the melt particles are large (cm diameter) and strongly vesicular. However, within the optimum range of explosive energy conversion, the particles are small (10-250 $\mu$m diameter) and weakly vesiculated. A similar textural relationship is observed in products of terrestrial volcanism. Eruptions involving a small water melt ratio domantly produce large, highly-vesiculated fragments greater than 250 $\mu$m diameter like plinian pumice and strombolian cinders. Optimum conditions for energy transfer produce base-surge blasts with a large fraction of weakly-vesiculated fragments less than 250 $\mu$m in diameter. Indeed, the fraction of fine fragments in a volcanic deposit is strongly linked to the degree of melt-water interaction in the vent. Planets with a near-surface layer containing volatiles should have appreciable surface areas composed of particles in the size range of 10 to 250 $\mu$m .

Second, particles formed by vapor explosions have a distinctive shape as revealed by scanning electron microscopy. Most SEM work to date has focused on glass particles from volcanic explosions (Heiken, 1974). Hydrovolcanic particles are weakly vesicular and pyramidal, as compared to the spongy, vesicular shape of magmatic particles which have experienced little effect of water-melt interaction. Small scale features of crystals produced by steam blast explosions are also distinct. Primary crystallographic faces, planar fractures, dish-shaped concavities, parallel steps, and small pits are typical (De Rita and others, 1981). The small-scale surface textures of experimental products have yet to be examined in detail. SEM techniques could therefore prove useful for recognition of vapor explosion products on other planets.

Third, grains produced by vapor explosions may be more strongly altered than grains produced in a dry environment. Melt particles with a large surface area in intimate contact with high-temperature vapors undergo rapid alteration. Thus, terrestrial products of "wet" hydromagmatic explosions are typically hydrated, altered to zeolites, and strongly cemented. Products of "dry" hydrovolcanic explosions generally lack these effects. The distinction between "wet" and "dry" conditions is based on the presence of a three-phase (water-steam-particles) vs. two-phase (steam-particles) system (Sheridan and Wohletz, 1981). Absorbed volatiles and secondary reaction products could be detected in vapor-explosion products on planetary surfaces using remote techniques.

Products of fuel-coolant type explosions should form a significant contribution to specific areas on planets containing a near-surface layer rich in volatiles. Because of their small grain size and vapor-rich transport media, their deposit morphology and distribution pattern would be greatly different from that of ejecta produced in a dry environment. Resedimentation of the particulate matter is also affected by the nature of the melt-volatile interaction. Some "dry" deposits composed of unconsolidated grains dominantly in the 10-250 $\mu$m size range might easily be resedimented through ambient planetary processes. Other "wet" deposits might show a high degree of lithification because of hydration, alteration, and secondary mineral cementation. Such deposits would be resistant to weathering forming erosional scarps, similar to lava flows. The progression from dry explosions to "dry" vapor explosions to "wet" vapor explosions would reflect an increase in volatile content in the contact zone of the melt with the surficial layer.

References

Colgate, S.A. and Sigurgiersson, T. 1973, Dynamic mixing of water and lava: Nature, 244, 552-555.

Corradini, M.L., 1981, Phenomenological modeling of the triggering phase of small-scale steam explosion experiments: Nuclear Science and Engineering, 78, 154-170.

De Rita, D., Sheridan, M.F., and Marshall, J.R., 1981, SEM surface textural analysis of phenocrysts from pyroclastic deposits at Baccano and Sacrofano volcanoes, Latium, Italy, in Whalley, W.B. and Krinsley, D.H. eds., SEM in Geology, Geoabstracts, Norwich, England.

Heiken, G., 1974, An atlas of volcanic ash: Smithsonian Contribution to Earth Science, no. 12, 101 p.

Nelson, L.S., Buxton, L.D., and Planner H.N., 1980, Steam explosion triggering: Corium-A and corium-E simulants and oxides of iron and cobalt studied with a floodable arc melting aparatus: Sandia National Laboratories, SAND79-0260, NUREGICR-9633.

Peckover, R.S., Buchanan, D.S., and Ashby, D.E., 1973, Fuel-coolant interactions in submarine volcanoes: Nature, 245, 307-308.

Sheridan, M.F. and Wohletz, K.H., 1981, Hydrovolcanic explosions: The systematics of water-pyroclast equilibration: Science, 212, 1387-1389.

Wohletz, K.H., 1980, Explosive hydromagmatic volcanism: Arizona State University, unpub. Ph.D. dissertation, 303 p.

# MELT-WATER INTERACTIONS: SERIES II EXPERIMENTAL DESIGN

Kenneth H. Wohletz, Los Alamos National Laboratory, P.O. Box 1663, MS987, Los Alamos, NM 87545
Michael F. Sheridan, Department of Geology, Arizona State University, Tempe, AZ 85287

Spontaneous vapor explosions resulting from the interaction of two fluids, one above the boiling temperature of the other, are common within the solar system. On earth these explosions are common at volcanoes where magma comes into contact with near-surface water (hydrovolcanism). Impact melts may also interact with surface waters, as concluded by studies of martian and terrestrial impact craters (1, 2, 3). Additionally, volcanism on Io may be a result of interaction of a hot silicate melt with a cooler sulfur fluid (4,5). Our work includes a review of steam explosion experiments, new experimental designs, and textural analysis of melt ejecta particles using scanning electron microscopy.

## 1. Previous Experimental Investigations

Extensive study of vapor explosions has been undertaken in the field of nuclear reactor safety (6). Experiments model the initiation and affects of possible steam explosions resulting from a core melt (fuel) interacting with a coolant (water) (7, 8, 9). Initial contact of the two fluids can generate dynamic pressure pulses that may cause spontaneous mixing of the two fluids resulting in large scale explosive heat exchanges. The prime focus of these studies has been the conversion efficiency of thermal energy to mechanical ($P\Delta V$) work. Experiments at Sandia National Laboratories have tested interaction of single (1 to 10 g) drops and large batches (10 to 20 kg) of molten metal in water. Thermodynamic and hydrodynamic modeling of the small-scale experiments has successfully predicted the degree of fuel fragmentation (particle size), the duration of the explosion, and peak pressures, all of which permit thermodynamic efficiency calculations. These experiments produce particles in the range of 10-1000 μm in diameter, peak pressures that reach 5 to 10 MPa in the order of a few milliseconds, and efficiencies in the range of 8 percent.

These above results compare favorably with ours at Los Alamos National Laboratory (3, 10) for experiments using a larger amount of fuel (100 kg). The mechanism of large-scale heat transfers produce by fluid mixing and fuel fragmentation have been studied by size and SEM analyses of particles. Particle median diameter decreases with increasing explosivity and ranges near 50 μm for optimum efficiencies. SEM micrographs show that surface area and ineqularity increases with decreasing particle size. These data correspond with recent studies of hydrovolcanic ash (11, 12).

## 2. The Series II Experimental Design

Previous experiments (3) resulted in estimates of thermodynamic efficiency, ejection phenomenology, and particle characteristics for burried explosions (Series I design) produced by the interaction of 100 kg of thermite melt with water. The new (Series II) design (fig. 1) includes the following changes: 1) The confinement chamber is smaller using only 10 kg of thermite and requires very little restoration maintenance; 2) the vent

opening is directed downward; 3) the chamber is fired above ground. These changes allow more accurate estimates of efficiencies based upon the lift-off acceleration and travel distance of the chamber, reduced experimental set up time, and facilitated collection of ejecta fragments. These experiments will determine optimum explosive conditions, a further refinement of data relating the melt-water ratio to explosive efficiency (3). Six experiments conducted thus far have established the operational system and show that other coolant materials of planetary significance, such as sulfur and dry ice, may be investigated.

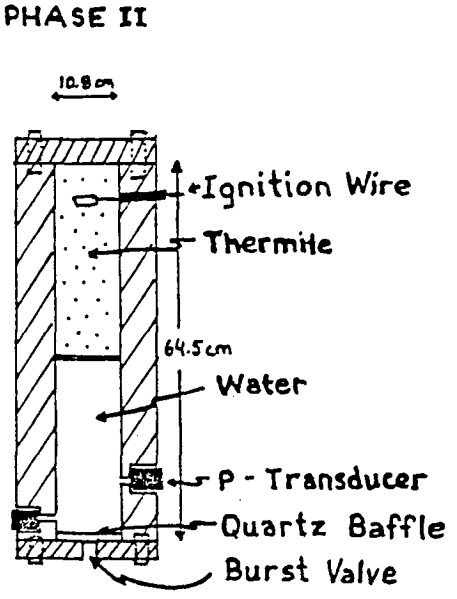


Fig. 1 Series II design of the melt-water interaction experiment. Varying amounts of thermite and water may be used in order to study explosive efficiency.

3. Particle Shape Analysis

The scanning electron microscope provides a method for determining morphological as well as chemical characteristics of ejecta particles formed during melt-water explosions. At this point we have only investigated particles from hydrovolcanic systems. Analysis of over 850 grains shows that three morphology types: vesicular, broken or blocky, and drop-like characterize most ash particles greater than 100 μm in diameter produced by hydrovolcanic explosions. The relative dominance of these morphology types are dependent upon ejection mode (surge or ballistic) and the deposit morphology (dunes, massive, planar, or airfall, Fig. 2). This relationship is a measure of explosive energy and nature of fragmentation resulting from mixing of magma and water. Particles less than 50 to 100 μm in diameter show morphologies that are irregular with high surface areas, and often agglomerates of smaller material. The change in particle morphology with decreasing size has been suggested (8) to be the result of increased frag-

mentation by fluid instabilities rather than by thermal fracturing evidenced in large particles.

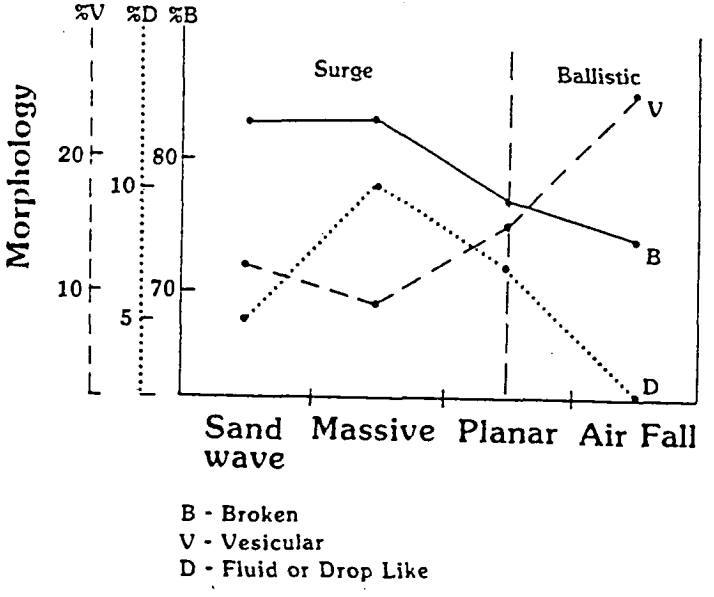


Fig. 2 The relative dominance of particle morphology types versus deposit morphology (sandwave-dunes, massive - channeled or hummocky, planar, and airfall) is also a function ejection mode. Deposit morphology is dependent upon explosion violence which decreases right to left.

References


1. Head, J.W. and Roth, R. (1976) Symposium on Planetary Cratering Mechanics, 50-52.
2. Kieffer, S.W. and Simonds, C.H. (1980) Rev. Geophys. Space Phyc., 18, 143-181.
3. Wohletz, K.H. and Sheridan, M.F. (1980) NASA Tech. Memo 82385, 143-181.
4. Cook, A.F., Shoemaker, E.M., and Smith, B.A. (1979) Nature, 280, 743-746.
5. Reynolds, R.T. and Peale, S.F. (1980) Icarus, 44, 234-239.
6. Sandia Laboratories (1975) SAND-74-0382, 472 p.
7. Corradini, M.L. (1980) Sandia Laboratories, SAND80-2131, 114p.
8. Buxton, L.D. and Benedick, W.B. (1979) Sandia Laboratories, SAND 79-1399, 62p.
9. Nelson, L.S., Duda, P.M. (1981) Trans. Amer. Nucl. Soc., 38, 453-454.
10. Wohletz, K.H. and McQueen, R.G. (1981) Amer. Geophys. Union Trans. (in press).
11. Wohletz, K.H. (1981) Geol. Soc. Amer. Nat. Meeting (in press).

# MORPHOLOGIC EVOLUTION OF THE 18 MAY 1980 CRATER AT MOUNT ST. HELENS, WASHINGTON

Daniel Dzurisin and Thomas J. Casadevall
U.S. Geological Survey, Vancouver, WA

The summit crater at Mount St. Helens was produced on 18 May 1980 by a massive landslide and ensuing lateral blast which devastated roughly 500 $km^2$ of countryside north of the volcano. The resulting horseshoe-shaped excavation on the volcano's northern flank was initially 730 m deep and 2.1 km (E-W) by 2.3 km (N-S) wide at the rim, with a nested inner crater 1.1 km in diamter. The volume of this initial excavation was approximately 2.3 $km^3$. Since its formation, the crater has been substantially modified by a host of geomorphic processes.

Ongoing eruptions have been the dominant agent responsible for crater infilling. Roughly 0.025 $km^3$ of pyroclastic material ejected during explosive eruptions since May 18 (May 25, June 12, July 22, August 7 and October 16-18 1980) have accumulated on the crater floor to an estimated depth of 100 m. In addition, extrusions in June, August, October and December 1980, and February, April, June, and September 1981 have built a dacitic lava dome roughly 150 m high, with an approximate volume of 0.03 $km^3$. An unknown, but presumably small, volume of new material may also have been added to the crater by shallow intrusion into the tephra fill on the original crater floor.

Mass wasting from steep crater walls has also contributed a substantial volume of material to the crater floor. Rapid slope failure and the abrasive uprush of erupted material on 18 May 1980 combined to produce steep, unstable walls susceptible to rockfalls and rock avalanches. Large rock avalanches in January and June 1981 traversed the crater floor and impinged on the dome; additional material is currently shed essentially continuously by smaller rockfalls onto the crater floor. The total volume of talus accumulated since May 1980 is estimated to be 0.005 $km^3$.

The primary erosive process operating in the crater has been incision into relatively unconsolidated 1980 pyroclastic deposits by surface runoff in the form of streams and mudflows. Intermittent streams fed by winter storms and spring meltwater have dissected the volcano's breached northern flank to a maximum depth of 15 m in the inner crater. Reworking of fines by wind

has not been volumetrically significant, but eolian redistribution of rockfall-generated dust often obscures visibility in the crater, and accounts for a mantle several cm thick on the crater floor.

In the near future, extrusion and continuing re-adjustment of the crater walls are likely to further infill the crater at a relatively high rate. Fluvial erosion will likely become increasingly important as more typical winters follow the exceptionally mild one of 1980-81, but accumulation will continue to exceed erosion until eruptions become less frequent and/or the crater walls become more stable.

Morphological Characteristics of Terrestrial Ash-Flow Tuff (Ignimbrite) and Related Pyroclastic Deposits. Charles W. Criswell and Wolfgang E. Elston, Department of Geology, Univ. New Mexico, Albuquerque, New Mexico 87131

## Introduction

The controversy over the importance (or existence) of extraterrestrial ash-flow deposits (especially on Mars) partly hinges on criteria by which such deposits can be identified (1). This is a preliminary attempt to classify terrestrial ash-flow deposits by morphological characteristics (useful in photographic images) and clast size (useful in future SLR images). The classification is based on field observations at Mount St. Helens, the Taupo zone (New Zealand), the Jemez Mountains and Mogollon-Datil field (New Mexico), and surveys of the literature. No single morphological feature is diagnostic; many can also be found in deposits as diverse as basalt flows, eolian and fluvial sediments, or glaciers. An array of criteria could be diagnostic.

Ash-flow tuff deposits are here classified as small ($<10km^3$), medium ($10-100km^3$) and large ($100-3,000+km^3$). In general, areal extent in $km^2$ is an order of magnitude greater than volume in $km^3$. All observed ash flows have been small or in the low end of the medium range.

## Characteristics of Vents

A. Small deposits: Vents are unlikely to have unique characteristics because small deposits are secondary features on rhyolite domes, andesitic stratovolcanoes, small basaltic calderas, etc.

B. Medium deposits: Transitional between small and large. Non-resurgent calderas predominate.

C. Large deposits: Vents, on top of low shields, are large calderas (diameter commonly $10^1km$), circular to elongated, commonly scalloped, with single or multiple ring-fracture zones with strings of convex lava domes; with or without central resurgent dome. No known extraterrestrial feature has this topographic form.

## Characteristics of Outflow Sheets

A. Tone: Uniform to mottled or streaked, generally light to medium.

B. Features influenced by pre-existing topography
1. Scour channels, especially on steep slopes, 0.1 to 10km long; 0.1 to 2km wide (2).
2. Subdued topography, filling of depressions and valleys, discontinuous veneers on high areas (3).

C. Primary surface features
1. Unstructured flows. Entire deposit may be unstructured (Valley of the Ten Thousand Smokes, Alaska, 1912, $11km^3$), or early unstructured deposits may become partly covered by structured deposits (Mount St. Helens, Washington, 1980, $0.2km^3$) (4).
   a. Surfaces: Gently inclined, flat or gently undulating, smooth, with local minor concentrations of pumice blocks (to 50cm).
   b. Pits and craters, formed by phreatic explosions, 2 to >100m diameter, rims and ejecta blankets low, ejecta exposed in lip is laminated, not overturned.
   c. Termini tapered
   d. Fumaroles: Mounds, pits, and discolored areas.
   e. Folds: In large deposits (5), folds (amplitude $10^0m$, wavelength $10^1m$) may occur near vents.
2. Structured flows (Fig. 1): Generally <10km long, <1km wide. Material ash- to block-size (4). During transport, ash particles partly concentrate in ash-cloud deposits; block-size pumice lumps tend to rise to tops of ash flows.
   a. Channels: Elongated zones between marginal levees (Fig. 1, C).
      i. Smooth surfaces, large proportion of lapilli.
      ii. Coarse-textured surfaces, large proportion of block-size pumice fragments, mainly in distal parts of channels.
      iii. Transverse profile concave in upper parts of channels, convex in lower parts due to drainage.
   b. Distributaries (Fig. 1, D): Single flow lobes split into multiple flow lobes, become bulbous near termini (Fig. 1, B).
   c. Longitudinal ridges (Fig. 1, LR): Generally associated with channels and distributaries. Mean material size coarser and better sorted than in channel deposits, largely lapilli- to block-size pumice or lithic clasts.
      i. Medial ridges, 0.5-2m high, $10^1-10^2m$ long, trains of pumice or lithic clasts, isolated or grouped in parallel rows.
      ii. Marginal ridges (levees), 1-3m high, may run for part or entire length of channels (Fig. 1, L). Consist of block-sized pumice clasts.

d. Transverse ridges
i. Primary dunes, $10^0$-$10^2$m long, 0.25-1.25m high, of very-fine-grained well-sorted ash-cloud deposits, isolated or marginal to ash-flow deposits.
ii. Flow folds in densely welded ash-flow tuffs (especially peralkalic varieties(5)). Amplitude 1-10m, wavelength 20-60m. Recumbent folds (axes dip toward source) grade into thrusts. Folds are aligned along concentric arcs, convex away from source. Example: Buckshot Ignimbrite, West Texas (6).
iii. Terminal ramps, i.e., imbricated deposits of pumice blocks concentrated near flow termini (Fig. 1, TR).
iv. Festoon- and eddy-like deposits of pumice blocks in distal parts ash-flows.
e. Lag deposits: Swarms of fines-depleted pumice. Also, accumulations of lithic clasts near vents (7).
f. Phreatic pits and craters, resemble those of unstructured ash-flow deposits.
g. Mounds
i. Tumuli, 2-5m high, 2-10m in diameter, circular in plan, steep to vertical flanks, breached or unbreached apices. May grade into discontinuous folds. Examples: Buckshot Ignimbrite, West Texas (22km$^3$) (6); Fantale, Ethiopia (8).
ii. Fumarole mounds, circular type 20-60m in diameter, 0.5 to 15m high; elliptical type 1.5-5m high, up to 600m long, flanks gentle or moderately steep, distribution generally random, fumarolic discoloration, associated with joints of rosette pattern. Example: Bishop Tuff, California (170km$^3$) (9).
h. Termini
i. Simple: lobes, commonly bulbous (4,10) (Fig. 1, B); steep fronts formed by coarse pumice clasts at maximum angle of repose.
ii. Crenulated, associated with transverse ridges (Fig. 1, CT).

D. Erosional Features
1. Surfaces: The entire unwelded upper parts of deposits are commonly stripped by erosion. Few, if any, details are preserved on large deposits.
2. Scarps
a. Vertical, 10-250+m, for simple cooling units.
b. Variable because of differential welding. Single steep face for simple cooling units, two or more steep faces separated by benches for compound cooling units.
c. Slump features: Hummocky deposits at base of scarps, from collapse of poorly welded or unwelded ash-flow tuff deposits.
d. Talus at base of scarp.
3. Joints
a. Columnar (vertical) formed by cooling of outflow sheet (11).
b. Rosette, formed around fumaroles (9).
c. Subhorizontal sheeting near tops of columns.
4. Tent rocks (11).
5. Erosional remnants, elongated parallel to direction of drainage or wind.
6. Mounds: indurated rock, concentric around circular fumaroles.
7. Eolian dunes, consisting of wind-transported ash-size particles from ash-flow and ash-cloud deposits.
8. Ridges: Indurated rock etched out along fissure-type or elliptical fumaroles.
9. Drainage patterns: On young unwelded ash flows, parallel (12) or dendritic drainage pattern develops on sloping pumice plains. In older welded deposits, drainage may approach trellis pattern, controlled by columnar joints.

References


1. Greeley, R. and Spudis, P.D., 1981, Rev. Geophys. Space Phys. 19, 13.
2. Sheridan, M.F., 1979, GSA Spec. Paper 180, 125.
3. Walker, G.P.L. et al., 1980, Nature 283, 286.
4. Rowley, P.D. et al., 1981, U.S.G.S. Prof. Paper 1250 (in press).
5. Wolff, J.A. and Wright, J.V., 1981, J. Volcanol. Geotherm. Res. 10, 113.
6. Anderson, W.B., 1975, Unpubl. M.S. Thesis, Univ. Texas, Austin
7. Wright, J.V. and Walker, G.P.L., 1977, Geology 5, 729.
8. Gibson, I.L., 1970, Contrib. Mineral. Petrol. 28, 89.
9. Sheridan, M.F., 1970, GSA Bull. 81, 851.
10. Deruelle, B., 1978, Bull. Volcanol. 41, 175.
11. Ross, C.S. and Smith, R.L., 1961, U.S.G.S. Prof. Paper 366.
12. Francis, P.W. and Baker, M.C., 1978, J. Volcanol. Geotherm. Res. 4, 81.

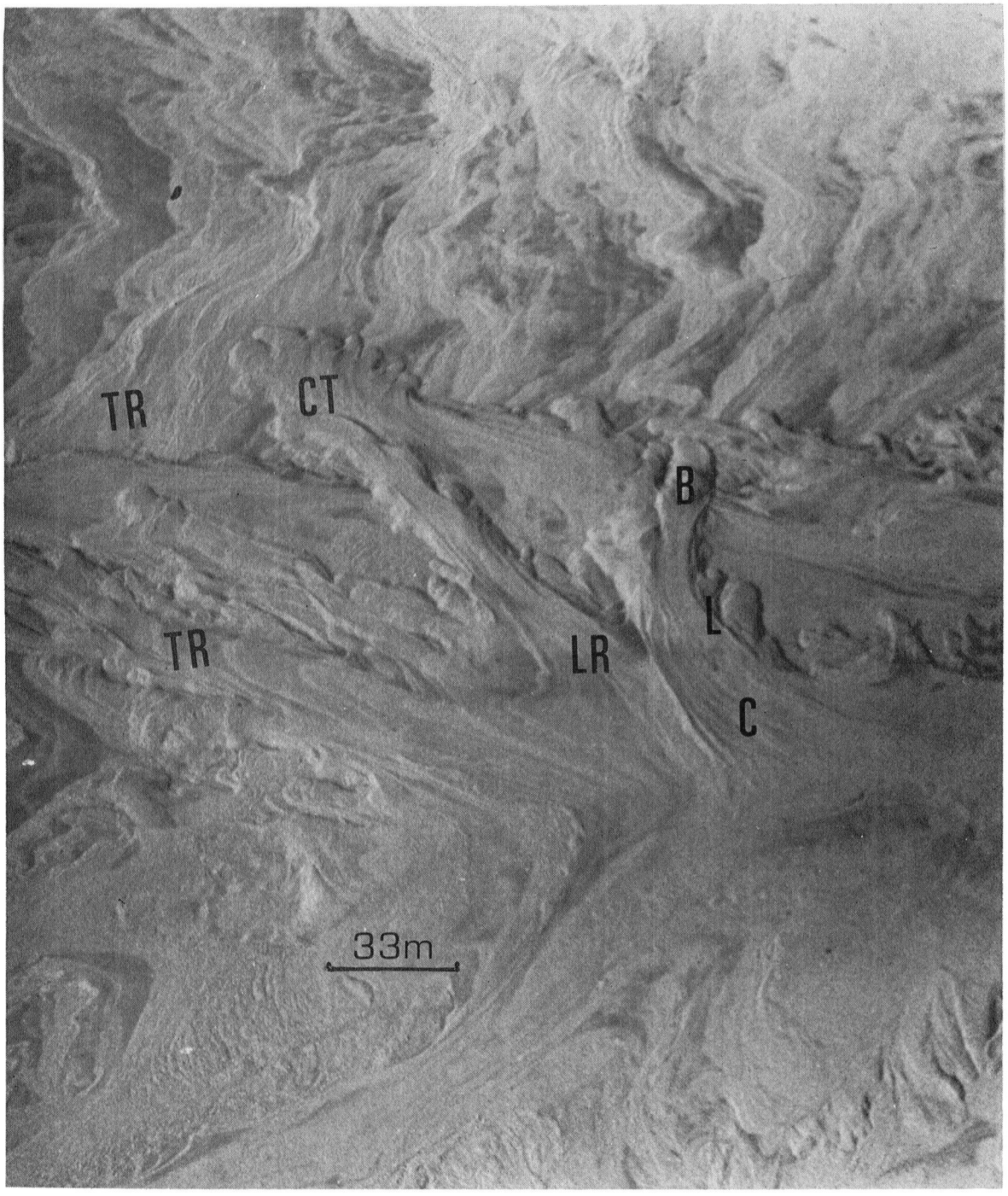


Figure 1. Structured pyroclastic flow deposit, Mount St. Helens, May 18, 1980. C-Channel, D-Distributary with bulbous and lobate termini (B), LR-Longitudinal ridges, TR-Terminal ramps, L-Levee, CT-Crenulated terminus.

CHARACTERIZATION OF ROCK POPULATIONS ON THE SURFACES OF MARS, VENUS, AND EARTH: A SUMMARY. J. B. Garvin, P. J. Mouginis-Mark, and J. W. Head, Dept. of Geol. Sci., Brown University, Providence, RI 02912.

Introduction. Rock populations on planetary surfaces reflect both local-scale and global-scale geologic processes [1]. Modes of formation, emplacement, and modification for individual blocks can be inferred from their morphology and morphometry (i.e. dimensions). This information can be related to planet-wide geologic phenomena such as volcanism, eolian erosion, chemical weathering, and meteorite impact. Over the past two years we have been establishing a data base for interplanetary rock population comparisons. Qualitative morphologic data concerning rock modification features (pits, flutes, facets, wind tails etc.), features diagnostic of a particular mode of origin (columnar joints, vesicles, flow bands etc.), and local environment have been collected from Viking lander images of Mars (VL-1, VL-2), Venera 9 and 10 panoramas of Venus, and from photographs of test sites in Egypt (WMB, GKR), Hawaii (MKS, HLM), and Iceland(ICB) [1,2]. Morphometric information (length and width axes) was also collected when viewing geometry was well-known. Table I summarizes some of the presently available data. Clustering analysis of the morphologic and morphometric data for Mars, Egypt, Iceland and Venus has been completed [1,6,7]. Power law fits to the rock size distributions available for martian, Hawaiian, and Egyptian sites, along with the determination of two-dimensional sphericity were also carried out [1,2,8]. Objectives in the martian analyses have been to infer 1) the types of rocks present at the Viking lander sites, 2) the emplacement mechanisms (i.e. debris flows vs. in situ lavas), and 3) modification histories (wind weathering vs. chemical and water-related erosion). Parallel studies of distinctive Earth environments provides an understanding of the basic processes operating at these scales.

Mars. [Table I; 1,3,4] VL-1 and VL-2 are quite similar in terms of general rock shape (form ratios of -0.25 to -0.30 indicate moderate elongation) and sphericity. However, rocks at VL-2 are generally larger than those at VL-1, where pebble size fragments dominate. The "b" parameter in a power law fit to the rock sizes (see Table I) at VL-1 is similar to disintegrated igneous boulders on Earth [5], or Tycho impact debris near Surveyor VII [5]. At VL-2, the "b" value is consistent with multiple fractured basalts as observed at Halemaumau (HLM) or near the summit of Mauna Kea (MKS). Both Viking rock populations have form ratios indicative of isotropic homogeneous igneous rocks (see ICB basalts in Table I) [1]. In terms of morphology, the VL-1 and VL-2 sites display highly pitted surfaces with abundant flutes. Most rocks are somewhat elongate and sub-angular. Small, shallow cavities abound at VL-1, whereas larger, deeper and more spherical cavities dominate VL-2 rocks. Wind features such as sediment moats, tails, and fillets (aprons) are more common at VL-1 than at VL-2, most likely due to the higher surface area block cover at VL-2 relative to VL-1 (20% vs 8%)[3,4]. Pit distributions on VL-1 blocks are typically uniform, whereas those at VL-2 are bimodal. Faceted rocks are common at VL-1, but much less so at VL-2. Large (cm size), multi-level cavities are observed at VL-2, but none can be seen at VL-1. These cavities resemble the small-scale tafoni (honeycomb weathering) that have been observed in a variety of salt weathering environments on Earth [9] as well as certain vesiculation patterns. While most rocks at the Viking lander 1 locality are at least slightly buried, many blocks at VL-2 appear to be perched, and no VL-2 rocks give the impression of a high degree of burial.

Clustering analysis of the morphologic data for VL-1 and VL-2 suggests that rock groups at VL-1 can be separated on the basis of surface texture, pit distribution, angularity, and linear features (fissures, bands, cracks). At VL-2, surface texture, angularity, and degree of elongation are the best rock class separation criteria. If modification features only are considered in clustering the data, cavity (i.e. pit) distribution, flute presence, and cavity size are the critical parameters in separating rock morphologic groups at VL-1, whereas degree of burial, cavity distribution, and presence of linear features (cracks, bands) are most diagnostic at VL-2 [1,7].

These preliminary analyses indicate fundamental differences in the rock populations at the two VL sites on Mars. These differences are best reflected in the styles of pitting in the rocks at the two localities. At present, we are conducting a detailed study of pits in near-field rocks at VL-1 and VL-2 in order to correlate them with volcanic (i.e. vesicular) or weathered (i.e. wind pitted or chemical) terrestrial rocks. At this stage in our analysis, it appears likely that the pits and flutes on VL-1 blocks are wind-related, while most of those visible on VL-2 rocks are related to the rock formation process and could be vesicles. Some VL-2 rocks display a pitting style that resembles tafoni in vesicular tholeiitic basalts observed on Hawaii, and could represent salt-weathering pits resulting from frosts [9].

The actual composition of the rocks at the Viking sites cannot be inferred from the analysis of VL images at this time. However, studies of a variety of lithologies under conditions similar to those on Mars in several ways can constrain the realm of possibilities. We have analyzed high resolution photographs of block fields in the Western Desert of Egypt [6,7], at two localities on the island of Hawaii [8,9], and at one site on Iceland in a fashion identical to that used for the Viking lander images. All of these terrestrial analog sites have extrusive igneous rock populations ranging from tholeiitic basalts to more alkalic basalts (Iceland and Mauna Kea).

Terrestrial analogs. (Western Desert of Egypt) Two basaltic localities in the hyperarid Gilf Kebir of Egypt were studied. The WMB site is a basalt plug that intruded the sandstones at Wadi Mashi during the Quaternary. The columnar jointed, wind pitted basalts at WMB are non-vesicular, aphanitic, and homogeneous. The GKR locality displays wind-fluted basalt fragments resting upon a desert pavement (reg) surface. Analysis of the morphologic data for these sites [6,7] reveals the importance of emplacement and modification processes in shaping a basaltic rock population under arid conditions. Wind pits and flutes are the only surface markings on the Egyptian basalts, and resemble VL-1 fragments quite closely. None display the high degree of pitting, or the deep cavities observed in many VL-2 rocks. We are using the Egyptian localities as end-members in which wind erosion is the dominant rock modification process on blocks not originally pitted from their formation process (i.e. vesicular). In addition, the WMB boulders have abundant columnar joints and linear features (cracks), both of which could be present in martian rocks. The GKR rocks were likely transported by floods caused by torrential rains in the desert peneplain. The VL-1 site lies near the mouth regions of several large channels in Chryse Planitia [3], and fluvial or flood transported fragments could be present there. Based on comparisons with the GKR fragments, however, VL-1 does not resemble a water-affected arid locality.

Hawaii: (Mauna Kea and Halemaumau) Two field sites in Hawaii have been studied in terms of their rock size distributions. Glaciated alkali basalt flows near the summit of Mauna Kea (MKS) are comparable to VL-2 in terms of their power law distribution (see Table I). Phreatic basalt ejecta from

Halemaumau pit crater in Kilaueau caldera (HLM) resembles VL-2 as well, but is more analogous to the Surveyor III site on the moon in terms of its power law distribution [5]. The basalts at MKS are vesicluar and elongated. They have been affected by wind, rain and snow, and are less angular than the recently emplaced (1924) massive tholeiite fragments at HLM. Both Hawaiian sites display rocks that are more spherical and elongate than martian or Egyptian ones (see Table I). Morphologic studies of these rocks are in progress.

Other localities: The Venera 9 and 10 localities on Venus have also been compared to the VL sites on Mars in terms of rock morphology [1,2]. The blocky Venera 9 site has a "b" parameter that indicates that the platy rocks there are very simply broken [5], like those at the VL-2 site on Mars. The Venera 13 and 14 missions to Venus in 1982 may provide better imagery of Venus, and permit more detailed Mars-Venus rock population comparison.

Table I: Summary of morphometric parameters for planetary surface block fields. N is size of population. N/A means "not available".

| Site | Location | N | Area ($m^2$) | Form* Ratio | Mean Diam. (cm) | Mean# W/L | Size Range (cm) | b@ | K@ | $R^2$ |
|---|---|---|---|---|---|---|---|---|---|---|
| VL-1 | Chryse Planitia, Mars | 240 | ∿ 7 | -0.25 | 5.8 | 0.634 | 1.8-21.3 | 0.81 | $3x10^4$ | 0.92 |
| VL-2 | Utopia Planitia, Mars | 210 | ∿ 7 | -0.30 | 7.3 | 0.631 | 1.3-25.1 | 0.62 | $1x10^4$ | 0.90 |
| MKS | Mauna Kea Summit Basalts, Hawaii | 162 | 4 | -0.49 | 6.9 | 0.720 | 2.2-57.0 | 0.58 | $1x10^4$ | 0.96 |
| HLM | Halemaumau Phreatic Ejecta, Hawaii | 137 | 4 | -0.56 | 6.6 | 0.740 | 1.3-59.0 | 0.61 | $1x10^4$ | 0.98 |
| WMB | Wadi Mashi Basalt Hill, Egypt | 101 | < 1 | -0.42 | 2.9 | 0.660 | 0.2-17.0 | 0.56 | 286 | 0.95 |
| GKR | Gilf Kebir Reg Basalts, Egypt | 51 | 9 | -0.56 | N/A | N/A | N/A | N/A | N/A | N/A |
| ICB | Iceland Alkali Basalts | 31 | ∿ 2 | -0.29 | N/A | N/A | N/A | N/A | N/A | N/A |
| Venera 9+ | Beta Regio (NE), Venus | 109 | >10 | -0.17 | 33.6 | 0.593 | 6.0-95.0 | 0.64 | $4x10^5$ | 0.90 |
| Venera 10 | Beta Regio (SE), Venus | 30 | >10 | +0.45 | N/A | N/A | N/A | N/A | N/A | N/A |

*Based on morphologic data
Values < 0 are elongate; Values > 0 are platy.

#W is width, L is length in cm; W/L is 2-dim. sphericity
Values near 1.0 are spherical.

@From power law regression of rock size data (d = rock diam.) : $N_{>d} = Kd^{(-3b)}$
b is slope in log N - log d plot, K is intercept.
Correlation $R^2 > 0.90$ in all cases.

+Based on orthographic Venera 9 panorama and map in Keldysh [1979].

References: 1] J. B. Garvin et al. (1981) The Moon & Planets 24, 355-387. 2] J. B. Garvin et al. (1980) LPS XI, 317-319. 3] A. B. Binder et al. (1977) J. Geophys. Res. 82, 4439-4451. 4] T. A. Mutch et al. (1977) J. Geophys. Res. 82, 4452-4467. 5] W. K. Hartmann (1969) Icarus 10, 201-213. 6] J. B. Garvin et al. (1981) LPS XII, 327-329. 7] J. B. Garvin (1981) NASA SP in press. 8] J. B. Garvin et al. (1981) NASA TM 82385, 238-240. 9] J. B. Garvin and P. J. Mouginis-Mark (1981) LPS XII, 330-332. 10] M.V. Keldysh (ed.) (1979) NASA TM 75706, 193 pp.

# Cenozoic Asian Volcanism.

J.L.Whitford-Stark. Department of Geology, University of Missouri, Columbia, Missouri, 65211.

Central and eastern mainland Asia remains one of the most enigmatic areas in the world for western geologists. The reasons for this are political, linguistic, the publication of information in obscure journals, and the extreme remoteness of much of the area. Even today, there are areas that have only been observed through Landsat imagery. Over the last several years the author has been compiling the more-readily obtainable information relating to Cenozoic volcanism in Asia and has attempted to synthesize that information to characterize the features of continental volcanism.

The area of the survey is extremely large, being approximately 21.7 x $10^6$ $km^2$ or roughly three times the size of North America and 1.25 times the size of Tharsis, comprising the eastern USSR, Mongolia, China, Burma, Thailand, Laos, Cambodia, Vietnam, Korea, and the Malay Peninsula. As few as a maximum of 13 volcanoes are reported to have erupted within the last few millenia. Some of these 13 eruption reports are unreliable while there are areas so isolated that an eruption could have gone unnoticed. The author has so far uncovered information relating to over 170 specific areas including over 200 named volcanoes and several hundred more unnamed volcanoes. These areas are shown in the accompanying figures. There remain, however, many areas for which no information has been obtained.

The predominant eruption style was one that led to the formation of plateau basalts and fault-controlled lava flows. Associated constructs are cinder cones and small shields. There are a few composite volcanoes; these being located on the east coast and in Burma. Some volcanoes on the Tibetan Plateau may have been Tuyas and large calderas have been identified in this area and possibly southeast Mongolia.

Excepting the east coast belt, the entire area is dominated by alkali-rich extrusives, particularly alkaline basalts and basanites. Four distinct chemical trends can be identified but generally there has been an increase in alkalinity with both decreasing age and increasing distance from plate boundaries.

Cenozoic volcanism appears to have been areally and volumetrically most significant during the Oligocene and Miocene periods and was probably related to the collision of the Indian and Eurasian plates and the opening of back-arc basins. Likewise, volcanism terminated in the Okhotsk-Chukotka belt with the establishment of volcanism on the Kamchatka Peninsula. Many of the continental eruptives appear to have been produced preferentially at former plate and microplate boundaries though grabens and strike-slip faults have also been important eruption centers(1).

References:
1) P.Molnar and P.Tapponnier(1975) Science 189, 419-426.

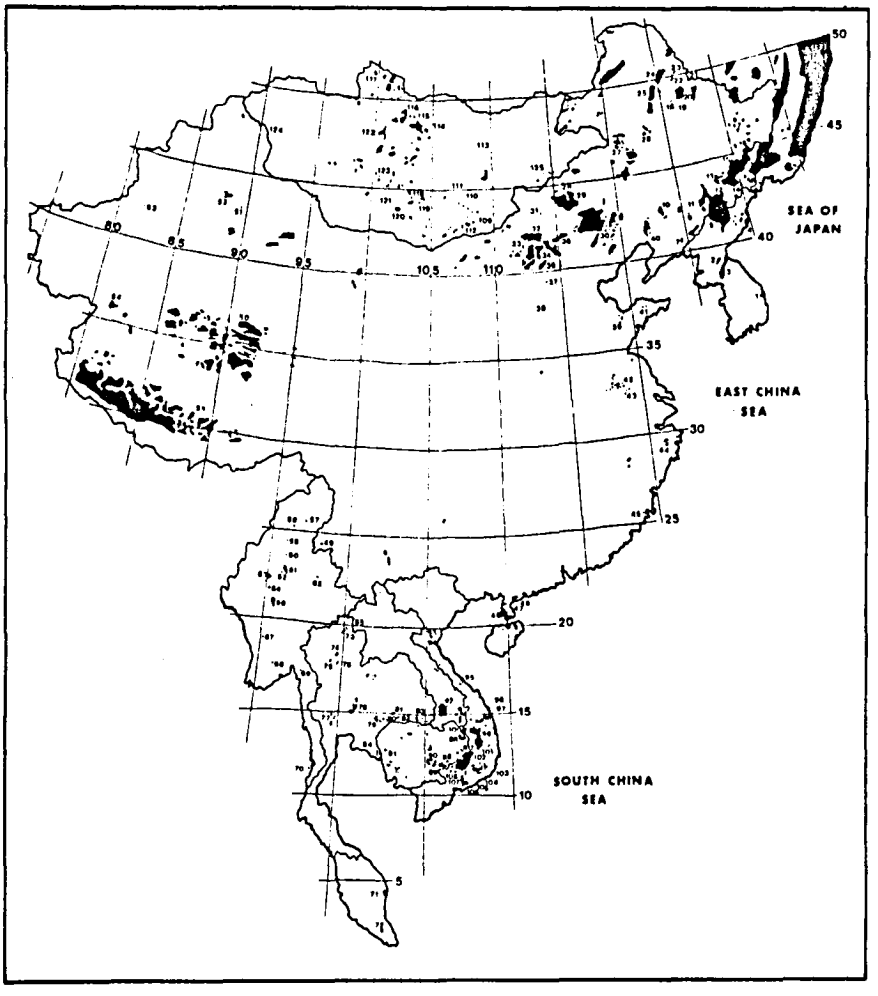


Figure 1: Distribution of Cenozoic basalts in southern Asia. Numbered locations are described in a forthcoming catalog. The representation of international boundaries is not necessarily authoritative

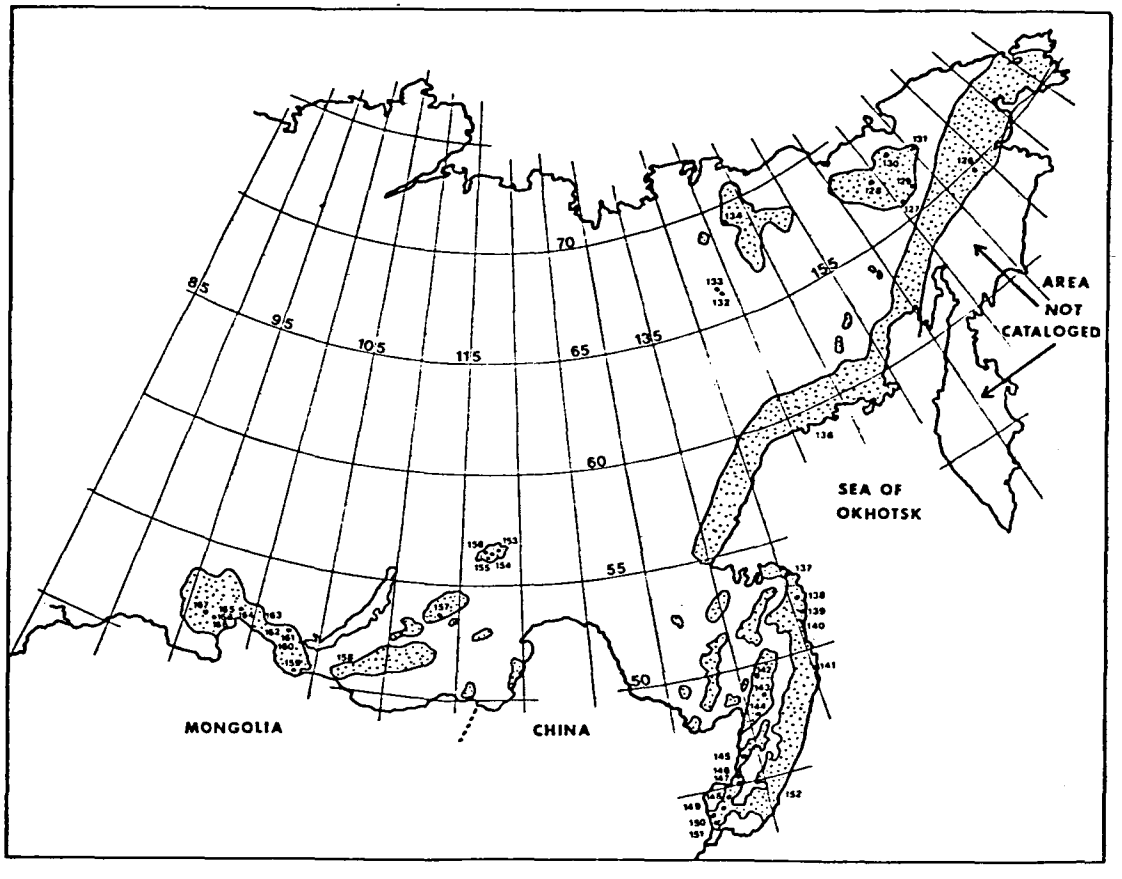


Figure 2: The distribution of Cenozoic basalts in northern Asia. Numbered localities are keyed to a forthcoming catalog. The respresentation of international boundaries is not necessarily authoritative.

# ILLUSTRATED GEOMORPHIC CLASSIFICATION OF ICELANDIC VOLCANOES

Richard S. Williams, Jr. and Elliot C. Morris, U.S. Geological Survey, Reston, Virginia 22092 and Flagstaff, Arizona 86001; and Sigurdur Thorarinsson, University of Iceland, 101 Reykjavík, Iceland

In 1959, Sigurdur Thorarinsson published his first complete classification of the 13 principal types of basaltic volcanoes of Iceland (Figure 1). In 1968, Thorarinsson published a modification of his earlier classification scheme. Both landform classifications were based on the relationship of the type of eruptive products (lava, lava and tephra, or tephra), number of eruptions (one or more than one), and the form of the eruptive vent (circular or linear). Aside from changing the type locality of one of the lava landforms (e.g., Trengslaborgir instead of Svörtuborgir), and deleting the lava fissure (e.g., Ögmundargjá) the two landforms classifications were very similar. Thorarinsson, in 1968, had, however, settled on 12 rather than 13 basic types of basaltic volcanoes of Iceland.

In 1980, Thorarinsson, working with Kristján Saemundsson, made a major modification to his initial classification scheme (Figure 2). The number of discrete basaltic volcano landforms were reduced to 11: the lava landforms have been reduced from 3 to 2, by transferring the lava crater (cone) row landform from the lava to the lava and tephra category; the stratified cone and stratified ridge have been deleted from the lava and tephra category; and two different types of crater row types are now represented in the lava and tephra category. In all three (1959, 1968, and 1980) classifications of the types of subaerial basaltic volcanoes of Iceland the five tephra landforms have remained the same. In the 1980 version the number of eruptions necessary to produce a given landform was also no longer considered to be a diagnostic characteristic and was dropped. The stratified (composite) cone or stratovolcano (Snaefellsjökull) and the stratified (composite) ridge (Hekla) landforms were also deleted from the 1980 classification scheme, because they are central volcanoes, being composed of basic, intermediate and acidic lavas and tephra.

In reviewing the three Icelandic basaltic volcano classification schemes (1959, 1968, and 1980) and from an extended discussion with Kristján Saemundsson in August 1981, a new classification of Icelandic volcanoes has been developed (Figure 3). The new classification scheme, still provisional, is based on the interrelationship of the following criteria: nature of the volcanic activity (effusive, mixed, or explosive); environment during formation (subaerial or subglacial (or submarine)); form of feeder channel (short fissure or tubular conduit or long fissure), and composition (basic, intermediate, or acidic). In addition, a volcano-like landform, the so-called pseudo-craters, is included as a separate category outside the classification scheme.

The ultimate objective of the research in developing a geomorphic classification of Icelandic volcanoes is to prepare a NASA Special Publication which will include vertical (stereopairs) and oblique aerial photographs, ground photographs, aerial thermographs, topographic and geologic maps, Landsat MSS and Landsat 3 RBV images, and Seasat SAR images, to properly illustrate each of the types of volcanoes, subaerial and subglacial (or submarine), found in Iceland. In combination with a supporting text the volume will be of special value to "students" of volcanic landforms on Earth, Mars, and Venus.

## References Cited


Thorarinsson, Sigurdur, 1959, The postglacial volcanism: III. in On the Geology and Geomorphology of Iceland (Thorarinsson, Sigurdur, ed.): Geografiska Annaler, v. 41, no. 2-3, p. 143-150.

Thorarinsson, Sigurdur, 1968, Iceland: Chapter 10 in A Geography of Norden, Sømme Axel, ed., J.W. Cappelens Forlag, Oslo, p. 204-234.

Thorarinsson, Sigurdur, and Saemundsson, Kristján, 1980, Volcanic activity in historical time; Chapter 3 in Geology of Iceland: Jökull, v. 29 (Special Issue), p. 29-32.


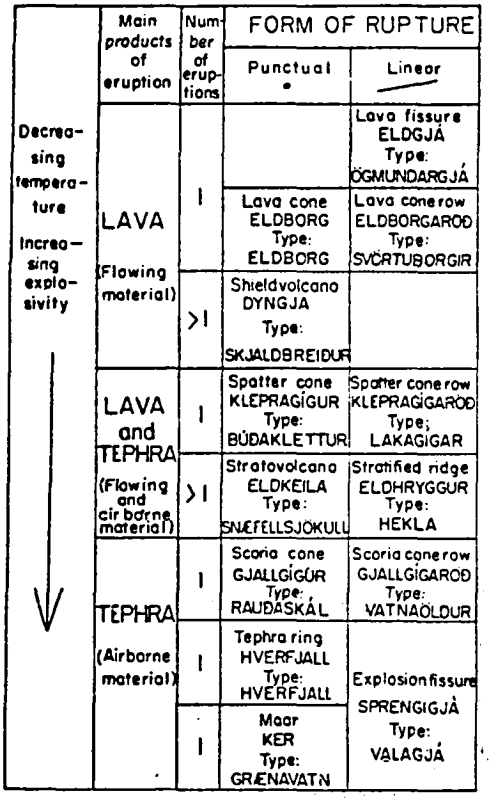


(From Thorarinsson, 1959, p. 145)

Figure 1. - The main types of Icelandic Volcanoes

Figure 2. - Types of Subaerial Basalt Volcanoes in Iceland

| Eruption products | | Form of feeder channel: Short fissure or tubular channel | Form of feeder channel: Long fissure | Addenda |
|---|---|---|---|---|
| Decreasing temperature; Increasing explosivity and production rate | Lava: Effusive activity | Lava ring Type: Eldborg near Krýsuvík | | Lava lake usual in crater |
| | | Lava shield Type: Skjaldbreidur | | The lava flows are mainly pahoehoe (Icel. *helluhraun*) |
| | Lava and tephra: Mixed activity | Agglutinate cone Type: Búrfell near Hafnarfjördur | Crater row Type: Threngslaborgir | The crater rows of mixed eruptions often develop craters of both types. The lava flows are mainly aa (Icel. *apalhraun*) |
| | | Scoria cone Type: Búdaklettur | Crater row Type: Vikraborgir | |
| | Tephra: Phreato-magmatic activity | Tephra cone Type: Raudaskál | Tephra cone row Type: Vatnaöldur | The volcanic activity is influenced by contact of magma with water |
| | | Tephra ring Type: Hverfjall | | |
| | | Maar Type: Grænavatn | Explosion chasm Type: Valagjá | |

(From Thorarinsson and Saemundsson, 1980, p. 31)

Figure 3. - Provisional Geomorphic Classification of Icelandic Volcanoes
(Modified from Thorarinsson, 1959 and 1968; and from Thorarinsson and Saemundsson, 1980)

INCREASING EXPLOSIVITY (DECREASING TEMPERATURE) ↓

**I - Icelandic Types of Basalt Volcanoes**

| NATURE OF VOLCANIC ACTIVITY | ENVIRONMENT DURING FORMATION | FORM OF FEEDER CONDUIT: SHORT FISSURE OR TUBULAR CONDUIT | FORM OF FEEDER CONDUIT: LONG FISSURE |
|---|---|---|---|
| EFFUSIVE ACTIVITY<br>Landforms resulting from flowing material | Subaerial | LAVA SHIELD<br>Type: Skjaldbreidur | LAVA SHIELD ROW<br>Type: Thjóðahraun |
| | Subglacial/ Subaerial | STAPI<br>Type: Herdubreid | SUBGLACIAL RIDGE<br>Type: Kálfstindar |
| | Submarine/ Subaerial | STAPI<br>Type: Surtsey | -- |
| | Submarine | SEAMOUNT<br>Type: Surtla | SUBMARINE RIDGE<br>Type: Eldeyjar |
| | Subaerial | LAVA RING<br>Type: Eldborg (Hnappadalssýsla) | -- |
| | Subglacial | * Type: Grettisbaeli | -- |
| MIXED ACTIVITY<br>Landforms resulting from flowing and/or airborne material | Subaerial | SPATTER CONE<br>Type: Búrfell (Hafnarfjördur) | SPATTER CONE ROW<br>Type: Threngslaborgir |
| | | SCORIA CONE<br>Type: Búdaklettur | SCORIA CONE ROW<br>Type: Vikraborgir |
| | | -- | MIXED CONE ROW<br>Type: Lakagigar |
| | Subglacial | * Type: Keilur | * Type: Fögrufjöll |
| EXPLOSIVE (OR PHREATO-MAGMATIC) ACTIVITY<br>Landforms resulting from airborne material | Subaerial | CINDER CONE<br>Type: Raudaskal | |
| | | TEPHRA RING<br>Type: Hverfjall | TEPHRA RING ROW<br>Type: Vatnaoldur |
| | | MAAR<br>Type: Graenavatn | MAAR ROW<br>Type: Valagjá |
| | Subglacial | * Type: Súlufell | * Type: Katlatjarnir |

**II - Volcano-Like Landforms (Basaltic) in Iceland**

| NATURE OF VOLCANIC ACTIVITY | ENVIRONMENT DURING FORMATION | NO FEEDER CONDUIT (Rootless "Volcano") |
|---|---|---|
| EFFUSIVE ACTIVITY | Subaerial (Saturated Soil) | PSEUDOCRATERS<br>Type: Skútustadir |

**III - Icelandic Types of Rhyolite Volcanoes**

| NATURE OF VOLCANIC ACTIVITY | ENVIRONMENT DURING FORMATION | FORM OF FEEDER CONDUIT: SHORT FISSURE OR TUBULAR CONDUIT | FORM OF FEEDER CONDUIT: LONG FISSURE |
|---|---|---|---|
| EFFUSIVE ACTIVITY | Subaerial | VOLCANIC DOME<br>Type: Hraunbunga | VOLCANIC DOMES<br>Type: Hrafntinnuhraun |
| | Subglacial | * Type: Sydri-Háganga | * Type: Hlíðarfjall |
| EXPLOSIVE ACTIVITY | Subaerial | MAAR<br>Type: Víti (Askja) | -- |

**IV - Icelandic Types of Central Volcanoes**
(Composition includes basic, intermediate, and acidic rock types)

| NATURE OF VOLCANIC ACTIVITY | ENVIRONMENT DURING FORMATION | MULTIPLE FEEDER CONDUITS AND FISSURES |
|---|---|---|
| MIXED ACTIVITY<br>Landforms resulting from flowing and airborne material | Subaerial/ Subglacial | COMPOSITE CONE<br>Stratified cone (stratovolcano) with summit crater<br>Type: Snaefellsjökull |
| | | COMPOSITE RIDGE<br>Elongated stratified cone with crestal fissure and crater(s)<br>Type: Hekla |
| | | COMPOSITE SHIELD VOLCANO<br>Contains a single (or multiple) caldera(s)<br>Type: Dyngjufjöll |

# THE GEOLOGY OF DYNGJUFJÖLL YTRI CRATER, NORTH CENTRAL ICELAND

Dean B. Eppler and Michael C. Malin, Department of Geology, Arizona State University, Tempe, AZ 85287.

Examination of aerial photography in preparation for the emplacement of eolian abrasion test sites in north central Iceland (Malin and Eppler, this volume) disclosed the existance of a small (∿ ½ km) crater-like form atop the palogonite ridge, Dyngjufjöll Ytri. Dyngjufjöll Ytri is west of Askja Caldera and is believed to have formed during the initial, subglacial eruptions of the Dyngjufjöll-Askja complex (Thorarinsson, 1958). The crater was noteworthy for its circularity, apparent raised rim, and subdued morphology (suggesting significant mantling by eolian debris). Owing to the crater's proximity to abrasion test site 1, we were able to investigate the geology of the crater during a three-day period in mid-August 1981. Our immediate goal was to determine, if possible, the mode of origin of the crater and to develop criteria by which the origins of similarly mantled craters (on Mars, for example) might be deciphered.

Owing to minimal topographic coverage, the crater was mapped using conventional brunton compass and tape measure techniques. Seven trasects gave profiles of the crater and established elevations for use in preparing a topographic map. Although reduction of these data is not complete, profiles indicated that the crater is an average of 26 m deep and ∿ 400 m wide along its east-west axis. A pronounced north-south asymmetry to the crater is most likely the result of infilling of sediments related to a northward dipping regional slope. Alternately, the asymmetry may reflect an initial asymmetry in form of the crater, enhanced by later infilling.

Rocks exposed in the crater have been grouped into three stratigraphic units; a lower palagonitic breccia (LPB); a basalt with abundant plagioclase phenocrysts (BPP), and an upper palagonitic breccia (UPB). The LPB is buff to tan, with rare clasts of rounded aphanitic basalt, lithologically dissimilar to the BPP, in its lowest exposures. The unit displays variable bedding, with cut-and-fill structures and abundant, fluvial crossbedding contrasting with more massive beds. The percentage of clasts increases upsection towards the BPP. The contact between the two units is marked by a baked zone ∿ 3.5 cm wide.

The BPP unit has euhedral, cm-sized plagioclase phenocrysts set in a fine-grained vesicular groundmass with microphenocrysts of olivine. Radial columnar jointing and lack of a baked zone along the contact with the UPB unit indicates BPP was extrusive rather than intrusive.

The UPB is lithologically distinct from LPB in its inclusion of abundant clasts of BPP. The unit is also highly variable with both massive and strongly crossbedded strata.

The crater appears to have formed by collapse rather than explosion. Sections of the northwest wall dip steeply into the crater (>40°) with stratigraphic order preserved. In some cases, the dip of beds within rotated blocks can be seen to change continuously from flat lying to steeply dipping, apparently indicating deformation occurred while the sediment was still soft. No planar, massive or surge beds such as described by Wohletz and Sheridan (1978) were observed radial to the crater

The interfingering of subaerial flows and palagonitic beds may indicate that the water level around the vent was fluctuating during eruption, allowing occasional subaerial eruptions in an otherwise subglacial or subaqueous eruption sequence. The cause of this fluctuation may be simply periodic retreat and resurgance of ice, or ice damming in the vicinity, forming temporary melt water lakes.

Our initial impression, gained from photo-interpretation, was that the crater was formed by explosive volcanism. This interpretation did not survive field evidence. Indeep, from the photographs alone, an impact origin might have been equally likely, had this crater been seen on Mars. Given our inability to recognize the origin of this crater by collapse (there being few diagnostic criteria for such phenomena at aircraft photo resolution), caution in interpretation of crater relationships on Mars and outer planet satellites, were devolatilization may lead to collapse, is clearly warrented.

References

Thorarinsson, S., 1958, The Orefajökull eruption of 1362: Acta Naturalia islandica, 2, 5-95.

Wohletz, K., and Sheridan, M., 1978, A model for pypoclastic surge: Geol Soc. Amer. Spec. paper 180, 177-195.

Cedar Butte - An Evolved Tholeiitic Volcano of the Eastern Snake River Plain, Idaho.

Michael A. Shelefka and John S. King, Department of Geological Sciences, State University of New York at Buffalo

Cedar Butte is a relatively small shield volcano located south of Arco, Idaho. It is approximately 10 km east of the rhyolitic dome known as Big Southern Butte which dominates the eastern Snake River Plain. Cedar Butte is a significant feature owing to the fact that it is composed of evolved tholeiites which are rare among the Snake River Group lavas of Pleistocene/Holocene age.

The petrologic relationships at Cedar Butte are complex but detailed mapping and sample analysis has demonstrated that the Cedar Butte construct originated from a seven phase fissure type eruption. Each phase is defined by an identifiable flow and a corresponding source area. The oldest flow is ferrobasalt and covered an area of about 6.4 square kilometers. The youngest flows are ferrolatites with the final eruptive event at the volcano being represented by a ferrolatite pyroclastic cone. Flow sequence is defined primarily on overlap and flow front relations. The location of Cedar Butte was a direct consequence of the intersection of the mid axis of the Eastern Snake River Plain with that of the Arco Rift Zone which trends approximately perpendicular to the mid axis. The Arco Rift Zone is sub-parallel to the Great Rift which is located 30-35 km to the west. Inasmuch as Basin and Range structure occurs both north and south of the Snake River Plain, it has been suggested that the rift zones are surface projections of Basin and Range bounding faults buried beneath the lavas of the Plain. Continuity of magnetic anomalies across the margins of the Plain reinforce this interpretation.

The composition range of the ruptive material at Cedar Butte is believed to have originated by fractional crystallization from an olivine tholeiite parent. Based both on field relations and geochemical data, rhyolite, which is found locally in intimate association with some of the mafic rocks of Cedar Butte, has been determined to be a remnant of an earlier rhyolitic episode which occurred in the region.

Inferno Chasm, A Construct on the Great Rift, Idaho

Harris Economou and John S. King, Department of Geological Sciences, State University of New York at Buffalo

Inferno Chasm is a volcanic construct associated with the Pleistocene-Holocene basaltic flows of the south central Snake River Plain. The Chasm is located in southeast Idaho approximately 50 km west of American Falls. Inferno Chasm, as well as several other vents, lie along Idaho's Great Rift System, an 80 km long extensional fracture zone which trends N 35 W (King, 1977). The alignment of these vents clearly shows that the rift zone is inherently associated with volcanism.

Field studies have indicated that early in its eruption Inferno Chasm was a low, broad shield volcano with slope angles of 2°-6°. This is typical of other shield volcanoes on the Snake River Plain. In the later stages of eruption, withdrawal of the magma occurred back into the main conduit leaving the central portion of the volcano unsupported. This in turn lead to a rapid inward collapse of the roof along radial lines of weakness. Fault scarps ringing the collapse zone indicate approximately 20 m of downward movement. The collapsed material was reincorporated into the partially molten crater floor.

Field studies have also indicated that Inferno Chasm's sinuous kilometer and a half long channel was formed by a single large outpouring of very fluid lava prior to collapse of the summit region. Furthermore these studies indicate that most of the lava vented at Inferno Chasm flowed westward through the channel. This suggests that the channel of Inferno as well as the regional land slope determined the general direction of lava flowage. However, some lava did flow in directions other than to the west. This occurred primarily prior to the formation of the channel and during periods of high volume lava extrusion when the transport capacity of the channel was exceeded. The levees bounding the channel attain a maximum height of approximately 30 m near the vent and progressively decline in height with increasing distance from the vent.

Several volcanic features similar to the Inferno Chasm channel have been located on the eastern Snake River Plain. Also similar volcanic constructs are known to exist on the Moon and Mars (Greeley and Schultz, 1977). Examination of Inferno Chasm's eruptive history and morphology will therefore aid in a clearer understanding of similar terrestrial and extraterrestrial volcanic processes.

King, J.S., 1977, Regional setting of the Snake River Plain Idaho, in Greeley and King, eds, Volcanism of the Eastern Snake River Plain, Idaho: A Comparative Planetary Guidebook, NASA, P. 45-58.

Greeley, R. and P. H. Schultz, 1977, Possible Planetary Analogs to Snake River Plain Basalt Features, In Greeley and King, eds, Volcanism of the Eastern Snake River Plain, Idaho: A Comparative Planetary Guidebook, NASA, p. 233-251.

# The Menan Complex, Eastern Snake River Plain, Idaho

Daniel Creighton and John S. King, Department of Geological Sciences,
State University of New York at Buffalo

Menan Buttes are part of a cluster of six volcanic vents aligned along a linear NNW trend and here defined as the Menan Complex. The Complex is located at the confluence of the Henry's Fork and Snake Rivers along the southern margin of the Eastern Snake River Plain, Idaho. Of the vents of this Complex, Menan Buttes are the two largest and most prominent. A smaller but less prominent feature is located between the Menan Buttes and is here defined as Center Butte. Island Butte (also here defined) is located about 2 km north of Menan Buttes on this linear trend and Twin Buttes are located to the south. All six constructs of the Menan Complex were formed through phreatomagmatic eruptions.

Menan Buttes are elliptical tuff cones composed primarily of basaltic material. The northern Butte is the largest of the two with long and short axes of 3.5 and 2.5 km respectively. It has maximum relief of 250 meters and its long axis, like that of the southern Butte, trends northeast. The two buttes exhibit greater accumulation of material to the northeast corresponding with the orientation of the long axes and this is believed to be due to the prevailing wind direction during eruption. Southern Menan Butte has axes of 3.0 and 2.0 km and 145 meters of relief. Both of the Menan Buttes rest on floodplain deposits of the Snake River.

Center Butte is similar to the Menan Buttes in composition but is much lower, with maximum relief of 20 meters. It is overlapped by both North and South Menan Buttes and appears to have been about the same diameter. The low height of this construct is due to a number of factors including erosion, style of eruption and volume of ejecta. The latter two factors are believed to have been of greatest significance.

Island Butte is a pyroclastic deposit defined by a single small (0.4 by 0.3 km) outcrop surrounded and almost completely buried by flow basalt. Maximum dimensions of this Butte cannot be accurately determined owing to burial but slight strike variation suggests a fairly large diameter body. The outcrop is composed of alternating beds of scoria and basaltic tuff. It is slightly concave to the east and the layers show a dip reversal suggesting that this outcrop marks the western rampart of Island Butte.

Twin Buttes are located 3 km from southern Menan Butte. They are arcuate remnants of two overlapping cones. Each is composed of significantly different proportions of scoria, basaltic tuff and fluvial sediments. Twin Buttes cover an area of approximately 1.0 by 0.5 km and have a maximum relief of 42 m above the surrounding Snake River floodplain.

The deposits of the Menan Complex are all believed to be of Pleistocene age. Center Butte is older than Menan Buttes as indicated by superposition. Age relations between Menan Buttes and Island Butte as well as Twin Buttes can only be subjectively stated. Hand specimen and outcrop appearance suggest that Island Butte is older than Menan Buttes. The more weathered appearance of the Island Butte tuff may be due to thermal interaction with the surrounding basalt rather than atmospheric weathering, however, leading to an erroneous conclusion. If hydrothermal effects from the basalt flow were minimal, Island Butte is probably

closer in age to Center Butte than to Menan Buttes. Twin Buttes are weathered to about the same degree as Menan Buttes.

Regional structural features of the area are NNW trending Basin and Range faults and NE trending faults associated with the mid axis of the Snake River Plain. The Rexburg Caldera Complex which encompasses the Menan Complex consists of several nested and overlapping calderas which were the source of significant rhyolitic volcanic deposits of Pliocene age. Statz and Albee (1966) described outcrops of these rhyolites in the Snake River Range, the Caribou Range and also in the Big Hole Mountains. Prostka and Embree (1978) cite control of caldera locations to be due to probable intersections of the regional fault systems. The orientation of the Menan Complex appears to be controlled primarily by Basin and Range trend and is independent of caldera structure. Evidence at Menan including abundant sanidine and some rhyolite xenoliths confirms the presence of caldera-related rhyolitic deposits in the subsurface.

Statz, M.H. and H.F. Albee, 1966, Geology of the Garns Mountain Quad, Bonneville, Madison and Teton Counties, Idaho: U.S.G.S. Bull, V. 1205, 122 p.

Prostka, H.J. and G.F. Embree, 1978, Geology and Geothermal Resources of the Rexburg Area, Eastern Idaho: U.S.G.S. Open File Report #78-1009, 14 p.

# Chapter 5

# AEOLIAN PROCESSES AND LANDFORMS

## SURFACE ROUGHNESS EFFECTS ON AEOLIAN PROCESSES: WIND TUNNEL EXPERIMENTS

*L.M. Reding, S. Williams, R. Leach, B.R. White, and R. Greeley, NASA-Ames Research Center Aeolian Consortium, Moffett Field, California 94035*

The presence of non-erodible surface roughness elements (pebbles, boulders, etc.) versus a smooth surface has a pronounced effect on several aeolian parameters, including threshold conditions and particle flux. Although some data for rough surfaces are available (Chepil, 1945), most experimental data for Mars involved smooth surfaces (Greeley et al., 1977). In order to obtain appropriate experimental data and to check theoretical models for Mars (e.g. Pollack, 1979), an investigation has been initiated in which threshold, flux, and boundary layer profiles are measured in the wind tunnel for a rough surface. The results presented here concern the first stage of the study and involve experiments conducted at one atmosphere surface pressure.

Pebbles 1 cm in diameter, spaced 1 cm apart were glued to the wind tunnel floor to produce a 'rough' surface. Boundary layer surveys were then made to obtain velocity profiles, both with and without erodible sand present. The boundary layer profiles were used to determine friction velocity ratios, $V_*/V_\infty$. This value was determined for various roughness heights and was found to increase as roughness increased. The straight log-height versus velocity plot confirmed the assumption inferred from the velocity profile that the boundary layer was turbulent. Next, wind friction threshold speeds, $V_{*t}$ were determined for 350 $\mu$m and 95 $\mu$m sand beds. The beds were superimposed over the pebble surface and $V_{*t}$ values were determined for various heights of the bed as it was allowed to erode. $V_{*t}$ was found to increase with increasing surface roughness (Fig. 1). Values for $V_{*t}$ where the roughness height was zero, and $V_{*t}$ determined for the smooth wind tunnel surface revealed similar values. Finally, particle flux, q (gm/cm$^2$/sec), as a function of height above the pebble base, and total flux, Q (gm/cm/sec), were determined for both sand sizes. The sand beds were 7.5 mm thick; q decreased with height; and Q increased with free-stream velocity, $V_\infty$. Interpolating both sets of data showed Q for the smooth surface to be slightly less than Q for the rough surface.

The results obtained in the rough surface wind tunnel may be applied to geologic cases on both Earth and Mars. Understanding the effects of wind on various sand surfaces enables prediction and control of sand movement, rates of erosion, ripple formation and migration and other aeolian related processes.

### Acknowledgement

This work was carried out during tenure on a Planetary Geology Program summer internship by LMR at NASA-Ames Research Center, 1981.

### REFERENCES

*W.S. Chepil, 1945. Dynamics of Wind Erosion: I. Nature of Movement of Soil by Wind, Soil Science 60, 305-320.*

*R. Greeley, B.R. White, J.B. Pollack, J.D. Iversen, and R.N. Leach, 1977. Dust Storms on Mars: Considerations and Simulations, NASA TM 78425, 29 p.*

*J.B. Pollack, 1979. Climatic Change on the Terrestrial Planets, Icarus, 37, 479-553.*

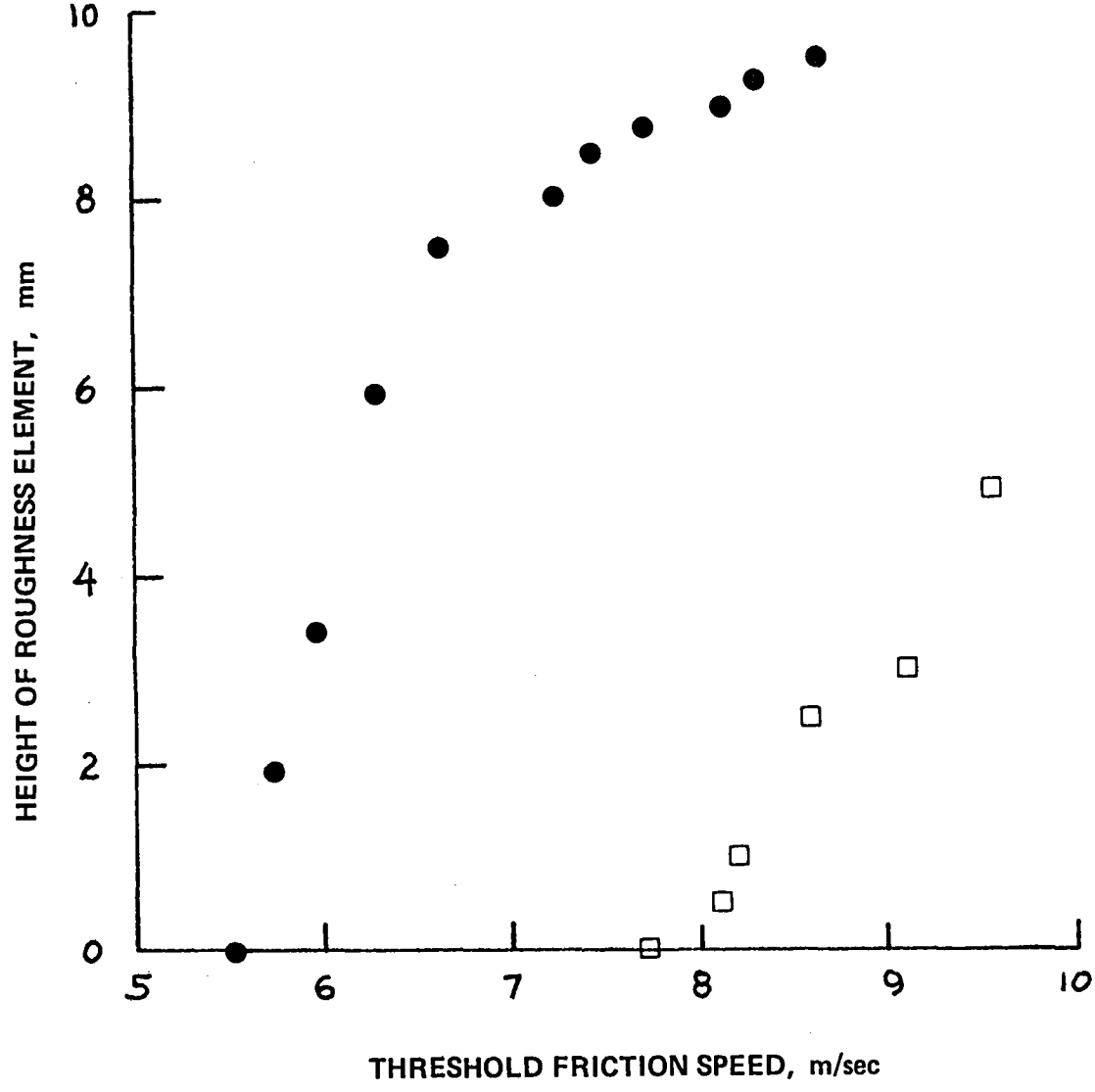


*FIGURE 1. Threshold friction speed as a function of surface roughness. 95 μm (solid circles) and 350 μm (open squares) sand sizes used.*

# FORMATION AND EVOLUTION OF PLAYA VENTIFACTS, AMBOY, CALIFORNIA

*S. Williams, Department of Physics, University of Santa Clara at NASA-Ames Research Center, Moffett Field, California 94035, R. Greeley, Department of Geology, Arizona State University, Tempe, Arizona 85287*

Drifts observed at the Viking Lander 1 site have been described as deposits of cohesive sediments that have been sculpted by the wind (Binder et al., 1977). In addition, many parts of Mars are mantled by deposits speculated to be of aeolian, fluvial, or volcanic origin. In some places, these deposits are currently being stripped away, presumably by wind erosion. Both mantling deposits observed from orbit and drifts seen at the landing sites appear to involve fine grained sediments of various degrees of induration; however, little is known about the mode(s) or rate(s) of erosion.

A possible analog to the stripping of these fine grained martian deposits occurs in the Mojave Desert at Amboy, California, where a playa deposit is currently being stripped by the wind. The deposit consists of approximately 25 cm of thinly bedded silts and clays overlying a lag gravel surface. Air photo analysis indicates that the playa was in the process of formation in late 1954, which provides an upper limit for the age of the deposits and, hence, a lower limit for the rate of erosion.

Observations of the playa and the evolution of the stripping were initiated in 1979. The stripping action of the wind sculpts the playa material into faceted mounds and ridges, which have a morphologic similarity to ventifacts. Sequential photographs (Fig. 1) and measurements of ventifact face retreat enable the stages of erosion to be determined; coupled with concurrent measurements of wind velocity, it is also possible to obtain rates of erosion. Erosion of playa material accurs in three modes: 1) lowering of the horizontal surface, 2) erosion related to 'micro' topographic features such as desiccation cracks, and 3) scarp retreat, which involves both erosional faceting and undercutting.

Because the deposit is only slightly indurated it is easily and rapidly eroded. For example, a single wind storm in the summer of 1981 resulted in scarp retreat in excess of 10 cm in some locations. Although data are limited at present, a maximum estimated erosion rate for that storm is 5 cm/hr for a storm of 3 hours duration and peak winds of 20 m/sec.

Continuing field studies will enable additional rates of abrasion to be obtained and a more refined model of playa ventifact evolution. These results will enable calibration of laboratory simulations for applications to studies of aeolian processes on Mars and Venus.

## REFERENCE

*A.B. Binder et al., 1977. J. Geophys. Res. 82, 4439-4451.*

*FIGURE 1a. Sequential photographs of a playa ventifact over a period of approximately 15 months. Image taken 10 May 1980.*

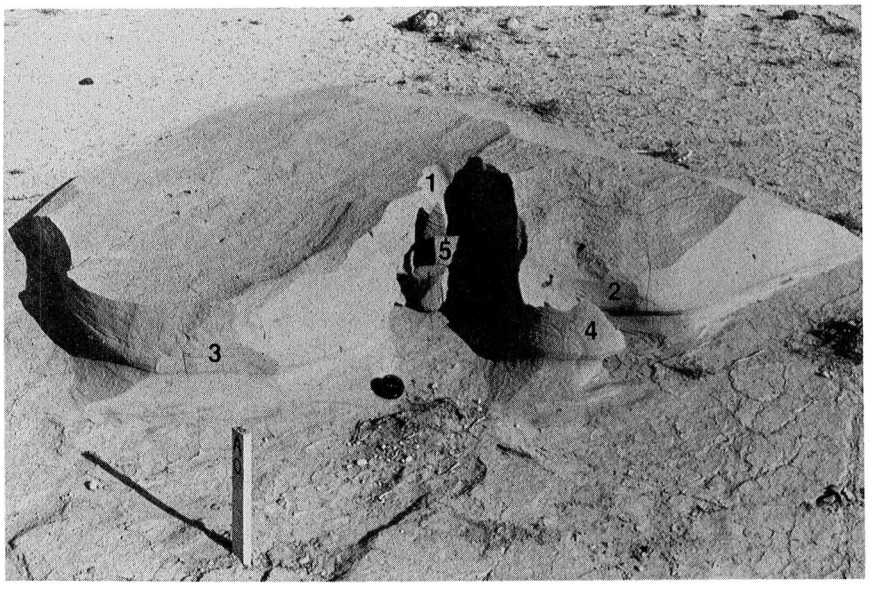


*FIGURE 1b. Sequential photographs of a playa ventifact over a period of approximately 15 months. Image taken 26 April 1981 showing erosion of grooves (1, 2), faceting of upwind face (3), erosion of a 'peninsula' (4), and undercutting and slumping within the large groove (5); 50 mm lens cap indicates scale.*

*FIGURE 1c. Sequential photographs of a playa ventifact over a period of approximately 15 months. Image taken 30 August 1981 showing joining of grooves and the complete removal of the 'peninsula'. Erosion occurring between b and c resulted principally from one wind storm. During this period there was no rain.*

## VENUSIAN SURFACE WIND TUNNEL

*R. Greeley, Department of Geology, Arizona State University, Tempe, Arizona 85287, J. Iversen, Department of Aerospace Engineering, Iowa State University, Ames, Iowa 50010, B. White, Department of Mechanical Engineering, University of California at Davis, Davis, California 95616, R. Leach and S. Williams, Department of Physics, University of Santa Clara at NASA-Ames Research Center, Moffett Field, California 94035*

A wind tunnel capable of simulating the aeolian environment on Venus has been installed at NASA-Ames Research Center as part of the Aeolian Consortium. The tunnel is currently undergoing dynamic testing, instrumentation, and calibration, and is expected to be operational to begin initial experiments in fiscal year, 1982. The facility consists of a closed-circuit wind tunnel approximately 6 m long by 3 m wide; the experimental test section is about 700 cm long by 20 cm in diameter. The wind tunnel is housed in the same chamber as the Martian Surface Wind Tunnel, and is operated through the same control room. The working fluid in the tunnel is carbon dioxide; for venusian simulations, the tunnel will operate at 35 bar pressure, which at ambient temperature produces the same fluid density (the critical parameter for most aeolian processes) for carbon dioxide as at 90 bar and 735 K, the nominal venusian environment. The wind tunnel will be used primarily for conducting particle threshold experiments, studying ripple dynamics, and determining particle fluxes and velocities.

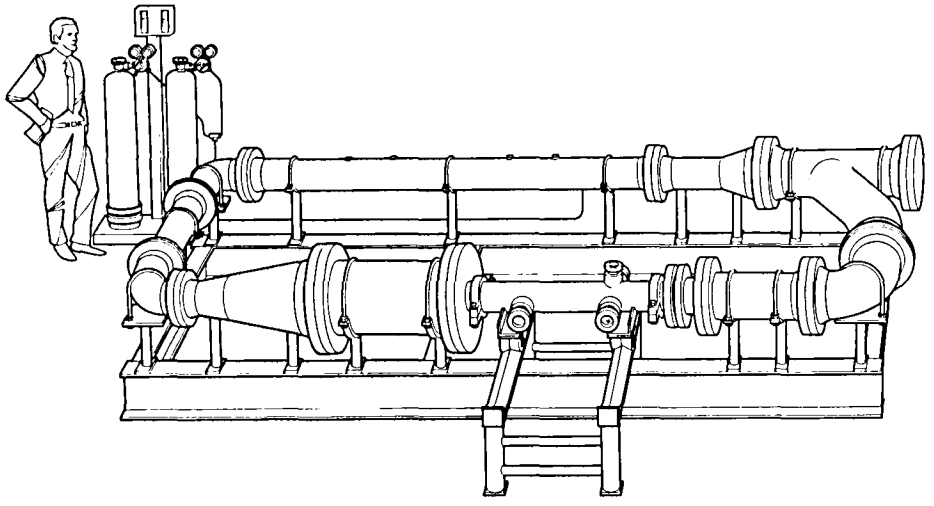

*FIGURE 1. Diagram of the Venusian Surface Wind Tunnel at NASA-Ames Research Center, Moffett Field, California.*

## SOIL TRANSPORT BY WINDS ON VENUS

*B.R. White, Department of Mechanical Engineering, University of California, Davis, California 95616,*
*R. Greeley, Department of Geology, Arizona State University, Tempe, Arizona 85287*

The rate of movement of surface material under a specified surface wind condition is of paramount interest for Venus. An estimate of the total amount of surface material transported by the wind may be made by examining the physics of the process. The force balance analysis on a control volume presented by White (1979) yields the material flux q, units of gm/[cm·s], as

$$q = \frac{C}{g} \rho (V_* - V_{*t}) (V_* + V_{*t})^2 \qquad (1)$$

where C is the constant of proportionality. Wind-tunnel experiments (White, 1979) have shown C to be a constant equal 2.61 for saltation processes at low pressures corresponding to martian surface pressures and at terrestrial atmospheric pressures. The physics of saltation on Venus would be expected to be the same as on Earth, as is the case on Mars. Hence, C = 2.61 in Equation (1) seems valid for estimating mass transport rates on Venus by saltation. A major problem of applying this equation to saltation on Venus is in knowing $V_{*t}$. The values of $V_{*t}$ will most likely have to be experimentally measured in a high-pressure wind tunnel. However, there is an analytical expression presented in Iversen and White, 1981, which uses variable pressure measurements to estimate threshold friction speeds for Venus. According to Iversen and White, the ratio of $V_{*t}$ between Earth and Venus is almost a constant value of 8.5 over a wide range of particle diameters from 0.1 to 1 mm, e.g.,

$$\frac{V_{*t_E}}{V_{*t_V}} = 8.5; \quad (\text{for } 0.1 \text{ mm} \leq D_p \leq 1 \text{ mm}) \qquad (2)$$

where the subscripts E and V represent the terrestrial and venusian cases, respectively.

A comparison of the rate of movement of surface material occurring during saltation may be made using Equation (1), which is,

$$\frac{q_1}{q_2} = \frac{\rho_1}{\rho_2} \frac{(V_* - V_{*t})_1 (V_* + V_{*t})_1^2 g_2}{(V_* - V_{*t})_2 (V_* + V_{*t})_2^2 g_1} \qquad (3)$$

where the subscripts 1 and 2 represent two different planets. Assuming a dynamically similar saltation between the planets, that is, the ratio of friction speed to threshold friction speed $V_*/V_{*t}$ is the same for both planets, yields

$$\frac{q_1}{q_2} = \frac{\rho_1 g_2}{\rho_2 g_1} \frac{V_{*t\,1}^3}{V_{*t\,2}^3} \qquad (4)$$

Now, using Equation (1) for the ratio of $(V_{*t})_E/(V_{*t})_V$ Equation (4) will produce an estimate of the ratio of q's between Earth and Venus for dynamically similar conditions, which is for 85 bar surface pressure and 700 K surface temperature on Venus,

$$\frac{q_E}{q_V} = \frac{1}{53.5}(0.894)(8.5)^3 = 10.3 \qquad (5)$$

for particle diameters from 0.1 mm to 1 mm. Hence, for wind speeds the same percentage above threshold on each planet, e.g., each 20 percent above their own respective saltation threshold friction speed, approximately ten times more material would be moved on Earth than on Venus. This result is due to the small trajectories of saltating venusian particles which

is in turn a result of the extremely dense atmosphere. A similar comparison (White, 1979) made between q's for Earth and Mars yields

$$\frac{q_E}{q_M} = 0.04 \qquad (6)$$

or

$$\frac{q_M}{q_V} = 250 \qquad (7)$$

for particle diameters from 0.1 mm to 1 mm.

**REFERENCES**

*J.D. Iversen and B.R. White, 1981. Saltation threshold on Earth, Mars and Venus, submitted to Sedimentology.*

*B.R. White, 1979. Soil transport by winds on Mars, Journal of Geophysical Research, 84, 4643-4651.*

# A METHOD FOR MODELING OF SMALL PARTICLE TRANSPORT

*J. Iversen, Department of Aerospace Engineering, Iowa State University, Ames, Iowa 50010, R. Greeley, Department of Geology, Arizona State University, Tempe, Arizona 85287, J. Pollack, NASA-Ames Research Center, Moffett Field, California 94035*

The atmospheric boundary layer wind tunnel has for some years been a useful engineering and scientific tool for studying, on a small scale, the effects of surface winds on natural topography and on man-made objects as well (Jensen, 1958; Cermak, 1971). More recently the boundary layer type of wind tunnel has been proven to be useful for studying the phenomenon of saltation of loose particulate material (Iversen et al., 1973, 1976a, 1976b, 1981a, Greeley et al., 1974a, 1976, 1980) and for modeling the topographic effects of saltating material at small scale (Iversen et al., 1973, 1975, 1976c, 1981b, 1981c, Greeley et al., 1974a, 1974b, Veverka et al., 1976, Howard et al., 1977). All of these investigations deal, for the most part, with sand-sized particles (62 to 2000 $\mu$m). It is evident, however, that particles of smaller size are very important in martian (and probably venusian) surface and atmospheric processes (Pollack et al., 1976, 1977) and that is the primary subject of the investigation.

A project involving the small scale simulation of dust transport was begun by one of the principal investigators (Iversen) in Denmark in January, 1981 (Jensen and Bjerregaard, 1981). This project involved the control of transport of dust from coal stockpiles at Danish power plants. The techniques perfected in this program can prove to be useful in the simulation of dust transport on Mars. The simulated particle materials ranged in particle diameter from 15 to 70 microns. A significant difference exists in particle transport for dust ($<$ 80 micron) and for sand ($>$ 80 microns). The dust particles travel primarily in suspension, carried mostly by turbulent fluctuations, whereas later particles are unaffected by turbulence and transport is mainly by saltation. The dust particles traverse irregular paths to great heights above the surface compared to sand particles, which have much lower, smoother trajectories. The differences in resulting drift formations, surface-bedform features, and topographic effects between blown sand and blown dust are enormous, but not much attention has been paid thus far to simulation of blown dust, primarily because of experimental difficulties.

Several experimental techniques have been evolved through the Danish coal dust research program. New methods of instrumentation technique were developed including (1) surface sampling, (2) isokinetic sampling, (3) surface visualization, and (4) topographic modeling. These techniques will be applied to planetary problems. For example, wind speeds in both the beginning and ending phases of Martian dust storms can be simulated. The beginning of the dust storm is simulated by prior distribution of dust on model surfaces. The ending of the storm is simulated by introducing material from above and upstream of the model at wind speeds below the threshold value. The former technique has been employed thus far only with sand-sized particles and the latter technique has not been employed at all except for terrestrial problems involving drifting snow (Iversen, 1981).

Two wind tunnels are available for dust simulations. The boundary layer wind tunnel at Iowa State University is 1.2 m by 1.2 m in cross-section with a maximum speed of 20 m/s. The low-air-density wind tunnel (MARSWIT) at NASA is approximately the same size, but the atmospheric pressure can be lowered to Mars values.

## REFERENCES

*J.E. Cermak (1975). Applications of Fluid Mechanics to Wind Engineering. A Freeman Scholar Lecture, Fluids Eng. 97:9-38.*

*R. Greeley, J.D. Iversen, J.B. Pollack, Nancy Udovich, B.R. White, 1974a. Wind Tunnel Studies of Martian Aeolian Processes, Proceedings, Royal Society of London, Series A, 341,331-360.*

*R. Greeley, J.D. Iversen, J.B. Pollack, Nancy Udovich, B.R. White, 1974b. Wind Tunnel Simulations of Light and Dark Streaks on Mars, Science, 183, 847-849.*

*R. Greeley, B. White, R. Leach, J. Iversen, and J. Pollack, 1975. Mars: Wind Friction Speeds for Particle Movement, Geophys. Res. Lett. Vol 3, No. 8, pp. 417-420.*

*R. Greeley, R. Leach, B. White, J.D. Iversen, J. Pollack, 1980. Threshold Wind-Speeds for Sand on Mars: Wind Tunnel Simulations, Geophy. Res. Lett. Vol 7, 121-124.*

*A.D. Howard, J.B. Morton, M. Gad-el-Hak, and D.B. Pierce, 1977. Simulation Model of Erosion and Deposition on a Barchan Dune: NASA CR-2838, 77 p.*

*J.D. Iversen, R. Greeley, J.B. Pollack, and B.R. White, 1973. Simulation of Martian Eolian Phenomena in the Atmospheric Wind Tunnel, Space Simulation, NASA Special Publication 336:191-213.*

*J.D. Iversen, R. Greeley, B.R. White, and J.B. Pollack, 1975. Eolian Erosion on the Martian Surface, part 1, Erosion Rate Similitude, Icarus 26:321-331.*

*J.D. Iversen, J.B. Pollack, R. Greeley, and B.R. White, 1976a. Saltation Threshold on Mars; The Effect of Interparticle Force, Surface Roughness, and Low Atmospheric Density, Icarus 29:381-393.*

*J.D. Iversen, R. Greeley, and J.B. Pollack, 1976b. Windblown dust on Earth, Mars, and Venus, J. Atmos. Sci. 33:2425-2429.*

*J.D. Iversen, R. Greeley, B.R. White, and J.B. Pollack, 1976c. The Effect of Vertical Distortion in the Modeling of Sedimentation Phenomena: Martian Crater Wake Streaks, J. Geophys. Res. 81:4846-4856.*

*J.D. Iversen, B.R. White, 1981a. Saltation Threshold on Earth, Mars, and Venus, in press, Sedimentology.*

*J.D. Iversen, 1981b. Drifting Snow Similitude-Transport Rate and Roughness Modeling, in press, Journal of Glaciology.*

*J.D. Iversen, 1981c. Comparison of Wind Tunnel Model and Full-Scale Drifts, in press, Journal of Industrial Aerodynamics.*

*M. Jensen, 1958. The Model-Law for Phenomena in Natural Wind. Ingeniφren 2:121-128.*

*V. Jensen and E. Bjerregaard, 1981. Modelforsφg over kulpartiklers fygning (Model Experiment of Coal Particle Drifting), unpublished project description.*

*J.B. Pollack, R. Haberle, J.D. Iversen, and R. Greeley, 1976. Estimates of the Minimum Wind Needed to Raise Dust on Mars, Icarus, 29, 395-417, 1976.*

*J.B. Pollack, D. Colburn, R. Kohn, J. Hunger, W. Van Camp, C.E. Carlston, and M.R. Wolfe, 1977. Properties of Aerosols in the Martian Atmosphere, as Inferred from Viking Lander Imaging data, Journal of Geophysical Research, 82, 4479 ff.*

*J. Veverka, C. Sagan, and R. Greeley, 1976. An Unusual Crater-Streak in Mesogaea, Icarus, Vol 27, pp. 241-253.*

# MARTIAN SEDIMENTS: EVIDENCE FOR SAND ON MARS

*A.R. Peterfreund, R. Greeley, and D. Krinsley, Department of Geology, Arizona State University, Tempe, Arizona 85287*

The nature of sediments on planetary surfaces provides important information on the processes that generate, transport, deposit, and destroy those sediments. On Earth, processes involving water dominate the sedimentary cycle. On the Moon, sedimentation is mostly the result of comminution due to meteoroid impacts. On Mars, sedimentation is currently dominated by aeolian processes; however, past sedimentation has also resulted from cratering, fluvial processes, periglacial phenomena, and volcanism. The types of sediments produced and the resultant landforms vary with each process. Thus, on Mars, a complex pattern of sedimentary activity is closely associated with the geologic history of the planet. What we see today is an ongoing modification by wind of the products of earlier processes. This review addresses the particular question of sand as related to the sedimentary history of Mars.

**Is there sand on Mars?** Although the answer to this question appears to be obvious, the presence of sand (particles 60 to 2000 $\mu$m diameter) and its physical and textural properties remain uncertain. Arguments against the widespread presence of sand include: 1) the relative absence of particles smaller than 100 $\mu$m diameter at the two Viking lander sites (1,2); 2) an apparent lack of quartz, the primary composition of terrestrial sand, on Mars (3); 3) aeolian models that suggest the self-destruction of saltating particles, or the 'kamakaze' effect (4); and 4) estimates based on laboratory simulations that abrasion by windblown sand would be exceedingly high (10-100 m/$10^6$ yr) (5). On the other hand, arguments for the widespread occurrence of sand are compelling. Martian dunes occur in a wide variety of geologic environments, but volumetrically are limited to a small number of areas (table 1). Terrestrially, dunes form by saltation of fine sand (125 to 250 $\mu$m); on Mars, there should be no substantial difference to this process (6). Observations of possibly active dunes (7) also strengthen the argument for sand, as saltation is required for dune migration. Viking Infrared Thermal Mapper (IRTM) observations also suggest the widespread presence of sand-sized particles based on estimates of thermal inertia which is sensitive to mean particle size. Low thermal inertia and high albedo regions are interpreted as mantled by silt-or smaller-sized particles (8) and account for less than 20% of the surface between +60° and -60° latitude. Most of the surface is dark and contains presumably coarser sediments than the mantled regions. A comparison of the IRTM data with photogeologic results shows that most wind streaks and dunes occur in regions that have thermal inertia values consistent with medium to fine sand-sized sediments (9). Evidence of sand on Mars can also be deduced from observations of recurrent aeolian activity (i.e., the presence of dust storms and the variability of surface albedo patterns). Experimental studies of particle motion in the martian aeolian environment show that the particle size most easily moved is fine sand ($\sim$ 100 $\mu$m) (10). These particles move by saltation and eject dust into suspension. Initiating particle motion without the presence of saltating sand requires extremely high wind speeds (e.g., for a bed of 10 $\mu$m particle threshold velocity would be $\sim$ 250 m/s) or an unusual mechanism such as dust injection (11). In fact, the regions of variable features and dust storm initiation contain sand-related landforms and thermal inertias consistent with sand.

Sand is likely to be common on Mars because of the wide range of geologic processes which can generate unconsolidated sediments. These processes are currently dominated by aeolian action; however, presumably past sand generation has occurred by cratering, fluvial processes, periglacial phenomena, mass-wasting, chemical and mechanical weathering and volcanism.

The total amount of sand in segmented aeolian deposits on Mars, however, appears to be an order of magnitude less than on the land area of the Earth. On Mars, dune fields account for 0.5% of the surface area; on Earth 4.4% of the land is covered by ergs (based on ergs > 12,000 $km^2$; (12)). A factor of 2 error is possible in this calculation, based on Viking imaging resolution and coverage.

**What types of sands are on Mars?** Sand is the product of a wide range of processes on Earth, and therefore is compositionally varied. However, the only sand-sized particles that survive for substantial geologic time are composed of quartz. This is due to both the abundance of large quartz grains derived from plutonic rocks, and the physical properties of quartz, particularly its hardness and resistance to chemical weathering. On the Moon, agglutinates, which are glass-bound comminuted rock, mineral and glass fragments, are the dominant sand-sized materials present in the soil (13, 14). Although attempts were made to collect crystalline sand-size particles at the two Viking Lander sites, all that were collected were aggregates of very fine particles (15). These aggregates are either electrostatically or chemically bound. Arguments for their occurrence have been made based on laboratory simulations (16, 17) which show that sand-sized particles abrade rapidly under martian conditions forming silt- and clay-sized particles which in turn become electrostatically-bound sand-sized aggregates. The survival of these particles in a saltating regime and their ability to form aeolian deposits remains a problem.

The evidence for crystalline sands on Mars can only be inferred from photogeologic studies and remote sensing investigations. The mechanisms for producing sand grains can be divided into two categories, primary and secondary. *Primary processes,* which introduce rock fragments, glass or minerals upon the surface, are meteoritic impact, explosive and effusive volcanism, tectonism, and weathering. The degree to which these processes have been active on Mars has declined with geologic time. *Secondary processes* are those that remobilize sediments and include: cratering, fluvial and periglacial processes, mass-wasting, weathering and aeolian abrasion. Unconsolidated sediments observed on Mars are the result of these secondary processes. Yardangs, which are erosional aeolian landforms that usually form in friable or indurated sedimentary deposits, are relatively common features in the equatorial region of Mars, particularly in regions proximal to large volcanoes. This suggests ignimbrites or lahars as possible source material (18). Many wind streaks, particularly splotch-related streaks, are also evidence of reworked deposits as they are often associated with intracrater deposits (9, 19). It appears that much of the sand on Mars consists of reworked sedimentary deposits and, as such, is compositionally as varied as in the primary processes of emplacement.

Remote sensing observations of sediments on Mars show a variety of characteristics indicative of composition. Earth-based near-infrared spectra indicate that a variety of sediment types must occur on Mars, ranging from what appear to be relatively unoxidized basalt fragments in some dark areas, such as Syrtis Major, to high desiccated mineral hydrates in bright areas such as the Arabia region (20). Correlations of IRTM data and orbiter color with photogeologic studies also suggest a wide range of sediment types on Mars (8).

In summary, sand grains on Mars are polygenetic and have a wide range of compositions and physical properties. While it has been shown that sand is an important element in regions of recurrent aeolian activity, the total abundance of free sand on the surface may be significantly less than on the land surface of the Earth. This implies either; 1) less sand is produced on Mars, 2) survivability of sand is low due to particle comminution, and/or 3) sand is 'trapped' beneath a surface crust. A combination of these factors appears likely.

## REFERENCES


1. *T.A. Mutch, 1976. Science 194, 87-91.*
2. *H.J. Moore, 1977. J. Geophys. Res. 82, 4497-4523.*
3. *I.J. Smalley and D.H. Krinsley, 1979. Icarus 40, 276-288.*
4. *C. Sagan et al., 1977. J. Geophys. Res. 82, 4430-4438.*
5. *S.H. Williams and R. Greeley, 1980. Lunar and Planet. Sci. XI, 1254-1256.*
6. *J.A. Cutts and R.S.U. Smith, 1973. J. Geophys. Res. 78, 4138-4154.*
7. *H. Tsoar et al., 1979. J. Geophys. Res. 84, 8167-8180.*
8. *H.H. Kieffer et al., 1977. J. Geophys. Res. 82, 4249-4291.*
9. *A.R. Peterfreund, 1981. Icarus 45, 447-467.*
10. *R. Greeley, 1980. Geophys. Res. Lett. 7, 121-124.*
11. *R. Greeley and R. Leach, 1979. NASA TM 80339, 304-307.*
12. *I.G. Wilson, 1973. Sed. Geol. 10, 77-106.*
13. *M.B. Duke et al., 1970. Proc. Apollo 11 Lunar Sci. Conf., 347-361.*
14. *J.F. Lindsay, 1976. Lunar Stratigraphy and Sedimentology, Elsevier, N.Y., 302 pp.*
15. *H.J. Moore et al., 1979. J. Geophys. Res. 84, 8365-8377.*
16. *R. Greeley, 1979. J. Geophys. Res. 84, 6248-6254.*
17. *D.H. Krinsley and R. Leach, 1981. Precam. Res. 14, 167-178.*
18. *A.W. Ward, 1979. J. Geophys. Res. 84, 8147-8166.*
19. *P. Thomas and J. Veverka, 1979. J. Geophys. Res. 84, 8131-8146.*
20. *R.B. Singer et al., 1979. J. Geophys. Res. 84, 8415-8426.*



*This work is supported by the NASA Planetary Geology Office, Mars Data Analysis Program, through Grants NSG-7548 and NAGW-24 to Arizona State University.*


TABLE 1. Martian Dune Regions

| | |
|---|---|
| North Pole (77 - 83°, 110 - 220°W) | ≅ 700,000 $km^2$ |
| South Pole (-70 - -60°, 165 - 220°W) | ≅ 25,000 $km^2$ |
| Argyre (-55 - -45°, 45 - 60°W) | ≅ 5,000 $km^2$ |
| Noaches (-60 - -45°, 325 - 350°W) | ≅ 5,000 $km^2$ |
| Minor Fields | area < 1,000 $km^2$ |

| | |
|---|---|
| Claritas Fossae | Syrtis Major Planitia |
| Syria Planum | Tempe Fossae |
| Solis Planum | Ares Vallis |
| Gangis Chasma | Lyot Crater |
| Hellas | NW of Hecates |
| NW Hesperia | Olympus Mons Aureole NW |
| Memnonia | |
| Sirenum | |

# AN EXPERIMENTAL STUDY OF THE BEHAVIOUR OF ELECTROSTATICALLY-CHARGED FINE PARTICLES IN ATMOSPHERIC SUSPENSION

Marshall, J.R., Krinsley, D. & Greeley, R., Department of Geology, Arizona State University, Tempe, Arizona 85287.

Greeley (1979) proposes that the precipitation of aeolian dust from the martian atmosphere may occur by the electrostatic agglomeration of silt/clay-size particles into sand-size aggregates. The experiments reported here were conducted to test this hypothesis.

Electrostatically-charged fine particulate (silt/clay-size) material was generated in a paddle-wheel device (described by Krinsley et al, 1979) from crushed basalt of sand size. Particle charging is a 'natural' product of the highly energetic comminution process and has therefore been postulated as being characteristic of martian aeolian material; the same device was employed by Greeley (1979) to produce aggregate material. Microscopic examination of the material showed it to consist of irregularly-defined electrostatic aggregates ranging in size from a few tens of microns to several thousand microns. Aggregates displayed a distinct tendency to form spheroidal clumps.

Approximately 200 grams of this aggregate material was placed at the base of a 1.5 m high, 0.1 m diameter glass column (Fig.1), then subjected to a momentary pulse of compressed air from a small (3 mm bore) nozzle (buried in the material) and allowed to settle out through the height of the column. The bulk of the material fell immediately to the base of the column upon cessation of the mobilizing air pulse. Silt-size particles blown into suspension were then observed to settle-out slowly over a period of something less than 30 seconds to leave what at first appeared to be a relatively stable, dense suspension of extremely fine material buoyed to some extent by residual air currents in the column. This fine suspension persisted only for a few seconds, however, before the sudden appearance of large, rapidly-falling aggregates of material. The aggregates were not of the spheroidal variety that composed the original material, but occurred as long threads and irregularly-shaped flakes (Fig.2). The largest of both the flakes and the threads were estimated to be between 5 and 10 mm in length. The threads fell with their long axes oriented in the direction of movement and each appeared to be pulled down by the weight of a small lump of material at one end (Fig.2).

Aggregation of particles was almost certainly an electrostatic process but aggregate growth could not be directly observed owing to the adherence of much of the fine material to the sides of the glass column. It is postulated, however, that the threads grew as tails behind falling lumps of material. Threads were also observed to grow in great profusion from plastic components within the apparatus and formed brush-like masses very similar in appearance to iron-filing whiskers around magnets; they were not observed to form on glass or metallic components.

The optical microscope revealed the threads to be finer than human hair but it could not be determined whether or not the finest of the threads constituted single-particle chains. The formation of electrostatic particle chains is not unique to basalt - the phenomenon is well known for atmospheric hydrocarbons (Russell, 1979).

The fact that aggregates occur with one, two and three-dimensional geometries (threads, flakes and spheres, respectively) may suggest some structural hierarchy relating the three geometries, but it is not clear why all three types should co-exist in an ostensibly uniform environment. It is suspected that the aggregation process occurs at some critical suspension density; the formation of aggregates may prevent this density from being exceeded. Aggregation from suspension could not be achieved after running the same material three or four times. This may indicate that only the finest material in the system contributed to the aggregates since this material was quickly lost through the air filter or left adhering to the walls of the chamber.

There are a number of implications of these findings for both terrestrial and martian geological processes. If this aggregation process were to occur on Mars, it would provide a mechanism for the rapid removal of dust from the atmosphere and the consequent 'shutting-down' of dust storms. Furthermore, material would tend to be dumped in relatively localized areas rather than dispersed widely by 'normal' settling modes. On Earth, this aggregation process may be active in the formation of accretionary lapilli in the eruption columns of volcanoes (Sheridan, personal communication) where high concentrations of very fine comminuted material occur in the presence of electrostatic charging. Sudden aggregation of material could contribute to column collapse. It is also possible that the turbulence of such a system may destroy aggregates as fast as they are formed.

The findings reported here are preliminary ones. At present, investigations are underway to determine if aggregation occurs at a critical dust density, at a critical level of charging, with various types of material and for a specific range of particle sizes. In addition, aggregates will be collected for SEM examination with the precipitation trap depicted in Fig.1 to determine the structures of the threads and flakes. Aggregate formation is not thought to be an artifact of the system since it occurs naturally in other materials not confined within experimental apparatus.

REFERENCES

Greeley, R., 1979. Silt-clay aggregates on Mars, J. Geophys. Res., 84 (no.B11) p. 6248-6254.

Krinsley, D., Greeley, R. & Pollack, J.B., 1979. Abrasion of windblown particles on Mars - erosion of quartz and basaltic sand under simulated martian conditions, Icarus, 39, p. 364-384.

Russell, P.A., 1979. Carbonaceous particles in the atmosphere: illumination by electron microscopy. In: Proc.carbonaceous particles in the atmosphere (ed.Novakov,T.), NSF and Lawrence Berkeley Lab. publication, p.133-140.

FIGURE 2. Aggregate Formation

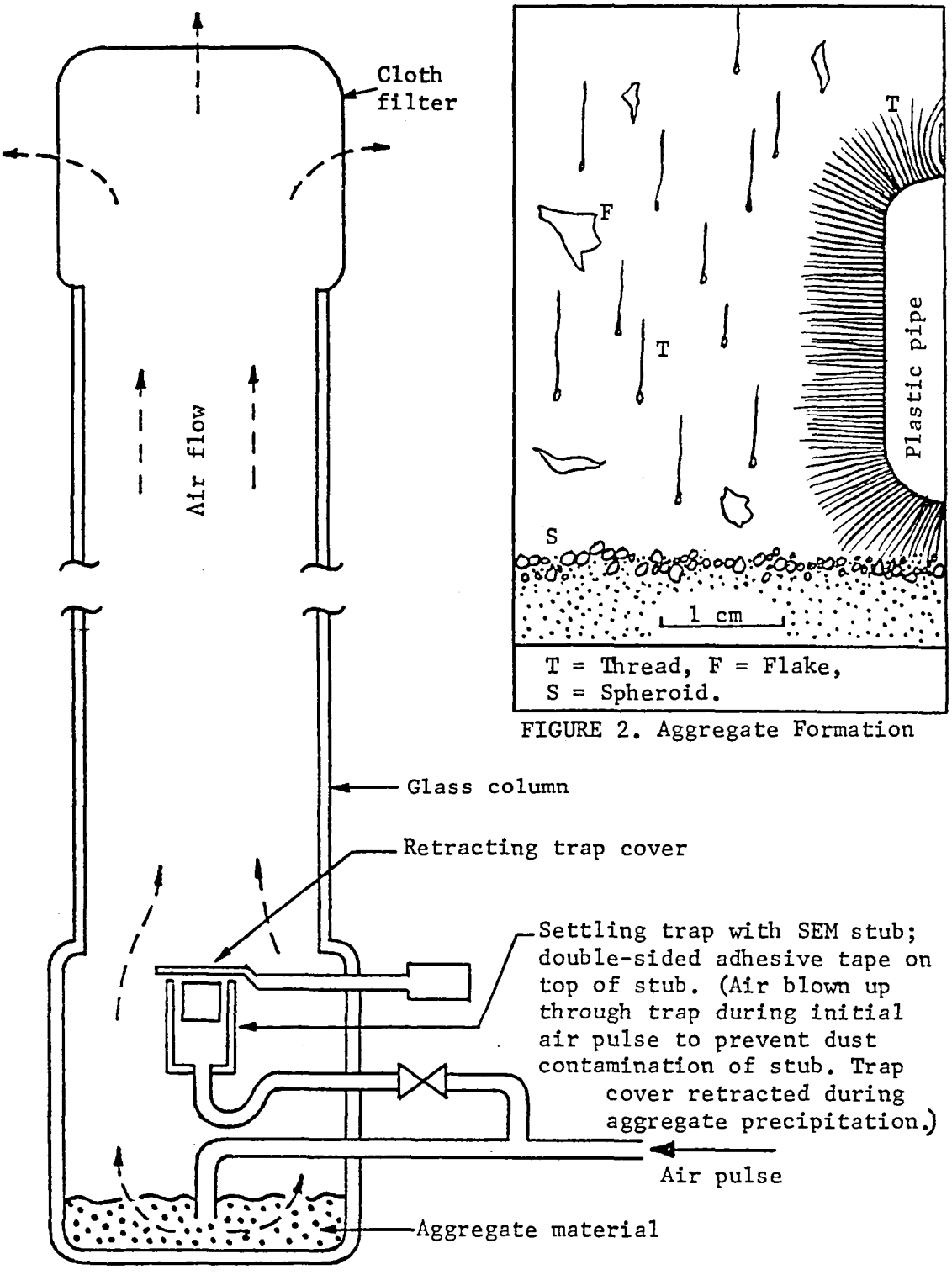


FIGURE 1. Aggregate Precipitation Device.

# AN EXPERIMENTAL INVESTIGATION OF MARTIAN ROCK DISINTEGRATION AT THE MICROLEVEL

Marshall, J.R., Stewart, G. and Krinsley, D., Department of Geology, Arizona State University, Tempe, Arizona 85287.

Aeolian erosion and deposition play a major role in the formation of the martian landscape (Sagan, 1973, McCauley, 1973, Cutts & Smith, 1973). Previous studies of martian aeolian abrasion have been concerned either with erosion of rock targets with sand-size particles (Williams, 1981) as determined by weight-loss measurements or the abrasion of sand particles themselves (eg., Krinsley et al., 1979). This study concerns the abrasion of rock surfaces (specifically basalt) by silt-size particles as revealed by scanning electron microscopy.

Flat basalt targets were impacted with silt-size (90-25 μm) quartz particles at velocities of 10, 20, 30 and 40 m/s in an atmosphere of $CO_2$ at 1-15 mb pressure. After abrasion, the targets were cleaned ultrasonically in acetone and examined in the scanning electron microscope.

At low (10 m/s) and high (40 m/s) velocities there were clear indications of abrasion by brittle fracture - most notably, the fairly common occurrence of lateral/median crack systems (associated with impact by sharp corners of particles, eg., Lawn & Wilshaw, 1975) and well-defined mineral cleavage. Lateral/median crack systems were found on the glassy matrix of the basalt; chipping by cleavage occurred on the feldspar crystals within the matrix. Some poorly-developed Hertzian cracks (associated with impact by rounded corners of particles, eg., Marshall, 1979) were observed in the matrix for 10 m/s impacts.

At intermediate impact velocities (20 & 30 m/s), the basalt developed an unusual surface layer composed of irregular lumps and flakes of material penetrated by shallow, open cracks (Fig.1). The surface layer did not appear to be more than a few microns deep. The fissure-like cracks appeared to have been formed by shrinkage of the surface layer; they did not look characteristic of cracks generated by impact. Micron-size particles littering the surface were, in many places, partially or almost wholly incorporated into the flakes and clumps comprising the surface layer. Partial melting and/or plastic deformation may have accounted for the overall appearance of the surface texture. This highly disrupted surface layer was found on both the glassy matrix and the feldspar crystals.

There is no obvious explanation for the occurrence of a disrupted surface at intermediate velocities. If the disruption is a product of plastic deformation or partial melting, it would be reasonable to expect its occurrence on targets impacted at 40 m/s where shear stresses and heating are highest. It is postulated, however, that the disruption is a function of the relationship between the amount of chipping and the amount of heat storage near the surface for a given impact velocity. Heat is generated in the target by impact; it is also carried away from the target in impact debris. Intermediate velocities could give rise to an 'optimum' interaction of these two opposing

processes so that sufficient heat is retained for partial melting and (enhanced) plastic deformation. At the lowest velocity, insufficient heat is generated for such surface alteration while at the highest velocity, the heat is instantaneously transported away from the target by a highly efficient chipping process. The shrinkage fissures visible in Fig.1 may be the result of localized cooling during bombardment or general surface cooling after cessation of the tests. Shrinkage will partially separate the surface from the body of the target in addition to causing vertical fissure systems. Heat accumulation within the target may have been aided by the relatively low thermal conductivity of the 1-15 mb atmosphere which is essentially a vacuum by terrestrial standards.

If a similar relationship between surface texture and particle velocity exists on Mars, it is possible to draw some conclusions concerning rock weathering on that planet. Firstly, since the surfaces produced by 20 and 30 m/s impacts are permeated by fissures and cavities (more so than surfaces produced by brittle fracture), they can store relatively large quantities of water or $CO_2$ ice. Chemical weathering should therefore be more pronounced on such surfaces. Secondly, abrasion debris produced by 20-30 m/s impact that is liberated into the aeolian environment should also be highly susceptible to chemical weathering owing to the disrupted nature of the material. Transmission electron microscopy will be used to determine the extent and nature of disruption in the surface layer.

Heat is always generated in a target bombarded by particles. The disrupted surface layer reported here suggests that this heat may be quite intense at an impact site. Surface-texture analyses by Krinsley et al. (1979) and Krinsley & McCoy (1978) corroborate this statement. This could be an important factor in aeolian abrasion on both Earth and Mars, irrespective of the type of surface texture present. Water (liquid or solid) contained within microfractures on a rock surface could melt or vapourize rapidly during particle bombardment if it is directly below the site of impact. Conversion of water to steam within a confined crack would generate very localized, but very intense, mechanical stresses with a potential for spalling material from the surface. High-temperature water (liquid or gas) may also give rise to short-term chemical reactions during the bombardment process. It is planned to test this hypothesis by controlling both the temperature and surface moisture content of a target undergoing particle bombardment.

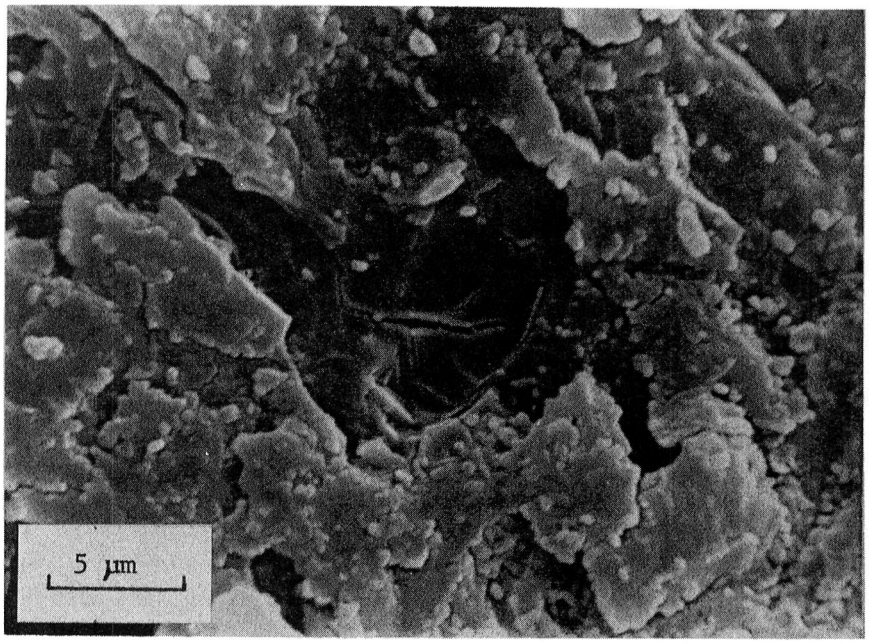


FIGURE 1. Disrupted surface on basalt (matrix) produced by 20-30 m/s impact of silt in a simulated martian environment.

## REFERENCES

Cutts, J.A. & Smith, R.S.U., 1973. Eolian deposits and dunes on Mars, J. Geophys. Res., 78 (no. 20) p. 4139-4154.

Krinsley, D., Greeley, R. & Pollack, J.B., 1979. Abrasion of windblown particles on Mars - erosion of quartz and basaltic sand under martian conditions, Icarus, 39, p. 364-384.

Krinsley, D. & McCoy, F., 1978. Aeolian quartz sand and silt. In: Scanning electron microscopy in the study of sediments (ed. Whalley, W.B.), Geo Abstracts, Norwich, England, p.249-260.

Lawn, B.R. & Wilshaw, R., 1975. Review indentation fracture: principles and applications, J. Mat. Sci., 10, p. 1049-1081.

Marshall, J.R., 1979. The simulation of sand-grain surface textures using a pneumatic-gun apparatus and quartz plates, Ph.D. Thesis, University College London, University of London, 301 pp.

McCauley, J.F., 1973. Mariner 9 evidence for wind erosion in the Equatorial and mid-latitude regions of Mars, J. Geophys. Res., 78 (no. 20) p. 4124-4137.

Sagan, C., 1973. Sandstorms and eolian erosion on Mars, J. Geophys. Res., 78 (no. 20) p. 4155-4161.

Williams, S., 1981. Calculated and inferred aeolian abrasion rates: Earth and Mars, M.S. Thesis, Arizona State University, 53 pp.

AN EXPERIMENTAL STUDY OF THE EROSION OF BASALT, OBSIDIAN AND QUARTZ BY FINE SAND, SILT AND CLAY

G. Stewart, D. Krinsley, and J. Marshall, Department of Geology, Arizona State University, Tempe, AZ 85287

Imaging data and experiments conducted by the Viking Landers indicate that a large amount of fine dust may be present at the Lander sites. For example, it has been proposed that possible wind-entrainable material at the two sites consists largely of 10 μm to 100 μm (diam.) particles (Shorthill et al., 1976) or possibly aggregates of clay (Moore et al., 1979). Furthermore, Huck et al. (1977) conclude that fine particles may be present in abundance over much of the martian surface, and a 200-year history of dust storm observations (Gierasch and Goody, 1973) supports this hypothesis. This information has prompted the question: to what extent do fine particles contribute to eolian abrasion processes? Our recent experiments indicate that the amount of abrasion due to impact by quartz particles 90 to 25 μm in diameter decreases much more rapidly with decreasing particle size and velocity than predicted by impact energy considerations ($S_A \alpha M_p V_p^2$) or experiments using larger sized particles (e.g. Greeley and Williams, 1979). They also indicate that clay particles on the surface of impacting grains or in the form of clay-silt aggregates may reduce abrasion by transferring themselves to the target and sheltering it from subsequent abrasion by larger particles.

Flat, polished plates of quartz, obsidian, and basalt were abraded by 90-63 μm, 63-45 μm and 50-25 μm commercial quartz, 90-63 μm and 63-45 μm Arizona Road Dust (A.R.D.), and 500-355 μm clay-silt aggregates in a whirling arm erosion device (Greeley and Williams, 1979) at velocities of 10, 20, 30 and 40 m/s in a $CO_2$ atmosphere at a pressure of 1-15 mb. Clay-silt aggregates were composed of quartz flour (one-third by volume) less than 90 μm in diameter and buff potter's clay (two-thirds by volume), commercial quartz was very clean and pure (>98% quartz), and the A.R.D. consisted mainly of quartz grains coated with clay particles.

The dependence of abrasion on particle velocity and mass was determined for targets impacted by commercial quartz using log-log plots of mass lost by the target per impact versus particle mass and velocity. The results indicate the following relationships: $S_A \alpha M_p^{2.03-1.37}$ and $S_A \alpha V_p^{2.03-3.16}$, where $M_p$ and $V_p$ are particle mass and velocity respectively. The discrepancies between these values and those predicted by the kinetic energy equation are not completely understood, but may be due to the fact that fewer particles of the total impacting mass contribute to brittle-fracture erosion at low impact energies, i.e. there is a kinetic energy threshold for impact fracture. This hypothesis is also supported by S.E.M. studies of the targets which indicate that the abrasion mechanisms change with kinetic energy and the fact that particle mass and velocity exponents change with target composition.

It was also found that A.R.D. was (on average) 72% less effective in abrading targets than 'clean' commercial quartz. Furthermore, erratic results as expressed by the velocity exponent were obtained when the susceptibility data was plotted against particle velocity (i.e. $S_A \alpha V_p^{0.68-3.31}$). This erratic behavior may, in part, be due to errors in weight-loss data resulting from adhering fines. However, S.E.M.

examination of quartz targets impacted at 20 m/s indicates that the erratic behavior is also due to the cushioning effect of adventitious fines on quartz grains which not only buffer the first few impacts, but transfer to and shelter the target from subsequent impacts.

Targets impacted by silt-clay aggregates also acquired a coating of fine particles which appeared much thicker than coatings on targets impacted by A.R.D. Although weight loss data from these targets were not gathered, S.E.M. examination of quartz targets impacted at 20 m/s and 40 m/s revealed no abrasion features. Hence, fine (clay) particles, either coating grains or as aggregates may shield targets from the impact of larger grains to a point where little or no abrasion occurs.

These experimental results have at least three implications for Mars and Earth. First, if wind-transported material is 'clean,' the amount of abrasion a target (ventifact or rock surface) may suffer will decrease more rapidly as particle size and velocity decrease (for particles less than 90 μm) than predicted by kinetic energy considerations. Second, if fine (clay) particles are present in or on the entrained material, these particles will transfer to the surface of the target and shelter it from abrasion by larger particles, thus reducing the rate of abrasion. Third, if fine (clay) particles are present in abundance, there may be no simple experimental or theoretical means at present to accurately predict rates of eolian abrasion. This is even more evident when one considers the aerodynamic complexities involved in the transport of fines. In relation to the Viking Lander sites, the low erosion rates inferred for these areas by Arvidson et al. (1979) could be explained partially or entirely by the sheltering capabilities of the fine soil materials present. This possibility is supported by Lander images which show soil components on the surface of larger rocks at the Lander sites (Saunders, 1977).

## REFERENCES


Arvidson, R., Guinness, E., and Lee, S., 1979, Differential aeolian redistribution on Mars. Nature, 278, p. 533-535.

Greeley, R., and Williams, S. H., 1979, Mars: Preliminary estimates of rates of wind erosion based on laboratory simulations. Lunar and Planetary Science Conf. X, p. 461-463.

Gierach, P. J., and Goody, R. M., 1973, A model of a Martian great dust storm, J. Atmos. Sci., 30, p. 169-179.

Huck, F. O., Jobson, D., Park, S., Wall, S., Arvidson, W., Patterson, W., and Benton, W., 1977, Spectrophotometric and color estimates of the Viking Lander sites, J. Geophys. Res., 82, p. 4401-4411.

Moore, H. J., Spitzer, C. R., Bradford, K. Z., Cates, P. M., Hutton, R. E., and Shorthill, R. W., 1979, Sample fields of the Viking Landers, Physical properties and aeolian processes, J. Geophys. Res., 84, (no. B14), p. 8365-8377.

Saunders, R., 1977, Sedimentary regimes on Mars, Reports of Planetary Geology Program, NASA TMX 3511, p. 144-145.

Shorthill, R. W., Moore, H. J., Scott, R. F., Hutton, R. E., Liebes, S. and Spitzer, C. R., 1976, The 'Soil' of Mars (Viking I), Science, 194, p. 91-97.

electrostatically bonded silt-clay aggregates are expected to settle to the ground during the waning stages of the dust storm and form deposits with dune-like morphology.

Although the electrostatic hypothesis for aggregate formation in plausible, it presents a new suite of problems. Electric charging of windblown particles occur by processes which operate in dust storms both on Mars and earth. In fact, terrestrial dust storms are known to be electrically charged. This would suggest that if electrostatically bonded aggregates can form dunes on Mars, they should also do so on earth. Yet, there are no reports of clay-dunes adjacent to non-saline dust sources on earth. On the other hand, dunes formed by transport, deposition and ultimate stabilization of salt-cemented clay aggregates are common. Another problem concerns the mechanical properties of the electrostatic aggregates. Marshall and others (1980) performed testing of wind tunnel-produced aggregates of crushed basalt. They point out that the aggregates have low penetration resistance and an ability to absorb the energy of an impacting body. The kinetic energy of an impact is not returned to the impactor by elastic recovery which means that the particles cannot saltate. This implies that dune formation would be difficult even if the aggregates are inherently strong enough to saltate without disintegration.

In light of the previous discussion of terrestrial saltbonded aggregates it it here proposed that the bonding agent on Mars is salt rather than electrostatic attraction. For salt to be a plausible aggregation agent on Mars one needs an adequate salt source and a mechanism for its cycling through the fine soil particulates. Farmer's (1976) data are consistent with seasonal (or perhaps diurnal) cycling of $H_2O$ between the atmosphere and the surface where the water resides as thin intergranular absorbed films. If the films become thick enough to behave as a bulk water phase, they should be capable of dissolving soluble materials, carrying the ions to the surface as part of the evaporatic phase of the cycle, and depositing a sulfate/chloride crust. A recent model of salt formation on Mars, proposed by Clifford (1980) and Huguenin (1980) calls for the existence of a planet-wide interconnected ground water system. The ground water supplies near-surface liquid water in several regions. As the water migrates into these regions from below it would produce extensive leaching and highly saline solutions. Evaporation of the brines should precipitate salts at or near the surface. Winds could disperse the salts planet-wide.

Viking XRFS-data strongly suggest the existence of clay minerals and salts at the lander sites. Whether the salts are produced locally through seasonal or daily cycling of water, or are brought in as aerosols from distant Martian "oases", their presence suggests that clay aggregate formation by salt crystal-bonding may be a common phenomenon on Mars.

Aggregates of fine particles may also be common on Io. Recent theoretical work on light scattering in rough and porous surfaces combined with Voyager photopolarimeter observations (Pang, et al., 1981) suggest that the surface of Io might be covered with aggregates of ash from Io's volcanoes. This opinion is based on studies of Io's phase curve (whole-disk brightness vs. solar phase angle) which permits a separation of the photometric effects of surface roughness and volume density. The particles present on Io's surface are sulfur and $SO_2$ frost. They have specific gravities of about 2.0 $g/cm^3$, yet the photometrically determined bulk density of surface material is 0.7 to 0.8 $g/cm^3$. This observation, combined with laboratory light scattering experiments on irregular, fluffy particles, determinations of particle sizes in Io's volcanic plumes, and estimates of Io's surface roughness, have lead to the conclusion that sulfur dioxide frost is not ubiquitously present as an optically thick layer on Io, neither is the sulfur present in coarse crystalline or colloidal form. Fluffy aggregates appear to be the best terrestrial analogs for particles on Io's surface.

Evidence for widespread occurrence of fine particle aggregates on Mars and Io is strong. The vastly different physical properties of such aggregates compared to those of the individual component particles in a dispersed state warrant

a detailed examination of terrestrial aggregates of potentially related origins. The aggregates responsible for clay dunes along Laguna Madre in Texas and other saline, semi-arid environments, probably constitute the most valid terrestrial candidate materials.

References.

Clifford, S. M., A model for the removal and subsurface storage of a primitive Martian ice sheet, NASA TM 82385, 405-407, 1980.

Coffey, G. N., Clay dunes, J. Geol. 17, 754-755, 1909.

Farmer, C. B., Liquid water on Mars, Icarus, 28, 279-289, 1976.

Greeley, R., Silt-clay aggregates on Mars, J. Geophys. Res. 84, 6248-6254, 1979.

Huguenin, R. L., Possible source of the Martian salts, NASA TM 82385, 502-503, 1980.

Hunt, G. R., L. M. Logan and J. W. Salisbury, Mars: components of infrared spectra and the composition of the dust cloud, Icarus, 18, 459-469, 1973.

Marshall, J., D. H. Krinsley and R. Greeley, Compression testing of electrostatic aggregates - analogs to sand grains on Mars, NASA TM 82385, 187-189, 1980.

Moore, H. J., R. E. Hutton, R. F. Scott, C. R. Spitzer and R. W. Shorthill, Surface materials of the Viking lander sites, J. Geophys. Res., 82, 4497-4523, 1977.

Mutch, T. A., R. E. Arvidson, A. B. Binder, F. O. Huck, E. C. Levinthal, S. Liebes, Jr., E. C. Morris, D. Nummedal, J. B. Pollack and C. Sagan, Fine particles on Mars: observations with Viking 1 lander cameras, Science, 194, 87-91, 1976.

Pang, K. D., K. Lumme and E. Bowell, Microstructure and particulate properties of the surfaces of Io and Ganymede: comparison with other solar system bodies, Proc. Lunar Planet Sci. Conf. 12th (in press).

Price, W. A., Physicochemical and environmental factors in clay dune genesis, J. Sed. Petrology, 33 766-778, 1963.

Toulmin, P., A. K. Baird, B. C. Clark, K. Keil, H. J. Rose, Jr., R. P. Christian, P. H. Evans and W. C. Kelliher, Geochemical and mineralogical interpretations of the Viking inorganic chemical results, J. Geophys. Res., 82, 4625-4634, 1977.

# CLAY AGGREGATES ON EARTH, MARS AND IO

Dag Nummedal, Department of Geology
Louisiana State University, Baton Rouge, LA 70803

Most terrestrial aeolian dunes are made of sand. This situation reflects the fact that sand-sized particles (60μm to 2000μm in diameter) are the dominant sediment population to be produced by weathering of common terrestrial igneous rocks. The conditions which permit sand to accumulate as aeolian dune forms, however, are also satisfied for aggregates of fine-grained materials. Aggregates of clay are common in terrestrial semi-arid regions where they often accumulate to form extensive, conspicuous clay dunes (Coffey, 1909). The dune form, therefore, is not diagnostic of sediment size.

Data on surface material properties on Mars and Io suggest that aggregates of fine materials may indeed be very common on these two bodies (Greeley, 1979; Pang, et al., 1981). Their existence can be inferred from various remotely sensed parameters, but the mechanics of their origin and the nature of the particle bonding elude direct determination. It is the objective of this paper to review the process responsible for most of the terrestrial clay aggregates and to argue in support of the hypothesis that similar processes might play a role in the formation of extraterrestrial aggregates.

Some of the best-developed terrestrial clay dunes form adjacent to saline wind tidal-flats of the south Texas coast. Price (1963) has described the areal extent, morphology and genesis of clay dunes near Corpus Christi and on the Rio Grande delta. These dunes typically are smooth ridges, less than 10 m high, with gentle stoss and lee slopes. Only on extremely rare occasions of abundant clay aggregate supply do slip faces develop. Aeolian scour of upwind slopes commonly leaves sculpted concave surfaces. These surfaces often reveal bedding due to color alternations in the clay and occasional interbedded silt and fine sand layers.

The initial step in formation of the Texas clay dunes is the desiccation and break-down of the crust of exposed salt flats. This crust may break by the growth of fine crystals of salts, the development and rupture of domal blisters, or the curling of suncracked polygon chips. The fragments break into sand-sized aggregates as they move in response to surface wind stress. High hygroscopicity and moisture retaining capacity of the clays provides the cohesive force necessary for the clay pellets to survive saltation transport.

Extensive drifts seen in the surface pictures at the VL-1 lander site strongly suggest aeolian movement and deposition of non-cohesive sand-sized material (Mutch, et al., 1976). Grain-size estimates based on different physical experiments at the lander site, on the other hand, suggests that the bulk of the material falls in the silt and clay range (Moore, et al., 1977). Even so, the VL-1 soil responded to retroengine exhaust more like dune sand than lunar nominal soil. Based on mineralogical modeling of X-ray fluorescence spectrophotometer (XRFS) determinations of elemental abundance, Toulmin, et al., (1977) proposed that the Martian soil is composed primarily of weathering products of mafic igneous rocks, dominately Fe-rich smectite clays. This inference is consistent with infrared spectral data obtained during the dust storms at the beginning of the Mariner 9 mission (Hunt, et al., 1973). Thus, the evidence is strong for the widespread existence of clays in the Martian soil, yet the morphology at the VL-1 lander site clearly reveals sand dune-like forms.

Greeley (1979) has addressed this problem and proposed a model calling for electrostatic bonding to agglomerate silt and clay-sized particles into sand-sized aggregates that are deposited as drifts and dunes. Laboratory testing in a Martian wind tunnel and field measurements demonstrate that electrification of small particles is likely to be an effective process during the Martian dust storms. The

# DUST AND SAND MOVEMENT ON MARS: PRESENT ACTIVITY AND ITS RELATION TO SEDIMENT DEPOSITS

Peter Thomas, Laboratory for Planetary Studies, Cornell University, Ithaca, New York 14853

Two lines of investigation, Viking Orbiter color data and complete global mapping of intra-crater splotches and associated streaks, have added significant information on present eolian transport on Mars and its relation to the main sediment deposits.

A. Color Data. Areas of contrast reversal of albedo features between red and violet images have been mapped for the entire planet (Fig. 1). Contrast reversal is restricted to crater splotches and associated streaks. Comparison with laboratory spectral measurements indicates that contrast reversal is most simply (not exclusively) explained by particle size effects in iron oxide mixtures; in particular, the presence or absence of micron-sized particles. The colors strongly suggest that many of the splotches and streaks have, at most, trivial amounts of the bright red dust widely dispersed on Mars. The splotches' association with dune deposits suggests recent saltation as the most likely mechanism for sorting out of micron-sized particles.

Colors and phase-related contrast change of bright steaks indicates that they can be explained as partial coverings of bright dust on a variety of substrates. The covering is thick enough in some streaks to provide a significantly different phase coefficient from that of surrounding areas. A more intricately textured surface in the streak area is the most likely explanation of the phase effects. The inverse effect is observed in dark streaks inferred to be erosional.

B. Global Distribution of Splotches and Associated Streaks. The latitudinal distribution of deposits and splotches and associated streaks is shown in Figure 2. Splotches show strong latitudinal grouping: into polar and low latitude belts. The difference between north and south is primarily caused by different numbers of craters. Of particular interest is the coincidence, at nearly all latitudes, of streak directions with splotch orientations: Material is being deflated from deposits by winds of the same directions as those that formed the intra-crater deposits.

C. Relation of Present Winds to Sediment Deposits.

1. Dune Distribution. Dunes are concentrated in three major regions of Mars: North polar erg, low latitude canyon, and crater dune fields in high southern latitudes. Estimates of volume have been made, and are plotted in Figure 3 along with the major meridional winds as shown by all wind streaks. The polar dune fields fall in areas of present seasonally reversing winds; this distribution can be formed from nearly any initial distribution of dune sand, provided the present winds are allowed to blow for periods greater than $10^6$ years. This would require the changing hemispherical asymmetry of climate to be strongly constrained by topographic and albedo effects on the efficiency of sand transporting winds.

2. Dust. Major dust deposits occur at both poles, but their present forms are severely modified by erosion. Wind streaks on and near the permanent frost caps suggest that at present there may not be net

deposition on the polar areas, a situation consistent with the geologic evidence of erosion. Present conditions thus are probably not those in existence during deposition of the thick deposits.

3. Dust and Sand. Dust and sand are associated in several settings on Mars in ways that are distinct from those on earth. The polar layered deposits have included or interbedded dune-forming material. The combination of the erosional state of these deposits, the polar dune field orientations, and the wind streak data, suggest that the polar layered deposits are the latest, but not ultimate, source of the polar dune sands. Dust and sand deposits also appear to coexist in many craters and may signify cycles of deposition at low latitudes as well.

D. Conclusions and Problems.

1. Active saltation and local sorting of dust and sand occurs now at a variety of settings and latitudes on Mars.

2. The accumulation of dune sand in latitudinal belts agrees with the present wind patterns and thus suggests that changes in hemispherical climate asymmetry may be modified by topographic and albedo effects.

3. Problems under study: a) Ways the different polar topography and albedo patterns can affect seasons of effective sand transport, b) mechanisms of transport and deposition that bring both dust and sand into the polar regions, and into the interiors of low latitude craters, and c) meteorological conditions needed to cause deflation rather than deposition in craters, with particular reference to terrestrial analogs.

This research is supported by NASA Grant NAGW 111.

Figure 1. Areas in which contrast reversal (VO Red/Violet filters) occurs on Mars. All are crater splotches or assorted streaks. All red/violet image pairs were searched; coverage of the planet is nearly complete.

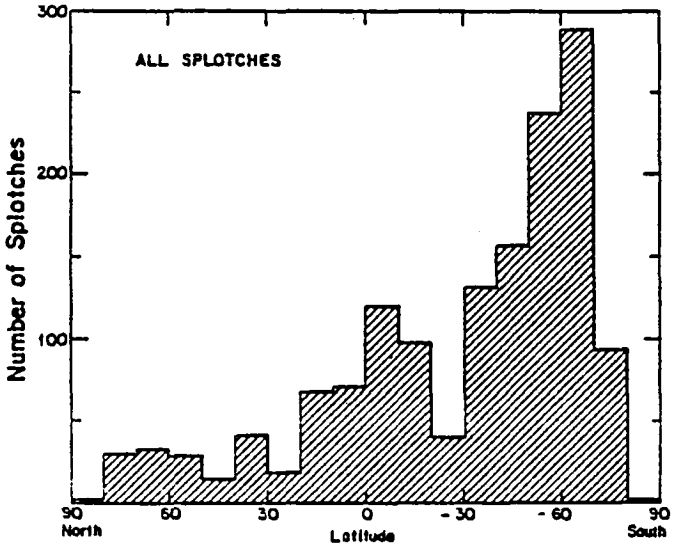


Figure 2a. Latitudinal distribution of depositional splotches. Although there are far more splotches at high southern latitudes than northern, the fraction of northern craters (> 20 km) with splotches is slightly higher.

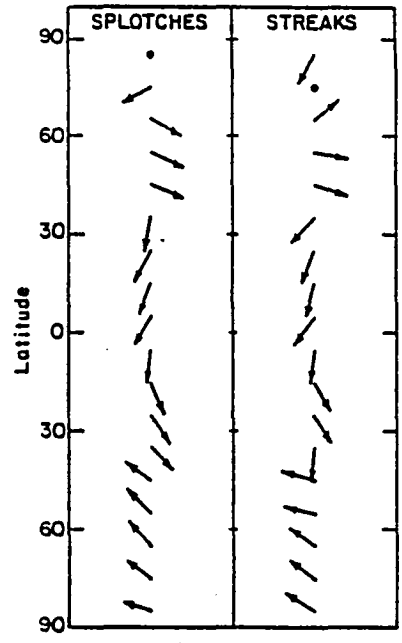


Figure 2b. Orientations of splotches and streaks by latitude. Wind directions responsible for splotches and streaks are similar for all areas, with the possible exception of very high northern latitudes.

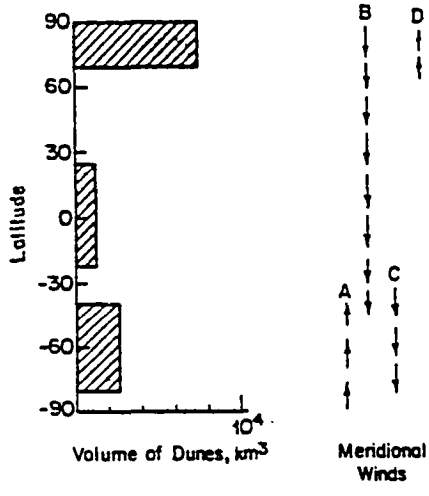


Figure 3. Main latitudinal concentrations of dunes: estimated volumes averaged over appropriate 10° latitude bins, and meridional wind patterns shown by all streaks. A) Southern summer, B) Southern spring/summer, C) Late southern summer, D) Northern summer.

COMPARISON OF AEOLIAN ACTIVITY IN ELYSIUM AND THARSIS.

S. Lee, P. Thomas, and J. Veverka, Laboratory for Planetary Studies, Cornell University, Ithaca, New York 14853

The Elysium and Tharsis regions have some of the greatest topographic relief on Mars, and are also notable for the presence of very distinctive aeolian features. In an effort to determine the factors controlling the formation and distribution of wind streaks on regional slopes, detailed mapping of the aeolian features in Tharsis and Elysium have been compiled from Viking Orbiter observations spanning more than a complete martian year.

Tharsis: Three basic types of wind streaks occur in Tharsis (Figure 1); the classification scheme used is that of Thomas et al. (1981):

(1) Crater-related bright depositional streaks [Type I (bright)] are found over much of the area and are predominantly directed downslope along the steepest topographic gradient. On the plains surrounding Olympus Mons, however, the streaks indicate winds describing a clockwise flow. This pattern is consistent with nighttime slope winds flowing down the flanks of the volcano (Gierasch and Magalhaes, 1981). Few temporal changes are found in the pattern of Type I (bright) streaks.

(2) Crater-related dark erosional streaks [Type I (dark)] are primarily found on the gently sloping plains to the south and west of Arsia Mons. These streaks are non-distinct following global dust storms. In late southern summer and early fall, dark streaks form in response to easterly winds of the global circulation. At other seasons, dark streaks form in response to downslope winds, often leaving two streaks of substantially different orientation from the same crater.

(3) Coalesced dark erosional streaks [Type I (dark) coalesced] which form over large areas, rather than behind craters and obstacles, comprise the dark collars formed on the flanks of the Tharsis volcanos. The slope winds generated in these areas are of sufficient velocity to erode dust from the surface, even though the ambient atmospheric pressure may be only a fraction of a millibar (Gierasch and Magalhaes, 1981). The collar outlines are extremely time variable, being very irregular following dust storms and becoming more sharply defined as the year progresses. The patterns are generally repeatable from year to year. Bright albedo areas [Type I (bright) sheet streaks] downslope of the collars form by deposition of the dust eroded from the upper flanks of the volcanos.

Elysium: Compared to Tharsis, the aeolian features in Elysium are stable throughout the year. The regional pattern appears little affected by topography (Figure 2):

(1) Type I (bright) streaks are the predominant type found. Over most of the region, the inferred winds (from the NE) follow the global circulation pattern expected during the time of major dust storms. The main deviation is noted near Elysium Mons, where the streaks indicate a clockwise flow, as in the case near Olympus Mons.

(2) Only minor occurrences of Type I (dark) streaks are found. The pattern is identical to that of Type I (bright) streaks in the same locale.

(3) Type I (dark) coalesced streaks are also quite rare, occurring only on the summit of, and very near the base of, Elysium Mons. An ill-defined dark collar, very near the summit of the volcano, is visible in some high-resolution images. Note that the dark region of Cerberus does not appear to be comprised of coalesced dark streaks (Chaikin et al., 1981).

Discussion: The pattern of winds in Tharsis is obviously controlled by regional topography, while the slopes of Elysium apparently have little effect on atmospheric circulation. The prominent examples of coalesced dark streaks which are highly visible, and highly variable, throughout the year in Tharsis are absent in Elysium. Apparently, slope winds which primarily determine the pattern of aeolian features in Tharsis are unable to dominate the global circulation pattern in Elysium. This difference may be explained by: (1) the slopes in Elysium are smaller than those in Tharsis, and (2) the thermal inertia of the surface material on most of Elysium is generally much higher than that in Tharsis (Palluconi and Kieffer, 1981), reducing the diurnal temperature differences found there. Both of these factors will effectively reduce the magnitude of slope winds.

This research was supported by NASA Grant NSG-7546.

REFERENCES:

Chaikin, A.L., Maxwell, T.A., and El-Baz, F. (1981). Temporal changes in the Cerberus region of Mars: Mariner 9 and Viking comparisons. Icarus 45, 167-178.

Gierasch, P., and Magalhaes, J. (1981). Slope winds on Mars: Interpretation of eolian features on volcanos. In preparation.

Palluconi, F.D., and Kieffer, H.H. (1981). Thermal inertia mapping of Mars from 60°S to 60°N. Icarus 45, 415-426.

Thomas, P., Veverka, J., Lee, S., and Bloom, A. (1981). Classification of wind streaks on Mars. Icarus 45, 124-153.

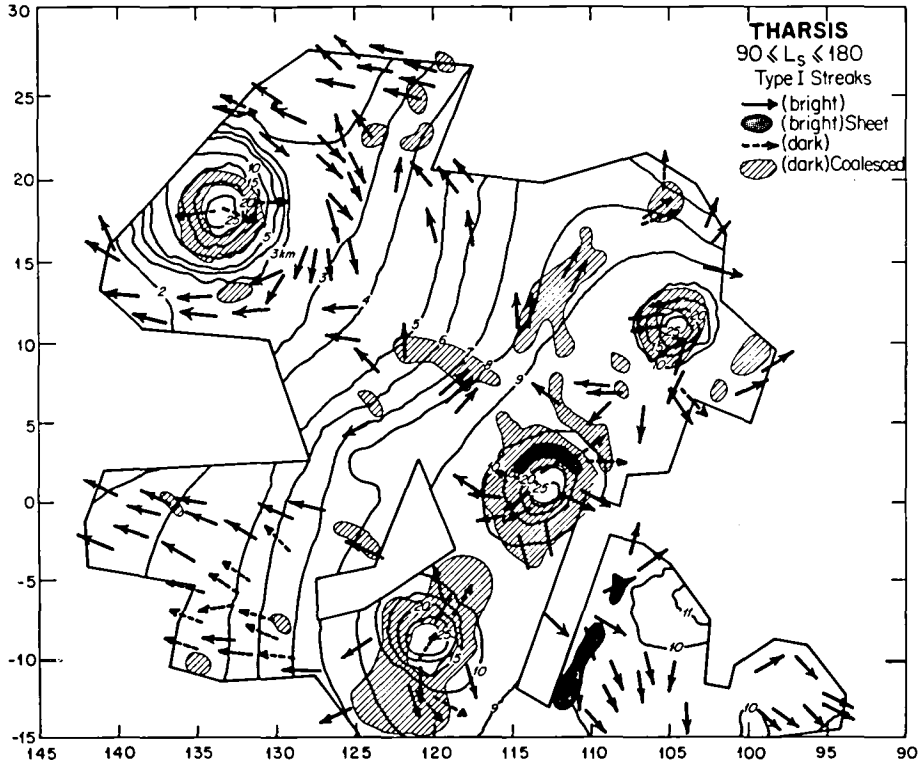


Figure 1. Wind streak map of Tharsis. Elevation contours are from U.S.G.S. topographic maps. Streak data were not obtained for areas outside the marked outlines.

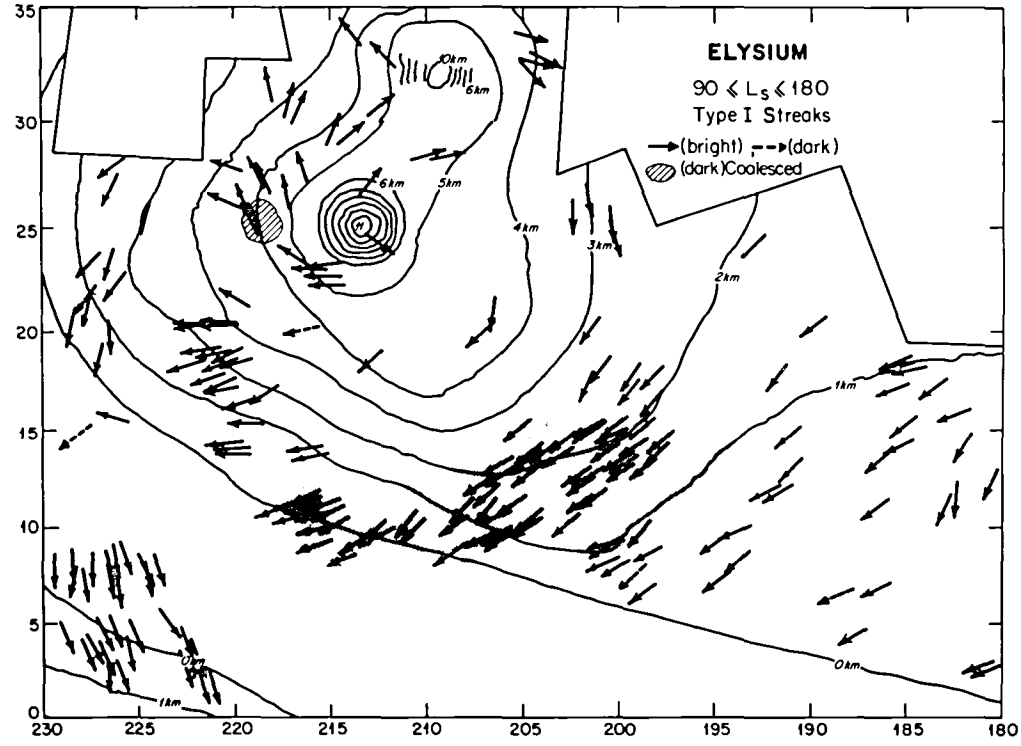


Figure 2. Wind streak map of Elysium. Data shown for one martian year after that in Figure 1. Cerberus is denoted by the shaded region.

EOLIAN STRATIGRAPHY OF THE WEST CENTRAL EQUATORIAL REGION OF MARS: VIKING LANDER 1 AND ORBITER COLOR OBSERVATIONS. Edwin L. Strickland, III
Dept. Earth, Planet. Sci. Washington University, St. Louis, Mo. 63130

Soil stratigraphic units recognized at the Viking 1 site correlate with color/albedo units seen in Viking Orbiter color images surrounding the site. Several of these units extend from the Lunae Planum highlands, west of Chryse, east to Schiaparelli basin and Sabaeus Sinus. Their morphology and contact relations vary little over this 8000 km. distance. Eolian mantle and bedrock geologic units are largely covered and obscured by these units. However, topography and (probably) meter-scale roughness have controlled the deposition and erosion of these eolian units. The sediments probably were transported into this region in eolian suspension, building up a succession of thin (less than meters thick) layers over wide regions. Progressive eolian erosion is now stripping these units, removing them in suspension, and exposing their stratigraphic sequence.

Distinct soil stratigraphic units are visible in color-enhanced images of the Viking 1 site. They are identified on the basis of color, texture, surface morphology, and contact relations (1). The uppermost unit is a thin, discontinuous, bright, and relatively "red"* soil. It probably is underlain by another thin and patchy layer: "green-blue" soil. "Blue drift" soils, generally covered by the "red" and "green-blue" soils, cover much of the site. Viking 1 landed straddling the edge of one of these drifts. A unique patch of crust-like "orange-red" soil was exposed at the edge of the drift, where retrorocket exhaust apparently scoured away a few centimeters of "blue drift" soil. The "blue drift" soil, and probably the "orange-red" soil, rest on the lowermost unit: "rocky blue" soil. A sixth soil unit, "dark red" soil, caps the "Big Joe" boulder near the lander, and surrounds several nearby boulder clusters. Its stratigraphic position is not well defined by the lander images, but it probably lies below the "blue drift" soil, and above the "rocky blue" soil. The soil units at the Viking 2 site, nearly halfway around the planet, greatly resemble those at the first site. This suggests that such soil units are widely distributed on Mars.

Study of color-enhanced Viking Orbiter images of regions near the Viking 1 site, and a natural color mosaic of the west-central equatorial region (2), suggests that the soil units observed by VL-1 can be observed from orbit, and extend laterally for thousands of kilometers. Chryse Planitia, at 1 and 4 km./pixel resolution, has a uniformly "red", moderately high albedo surface. These images were taken during the extended mission, when the Viking 1 site's soils were covered by a thin layer of bright "red" dust. This was deposited during the first winter; the bright "red" soil observed earlier may have been the deposit of previous dust storms. Other color/albedo units around the Chryse basin lose contrast and fade-out as they enter the basin. This unit, called here the Xanthe unit (after the classical bright albedo feature of west Chryse) is the uppermost unit in the Orbiter color/albedo stratigraphy.

At the mouth of Kasei Vallis, N. W. of Chryse, dark albedo features show dark "blue" and possibly "blue-green" colors. Similar features to the N. E. and E. form Niliacus Lacus at the southern end of Mare Acidalium. Craters McLaughlain and OXI-Lu have dark "blue" crater streaks that merge with the edge

* Colors referred to are relative to scene averages, as displayed in color-enhanced images.

of Niliacus Lacus. Further east, in Oxia, isolated dark "blue" crater streaks occur, and to the S. and S. W., they merge to form the classical dark albedo features of Oxia Palus, Sinus Meridiani, Margaritifer Sinus, and Aurorae Sinus. This unit, the Sinus Meridiani unit, is bordered throughout this region by a bright "red" border, against darker, intermediate albedo "red" surfaces.

The bright "red" border widens along the margins of the dark markings near the equator. It forms independent crater streaks, caps mesas in the channels entering S. E. Chryse, and forms irregular patches along the border of Lunae Planum and the S. Chryse highlands. This unit may be called the Eos unit, where it separates Aurorae Sinus and Margaritifer Sinus.

The intermediate albedo "red" unit, the Oxia unit, extends without interruption from the Lunae Planum highlands, across the S. Chryse highlands, the mouths of Simud, Tiu, and Ares Valles, the cratered plains of Oxia, nearly to the rim of the Schiaparelli basin. Here, and to the north, the Oxia unit terminates against the brighter "red" cratered highlands of west Arabia (Moab in the old nomenclature). Along the southern half of this border, it forms dark "red" crater tails against the Arabia unit, as the Eos unit does against Oxia in the S. Chryse highlands, and the Sinus Meridiani unit does against the Eos unit in Oxia Palus. Crater ARA-Sn, at 16°N., 347°W., ideally shows the sequence of these units. An irregular dark "blue" patch of Sinus Meridiani unit in the center is surrounded by a thin bright border of Eos unit and a wider dark border of the darker "red" Oxia unit, against the moderately bright "red" background of the Arabia unit. The Oxia unit is always separated from the Sinus Meridiani unit by the Eos unit, except near the mouth of Kasei Vallis, where contact relations may be obscured by patches of the Xanthe unit, and near the Schiaparelli basin, where complex albedo patterns and a sixth unit obscure contact patterns.

The sixth unit, the Deucalionis unit, forms the bright classical albedo feature of Deucalionis Regio, south of Sinus Meridiani and Sinus Sabaeus. Here, bright patches on Sinus Meridiani unit in crater bottoms, and bright crater streaks abruptly merge to form a nearly continuous bright region. To the south, in Pandorae Fretum, irregular patches and dark lines reappear. At the west end of Pandorae Fretum, the bright Deucalionis unit breaks up, exposing typical materials of the Sinus Meridiani unit. Between Orbiter 1 revolutions 593 and 669, several dark "blue" patches of Sinus Meridiani unit appeared or darkened south of Schiaparelli basin and Sinus Sabaeus. Pandorae Fretum regularly darkens during the martian southern summer. Dark streaks and patches similar to those in this region, but further south, enlarged and darkened during the Mariner 9 mission. These are thought to form by eolian stripping of a thin layer of bright dust from a darker surface. The Deucalionis unit, like the Xanthe unit, probably consists of a thin dust deposit from the annual dust storms.

Unambiguous evidence of the vertical stratigraphic sequence of these units is rarely available in Orbiter imagery at kilometer resolution. To obtain more information on the contact relations of these units, several higher resolution black and white images of selected features were databased. This procedure removes most camera signatures, illumination shading, and projects the images into Mercator projection. These images will be combined with color information from the km. resolution color images to yield synthetic high-resolution color images. A unique 20 m./pixel color image S. of Schiaparelli basin is also being prepared.

# EOLIAN STRATIGRAPHY: WEST CENTRAL EQUATORIAL REGION

Strickland, E. L., III

Becquerel crater (8.4°W., 21.3°N.), in the Oxia Palus region, contains dark "blue" soils that form dune masses, and less dark, featureless "blue" patches. The dunes are not well resolved at 75 m./pixel resolution, but appear to have maximum dimensions of about 300 meters. Surrounding the dune fields, and extending downwind (southwest) from them, are areas with higher albedo and weaker "blue" coloring. Some areas may have "blue-green" color. These members of the Sinus Meridiani unit are surrounded by the higher albedo border of the Eos unit. That unit forms several crater tails downwind of small craters on the floor of Becquerel, against the darker Oxia unit. The Sinus Meridiani unit probably consists of small "blue" drifts, ≤75 m., resting on the bright "red" Eos unit. The Oxia unit surrounding these units is then interpreted as the lowest of these three units.

The topography of Becquerel crater, and the smaller craters in this area is quite subdued, and little difference is visible between the areas covered by these three units. Relief may be slightly sharper in the "blue" crater tail region, as suggested by Kieffer, et al. (2). They suggest that the crater tails are areas of turbulent wind scour, where dark "blue" bedrock is exposed. However, this cannot be reconciled with the subdued, mantled character of the southern rim of Becquerel, and fails to explain the consistant relation of dark "blue" splotches in crater floors with "blue" wind tails downwind of them. These dark streaks do not resemble the dark erosional streaks and patches of Pandorae fretum. Finally, their hypothesis does not explain the systematic appearance of one unit as crater tails near its border with only one of its adjacent units. Perhaps previous erosion of mantle deposits downwind of craters produced greater meter-scale roughness, that now impedes erosional stripping of these units.

One additional unit in crater Becquerel is the Bequerel Cratered Plateau. This bright "red" plateau shows concentric banding resembling the layered terrain of the polar regions. It has a sharp, unmantled appearance, and looks severely eroded. Yardang grooves cross most of its surface where it has been imaged at high resolution. Similar materials form layered plateaus in Henry crater (11°N., 336°W.), nearby ARA-Ng, and "White Rock" to the south. These units, with superimposed craters, are clearly much older than color/albedo units that dominate the west central equatorial region of Mars.

(1) Strickland, E. L., III (1979) Proc. Lunar Planet. Sci. Conf. 10th., P. 3055-3077.
(2) Kieffer, H. H., et al. (1981) submitted to Proc. Lunar Planet. Sci. Conf. 12th.

Table. Preliminary stratigraphic columns.

| Viking 1 Site | | West Central Equatorial Region |
|---|---|---|
| "Bright Red" soil | ? | Bright "red" Xanthe and Deucalionis units |
| "Green-blue" soil | ? | Dark "blue" and possible "blue-green" Sinus Meridiani units |
| "Blue drift" soil | | |
| "Orange-red" soil | ? | Bright "red" Eos unit |
| ? "Dark red" soil | ? | Intermediate "red" Oxia unit |
| "Rocky blue" soil | x x | Bright "red" Arabia unit |

SKETCH MAP OF THE EOLIAN UNITS OF THE WEST CENTRAL EQUATORIAL REGION OF MARS. Edwin L. Strickland, III, Dept. Earth, Planet. Sci., Washington Univ., St. Louis, Mo. 63130

Six stratigraphic units of eolian sediments have been identified in a natural color Viking Orbiter mosaic of the west central equatorial region of Mars (1). The region stretches 8000 km. from the Lunae Planum highlands east to the western Arabia highlands. The figure shows a preliminary sketch map of these units. Thomas and Veverka (2), report that the dark "blue" crater streaks in the Oxia region lengthened between the Mariner 9 and Viking missions, and during the Viking missions. They attributed these changes to deflation of dark material from dune masses in the craters' floors, and downwind transport and re-deposition of these materials.

References: (1) Strickland, E. L., III, Eolian Stratigraphy of the West Central Equatorial Region of Mars: Viking Lander 1 and Orbiter Color Observations. (these Abstracts). (2) Thomas, P., and Veverka, J., J. Geophys Res. (1979) 84, B14, 8131-8146.

Figure 1.

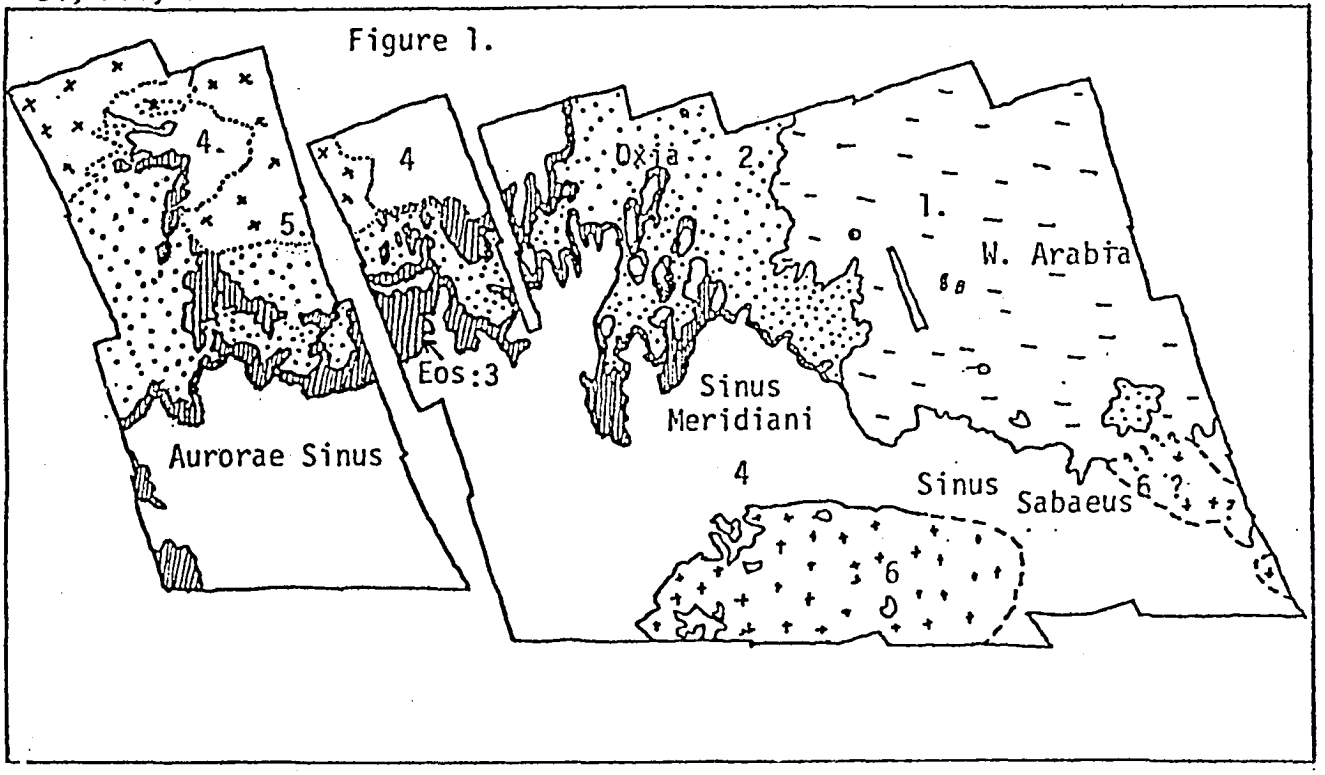


Stratigraphic sequence:

----- Uncertain boundaries

5 Xanthe

6 Deucalionis

4 Sinus Meridiani

3 Eos

2 Oxia

1 Arabia

# WIND-MODIFICATIONS OF THE CHRYSE CHANNELS

Dag Nummedal, Department of Geology
Louisiana State University, Baton Rouge, LA 70803

Ten years after the discovery of the large Martian channels by Mariner 9 there are still numerous contending hypotheses regarding their origin. Catastrophic fluvial floods, mudflows, glaciers and wind are all considered, by different investigators, to have been the dominant agents of channel sculpture (Lucchitta, 1981). The apparent reason for this bewildering array of hypotheses is that most investigators attempt to fit one formative process to the entire en-channel morphologic assemblage. What is needed at this stage is an approach which will permit discrimination of the morphologic imprints of primary and secondary channel processes. The objective of this study is to outline one such possible approach.

It has long been recognized that post-formational modification of the large channels has been severe (Baker and Kochel, 1979). Side-wall slumps and talus slopes, channel-floor lava flows and aeolian etching provide abundant evidence of such modification. There is strong support for the view that aeolian abrasion of Martian bedrock has been rather ineffective over the last 3 billion years (Arvidson et al. 1979). Yet, some investigators argue on theoretical grounds that the bulk of the channel volume could have been carved by aeolian activity (Cutts and Blasius, 1981). This, presumeably, implies great antiquity of the channels or local deposits of easily erodable materials. Great antiquity is inconsistent with en-channel crater frequency counts (Masursky et al. 1980) and dramatic differential aeolian erosion rates are geologically untenable.

It is here proposed that the aeolian modification of pre-formed fluvial channels has been much greater than previously recognized. The winds responsible for this modification followed circulation patterns similar to those of the present; the funneling of winds in many narrow channel passages greatly enhanced their ability to abrade, and deposits of possible fluvial origin within the channels could have provided materials much more susceptible to aeolian erosion than the surfaces where Arvidson et al. (1979) did their aeolian crater erosion study.

Ares and Kasei Valles provide ample evidence for large-scale aeolian channel modification. In both channels the present winds blow from the Chryse Basin upchannel towards their heads. Dark and bright wind streaks on the channel floor and the adjacent cratered uplands clearly delineate the present aeolian sediment dispersal patterns (fig. 1). Data from the Viking Infrared Thermal Mapper can be interpreted in terms of surface sediment texture. Texture information is most directly obtainable from the thermal inertia data. As seen in figures 2 and 3, thermal I R values range from as low as $I = 3 \cdot 10^{-3} cal/K \cdot s^{\frac{1}{2}} cm^2$ to a high of $I = 12 \cdot 10^{-3} cal/K \cdot s^{\frac{1}{2}} cm^2$. If the surface material was homogenous this would correspond to grain sizes of about 50 μm and 2 mm, respectively (Kieffer et al. 1977). Alternatively, a higher I-value could imply a greater admixture of large clasts, duricrust or bedrock.

The importance of the thermal data in this discussion lies in the pattern. In Kasei Vallis (fig. 2) thermal inertia is highest at the mouth; it decreases monotonically upstream. This is consistent with the wind streaks: the wind has effectively deflated the region at the Kasei Vallis mouth and left behind a deflation pavement or coarse sand. Such a surface composition is also consistent with the low solar albedo (A = 14%) at the mouth of Kasei Vallis.

In Ares the pattern is not so simple. Thermal inertia generally decreases upstream, except in the "big bend" region where it attains a local high of $I = 11 \cdot 10^{-3} cal/K \cdot s^{\frac{1}{2}} cm^2$. This same region corresponds to a low in solar broadband albedo (fig. 3) again suggestive of an area subject to aeolian deflation or coarse-grained sediment deposition.

Relating these thermal and albedo observations back to the morphology one finds the following correlations. Kasei Vallis is oriented directly into the regional wind. It is therefore subject to potentially intense aeolian abrasion. Kasei Vallis has a dramatic and consistent upstream decrease in thermal inertia and increase in solar albedo indicating a change from an erosional to a depositional wind regime. Finally, Kasei Vallis is the most profoundly grooved of all the large Chryse channels. It is here contended that these correlations are not fortuitous; rather, the Kasei Vallis grooves are etched by wind. In Ares Vallis the most intense aeolian sculpture would be expected in the high thermal inertia "big bend" region. A close look at the channel floor remnants in that area demonstrates that they are shaped as yardangs in response to up-channel winds.

One may conclude from this that medium-scale channel morphology; features such as groove, hills and etched terrain, are at the very least greatly modified by, and probably formed by, aeolian erosion.

References

Arvidson, R. E., E. Guiness, and S. Lee, Differential aeolian redistribution rates on Mars, Nature, 278, 533-535, 1979.

Baker, V. R., and R. C. Kochel, Martian channel morphology: Maja and Kasei Valles, J. Geophys. Res., 84, 7961-7983, 1979.

Cutts, J. A., and K. R. Blasius, Origin of Martian outflow channels: the aeolian hypothesis, J. Geophys. Res., 86, 5075-5102, 1981.

Kieffer, H. H., T. Z. Martin, A. R. Peterfreund and B. M. Jakosky, Thermal and albedo mapping of Mars during the Viking primary mission, J. Geophys. Res., 82, 4149-4291, 1977.

Lucchitta, B. K., Origin of Martian outflow channels: wind, water, mud, or ice?, Third Internat. Colloquium on Mars (abstract), 137-138, 1981.

Masursky, H., A. L. Dial, Jr., and M. E. Strobell, Martian channels - a late Viking view, NASA Tech. Memo. 82385, 184-187, 1981.

Thomas, P., and J. Veverka, Seasonal and secular variation of wind streaks on Mars: an analysis of Mariner 9 and Viking data, J. Geophys. Res., 84, 8131-8146.

Fig. 1. Global distribution of wind streaks on Mars (from Thomas and Veverka, 1979). Locations of Ares and Kasei Valles are indicated.

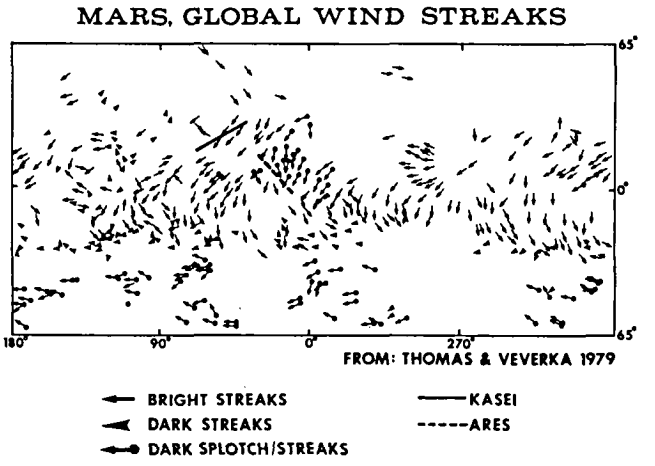


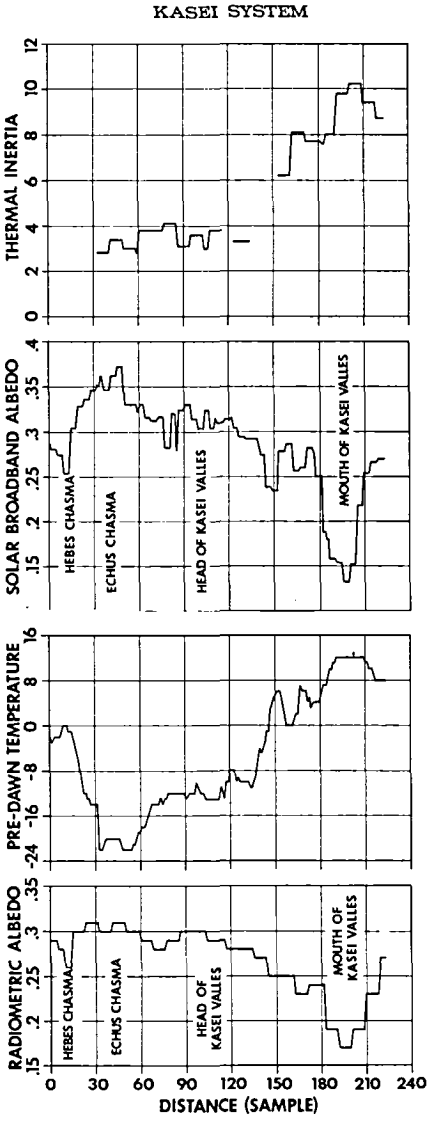


Fig. 2. Longitudinal profiles of Viking IRTM - data and solar albedo in the Kasei Vallis system.

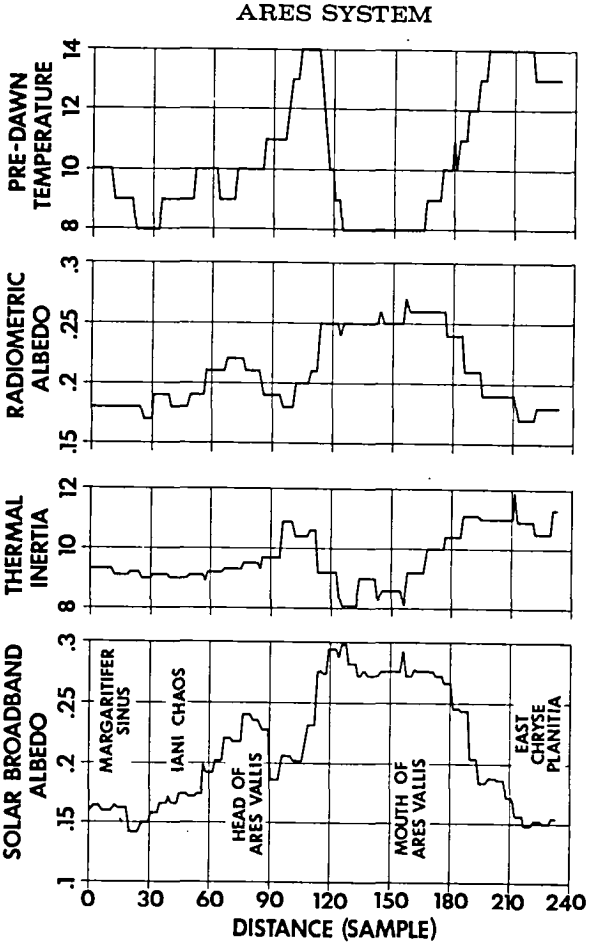


Fig. 3. Longitudinal profiles of Viking IRTM - data and solar albedo in the Ares Vallis system.

# CRESCENT-SHAPED PITS ON MARS

Dallas D. Rhodes, Department of Geology, Whittier College, Whittier, California 90608 (NASA Summer Faculty Fellow, Jet Propulsion Laboratory, Pasadena, California 91103) and
Tina Neal, Department of Geology, Arizona State University, Tempe, Arizona 85281

Crescent-shaped pits exist at a number of places on the martian surface. An excellent example of the crescent-shaped pits is located near -11, 178 (fig. 1). This area illustrates some of the characteristics of the pits. These features always occur in groups. In the area of figure 1, there are 32 distinct pits. At another site located 375 km southwest of Olympus Mons, there are more than 100 pits. The pits occur on generally smooth or grooved surfaces, suggesting fine-grained material. They vary considerably in size. The pits located in the vicinity of figure 1 have lengths (measured from the center line of the tips to the apex of the convex side) that range from 0.63-1.96 km. The widths (measured from tip to tip) vary from about 0.60-1.80 km. Pits seen at other locations are roughly comparable in size. The depth of the pits is unknown, but it appears to vary directly with size.

The origin of these features is uncertain. Four types of geomorphic features on Earth have a regular crescentic shape and might be analogs for the martian pits. These features are 1) various kinds of fractures and gouges produced by glacial erosion, 2) scour marks produced by flow separations, 3) crescentic hollows observed in the Arabian desert, fuljis, and 4) sand dunes.

The various kinds of crescentic marks produced by glacial erosion are unlikely analogs. They are orders of magnitude smaller than the martian pits and generally have a more open, or lunate form. Flow separations around obstacles are capable of producing crescentic hollows similar in shape to the pits. However, detailed examination of pictures of the martian pits does not reveal objects that might have initiated separations of the size required to scour the pits.

Fuljis appear to be very similar in form to the martian pits (fig. 2). These features are known only from the Nafud, the Great Red Desert of northern Arabia. They were first noted by W.S. Blunt (1880), according to Holm (1960). Lady Anne Blunt (1881) (as cited by Phillips, 1882) described the fuljis as "great horseshoe hollows" which are scattered over the surface. The area of the depressions varies from "an acre to a couple of hundred acres". The diameter of the largest depression measured was at least 0.4 km, and the maximum depth was reported to be 85 m. The origin of the fuljis is unclear from the reports of Phillips (1882) and Holm (1960), but the A.G.I. Glossary (Gary et al., 1972) definition indicates that the depressions are open spaces between closely packed barchan dunes. This interpretation appears to be hard to justify in

terms of what can be seen in figure 2. However, the morphology of the fuljis does seem to be very similar to that of the martian pits, and they should receive more study.

A fourth possibility is that the pits are barchan dunes that have had their form inverted. Topographic inversion could be accomplished by a three step process. First, barchan dunes are formed on a smooth, barren surface (fig. 3a). Second, the dunes were partially or completely buried (fig. 3b). A wind transported sediment is most likely to have engulfed the dunes because a more energetic process would probably have destroyed them. Fine-grained pyroclastic material is a possibility and is especially well suited for this model because it could be welded into a relatively resistant covermass. The third step in the process involves winnowing of the loose sand from the resistant covermass, leaving behind a partial mold of the dune (fig. 3c). Topographic inversion of dunes is not known to have occurred on Earth; therefore, this model is hypothetical. However, the similarity of the pits to a field of barchan dunes is remarkable. Furthermore, there is evidence of aeolian erosion (yardangs) in the areas where the pits are found, and most of the localities are associated with volcanic terrains.

Other possible explanations for the crescent-shaped pits can be conceived. They might be collapse features resulting from the loss of volatiles in the subsurface. The pits might also be incipient yardangs or features etched along existing rock structure by the wind (Ward, personal communication). Whatever the origin of the pits, they are widely distributed geomorphic features which merit further investigation.

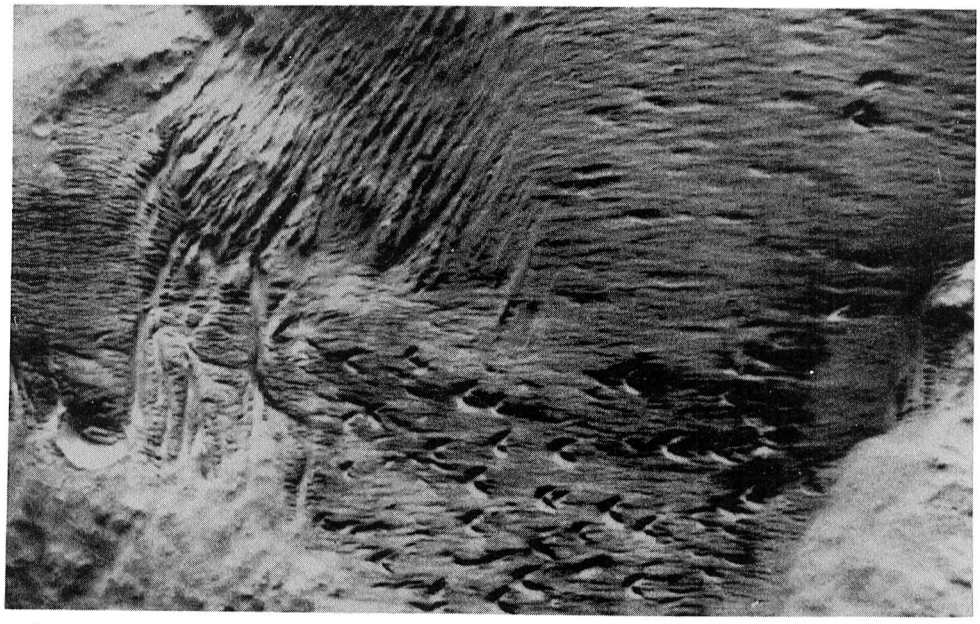

Figure 1. Crescent-shaped pits located near -11, 178. Light is from the top of the picture. (VO image 438S03.)

## REFERENCES

Blunt, A., 1881, A pilgrimage to Nejd, the cradle of the Arab race, Volume 1: London.

Blunt, W.S., 1880, A visit to Jebel Shammar (Nejd): Proceedings of the Royal Geological Society, v. 2, p. 81-102.

Gary, M., McAfee, R., Jr., and Wolf, C.L., ed., 1972, Glossary of geology: Washington, American Geological Institute, 805 p.

Holm, D.A., 1960, Desert geomorphology in the Arabian Peninsula: Science, v. 132, p. 1369-1379.

Phillips, J.A., 1882, The red sands of the Arabian Desert: Quarterly Journal of the Geological Society of London, v. 38, p. 110-115.

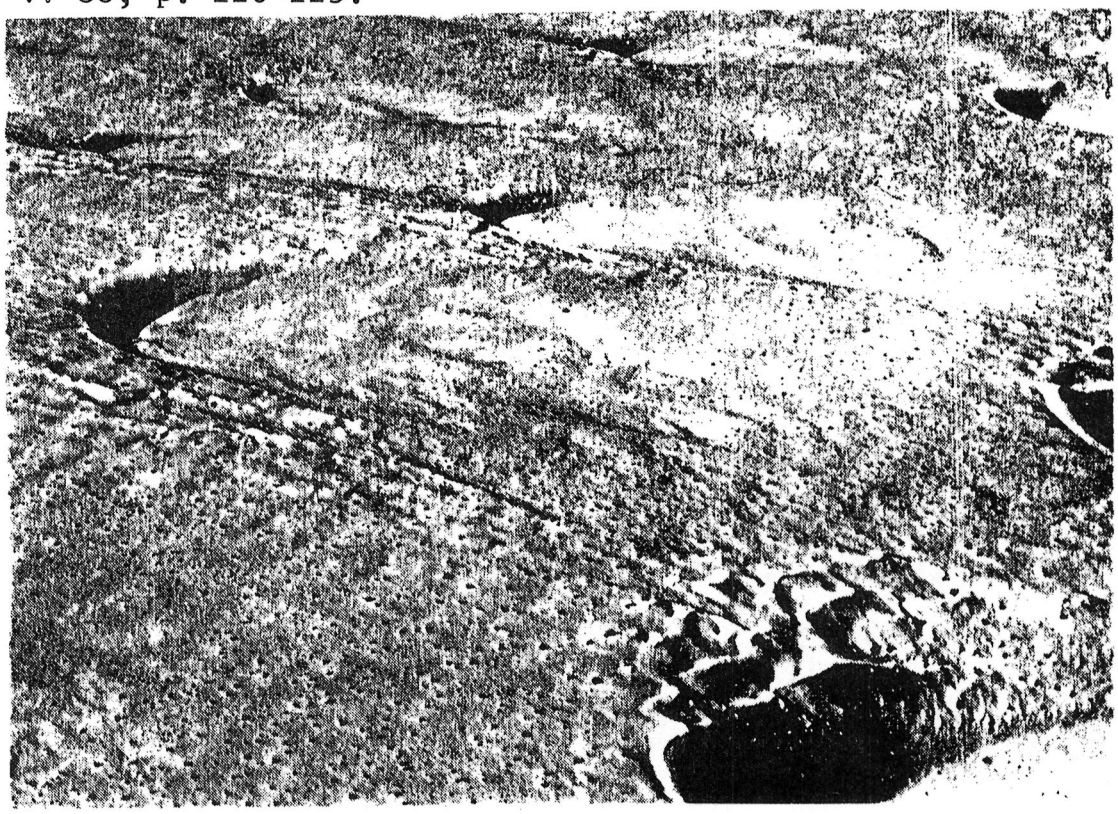

Figure 2. Fuljis, giant crescentic hollows in the Great Nafud Desert of northern Saudia Arabia. (Photograph by the Arabian American Oil Co.)

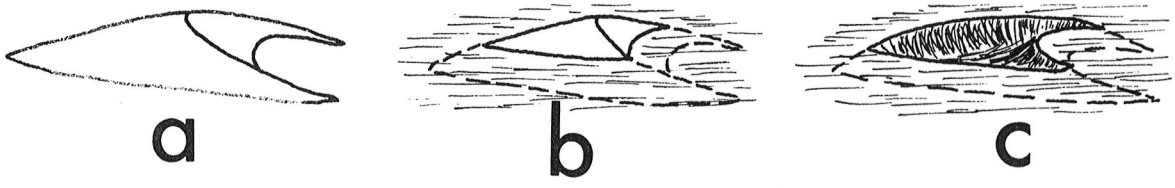


Figure 3. Model for the formation of inverted barchan dunes.

# EOLIAN EROSION OF POORLY CONSOLIDATED SEDIMENTARY BLANKETS ON MARS: A SMALL-SCALE TERRESTRIAL ANALOG

Brook, George A., Department of Geography, University of Georgia, Athens, GA 30602

A relatively young mantling deposit of debris surrounds both polar regions of Mars and extends towards the equator to latitudes 30° to 40° north and south. Soderblom et al. (1973) argue that the mantle was derived by wind erosion of sedimentary deposits in the polar regions. In addition, equatorward of 30° N and S are localized eolian or fluvial deposits such as those of the Chryse Planitia (Greeley et al. 1977, p. 4105). Many of these deposits have been molded by eolian deflation.

The Martian polar regions are characterized by pitted and etched terrains. Pits are closed depressions 0.5 to several tens of km across and up to 400 m deep which have abrupt walls. Sharp (1973) notes that in many areas the shapes and patterns of pits reflect either control by structures in the pitted blanket sediments, or some directional property of the eroding agent. In some areas, however, a lack of consistency in shape and arrangement is common. Etched terrain is an advanced stage in pit development. Expanded pits coalesce to produce large bedrock areas denuded of the overlying mantle. Although most common in polar regions etched terrain has also been described by Greeley et al. (1977) in the southeastern part of the Chryse Basin. Of particular importance is that wall recession in Martian pitted and etched terrains is apparently caused by an undermining process. Sharp (1973) suggests that undermining may result from the presence of a more consolidated surface layer. One possibility is that such a layer may be more consolidated because of a higher concentration of frozen volatiles.

Eolian deflation on marine beaches with a surface crust of salt-cemented sand called a salcrete (Yasso 1966) results in the formation of a micro topography similar to that in Martian pitted and etched terrain (Figs. 1 and 2). In beach sand deflation is concentrated in orthogonal and dendritic tension cracks which are thought to develop in the salcrete crust due to differential compaction of the underlying sand as it dries. Wind scours out the cracks to form small pits, intersecting linear troughs, and sinuous channels. In form, the sinuous channels, which are not continuous over long distances, closely resemble much larger channels on Mars (Fig. 1B). Schumm (1974) has suggested that many Martian channels may be modified sinuous tension fractures--observations in salcreted beach sand would suggest a similar conclusion. Deflation causes pits, troughs, and sinuous channels to grow and coalesce to form flat-floored, irregularly-shaped depressions one to several cm across. The depressions have steep to vertical walls due to undercutting of the salcrete layer by wind, small mesas and buttes capped by salcrete rise from their floors. Ultimately the original salcreted surface is replaced by a lower-level non-salcreted sand surface surmounted by wind sculpted yardangs. Observations on salcreted beach sand have shown that tension cracks control the shapes

of deflation hollows initially but that during later stages of erosion depression walls and mesa and butte walls are aligned either parallel or perpendicular to the predominant wind direction.

All stages in the deflation of salcreted beach sand have been identified at larger scale (km rather than cm) in pitted and etched terrains on Mars. The similarity of form suggests that these Martian topographies are indeed produced by deflation of weakly consolidated sediments capped by a slightly more consolidated layer. It also suggests that deflation operates in tension cracks some of which may have been produced by differential compaction of the sediments after deposition, others by tectonic processes. Evidence from salcreted beach sand indicates that distinct preferred orientations in pitted and etched regions may reflect tension crack geometry or prevailing wind directions depending upon the stage of erosion.

References

Greeley, R., Theilig, E., Guest, J. E., Carr, M. M., Masursky, M., and Cutts, J. A. (1977). Geology of the Chryse Planitia. J. Geophys. Res., 82: 4093-4109.

Schumm, S. A. (1974). Structural origin of large Martian channels. Icarus, 22: 371-384.

Sharp, R. P. (1973). Mars: South polar pits and etched terrains. J. Geophys. Res., 78: 4222-4230.

Soderblom, L. A., Kreidler, T. J., and Masursky, H. (1973). Latitudinal distribution of a debris mantle on the Martian surface. J. Geophys. Res., 78: 4117-4122.

Ward, A. W. (1979). Yardangs on Mars: evidence of recent wind erosion. J. Geophys. Res., 84: 8147-8166.

Yasso, W. E. (1966). Heavy mineral concentrations and sastrugi-like deflation furrows in a beach salcrete at Rockaway Point, New York. J. Sediment. Petrol., 36: 836-838.

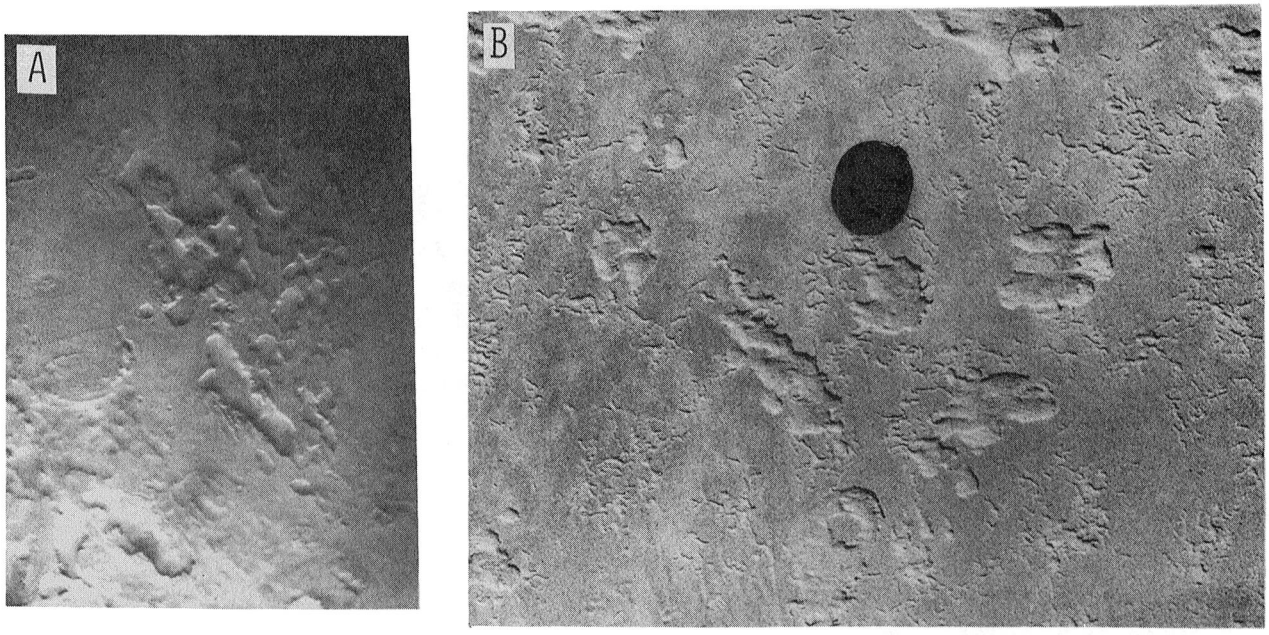


Fig. 1 Etched terrain at 79°S, 90°W (A) compared with morphologically similar deflation hollows in a salcreted beach surface, Hilton Head Island, South Carolina (B). Note the sinuous deflation channels in the beach surface. The Viking Orbiter image (A) covers an area of approximately 278 x 196 km. The camera lens cap shows the scale of (B).

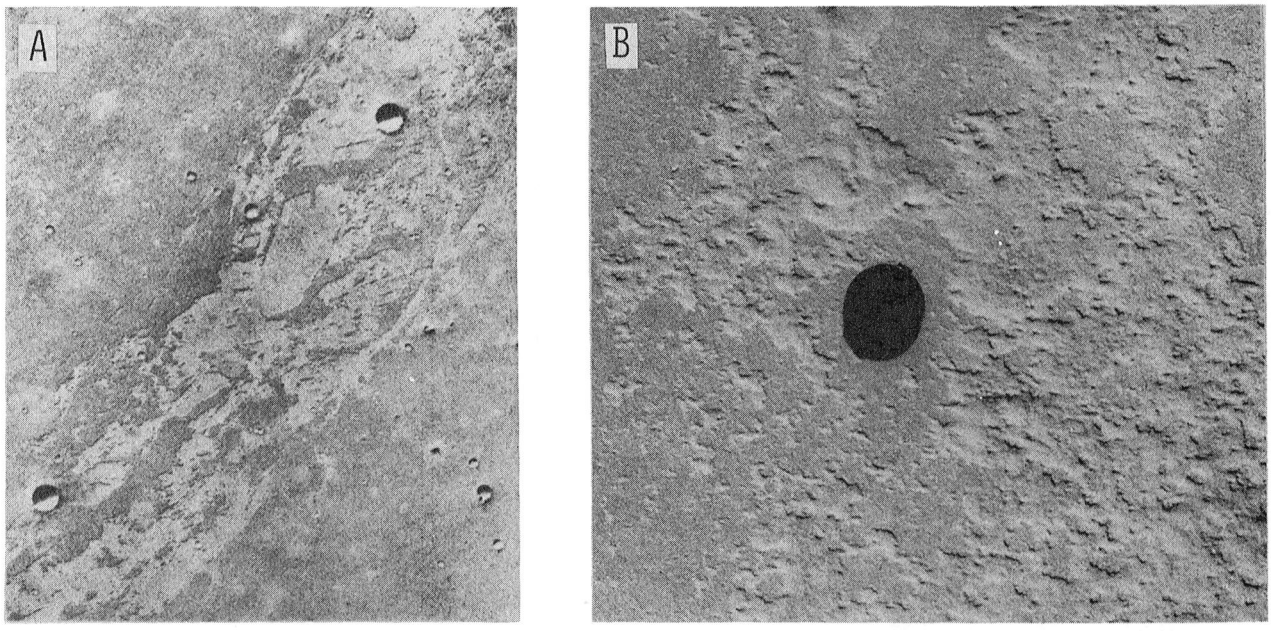


Fig. 2 Etched terrain in the Chryse Basin at 18°N, 35°W (A) compared with a deflated salcreted beach surface (B). The Viking Orbiter image covers an area of approximately 30 x 25 km. Pitted and lineated plains in the Iapygia region of Mars (Ward, 1979, Fig. 14) have an almost identical morphology, although at a larger scale, to that shown in (B).

# FIELD MODELING OF THE RESPONSE OF VARIOUS DESERT SURFACES TO THE LONG- AND SHORT-TERM EFFECTS OF THE WIND -- MARS APPLICATIONS

J. F. McCauley, M. J. Grolier, C. S. Breed, D. J. MacKinnon, and G. H. Billingsley, U.S. Geological Survey, Flagstaff, AZ 86001

The effectiveness of the wind as a geologic agent on Mars has been a subject of controversy since the earliest days of systematic telescopic study of the planet. Mariner 9 and Viking data have stimulated further arguments on its relative importance in landscape evolution. Much of this uncertainty stems from inadequate knowledge of the power of the wind in various desert environments on Earth. Theoretical studies based on modifications of Bagnold's (1941) classical theories fall short of truly satisfying explanations for features observed in both orbital and lander pictures of Mars. Wind tunnel experiments, including those on aggregates, also fail to provide comprehensive solutions to observations on apparent wind pattern trends, surface color variations, and the distribution of dunes on Mars.

One operational system that will help provide detailed quantitative data on wind behavior in different desert environments is being used by the U.S. Geological Survey's "Desert Winds Project." Almost 10 years ago a technological breakthrough occurred providing an opportunity to greatly augment our quantitative data base in desert geology. Satellite relay, data collection platforms (DCP's) coupled with electronic microprocessors became commercially available. These machines can accept, store, process, and transmit to and from satellites (preferably the geostationary type) data from arrays of various types of field sensors tailored to the needs of individual geoscientists. These automatic, solar-powered, low maintenance stations can be emplaced in remote desert areas of special interest, unlike the National Weather Service stations that are usually located at or near airports and that provide lower-resolution data. Investigations (mostly qualitative) of deserts in South America, North Africa, Central Asia, the southwestern United States, and particularly our work on the dust storm of 1977 in the U.S.A. (McCauley and others, in press) made clear the need for high-resolution geo-meteorological data, both for better resource management of the world's deserts and for possible Mars applications. Consequently a modest "Desert Winds Project", was established in 1979 as part of the Energy Lands and Climate Programs of the U.S. Geological Survey. The principal objective is a long term study of the geologic role of wind, relative to other processes, in the five distinctive desert regions of the southwestern United States, using non-attended DCP's coupled with an array of "off the shelf" meteorological devices. Three of these "Geomet" stations are now operational; they are located on the Navajo Reservation, on the Ranegras Plain west of Phoenix, and near Yuma. Each was positioned after extensive site studies and detailed geological mapping of the surficial geology around each station. Photo stations have been established on various surficial units around each station to provide long term, repetitive coverage of physical changes and their relations to the Geomet data (McCauley and others, in press). These machines currently measure windspeed and wind direction, including peak gusts, air and soil temperature, precipitation, and barometric pressure, and provide six-minute averages of each parameter around the clock. These data are automatically relayed each hour by way

of the Geostationary Orbit Environmental Satellite (GOES 4), to the U.S. Geological Survey Computer Facility in Flagstaff, Ariz., where the data can be analysed in near-real time. Two more stations are planned in the remaining distinctive desert regions of Arizona.

The U.S. Geological Survey computer facilities at Flagstaff record time histories of meteorological events for each station but emphasis to date has been on severe windstorms. The results of one such event at the Gold Spring Site, located amidst a large field of ENE-trending linear dunes on the Moenkopi Plateau, is shown in figure 1.

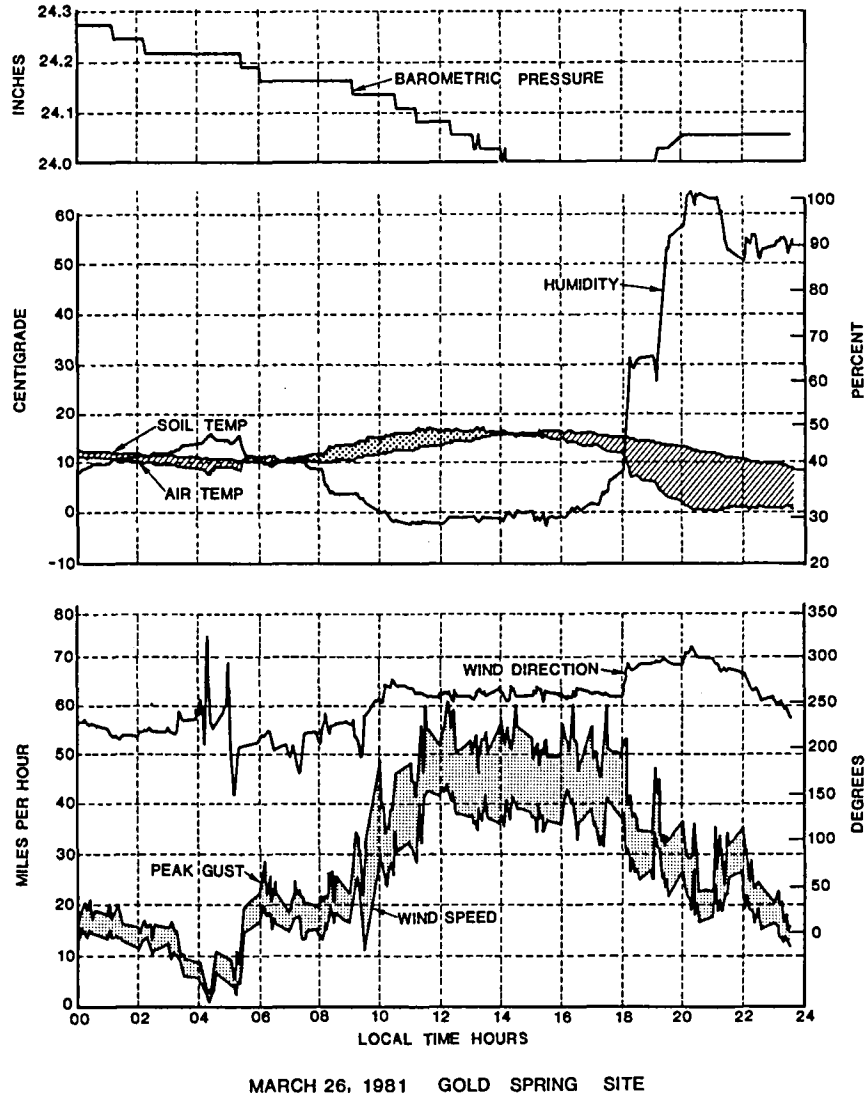


Figure 1. Results obtained at the Gold Spring Geomet station for March 26, 1981. The hatched area in the middle graph shows the soil temperature on excess of the air temperature, the dotted area shows the reverse situation. The dotted area in the lower graph shows the excess of the peak gusts over the six-minute average of the wind speed. According to the 3rd power law of sand transport it is these peak gusts that probably do most of the work of the wind.

Note that both the averaged winds and peak gusts were above 15 mph (except from about 4AM to 6AM) throughout the day; from 10AM to 4PM winds were generally above 40 mph from the WSW. A number of more intense wind storms of shorter duration have been recorded at the Vicksburg site, near Phoenix, as mentioned in a companion report (Krinsley and others, this volume). Analyses of quantitative meteorologic data, acquired over several years, will be combined with detailed geologic field studies and repetitive photographic coverage around each machine to provide a basis for comparing wind effectiveness in deserts of differing geologic and climatic types. The quantitative data base produced, unlike that of existing weather stations, should be of sufficient resolution and over a long enough time to contribute to a better understanding of desert processes in general and the role of the wind in particular.

Different patterns of wind activity and surface response are already evident in the data recorded from the different subtypes of the Arizona desert being monitored. These differences indicate the complexity of desert environments as a whole, and the difficulty of applying a single theoretical or experimental model of wind processes to desert landforms on Mars, where features seen undoubtedly also have formed in different climatic environments.

We are currently planning to retrofit all machines with a modified sand trap of the type described by Fryberger and others (1979). The eight directionally divided storage bins of his mechanical device will be replaced by a tipping bucket assembly like that used on our existing precipitation sensor. Thus the actual sand flux passing near the machine can be measured, transmitted automatically, and compared to in situ wind and other data seen in figure 1. We also have initiated abrasion experiments using "virgin" quartz grains mounted on two of our machines and will be adding the necessary equipment to the third (Krinsley and others, this volume).

References:

Bagnold, R. A., 1941, The Physics of Blown Sand and Desert Dunes: Chapman and Hall, p. 1-256.

Fryberger, S. G., Ahlbrandt, T. S., and Andrews, S., 1979, Origin, sedimentary features, and significance of low-angle eolian "sand sheet" deposits, Great Sand Dunes National Monument and vicinity, Colorado: Journal of Sedimentary Petrology, v. 49, no. 3, p. 733-746.

Krinsley, D. H., Marshall, J., McCauley, J. F., Breed, C. S., and Grolier, M. J., 1982, Production of fine silt and clay during natural eolian abrasion, this volume.

McCauley, J. F., Breed, C. S., Grolier, M. J., and MacKinnon, D. J., The U.S. dust storm of February, 1977, in Pewe, T. (ed.) Desert Dust: Geological Society of America Special Paper 186, in press.

SERRATED EOLIAN DEPOSITS IN CHINA'S NORTHWESTERN DESERTS AND THEIR COMPARISONS TO DARK SPLOTCHES ON MARS.

Farouk El-Baz and L. S. Manent, National Air and Space Museum, Smithsonian Institution, Washington, D.C. 20560.

Landsat images reveal several areas of dark, serrated-edge deposits in eastern Turpan depression and western Dzungarian Desert basin, both in the province of Xinjiang, China (Fig. 1). These deposits are the results of eolian action, where the wind erodes and redistributes enormous quantities of debris in this northwestern part of China. Such deposits are similar in overall appearance to the jagged-edged dark splotches photographed by Mariner 9 and Viking spacecraft. Comparisons are here made to identify the causes of the serrated outlines and their possible relationship to local topography.

The Turpan depression is an intermontane, interior drainage basin with the Bogda Mountains to the north and the Kuruktag Mountains to the south. East of the depression is Sand Mountain, a 2,500 $km^2$ dune field with various types of dunes. Lake Aydingkol is located at the southernmost part of the depression and includes the lowest point in China, 154 m below

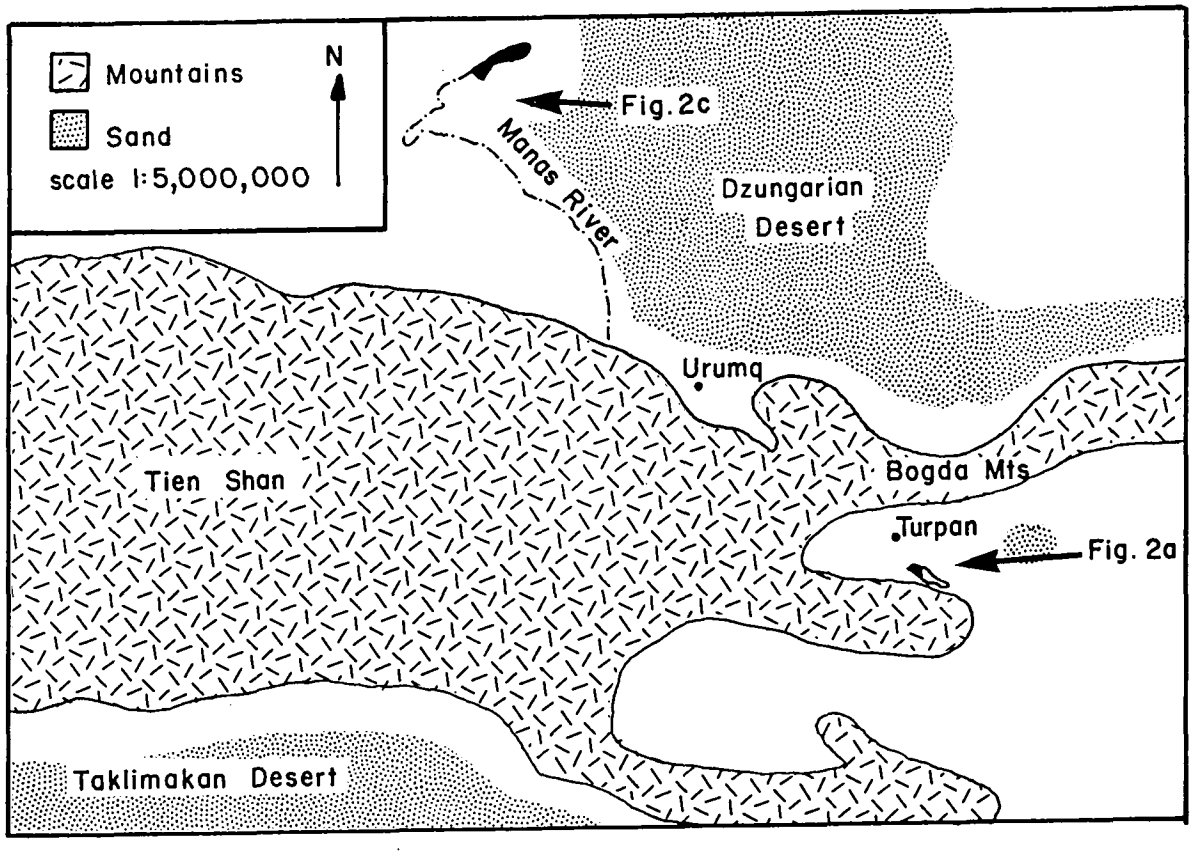


Figure 1. Map of part of Xinjiang province, northwestern China, showing the location of the two regions with dark streaks and splotches.

sea level (Xia, 1980). South of Lake Aydingkol is a field of east-west oriented yardangs (El-Baz, 1980). The wind direction, measured at Turpan is east-northeast.

Dark streaks and splotches concentrated in the southeast corner of the Turpan depression, particularly just west of Sand Mountain (Fig. 2a) were measured from computer-enhanced Landsat imagery. The largest of these splotches is composed of several streak segments. Individual streaks measure between 2 km to 10.5 km long and 0.1 km to 1.43 km wide. These streaks are present on the lee side of patches of agriculture, where the height of poplar trees, usually used as wind breaks (El-Baz, 1980), does not exceed 20 meters.

The Turpan serrated deposits are particularly similar to dark splotches west of Solis Planum in the Thaumasia Quadrangle of Mars (Fig. 2b). In the latter, dark splotches and streaks also occur in the lee of topographic obstacle. The obstacles in this case are small craters, which makes it similar to the case of wind streaks in the lee of craters and knobs in the Cerberus region (El-Baz et al., 1979; El-Baz and Maxwell, 1980; Chaiken et al., 1981). Some of the streaks and splotches start at points where the resolution of the images is inadequate to discern any obstacles.

In the Dzungarian basin, which is located north of the Tein Shan range at N45°25' E86°20', an area just southeast of Manas Lake contains splotches and streaks (Fig. 2c). East of the streaks is a very large dune field composed of various types of dunes. The wind direction in this region, as deduced from corrasion features and streak orientation, is to the southeast. Here, the streaks also appear to form in the lee of small obstacles. They vary in length from 1 km to 13 km and in width from 0.1 km to 1.2 km. These dark areas are similar to those east of Arsia Mons in the Phoenicis Lacus Quadrangle of Mars (Fig. 2d).

From this preliminary study it appears that in the Chinese deserts, serrated-edge eolian deposits have developed in response to obstacles in the way of the wind. Minor topographic rises, smaller than the resolution elements of the Viking images of Mars may have similarly been responsible for the generation of serrated-edge dark splotches on Mars.

References

Chaikin, A.L., Maxwell, T.A. and El-Baz, F. (1981) Temporal changes in the Cerberus region of Mars: Mariner 9 and Viking Comparisons. Icarus: 45, p. 167-178.

El-Baz, F. (1980) Journey into Northern China. Explorers Journal: 58, p. 60-65.

El-Baz, F. and Maxwell, T.A. (1980) Comparison of wind streak form in Egypt and on Mars. Reports of Planetary Geology Program - 1980, NASA TM-82385, p. 292-294.

El-Baz, F., Breed, C.S., Grolier, M.J., and McCauley, J.F. (1979) Eolian features in the Western Desert of Egypt and some applications to Mars. J. Geophys. Res.: 84, p. 8205-8221.

Xia, X.C. (1980) Turpan Basin. Xinjiang People's Press, (in Chinese), p. 5.

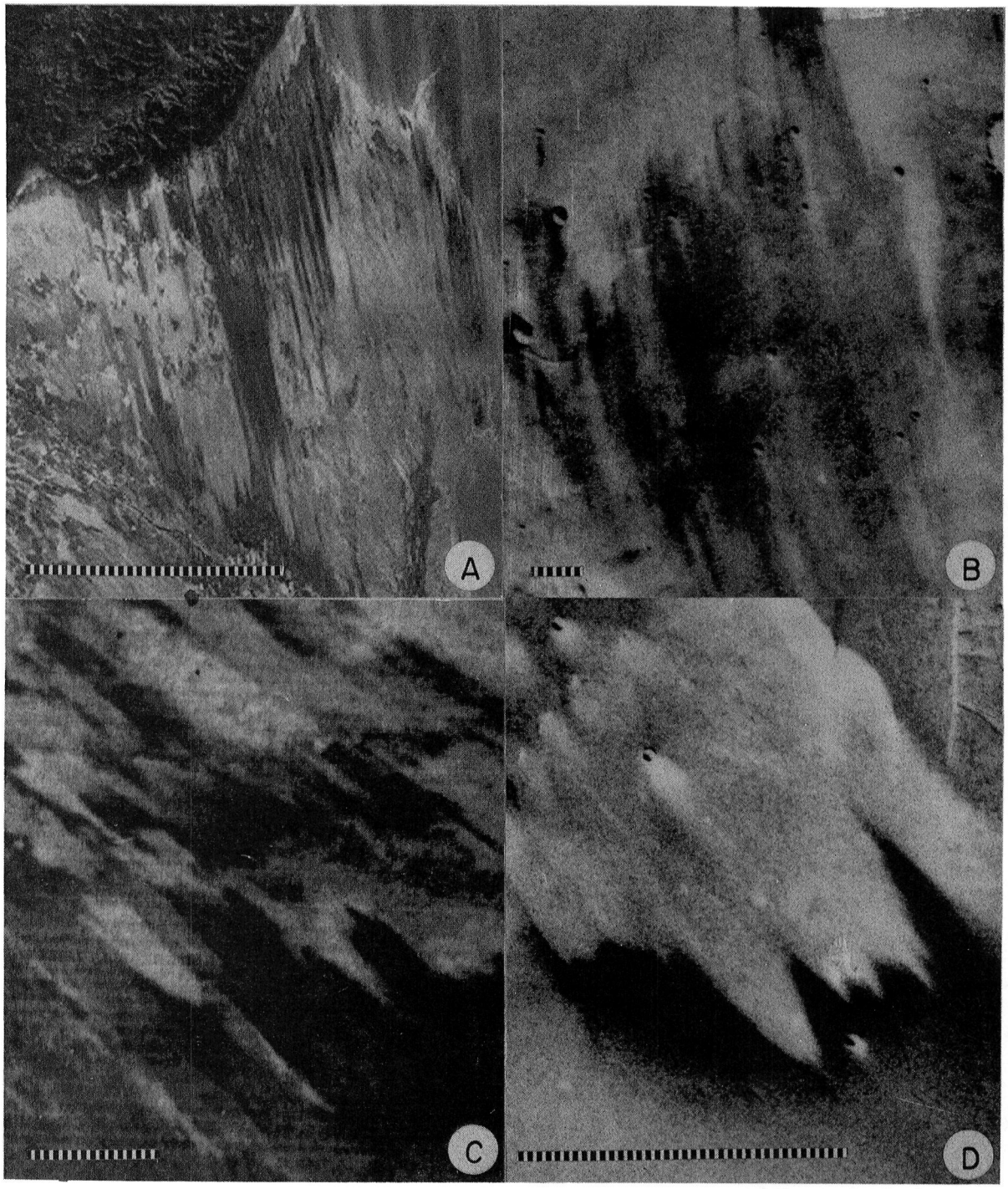


Figure 2. Comparison of wind streaks and splotches in deserts of northwestern China and on Mars: (A) Streaks emanating from a sand field in the Turpan depression; (B) Streaks west of Solis Planum on Mars; (C) Serrated dark splotches southeast of Manas Lake on the western edge of the Dzungarian Desert, northwestern China; (D) Splotches east of Arsia Mons on Mars. Scale bars 10 km.

# DUNE FORMS IN THE GREAT SAND SEA AND APPLICATION TO MARS.

Farouk El-Baz, National Air and Space Museum, Smithsonian Institution, Washington, D.C. 20560 and Monique Mainguet, Laboratoire de Géographie Physique Zonale et d'Études des Paysages en Roches Sédimentaires, Université de Reims, Reims, France.

The Great Sand Sea was so named by the German explorer Gerhard Rolfs who explored parts of it in 1874 and described it as sand dunes with sand in between, where at distances of 2 to 4 km "one sand ridge followed the other, and each was over 100 m high" (Bagnold, 1935, p. 172-173).

As measured by Gifford et al. (1979) the areal extent of the part of Great Sand Sea in the Western Desert of Egypt is 72,000 $km^2$. However, several additional arms of the sand sea in the same desert may also be considered part of it. These include the sand fields of Sitra (2,100 $km^2$), El-Quss Abu Said (800 $km^2$) and Uweinat (31,500 $km^2$), giving a total of 106,400 $km^2$.

The Great Sand Sea begins in the northern part of the Western Desert just south of El-Diffa plateau. It continues southward for 600 km before the dunes are deflected by the Gilf Kebir plateau and associated highs (Fig. 1a). In the northern part there are few sand-free areas. Numerous 2-10 km long crested linear and sinuous dunes arise from a blanket of sand (Fig. 1b). The distance between the crests of these dunes is usually less than one kilometer.

In the southern part of the Great Sand Sea, large and gently sloping whaleback dunes abound. These are usually over 20-70 km long and 2-5 km wide. They are often separated by essentially sand free corridors several kilometers in width (Fig. 1c). Bagnold (1935, 1941) noted that these dunes are usually overlain by crested linear dunes or seifs. He correctly recognized that the latter move along the spines of the relatively static whalebacks. This led him to the assumption that the whaleback dunes became so large that they no longer could move, and thus, were rendered static by their own bulkiness.

We propose, however, that while the seifs on their crests are depositional features, the whalebacks are erosional landforms. This proposal is based on the following observations:

1. The width of the interdune areas increases nearer the southern edge of the Great Sand Sea (Fig. 1c).
2. Sand is transported in the interdune corridors as indicated by a thin sheet of sand that ends at the southern termination of the dunes (Fig. 1c), and less abundantly by barchan and parabolic(?) forms in the interdune corridors (Fig. 1d).
3. Accumulations near and on top of the whalebacks resemble bundles of dunes in the Qattara area north of the Great Sand Sea and in the Fachi-Bilma sand sea in Chad-Niger (Fig. 2, left).
4. Nearly parallel corridors between high ridges are easily formed by wind erosion, as in the case of corrasion features and yardang fields (Fig. 2, right) in both solid rock and lacustrine sediments.

Our proposal is explained by the following model. Sand, over 100 m in thickness, is deposited during fluvial periods in a low basin; fluvial periods result in the generation of most of the sand. During dry periods the sand is moved by the wind which creates the crested dunes of the

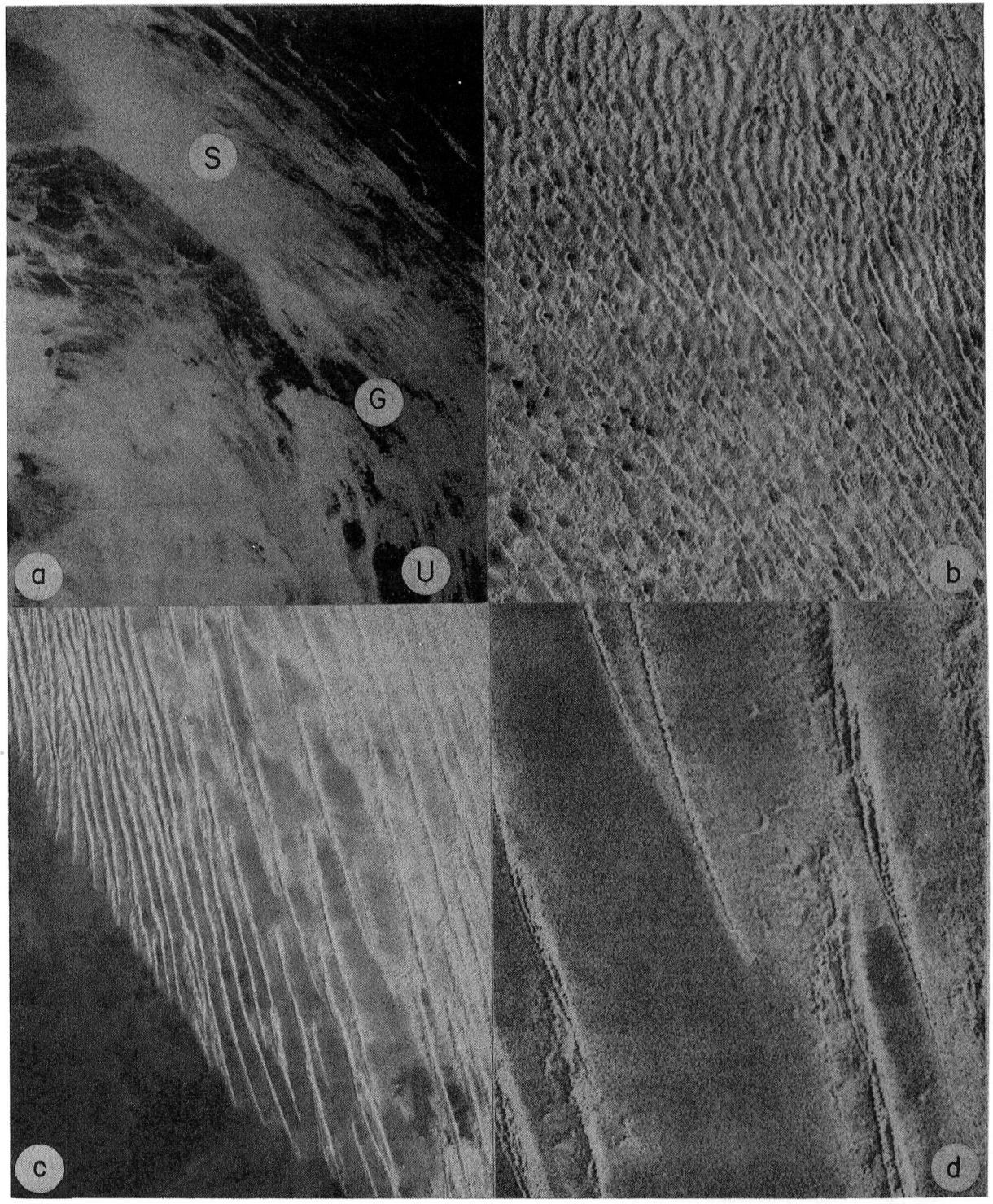


Figure 1. (a) Great Sand Sea, S, Gilf Kebir plateau, G, and Gebel Uweinat, U, in the Western Desert of Egypt; (b) Northern part of Great Sand Sea; (c) Southwestern edge of Great Sand Sea; (d) Enlargement of barchans (lower left corner) and parabolic(?) forms (right center) in the interdune corridors.

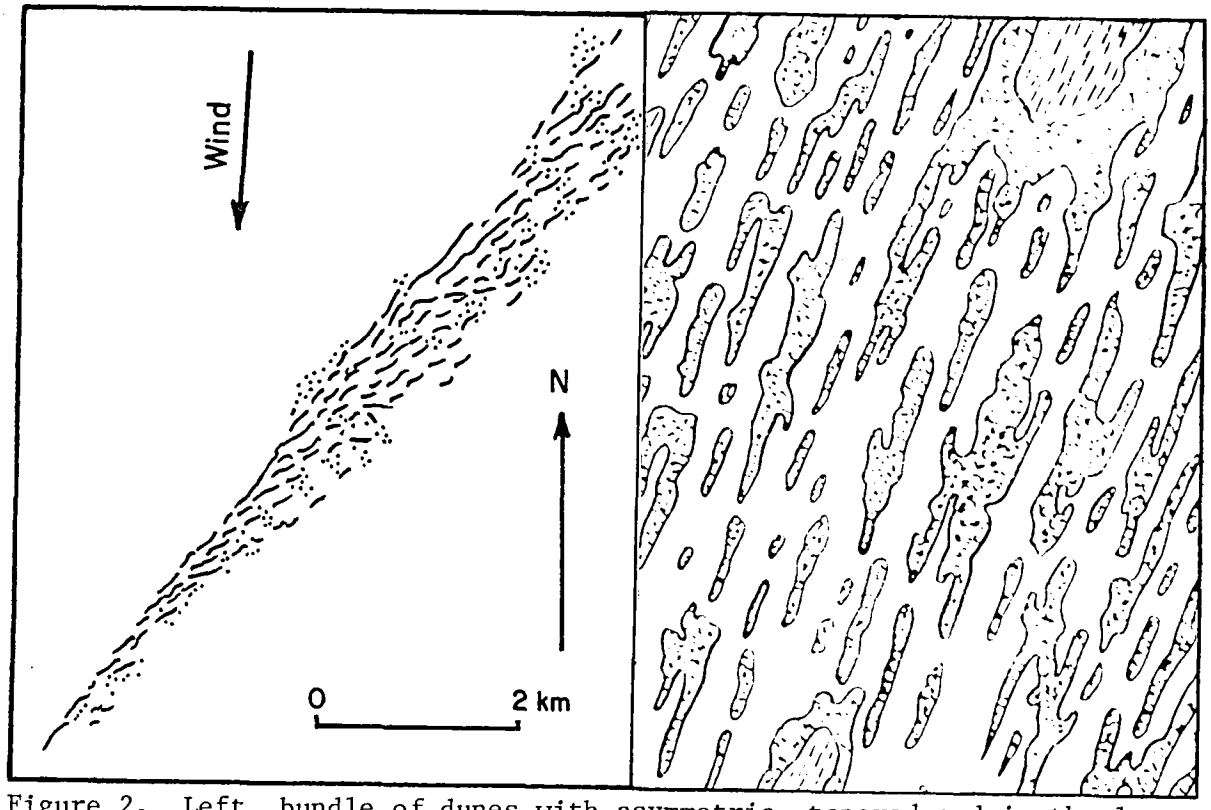


Figure 2. Left, bundle of dunes with asymmetric, tapered end in the lee of the wind (from Mainguet and Callot, 1978). Right, yardangs and corridors in the Lop Nor region (from Hedin, 1905, p. 61).

northern part of the Great Sand Sea. In the southern part, where the sand deposit is thinner the wind more easily erodes the sand and creates the nearly parallel corridors leaving whaleback-like ridges. The transported sand forms the crested, shifting dunes, and the whaleback ridges remain static except for the loss of sand.

This model may be applicable to dune forming processes on Mars. Areas of eroded, loose deposits in the equatorial region of Mars display ridges separated by corridors in a similar fashion. Such dune-like forms may have also formed by wind erosion rather than wind deposition.

References

Bagnold, R.A. (1935) Libyan Sands. Hodder and Stoughton, London.
Bagnold, R.A. (1941) The physics of blown sand. Methuen, London.
Gifford, A.W. et al. (1979) NASA SP-412, v. 2, p. 219-236.
Hedin, S. (1905) Journey in Central Asia 1899-1902, GSSA, Stockholm.
Mainguet, M. and Callot, Y. (1978) Erg de Fachi-Bilma, CNRS, Paris.

# EOLIAN PROCESSES IN ICELAND'S COLD DESERTS

Michael C. Malin and Dean B. Eppler, Department of Geology, Arizona State University, Tempe, AZ 85287

Strong, nearly constant winds, abundant sand- and silt-sized particles of basaltic composition, and extremely limited erosion by runoff make Iceland's volcanic deserts excellent locations to quantify rates and vigor of various eolian processes, particularly those which may also operate on Mars. To examine these processes, long- and short-duration exposure test sites were established in Iceland. Two specific processes were actively studied: 1) eolian abrasion of volcanic materials by volcanic materials, and 2) establishment of reg surfaces (concentrations of stones at the surface).

## Eolian Abrasion

Three test sites were established: 1) Dyngjufjalladalur (west of Askja), 2) Vaðalda west flank, and 3) Vaðalda dunes (west of Vaðalda). Site 1 was selected on the basis of large scale ventification of m-sized blocks of palagonitic breccia. Site 3 was selected as a site of maximum abrasion, as the dune surface is active (although the dune mass itself appears fixed). Site 2 was selected as a site intermediate in sand supply, surface roughness, and because it most resembled in appearance the Viking Lander 1 site. Each test site includes the following materials: 1) a 160 cm plexiglass rod, to measure height of maximum abrasion and direction of most erosive wind-blown material; 2) sand collectors at 7, 14, 21, 35, 80, and 160 cm height, facing the direction of principal wind as measured in the field during the preceeding 24 hours; 3) three sand collectors at 21 cm height facing 90°, 180°, and 270° to the principal wind direction; and 4) abrasion targets. Abrasion targets were 3.5 cm x 3.0 cm x 0.5 cm slabs of basalt, welded, and non-welded Bishop Tuff. Each slab was polished, and then one-half was "pre-abraded" by commercial sandblasting, in order to examine variations in abrasion owing to surface fracture characteristics. Targets were deployed on wooden posts at heights of 7, 14, 21, and 35 cm, facing into and at 90°, 180°, and 270° with respect to the principal wind direction.

Sand was removed from the collectors after 12 and 23 days; short duration targets were removed after 23 days and replaced with long duration targets. These shall remain in place for several years. Wind speed and direction observations were made when in residence at each site ($\sim$ 5 days at each site). Samples of native materials are still in transit. Thus we cannot as yet report on flux rates. However, we transported the abrasion targets in our gear and can report on preliminary findings.

1) Control targets, prepared exactly as were those to be deployed, transported to Iceland, but not deployed, showed mass changes of $\sim 1.6 \times 10^{-3}$ gm/cm$^3$ for basalt, $2.8 \times 10^{-3}$ gm/cm$^2$ for welded tuff, and $9.5 \times 10^{-3}$ gm/cm$^2$ for non-welded tuff, principally reflecting unbound water not totally released during heat treatment applied during sample preparation.

2) No systematic mass loss (either as function of height or wind azimuth) was detected in 21 days exposure on any sample at Site 1. Field observations showed that, even in winds gusting to 22m/sec(50 mph), little

sand was available for transport. Coarser particles were moved, however rarely, and particles to 5 mm were collected at heights of 1.5m. Individual impact sites on polished surfaces will be examined using SEM to study the role of occassional, highly energetic impacts in surface abrasion.

3) Very slight systematic mass loss was seen at Site 2, principally from the non-welded targets. Greatest losses were from the 0° or principal wind facing surfaces, followed by the 90°, 270° and 180° surfaces, in the ratio 1:0.6:0.4:0.2. This is consistant with field estimates of wind directions and strengths. This trend was displayed by all three materials, although the magnitude of the mass losses for the basalt and some of the welded tuff specimens were within the statistical error associated with the control group, and cannot be reported without caution. However, the non-welded samples at 0°, 90°, and 270°, all displayed losses at least 2½ times any of the controls (at 35 cm height) and increasing mass loss with decreasing height showed strong correlation. Maximum mass loss was $8.3 \times 10^{-2}$ gm/cm$^2$, or approximately 0.7 mm in 22 days.

4) Greatest changes were seen at Site 3, where, over observational periods extending from 24 hours to 5 days, mean wind speed was 5 m/sec (∿10 mph) blowing for 20 hours/day. Saltation was observed at least 10 hours/day. Systematic changes with azimuth were somewhat less clear than at Site 2, but correlation of mass loss with height was stronger. Greatest mass loss (non-welded tuff at 7 cm) was 0.099 gm/cm$^2$ or about .83 mm in 24 days. Maximum basalt abrasion was about 30 μm in 24 days.

Surface Concentration of Stones

In order to examine the processes by which stones larger than those that can be wind-transported became concentrated on surfaces, several test sites were established. At each site, a 1-m$^2$ area was cleared of surface stones, each being measured, and staked for future reference. These areas will be used to observe inwashing of stones from up-hill slopes and/or deflation of fines to establish new concentrations. A 50 cm x 50 cm x 50 cm trench was dug at each site to give stratigraphic control on abundance of large stones and fines. Selected stones were painted and placed at specific depths as these trenches were filled: we hope to examine differential frost heaving of coarser fragments in these plots. These sites are long duration experiments.

However, during the emplacement of several sites, wind conditions and abundant saltating sand made possible "real-time" observation of the creation of stone concentrations. It was clear that a feedback mechanism was at work, creating an equalibrium surface. The spacing and concentration of stones (and the removal of inter-stone fines) depended on the size and height of stones and the path of the saltating sand on its downward trajectory. In these observations we find good field evidence in support of ideas presented by Chepil (Soil Science 69, 149, 1950). It is possible these observations will allow us to asses the wind regime under which the Viking Lander 1 and 2 site stone concentrations were established. Preliminary calculation suggests a wind speed lower than the present threshold velocity. This may mean that the stone spacing (reflecting the distribution of fines) may date from a period when the atmospheric pressure was greater.

Seasonally-Reversing Transverse Dunes in the California Desert: An Analog for Some Dunes on Mars

Smith, Roger S. U., Department of Geological Sciences, University of Texas at Austin, Austin, TX 78712

Some transverse dunes reverse their slip-face orientations from season to season and exhibit little net migration over tens of years. Preliminary investigations indicate that these dunes are morphologically distinct from non-reversing transverse dunes and that both sorts occur on Mars, each probably representing different wind conditions.

Reversing transverse dunes are long, narrow and straight to gently curved ridges arranged parallel to one another, with local forked junctions where a single ridge splits into two parallel ones. Their steep sides are roughly symmetrical below the reversing crest and these dunes seem to develop best on immobile substrates. Migratory transverse dunes differ in that their ridges are stubbier, less parallel and scalloped to cuspate in plan with fewer branches and asymmetrical in cross section. Migratory transverse dunes may break up into well-developed barchans, but their reversing cousins break up into narrow, steep-sided ridge segments that may migrate but lack barchan horns.

The behavior of reversing transverse dunes can be documented from long-term air-photo records supplemented by field observations. Preliminary evaluation of a 34-year record from Cadiz Valley, CA, and of a 29-year record from Stovepipe Wells, Death Valley, CA, indicates that southeast-facing slip faces develop during winter and spring but reverse to northwest-facing during summer and fall. Along the east side of Cadiz Valley, the net migration rate of ridges about six meters tall has been less than one meter per year, sense varying, but individual, broken-up segments of ridges about two meters tall have moved southeast at four to eight meters per year. Along the southwest margin of the Stovepipe Wells field, dunes have averaged up to five meters per year of southeastward migration and up to two meters per year northwestward along the field's northeast margin, producing net contra-clockwise ridge rotation of 0.004 to 0.005 radians per year. Clearly, these dune ridges will become less and less transverse to wind with time at their present rate of roation and would become sharply oblique to wind within a few hundred years. It is not known how oblique to wind they now are, how old they are or what forms they may evolve into. Although no wind data are available from nearby stations, nearby longitudinal dune features at both Cadiz and Stivepipe Wells suggest a westerly wind component oblique to the transverse ridges, but its effect and significance remain problematic in the absence of eastward or northeastward ridge advance.

Classic star dunes occur south of the Stovepipe Wells dunes and incipient ones occur north of the Cadiz Valley dunes. Active or fixed forms similar to those of reversing dunes seem common within some fields of star dunes, consistent with the notion that star dunes represent a balance between opposing winds of comparable intensity. In some places, the nodes where dune ridges fork seem to represent incipient star dunes, but an evolutionary sequence from small to large forms has not been demonstrated.

Preliminary inspection of Viking imagery suggests that ridges arranged like the reversing transverse dunes in the California desert occur along the margins of some martian dune fields, where ridge spacing gets distinctly narrower than in the fields' interiors. At a local crest-to-crest spacing of less than 0.5km, ridge pattern can be resolved but not morphology, and these features are substantially larger than the California ones (spacing less than 0.1km). The linearity and forking of larger transverse ridges in some fields' interiors may likewise represent dune reversal, perhaps on time scales longer than seasonal.

# PRODUCTION OF FINE SILT AND CLAY DURING NATURAL EOLIAN ABRASION

D. H. Krinsley and J. Marshall, Dept. of Geology, Arizona State University, Tempe, AZ 85287; J. F. McCauley, C. S. Breed, and M. J. Grolier, U. S. Geological Survey, Flagstaff, AZ 86001

Well rounded grains are characteristic of eolian materials in large, hot deserts, and abrasion experiments have demonstrated that rounding occurs rather rapidly (Kuenen, 1960; Krinsley, unpublished information). During recent years, we have studied the surface roughness or texture of eolian grains collected from the large deserts of the world (e.g., Margolis and Krinsley, 1971). Very few fresh abrasion features were noted, even on grains collected from dunes that migrate about 2.5 m per year in the Western Desert of Egypt (Breed and others, 1979). Cleavage plates and fractures showing massive overlays of precipitated silica are generally observed. Kuenen (1960) has shown that damage to sand abraded in an eolian regime falls off rapidly as roundness increases, and that polished grains are virtually immune to damage; if so, the highest rate of abrasion must occur during the initial stages of transport. We have formulated some ideas about differences between terrestrial and martian abrasion rates and particle surface textures, based on laboratory simulations (Greeley and others, 1974; Krinsley and others, 1979; Williams, 1981); thus information about the rates at which natural surface textures develop on Earth might permit us to model natural martian surface comminution and the resulting size, shape and amount of debris produced.

Although abrasion processes have been simulated in the laboratory, the abrasion of 'virgin' quartz particles in a natural eolian regime does not appear to have been studied. We therefore placed crushed Brazilian sand-size quartz particles in a natural eolian environment where wind velocity and direction, precipatation, and other meteorological parameters that affect eolian processes are being monitored by the U.S. Geological Survey's Desert Winds Project (McCauley and others, this volume and in press). Quartz particles with diameters of 5000, 2000, 1000, 500, 250, 125, and 60 μm were mounted on anodized aluminum plates and attached to the Desert Winds Geomet Station at Vicksburg, Arizona at elevations of 30 cm and 212 cm above ground level on May 28, 1981. These grains were not free to saltate and self-abrade. However, our experiments permitted us to study damage on surfaces oriented in different directions with respect to the major wind direction, and to retrieve single grains after they had been subjected to natural conditions for given periods of time.

This first experiment revealed definite eolian abrasion, probably as a result of a severe windstorm that struck the area on July 10, 1981. Unfortunately, the meteorological data for that day, though recorded, were lost in satellite transmission, but eyewitness accounts of high winds estimated in excess of 150 km per hour include reports that the roof of a nearby house was blown away. Field observations following this storm indicate that coarse sand grains as large as 0.8 cm in diameter were moved during this event. Another less violent windstorm on August 8 reached peak gusts recorded at 140 km per hour, with average wind speeds in excess of 80 km per hour for 36 minutes. Some of the mounted grains, particularly those

near the ground, were blown off their mounts by the wind during the July 10th event; some that remained were removed by the authors on July 22, 1981 and studied with scanning electron microscope (SEM). Most of the abrasion observed on the grains removed for SEM study was probably caused by the particle flux generated by the windstorm on July 10. The extremely high velocity of the wind, though occurring over a fairly short period of time, appears to have been every effective. Perhaps it is the infrequent high speed winds of such relatively rare events that produce most of the abrasion effects observed on sand grains from desert environments.

Kuenen (1960), and Krinsley and Takahashi (1962) reported that eolian abrasion in the laboratory is initiated on edges of irregular quartz grains and then spreads over their entire surfaces. Our results indicate that the same process prevails in nature. Edges of grains that were oriented directly into the prevailing wind were most heavily abraded, while edges oriented in other directions were abraded to a lesser degree. Grains that were mounted above the saltation curtain (212 cm above ground level) were the least abraded. Those mounted within the saltation curtain (30 cm above the ground) were more heavily abraded. Abrasion generally decreased with decreasing grain diameter. The material produced is mostly the size of fine silt and clay as determined from SEM photographs of particle edge-abrasion.

Textural features observed include conchoidal fractures, upturned eolian plates, (Krinsley and Doornkamp, 1973) and lateral-vent chipping (Lawn and Wilshaw, 1975). The last results from impact by sharp indenters. Binocular-microscope study of the coarse sand-size material collected around the Vicksburg site shows most of the windblown debris to be quite immature and angular, which explains the apparent absence of Hertzian fractures which are characteristic of round indenters (Marshall, 1979). Lateral-vent chipping appeared singly on original flat fracture surfaces that were oriented toward the wind. This feature was also occasionally found on the edges of abraded ridges in association with upturned plates and conchoidal fractures. It should also be noted that large areas on the grains away from edges were completely smooth and had suffered no abrasion.

McKee and others (1979) suggest that single impacts would produce both silt- and clay-size particles. Results of our experiment indicate that initial abrasion on irregular, sand-size targets produces clay-size particles in much greater abundance than coarser, silt-size debris. In addition, McKee and others (1979 and some unpublished data) show that after a surface has been roughened, most of the particles that are removed during abrasion are of clay size. If such is the case with basalt and other rocks and minerals characteristic of the martian surface, it would help to explain the apparent predominance of fine particles on Mars. Stewart and others (1982, this volume) suggest that the transfer of fine particles to targets during impact reduces the amount of abrasion and may even cause an increase in mass of the impacted surface. Thus more surface protection may occur on Mars than on Earth, resulting in a lower erosion rate on the martian surface.

References:

Breed, C. S., McCauley, J. F., Grolier, M. J., and Witbeck, N., 1979, Eolian depositional features in the western Desert of Egypt: comparison with Mars: National Aeronautics and Space Administration Technical Memorandum 80339, p. 282-285.

Greeley, R., Iversen, J., Pollack, J., Udovich, N., and White, B., 1974, Wind tunnel studies of Martian aeolian processes: Proceedings, Royal Society of London, p. 331-360.

Krinsley, D. and Takahaski, T., 1962, The surface textures of sand grains, and application of electron microscopy: Science, v. 135, p. 923-925.

Krinsley, D. and Doornkamp, J., 1973, Atlas of Quartz Sand Surface Textures: Cambridge University Press, Cambridge, 91 p.

Krinsley, D., Greeley, R. and Pollack, J., 1979, Abrasion of windblown particles on Mars-erosion of quartz and basaltic sands under simulated Martian conditions: Icarus, v. 39, p. 364-384.

Kuenen, Ph. H., 1960. Experimental abrasion. 4. Eolian action. Journal of Geology, v. 68, p. 427-449.

Lawn, B. and Wilshaw, R., 1975, Review - Indentation fracture: principles and applications: Journal of Material Science, v. 10, p. 1049-1081.

Margolis, S. and Krinsley, D., 1971, Submicroscopic frosting on eolian and subaqueous quartz sand grains: Geological Society of America Bulletin, v. 82, p. 3395-3406.

Marshall, J., 1979, The Simulation of Sand-Grain Surface Textures using a Pneumatic-Gun Apparatus and Quartz Plates: Ph.D. Thesis, University College, London.

McCauley, J. F., Grolier, M. J., Breed, C. S., Mackinnon, D. J., Helm, P. J., and Billingsley, G. H., this volume, Field modeling of the response of various desert surfaces to the long and short term effects of the wind--Mars application.

McCauley, J. F., Grolier, M. J., Breed, C. S., Mackinnon, D. J., Helm, P. J., Billingsley, G. H., Doyle, K. B., McCauley, C. K., and Cook, D. A., Remote monitoring of processes that shape desert surfaces in Klemas, V. (ed.), Remote Sensing of Earth Resources and Environment, University of Delaware, in press.

McKee, T., Greeley, R. and Krinsley, D., 1979, Simulated eolian erosion of quartz, in 37th Annual Proceedings Electron Microscopic Society of America, Bailey, G. (ed.), San Antonio, TX, 624-625.

Stewart, G., Krinsley, D., and Marshall, J., this volume, An experimental study of the erosion of basalt, obsidian and quartz by fine sand, silt and clay.

Williams, S., 1981. Calculated and inferred aeolian abrasion rates: Earth and Mars: M. S. Thesis, Arizona State University, Tempe, AZ.

# Chapter 6

# FLUVIAL, PERIGLACIAL AND OTHER PROCESSES OF LANDFORM DEVELOPMENT

# CHRONOLOGY OF CHANNELS IN CHRYSE PLANITIA MARS

Cutts, James A., Lewis, Blake H., and Blasius, Karl R., Planetary Science Institute, Science Applications, Inc., 283 S. Lake Ave., Suite 218, Pasadena, CA 91101

Despite intensive research, much remains to be learned about the geologic history of Chryse Planitia and surrounding terrains. As part of our participation in the Mars Channel Workshops, we have been concerned with three aspects of that history: (1) the chronology of emplacement of different geologic units, (2) the role of structural control in the development of chaotic terrain, and (3) the complementary roles of collapse and flow in the evolution of channel landforms. This report is concerned with the first aspect. The major result of this study is that the erosion phase of outflow channel formations was limited to a comparatively narrow window in martian history.

Chronology of Chryse Planitia - A new study of ages of different units in Chryse basin region was presented at the Mars Channel Workshop, Flagstaff, Arizona, September 28 - October 1, 1980 (Ref. 1). Terrains were divided into five groups (Table 1), each with two subgroups, on the basis of morphologic similarities and arranged in an age sequence based on stratigraphic relationships. Relative crater densities (R) on each set of surfaces (see definition in Ref. 2) are compared in Fig. 1, which also includes observations on the group of rille-like channels in Western Chryse Planitia (Maumee, Vedra, and Bahram Valles).

The original crater counts (Ref. 1) exhibit the following characteristics:

- The Group 1 (prechannel plains) and Group 3 (outflow channel) surfaces have well behaved crater populations with approximately constant values of relative density between D=1km and 8km.

- There is a sharp upturn in relative density below D=1km for the Group 3 population which is not found in the Group 1 population and which may be a consequence of selective enhancement of secondary craters by deflation.

- Other possible shape differences occur in Group 2 (chaotic terrains) and Group 4 (post-channel plains). In the first case this appears to be an effect of terrain roughness; in the second case no ready explanation exists but the result is only marginally significant statistically.

Reduced crater densities obtained by least squares analyses (Ref. 1 and Fig. 1) are consistent with the following scenario for the evolution of the region:

(a) The oldest event dated is the formation of rille-like channels and associated plains (Group 1R). These surfaces are very close in time of formation to the global event (Ref. 3) which obliterated all craters on Mars below 1km diameter which has an estimated age of log R=-2.1 (Ref. 1).

(b) Extensive plains (Group 1A & 1B) formed in Lunae Planum and Chryse Planitia (Log R ~ -2.25).

(c) Collapse terrains (Group 2) and outflow channel (Group 3) erosional features developed at the expense of these plains surfaces. Rough collapse terrains are difficult to date using impact crater densities and crater densities are uncertain. Outflow channel erosional forms have significant lower densities (Log R ~ -2.45) than the plains in which they are formed.

(d) Erosional channels in southern Chryse are postdated by extensive plains (Group 4) with Log R ~ -2.55.

(e) Much younger deposits also occur in channels and collapse terrains. The extensive volcanic deposits in Kasei Vallis can be dated at Log R ~ 3.1, however, local eolian deposits in southern Chryse collapse terrains are so small in area that no meaningful ages can be derived.

Discussion - This scenario limits outflow channel formation to a comparatively short period in martian history (Fig. 1) in apparent conflict with the conclusions of Masursky et al. (Ref. 3) that channel formation spanned a longer interval of time. However, there is not necessarily a real conflict in observations here because Masursky et al. (Ref. 3) group all the channels in the Chryse region together whether of outflow or rille-like form. They also include ages on channels which have been embayed with volcanics postdating the outflow channeling episodes. With these liberal criteria for channel terrains we would also find that channels "formed" over a large period of martian history.

Much more significant to us is the fact that the development of streamlined islands and erosional grooves associated with outflow type channels was limited to a very narrow interval in the planet's history. How narrow was this window and how do the Log R values given in Fig. 1 convert to the cumulative crater numbers that other workers have used? Using conversion factors between relative and cumulative densities given in Ref. 1, we estimated crater number (N), i.e., cumulative crater density for a $10^6 km^2$ area at 1km diameter constraining the slope of the curve to a fixed value (Fig. 1). Pre-channel plains (Group 1A & 1B) formed at about CN=3000; outflow channel formation at about CN=1550; and post-channel deposits formed almost immediately afterward near CN=1475. A comparatively narrow Chryse outflow channel formation period of CN=1500 to 2100 is also reported by Carr (Ref. 5). Further work is needed to refine these ages and better define their uncertainties.

References - (1) J.A. Cutts and K.R. Blasius, Science Applications Report #1-142-500-01. (2) Crater Analysis Techniques Working Group, Icarus 37, 467-474, 1979. (3) H. Masursky, A.L. Dial and M.E. Strobell, Third Mars Colloq. Abstracts, 148-152, 1981. (4) C.R. Chapman and K.L. Jones, Earth Planet. Sci. 3, 515-540, 1977. (5) M.H. Carr, Third Mars Colloq. Abstracts, 36-38, 1981.

TABLE 1: GROUPINGS OF CHRYSE BASIN TERRAINS USED FOR AGE ESTIMATES

| GROUP | DESCRIPTION | SELECTION CRITERIA |
|---|---|---|
| 1 | PRE CHANNEL PLAINS | TERRAINS CUT BY FRACTURE SYSTEMS RELATED TO CHAOTIC TERRAIN |
| R | RILLES & ASSOCIATED PLAINS | |
| A | LUNAE PLANUM | |
| B | CHYRSE PLANITIA | |
| 2 | COLLAPSE TERRAIN | FLOORS OF COLLAPSE BASINS WITHOUT FLOW FEATURES OR LATE-STAGE LAYERED DEPOSITS |
| A | HUMMOCKY TERRAIN | |
| B | SMOOTH PLAINS | |
| 3 | CHANNEL FLOORS | AREAS WITH THE LINEAR EROSIONAL FORMS CHARACTERISTIC OF OUTFLOW CHANNELS |
| A | IN KASEI VALLIS | |
| B | IN SOUTHERN CHRYSE CHANNELS | |
| 4 | EARLY POST CHANNEL DEPOSITS | DEPOSITS THAT APPEAR TO POSTDATE CHANNEL EROSIONAL FORMS WITH SUBSTANTIAL CRATER POPULATION |
| A | IN KASEI VALLIS | |
| B | IN SOUTHERN CHRYSE CHANNELS | |
| 5 | LATE POST CHANNEL DEPOSITS | DEPOSITS OVERLYING FLOW-MODIFIED OR COLLAPSE TERRAINS |
| A | VOLCANIC THARSIS UNIT | |
| B | YOUNG SEDIMENTS | |

FIG. 1: STRATIGRAPHIC AND IMPACT CRATER AGE RELATIONSHIPS COMPARED: CHRYSE BASIN REGION

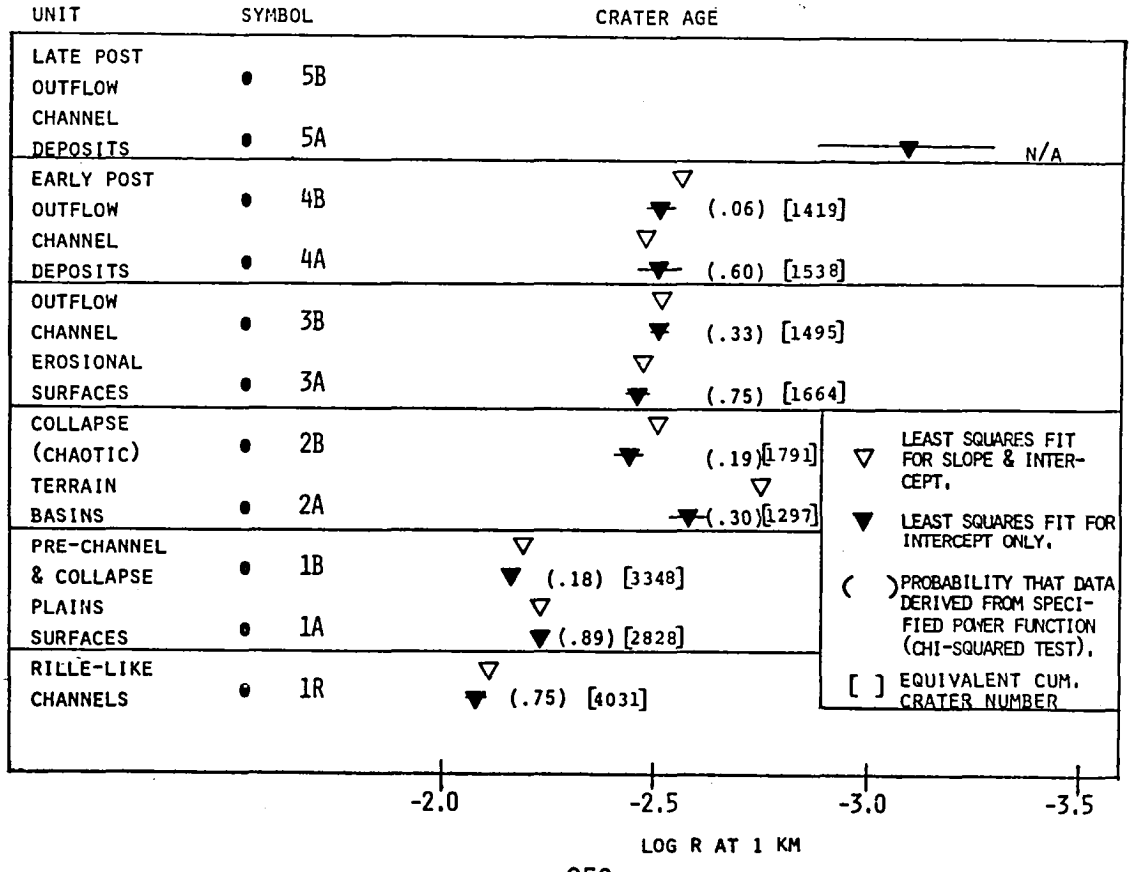

CHAOTIC TERRAIN AND CHRYSE BASIN OUTFLOW CHANNELS: STRUCTURAL CONTROL AND EVOLUTION

James A. Cutts, Jose Helu, and Karl R. Blasius, Planetary Science Institute
Science Applications, Inc., 283 S. Lake Ave., Suite 218, Pasadena, CA 91101

INTRODUCTION - The chaotic terrain and Chryse basin outflow channels form the northeastern extension of the Valles Marineris -- an enormous canyon system spanning more than one-quater of the equatorial girth of Mars. In this report we describe the structural patterns in the chaotic terrain regions and examine evidence for the combined effects of structural control and flow on landform evolution.

STRUCTURAL PATTERNS - In studies of the Mariner 6 images of martian chaotic terrain, Wilson et al. (Ref. 1) found that lineaments in these terrains showed preferred orientations. They concluded that chaotic terrains exhibited tectonic control and not the random "mudcrack style" patterns that might develop by ground ice decay in an unstressed crust. We have reexamined the role of tectonic control on chaotic terrain development using the Viking Orbiter imagery which provides orders of magnitude increase in coverage, resolution, and quality over Mariner 6 data. We have mapped out prominent linear features bounding chaotic terrain basins and the blocks interior to those basins. We have generated rose diagrams indicating the occurrence of lineaments with different orientations (Fig. 1).

The structural patterns of the Chryse region have the following characteristics: (1) Lineament orientations are much more varied than Wilson et al. (Ref. 1) found in the Mariner 6 data set. This is not surprising given the greater coverage and resolution of the Viking Orbiter data. (2) Despite the fact that we did not map subtle linear features but prominent scarps and fractures there is a noticeable suppression of the detectability of lineaments oriented parallel to the illumination azimuth. This effect has been discussed recently by Wise (Ref. 2), and it must be taken into account in interpreting these rose diagrams. (3) There are substantial differences in the lineament rose diagrams for different basins. From this we infer differences in the geologic structures influencing development of chaotic terrain basins. (4) Basins tend to be most similar to their neighbors in their lineament rose diagrams (they also resemble their neighbors in depth and visual morphology). There are suggestions of systematic regional shifts in the orientation of structural features. One family of lineaments exists with a generally northerly trend which "veers" with location on the planet from west of north in the western and northern regions to east of north in the eastern and southern regions. A similar change is apparent with a second family of generally east-west trending lineaments. Their orientations appear to veer to the southeast moving from west to east. (5) The most prominent lineaments appear to be roughly orthogonal to one another in three of the eight basins. In Eos Chasma there is a suggestion of two orthogonal sets of lineaments.

These observations are of interest in the context of the tectonic hypothesis for the development of chaotic terrain. Blasius et al. (Ref. 3) proposed that contrasts in morphology and erosional style between chaotic terrain and troughed terrain are caused by differences in geologic setting including

tectonic control and near surface materials. The systematic regional shifts in orientations of structures and the corresponding trends in terrain morphology tend to corroborate the hypothesis of gradational changes in crustal stress conditions. However, mechanisms for formation of chaotic terrain involving melting and ablation of subsurface volatiles (Ref. 4) cannot be ruled out.

FLOW SCULPTURE OF COLLAPSE TERRAINS - Although the specific mechanisms of collapse and mass wasting in chaotic terrains are not uniquely defined, a fairly clear cut picture now exists of this stage of their evolution. Preexisting structures apparently controlled the orientations of the scarps bounding collapse basins and the horsts and blocks within these basins. The intervening rock ridges within these basins were then apparently isolated and ultimately destroyed by the enlargement and coalescence of lowland surface in the manner described by Brook (Ref. 5). Thus, a lower elevation plain surmounted by residual towers replaced the upland plateau.

A scenario for further evolution of these lowland terrains presented here is somewhat more speculative. In our view, entire lowland basins expanded and coalesced to leave large angular plateau fragments (Fig. 2b), an example of which appears at $8^{o}N$, $31^{o}N$ in VO frame 651A4. Some of these angular fragments have been preserved; others have been reduced by mass wasting, but still others have entered another phase of evolution under the action of the flow processes responsible for the sculpture of outflow channels (Fig. 2d). It seems quite plausible that many of the streamlined plateau remnants that characterize the outflow channels of Ares, Kasei and Simud/Tiu formed originally as angular plateau remnants and were streamlined to their present form by the outflow channeling process. This two-stage model is preferable to a pure flow sculpture model which requires that shallow rims of craters somehow diverted the enormous outflow channel flows.

SUMMARY AND IMPLICATIONS - Orientations of lineations in the chaotic terrains suggest gradational place-to-place changes in structural control of these basins. This is consistent with the hypothesis (Ref. 3) that chaotic terrain is one manifestation of a varied environment of extensional tectonics within and adjacent to the Valles Marineris. Erosion by large scale flows may have preferentially acted within areas previously modified by collapse. Streamlined plateau remnants can therefore be best understood by collapse and flow occuring sequentially or in concert. Consequently, estimates of the amount of material excavated by erosive flow (Ref. 6) should be scaled back. Correspondingly, other sources must be sought for sedimentary material now forming polar layered deposits (Ref. 7) and possibly equatorial sedimentary deposits (Ref. 8).

REFERENCES - (1) Wilson, R.C. et al., GSA Bull. 84, 741-748, 1973. (2) Wise, D.U., NASA TM 82385, 439-441, 1980. (3) Blasius, K.R. et al., JGR 82, 4067-4091, 1977. (4) Sharp, R.D., JGR 78, 4073-4083, 1973. (5) Brook, G.A., Third Int. Colloq. on Mars, 31-33, 1981. (6) Cutts, J.A. and K.R. Blasius, JGR 86, 5075-5102, 1981. (7) Cutts, J.A., JGR 78, 4231-4249, 1973. (8) Schultz, P.H. and A.B. Lutz-Garihan, Third Int. Colloq. on Mars, 229-231, 1981.

CHRYSE HYDROGRAPHIC BASIN, MARS - A PROGRESS REPORT.
Harold Masursky, A. L. Dial, Jr., M. E. Strobell (U. S. Geological Survey, Flagstaff, Arizona 86001); G. S. Downs, (J.P.L., Pasadena, CA); Tommy Thompson, (PSI, Pasadena, CA)

Radar observations of Mars made at the Goldstone facility (1971-1980) have been reduced to a common ephemeris; the measurements are accurate to 100 m [1,2]. Twelve radar traverses have been made in the Chryse Planitia area and an additional 12 in the canyon area to the south. These profiles were plotted on the newly completed unpublished airbrush map of the basin at a scale of 1:5 million and on a 1:5 million scale reduction of the 1:2 million scale photomosaic maps. Long profile slopes can be determined for the first time from these data. Channel depths range from 300 m to 1.5 km below the adjacent cratered terrain; the deepest section is about 2 km. The northward slope of Ares and Tiu Valles is 1.7m/1km over a 600 km reach; Simud Valles slopes about 0.5m/km over a 450 km reach. According to Baker [3,4] the long profiles of Washington/Oregon scablands have the following slopes: Chaney-Palouse tract, 3 to 4 m/km; Grand Coulee, 2 m/km and Lake Missoula outflow reach, 1m/km. Shown in figure 1 are parts of three of the radar profiles across the channels in Chryse Planitia and one across Capri Chasma and Aureum Chaos. Extrapolating the Aureum profile, the chaotic area is about 2 km (1.4 km where measured below the surrounding terrain. It is possible that the collapse is due to melting of subsurface ice that escapes and supplies the channel water. In most other chaotic areas no radar signal is received as the texture apparently is too rough, as are the summits of the big shield volcanoes. Crater counts are shown in figure 2 for seven parts of five channels made from high resolution Viking pictures. Differences in relative crater densities are clearly shown; the range in age of these channels is large. Mawrth, is the oldest channel (20,000 craters at the 1 km intercept using the Neukum [5] method/$10^6$ sq. km. The old region in Ares is intermediate (2500 craters/$10^6$ sq. km) and inner Ares the youngest (600/craters/$10^6$ sq. km). Old and young Kasei are very similar to Ares in crater densities. It is inferred that these channels formed over a long period of time [6,7,8] and that the big channels probably have several episodes of water flow with the broad, widespread flows earlier and the confined inner channel cutting later. The source areas for the big channels differ markedly. Ares originates in many chaotic areas probably made by ice melting and collapse that feed into the main channel. The crater age of the widespread channel is greater than the narrow incised channel. The same is true for Kasei, but it originates in linear closed depressions of "normal" canyon type (Echus Chasma, Hebes Chasma) that may have fed the channel by spring fed flow carrying fine grained material from the collapsed areas that don't exhibit chaos complexes. There were at least two waterflow episodes and there may have been many, leading to the observed restricted channel flow each time and not forming "lakes" when the water reached the lowlands, as would have been the case if there had been only one massive flood. The water might have been lost by evaporation and underflow before lakes could form as is true in many terrestrial desert areas.

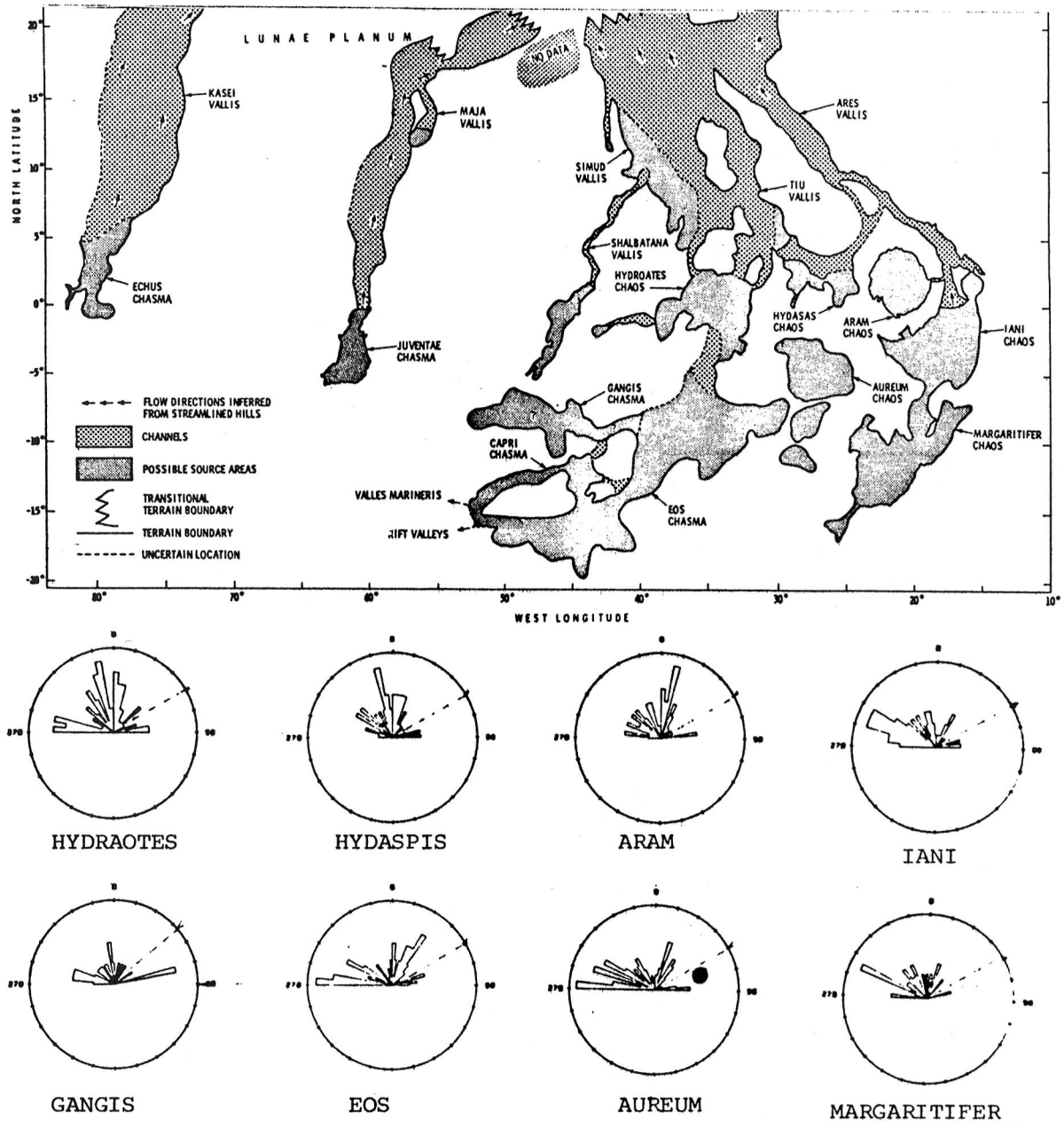


Figure 1: Rose diagrams of orientations of linear features in major chaotic terrain basins. Rose diagrams for the eastern troughs (Coprates Chasma) resembles that for Eos Chasma. Dashed lines indicate illumination direction.

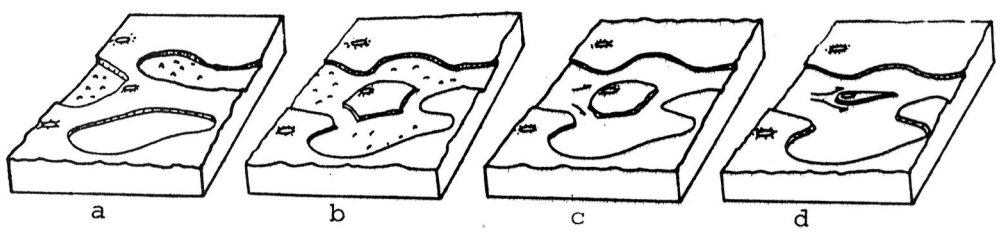


Figure 2: Evolution of chaotic terrain by collapse and flow.

Maja Valles has both types of source areas. Simud has a low elevation area in its mid reach that may be due to sag after volcanic flooding. This low area is marked by subdued chaos texture as are the tectonically lowered chasma bottoms in the Valles Marinaris complex.

References


1. Downs, G. S., Green, R. R., Reichly, P. E., 1978 Radar Studies of the Martian Surface at centimeter wavelength: the 1975 opposition Icarus, v. 33, p. 441-453.
2. Roth, L. E., Downs, G. S., Saunders, R. S., Schubert, G., 1980, Icarus, v. 42, p. 287-316.
3. Baker, V. R., 1973, Paleohydrology and Sedimentology in Eastern Wa., G. S. A. Spec. Paper 144, 79 p.
4. Baker, V. R. and Nummedal, Dag, 1978, The Channeled Scabland, NASA Planetary Geol. Prog., 186 p.
5. Neukum, G., Hiller, K., 1981, Martian Ages, J.Geophys. Res., v. 86, 0. 3097-3121.
6. Masursky, Harold, Dial, A. L., Jr., and Strobell, M. E., 1980, Martian Channels - A late Viking view: in Reports of Planetary Geology Program,1980-1981, NASA Tech. Mem. 82385, p. 184-187.
7. Masursky, Harold, Strobell, M. E., and Dial, A. L. Jr., 1979, Martian Channels and the Search for Extra terrestrial Life, J. Mol. Evol. v. 14, p. 39-55.
8. Masursky, Harold, Boyce, J. M. Dial, A. L. Jr., Schaber, G. G., and Strobell, M. E., 1977, Classification and Time of Formation of Martian Channels based on Viking Data, J. Geophys. Res., v. 82, p. 4016-4038.


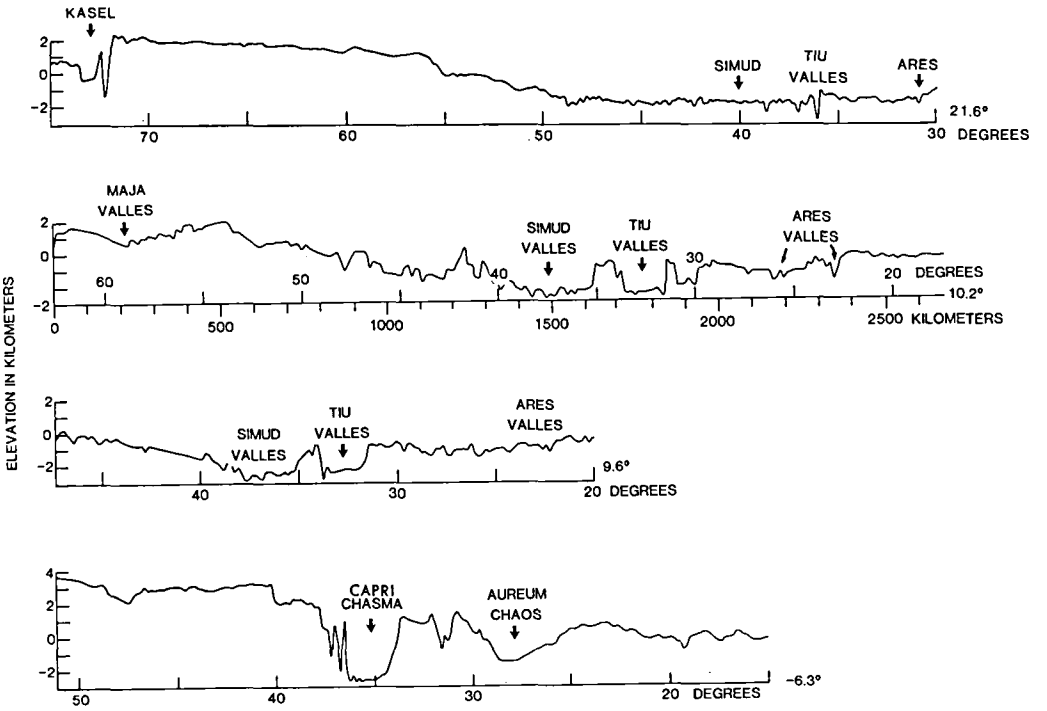


Figure 1. MARS-CHRYSE BASIN PROFILES

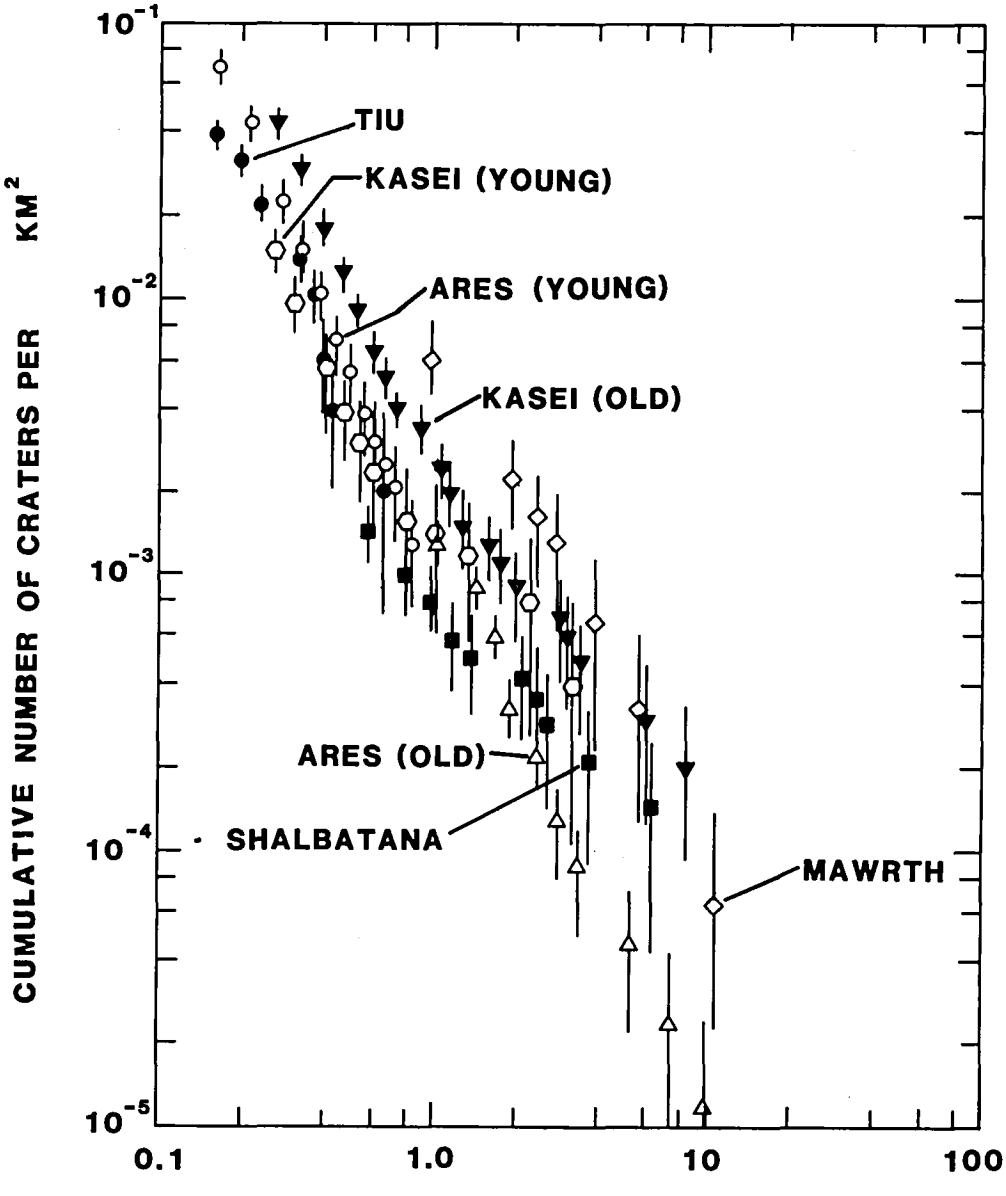
CUMULATIVE NUMBER OF CRATERS PER KM²
10⁻¹
10⁻²
10⁻³
10⁻⁴
10⁻⁵
TIU
KASEI (YOUNG)
ARES (YOUNG)
KASEI (OLD)
ARES (OLD)
SHALBATANA
MAWRTH
0.1
1.0
10
100
CRATER DIAMETER IN KILOMETERS

Figure 2.

# STREAMLINED ISLANDS: AN ANALYSIS OF THEIR MINIMUM-DRAG SHAPE

Komar, Paul D., School of Oceanography, Oregon State University,
Corvallis, Oregon 97331

The streamlined 'islands' or outliers found in martian outflow channels such as Maja and Kasei Valles have inspired considerable interest and debate since their discovery (Carr et al., 1976; Baker and Kochel, 1979). The loess hills of the Channeled Scabland in eastern Washington have also been scoured into streamlined shapes (Baker, 1973). Other streamlined landforms include the yardangs produced by wind erosion, longitudinal river bars, and drumlins produced by ice flow. The present investigation includes only those forms produced by turbulent flows, thus excluding drumlins.

It is generally recognized that the streamlined island shape must represent or approach an "equilibrium" form that provides the least amount of resistance to the fluid flow. This condition is best described by Baker (1979) who pointed out that the streamlined shape represents the best compromise between the form drag and the skin friction to yield the smallest total drag. With a fixed island width, W, perhaps controlled by the presence of a crater or other flow obstacle, a progressive increase in the island length L would decrease the form drag due to the streamlined shape eliminating flow separation, but would increase the skin friction. There must be a certain length or L/W ratio where the total drag, the sum of the form drag and skin friction, will be a minimum.

This study involves a combination of reanalyses of existing measurements of drag on streamlined shapes, and flume experiments that examine the development of the streamlined form in water flows. Most of the available data come from wind tunnel experiments investigating the drag on airfoils. The majority of these experiments are with asymmetrical airfoils rather than with the nearly symmetrical shapes common in the streamlined islands found in the martian channels. Hoerner (1958) provides many graphs that are useful in this analysis, but the most suitable data set is that of Fage et al. (1929). They worked with seven streamlined shapes (Joukowski Sections) with length/width ratios ranging 2.48 to 18.15. A series of

wind speeds yielded the total Reynolds number range $Re = u_o W/\nu = 3 \times 10^4$ to $3 \times 10^5$ where $u_o$ is the mean-flow velocity. It should be noted that even though the experiments were performed in air, the results will be applicable to any turbulent Newtonian fluid including water. Fage et al. directly measured the total drag and the form drag. The skin friction was determined by subtracting the form drag from the total drag.

The accompanying figure shows an example of the measurements of Fage et al. (1929), reanalyzed in this study. The results are presented in the form of drag coefficients. For example, $C_d$ is the drag coefficient for the total drag, given by

$$C_d = \frac{\text{Total Drag}}{0.5\ \rho\ W\ u_o^2}$$

where $\rho$ is the fluid density. The drag coefficients for the skin friction, $C_s$, and form or pressure drag, $C_p$, are similarly defined. Of most interest to the present application, it is seen that the total drag as indicated by $C_d$ reaches a minimum at a length to width ratio approximately in the range 3 to 4. This result corresponds closely to the measurements of Baker (1979) of the L/W ratios of islands in Maja Vallis, Kasei Vallis and the Channeled Scablands. All of Baker's data yielded $L/W \simeq 3$, but the martian islands tended to be slightly more elongate than the Scabland counterparts, yielding $L/W \simeq 4$. These results therefore tend to support the hypothesis that the islands found in the martian channels were most likely sculptured by a turbulent fluid (probably water, but air cannot be excluded as a possibility on the basis of these measurements alone).

Within the range of Reynolds numbers included in the experiments of Fage et al. (1929), the results are independent of this parameter. It was initially hoped that the observed geometries of the Martian streamlined islands would provide an indication of the flow Reynolds numbers which created them, but this does not now seem possible.

The above analyses give no indication of how an island achieves a streamlined form starting from some amorphous shape, nor how long a flow duration is required to achieve equilibrium. Flume experiments are now underway to investigate these aspects.

References

Baker, V.R. (1973) Paleohydrology and sedimentology of Lake Missoula Flood-in eastern Washington: Geol. Sco. Amer. Special Paper 144, 79pp.

Baker, V.R. (1979) Erosional processes in channelized water flows on Mars: Jour. Geophys. Res., v. 84, n. B14, p. 7985-93.

Baker, V.R., and R.C. Kochel (1979) Martian channel morphology: Maja and Kasei Valles: Jour. Geophys. Res., v. 84, n. B14, p. 7961-83.

Carr, M.H. et al. (1976) Preliminary results from the Viking orbiter imaging experiment: Science, v. 193, p. 766-776.

Fage, A., V.M. Falkner, and W.S. Walker (1929) Experiments on a series of symmetrical Joukowski sections: Gt. Britain Aeronautical Res. Comm., Reports and Memoranda, No. 1241, H.M.S.O., London.

Hoerner, S.F. (1958) Fluid-Dynamics Drag: publ. by author, 402 pp.

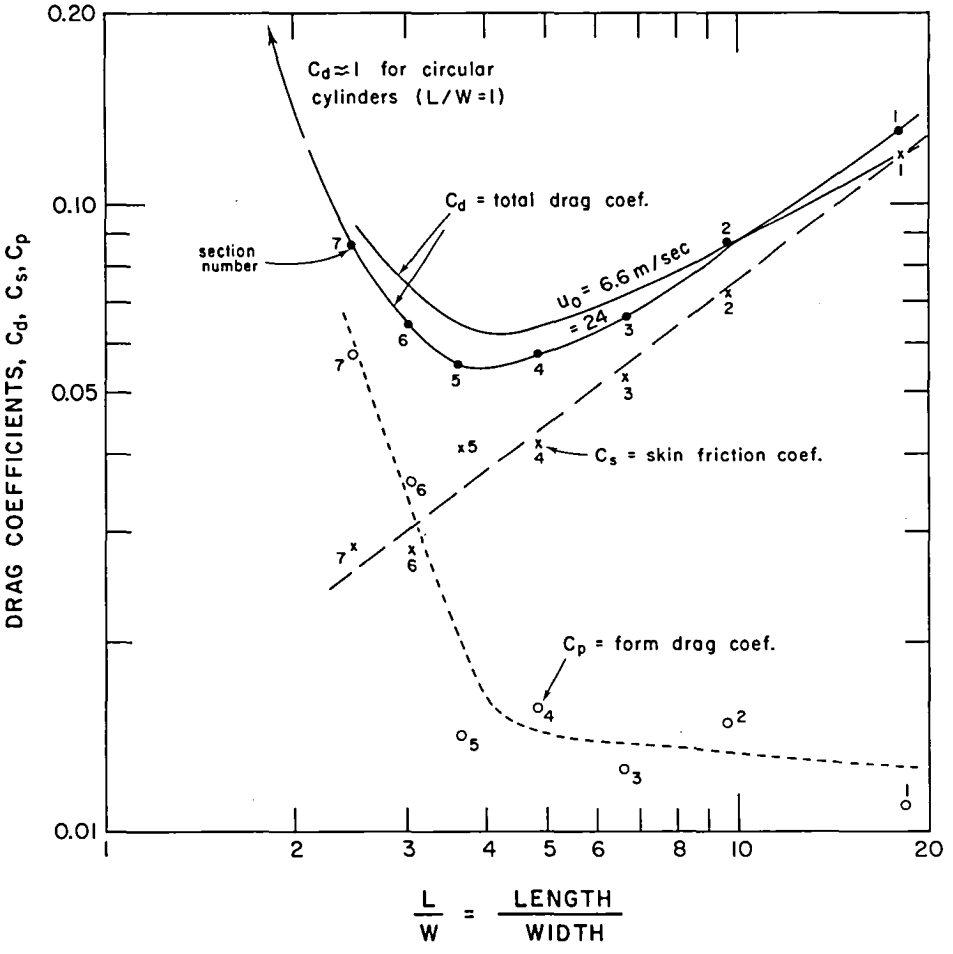

# THE ROLE OF KINEMATIC WAVES IN SEDIMENT TRANSPORT DURING CATASTROPHIC FLOODING

David E. Thompson, Jet Propulsion Laboratory, California Institute of Technology, Pasadena, CA 91109

This study is a two-part theoretical assessment on alluvial bed scour and depositional features which are formed and modified during catastrophic flooding of highly sediment-laden fluids. The analysis is constrained from two sources: (1) from data gathered on scour and depositional interrelationships along the Alsek River channel in Yukon Territory, Canada, down which catastrophic floods regularly occur from drainage of ice-dammed Lake Alsek, and (2) from theoretical hydrographs created for the Lake Alsek flood, developed by applying a peak discharge hydrograph predictor model to the basin characteristics of glacial Lake Alsek and by imposing assumptions concerning transport of water through glacial ice. These two sources allow analysis of the hydraulic characteristics of the Lake Alsek flood and assessment of the size and type of debris participating in the flood, both in lacustrine drainage and in intense scour and channelling downstream of the ice dam. The analysis contained in this study is an assessment of the role of kinematic waves in sediment transport during catastrophic flooding. The approach is (1) to analyze the response, migration, and stability of bedforms following intense hydraulic changes wherein the fluid itself is not heavily deris laden, and (2) to follow the growth, intensification, and dissipation of what might be termed sediment concentration shocks in fluids which are heavily debris laden or which carry a high concentration of sediment in suspension. Both the bedforms and the sediment concentration shocks propagate as kinematic waves, although in the shock analysis, consideration of sediment diffusion and nonlinear flow interations is included wherein the velocity of propagation is itself a function of concentration.

A detailed approach of the analysis is as follows. First, from several seasons of field work in the Alsek River valley, a characterization has been made of the size and type of debris and sediment which participates in the Lake Alsek floods. Further, an assessment has been made of the degree of scour present, of the interrelationships between scour and channelling, and of flood depth both upstream of the ice dam where giant gravel dunes occur as sets on bars, and downstream of the ice dam where more intense scour and channelling occurs. Next, both from terrace distribution on airphotos and from lake shoreline measurements in the field, realistic hypsometric data of lake surface area as a function of depth has been gathered. Thus lake volume, distribution, and basin geometry is known. This allows initial development of a theoretical hydrograph for the Lake Alsek flood (see Thompson, 1980). Then, in order to set the peak discharge of the hydrograph to that required from the flood hydraulic data on scour features below the ice

dam, lake temperature and ice tunnel closure parameters are set. The tunnel closure parameter, for a known basin geometry, constrains the effective roughness and turbulent heat transport through the ice tunnel which allows the leaking of Lake Alsek and the eventual flood. In addition, laboratory stability criteria (Richardson, 1968) for horseshoe vortex scour and dune form provide effective Reynolds and/or Froude numbers of the flood which constrain the peak of the theoretical hydrograph. Finally, a well-constrained theoretical hydrograph for the Alsek flood is created which includes the degree of geomorphic work represented by remnant scour and depositional features and the degree of sediment carried in suspension. This phase of the project is completed.

The second phase of the analysis is currently underway. Here it is taken as given that the flood hydrograph is known, and that sediment concentrations at various points along the flood reach in the Alsek valley can be realistically hypothesized. Stability criteria for the large transverse gravel dunes on megabars and for the horseshoe vortex scour are known because flood depth and hydrograph record are known. Thus, the analysis now concentrates on how initial features are modified during changes in the flood, how the stability is affected by changes in both hydraulics and in sediment concentration, and how bedforms migrate or how new modal sets are developed. This first aspect of the analysis tests modification of bedforms to changes in flood hydraulics, parallels that by Fredsøe (1979), but relates specifically to the Alsek flood. Next, the analysis approaches the problem of development and effect of shock propagation in sediment concentration on the bedforms. Basically, here the analysis is an application of Burger's equation (Whitham, 1974, chapter 4), including shock structure development, wherein the shock front is distinguished by a step in density and sediment concentration acting on the bedforms as if a change in fluid viscosity (or erosion potential) were occurring. This requires an analytic representation between sediment concentration functions and fluid viscosity, applicable at hyperconcentrations of debris in the fluid. Finally, the analysis attacks the problem of migration by kinematic waves of the bedforms (or of the sediment concentration fronts) in response to (or as a function of) actual fluid viscosity changes.

The research is supported under NASA contract NAS 7-100.

REFERENCES

Fredsøe, J., 1979, Unsteady flow in straight alluvial streams: modification of individual dunes: Jour. Fluid Mech., vol. 91, part 3, pp. 497-512.

Richardson, P.D., 1968, The generation of scour marks near obstacles: Jour. Sed. Petrol., vol. 38, no. 4, pp. 965-970.

Thompson, D.E., 1980, Relation of scour by catastrophic flooding to peak discharge from jokulhlaup hydrographs: Niagara Falls, N.Y., in Proc. Third Coll. on Planetary Water, Oct. 1980, pp. 30-35.

Whitham, G.B., 1974, Linear and Nonlinear Waves: New York, John Wiley and Sons, 636 p.

# CATASTROPHIC FLOODS OF THE JÖKULSÁ Á FJÖLLUM, ICELAND

Michael C. Malin and Dean B. Eppler, Department of Geology, Arizona State University, Tempe, AZ 85287

Catastrophic floods (jökulhlaups) of the Jökulsá á Fjöllum in north central Iceland have been examined by Thorarinsson (1, 2, 3), Tómasson (4), Saemundsson (5) and Einarsson (6). Most of these studies were related to a desire to understand the hydrology of the Jökulsá á Fjöllum, the largest river in Iceland and the one seeming, at first glance, the most ideal for hydroelectric development. Among the aspects that suggested it as a major resource in Iceland was its relatively high and sustained yearly discharge and its deep canyon throughout most of its northern reach. However, it is this canyon, and the large, dry cataract Ásbyrgi, that have brought to the forefront discussions of enormous jökulhlaups, for the canyon is tremendously underfit by the present river and its historic (fifteenth to eighteenth centary) floods. Tómasson estimates discharges of $\sim 4 \times 10^5 m^3/sec$, using several different methods, including estimating a flood filling the canyon, and using the Manning equation and measurements of present day topography. Given these large discharges, exotic surface forms as seen in aerial photographs (including teardrop-shaped islands up to 5 km in length), and a length comparable to some martian channels (7), we have examined several specific aspects of this flood, in the hope of shedding light on several of the most persistant problems of martian channels, namely: 1) where did the fluid come from; 2) what was the viscosity of the fluid (ice, mud, water or air); 3) how was canyon excavation accomplished; 4) where did the debris load go and can it be recognized today; 5) how did the fluid behave in unconfined reaches; and 6) are there diagnostic characteristics of water floods that cannot be mimiced by other fluids?

Field observations, taken during July and August 1981, have yet to be totally correlated, but preliminary findings suggest several points:

1) Cataracts, "scabland" plucking of bedrock, broad lemniscate forms, (principally erosional), occassional megaripples and depositional tails are the principal characteristic large-scale features of catastrophic floods. We found no evidence of linear grooving at scales greater than 1-2 m width and a few 10's m (maximum) in length.
2) It is extremely difficult to distinguish glacial from flood debris from single-location studies. Some glaciers transport well-rounded debris, some floods transport angular material (derived by local plucking and not transported over long distances). Generally, flood debris was more rounded and significantly better sorted. It is far easier to distinguish debris origin at thoughtfully selected locations: depositional tails, megaripples along channel margins and boulder fields up-stream of cataracts provide the best evidence, from the load standpoint, of catastrophic flood.
3) Among these latter areas, a 1 $km^2$ field of well-sorted, well-rounded boulders about 3 m dia. each occurs west of Dettifoss, just south of the first major cataract. The only megaripples seen were variable in wavelength and amplitude (becoming larger to the north - downstream), but averaged 20 m wavelength, with stoss amplitudes of $\sim$1 m, lee amplitude of 1.5-1.7m, and material is principally between 2 and 10 cm

diameter (largest ∿ 1.5m).

4. Our estimates of discharge, based on plunge pool geometry, splash marks, etc., suggest a discharge of ∿ 3 x $10^5 m^3$/sec at Ásbyrgi, similar to Tómasson's estimates.
5. In unconfined reaches, flood effects are extremely difficult to detect and interpret. In particular, flood margins are nearly invisible. Typical depths diminish to a few m, and the thickness and caliber of debris now mantling the surface (where it can be distinguished from later fluvial and eolian debris) indicate movement not unlike mud-flows. Little debris is found within or atop the walls of the canyon of the Jökulsá; the abundance of it headward suggests the flood may have dropped most of its load in locations proximal to its source. The effect may have resembled the gradual "de-watering" of a fluid mudflow, much as observed at Mount St. Helnes after its eruptions of 1980.
6. Evidence of some over-topping of very high obstacles, yet general absence of great amounts of debris in such sites and the generally low "high-water-line" of the proximal reaches of the course suggests a surging nature to the flood, reflecting perhaps variations in the nature or geometry of the outlet, or kinematic waves within the flow itself.

More detailed analysis, and the application of these analyses to the outstanding problems of martian channel formation, are currently in progress.

References:


1) Thorarinsson, S. (1950) Jökulhlaup og eldos á jokulvatnasvaedi Jökulsár á Fjöllum. Náttúrufraedingurinn 20, 113-133.

2) _____ (1959) Some geological problems involved in the hydro-electric development of the Jökulsá á Fjöllum. Report to the State Electricity Athority, Reykjavik. 35 pp.

3) _____ (1960) Der Jökulsá-Canyon und Ásbyrgi. Petermanns Geographisch Mitteilunger 104, 154-162.

4) Tómasson, H. (1973) Hamfhrahlamp í Jökulsá á Fjöllum. Náttúrufraedingurinn 43, 12-34.

5) Saemundsson, K. (1973) Straumrákadar klappin í kringum Ásbyrgi. Náttúrufraedingurinn 43, 52-60.

6) Einarsson, T. (1976) Tilgáta um orsök hamfarahlaupsins í Jökulsá á Fjöllum og um jardvisindalega þydingu þessa mikla hlaups. Jökull 26, 61-64.

7) Malin, M.C. (1980) Geomorphic processes in Iceland's Cold Deserts: Mars analogs (Abs). Reports of Planetary Geology Program, NASA TM-82385, 367-368.

# SEDIMENTARY PROCESSES ALONG THE SAGVANIRKTOK RIVER, CENTRAL ARCTIC SLOPE, ALASKA

Jon C. Boothroyd, Department of Geology, University of Rhode Island, KIngston, RI 02881; Barry S. Timson, The Mahoosuc Corporation, Augusta, ME 03240

The Sagvanirktok River is the second-largest river (after the Colville) on the Arctic Slope of Alaska with a drainage basin area of 14,364 $km^2$ and a length of 267 km (Fig. 1). Maximum discharge recorded during spring breakup was 2320 $m^3\ sec^{-1}$ (cms) (USGS, 1975); flow declines to essentially zero during the winter freeze. The Sag flows through terrain underlain by continuous permafrost ranging up to 300 m in thickness adjacent the delta at Prudhoe Bay on the Beaufort Sea. Thawing and formulation of an active layer of variable thickness each year contributes to solifluction and debris flow processes on slopes adjacent to the river. Field work during the 1981 season concentrated on: 1) clast size and bar morphology of the Sag River; 2) processes on selected slopes and terraces adjacent to the Sag; and 3) morphology and processes on a debris fan on the flank of the Franklin Bluffs erosional remnant.

The Sag is a coarse-gravel, braided river that is degradational through most of its length, becoming aggradational only on the last 20 km of delta plain. Clast size was measured at 21 stations along a 160 km reach of the river from the foothills of the Brooks Range to Prudhoe Bay. Average largest clast size decreases from a maximum of 49 cm (long axis) to 7 cm on the delta plain. Bars formed from imbricated clasts of up to 135 cm long axis are present where the river flows through end moraines of the Late Pleistocene Itkillik glaciation (Hamilton, 1978). Active bars are a combination of longitudinal bar complexes and large transverse bars. Many transverse bars are formed at the end chutes incised into low terraces of the inactive fluvial plain. Formation of chutes is due to blockage of the river by ice derived from icings (aufeis). Icings form by repeated overflows of water on the river ice cover (that is, frozen to the river bed) due to intermittent thawing or, more importantly, a groundwater source (Hall and Roswell, 1980; Sloan et al., 1976). Spring breakup results in ice drives that may jam up and direct the river laterally to an unoccupied part of the fluvial plain.

Numerous small alluvial fans have formed along the Franklin Bluffs erosional remnant (Fig. 1). The fans are less than 1 km in length with gradients ranging from 100-200 m $km^{-1}$. Coarse gravel is transported down the fans to the Sag River primarily by debris flows. Sieve lobes are prominent at the ends of U-shaped channels. The flows are fed by runoff during spring breakup, melting of ground ice during the thaw season, and by groundwater-fed springs (small icings).

The Sagvanirktok River system, including selected tributaries (Fig. 1), is important because it is a degradational river flowing through con-

tinuous permafrost with active slope processes on adjacent valley walls and erosional remnants. Icings also may play an important role in determining the morphology of the river.

## REFERENCES CITED

Hall, D.K., and Roswell, C., 1980, Analysis of the origin of aufeis feedwater on the Arctic Slope of Alaska: NASA Tech. Memo. 81992, 41p.

Hamilton, T.D., 1978, Surficial geologic map of the Philip Smith Mountains quadrangle, Alaska: U.S. Geol. Survey Map MF-879A.

Sloan, C.E., Zenone, C., and Mayo, L.R., 1976, Icings along the trans-Alaska pipeline route: U.S. Geol. Sirvey. Prof. Paper 979, 31p.

U.S. Geological Survey, 1975, Water resources data for Alaska, water year 1975: U.S. Geological Survey Water Data Rept. AK-75-1, 410p.

Figure 1. Location map of Sagvanirktok River, Central Arctic Slope, Alaska.

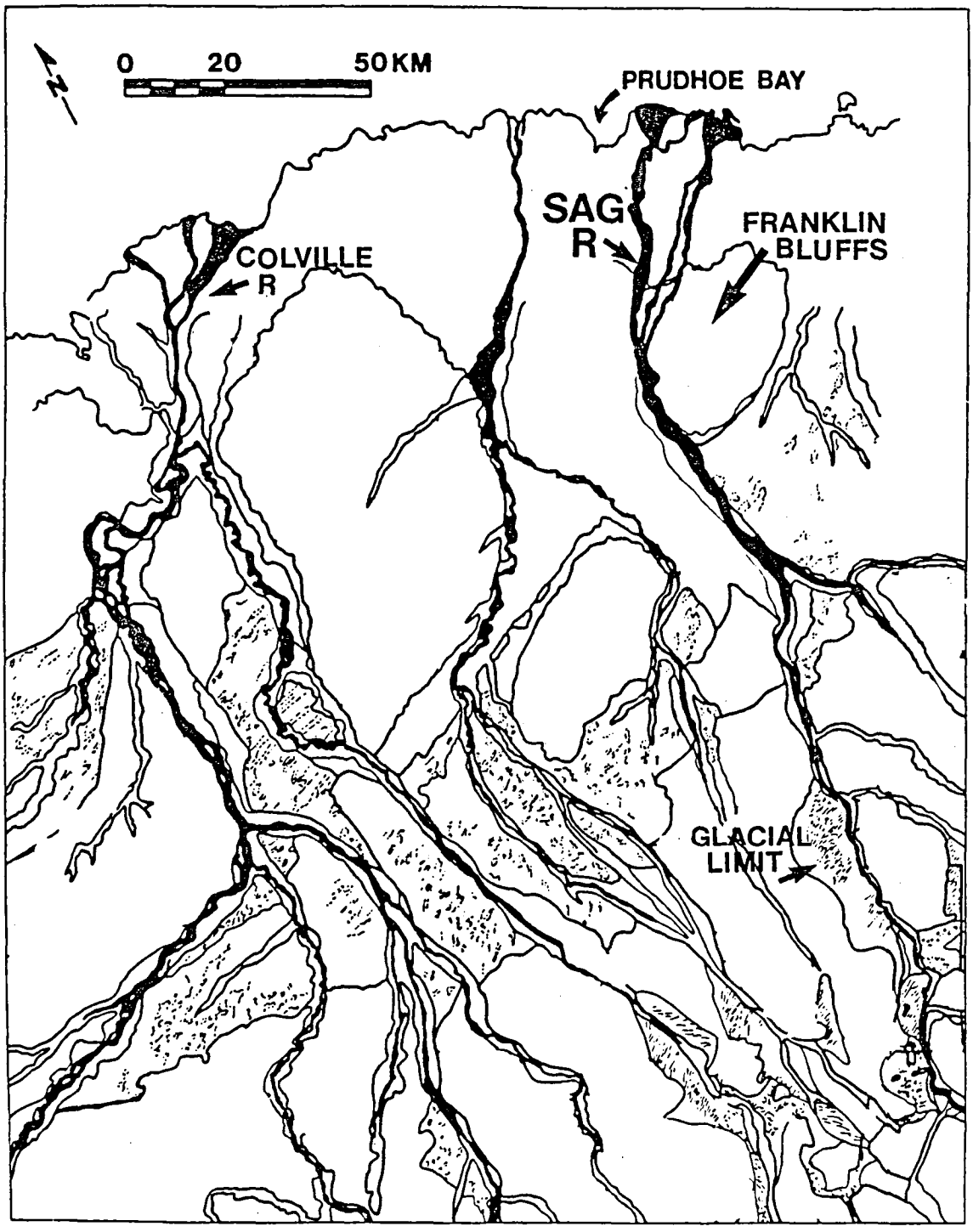
0 20 50KM
PRUDHOE BAY
SAG R
FRANKLIN BLUFFS
COLVILLE R
GLACIAL LIMIT

Vesiculation and Lithification Behavior of Saline Muds in near Vacuum

Laurie A. Johansen, Jet Propulsion Laboratory

Liquid water is not stable on the Martian surface because of the low atmospheric pressure (except for certain exotic brines). As a result, mud exposed to Martian surface conditions is not stable. It will boil and freeze, producing a vesicular icy mud. The ice will eventually sublime leaving a sediment and salt residue. This phenomenon was studied in a laboratory using a vacuum chamber. Vesiculation of mud upon exposure to near vacuum occurs in a wide range of sediment size and compositions. Varying the amount of water results in different textures in the end product varying from tuff-like to macroscopically vesicular. Bulk densities ranged from 0.1 to 1.9 $g/cm^3$. Due to the porosity, the bulk thermal ineria is very low. Scanning electron microscope images were taken of the microstructure of the clods which showed vesicles and ice crystal cavities bvetween 10-100 microns although vesicles have been up to a centimeter in size.

When salt solution is used to make the mud, the clods become stronger. Magnesium sulfate produces harder clods than sodium chloride. Also, longer drying times appear to strengthen the clods. The strongest clod formed so far was formed of montmorillonite and magnesium sulfate. It was dried at a rate such that it was half dry at 8.5 days and failed under an unconfined compressive load of about 500 psi. In comparison, the weakest concretes fail at about 800 psi. It is difficult to chip cemented clods this strong and they may be superficially mistaken for rock. This is strong enough to support its own weight to a height of about 70m (420m optimistic limit, 28m pessimistic ).

Subsequent exposure to moisture greatly weakens the clods. They diaggregate immediately on exposure to liquid water. Even Southern California atmospheric moisture has a clearly qualitatively noticible and measurable effect within a few minutes.

This behavior has interesting implications for the Martian surface. Evidence of surface flows attest to the presence of water at times on the surface. The presence of duricrust suggests that local concentrations of salts can occur. It appears that the opportunity for forming these salt cemented clods exists.

The mudflows on Mars are generally associated with either volcano-tectonic activity, or meteorite impact. In the case of volcanic activity, the flows may eminate from near a volcanic center or a fissure. Their areal appearance may be indistinguishable from true lava flows at the resolution of Viking images. If mud is a common constituent of the Martian crust, mud flows and mud volcanism associated with volcano-tectonic activity may be more significant than presently concidered.

This material is strong enough to be significant in forming landforms on Mars. Furthermore, the large size of the potential flows implies longer drying times than I have been able to achieve in the laboratory. Since longer drying times are apparently significant in increasing the materials strength, the Martian material may be conciderably stronger than the 500 psi I have measured.

It is possible that the rocks around the Viking landers are salt cemented vesicular clods. Viking landers attempted to sample rocks in their vicinity but were unable to in spite of numerous attempts. Each time a suitable particle was pressed it disintegrated, and the fragments had a higher salt content. Thus the clods were interpreted to be a part of the duricrust. If one examines images of the area it appears remarkable that no rock fragments were recovered since the smaller rocks appear to form a broad gradation of sizes up to the size of the vesicular rocks around the landers. Rocks were pushed and chipping was attempted. The rocks tested did not chip even though $10^8$ pascals (Moore, et al 1977) (14,696 psi) were exerted on them. This is all we know concerning the strength or composition of the rocks. If the rocks were in fact salt cemented clods, the inability of the lander to sample a rock would be explained. However either the salt cemented clods would have to be slightly over an order of magnitude stronger. This is concievably possible but not yet demonstrated in the laboratory.

If the surface materials are made of this sort of material then its water erosion characteristics would be very different from that of basalt. It would take much less water to produce a channel, or degrade the rock. A rising water table could lead to liquefaction and collapse. This may also have effects on the structural appearance of the channels.

Exposure of saline mud to the Martian conditions of low atmospheric pressure could produce hard vesicular rocks composed of salt cemented fines. Such exposures have been hypothesized to have occured by meteorite impact and by tectonic and thermal processes at work on Mars.

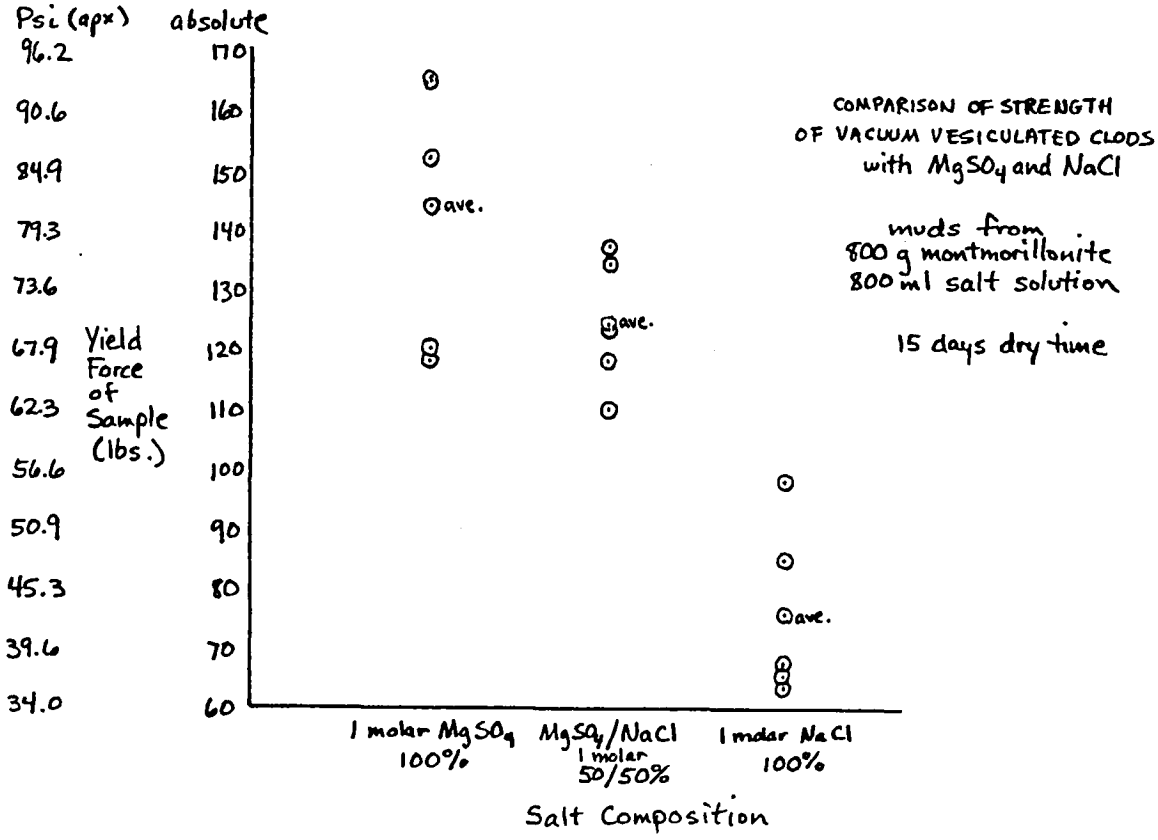

References

Moore, H., R. Hutton, R. Scott, C. Spitzer, and R. Shorthill, "Surface Materials of the Viking Landing Sites", JGR, Vol. 82, No. 28, Sept. 30 1977, p 4497-4523.

Johansen, L., "Mud as a Pseudo-Volcanic Rock Magma", Proc. Third Coll. on Planetary Water, Niagara Falls, New York, 27-29 Oct. 1980, p113-115.

# SAPPING PROCESSES AND THE DEVELOPMENT OF THEATRE-HEADED VALLEYS

Laity, Julie E. and R.S. Saunders, Jet Propulsion Laboratory, California Institute of Technology, Pasadena, CA 91109

Deeply entrenched theatre-headed canyons are widespread on Mars. The lack of any compelling evidence for rainfall or surface flow on Mars (Pieri, 1980), as well as the geographically scattered distribution of channels (suggestive that water for valley growth was supplied from lithospheric rather than atmospheric sources)(Sharp and Malin, 1975) argues strongly that the Martian small valleys developed by groundwater, groundice, or throughflow processes that caused sapping of the valley walls and resulted in headward and lateral extension of the valleys. The morphology of the valleys, characterized principally by the development of theatre-headed terminations, is generally believed to indicate sapping. Canyons with morphology and drainage pattern strikingly similar to those on Mars are developed within the Navajo Sandstone in the Glen Canyon region of the Colorado Plateau, and these valleys were investigated to examine feature/process relationships. Geomorphologic similarities between the Martian and terrestrial valleys include cuspate-shaped valley heads, large scale, nearly constant valley width from source to outlet, high and steep valley sidewalls, hanging valleys, and a large degree of structural control. A major objective of the field study was to assess the relative roles of overland, through, and groundwater flow processes in feature formation and to determine if the development of the observed morphologies characterizes the sapping process.

Evidence that Sapping is the Governing Process in the Development of Theatre-headed Valleys in the Navajo Sandstone:

1. Theatre-headed valleys do not occur in all lithologies on the Colorado Plateau. In the Glen Canyon region they are best developed in the Navajo Sandstone. The occurrence of theatre-headed valleys here is due to a unique interplay of lithologic, structural, and stratigraphic factors. The Navajo Sandstone is a highly transmissive aquifer underlain by impermeable rocks of the Kayenta Formation. Groundwater tends to emerge at seeps in the cliff wall at the zone of contact. Groundwater seepage results in slow grain release, enlarging cavities or alcoves, and undermining basal support for the cliff to cause eventual mass movement failure of the canyon head or sidewalls (Laity, 1980).
2. Within the Navajo Sandstone two populations of valleys were identified with markedly different geomorphic features. The first group, morphologically analogous to Martian small valleys, exhibits theatre-heads, longitudinal profiles with high step-like discontinuities, and commonly asymmetric, structurally controlled network patterns. The second group is characterized by tapered terminations of first-order tributaries, a relatively smooth concave-up profile, and a more dendritic appearing network pattern. The differences in form of these valley types are attributed

primarily to structural constraints that determine the relative effectiveness of overland flow and groundwater (sapping) processes. Of particular importance to the direction of valley growth is the dip direction of the beds. Where groundwater converges towards the canyon head and runoff values are low, headcuts develop; where groundwater flows downdip away from valley heads and seepage is minimal, and where runoff is high, profiles are concave-up and theatre-heads do not occur.

3. The distribution of springs and relative discharge of groundwater along canyon walls are compatible with a general model of drainage extension by sapping processes. Dunne (1980) and others propose that groundwater discharge should be greatest at the canyon head and decrease distally from it. Seepage discharge measurements were made in two large canyons in the study area. Springs at the theatre-heads comprised 20-40 percent of total flow, with sidewall springs and lateral inflow directly into the channel contributing the remainder. The significant percentage of discharge derived from the head spring and the measured decreasing rate of inflow in a downstream direction support a model of headward growth by sapping processes.

4. In addition to the quantitative estimate of baseflow fed by groundwater seepage, alcove distributions also provide morphological indicators of processes forming and modifying the canyons. Alcoves growing at the Navajo/Kayenta contact were classified as either wet or dry, according to the amount of observable seepage. Dry alcoves may represent non-contemporaneous features and/or alcoves that are presently enlarging at a much slower rate than wet alcoves. The observation that wet alcoves are concentrated near canyon heads, and that dry alcoves are more common in the lower reaches of the valleys is consistent with valley growth by sapping.

5. As groundwater flow is particularly sensitive to bedrock fractures and to changes in gradient resulting from regional folding, the strong correlation between these factors and canyon growth is indicative of a major role played by sapping in valley evolution. Network patterns of theatre-headed valleys suggest strong control by structural factors: they are commonly highly asymmetric, show unusual constancy of tributary junction angles into the mainstream, and exhibit pervasive parallelism of tributary orientation over large geographic areas. An analysis of air photographs and of rose diagrams illustrating canyon, runoff channel, and joint orientations also revealed several structural relations that argue for the formation of theatre-headed valleys by groundwater flow. It is notable that theatre-headed canyons are found principally on surfaces with low dip angles, favoring a large proportion of infiltrated water and thereby having less surface runoff: as the dip angle steepens, surface runoff increases and there is a resultant change in canyon morphology towards narrower valleys with tapered terminations.

In addition, a detailed examination of individual drainage basins reveals that the directionality of canyon growth often varies considerably from that of runoff channels. This is particularly evident where the

presence of soil or other cover materials masks surface jointing and causes a more random orientation of the runoff channels, but the canyons nevertheless remain in alignment with the regional fracture system. It can be inferred from these observations that canyon orientation is largely the result of groundwater seepage related to fractures sensed at depth, rather than of waterfall erosion along the path of plateau streamflow.

6. The form of the longitudinal profile and field observations of the headscarp do not support the hypothesis of theatre-head development by knickpoint retreat and waterfall erosion. The notches through which runoff flows at the top of the headwall are generally very narrow and represent an insignificant fraction of the total relief or breadth of the theatre-head. This geometrical relationship suggests that the discharge carried to the falls is insufficient to create, through spray radius and mechanical erosion, scarps of the magnitude developed. Furthermore, headscarps are best developed in networks where the contribution of overland flow to the headscarp is small. As the flow volume increases, these steps in the longitudinal profile are smoothed out. Theatre-heads are not developed in drainage basins where, owing to the dip of the beds, groundwater moves in a direction away from the canyon headwalls.

Conclusions

The primary erosional mechanism for the development of theatre-headed canyons in the Navajo Sandstone appears to involve groundwater sapping processes: overland flow does not explain the relationships in as reasonable or consistent a manner. The strong relationship between valley form and type of erosional process is evidenced by the development of two morphological populations of valleys within the same lithologic and climatic environment - the development of each is tied to the relative effectiveness of overland flow or groundwater flow processes. Structure, primarily bed dip, is the principal control. Although the constituent materials, scale, climate, structure or groundwater conditions of Mars cannot be replicated in any Earth analog, the striking form similarities to the Colorado Plateau and the strong process/feature relationships observed there suggest that at least gross geomorphic processes may be similar and that sapping processes are indicated for the Martian valleys.

REFERENCES:

Dunne, T., 1980, Formation and controls of channel networks: Progress in Physical Geography, v. 4, no. 2, p. 211-239.

Laity, J.E., D.C. Pieri, and M.C. Malin, 1980, Sapping processes in tributary valley systems: Reports of Planetary Geology Program, 1979-1980, NASA TM 81776, p. 295-297.

Pieri, D.C., 1980, Martian valleys: Morphology, distribution, age, and origin: Science, v. 210, p. 895-897.

Sharp, R.P., and Malin, M.C., 1975, Channels on Mars: Geological Society of America Bulletin, v. 86, p. 593-609.

Groundwater sapping in sediments: Theory and experiments. Alan D. Howard and Charles McLane, Department of Environmental Sciences, University of Virginia

Viking imagery of Mars has revealed many crudely dendritic channel networks that are suspected to have originated by groundwater sapping processes. Although sapping processes are increasingly being recognized as important contributors to the development of headwater channels in many terrestrial drainage basins, sapping is generally masked by the effects of overland flow. Because of this, there has been almost no quantitative investigation of sapping processes or of the morphology of valley systems developed primarily by sapping. Our project involves several related efforts: 1) Quantification of sapping rates as a function of flow under conditions similar to natural groundwater flow towards valleys; 2) Experimental development and monitoring of small-scale sapping networks developed in fine sediments; 3) Development and use of digital computer groundwater groundwater flow models for prediction of flow conditions at sapping faces; 4) Use of the above information to develop computer simulation models of the development of drainage networks by sapping processes; and 5) Comparison of the morphology of channel networks developed by 4) with presumed Martian analogues to determine the likelihood of sapping as the dominant Martian process and the groundwater volumes and rock types that would be required.

The initial phases of the study are being concentrated in elucidation of the mechanics and morphological results of sapping processes in fine-grained sediments. Although sapping processes on Mars are likely to occur in rock or partially consolidated sediments containing large grain sizes, study of sapping processes in fine sediments is an important stepping stone towards a more general understanding, because sapping in noncohesive or slightly cohesive sands, silts, and clays occurs on temporal and spatial scales which can be monitored and quantified for comparison with theoretical and simulation models, and the miniature drainage networks developed by sapping in five sediments are morphologically quite similar to larger terrestrial and Martian channel systems presumed to be formed by sapping this similarity is almost certainly not coincidental.

We are investigating both the threshold of erosion and the rate of erosion of a variety of fine-grained sediments in a simple chamber approximately two feet high by about 8 feet long and two inches thick (Figure 1). The flow patterns that can be achieved in this chamber are quite similar to natural groundwater flow towards valleys, and the flow lines and hydraulic gradients should be directly comparable to their larger counterparts for similar geometries and Darcian flow.

The mechanics of erosion of slopes by seepage can be analyzed by considering the bulk stability of the soil, under the assumption that seepage erosion will commence under about the same conditions that the surface layers of the soil become unstable. It is assumed that the conditions along the slope vary gradually, so that when considering slope stability for a small slope element (Figure 2a), the forces on the upslope and downslope sides (A-B and C-D) are equal and opposite, and so need not be considered. The following forces must be placed in equilibrium: 1) The buoyant weight of the soil ($G_b$ a d), where $G_b$ is the buoyant unit weight of the soil and a and d are the dimensions of the soil prism; 2) The resultant of the boundary normal efective

stresses ($N_e$); 3) The resultant of the shear stresses acting over the boundary of the element (T); 4) The seepage force, which is the product of the volume of the element times the unit weight of water, $G_w$, times the gradient, I ($G_w$ I a d). For seepage flowing towards the slope at an angle (Figure 2b), the hydraulic gradient equals:

$$I = \text{Sin}\,\phi / \text{Cos}\,(\psi + \phi),$$

where  is the slope angle. Forces acting normal ($N_e$) and parallel (T) to the lower surface (B-C) are the projected components of the seepage force and the buoyant unit weight:

$$N_e = G_b \text{ a d Cos } \phi - I\, G_w \text{ a d Sin } (\psi + \phi),$$
$$T = G_b \text{ a d Sin}\phi + I\, G_w \text{ a d Cos } (\psi + \phi).$$

For noncohesive soils seepage erosion may be expected to begin near the conditions where the soil near the surface becomes unstable and where there is seepage from the soil face. A general failure law for noncohesive soil is:

$$T_c = N_e \text{ Tan}\,\theta,$$

Where $T_c$ is the critical shear force and $\theta$ is the characteristic angle of internal friction for the soil. Substituting from the above equations, conditions of limiting stability should be reached when:

$$\text{Tan}\,\theta = [G_t \text{ Sin}\,\phi\,]/[G_b \text{ Cos } \phi - G_w \text{ Sin}\phi \text{ Tan } (\psi + \phi)],$$

Where $G_t$ is the total unit weight of the soil ($G_b + G_w$). Solution of this equation for the maximum stable slope angle, $\phi_m$, are shown in Figure 3 as a function of $\psi$ for assumed values of $G_b$, $G_w$, and as shown. Also shown are the values of the hydraulic gradient, I, and the component leading to seepage and capable of transporting soil) $I_n$ = Sin $\phi$ Tan ($\psi + \phi$). Note that sapping on sloping surfaces may occur for hydraulic gradients as low as about 0.3 (compared to a value of 1.3 for the "quicksand" case of $\psi = 90^o$ and $\phi = 0^o$). On an active seepage erosion face, the backcutting should assure that the slope angles in the zone of active erosion lie on the critical curve of Figure 3. In soils with a mixture of grain sizes, smaller grains may be removed from between the larger (suffusion) for hydraulic gradients lower than those given by the formula.

Preliminary experiments with sand in the experimental chamber suggest sapping begins under overall hydraulic gradients as low as about 0.08 (measured as the elevation loss over the length of the flow divided by the length) and that the rate of sapping is roughly proportional to the excess of the hydraulic gradient above the critical gradient (Figure 4). This low overall gradient may be consistent with the theoretical prediction (0.3), because groundwater flow models indicate that hydraulic gradients near seepage faces are greater than the overall gradient. The two-dimensional measurements will be extended to three dimensions in sand-box experiments of drainage network development by groundwater sapping.

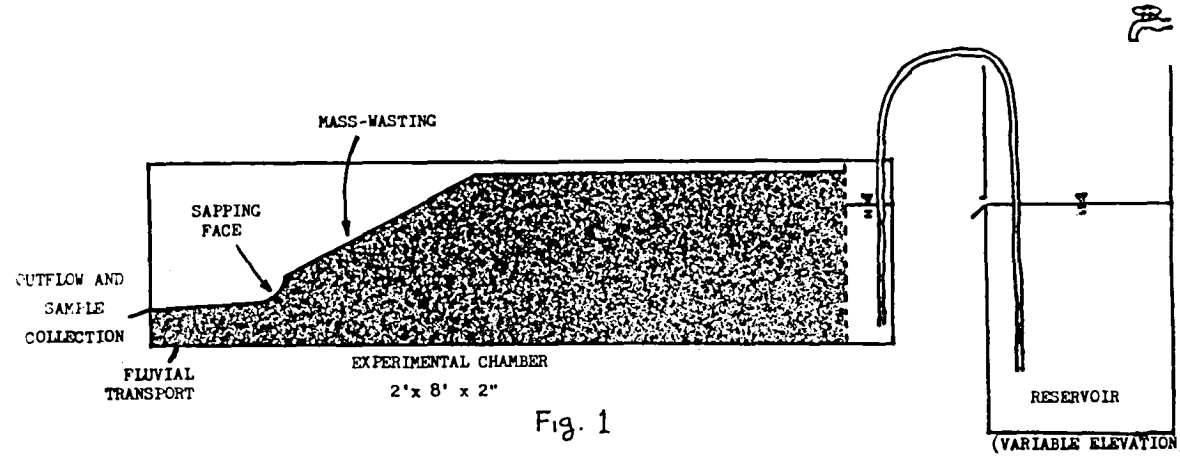


Fig. 1

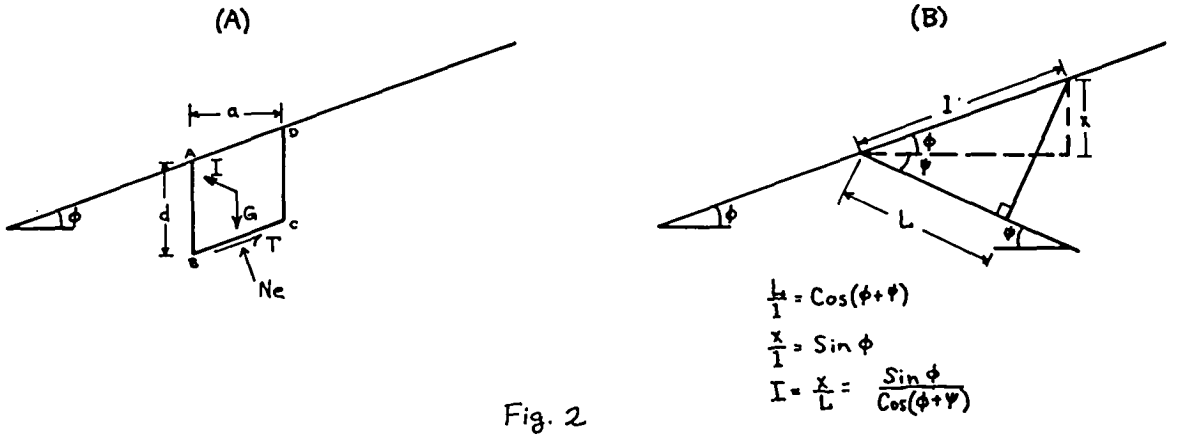


$\frac{L}{l} = \cos(\phi+\psi)$

$\frac{x}{l} = \sin\phi$

$I = \frac{x}{L} = \frac{\sin\phi}{\cos(\phi+\psi)}$

Fig. 2

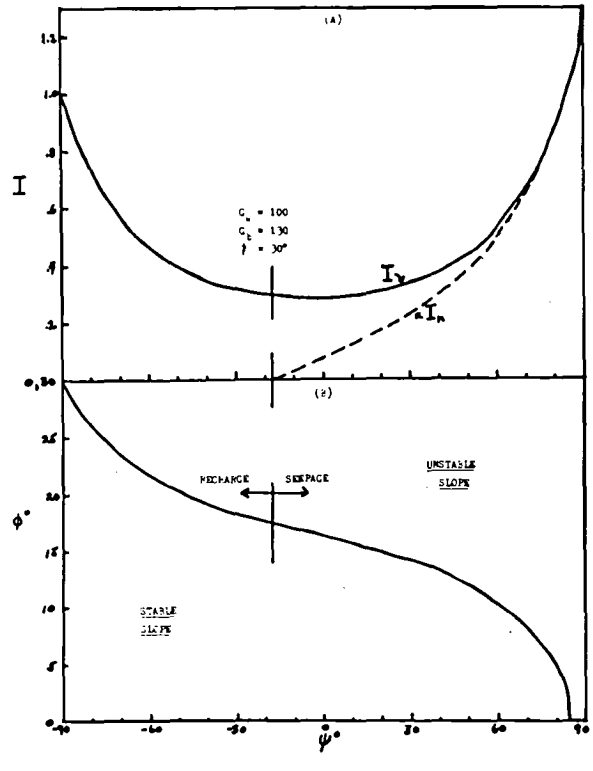


Fig. 3

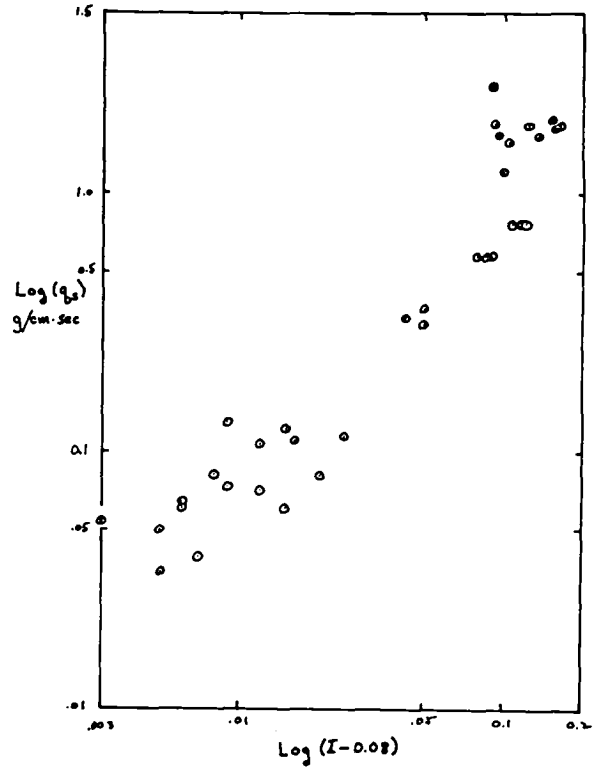


Fig. 4

ETCHED PLAINS AND BRAIDED RIDGES OF THE SOUTH POLAR REGION OF MARS: FEATURES PRODUCED BY BASAL MELTING OF GROUND ICE?

Alan D. Howard, Department of Environmental Sciences, University of Virginia.

The etched plains of the south polar region of Mars (1) (alias pitted plains (2) and pitted and etched terrain (3)) are composed of small-to-large, irregular, steep-sided, round- or flat-bottomed pits incised into a smooth upland surface. The bottom of some pits expose underlying crated plains. Little layering is exposed on the pit walls.

Narrow braided ridges (Figs. 1, 2, and 3) are a conspicuous local feature of the south polar region (forming the Dorsa Argentia) which have been noted on Viking imagery by many observers but not described in the literature. Individual ridges are characterized by a narrow width (less than 1 km), a meandering plan form (wavelength about 15 km), a great length of some of the ridges (150 or more km), frequent splitting and merging (braiding), and the absence of obvious structural control. The ridges are superimposed upon sparsely cratered plains and they commonly cross large to medium sized craters (although the age relationships are often obscured because the ridges are deflected to follow the rim of the crater). However, several small craters seem to be superimposed upon the ridges, indicating that ridges are old compared to the polar layered deposits but young compared to cratered terrains. The main occurrence of the ridges is organized into a "train" of braids extending from about 78°S 10°W to 70°S 70°W, although scattered ridges occur elsewhere on the smooth plains unit of (1), and some disappear under the polar layered deposits. Similar ridges apparently occur locally elsewhere on the planet (M. Carr, personal communication).

At their southward and eastward termination the ridge system of Dorsa Argentia appears to be covered by etched plains material (Fig. 2, locations marked "X"), indicating either that they are older than the etched plains or that they have formed as a modification of that unit and subsequently erosionally exposed, the view suggested here. This relationship, plus a locally distinct boundary between the unpitted portions of the surface of the etched plains and the surrounding smooth plains (dashed lines on Figs. 2 and 3) indicates that the etched plains are not a modification of smooth plains material as suggested by (1), but are a younger deposit superimposed upon the smooth plains and subsequently eroded.

Interpretation: The etched plains have been interpreted by all previous observers to be an erosional modification of massively structured sedimentary blanket, probably a fine-grained deposit of eolian or volcanic origin (1,2,3,4). They have interpreted the erosional agent to be eolian stripping. Arguments in favor of eolian erosion include a prevalence of eolian erosional and depositional landforms in the south polar region (4), the occurrence on Earth of eolian deflation basins (albeit shallower) (3), local elongation of the pits show little preferred wind direction (4) (although most of the pits along preferred orientation except perpendicularity to a possible regional slope), the absence of obvious structural control to the scarp edges bordering the pits, and apparently structurally-intact cratered plains exposed in pit bottoms (3) (the last two arguments appear to rule out an origin through basin faulting). The eolian hypothesis requires the presence of a caprock or surficial lag deposit to account for the localized rather than general scour (4), and mass-wasting of the marginal pit scarps has obviously modified and widened the pits (3).

A different hypothesis is advanced here; the pits are interpreted to be formed by basal melting of ground ice (which, of necessity would have to be a major component of the etched plains unit) and the braided ridges are considered to represent basal outflow channels from this melting which were laterally and vertically confined by ground ice.

Several investigators in informal discussions have raised the possibility that the braided ridges are eskers, that is, fluvial sediments laid down by basal melting of a thick ice cover, now ablated. The morphological comparisons are favorable, particularly their occurrence as ridges, the narrow width relative to the wavelength of the meandering (due to ice-confined channel walls), and the braided pattern of the ridges. Open-channel flow is argued against by their narrow width, positive relief and their crossing of crater rims without apparent erosional modification. Former channel deposits with inverted relief created by erosion have been found on Mars (5), but they are relatively wide (compared to wavelength), flat-topped features. Unfortunately, a lack of quantitative studies of morphology of terrestrial esker systems and the poor quality of published maps has prevented a more detailed comparison. The source of the sediments forming the putative eskers would be derived both from debris or dust in the ice and from erosion of cratered plains beneath the ice. The disappearance of certain of the ridges beneath the etched plains suggests that at least some of the source deposit may remain as the etched plains, and that the pits have formed by basal sapping of ice and debris composing the etched plains deposit. A high ice content in these deposits would be required, but this has already been implicated to be present because of the scarp-wall sapping (3). Some of the pit bottoms expose apparent ridges aligned with the long dimension of the pits, suggesting that they may be equivalents of the braided ridges. It has been suggested that the polar layered deposits may be episodically subject to basal melting (6). Although the massive etched plains deposits seem to be stratigraphically distinct from the layered deposits, they may reflect such basal melting.

The scenario outlined above faces several difficulties. The area of strongest development of the braided ridges (Dorsa Argentia) offers no other evidence of an ice cover (e.g., moraines, grooving, or remnant deposits). Secondly, many contacts of the etched plains deposits with the adjacent smooth plains near the braided ridges seem uneroded (Fig. 3) (e.g., the size of the pits diminshed gradually near the contact, suggesting an original thinning of the deposit). Thus, if the channels were confined during their origin, a complex stratigraphy and a hypothetical ice cover distinct from the etched plains unit are required. Finally, there is no clearly-identifiable lateral extension of the ridge system into outwash channels or fans.

The braided ridges and associated etched plains are clearly intriguing and important features that deserve further study. If they have formed as outlined above, then they share a close relationship to periglacial features elsewhere on the planet, with the distiction being the occurrence of melting from the bottom rather than the top in the cold polar region.

REFERENCES: (1) Condit, C.D. and Soderblom, L.A., 1978, U.S. Geol. Survey Map I-1076; (2) Murray, B.C., Soderblom, L.A., Cutts, J.A., Sharp, R.P., Milton, D.J., and Leighton, R.B., 1972, Icarus, 17, 328-345; (3) Sharp, R.P., 1973, J. Geophys. Res. 78, 4222-4230; (4) Cutts, J.A., 1973, J. Geophys. Res., 78, 4211-4221; (5) Rhodes, D.D., 1980, NASA TM-82385, 397-399; (6) Clifford, S.M., 1980, NASA TM-82385, 405-407.

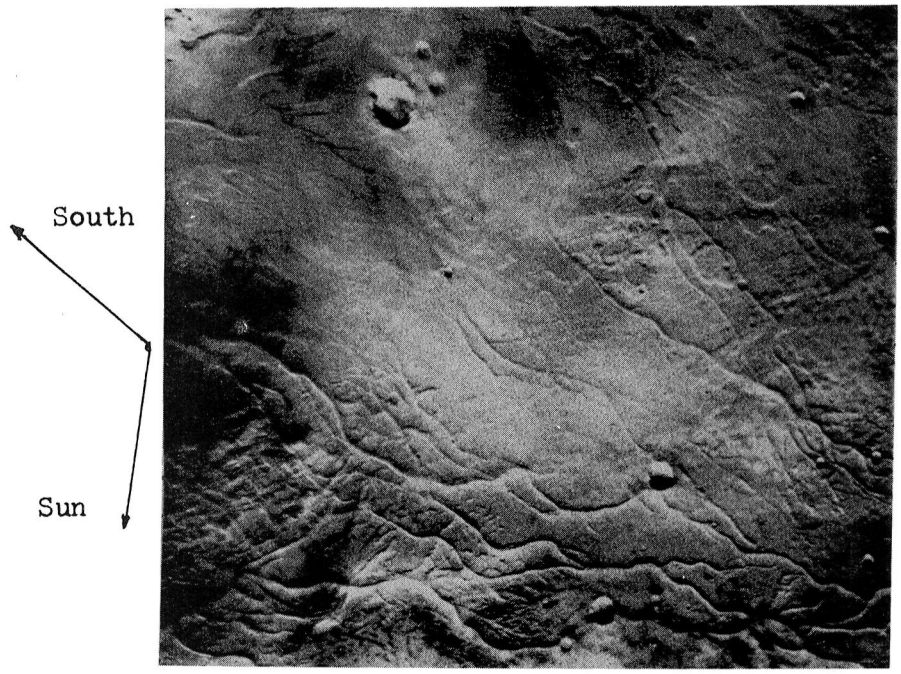


Figure 1: Image 421B53. Image width about 210 Km. Braided ridges disappear beneath etched plains and smooth, young layered? deposits in upper left corner. Picture center at -77.7°S 40.4°W.

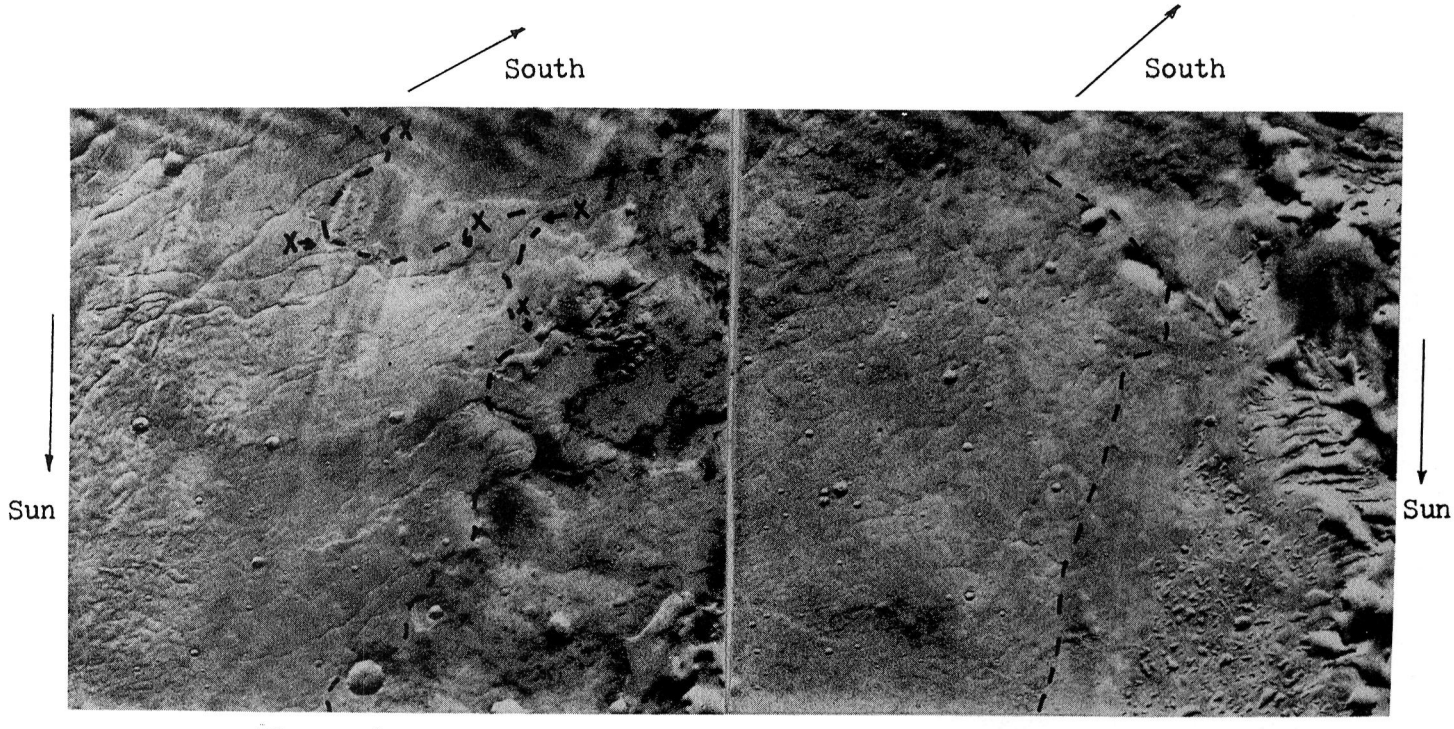


Figure 2

Figure 3

Images 390B85 (left) and 390B89(right). Picture widths about 210 km. Centers at -78.6°S 48.8°W and -75.7°S 62.9°W. Sparsely-cratered plains to left of dashed line, etched plains to right. "X's" mark disappearance of braided ridges beneath etched plains, which also occurs (less distinctly) elsewhere on pictures.

# GEOMORPHIC IMPLICATIONS FROM MARTIAN GROUND ICE

Lisa A. Rossbacher* and Sheldon Judson, Department of Geological and Geophysical Sciences, Princeton University, Princeton, NJ 08540 (* Current address: Department of Geology, Whittier College, Whittier, CA 90608

## Evidence for water ice

The body of evidence for water ice on Mars has grown with continued study of Viking data. Direct evidence comes from studies of atmospheric water vapor (1) and observations of the north polar cap (2). Indirect evidence includes a variety of martian landforms of probable ice-related origins, such as debris flows (3,4), table mountains (5), patterned ground (6), and thermokarst (7,8), supported by theories for atmospheric evolution (9). With the accumulated evidence acquired to date, the significance and implications of water ice on Mars can be reevaluated.

## Significance and implications

Because water ice has created a variety of landforms, it represents a powerful agent in landscape modification. This suggests that water ice may contribute to other processes operating on Mars, including, most importantly, weathering. Water is important in weathering processes on Earth; thermal weathering in the presence of even small amounts of water is significantly more effective than temperature variations under dry conditions. Small amounts of water could enhance physical weathering processes, as well as chemical ones (10), greatly.

The widespread evidence for water ice on Mars implies that some other related processes may be important phenomena. One of these is nivation. This process was first described by Matthes in 1900 (11), and it combines freeze-thaw cycles with mass wasting. The dominant climatic factors controlling nivation on Earth are a high frequency of freeze-thaw cycles, a low evaporation rate, and sufficient water-ice cover (12).

On Mars, many amphitheater heads of small valleys in the Valles Marineris region strongly resemble terrestrial nivation hollows. The only terrestrial analog suggested to date has been hollows formed by sapping (13). Sapping and nivation are similar processes; both involve undermining of basal support of walls, but nivation is confined by snowpack cover. Many of the martian valleys have near-circular heads and are elongate. On Earth, depressions with an ephemeral snow cover are deeper and more circular; where the snow cover persists throughout

the year, the depressions become elongate. The influence of bedrock structure becomes more pronounced on steeper slopes, which also explains the elongation of some depressions (13). Through field work in the Colorado Front Range, Thorn (14) determined that nivation intensifies mechanical weathering by increasing the effeciency of the freeze-thaw cycle; nivation also enhances chemical weathering by a factor of 2 to 4 times.

Frequent freeze-thaw cycles occur on Mars under current climatic conditions (15), but a higher atmospheric volatile content is needed to fulfill the other climatic requirements. In theory, frost deposits should extend to 10°N during southern winter and not quite to the equator during northern winter (16). Frost is most likely to persist past local sunrise only in shaded areas, which makes identification on orbiter images difficult.

## Role in geomorphic history

Most of the geomorphic processes related to water ice are too slow to have been observed over the 2 Mars years recorded in detail by Viking. Evidence for water ice from crater morphologies reflects a relative antiquity, but crater counts on areas with curvilinear terrain, possibly formed by solifluction and ice-cored ridges (7), indicate resurfacing. The requirements for nivation include a low evaporation rate and adequate water-ice cover; these are not met by current martian conditions. However, a denser atmosphere would meet these criteria. Nivation, and presumably related processes, might then have been active early in the planet's history. The possibility that the atmospheric density and volatile abundances have varied with the orbital parameters also needs to be considered.

## Energy budgets

An evaluation of the geomorphic energy budget for Mars remains a valid consideration (17). Energy budgets provide an organizing concept that can provide a key to the similarities and differences between environments. Planetary-energy studies may advance our understanding of global energy and volatile resources; eventually, martian energy budgets may aid evaluation of prospects for a manned mission to Mars. Until more data are collected, the conclusions about the martian energy budget will remain tentative, but this type of analysis may reveal avenues of investigation for future unmanned scientific missions. Particularly relevant to the possibility of near-surface water is the study of microclimates and small-scale energy systems.

The current geomorphic energy regime on Mars has a low energy level compared with earlier periods in the planet's history, and it is not clear whether ground ice plays an active role today. However, it clearly influenced landform development in the past, and water ice still affects the surface through polar deposits, frost, and weathering processes.

This work was supported by NASA Grant NSG-7568.

## REFERENCES CITED

(1) Farmer, C.B., and P.E. Doms (1979). J. Geophys. Res. 84, 2881-2888.
(2) Kieffer, H.H., S.C. Chase, Jr., T.Z. Martin, E.D. Miner, and F.D. Palluconi (1976). Science 194, 1341-1344.
(3) Squyres, S.W. (1978). Icarus 34, 600-613.
(4) Squyres, S.W. (1979). J. Geophys. Res. 84, 8087-8096.
(5) Allen, C.C. (1979). J. Geophys. Res. 84, 8048-8059.
(6) Helfenstein, P., and P. Mouginis-Mark (1980). Proc. Lunar Sci. Conf. XI, p. 429-431.
(7) Rossbacher, L.A., and S. Judson (1980). Repts. Planet. Geol. Prog., 1979-1980 (NASA TM 81776), p. 283-285.
(8) Rossbacher, L.A., and S. Judson (1981). Icarus 45, 39-59.
(9) Pollack, J.B., and D.C. Black (1979). Science 205, 56-59.
(10) Huguenin, R.L., K.J. Miller, and W.S. Harwood (1978). Colloq. Planet. Water and Polar Proc., 2nd, Proceedings, p. 83-94.
(11) Matthes, F.E. (1900). U.S. Geol. Surv. 21st Ann. Rept. 1899-1900, Pt. 2, 167-190.
(12) Russell, R.J. (1933). Bull Geol. Soc. America 44, 927-949.
(13) Laity, J.E. (1980). Repts. Planet. Geol. Prog. - 1980 (NASA TM 82385), p. 358-360.
(14) Thorn, C.E. (1976). Bull. Geol. Soc. America 87, 1169-1178.
(15) Evans, N., and L.A. Rossbacher (1980). Repts. Planet. Geol. Prog. - 1980 (NASA TM 82385), pp. 376-378.
(16) Balsamo, S.R., and J.W. Salisbury (1973). Icarus 18, 156-163.
(17) Rossbacher, L.A., and S. Judson (1980). Repts. Planet. Geol. Prog. - 1980 (NASA TM 82385), p. 364-366.

# SOME THERMODYNAMIC RELATIONSHIPS GOVERNING THE BEHAVIOR OF PERMAFROST AND FROZEN GROUND

Duwayne M. Anderson

State University of New York at Buffalo

It is well established that water-ice occurs in the surface materials of Mars and that temperature regimes are such that ice-rich permafrost may be present in many localities. Water-ice is also thought to be a major constituent of the surface materials on Europa, Ganymede, Callisto, and several of the moons of Saturn.

When ice exists in intimate contact with silicate minerals and other solids a thin interfacial transition layer is present. Recent discussions of this topic in connection with planetology have centered on the nature, properties, and behavior of this layer (Anderson 1979, 1980). In brief, this transition layer possesses the properties of a two-dimensional fluid and is, therefore, referred to as "unfrozen water". The viscosity of this unfrozen, liquid-like water is considerably higher than that of pure water as inferred from nuclear magnetic resonance data and there is evidence of heterogeneity in this interfacial transition zone by phase changes in the range -40°C to -50°C. These major phase changes appear to be dependent upon the nature of the adjacent silicate surface or other solid phase. Below about -80°C the liquid-like behavior of the interface ceases and behavior more characteristic of solids is observed. The thickness of the unfrozen water interface varies with temperature, pressure, and concentration of dissolved substances. The relationships have been extensively studied and discussed and in general are exponential in nature.

The existence of a mobile interfacial fluid facilitates the transport of ionic species through frozen ground and also the response (by regelation) of the ice and mineral particles to changes in temperature and stress fields toward an equilibrium

or steady state configuration. The equilibrium among phases present in frozen ground can be described by appropriate thermodynamic relationships derived for heterogenious systems. The variables needed to define the thermodynamic state of this heterogenious mixture of ice, unfrozen water, and mineral matter are temperature, pressure, and composition. Other variables such as electrical gradients, gravitational fields, etc. are usually neglected but can be included if appropriate or needed. The defined thermodynamic functions required are: The partial molar free energy of the substance under discussion, in this case water ($\bar{F}$); the partial molar enthalpy ($\bar{H}$); the partial molar entropy ($\bar{S}$); and the activity (a). Also needed in the discussion are: The partial molar volume ($\bar{v}$); the partial molar heat capacity ($\bar{c}$); and the freezing point depression ($\theta$). Although thermodynamic theory proceeds from a basis in first principles from which "ideal behavior" can be predicted the theory ultimately becomes empirical because of complex interatomic and intermolecular behavior that as yet is too complex to have been sufficiently understood and described in terms ammenable to inclusion. Consequently, recourse is invariably made to empirical data which are then directly related to the partial molar quantities listed. When the empirical data are accurate and known with sufficient completeness, equilibrium relationships can be predicted with confidence and accuracy. Enough work has now been done to allow the ready determination or prediction of the following phenomena in permafrost and/or frozen ground: The freezing point depression ($\theta$); the latent heat of freezing or thawing; the variation in thickness of the unfrozen water interface separating ice from mineral surfaces as a function of temperature, pressure, and concentration of dissolved substances; the direction of movement of water through frozen ground in response to temperature or electrical field gradients; the maximum, equilibrium pressure that may be developed in or sustained by frozen ground at varying temperatures below freezing.

Consider a mixture of ice and an assembly of silicate minerals for which adequate data on their surface properties, etc. is available (e.g. an assembly of clay minerals, quartz, etc.). Assume that such variables of state as the interfacial area, the composition of the water and other constituents present are constant and invarient. Under these conditions the equilibrium existing between the unfrozen water and the ice present can be described in terms of their respective partial molar free energies and the dependence of these quantities upon temperature and pressure. At equilibrium the partial molar free energies of the unfrozen water and ice present are equal. At slightly different temperatures and pressures, T + dT and P + dP:

$$\bar{F}_u + d\bar{F}_u = \bar{F}_i + d\bar{F}_i \ . \qquad (1)$$

It follows that

$$d\bar{F}_u = d\bar{F}_i \qquad (2)$$

Taking the total derivative of Eq. (2) and identifying the partial derivatives as the partial molar volume $\bar{V}$ and the partial molar entropy $\bar{S}$, respectively, we obtain

$$d\bar{F}_u = \bar{V}_u dp - \bar{S}_u dT \qquad (3)$$

and

$$d\bar{F}_i = \bar{V}_i dp - \bar{S}_i dT. \qquad (4)$$

Equating and rearranging Eqs. (3) and (4) results in

$$\frac{dp}{dT} = \frac{(\bar{S}_i - \bar{S}_u)}{(\bar{V}_i - \bar{V}_u)} \qquad (5)$$

By definition

$$\frac{\Delta \bar{H}_f}{T} = (\bar{S}_i - \bar{S}_u). \qquad (6)$$

in which $\Delta \bar{H}_f$ is the difference in partial molar enthalpy between ice and water. Substitution of this identity in Eq. (5) yields

$$\frac{dp}{dT} = \frac{\Delta \bar{H}f}{T \Delta \bar{V}}. \qquad (7)$$

This is a form of the Clausius-Clapeyron equation describing the phase relationships for ice and the unfrozen water interface in a frozen mixture. The relationships are shown in schematic form in Figure 1 for water and ice in a montmorillinite clay mixture. Equation 7 describes the lines a-a", b-b", etc. in Figure 1.

Two principle factors determine the position of lines b-b", c-c", and d-d", that depict the liquid-solid equilibrium for three water contents. First is the lowered freezing temperature, T, of the drier material (thinner interfacial water), or in other words, a greater freezing point depression. Secondly, there is a reduction in the latent heat of freezing, $\Delta \bar{H}_f$ at lower temperatures. Available estimates of $\Delta \bar{H}_f$ compared with measured freezing point depressions indicate that, of the two opposing effects, the decrease in $\Delta \bar{H}_f$ at lower temperatures is the stronger function and predominates. For this reason Figure 1 is drawn to show progressive decreases in slope of the solidus-liquidus line with decreasing water content.

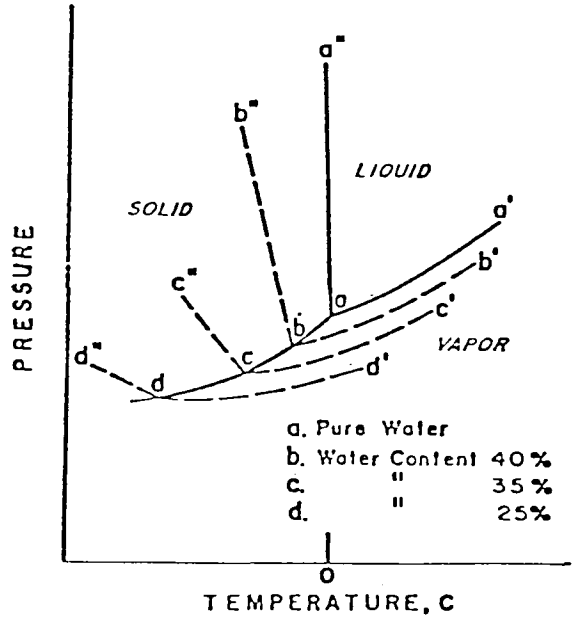


Figure 1. Schematic phase diagram for water imbibed by montmorillonite showing the effect of clay surfaces on the vapor pressure, the freezing point, and the slope of the solid-liquid equilibria (not to scale).

The partial molar volume change associated with freezing the interfacial water could be an important factor if, like T, it can become very small. The specific volume of ice is about 10% greater than that of water at 0°C, but the specific volume of the unfrozen interfacial water next to montmorillonite surfaces is at least 3% greater than that of pure bulk water so that $\Delta \bar{V}$ in this case must be of the order of 7%. It appears that as the temperature is lowered, $\Delta \bar{V}$ for a given thickness of interfacial water is further reduced. The rate of decrease and the final, limiting value, however, have yet to be determined. It is believed, however, that in comparison with the influence of $\Delta \bar{H}_f$ and T, the effect is minor and that the slopes given in Figure 1 are qualitatively correct.

The consequences of decreasing slopes of the solidus-liquidus lines with decreasing water contents are several. The most obvious is that ice pressed against montmorillonite surfaces is more susceptible to pressure melting than normal, and that the application of pressure at constant temperature leads to an increase in the thickness of the unfrozen water interface. This is important in the theory of ice segregation and frost heaving, for at a given temperature below freezing, the build-up of heaving pressures or the external application of pressure acts

to increase the thickness of the interfacial water above that which would otherwise prevail.

The movement of particles suspended in ice along thermal gradients has been demonstrated at temperatures near 0°C. The application of pressure is thus expected to enhance the rate of particle migration at a given temperature, and the application of sufficiently high pressure could induce particle migration at temperatures lower than ordinarily experienced.

In terrestrial environments subject to annual freezing and thawing, frost heaving results in the progressive elevation of the ground surface from 10cm to 30cm during winter. The process is terminated by spring thaw. If the length of the winter season were doubled the extent of frost heaving would be correspondingly increased. In regions of the earth where permafrost occurs, annual freeze thaw is confined to the upper few meters of the ground and frequently freezing occurs simultaneously from the top downward and the bottom upward. The resulting confinement of unfrozen soil in between results in considerable deformation and churning of the ground. Even when the soil is solidly frozen, redistribution of water and the growth of ice lenses occurs. Water is continually transported through the unfrozen liquid interfaces toward regions of lower and lower temperatures. Particle rearrangement and the continual deformation of the frozen ground result. The variety of geomorphic land forms characteristic of permafrost and frozen ground are formed by an interplay of processes involving the transport and redistribution of material in the unfrozen interfacial water and the processes associated with thermal expansion and contraction of the frozen earth and ground water. Similar phenomena are to be expected on Mars and the other planetary bodies where ice is found intermixed with silicate minerals. Unfamiliar land forms and surface features are expected on these planetary bodies where the extremes of temperature and pressure greatly exceed thosecommonly occuring on the earth.

## REFERENCES


Anderson, D. M. Water in the Martian Regolith, Comparative Planetology, 219-224, Academic Press, Inc., 1978.

Anderson, D. M. The Role of Interfacial Water and Water in Thin Films in the Origin of Life. Proceedings NASA Conference on Life in the Universe, Ames Res. Center, Moffett Field, CA., June 1979. (in press)

Anderson, D. M. Tice, A. R., Low Temperature Phase Changes in Montmorillonite and Nontronite at High Water Contents and High Salt Contents. Cold Regions Science and Technology, 3: 139-144, 1980.

# ANALYSIS TOWARDS A DYNAMIC ORIGIN FOR THE FORMATION OF SUBGLACIAL LONGITUDINAL GROOVING IN SEDIMENT OR BEDROCK

David E. Thompson, Jet Propulsion Laboratory, California Institute of Technology, Pasadena, CA 91109

Because of recent hypotheses concerning the origin of longitudinal grooving on Mars as being glacial or subglacial in origin (Lucchitta, 1980; Lucchitta, et al., 1981), and because neither dynamic nor firm kinematic assessment of the potential for glaciers to erode in a preferred longitudinal sense has been carried out on which to base such hypotheses (partial exception of Shaw and Freschauf, 1973), analysis is now underway which purports to examine the development of subglacial longitudinal grooving through means of stable secondary helicoidal flow patterns in basal glacier ice. Analysis includes both stress and temperature dependence in the viscosity whereby the effect of both enhanced flow strain rates and advected temperature gradients leading to shear heating in the ice can be addressed. Furthermore, the effect of widely different temperature gradients such as would be apparent between terrestrial and martian glaciers, and even between temperate and polar glaciers on earth, can be incorporated into the analysis. More importantly, previous work (Thompson, 1979) has shown that the growth of perturbations in glaciers into stable secondary flow patterns requires (1) analysis which incorporates three-dimensional perturbations imposed on realistic primary flow states so that strain softening of the glacier ice can occur through the flow law, or (2) a flow law which is dependent on both the second and third strain rate invariants. This analysis thus incorporates these more realistic assumptions in order to determine the actual conditions under which glacier ice can dynamically develop helicoidal flow fields which are maintained in the primary flow.

Theories of erosion by glaciers do not have to be dynamical as has been aptly demonstrated by Shaw and Freschauf (1973) and by Boulton (1979) and Boulton and Jones (1979). Kinematic theories are discussed in general, and their applicability to deformation of unconsolidated debris or to bedrock erosion is evaluated. However, one difficulty with kinematic theories is that they cannot explain the ubiquitous uniformity of glacial grooving in regions of Arctic Canada and Alaska or in Fennoscandia. Indeed, a kinematic description cannot address observed selective deposition of distinguishable bedrock lithologies, repeated at uniform distances down glacier, as discussed by Drake (1972). For this reason, this analysis deals more with the development of a dynamical theory for the origin of longitudinal grooving. The stability criteria developed help determine the conditions whereby glaciers or ice sheets can access different smaller scale flow fields for erosion at the ice-bedrock interface and what thermal regimes are required for flow enhancement or erosion at all.

This research is supported under NASA contract NAS 7-100.

REFERENCES

Boulton, G.S., 1979, Processes of glacier erosion on different substrata: Jour. Glaciology, vol. 23, no. 89, pp. 15-38.

Boulton, G.S., and A.S. Jones, 1979, Stability of temperate ice caps and ice sheets resting on beds of deformable sediment: Jour. Glaciology, vol. 24, no. 90, pp. 29-43.

Drake, L.D., 1972, Mechanisms of clast attrition in basal till: Geol. Soc. America Bull., vol. 83, pp. 2159-2166.

Lucchitta, B.K., 1980, Glacially grooved valley floors on earth and Mars: Reports of Planetary Geology Program, NASA TM 82385, pp. 381-382.

Lucchitta, B.K., D.M. Anderson, and H. Shoji, 1981, Did ice streams carve martian outflow channels?: Nature, vol. 290, p. 759-763.

Shaw, J. and R.C. Freschauf, 1973, A kinematic discussion of the formation of glacial flutings: Canadian Geographer, vol. 17, no. 1, p. 19-35.

Thompson, D.E., 1979, Stability of glaciers and ice sheets against flow perturbations: Jour. Glaciology, vol. 24, no. 90, pp. 427-441.

A COMPOSITE ORIGIN FOR MARTIAN OUTFLOW CHANNELS

B. K. Lucchitta, U.S. Geological Survey, Flagstaff, AZ 86001

The origin of martian outflow channels has been ascribed to erosion by lava [1], liquid alkanes [2], wind [3], catastrophic floods [4], mudflows [5], and ice [6]. Even though some channels may be eroded by lava erosion, the hypotheses most often considered are origin by wind, flood, mud, or ice. All of these rely primarily on morphologic comparison between channel features and those formed on Earth by these agents.

The wind hypothesis, championed by Cutts and Blasius [3], envisions that atmospheric currents with suspended or saltating particles formed the channels by plucking or abrasion. Supporting evidence for this hypothesis include: many streamlined forms in the channels resemble wind-carved yardangs; wind erosion is active on Mars at present and can take place on very gentle slopes; and the volume of the source area is not restricted. A disadvantage is that the wind is unlikely to form channelized air currents or to emerge from well-circumscribed areas, such as the chaotic terrain. Also, uniform gradients and integrated drainages suggest fluid flow, and the sinuosity of outflow channels is generally more pronounced than sinuosities found in wind-streaked terrains. However, valley winds may well have eroded channel walls and floors after the original channel was formed.

The catastrophic flood hypothesis, proposed by Baker and Milton [4] depends primarily on morphologic similarities between the martian outflow channels and those created by the catastrophic Spokane flood that formed the Washington scablands. Similarities, which have been documented extensively, are expressed by the overall and anastomosing flow patterns of the channels, streamlined islands, and shape of the longitudinally grooved floors. However, differences in scale remain a major problem: martian channel features are, on the average, much larger than their proposed terrestrial analogs. Not even the discharges calculated by Carr [7] for possible catastrophic outburst from the chaotic terrain on Mars are sufficient to account for the depth of water that would be needed to form the deep, wide grooves on the martian channel floors.

The mudflow hypothesis, advocated by Nummedal and Prior [5] proposed collapse of metastable sedimentary units in response to a seismic event or to shear during sliding, resulting in spontaneous liquefaction or retrogressive flow slides. The collapsed areas formed the chaotic terrain; the flow slides carved the channels. Striking morphologic similarities are seen between liquefaction slides in Norway, submarine liquefaction slides on the Mississippi delta [5], and the martian chaotic terrain. All are widened, collapsed areas that have slump-blocks at the heads, narrow channel outlets, and scarps near the outlet that face uphill. These similarities strongly suggest that a mudflow-like process may have operated in the source areas of the channels. A problem with the mudflow hypothesis lies in the high speeds required to maintain flow along the lower channel reaches. The potential energy that initially caused high rates of flow could hardly

be effective in the lower channel reaches, 1,000 to 2,000 km downstream. In these areas, flow would be propelled by gravity, driven by the local gradient, and mudflows would become catastrophic floods that are highly charged with debris. Therefore mudflows, like catastrophic floods, would seem to require unreasonably high discharge rates.

The ice stream hypothesis proposes that many of the channel features were carved by creeping masses of ice [6]; it is based on morphologic similarity of channel forms to terrestrial forms sculptured by glaciers, ice streams, or continental ice sheets. Similarities include: anastomosis of channels, U-shaped valleys, sinuosity of valleys, streamlined islands, longitudinal scour on valley walls, and grooves on channel floors. A problem with this hypothesis is the difficulty of moving glacial ice under martian conditions of low gravity, low temperature, and low gradient on the channel floors. However, if the ice were warm-based and wet at the sliding contact, this problem would be less severe. Grooves on the channel floors, which suggest erosional and depositional processes, infer warm- and wet-based ice. Similar grooves under terrestrial ice sheets are drumlinoid forms that also formed by erosion or deposition [8]. Such glacial grooves or flutes are preferentially formed on Earth by thin, wet ice that is loaded with debris and is sliding rapidly over low gradients [8]. Thus, flute-forming ice masses appear to have many characteristics in common with extremely viscous mudflows that are travelling on low gradients.

The above consideration suggests that mudflows and the flute-forming fluid that carved martian channels are related. Other landforms, as discussed above were probably formed by flooding or by the wind. Therefore, the following composite origin is suggested for the outflow channels. The channel-forming fluid emerged from the chaotic terrain as liquefaction mudflows that became more viscous and moved more slowly downstream, where the liquid was frozen and the channels choked in the manner of ice drives. Such slugs of debris may have moved through the channels as hybrids between very viscous mudflows and very debris-rich and wet glaciers; confined brines at their base may have buoyed the flow locally. Increased friction on steeper gradients may have partly liquefied the material so that it reverted, in some places, to true mudflows or floods. The debris was carried into the northern plains where it may have created some of the irregular topography seen in that region. After the channels were formed, wind erosion modified many of the previously developed landforms.

References

[1] Schoenfeld, E. (1977) Martian volcanism. In Lunar Science VIII, p. 843-845. Lunar Science Institute, Houston.

[2] Yung, Y. L. and Pinto, J. P. (1978) Primitive atmosphere and implications for the formation of channels on Mars. Nature 273, 730-732.

[3] Cutts, J. A. and Blasius, K. R. (1981) Origin of martian outflow channels: the eolian hypothesis. J. Geophys. Res. 86, 5061-5074.
[4] Baker, V. R. and Milton, D. J. (1974) Erosion by catastrophic floods on Mars and Earth. Icarus 23, 27-41.
[5] Nummedal, Dag and Prior, D. B. (1981) Generation of martian chaos and channels by debris flows. Icarus 45, 77-86.
[6] Lucchitta, B. K., Anderson, D. M., and Shoji, H. (1981) Did ice streams carve martian outflow channels? Nature 290, 759-763.
[7] Carr, M. H. (1979) Formation of martian flood features by release of water from confined aquifers. J. Geophys. Res. 84, 2995-3007.
[8] Menzies, J. (1978/1979) A review of the literature on the formation and location of drumlins. Earth-Sci. Revs. 14, 315-359.

# GEOMORPHIC MAPPING OF CAPRI CHASMA

Jon C. Boothroyd, Department of Geology, University of Rhode Island, Kingston, RI 02881; Barry S. Timson, The Mahoosuc Corporation, Augusta, ME 03240

Geomorphic mapping of Capri Chasma, following the general format of Baker and Kochel (1979), has been carried for the area centered on 5S, 35W. The chasma in this area is a proximal outflow channel feeding Tiu and Simud Valles. The terrain has been divided into nine basic geomorphic units that are further subdivided for a total of 17 sub-units.

Smooth plains, cratered plateau, and craters follow the mapping scheme of Saunders (1979). The wide valley floor contains both large (30-40 km long), and smaller, erosional remnants showing the effects of multiple fluid flows. Chaotic terrain in various stages of collapse and burial are present. The valley walls have well-defined but discontinuous terraces. Later debris flows and slumps have modified most of the above units.

It is apparent that the valley has been subject to multiple episodes of fluvial flow, perhaps by sediment or ice-charged water or by debris flows. Between-flow and post-flow secondary modification to the walls and floor of the valley occurred by cratering, mass-wasting, and eolian processes. Mass-wasting appears to be the dominant secondary process, affecting many of the earlier craters as well as the valley walls. The last stage of secondary modification may be due to eolian processes that have sculpted the small remnants and chaotic terrain on the valley floor and terraces. The complete suite of mass wasting and collapse, secondary modification features suggests that the melting of ground ice or subpermafrost water played at least some role in the development of the landscape.

## REFERENCES CITED

Baker, V.R., and Kochel, R.C., 1979, Martian channel morphology; Maja and Kasei Valles: Jour. Geophy. Research, v. 84, No B14, p. 7961-7983.

Saunders, R.S., 1979, Geologic map of the Margaritifer Sinus quadrangle of Mars: U.S. Geol. Survey Map I-1144 (MC-19).

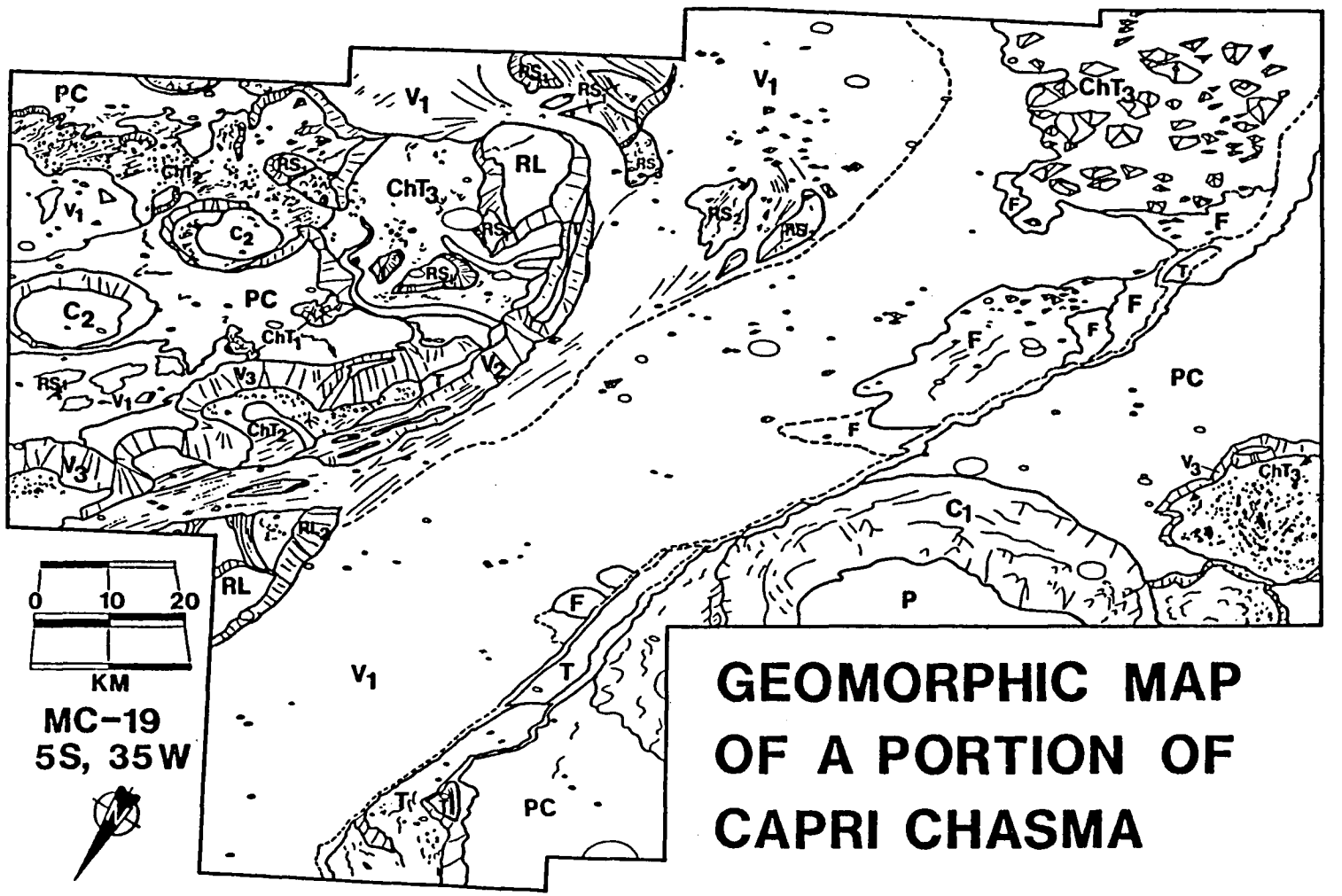


# GEOMORPHIC MAP OF A PORTION OF CAPRI CHASMA

# GEOMORPHIC UNITS: CAPRI CHASMA, M-19 (5S, 35W)

- P SMOOTH PLAINS
- PC CRATERED PLATEAU
- C CRATERS
  - 1 RIMMED
  - 2 SUBDUED
- RL REMNANTS, LARGE
  - 1 REMNANT SURFACES
  - 2 SCARP/SLOPES & TALUS
- RS REMNANTS, SMALL
  - 1 UNMODIFIED
  - 2 FLOW - MODIFIED
  - 3 COLLAPSED MASS
- ChT CHAOTIC TERRAIN
  - 1 IN PLACE
  - 2 DISPLACED
  - 3 BURIED
- T TERRACES
- V VALLEYS
  - 1 VALLEY FLOOR
  - 2 VALLEY WALL
  - 3 VALLEY HEAD CUTS
- F DEBRIS FLOWS/ SLUMPS

PRELIMINARY COMPARISON OF INSELBERGS IN THE CERBERUS REGION OF MARS TO TERRESTRIAL ISOLATED HILLS IN ARID, HUMID, AND GLACIAL TERRAINS.

L. S. Manent and Farouk El-Baz, National Air and Space Museum, Smithsonian Institution, Washington, D.C. 20560.

Inselbergs and knobs on Mars have been compared to isolated hills in eolian environments. Specifically, we have discussed the analogies between inselbergs and knobs in the Cerberus region of Mars and isolated hills and yardangs in the Farafra region in the Western Desert of Egypt (El-Baz and Manent, 1980). However, the Cerberus inselbergs have not previously been compared to hills in other than eolian environments.

In this study we compare inselbergs in the Cerberus region of the Elysium Quadrangle to hills in arid, humid and glacial regions. The purpose is to see if the martian inselbergs are analogous to terrestrial landforms formed by eolian, fluvial or glacial erosion. The terrestrial isolated hills were stereographically studied using aerial photographs. The same parameters used to measure the hills in Farafra and Cerberus by El-Baz and Mananet (1980) were used to measure those in two areas selected at random in Puerto Rico and the state of New York.

Near Palmyra, New York, N43°08', W77°14', an area exposed to glacial erosion is characterized by isolated hills or drumlins (Fig. 1) that were formed by ice moving south from the Ontario basin. Drumlins, in general, are smooth, dome-shaped, streamlined hills formed by the process of advancing or retreating glacial ice. They are oval in shape and range from less than 0.4 km to over 3 km in length and are usually 3 to 5 times longer than they are wide. The measured drumlins in the Palmyra area range from 200 m to 600 m in width and 0.5 km to 1.7 km in length. The width to length ratio is 0.37 with a standard deviation of 0.07.

In Puerto Rico, two areas located at N18°26', W66°49' and N18°24', W66°26', also exhibit asymmetrical isolated hills. Most of these are mogotes, which are large isolated hills associated with a karst landscape (Fig. 2). In Puerto Rico, this landscape is modified by fluvial erosion

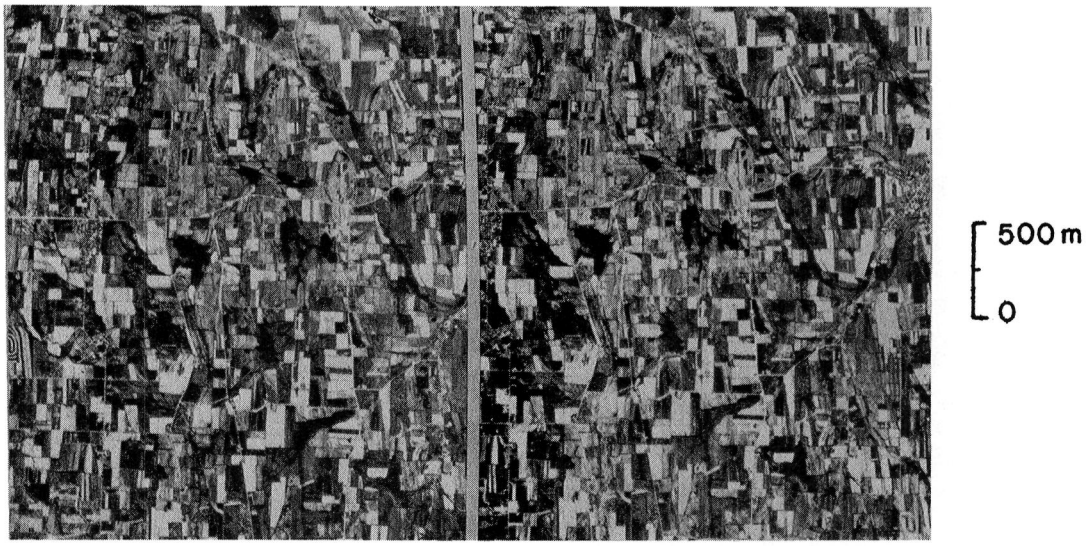


Fig. 1. Stereo pair showing hilly glacial terrain near Palmyra, New York.


Fig. 2. Aerial photograph of isolated hills east of San Juan, Puerto Rico.

during alternating wet and dry episodes. These hills range in width from 40 m to 150 m and in length from 50 m to 250 m. Mogotes rise from blanket sand deposits to heights between 30 and 50 meters. The width to length ratio is 0.73 with a standard deviation of 0.16.

In the Farafra depression in the Western Desert of Egypt, major escarpments were shaped by pluvial action. However, during dry climatic periods, such as the present time, isolated hills are shaped by eolian erosion (Fig. 3a). The widths of these isolated hills range from 4.1 m to 18.4 m and their lengths range from 7.1 m to 44.3 m. Also, in the same area 26 yardangs were measured ranging in width from 0.41 m to 10.2 m and in length from 0.87 m to 15.4 m. The width to length ratio of the Farafra isolated hills and yardangs is 0.65 with a standard deviation of 0.16. These landforms were compared to inselbergs in the Cerberus region of Mars (Fig. 3b), which range from 0.65 km to 16 km in width and 0.88 km to 28 km in length. Width to length ratio of these martian landforms is

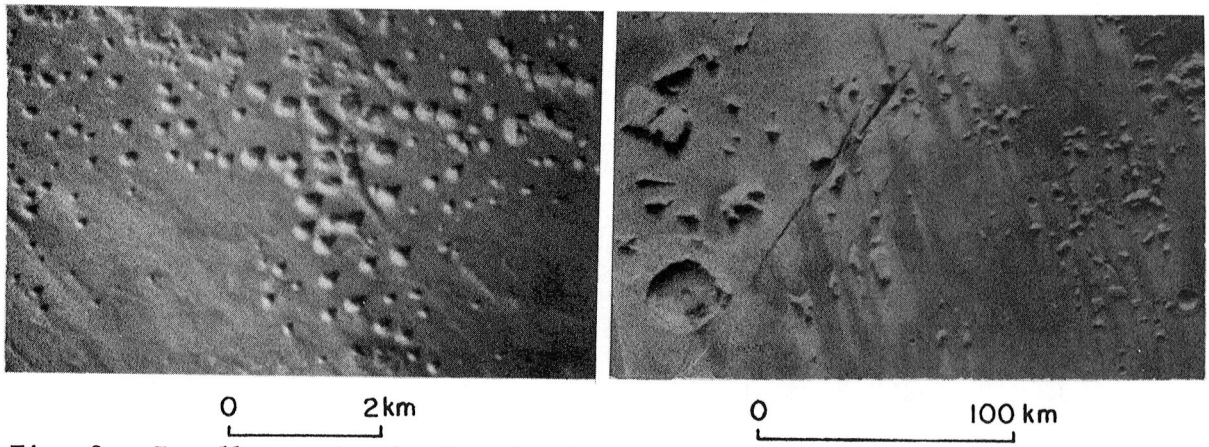


Fig. 3. Inselbergs in the Farafra Depression, Western Desert of Egypt (left) and isolated hills in the Cerberus region of Mars (right).

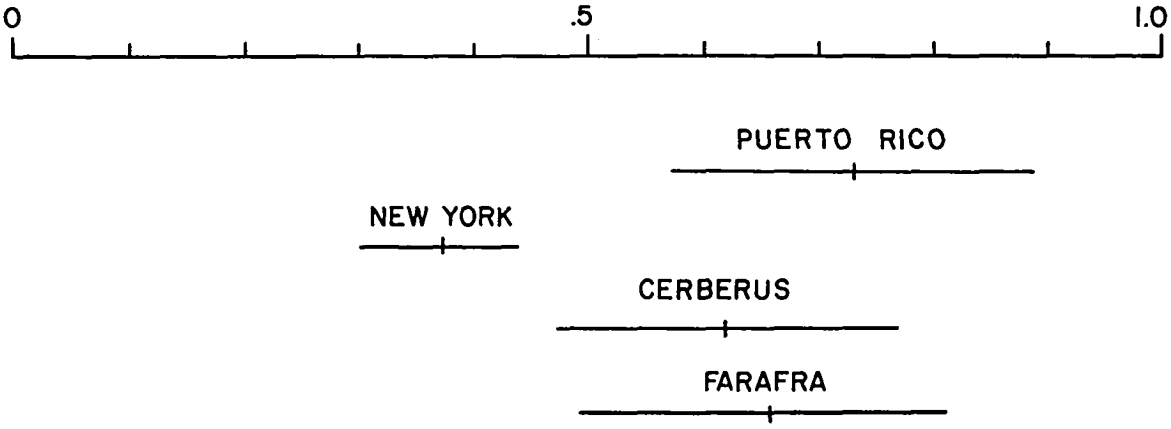


Fig. 4 Width to length ratio of isolated hills with standard deviation.

0.62 with a standard deviation of 0.15 (El-Baz and Manent, 1980).

A comparison between the width to length ratio of the four areas is shown in Figure 4. It shows that inselbergs and knobs in the Cerberus region of Mars and isolated hills and yardangs in the Farafra region of the Western Desert of Egypt have similar dimensions. These differ from the dimensions of the hills in New York and Puerto Rico. This lends additional support to the proposition that inselbergs and knobs in the Cerberus region of Mars are more likely to have formed by eolian erosion than by fluvial or glacial processes. Furthermore, the presence of wind streaks in the lee of both the martian and Egyptian isolated hills (El-Baz and Maxwell, 1980) enforces the importance of eolian action in their formation.

It is recognized that this preliminary observation has resulted from the study of a few isolated cases, and its validity must be further checked. We plan to study several other areas on Mars, together with additional areas in terrestrial arid, humid and glacial environments.

References

El-Baz, F. and L.S. Manent (1980) Comparison of knobs in the Cerberus region of Mars and eolian knobs in the Farafra depression, Western Desert of Egypt. Reports of Planetary Geology Program - 1980, NASA Tech. Memo. 82385, p. 295-297.

El-Baz, F. and T.A. Maxwell (1980) Comparisons of wind streak form in Egypt and on Mars. Reports of Planetary Geology Program - 1980, NASA Tech. Memo. 82385, p. 292-294.

# SUBSIDENCE DEPRESSIONS ON MARTIAN PLATEAU TERRAINS

J. J. Fagan, D. Weiss, J. Steiner, O. L. Franke,
Department of Earth and Planetary Sciences,
City College of CUNY, New York, N.Y. 10031

The question of the relative ages of the northern lowland plains of Mars and the plateau-like uplands bordering on the south has occupied many workers (3 ). One reason for the assumption of great age for the plateaus has been the apparent abundance of impact craters in these regions. However, study of Viking Orbiter images of the plateaus, especially in the fretted terrain area (4), makes it clear that not all of the numerous circular depressions are of impact origin. Circular pits, often aligned along the upper reaches of valleys have been noted in connection with analysis of landforms possibly formed by thermo-karst collapse (1).

It also now seems clear that many of the large, non-aligned circular depressions in the plateau regions near the northern lowland plains do not have the typical form of impact craters (Fig.1) but appear to result from subsidence of the plateau surface. A similar origin has been suggested for small depressions near Olympus Mon and Valles Marineris (2).

Evidence for the origin of certain plateau depressions by subsidence rather than direct impact includes a number of observations: 1. walls of the depressions are usually quite sharp at the rim and the base, suggesting relatively recent scarps; 2. lack of the ejecta typical of recent impacts; 3. typical subcircular outline of the rim with some linear edges apparently controlled by the fractures that stretch across large areas of plateau terrain; 4. relatively flat floors within most of these depressions are uncharacteristic of impact craters; 5. occasional examples of these steep-walled depressions appear to cut across the ejecta pattern of adjacent impact craters (Fig. 2), suggesting subsidence later in time than the impact and making it unlikely that the depression could be an old eroded impact crater.

Subsidence of the plateau surface to form steep-sided depressions seems to have taken place in one of two ways: 1, the entire central region sinks downward as one mass along fracture lines (Fig. 3A) or 2, the central region breaks up into a number of smaller segments which eventually waste away leaving the depression (Figs. 3B and 4).

In some instances, subsidence depressions enclose smaller, concentrically-positioned depressions which appear to be impact craters. In Figure 5, the inner depression appears

to be impact-produced; it is of youthful appearance yet displays no ejecta and has not affected the walls of the outer depression. It seems probable that ejecta corresponding to the inner crater lies buried below enclosing plateau layers; i.e., the impact occurred prior to laying down of plateau strata and served as the focus of the later collapse that formed the outer, larger depression (Fig.6). As settling of overlying layers proceded, the ancient crater was exhumed in the center of the developing depression.

If this interpretation is correct, it may be inferred that ancient impact craters underly many of the larger subsidence craters but usually have not been uncovered because of "incomplete" subsidence or less erosion. The specific processes involved in collapse and removal of the missing plateau materials are uncertain, although wastage of ground ice has been suggested as a cause of some surface collapses(2).

It seems probable that the location of collapse depressions depends on the existence of craters and other topographic features of a more ancient terrain that underlies the plateau strata. The existence of this underlying terrain is also suggested by those impact craters partially exposed by wastage of the irregular edges of the plateau to be seen in a number of places in the fretted terrain.

To conclude, many of the larger, near-circular depressions in the plateau regions bordering the northern lowland plains appear to result from surface subsidence rather than from impact onto that surface. When the number of such depressions is added to that of the abundant small pits, aligned with channels, also not representing impacts, the plateau surface takes on an aspect of being younger than it is normally assumed to be.

References:

1. Brook, G.A.(1979) Terrestrial and Martian Rock Labyrinths, NASA Tech Mem 80339, 42-46.
2. Rossbacher, L. and Judson, S.(1980) Thermokarst on Mars, NASA Tech Mem 1776, 283-285.
3. Scott, D.H.(1978) Mars, Highlands-Lowlands: Viking Contributions to Mariner Relative Age Studies, Icarus, 34, 479-485.
4. Sharp, R.P.(1973) Mars: Fretted and Chaotic Terrains, J. Geophys. Res., 78, 4073-4083.

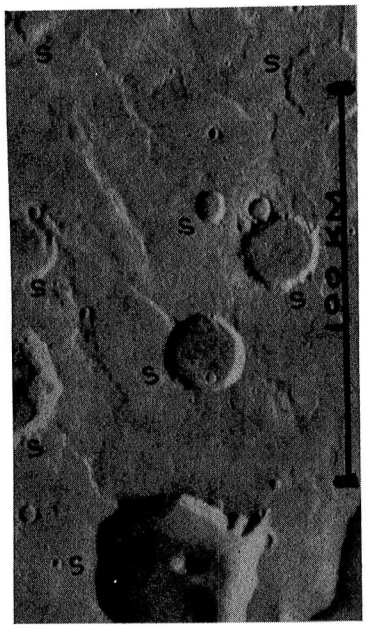


Figure 1. Typical collapse depressions (S). Highland plateaus: 673B69

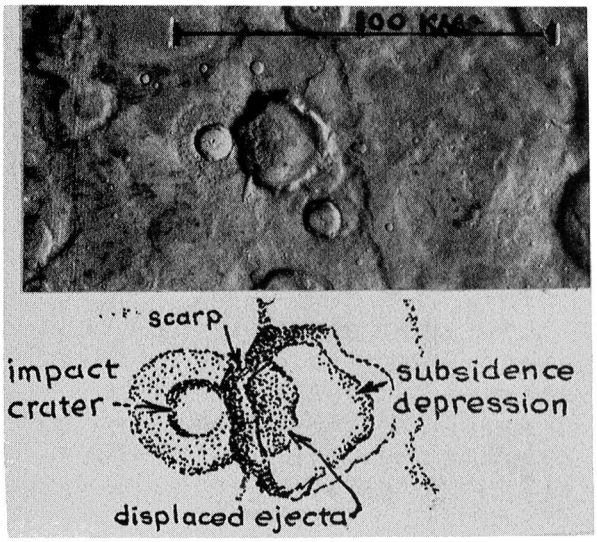


Figure 2. Subsidence depression intersecting an older impact crater: 569A29 (top). Sketch to clarify below.

Figure 3 (below) Hypothetical stages in formation of subsidence depressions: A. collapse of central region as a single unit; B. collapse of central region as separate blocks

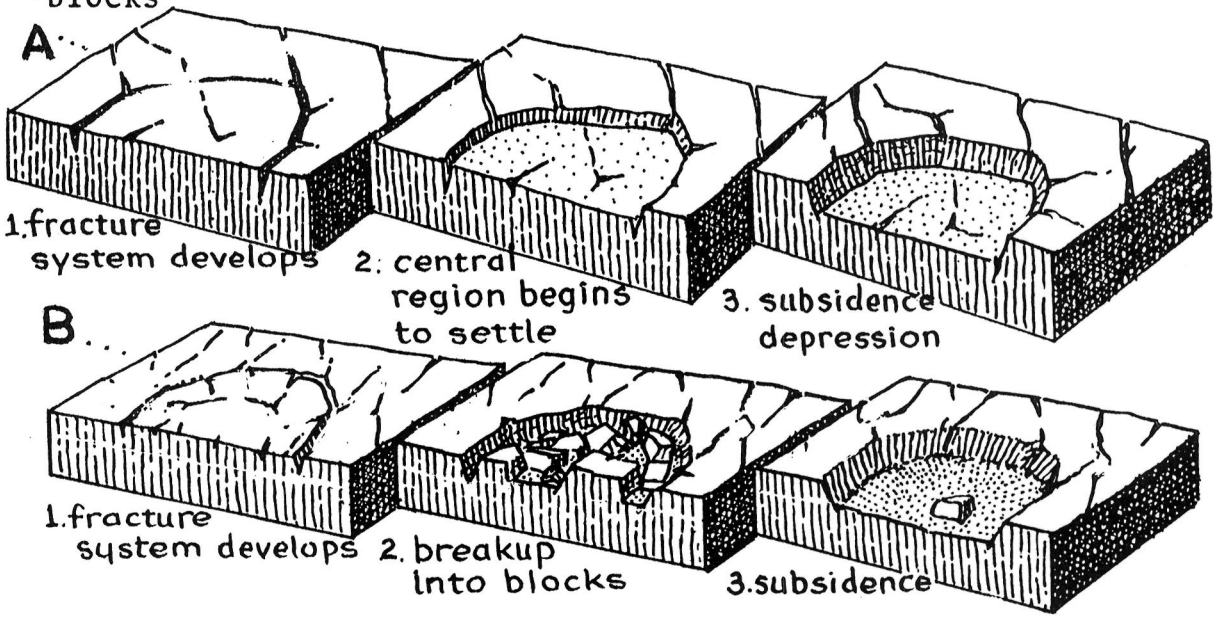

Figure 4. Large subsidence depressions on highland plateaus showing breakup of collapsed surface
534A23

Figure 5. Crater exposed by apparent subsidence of overlying plateau strata.
675B56 (right)

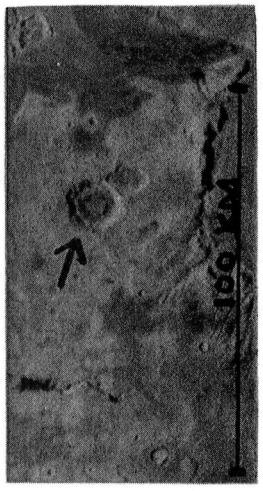

Figure 6 (below). Hypothetical sequence of stages in formation of a subsidence depression by collapse of strata once overlying an impact crater.

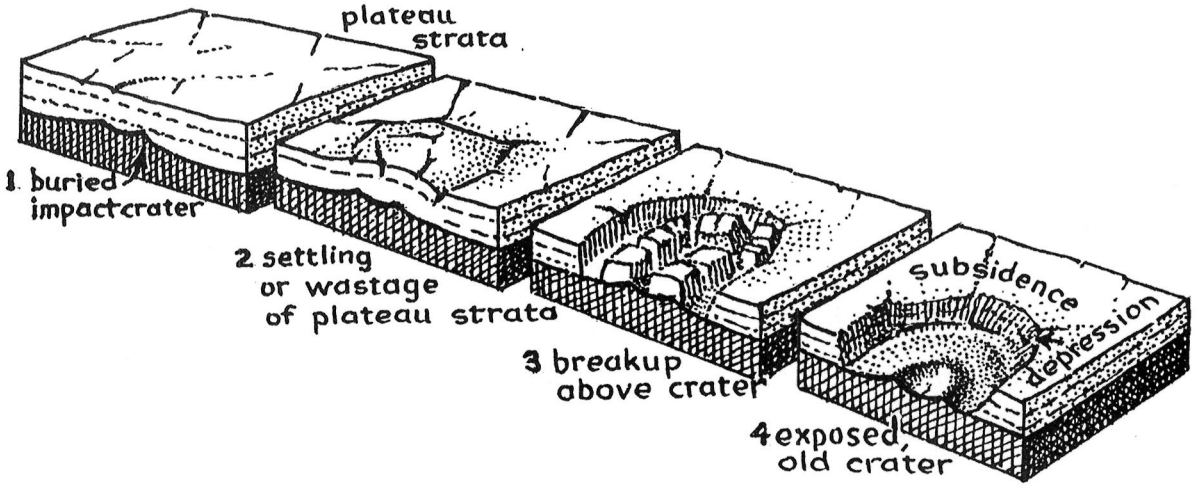

# A MORPHOLOGICAL COMPARISON OF DEPRESSIONAL FEATURES IN PLATEAU MATERIALS OF THE DEUTERONILUS MENSAE REGION BASED ON ELLIPSOIDAL CHARACTERISTICS

J. Steiner, C. Sodden, D. Weiss, J. J. Fagan, O. L. Franke
Department of Earth and Planetary Sciences
City College of CUNY, New York, N. Y. 10031

Meteorite craters and karst-like depressional sinks comprise at least two morphologically distinct classes of small basins in the Deuteronilus Mensae region of Mars. Quantitative descriptions and comparisons of these small landforms are of use in extracting information on possible evolutionary interrelationships between the two forms, as well as on erosional processes, relative ages, and perhaps bedrock lithologies. Several numerical procedures are in use which aid in the construction of three-dimensional analogues of basin forms (1,2) it now seems appropriate to begin to evaluate the possible importance of including non-circularity as a morphological parameter.

Non-circularity has been recognized as potentially indicative of layered bedrock, rill features in bedrock, and the glancing angle of impacting meteoritic materials (3,4). Wolfe (5) quantitatively defined non-circularity through Fourier series approximations to digitized crater outlines on a photomosaic base, adopting the amplitude of the second harmonic as an appropriate expression of elongation. Computer approximations to crater (basin) outlines by use of standard least squares techniques seem to constitute an important alternative approach. Quadratic fits are directly interpreted as ellipses with a standard definition for elongation (eccentricity). Goodness of fit criterion for such approximation are well understood.

Using eccentricity, area, correlation coefficient, and north angle (defined herein by the major axis in the north-direction and the longitude line passing through the center of the ellipse), it is possible to evaluate whether non-circularity of studied features in the plateau area is sufficiently pronounced to be useful as a geologic indicator. Of present interest are comparisons of ellipsoidal parameters of plateau craters with those on the adjacent lowland plains, and the degree to which various parameters can be used to define set criterion.

## Method

Oblique orthographic projections are defined in terms of the geocentric-latitude-longitude coordinates of the center of the

image (6). This point (pixel) is directly recoverable in images based on digitized magnetic tapes and stored in an interactive display system, but this point can only be approximated from photo-images using the digitizing method. Present inverse calculations, based on the Elliott and Schwartz method, rely on generating an image map of the box defined by the latitude-longitude lines derived from SEDR annotations. Computer manipulations of digitized photo-outlines constructed in house enable a best-fit approximation of a tablet-to-photo image overlay match. This match is used to assign photo center coordinates with a reasonable level of confidence and hence to use the inverse imaging techniques. Alternatively, matched photo outlines can be inverse-mapped by using any corner as origin and radial axes as a basis for an iterative approach.

Digitized basin outlines were input to the KW1KR8 multiple regression computer program (7) with second and third degree fit options excersized. Coefficients for quadratic and higher order surfaces were output together with respective coefficients of correlation to standardized files and calculated to ellipsoidal and other simple geometries. Eccentricity as used herein is defined as the ratio of c/a, where c is $(a^2-b^2)^{1/2}$ and a and b are denominators in the formula:

$$\frac{x^2}{a^2} + \frac{y^2}{b^2} = 1 \qquad a \geq b > 0.$$

The eccentricity index varies from 0 to 1 and indicates the degree of departure from circularity (zero is a perfect circle and unity is a straight line). Data used in the following section were not corrected for the minimal distortion deriving from the oblique orthographic projection method. The resolution of a given point is 0.005 inches using a modified Tektronix 4662 interactive digital plotter, which translates to $\pm$ 0.01 kilometers for the medium resolution photos.

## Sample Results

The digitized results for small area (to 200 $km^2$) impact craters can be used to illustrate the use of erecting morphologic profiles based on ellipsoidal criteria. Using 237 plateau craters and 188 plains craters the average elongation of plateau craters as opposed to plains craters is 0.355 $\pm$ 0.080 compared to 0.338 $\pm$ 0.09 in eccentricity (figure 1). Interestingly, least squares approximations to data show intercepts at 0.35 and 0.33 respectively, which evidently support the stated resolution of about 0.01 km on images digitized. The absence of increased scatter over the low-area range supports a maintenance of resolving power almost to vanishingly small crater sizes.

Two weak maxima are distinguishable at eccentricities of 0.4 to 0.5 (1-10 $km^2$) and .30 to .35 (about 20 $km^2$) centers. These groupings are not present in plains crater populations, although related clustering is mirrored in north angle plots against both area and eccentricity. A representative plot of the latter is shown in figure 2 with the smallest area (ca.10 $km^2$) group centered on angles of about 15° north angle compared to a broad diffuse band of samples situated over a higher angle range of about 35 to 50 degrees. Eccentricity data in conjujunction with other ellipsoidal properties of crater outlines can thus be used to identify tentative crater sets which can be examined for overall morphologic similarities. Since the preponderance of data in present files stem from fluidized craters of type E (8), the depicted clusters represent embryo data sets which can be further elaborated and targeted against other crater sets of diverse morphology.

References


1. Mouginis-Mark, P.J. and Wilson, L., 1981, Computers and Geosciences, v. 7 p. 33-45.
2. Davis, P.A. Eliason, E. M., and Soderblom, L.A., 1981, Third International Colloqium on Mars, p. 56-58.
3. Quaide, W. L., and Oberbeck, V. R., 1968, J. Geophys. Res., v. 73, p. 5247-5270.
4. Eppler, D. T., Nummedal, D., and Erhlich, R., 1977 in Impact and Explosion Cratering, ed. by Roddy, D. J., Pepin, R.O., and Merrill, R. B., p. 511-526.
5. Wolfe, R.W., 1980, NASA-TM 82385, p. 164-166.
6. Elliott, D. A. and Schwartz, A.A., 1977, JPL 77-7, 24 pp.
7. Esler, J.E., Smith, P.F., and Davis, F.C., Computer Contribution 28, Kansas Geol. Surv., 31 pp.
8. Mouginis-Mark, P., 1979, J. Geophys. Res., v. 84, p. 8011-8022.

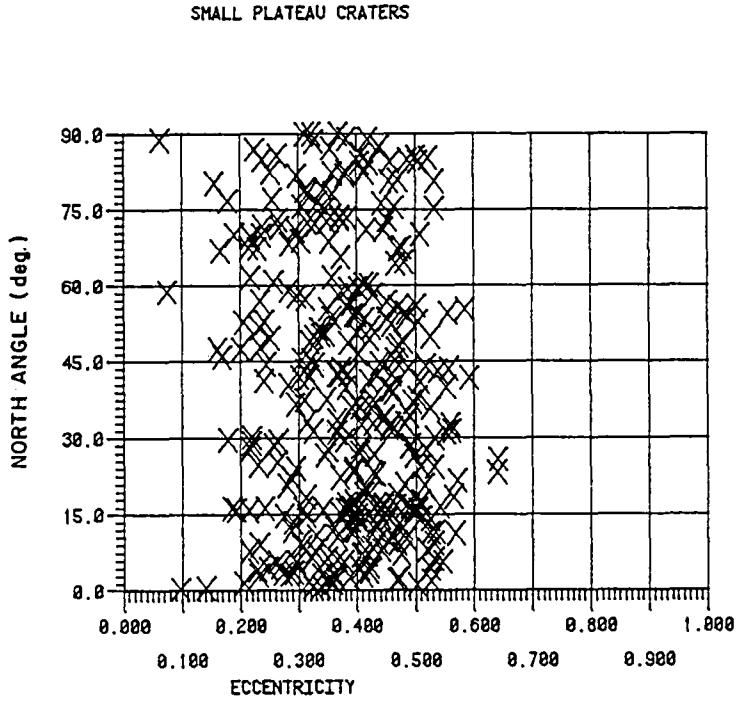


Figure 2. Distribution of north angles for 237 small impact craters.

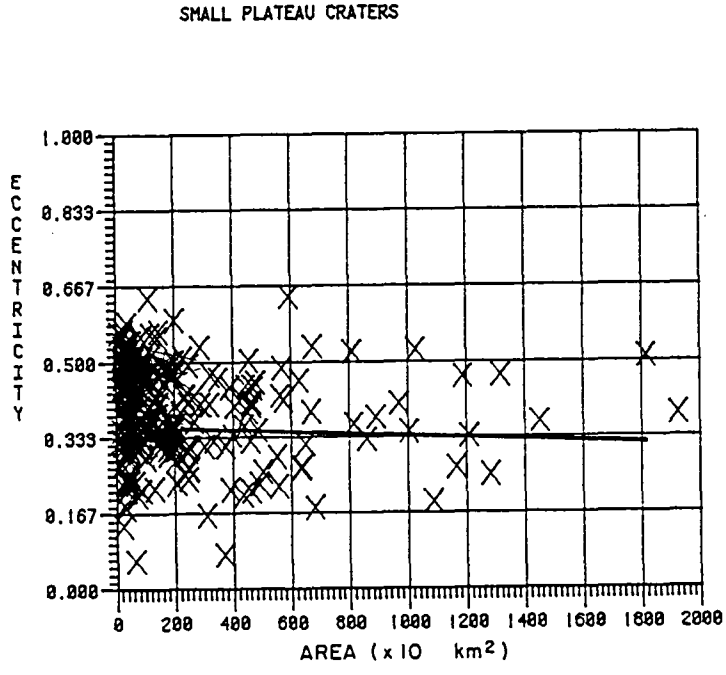


Figure 1. The distribution of eccentricities for 237 small impact plateau craters, Deuteronilus Mensae region.

# EXHUMED TOPOGRAPHY - A REVIEW OF SOME PRINCIPLES

Dallas D. Rhodes, Department of Geology, Whittier College, Whittier, California 90608 (NASA Summer Faculty Fellow, Jet Propulsion Laboratory, Pasadena, California 91103)

Exhumed landforms are topographic features that were created by surficial processes, buried by a covermass, and later exhumed or resurrected to such a degree that they constitute an important part of a present-day landscape. Many areas of exhumed topography have been recognized on Earth. These exhumed landforms vary considerably in age (from Precambrian to Pleistocene), in size (from regional scale to individual landforms), and in origin. Each is a record of the geomorphic conditions at the time they were created and can be used to help reconstruct the geologic history of the area.

Areas of exhumed topography may also exist on Mars. Sharp (1973) stated that some physiographic forms and relationships in south-polar plains could be explained as exhumed topography. The Viking orbiter images have revealed numerous features that may be examples of exhumed topography. Because exhumed landforms may constitute an important part of the martian landscape, a review of the literature dealing with exhumation of terrestrial features is in progress. This is a report on that review, summarizing some of the principles involved in the exhumation of landscapes.

By definition, exhumed landscapes were originally created by surficial geomorphic processes. This requirement excludes some features, like stripped structural surfaces, which have been mistakenly called exhumed. Also excluded are features that are seen only in cross-section, commonly as unconformities. Many older papers on exhumed topography concern the resurrection of peneplaned surfaces - "fossil peneplains". Considering the disrepute in which the peneplanation concept is now held, the geomorphic history of such areas is subject to complete reinterpretation. In order for a feature or landscape to be correctly termed "exhumed", it must have undergone a sequence of events that includes: (1) creation of the original topography; (2) a change in the original environmental conditions; (3) burial as a result of new conditions; (4) a period of interment; (5) another change in environment and/or base level; and (6) exhumation.

A variety of geomorphic features has been exhumed on Earth. These forms include sinkholes in karst topography; marine erosional features such as barrier islands and sea cliffs; glacial features, including moraines and grooved bedrock surfaces; fluvial landscapes of varying relief; and impact structures. Depositional aeolian features have not been found as exhumed landforms, presumably because they

are too easily destroyed.

Burial of landforms requires a major change in the environment or base level of the area. With the onset of new conditions, the landforms become relicts. Relict landforms and landscapes are, by definition, in disequilibrium with their environment. Therefore, to a great extent, the degree of preservation depends upon the speed with which old landforms are buried. Two other factors also help to determine preservation. They are the relative resistance of the rocks from which the landscape was created (the undermass) and the geomorphic energy of the new environment. For a given set of conditions, determined by rate of burial, resistance of the undermass, and energy of erosional processes, low-relief topography will be less modified during burial than will more rugged landscapes. Commonly cited figures for the paleorelief on exhumed surfaces are on the order of a few tens to a hundred (30-150) meters. However, with rapid burial and a resistant undermass, more than 300 meters of paleorelief may be preserved (Martin, 1968).

The burial of a landscape marks a major change in environment, tectonic activity, or volcanic activity in an area. The areal extent of the buried topography reflects the magnitude of the change. On Earth, major changes result from regional tectonic activity, which can be correlated with crustal plate movements, and global climate and sea-level changes associated with glaciation. Martin (1968) found that the greatest number of buried landscapes date from the end of the Precambrian, the Silurian, the Mississippian, and the Tertiary. Periods of major change in surface processes on Mars are related to the inferred denser early atmosphere of the planet, which produced more intense aeolian activity (Pollack, 1979), and possibly periods of pyroclastic volcanism (Greeley and Spudis, 1981), and to climatic fluctuations associated with orbital variations (Ward, 1974). In all instances, the change affects an area larger than that buried. This is true because the covermass source must be outside the buried area; otherwise, the landscape would be modified to produce the required material. Thus, on both Earth and Mars, exhumed topographies date from times of significant geologic change.

The depth, duration, and degree of burial, whether partial of complete, affect the preservation of landscapes. The depth of burial is important because it influences the weathering or endogenetic processes which may act on the older topography. The period of interment will vary for the higher and lower parts of the topography. If the rate of

burial is slow in comparison to the relief on the landscape, or if the area is only partially buried, there may be significant changes in the higher elevations of the landscape due to continued erosion.

Exhumation commences with another change in climatic or tectonic environment. The time period required for the exhumation of the landscape and the degree of modification of the landscape during exhumation will depend on the depth of burial, the energy of the erosional processes, and the resistance to erosion of both the covermass and the undermass.

The criteria that can be used to recognize exhumed topography include: adjustment of topography to structure in recently glaciated areas (Ambrose, 1964); discordant (superposed) drainage on an otherwise-adjusted topography (Cotton, 1945); residual materials, hardpans, duricrusts, and paleosols (Fisher, 1964); and isolated pockets of young sedimentary rocks (inliers) on an older surface and outliers of older rocks poking through a younger cover (Ambrose, 1964). As a generalization, surface features of great age are more likely to have been recently exhumed than to have remained intact for very long periods of time.

The study of exhumed topography is a part of paleogeomorphology. Resurrected landscapes are records of environmental and geologic conditions effective at the time of their formation. Exhumed landforms provide valuable insights into the geologic history of Earth, and they may also be an important part of the geologic record on Mars.

REFERENCES CITED

Ambrose, J.W., 1964, Exhumed paleoplains of the Precambrian shield of North America: Am. J. Sci., v. 262, p. 817-857.

Cotton, C.A., 1945, Geomorphology (4th ed.): New York, John Wiley and Sons, Inc., 505 p.

Fisher, R.V., 1964, Resurrected Oligocene hills, eastern Oregon: American Journal of Science, v. 262, p. 713-725.

Greeley, R., and Spudis, P.D., 1981, Volcanism on Mars: Reviews of Geophysics and Space Physics, v. 19, p. 13-41.

Martin, R., 1968, Paleogeomorphology; in Fairbridge, R.W., ed., The encyclopedia of geomorphology: New York, Reinhold Book Corporation, p. 804-812.

Pollack, J.B., 1979, Climatic change on the terrestrial planets: Icarus, v. 37, p. 479-553.

Sharp, R.P., 1973, Mars: Fretted and chaotic terrains: Journal of Geophysical Research, v. 78, p. 4073-4083.

Ward, W.R., 1974, Climatic variations on Mars: I. Astronomical theory of insolation: Journal of Geophysical Research, v. 79, p. 3375-3386.

# A PRELIMINARY SURVEY OF SLOPE AND RELATED FEATURES AT AND NEAR THE BOUNDARY BETWEEN THE PLATEAU-FRETTED TERRAIN AND NORTHERN PLAINS OF MARS

O. L. Franke, J. Steiner, D. Weiss, J. J. Fagan
Department of Earth and Planetary Sciences
City College of CUNY, New York, N. Y. 10031

The boundary between the "fretted, hummocky terrain" (Mutch and others, 1976) and the northern plains of Mars in our area of study (25°-50°N, 270°-360°W) is characterized by steep escarpments. Often these escarpments attain heights of 1 - 2 Km (Carr, 1980, Mutch and others, 1976; Sharp, 1980) and are virtually unbroken for lengths of tens of kilometers. Similar escarpments have also been noted in the valleys that cut the upland plateau in the study area. Despite their prominence across the Martian landscape, very few quantitative descriptions and detailed geometric and mechanical analyses have been undertaken to explain the maintenance of these escarpments.

We have begun a preliminary survey of slope features in the study area which includes both description and detailed analysis. The descriptive phase involves measurement of slope heights and angles of both bedrock surfaces and debris aprons using standard photogrammetric techniques for Martian terrains. In addition, determinations of valley cross-sections and longitudinal profiles, as well as data collection pertaining to the dimensions of landslide features, the mapping of the height, direction, and extent of the scarps, debris aprons and topographic benches are underway.

The primary focus of the analysis phase is the application of standard equations and techniques for the analysis of slope stability developed in soil mechanics (Schuster and Krizek, 1978; Taylor, 1948; Terzaghi, 1950; Zaruba and Mencl, 1969) to the measured slope data. Some combination of the relevant physical parameters expressed in these equations must exist for the slope-forming materials of Mars to allow the observed large slope heights and steep slope angles to exist. Some of the relevant parameters in this problem are indicated in a formula based on a method of slope stability analysis by Culmann (Taylor, 1948),

$$\frac{c_d}{\gamma H} = \frac{1-\cos(i-\phi_d)}{4\sin i \cos\phi_d}$$

in which $c_d$ is the average value of developed cohesion, $\phi_d$ is the average value of developed friction angle, $i$ is the inclination angle of slope, $H$ is the slope height, and $\gamma$ is the unit weight (weight density) of the slope material.

This formula assumes a plane surface of failure through the toe of the slope and no seepage. Despite its limitations, it gives results for very steep slopes. Of the parameters listed above slope inclination (i) and slope height (H) are being measured from the imagery, and a range of reasonable values for unit weight ($\gamma$) can be assumed. Two parameters, representing cohesion and angle of internal friction of the slope forming materials, remain as unknowns. Thus, only combinations of values for these two parameters that are consistent with the other parameters will be determined.

The above formula is included primarily as an aid in discussion. The investigation will rely on other more general and powerful techniques of slope stability analysis, which assume more realistic failure surfaces and include the effects of seepage.

The above discussion indicates that, analogous to other physical-parameter investigations on Mars, analysis cannot provide a unique set of physical parameters for the Mars materials in any given problem. However, this analysis will hopefully provide a range, i.e. a set of constraints, on values of the relevant material parameters. The range in plausible parameter values obtained in the analysis will be compared to measurements of these parameters on earth materials that might be similar to materials occurring on Mars. Such comparison may permit a decrease in the range of plausible parameter values.

References:

Carr, M., 1980, The morphology of the Martian surface, Space Science Reviews, vol. 25, p. 231-284.

Mutch, T., et al, 1976, The geology of Mars, Princeton University Press, 400 p.

Schuster, R. and R. Krizek (editors), 1978, Landslides--- analysis and control, Transportation Research Board, Special Report 176, National Academy of Sciences, 234 p.

Sharp, R., 1980, Geomorphological processes on terrestrial planetary surfaces, Am. Rev. Earth Planet. Sci, vol.8, p. 231-61.

Taylor, D., 1948, Fundamentals of soil mechanics, John Wiley, 700 p.

Terzaghi, K., 1950, Mechanics of landslides, in Application of Geology to Engineering Practice (S. Paige, editor),Berkey volume, Geological Society of America, p. 83-124.

Zaruba, Q. and V. Mencl, 1969, Landslides and their control, Elsevier, 214 p.

# MODIFICATIONS OF ESCARPMENTS ALONG CHANNELS AND PLATEAUS ON MARS

R. Craig Kochel, Department of Geology, State University College, Fredonia, NY 14063, and Victor R. Baker, Department of Geosciences, University of Arizona, Tucson, AZ 85721

Escarpments of several kilometers relief are well-developed in Martian equatorial regions such as Valles Marineris (Lucchitta, 1978, 1979), along the rim of Chryse Planitia (Baker and Kochel, 1979; Kochel and Baker, 1980), and in mid-latitude regions of fretted terrain (Sharp, 1973; Carr and Schaber, 1977; Squyres, 1978, 1979). Suggested origins for these escarpments include faulting, sapping of ground-ice and subsequent collapse, volcanic processes, and catastrophic flood erosion. Once formed, these escarpments are extensively modified by mass wasting processes resulting in up to several kilometers of escarpment recession.

Escarpments along western Kasei Vallis outflow channels are irregular in plan and can be classified according to the spacing and genesis of irregularities or reentrants along the upland edge. Three scales of reentrant spacings occur. Megascale reentrants are spaced regularly 60 to 70 km apart and occur as tributary valleys and/or broad, crescentic forms (Figure 1). These large-scale forms appear to be structurally controlled by more or less regularly-spaced joints, faults, and/or wrinkle ridges. Structural features are zones of weakness that act as foci for maximum rates of backwasting. Mesoscale features are expressed as arcuate or blocky forms randomly spaced between 10 and 50 km along channel walls. These intermediate sized irregularities are caused by large slumps, craters, and minor structural features. Microscale features spaced less than 5 km apart appear to be semi-regularly spaced and owe their origin to small craters and rockfall chutes.

Tributary valleys to the main Kasei Vallis channel are regularly-spaced in accord with the regional fracture density of the regolith. Tributary valleys are linear and elongated parallel to structural features. Their juncture angles with the main channel average between $75^{0}$ and $90^{0}$. These tributary valleys probably developed by sapping of ground-ice and/or piping along structurally weak zones. Figure 1 (sites A) show incipient valleys headward of the tributary valley from which material appears to have been removed by subsurface piping. In cross-section, tributary valleys are rectangular, have smooth floors, and terminate headwardly by tapering to V-shaped valleys (Figure 1, sites B) or wide, blunt, cirque-like box canyons (Figure 1, sites C). Valley floors appear to be mantled with extensive aprons of debris that wasted from adjacent valley slopes as these tributaries expanded headwardly.

Debris accumulations occur at the base of most escarpments while others are free of slope debris. Slopes associated with debris accumulations may be smooth or irregular. In general, smooth slopes occur above the most areally extensive debris aprons. These debris aprons commonly extend 25 to 30 km from escarpments in regions of fretted terrain (Squyres, 1978, 1979; Kochel and Baker, 1981). Debris aprons appear lobate in cross-section and exhibit lineations on their surfaces. Lineations are generally perpendicular to the strike of the escarpment and parallel to presumed flow

directions. However, transverse ridges sometimes occur upslope of obstacles and along terminal zones of the debris aprons where compressional forces would be expected to be maximized (Squyres, 1978; Kochel and Baker, 1980). Irregular, highly serrated escarpments occur on spur and gully slopes. At the base of these gullies (chutes) are talus cones. Along extensive escarpments adjacent talus cones merge to form talus aprons.

Escarpment sections that have experienced large slumps typically lack debris at their base (Figure 1, sites D). One area of Kasei Vallis (Figure 1, sites E) have depressions or moats along channel walls and around isolated plateau remnants.

Channel floors typically show evidence of substantial modification since their formation during channeling events. Channel widths have been enlarged by several kilometers (Figure 1, sites F). In other areas, structural lineaments abruptly disappear and are replaced by smooth, crater-free channel floors. Smooth floors may be areas of deposition by igneous, eolian, or mass wasting processes. In some areas channel floors have been excavated along structural trends. Enlargement of the fractures, probably by sapping processes, results in rectangular inner channel networks (Figure 1, sites G).

Slope backwasting is a major process responsible for modifying Martian landscapes. Escarpment retreat accounts for several km of postdiluvial widening of outflow channels, formation of extensive tributary networks, and etching of channel floors and bedforms. In fretted regions, backwasting may be the dominant surficial modifying process causing breakup of upland plains units.

References Cited:


Baker, V. R., and R. C. Kochel, 1979, Martian channel morphometry: Maja and Kasei Vallis: J. Geophys. Res., v. 84, p. 7961-7983.

Carr, M. H., and G. G. Schaber, 1977, Martian permafrost features: J. Geophys. Res., v. 82, p. 4039-4054.

Kochel, R. C., and V. R. Baker, 1980, Backwasting and debris accumulation along Martian escarpments: Proc. 3rd Colloq. on Planetary Water, Niagara Falls, NY, Oct. 27-29, 1980, p. 53-58.

Kochel, R. C. and V. R. Baker, (in press) Degradation of Martian escarpments: Backwasting and debris accumulations: (Abs) Proc. 12th Lunar and Planet. Sci. Conf., Houston, TX, Mar. 16-20, 1981.

Lucchitta, B. K., 1978, Morphology of chasma walls, Mars: J. Research, U. S. Geol. Survey, v. 6, p. 651-662.

Lucchitta, B. K., 1979, Landslides in Vallis Marineris, Mars: J. Geophys. Res., v. 84, p. 8097-8113.

Sharp, R. P., 1973, Mars: Fretted and chaotic terrains: J. Geophys. Res., v. 78, p. 4073-4083.

Squyres, S. W., 1978, Martian fretted terrain: Flow of erosional debris: Icarus, v. 34, p. 600-613.

Squyres, S. W., 1979, The distribution of lobate debris aprons and similar flows on Mars: J. Geophys. Res., v. 84, p. 8087-8096.

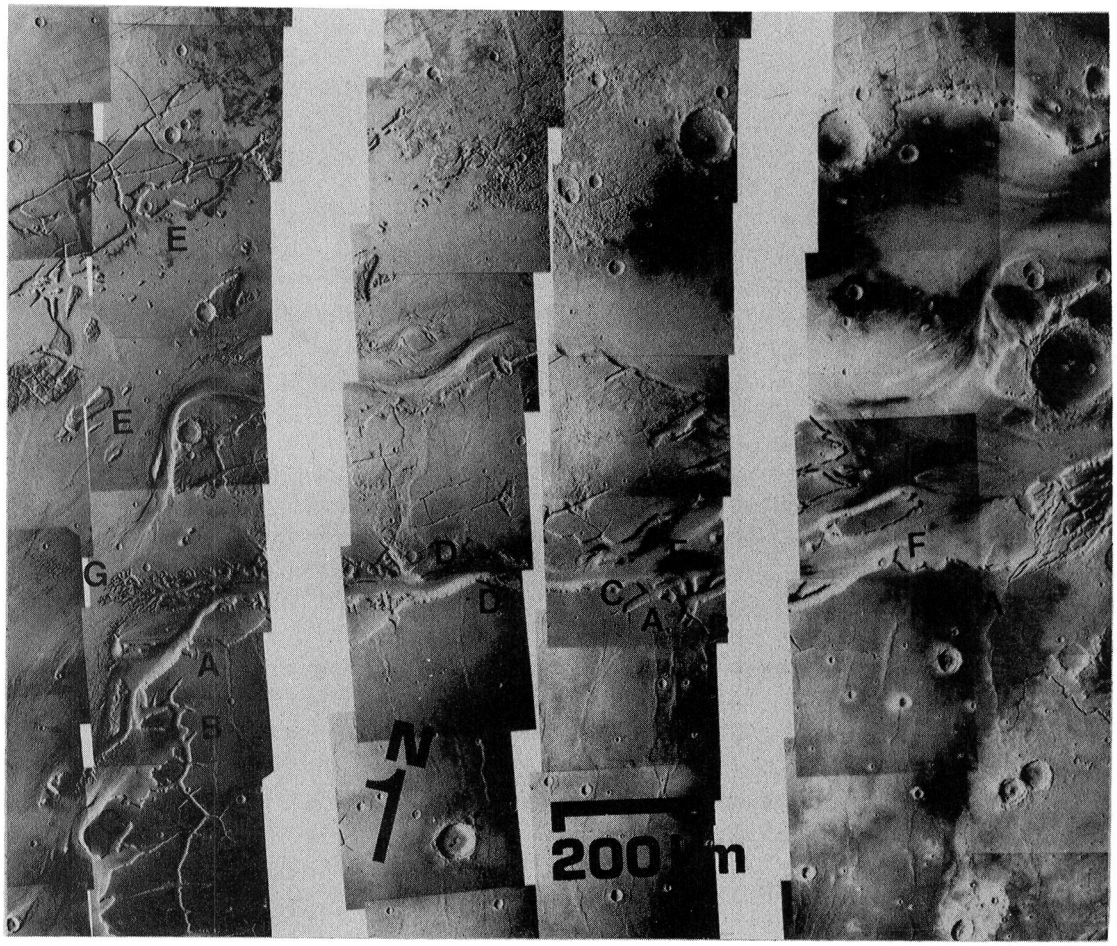


Figure 1. Part of Viking photomosaic 211-5642 showing western Kasei Vallis channels and related features. Photo is centered at approximately 24° N, 70° W. Lettered sites are discussed in the text.

# EVOLUTION OF THE SPUR AND GULLY TOPOGRAPHY ON THE VALLES MARINERIS WALL SCARPS

P. C. Patton, Department of Earth and Environmental Sciences, Wesleyan University, Middletown, CT 06457

The morphology of the Valles Marineris wall scarps has been described by a number of investigators (Sharp, 1973; Blasius and others, 1977; Lucchitta, 1978a, 1978b). A major slope form present throughout the canyon system are networks of scarp gullies with their intervening divides. These slope systems have been termed spur and gully topography (Lucchitta, 1978a) and clearly represent erosion and sediment transport on the scarp face. The regional variation in the morphology of these slope systems suggests that the spur and gully topography undergoes a systematic progressive degradation with time.

The evolution of the spur and gully topography can be most clearly seen in Ius Chasma. In the eastern segment of the chasma the slope base is created by an abrupt straight scarp which is interpreted as a fault scarp (Blasius and others, 1977). The spur and gully topography is well developed with a high density of erosional gullies on the slope. The lowered base level of the slope system created by the fault scarp is probably responsible for the fine-textured erosional topography. With increasing distance to the west in Ius Chasma the spur and gully slopes have a more degraded appearance with fewer spurs near the base of the scarp. Well defined fault scarps are not present at the base of these slopes.

These observations of slope evolution can be quantified by mapping and measuring the topology of the spur and gully networks. In the preliminary analysis slope networks were defined by the master spur which intersected the slope crest. The spur network branched downslope. The boundaries of the slope system were defined by the major gullies separating the spurs and by the break in slope at the scarp base. Spur networks were quantified using the network ordering system of Shreve (1966). The furthest downslope unbranched spurs were designated first-order spurs and successive upslope links were the sum of the total external links. The following attributes of the slope networks were measured: slope area, slope length, total number of first-order spurs, total length of spurs, spur density and first-order spur frequency.

Correlations between the measured morphometric parameters provide insight into the processes of slope modification. There is a strong correlation between slope area and slope length. Slope length increases as the square root of area indicating that slope systems increase in width at an equal rate. Increases in width are caused by piracy of adjacent slope systems because of the unequal rate of headward growth at the slope crest. Therefore, with increasing erosion of the slope crest and increasing size of the slope system there is an increase in the sinuosity of the scarp crest. The data on spur density confirm that those slopes with the highest density of spurs are associated with the linear basal fault scarp. The slopes which are more degraded in appearance lack the high number of first-order spurs and their spur density is largely a result of longer but fewer

first-order spurs. These data illustrate the evolution of the first-order spurs. On slopes where the transport processes are efficient, erosion and transport of debris extends to the slope base. The first-order spurs that form at the scarp base are evidence of the high rate of transport relative to debris production. As the rate of debris removed from the scarp base declines debris would be stored in the gullies while the spurs continue to erode. Eventually the relief between spurs and gullies would decline and these forms would merge to create a smooth slope. Therefore, the downslope spurs would be the first to be abstracted from the network. As this occurs the density of the spur system becomes more a function of the longer spurs which were interior links. The overall density of the spur network also declines because of the large slope area that eventually becomes buried in debris. If the erosional development of the scarp face is controlled by base leval changes caused by faulting, then the morphometric data on spur and gully topography can be used as a relative index of tectonic activity.

The preliminary results indicate that mapping and analysis of slope forms in Valles Marineris may provide information on the evolution of the scarps. Additional study of scarp morphology throughout the Valles Marineris is being undertaken to refine the initial observations. One important implication is that scarp morphology may be an indicator of the tectonic processes in the trough systems. In this manner the geomorphic mapping may define the degree of tectonic activity in the same fashion that recent investigations of the morphology of mountain fronts in the Basin and Range Province of the western U.S. have been used to delineate fault zones of varying tectonic activity (Bull and McFadden, 1977; Wallace, 1978).

## References Cited


Blasius, K. R., Cutts, J. A., Guest, J. E. and Masursky, H., 1977, Geology of Valles Marineris: First analysis of imaging from the Viking orbiter primary mission: Jour. of Geophy. Research, v. 82, p. 4067-4091.

Bull, W. B. and McFadden, L. D., 1977, Tectonic geomorphology north and south of the Garlock Fault, California: in Doehring, D. O., ed., Geomorphology in arid regions, Publications in Geomorphology, Binghamton, N.Y., p. 115-136.

Lucchitta, B. K., 1978a, Morphology of chasma walls, Mars: U. S. Geol. Survey Journal of Research, v. 6, n. 5, p. 651-662.

Lucchitta, B. K., 1978b, A large landslide on Mars: Geol. Soc. Am. Bull., v. 89, 1601-1609.

Sharp, R. P., 1973, Mars: troughed terrain: Jour. Geophy. Research, v. 78, p. 4063.

Shreve, R. L., 1966, Statistical law of stream numbers: Jour. Geol., v. 74, p. 17-37.

Wallace, R. E., 1978, Geometry and rates of change in fault-generated range fronts, north-central Nevada: U. S. Geol. Survey Jour. of Research, v. 6, n. 5, p. 637-650.

MORE ON LANDSLIDES - VALLES MARINERIS

B. K. Lucchitta, K. L. Kaufman, and D. J. Tosline, U.S. Geological Survey,, Flagstaff, AZ 86001

A topographic map of the Coprates Northwest Quadrangle of Mars (approximate scale 1:2 million; contour interval, 1 km) permitted quantitative studies of some landslides in Valles Marineris. Stereographic images at resolutions near 100 m/line pair covering parts of Ius, Ophir, Candor, and Melas Chasmata have allowed detailed photogeologic analysis. The quantitative data show that martian landslides differ from terrestrial slides, and the photogeologic observations support the contention that martian landslides are lubricated by water [1,2].

Terrestrial landslides are commonly compared by plotting the volume of a slide against the tangent of its slope from the head of the landslide scar to the tip of the slide deposit. The slope is an approximate measure of the coefficient of friction [3] and, inversely, the efficiency of the slide. Volumes of slides are difficult to obtain on Mars; therefore we plotted the more easily obtained areas of several martian and terrestrial slide deposits against the tangents of their slopes. The results (Fig. 1) show that the landslides, even though highly scattered, increase slightly in efficiency with increasing areas of the deposits. However, because landslides vary widely in thickness, their areas are poor approximations of their true mass, and the results of Figure 1 are highly tentative. Also, differences in gravity between Mars and Earth must be considered when comparing martian and terrestrial landslides.

In order to overcome the limitations mentioned above, a few landslides were found in Valles Marineris whose volumes could be obtained by computing the volume missing from landslide scars. Weights were estimated from the calculated volumes, because weights include a term for gravity. Volumes of terrestrial landslides, graphed by Scheidegger [3], were similarly transposed into weights, and all weights were then plotted against slope tangents (Fig. 2). Scheidegger's [3] correlation curve (slope, -0.16) is given on the graph by a dashed line. The graph shows that the plotted martian landslides - all larger than terrestrial slides - do not fall on Scheidegger's curve. Terrestrial landslides show increased efficiency with increased weight, but martian slides apparently retain their efficiency regardless of weight. Either landslides have a threshold size above which they do not increase in efficiency with increasing size, or martian landslides are different from terrestrial ones. The difference may be due to composition, water content, entrainment of air, substrate material, or other factors.

Relief shown on the topographic map also permitted calculation of speeds for some landslides. Wherever landslides move through topographic lows and thence uphill on opposite slopes, the attained heights correspond to minimum speeds that can be calculated. In Table 1 we compare the speeds of martian landslides to terrestrial speeds, and show that martian landslides are generally faster; the Huascaran landslide in Peru, which fell from great height and involved ice and water [4], is an exception.

One major question about martian landslides is whether they were dry or wet. Lucchitta [2] previously argued for wet landslides and the following observations corroborate the proposition: 1) Landslide flow lobes emerge from some landslide slump masses at right, or even acute, angles to the main direction of movement, and invariably flow downhill. 2) Small sinuous channels emerge locally from landslide deposits, and entire landslide lobes merge in places with apparent channels that are smoothly graded toward the nearest topographic low. 3) Small landslides have marginal levees, a form that is common on terrestrial mudflows. 4) All landslides that have flow lobes extending far out onto the chasma floors come from chasma walls or erosional remnants of wall rock. None come from the layered deposits on the floors of the chasmata, even where the layered deposits are as high and as steep as the walls. Apparently the wall material flowed easily; the interior deposits did not. A likely explanation is that the wall rocks contained much water [5]. 5) Large terrestrial landslides are generally dry, the difference between terrestrial and martian landslides, shown in Figure 2, may be due to a higher water content of the martian slides. 6) The Huascaran landslide in Peru is the only terrestrial landslide with a speed similar to that of martian slides, and it contains ice and water; the high martian speeds may also have been facilitated by water lubrication. Even though none of the above criteria furnish proof that the martian landslides were wet, when considered together, they strongly support the hypothesis that martian landslides contained water and may have been similar to gigantic mudflows.

References

[1] Lucchitta, B. K. (1978) A large landslide on Mars. Geol. Soc. Am. 89, p. 1601-1609. [2] Lucchitta, B. K. (1979) Landslides in Valles Marineris. J. Geophys. Res. 84, p. 8097-8113. [3] Scheidegger, A. E. (1973) On the prediction of the reach and velocity of catastrophic landslides. Rock Mech. 5, p. 231-236. [4] Plafker, G. and Erickson, G. E. (1978) Mechanism of catastrophic avalanches from Nevados Huascaran, Peru, in (Barry Voight, ed) Rock slides and avalanches, p. 277-314. Elsevier, Amsterdam. [5] Carr, M. H. (1979) Formation of martian flood features by release of water from confined aquifers. J. Geophys. Res. 84, p. 2995-3007.

Table I Speed of Landslides

| Earth | km/hr | Mars | km/hr |
|---|---|---|---|
| Vaiont, Italy | 90 | Ius, east | 250 |
| Elm, Switzerland | 150 | Tithonium, center | 250 |
| Madison, Montana | 160 | Ius, west | 300 |
| Gros Ventre, Wyoming | 165 | Ius, center | 300 |
| Frank, Alberta | 175 | Tithonium, east 1 | 300 |
| Blackhawk, California | 235 | Tithonium, east 2 | 300 |
| Huascaran, Peru | 360 | Candor | 400 |
| | | Melas | 450 |

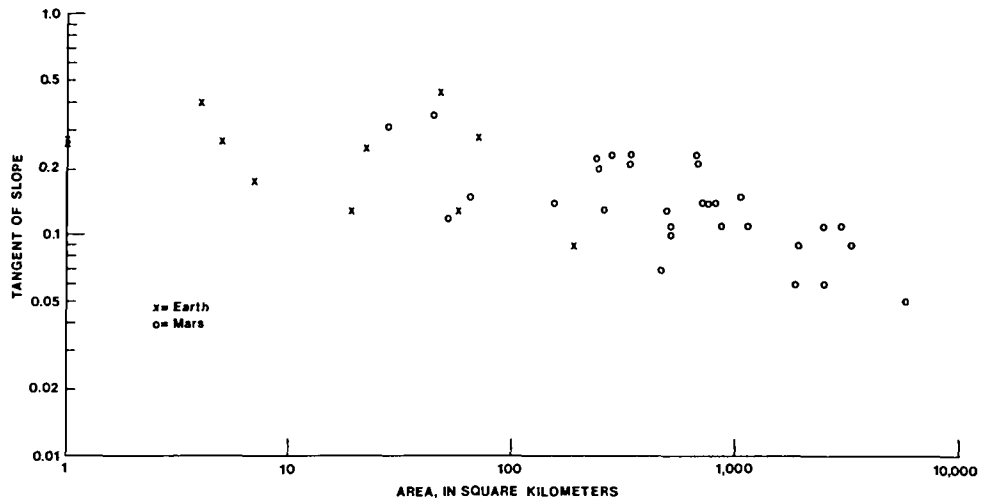


Figure 1. Comparison of areas of landslides plotted against tangent of slope from head of scar to tip of deposit.



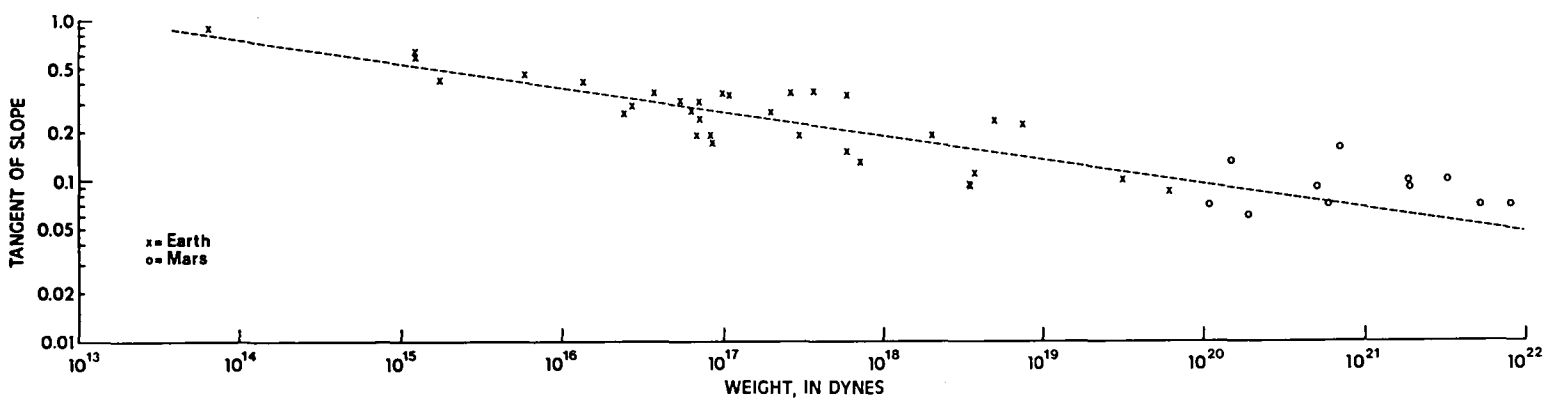


Figure 2. Comparison of weights of landslides plotted against tangent of slope. Terrestrial data and dashed correlation curve from Scheidegger [3].

AUSTRALIAN ANALOGS TO GEOMORPHIC FEATURES ON MARS

Victor R. Baker, Department of Geosciences,
University of Arizona, Tucson, Arizona 85721

The remarkable tectonic stability of the Australian continent has favored the prolonged action of denudational processes, yielding extensive erosion surfaces of low relief. In the arid interior of central Australia inselbergs and other relict landforms rise above the erosional plains. The region west of Alice Springs displays eroded impact structures, active eolian features, and relict fluvial landforms.

The Gosses Bluff impact structure probably formed during the early Cretaceous (1). The structure is now deeply eroded such that most of the crater floor breccia has been removed, exposing a resistant central core of uplifted sandstone. Breaches and notches through this central uplift area illustrate the superposition of a drainage system from an ancient land surface. The Henbury Craterarea provides an interesting contrast to Gosses Bluff. The Henbury impacts are probably Holocene in age (2). The craters are undergoing active dissection by a drainage system whose predecessor they disrupted. Both Henbury and Gosses Bluff have important similarities to the relationships between craters and small valley networks in the heavily cratered terrain of Mars.

Erosion in central Australia involved an ancient epoch of deep weathering, probably in a tropical climate of Tertiary age (3). Subsequent Tertiary and Pleistocene climate change to arid conditions was accompanied by stripping of the weathered mantle, producing an etched surface of geomorphic complexity. The analogous process on Mars may have been the prolonged influence of the deep permafrost and underlying water on the impact breccia of the megaregolith. Material below in the permafrost zone could have been cemented by diagenetic alteration, allowing the unaltered ice-cemented regolith to be more easily stripped by prolonged denudational processes (4). The result would be etched erosion surfaces developing in front of adjacent high escarpments, many of which are held up by resistant caprocks on Mars. A key relationship is that between the northern plains and the heavily cratered plateaus.

A possible Australian analog to the latter is the great block of resistant sandstone and conglomerate (Middle Proterozoic Kombolgie Formation) that comprises the Arnhem Land Plateau. The sandstone acts as a caprock, protecting the underlying weaker rocks from erosion. Removal of the latter from the base of the sandstone has produced an immense escarpment separating the high sandstone plateau from an extensive erosion surface developed on the weaker rocks. The escarpment retreats by a sapping process, but the influence of faults, joints, and anticlines has resulted in great embayments and inliers of the lowland surface. Outliers of the resistant caprock were isolated by escarpment retreat to form inselbergs. Portions of the plateau were eroded to form a great labyrinthine complex of intersecting linear troughs. The troughs are aligned along joint and fault planes. Although some contain active streams, the dominant process of trough development was sapping and mass movement along the faces of bounding scarps.

The Katherine Gorge illustrates the fluvial process influence in Arnhem Land (5). The gorge developed by fluvial exploitation of structural troughs along the plateau margin. The capacity of the upper gorge is not sufficient to convey the largest flood discharges. This resulted in the formation of an anastomosing reach of bedrock scabland. The Katherine Gorge illustrates the floodwater invasion of a trough formed by sapping and hillslope processes. These relationships are similar to some that prevail for the small valley networks and fretted terrain of Mars. Although ground ice wastage probably served as the primary agent for Martian valley development, the temporal sequence of that development appears quite similar to that observed in Arnhem Land.

The interior plainsland deserts of Australia can experience immense floods when tropical air masses make incursions from the north. A spectacular example occurred in January, 1974, when over 800 mm fell in the headwaters of Coopers Creek, Diamantina River, Hamilton River, and other drainages of southwestern Queensland. This rain was associated with a tropical storm that displayed unprecedented strength and southward penetration. The flood waters were conveyed through a lowland characterized by sand dunes and gentle folds in duricrusted sedimentary rocks. The gradient of Cooper Creek averages less than 30 cm per kilometer through southwestern Queensland. As a result, the flood water spread over immense regions, as much as 60 km wide for Cooper Creek alone.

The rare incursion of such floods into the arid Australian interior plainslands results in a pattern of anastomosing channelways and streamlined residual land elements. The expansion and constriction of the reticulate channel complexes is controlled by the folding in an analogous manner to the influence of mare-like ridges on outflow channeling in the western Chryse Basin (6). The Martian terrain has been interpreted to have experienced relatively shallow, but areally extensive flooding (7).

The hyperarid deserts of northeast Africa (8) and the cold-dry deserts of Antarctica (9) are probably the appropriate analogs for modern Martian conditions. However, because of tectonic stability, the profusion of very ancient relict landscapes, the occasional spectacular influence of fluvial processes, and the abundant eolian modification of structural and fluvial landforms, central Australia is an important analog to ancient conditions on Mars.

References. (1) D.J. Milton, and others, Science 175, 1199-1207 (1972).
(2) D.J. Milton, U.S. Geol. Survey Prof. Paper 599-C, C1-C17 (1968).
(3) J.A. Mabbutt, Z. Geomorph. 9, 82-114 (1965).
(4) L.A. Soderblom and D.B. Wenner, Icarus 34, 622-637 (1978).
(5) V.R. Baker, G. Pickup, and P. Russell, Geol. Soc. Amer. Abstracts with Programs 12, 382 (1980).
(6) R. Greeley and others, Jour. Geophys. Res. 82, 4093-4109 (1977).
(7) V.R. Baker and R. C. Kochel, Jour. Geophys. Res. 82, 7961-7983 (1979).
(8) McCauley and others, Jour. Geophys. Res. 84, 8222-8232 (1979).
(9) E.K. Gibson, Jr., NASA Tech. Memo. 82385, 199-201 (1980).

COMPARATIVE RATES OF GEOLOGIC PROCESSES ON VARIOUS TERRESTRIAL TYPE BODIES

Cutts, James A., Planetary Science Institute, Science Applications, Inc., 283 S. Lake Ave., Suite 218, Pasadena, CA 91101

INTRODUCTION - Observations of the terrestrial planets and Galilean satellites acquired in recent years provide information on the rates of geologic processes on these bodies. Data have been assembled on the rates of geologic processes on Mars, Venus and Io and compared with those for the Earth. These data yield some surprises: contrary to a widely held view (Ref. 1) some parts of Mars are more active geologically than most of the Earth's surface.

VERTICAL DEPOSITION AND EROSION - Following an approach developed for the Earth by Fischer (Ref. 2) and elaborated upon by Schwarzacher (Ref. 3) we have compiled data on sedimentation rates in a variety of terrestrial and planetary environments. We have reduced estimates of erosion and deposition rate to units of μm/year sometimes termed Bubnoffs (B) after the German sedimentologist of that name.

Earth - On the Earth, rates of geologic processes are quite variable ranging from the deposition rates of deep sea clays which can be less than 1B to the deposition rates of terrigenous sediments which can exceed 1000B. Included in Fig. 1 is the rate of accumulation of annual and perennial ice on the Earth which makes for some interesting comparison with ice accumulation on Mars.

Mars - The estimated rates of deposition and erosion on Mars span many orders of magnitude. Although some of the variation arises from the differing assumptions of different investigators there are clearly enormous geographic differences in deposition and erosion rates on Mars.

In some parts of the planet such as the VL-1 site, long-term rates of erosion and/or deposition have been incredibly small. This indicates that eolian erosion has been ineffective despite theoretical calculations and laboratory experiments to the apparent contrary (Refs. 4, 5). Furthermore, it implies negligible long-term deposition by volcanic and eolian action, although there has been periodic redistribution of eolian materials by wind (Ref. 6). The VL-2 site appears to have experienced more rapid erosion than the VL-1 site. The eroded equatorial deposits of either ignimbritic (Ref. 7) or eolian origin (Ref. 8) manifest even higher erosion rates although no rate estimates have been published. Very high erosion rates also occurred during the planet's early history when various types of channel feature formed, but estimates of these rates are highly model-dependent.

Some of the highest deposition rates on Mars are found in the polar regions. Photogeologic estimates (Ref. 9) and theoretical estimates (Ref. 10) are in rough agreement and have been used to argue for high contemporary equatorial erosion rates. More recently it has become apparent that sediment recycling is important and that extremely high erosion rates occur in parts of the south polar region (Ref. 11).

Io - This extraordinary body exhibits extremely high global rates of volcanic deposition (Ref. 12) comparable to the rate of accumulation of martian polar deposits. The total annual mass transport of material by volcanism on Io may

be larger than the annual transport of suspended sediment from the rivers of the Earth (Fig. 2). Erosion by energetic particles which was believed to be the most significant surface process before the discovery of volcanism on Io (Ref. 13) has reemerged as a possibly significant process in the evolution of Io and Europa (Ref. 14).

Moon - Processes of impact regolith formation and soil development on the Moon are difficult to characterize in terms of simple rates of erosion and deposition. Instead, the soil, and perhaps the entire regolith, experiences an evolutionary process during which the constituents develop into mature forms. Perhaps one exception is the erosion of rocks which can be related to a roughly linear process of ablation by micrometeoritic impact, although even here the effects of rock splitting larger impacts perturb the simple picture (Ref. 15).

Venus - On Venus in the absence of a micrometeoritic flux and eolian abrasion (Ref. 16) the rate of erosion may be extremely low ($<10^{-6}$B) unless chemical weathering is effective. Deposition rates on the other hand may be comparatively high. If Campbell and Burns (Ref. 17) are correct in inferring a comparatively active volcanic history for Venus from observed crater populations then deposition rates may be as high as a few Bubnoffs. On the other hand, if radar crater signatures are being obliterated by a thin veneer of sediment (Ref. 18) then the overall sedimentation rate may be down in the $10^{-3}$B range which could be produced by global deposition following large impacts (Ref. 18).

HORIZONTAL TRANSPORT - Rates of geologic processes described above refer to changes taking place in a vertical direction. On the Earth, changes taking place in a horizontal direction, e.g., the advance of a sedimentary lobe, can be orders of magnitude more rapid than vertical changes. This is also true on other bodies, e.g., eolian sedimentation on Mars. In Fig. 3, we depict theoretical estimates of the annual advance of a sand deposit as a function of the thickness of that deposit for several assumed values of the potential sand transport rate. Since the rates vary inversely as thickness, thin layers can experience annual advances or retreats of kilometers.

Direct observational data to demonstrate that the potential for sediment transport is actually realized on Mars are not well documented. Many workers have reported changes in the positions of thin veneers of eolian materials of tens of kms (e.g., Ref. 19). However, there is considerable uncertainty about the thickness of these deposits and whether the material was transported in a ground-hugging saltation sheet, and these observational data have not been included in Fig. 2. Observations have also been reported of changes in the positions of sand dune ridges and sheets from imaging data (Ref. 20) and radar reflectivity data (Ref. 21). In neither case is the interpretation the only one nor universally accepted as valid. However, these kinds of data will allow us to refine measurements of horizontal sand transport in future.

SUMMARY AND DISCUSSION - Planetary surfaces experience depositional and erosional processes at many different rates. Eolian sedimentation rates in the polar regions of Mars are high even by terrestrial standards. Annual transport of volcanic material to the surface of Io may exceed the total suspended sediment transport of the Earth's rivers.

REFERENCES - (1) Head, J.S. and S.C. Solomon, Science 213, 62-76, 1981. (2) Fischer, A.G., Geol. Soc. Am. Bull. 80, 546-552, 1969. (3) Schwarzacher, W., Sedimentation Models and Quantitative Stratigraphy, Elsevier, 1975, 382 p. (4) Sagan, C., JGR 78, 4155-4162, 1973. (5) Williams, S.H. and R. Greeley, LPSC XI, 1254-1256, 1980. (6) Arvidson, R.E., E.A. Guinness and A.P. Zent, Third Int. Colloq. on Mars (abstr.), 6-8, 1981. (7) Scott, D.H. and Tanaka, K.L., NASA TM 82385, 255-257, 1980. (8) Schultz, P.H. and A.B. Lutz-Garihan, Third Int. Colloq. on Mars (abstr.), 229-231, 1981. (9) Cutts, J.A. et al., Science 194, 1329-1337, 1976. (10) Pollack, J.B. et al., JGR 84, 2929-2945, 1979. (11) Howard, A.D. and J.A. Cutts (this report). (12) Johnson, T.V. et al., Nature 280, 746-750, 1979. (13) Matson D.L. et al., Astrophys. J. 192, L43-L46, 1974. (14) Dessler, A.J., Icarus 44, 291-295, 1980. (15) Hörz, F. et al., The Moon 13, 235-258, 1975. (16) White, B.R., Icarus 46, 226-232, 1981. (17) Campbell, D.B. and B.A. Burns, JGR 85, 8271-8281, 1980. (18) Cutts, J.A. et al., Icarus, 1981, in press. (19) Sagan, C. et al., 1973. (20) Tsoar, H. et al., JGR 84, 8167-8180, 1979. (21) Cutts, J.A. and S.J. Keihm, Icarus, 1981, in press. (22) Milliman, P., Oceanus 24, 3-10, 1981. (23) Morales, C., Saharan Dust, Mobilization, Transport and Deposition, Wiley, 1979, 293 p.

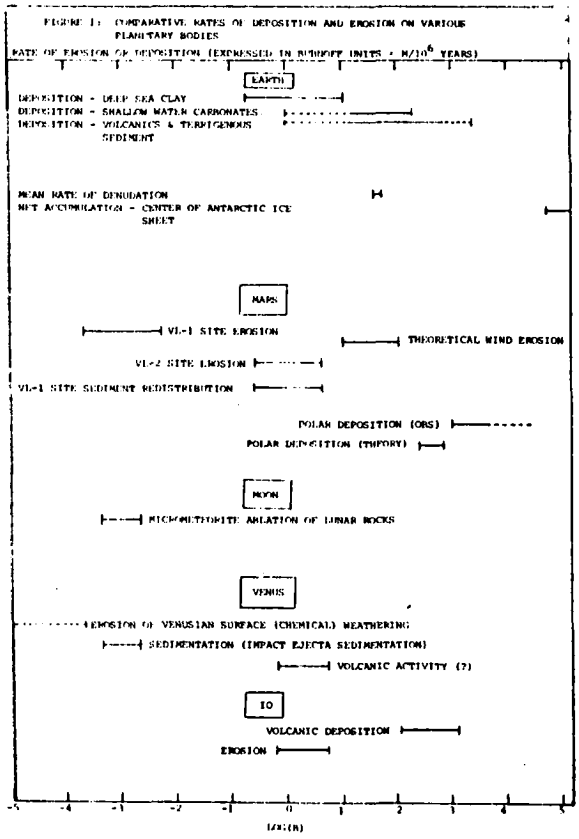


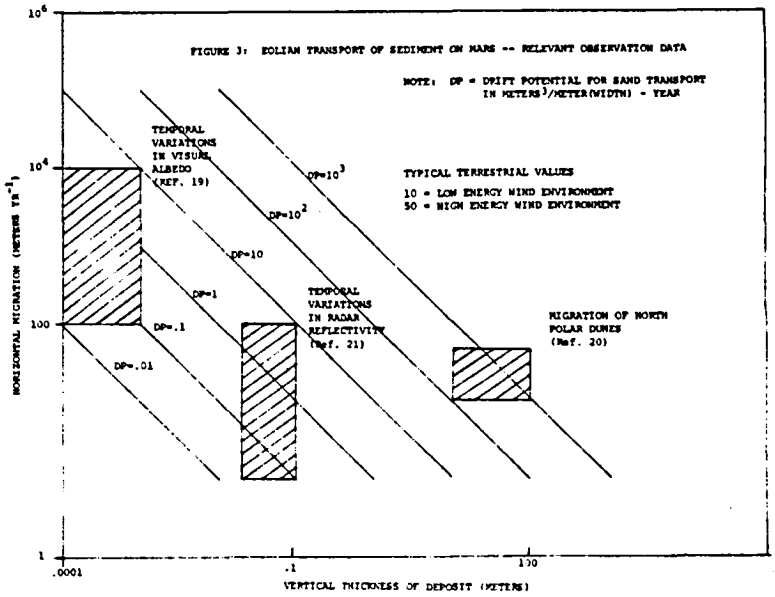


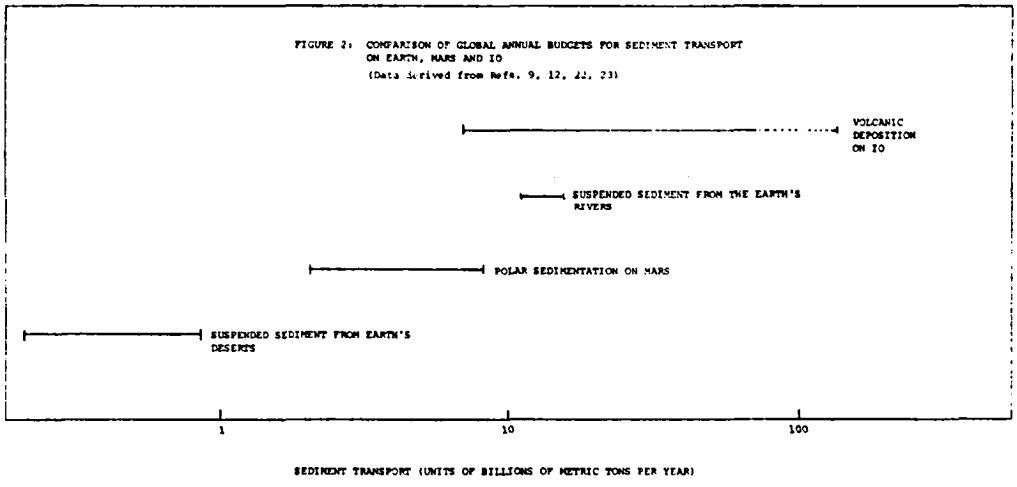

# Chapter 7

# MARS POLAR DEPOSITS, VOLATILES AND CLIMATE

TOPOGRAPHY AND STRATIGRAPHY OF MARTIAN POLAR LAYERED DEPOSITS

James A. Cutts and Karl R. Blasius, Planetary Science Institute, Science Applications Inc., 283 S. Lake Ave., Suite 218, Pasadena, CA 91101; and Alan D. Howard, University of Virginia, Charlottesville, VA 22903

Introduction - Quantitative measurements of the topography and stratigraphy in the martian polar layered deposits are needed to unravel the complex geology of this part of Mars (Ref. 1) and for exploring hypothesis of climate control of stratigraphy (Ref. 2). Here we describe recent work to compare photogrammetric and photoclinometric data for various test sites in the polar layered deposits and examine the kinds of measurement techniques that are needed to fully exploit the potential of the Viking Orbiter imagery.

Comparison of Stereophotogrammetric and Photoclinometric Measurements of Polar Topography - The finest resolution topographic and stratigraphic data for layered deposits is north polar imaging acquired by the Viking 2 Orbiter. High quality stereo imaging at about 50m/pixel occurs for a significant fraction of the terrains (Fig. 1). Monoscopic coverage is nearly complete under summer conditions of partial defrosting and spring conditions of complete surface frost cover. The last data set may contain the highest resolution topographic data on outcropping strata and other low relief landforms if it can be successfully analyzed using photoclinometry. It is our long range plan to use selected high quality stereogrammetric measurements to constrain the parameters of photoclinometric solutions for topography. Howard et al. (Ref. 3) describe the photoclinometric profiling technique we have developed and present profiles across north polar layered deposits mantled by annual polar cap ice. Here we describe the stereogrammetric data and make a comparison of the independent results of the two techniques. The thicknesses of resolved bands or strata in the areas studied are discussed.

As described by Ruiz et al. (Ref. 4) and Blasius and Cutts (Ref. 5) digital photogrammetric techniques have been developed for and applied to Viking Orbiter stereo imaging. High resolution topographic maps have now been compiled for three areas on the north polar layered deposits (Figs. 1 and 2).

The area of the third topographic map compiled from stereo images (Fig. 2) was also the subject of photoclinometric analysis (Ref. 3). Here we show these two techniques yield similar results allowing the higher resolution photoclinometry data to be used for stratigraphic studies. The results also suggest that photogrammetry may provide useful constraints on photoclinometric solutions. In Fig. 2 we show the locations of photometrically derived elevation profiles from image 566B75 relative to the topographic map contours derived stereophotogrammetrically. The dots are the locations of the individual point elevation measurements from the stereo pair which formed the basis for the contour map. We compare the two data sets by displaying the photoclinometric profiles along with point elevation measurements which occur within a specified range of the profile (dots in Fig. 2). In Figs. 3a, 3b and 3c we show three profiles and photogrammetric data points within a range of 50 pixels on each side of the profile.

the photogrammetric data have been adjusted in two ways to facilitate comparison. The photoclinometric analysis assumed the "basement" surface below the layered deposits is level. We have tilted the stereo model slightly to approximate this condition. The tilts induced are $0.28^{o}$ about the axis defined by sample number 550 and $0.58^{o}$ about the orthogonal axis along line 700. These rotations are within the range of estimated error ascribable to uncertainty in camera pointing (Ref. 5). In addition to the slight rotation, gross vertical offsets were also removed. This step has no scientific significance since photoclinometry yields no estimate of absolute surface elevation.

In Fig. 3a elevation changes in more or less a straight line along profiles 1, 2 and 3 are compared to photogrammetric data. The latter show considerable scatter, but with a slight rotation of about 200m over 500 pixels (22.5km) (about $0.5^{o}$) the profile would represent a good fit to the data points.

In Fig. 3b profiles 4, 8 and 9, which include a dogleg, show similar agreement with point stereo measurements. Finally, in Fig. 3c a smaller amount of stereo data compares favorably with the photoclinometric profile with allowance for about the same $0.5^{o}$ rotation as seemed present in the comparison of Fig. 6a.

The rotational incongruities between the two topographic data sets are to be expected not only because of uncertainty in stereo model orientation, but because of assumptions which contributed to the photoclinometric solution. Work conducted thus far (Ref. 3) shows the tilt of elevation profiles is quite sensitive to the brightness level which is assumed to correspond to a level surface. This value is dependent upon the photometric correction applied to the image to remove large scale camera-induced photometric error. Because of systematic effects found, we expect to be able to substantially improve upon this camera shading correction procedure.

Future Directions - Software improvements to provide for direct calculation of stereophotogrammetric profiles from the digital imagery would have immediate advantages in productivity. Additionally, we plan to incorporate image shaping algorithms to improve correlation performance on the sloping surfaces of the polar strata. We envisage a two-pass procedure for processing stereo pairs: in the first pass we orient the stereo model using two-dimensional image mathcing of features on flat surfaces; in the second stage we match imagery in local areas using one-dimensional image shaping and matching (Ref. 6). This should also improve the accuracy of relief measurements on the sloping surfaces where polar strata are exposed. On these sloping surfaces correlations are poorly constrained in directions parallel to the layers. These measurements would be implemented on our PDP-11/70 based interactive image processing facility. We are presently developing under separate sponsorship a stereo ranging system using digital television images which has some of the features described.

References - (1) Howard, A.D. and Cutts, J.A. (this report). (2) Cutts, J.A. (this report). (3) Howard, A.D. et al., Icarus, in press, 1981. (4) Ruiz et al., JGR 82, 4189-4202, 1977. (5) Blasius, K.R., and Cutts, J.A., Icarus, in press, 1981. (6) Keating et al., Proc. ACSM-ASP, 1975.

## Figure 1

One of 12 outline maps showing the distribution of Viking Orbiter high resolution stereo imagery of north polar layered deposits. The area of heavily striping shows area covered by two of the three stereo maps compiled in this study. The third at 79°N, 334°W is reproduced in Fig. 2.

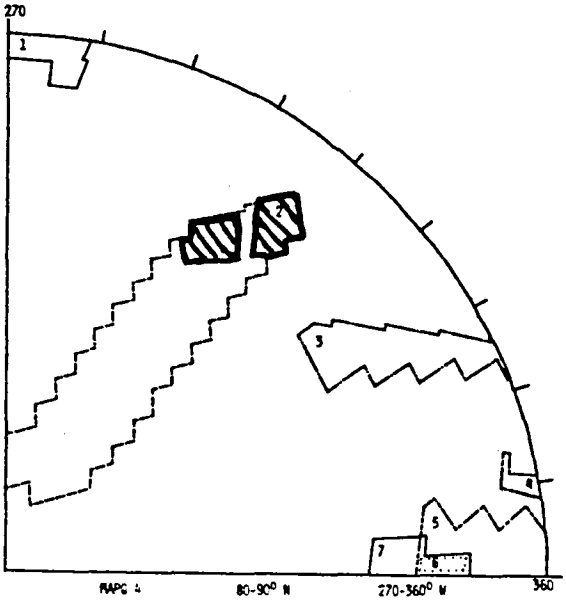


## Figure 2

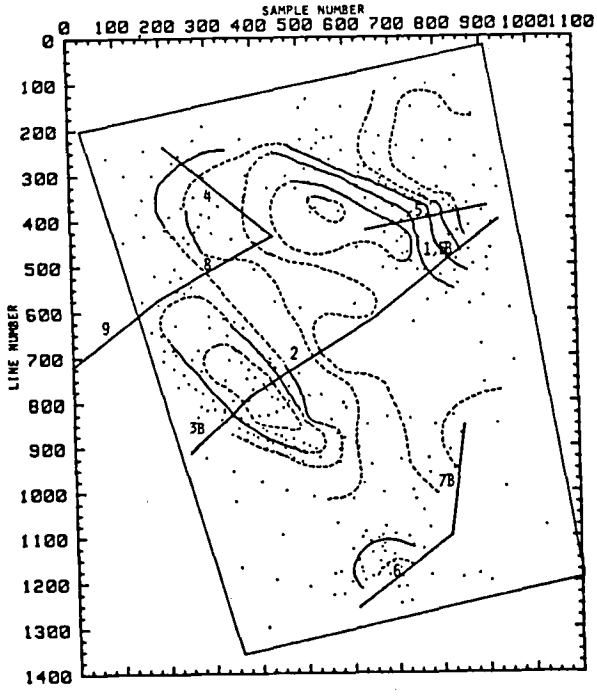


## Figure 3

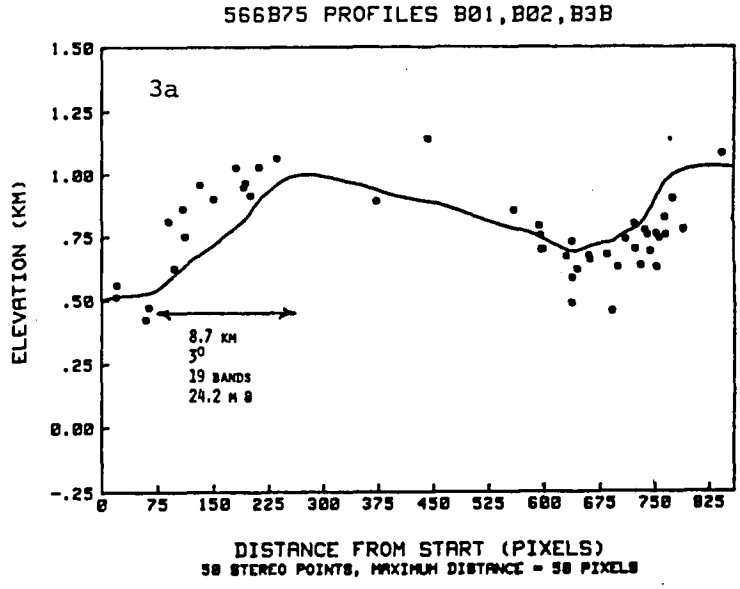


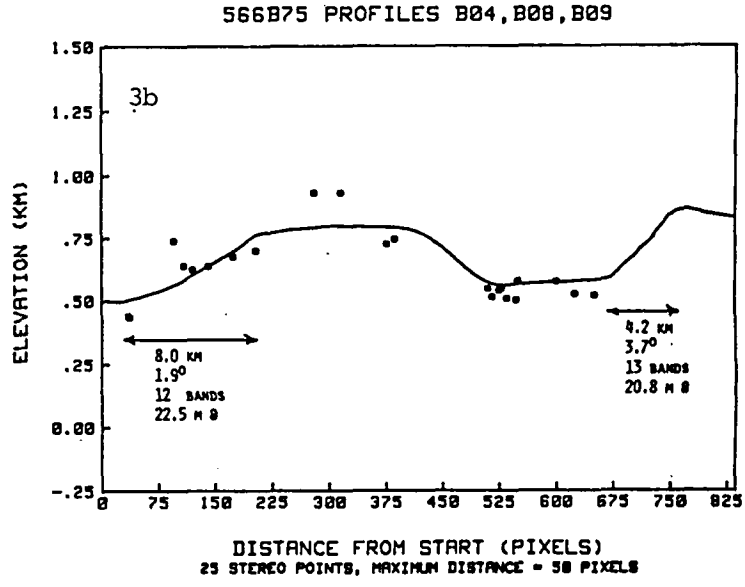


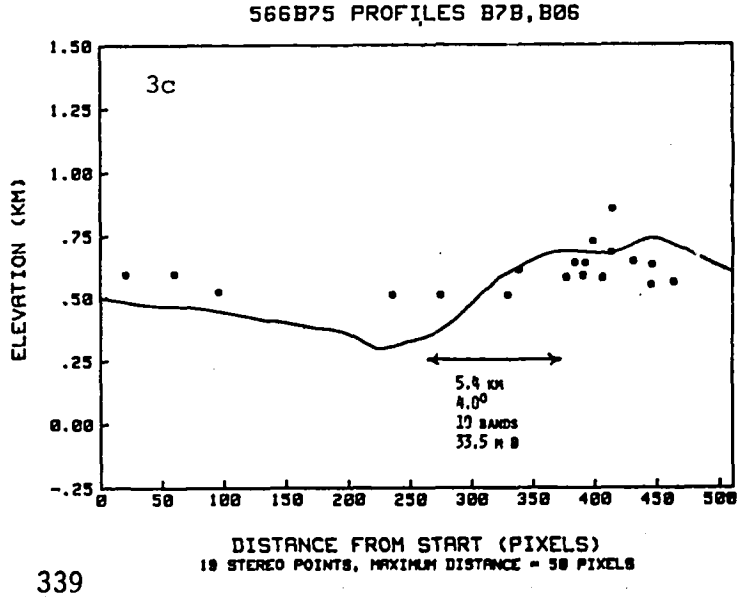

# UNIFORM DEPOSITION RATE AND CLIMATE MODULATED DEPOSITION RATE MODELS OF MARTIAN POLAR LAYERED DEPOSITS

Cutts, James A. and Karl R. Blasius, Planetary Science Institute, Science Applications, Inc., 283 S. Lake Ave., Suite 218, Pasadena, CA 91101

Polar layered deposits on Mars (Ref. 1) are now widely thought of as a geological expression of long term quasi-periodic variations in the martian climate. One possibility is that variations in the orbital/axial elements of Mars (Refs. 2, 3) which are large enough to affect the martian climate (Refs. 2, 4, 5, 6, 7, 8, 9, 10) are recorded in the deposits. Other possibilities such as variations in the output of the sun and episodic variations in the supply of volatiles at the martian surface still cannot be excluded. Here we review a modeling approach that is being used to predict the quantitative effects of astronomical variations on polar stratigraphy.

In last year's work we reported new topographic measurements of the polar deposits. Our data now indicate typical layer thicknesses may be as low as 15 meters (Ref. 11). Using improved photogrammetric and photoclinometric techniques (Ref. 12) there are the prospects of measuring individual layer thicknesses and defining sequences of layered strata in detail. Potential success in making these refined measurements forms a significant part of the inspiration for developing an improved theoretical understanding of polar layered deposit formation.

In recent work (Ref. 13) two broad classes of models have been considered. Uniform deposition rate models assume that the major constituent of the layered deposits is laid down at a constant rate. Climate is assumed to change the concentration of some minor constituent which modifies locally the resistance to erosion of the deposited materials. Climate-modulated deposition rate models assume that the deposition rate of the major constituent is controlled by climate. Discrete layers are defined by intervals during which deposition slowed down or temporarily ceased. Conceptually they resemble models for the formation of terrestrial or ocean margin sedimentary records where there are hiatuses in deposition in association with glaciation or change of sedimentary base level. The two types of models are illustrated and described in Fig. 1.

We have also developed models which have a physical basis in meteorology and surface processes on Mars and which include the controlling effects of eccentricity and longitude of perihelion as well as obliquity. Two specific climate-modulated deposition rate models have been formulated in physical detail: in one case, the major constituent is dust, in the other case, it is water ice. The effects of varying the threshold obliquity condition for sedimentation (Fig. 1) have also been examined. For certain ranges of threshold values the stratigraphic models are characterized by a single anomalously thick layer followed by a series of thinner ones; in the remaining range the layer thickness has only a slight quasi-periodic modulation. Pattern recognition techniques are being developed for distinguishing characteristics of particular models.

The characteristics of sediment accumulation at the margins of the perennial ice caps are also being explored. Some of the approaches taken to study sedimentation variations at the ocean margins during globally synchronous

changes of sea level (Ref. 14) are being applied here. Models for the mode of formation of polar troughs, which are the most controversial of all the martian polar landforms, are also being examined.

The geologic investigation of the martian polar regions is continuing to yield rich results. Mars is unique among Earth's neighbors in recording a history of its climatic experience. In investigating that history we are learning about mechanisms of climate change that Mars may share with Earth.

REFERENCES - (1) Murray, B.C. et al., Icarus 17, 328-245, 1972. (2) Ward, W.R., Science 181, 260-262, 1973. (3) Ward, W.R. et al., JGR 79, 3387-3395, 1974. (4) Briggs, G.A., Icarus 23, 167-191, 1974. (5) Fanale, F.P. et al., JGR 79, 3397-3402, 1974. (6) Fanale, F.P. et al., JGR 83, 2321-2325, 1978. (7) Pollack, J.B., Icarus 37, 479-553, 1979. (8) Toon, O.B. et al., submitted to Icarus, 1981. (9) Cutts, J.A. et al., Science 194, 1329-1337, 1976. (10) Cutts, J.A. et al., JGR 84, 2975-2994, 1979. (11) Blasius, K.R. et al., submitted to Icarus, 1981. (12) Howard, A.D. et al., Icarus (in press). (13) Cutts, J.A. et al., submitted to Icarus, 1981. (14) Pitman, W.C. (abstract), Ancient Sea Level Changes Symposium, Lamont-Doherty Geological Observatory, 1979.

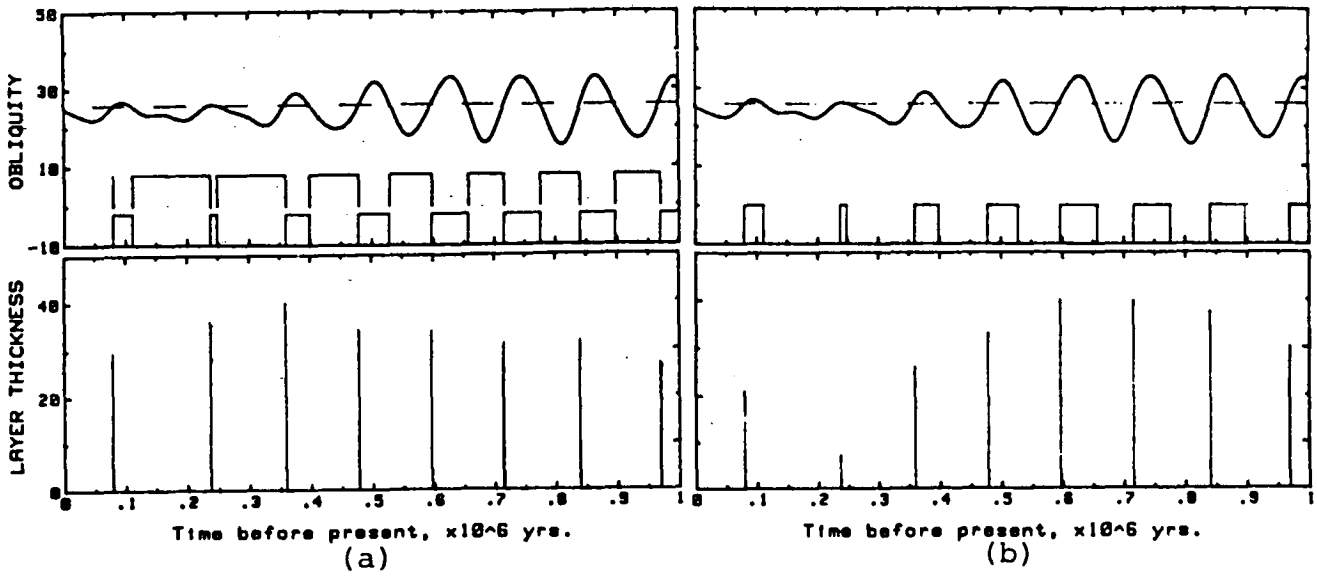


Figure 1(a): Continuous Deposition Rate Model for formation of polar layered deposits. Deposition of material A or B which differ only in a minor constituent is determined by the value of a function of obliquity, eccentricity, and longitude of perihelion. In this example, the function is proportional to obliquity, and the material type changes when obliquity crosses 26° terminating a period of accumulation of material B; a photogeologically recognizable layer is formed. The thickness of each completed layer as a function of completion time appears in the lower plot.
Figure 1(b): Climate-Modulated Deposition Rate Model for formation of polar layered deposits is similar to the Continuous Deposition Rate Model (Fig. 1a) in that a function of the orbit/axial elements controls deposition. It differs from the latter in that no deposition occurs when the function (here merely the obliquity) falls below threshold. A different pattern of layer thickness as a function of completion time results.

DIAGNOSTIC STRATIGRAPHIC RELATIONSHIPS IN AREAS OF COMPLEX TOPOGRAPHY ON POLAR LAYERED DEPOSITS. Alan D. Hoawrd, Univeritys of Virginia, James A. Cutts and Karl R. Blasius, Planetary Science Institute.

In most areas of the Martian polar regions which are underlain by layered deposits the topography is quasi two-dimensional in that it is composed of sub-parallel troughs and scarps. Currently-viable scenarios for the origin of these topographic features (1,2,3,4,5) have as a common element the building up of the intertrough flats by deposition of ice and dust modulated by quasi-cyclical climatic changes (6,7). The theories differ in whether poleward-facing trough walls are sites of deposition (2,3,5) or stability (4) (no erosion or deposition) and whether the equatorward-facing scarps and trough walls are mildly (3,4) or strongly (1,2,5) erosional. In addition, there is the possibility that quasi-cyclical climatic changes may produce episodes of general erosion on the layered deposits. Because of the two-dimensional topography and the limitation of layer exposures to equatorward-facing slopes, a wide range of spatio-temporal histories of deposition and erosion (including unconformities) can occur but still produce regular sequences of exposed layers.

However, local areas of the polar caps have complex topography with strongly curved and intersecting troughs and scarps. Such areas are potentially more diagnostic of stratigraphic history both because the non-parallelism of scarps exposing layers allows a three-dimensional view of stratigraphic relationships and also because the different scenarios of layer deposition should leave characteristic signatures (e.g., unconformities) as a result of the shifting of locii of deposition and erosion. Furthermore, areas of three dimensional topography locally have slopes whose strike approaches a north-south orientation. Such slopes are transitional in behavior between the poleward- and equatorward-facing trough walls; they fluctuate between erosion and deposition during the quasi-cyclic climatic changes.

An example of stratigraphic relationships in an area containing a trough junction is shown in Figures 1-4, which is centered at 81.6 N and 308.7 W and has stereoscopic imagery (77B21 and 77B51). Figure 2 shows locations discussed below and mapping units characterizing the north and south polar landscapes. Areas marked "L" are exposures of layered deposits, "S" designates relatively level expanses of smooth ice-covered terrain which appear to be the deposition sites of ice and dust forming the layered deposits, and "B" indicates a newly-recognized unit called banded terrain characterized by partial summer-time defrosting which reveals diffuse, irregular bands. Banded terrain generally occurs on poleward-facing trough walls and locally on slopes with a north-south strike. Banded terrain to most likely to have resulted from slight erosion of the feather edges of transgressive layer sequences on the poleward-facing trough walls, although it may also be produced by differential defrosting of wavy topography produced by recent layer deposition over the edges of previously-deposited layers of more limited distribution. The former interpretation is supported by local occurances of layers in the layered terrain being laterally traceable to equivalent bands, as near localities "A" and "B". The contact between banded and the smooth ("S") terrain is gradational, but the banded terrain generally unconformably overlies the layered deposits as indicated by dashed lines in Figure 2. Unconformities within the layered deposits are indicated on Figure 2 by dashed lines. Figure 3 shows the exposed layers of layered terrain and well-defined layers in banded terrain. Figure 4 is an interpretation of the topography based upon parallax measurements from the stereo pair. The contours are relative (9 - 10 scale), and the lack

of correction for viewing geometry may have introduced a systematic tilt bias to the contours. Comparison with a photogrammetric analysis of these images where these effects have been corrected for (4) suggests that each contour represents about 120 meters of relief. The more detailed contours compared to the map in (4) is due to a greater subjective interpretation of the data (e.g., contours were constrained to follow outcropping layers and the strike of linear features on the image to a degree consistent with the data).

One trough trending NW-SE (X-X' in Figure 2) is intersected by a curving trough which at the intersection (Y') trends NS-NE (Y-Y'), resulting in complex topography at the zone of intersection. The areas of smooth terrain often have appreciable slopes of different strike relative to each other (the model may have an overall tilt). The steeper, northward-facing trough walls occur as either smooth or banded terrain. The outcropping layers near the crest of the trough Y-Y' at location "A" are conformable to the boundary between the two units, but are sloping relative to other areas of smooth and banded terrain. This area of relative tilt of the exposed layers occur where the smooth terrain at "B" forms the northeastward-facing wall of the trough X-X'. The layers exposed near the top of the short scarp at locations "C" and "G" also have strong relative tilt. The local relative tilt of the uppermost layers strongly suggests that they have been deposited beneath adjacent smooth and banded terrain, and that the broad-scale topographic features (e.g., the troughs) existed prior to their deposition, although they have been modified as a result of the deposition and possible erosion of exposures of layered deposits. A well-defined unconformity occurs within the layered terrain at location "E", located about 5-10 layers from the topmost exposed layer on the trough wall. Figure 5 presents one interpretation of the stratigraphic relationships along cross-section Z-Z', illustrating the unconformities at "E" and "A" in Figure 2 (between units 5 through 7 in Figure 5). According to this interpretation, some erosion of layers deposited prior to deposition of unit 6 occured on the northeast-facing trough wall near "B". The banded terrain is interpreted to be exposure of layers 7 through 9, which are either the depositional edges of these layers or the result of their slight subsequent erosion. Slight-to-strong erosion of the two scarps of layered deposits has probably occured during the time interval recorded by layers 1-9.

REFERENCES: (1) Howard, A.D., 1978, Icarus, 34, 581-599; (2) Howard, A.D., 1979, NASA TM-80339, 103-105; (3) Squyres, S.W., 1979, Icarus, 40, 244-261; (4) Cutts, J.A., Blasius, K.R., and Roberts, W.J., 1979, J. Geophys. Res., 84, 2975-2994; (5) Toon, O.B., Pollack, J.B., Ward, W., Burns, S.A., and Bilski, K., 1981, Icarus, in press; (6) Ward, W.R., 1979, J. Geophys. Res., 79, 3375-3386; (7) Cutts, J.A., and Lewis, B.H., 1982, submitted to Icarus.

Fig. 1.

Fig. 2.

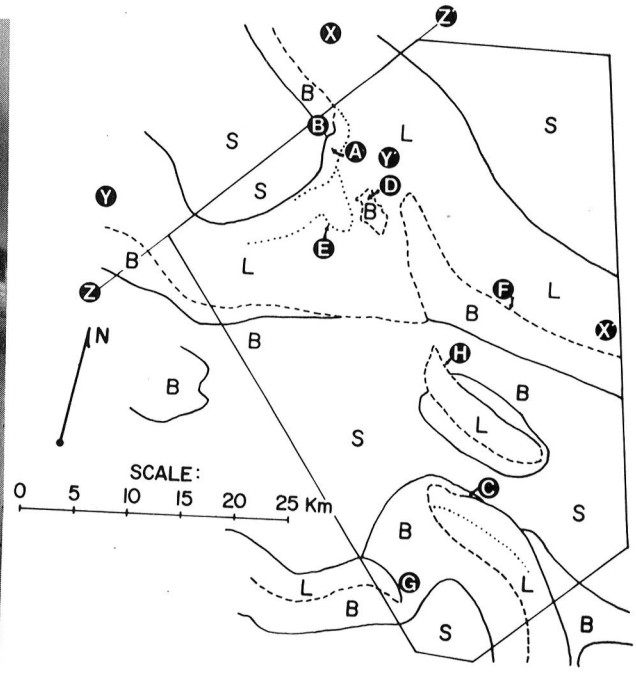


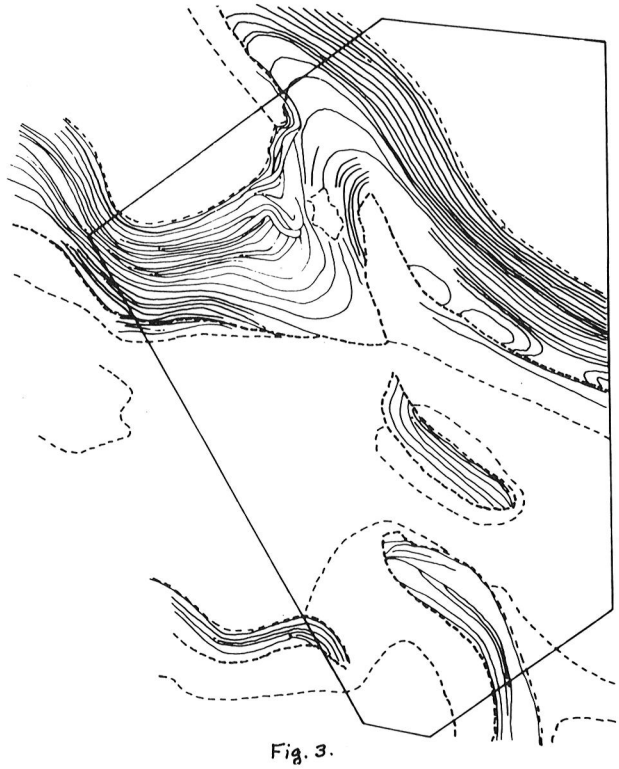

Fig. 3.

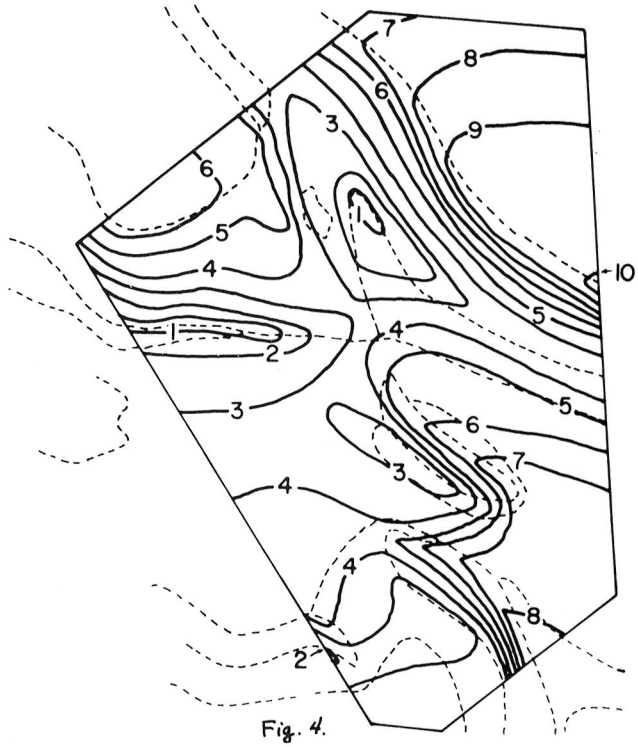


Fig. 4.

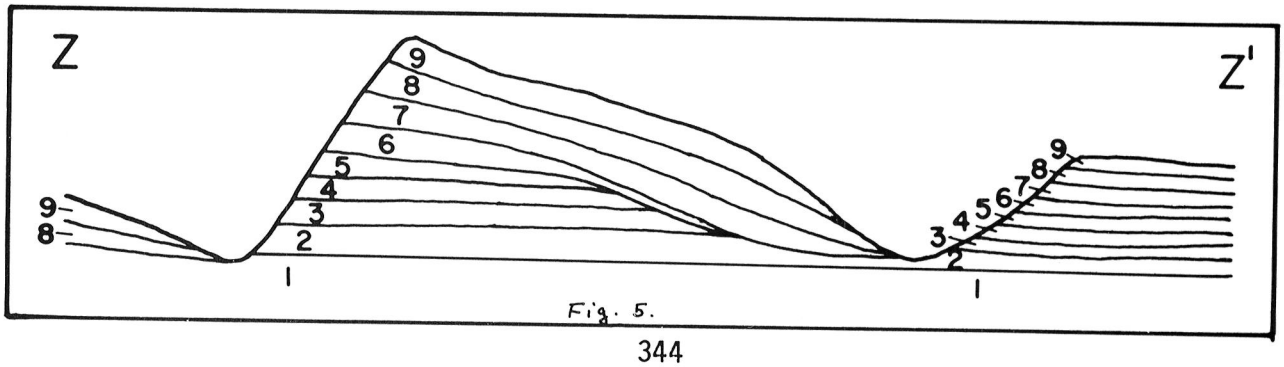


Fig. 5.

# WORKSHOP ON QUASI-PERIODIC CLIMATIC CHANGES ON MARS AND EARTH

James A. Cutts, Planetary Science Institute, Science Applications, Inc., 283 S. Lake Ave., Suite 218, Pasadena, CA 91101; Alan D. Howard, University of Virginia, Charlottesville, VA 22903; James B. Pollack and Owen B. Toon, Ames Research Center, NASA, Moffett Field, CA 94035

A workshop was held at the NASA Ames Research Center, Moffett Field, California, February 24-26, 1981, and its purpose was to bring together planetary geologists, planetary atmospheric physicists, celestial mechanicians, and researchers studying the terrestrial climate record to exchange information and ideas and advance our knowledge of the climatic history of Mars and earth.

The workshop agenda was structured as four topical areas: Mars Geologic Record, Mars Seasonal Cycles and Atmospheric Processes, Mars Climate Models, and Terrestrial Geological Record and Climate Modeling. The program was organized around a number of invited presentations; other participants joined in the question and answer period following each talk and in formal discussion sessions. The contributions on terrestrial climate change were broad reviews of current work; the contributions on Mars were more detailed and included critiques of current models and interpretations.

A fairly detailed summary of the workshop is published elsewhere (Ref. 1) and papers presented at the workshop will appear in a Proceedings Volume (Ref. 2). Here we summarize some of the future research needs that were discussed and which are desirable for future progress in Mars climate studies.

GEOLOGICAL DATA - Improved startigraphic data of individual layer thickness and trough geometry is needed to provide a basis for testing hypotheses that climatic cycles control thickness of polar layer and composition and to define unconformities that may correspond to long intervals of nondeposition in the historic record. Also, such data may help to resolve the question of whether or not the troughs in the layered deposits can migrate laterally as the uniformitarian model implies.

It is also important to determine if types of quantitative data other than layer thickness can be extracted from imaging data and used to constrain climate models. Possibilities include layer composition defined from layer albedo or slope and spacing of polar undulations.

Improved determinations of the density of the north polar layered deposits could result from refinements in the gravity and topographic data. Density places strong constraints on the composition of layered deposits (in particular, the relative proportions of dust and ice).

It is highly desirable to place better constraints on the thickness of the regolith, particularly at subpolar latitudes. In most modern theories of the manner in which astronomical verifications can cause climate changes on Mars, redistribution of $CO_2$ between the regolith and atmosphere plays an

important role. But the magnitude of the resulting atmospheric pressure oscillations depends in part on the depth of the regolith.

MODELING APPROACHES: CURRENT ATMOSPHERE - Further work on the circulation models is needed to understand better the transport of dust and water to and from the poles, to define their key source regions (e.g., the role of the regolith in the case of water), and to assess the factors determining the occurrence of permanent $CO_2$ ice caps. At present, the models do not adequately represent the transport of either substance, but techniques are under development to deal with this problem. It is now necessary to consider interactions among dust and volatile cycles to improve our knowledge about the seasonal cycles of these materials on present day Mars. Such an improvement will lay a solid basis for determining the effects of astronomical variations on long-term cycles.

MODELING APPROACHES: RESPONSE TO ORBITAL-AXIAL VARIATIONS - For the most part, past models of the responses of the Martian climate system to the astronomical forcing functions have involved separate considerations of the dust, water and $CO_2$ cycles and have used one-dimensional models (i.e., local heat and mass budgets). They have also been constructed without allowing for transport effects explicitly. Future approaches should involve consideration of coupled effects between the various cycles and the influence of dynamics. For example, the deposition of dust in the polar regions resulting from dust storms can significantly alter the albedo of the polar ice deposits and profoundly affect the polar heat budgets and, thereby, the $CO_2$ and $H_2O$ cycles. Also, in certain cases, the use of two-dimensional models, with perhaps paramaterized eddy transport, would help to define better the influence of atmospheric dynamics on some of the cycles.

Finally, it would be worthwhile to construct more explicit models of the actual formation and evolution of the polar layered deposits themselves to study the factors that influence the accumulation and ablation of dust and ice in the polar regions and the resulting geometry. Coupled models of the atmospheric water vapor and dust cycles would be needed for this purpose. Techniques for comparing observational data with the predictions of theory must also be refined to handle the large number of variables in the simulations.

ACKNOWLEDGEMENTS - The organizers would like to thank the principal speakers at the workshop: John Imbrie, Nicholas Christie-Blick, Warren Wiscombe, Edward Birchfield, Isaac Held, William Ward, Alan Peterfreund, Karl Blasius, Ronald Greeley, Michael Malin, Bruce Jakosky, Donald Davies, Phillip James, David Paige, Fraser Fanale, Rich Zurek, Conway Leovy, Robert Haberle, and Steve Squyres. Michael Carr, Richar Goody, and Frank Palluconi are appreciated for their excellent summary presentations. The workshop was sponsored by the Planetary Geology, Planetary Atmospheres, and Climate programs of the National Aeronautics and Sapce Administration.

MARS: THEORETICAL AND EXPERIMENTAL STUDIES OF REGOLITH-ATMOSPHERIC-CAP $CO_2$ EXCHANGE AND CLIMATE CHANGE

F.P. Fanale, Hawaii Institute of Geophysics, U. of Hawaii, W.B. Banerdt and R.S. Saunders, Jet Propulsion Laboratory, California Institute of Technology, and J.R. Salvail, Hawaii Institute of Geophysics.

Our quantitative models estimate the effects of astronomically driven surface insolation variations (Ward et al., 1974, 1979) on $CO_2$ exchange among the Mars regolith, atmosphere, and polar cap reservoirs (c.f. Fanale and Cannon, 1979; Toon et al., 1980.) In these new models the deep regolith is divided into many segments: various depths and latitudes. A time-temperature history is calculated for each, based on astronomical insolation theory. The atmosphere continues to reequilibriate with all segments in the warming and cooling regolith buffer. We find that at high obliquities atmospheric $PCO_2$ is determined by regolith temperatures and conservation of chosen total $CO_2$ mass ($\Sigma CO_2$). At low obliquities, this pressure drops to values allowing condensation on high albedo areas near the poles. In the first mode the cap mass is zero, the regolith buffers the atmospheric pressure, and the $\Sigma CO_2$ in the atmosphere plus regolith is constant. In the second, the atmospheric pressure is controlled only by the temperature of the surface $CO_2$ reservoir (cap) and the regolith adjusts its $CO_2$ content to satisfy that atmospheric $PCO_2$, laboratory-determined adsorption laws, and temperatures of each of its segments. In this mode the cap mass in not zero but is a free parameter which is adjusted so the total $CO_2$ in all three operative reservoirs equals the input $\Sigma CO_2$.

Table I shows some results. Maximum and minimum pressures attained during the pre and post Tharsis obliquity cycles are given, as are maximum values of cap mass. Models for ground basalt and clay regoliths are given (experimental data on amorphous gels is currently being obtained). For each, exchange is governed by analytical expressions which fit our laboratory adsorption data for the field of $PCO_2$'s and T's in question. A variety of thickness-latitude distributions for the regolith are examined as well, since, like the mineralogy of (especially) the deep regolith, these are currently uncertain for Mars. Constant regolith thickness models (Table I) have the virtue of simplicity. Also given are stepped models in which the equatorial regolith has negligible thickness, the middle thickness regolith has a thickness of 200 km and the near polar thickness is given. While total regolith mass and total $CO_2$ mass seem to be arbitrary imput parameters, we prefer (Table I) models which do not assume such small regolith or such high available $CO_2$ inventories that a huge surface $CO_2$ cap - not observed - is currently demanded.

In all our models (a few of which are presented here) certain conclusions recur:

1. The regolith and a sometimes huge $CO_2$ cap are the major $CO_2$ reservoirs on Mars. The atmosphere is a limited conduit through which $CO_2$ flows between those two large reservoirs.
2. The contention for exchangeable $CO_2$ between the two large reservoirs (the "ocean" of adsorbed $CO_2$ in the regolith and a sometimes huge surface $CO_2$ cap) shifts periodically in response to obliquity ($\theta$)

variation. At lowest θ a huge $CO_2$ cap (not presently observable) forms and buffers the atmospheric $PCO_2$. At high θ there is no $CO_2$ cap and the regolith buffers the atmosphere, severly restricting the maximum pressures. Among several reasons, the main reason why the reservoirs alternate domination is that the caps experience a maximal thermal wave because of proximity to the pole plus lack of attenuation by overlying regolith, but the time-temperature history of the regolith is much more muted.

3. The mass of the $CO_2$ cap which appears at each low in the θ cycle is up to 1 x $10^{21}$ grams in plausible models. As $CO_2$ flows from one reservoir to the other each $10^5$ years, it flushes out atmospheric $O_2$ at a sufficient rate to surpress $^{18}O$ enrichment as required by Viking observations.
4. As the cap and regolith reservoirs wax and wane the atmosphere experiences extensive pressure variation. At lowest θ , when buffered by the cap, $PCO_2$ falls to ∿0.1 mb (∿0.02 mb if Pre-Tharsis). At highest θ a $PCO_2$ maximum is achieved which is probably 8-15 mb. (11-25 mb pre-Tharsis).
5. This buffering of the atmosphere alternatively by the caps and the regolith has controlled Mars' climate through much of its history. Table I implies great changes in polar cap configuration and (with periodic x100 pressure variations) the ability of the atmosphere to transport dust (Greeley et al., 1981). This would seemingly be sufficient to explain the layered terrain growth (Cutts et al., 1979). Occurrance of extensive gully systems, (only) in earliest Mars history, suggests superimposition of "non harmonic" or "non periodic" effects on the clockwork mechanism described. Among such processes are the gradual growth or redistribution of the regolith, or a change in mineralogy, increased atmospheric heat transport to the poles, gas/dust greenhouse effects, $CO_2$ imcorporation into carbonates. Viking data may imply a regolith specific surface area (Ballou et al., 1978) generally compatible with those used in our models. Also the "flushing" rate is about the same as that required for $^{18}O$:$^{16}O$ stabilization (McElroy et al., 1976). Another possible test will be determining whether $^{15}N$ enrichment would occur too efficiently or too slowly on the average over Mars history given the atmospheric $PCO_2$ history envisioned (c.f. Fox, 1981).

We also examined the suggestion of Dzurisin and Ingersoll (1975) that isothermal buffering of the seasonal pressure "wave" might decrease its amplitude and shift its phase. We tested, in the laboratory, a theory for migration of $CO_2$ in a cold, porous, highly absorbing soil developed by Toon et al. (1980 modifying a relation given by Barrer (1967). The apparatus and techniques we used are described elsewhere in the volume. Our results confirmed applicability of the theory under Mars T and $PCO_2$ conditions down to -70° C, and also suggested applicability at lower temperatures. Values of D for $CO_2$ diffusion through the montmorillonite soil used in our experiments at -40° C and -70° C were 2.5 x $10^{-2}$ and 1.1 x $10^{-2}$ $cm^2$ $sec^{-1}$. These were in keeping (within ∿50%) with theoretical predictions based on adsorptive properties we measured for a sample of soil even though application as low as -70° C required a correction of x50 (downward) for the diffusion constant due

to adsorption slowing of the diffusion. Our results indicate some soils might indeed provide effective isothermal buffering, but at martian temperatures the silty material in soil decreases rather than increases its $CO_2$ buffering ability. This is because the increase in buffering capacity per gram accomplished by adding fine weathering products is largely counterbalanced by decrease in diffusion rates owing to time spent in the adsorbed layer vs. pore gas. This leaves simple blockage of small pore spaces as the major effect, thus thwarting effective $CO_2$ buffering. With $D = 1.1 \times 10^{-2}$ $cm^2$ $sec^{-1}$ we calculate that soil used in our experiment could diminish an ab initio P wave of 2 mb by only ∿5%. We believe slowing of diffusion by adsorption as indicated by our measurements is the probable reason why isothermal buffering of the seasonal pressure wave has not been identified (Hess et al., 1979). It should be noted that these adsorption-slowed vapor diffusion rates, while blunting the effectiveness of seasonal isothermal buffering, are still much greater than thermal diffusivities for soils, hence vapor diffusivity limits do not restrict long term Θ-driven $CO_2$ exchange discussed above. We also evaluated thermally driven seasonal exchange. We find that process could produce notable pressure effects only if released gas is restricted to the latitude where it was desorbed for a substantial portion of the season. More likely, if desorbed $CO_2$ is allowed to mix latitudinally, the effects could be undetectable in the presence of effects due to sublimation and condensation of the annual caps.

References: Ballou, E.V. et al., Nature 271, 644-645, 1978. Cutts, J.A. et al., J.G.R. 84, 2975-2994, 1979. Dzurisin, D. and Ingersoll, A.P., Icarus 26, 437-440, 1975. Fanale, F.P. and Cannon, W.A., J.G.R. 24, 3397-3402, 1974. Fanale, F.P. and Cannon, W.A., J.G.R. 83, 2321-2325, 1978. Fanale, F.P. and Cannon, W.A., J.G.R. 84, 8404-8414, 1979. Fox, J.E. et al., J.G.R., in press, 1981. Greeley, R. et al., Icarus, in press, 1981. Hess, S. et al., J.G.R. 82, 4559-4573, 1979. McElroy, M. et al., Science 194, 70-72, 1976. Toon, O.B. et al., Icarus, in press, 1980. Ward, W.R. et al., J.G.R., 243-259, 1979. Ward, W.R. et al., J.G.R. 79, 3387-3395, 1974. Barrer, R.M., in The Solid-Gas Interface Vol. 2, 557-609, Dekker, N.Y., 1967.

TABLE I

| Regolith Model | Max. Pressure Post Tharsis (mb) (Θ=37.1°) | Max. Pressure Pre Tharsis (mb) (Θ=50°) | Min. Pressure Post Tharsis (mb) (Θ=11.7°) | Min. Pressure Pre Tharsis (mb) (Θ=9°) | Max. Cap Mass Post Tharsis ($x10^{17}$kg) | Max. Cap Mass Pre Tharsis ($x10^{17}$kg) |
|---|---|---|---|---|---|---|
| Ground Basalt 1000 m constant | 9.70 | 12.8 | .105 | .019 | 6.78 | 9.64 |
| $\Sigma$ $CO_2$ = 350 g/cm$^2$* | 8.61 | 11.0 | | | 7.02 | 9.88 |
| Ground Basalt 1000 m stepped** | 9.69 | 13.4 | .105 | .019 | 2.98 | 4.30 |
| $\Sigma$ $CO_2$ = 200 g/cm$^2$* | 8.42 | 11.5 | | | 3.16 | 4.48 |
| Nontronite (Clay) 1000 m stepped** | 13.2 | 23.9 | .105 | .019 | 15.0 | 17.8 |
| $\Sigma$ $CO_2$ = 1,400g/cm$^2$* | 10.2 | 17.6 | | | 16.2 | 18.7 |
| Nontronite (Clay) 100 m constant | 15.1 | 21.3 | .105 | .019 | 2.63 | 3.07 |
| $\Sigma$ $CO_2$ = 250 g/cm$^2$* | 14.3 | 20.2 | | | 2.69 | 3.13 |
| Nontronite (Clay) 400 m stepped** | 15.1 | 25.4 | .105 | .019 | 8.39 | 9.98 |
| $\Sigma$ $CO_2$ = 800 g/cm$^2$* | 12.3 | 20.3 | | | 9.06 | 10.5 |

*This is the particular value for each model of various arbitrarily chosen values of total $CO_2$ inventory in g/cm$^2$ at which a permanent polar $CO_2$ cap begins to form at $\approx$ 25° obliquity for the post Tharsis case. This corresponds to presently observed conditions on Mars (Θ=25.2°)

**See text for the definitions of the two stepped cases.

***The two numbers in each block represent values using two different values of thermal diffusivity. For the upper numbers $\alpha = 15.068 m^2 yr^{-1}$. For the lower numbers $\alpha = 2.389 m^2 yr^{-1}$. See Text for explanation of these values.

VIKING MAWD OBSERVATIONS AND REGOLITH WATER VAPOR SOURCES ON MARS

R.L. Huguenin and S.M. Clifford, University of Massachusetts, Dept. of Physics/Astronomy and B.W. Hapke, University of Pittsburgh, Dept. of Geology/Planetary Sciences.

Viking Orbiter MAWD (Mars Atmospheric Water Detector) data have been used for several atmospheric transport and vapor source models. Farmer and Doms (1979) proposed that vapor was transported north (during the 1977b storm) with deposition north of 60° latitude. Jakosky and Farmer (1981) argued for a net southward transport with significant regolith buffering. Davies (1981) suggested alternatively that the $H_2O$ is derived from the poles with no net transport to or from the caps. Despite the major differences between models, they have in common the proposal that there are probably no net annual regolith water vapor sources in the equatorial regions of Mars. This was particularly emphasized by Jakosky and Farmer (1981). It is proposed here that the various transport models and particularly arguments against southern hemishpere net annual regolith vapor sources may not be valid, due primarily to detectivity and aerosol masking limitations.

Indeed it has been proposed, based on other data sets, that Solis Lacus and Noachis-Hellespontus may in fact be net annual southern hemisphere vapor source regions. The evidence is based on the observational record (past telescopic, Mariner 6/7, Mariner 9 and Viking) of the occurrence and behavior of condensate features on the planet( Huguenin et al., 1979; Huguenin and Clifford, 1980, 1981) and on radar data (Zisk and Mouginis-Mark, 1980).

It was estimated that maximum regolith outgassing rates (during late southern spring) may be $\gtrsim$ 1 mg $cm^{-2}$ $sol^{-1}$ over each of the two source regions (Huguenin and Clifford, 1981). This would be equivalent to a column $H_2O$ abundance of $\gtrsim$ 10 precipitable microns over each source area. During most of the year, however, daily release rates were predicted to be substantially lower (column abundances probably < 1 pr micron per sol), with a total annual release estimated to be $\sim 10^2$ mg $cm^{-2}$ from each source region (equivalent to $\sim 10^{-1}$ $km^3$ ice). It was further argued, based on the observed onsets of cloudiness and regolith adsorption/desorption models, that the highest $H_2O$ vapor release rates may have occurred shortly after sunrise (0700-0900) when heating rates were maximum ($\sim 15°$ $hr^{-1}$). By the time of the MAWD observations (1000-1600 hours), then, most of the vapor should have been in the atmospheric column. A variety of factors may have prevented its detection, however.

Firstly, even in the absence of masking effects and other complicating factors discussed below, the detectability of the water vapor from the proposed source regions (Solis Lacus and Noachis-Hellespontus) would be questionable. The MAWD was a reflectance spectrometer that measured the absorption of solar radiation reflected from the martian surface at the 1.38 μm water vapor absorption band. Instrument sensitivity was such that $\lesssim$ 1 precipitable micron (column abundance) could be detected. During much of the non-storm season estimated daily outgassing volumes

(< 1 pr. micron) would have been near or below the detection limit. During storm seasons predicted outgassing rates would produce daily column abundances that exceed $\sim$ 10 precipitable microns. The $\sim$ 10 pr μm lower limit would be comparable (within a factor of $\sim$ 2) to observed column abundances in the proposed source regions during all but the most dust-contaminated periods, and detectability (even in the absence of masking particulates) would be questionable. It is uncertain what the average column abundances actually were in the dusty hemisphere during the storm season, and hence it is uncertain how high the column abundances would need to have been to be detected as anomalies. During southern spring-summer seasons in the 1960s, for example, (and this was pointed out by Jakosky and Farmer, 1981) when dust storms were concentrated in the northern hemisphere, average water vapor abundances exceeded 50 pr μm (disk averaged column abundances). Largest abundances occurred over the southern hemisphere and could have reached 150 pr. microns in some locations.

Such abundances may have been prevalent during the 1977 southern summer seasons as well. During the 1977a storm period, measured global vapor abundances fell by 30 percent compared to the pre-storm value and during the second storm measured amounts of vapor fell by nearly 70 percent. In the southern hemisphere local column abundances dropped to their lowest values (2-8 microns) at the times of the storms, and this occurred at a time (particularly during the second storm) when clouds and fogs were in maximum abundance. Some canyon condensate fogs were seen in images at the warmest latitudes and times of the year (near perihelion) that survived the warmest time of the day (lasting to at least 3:00 pm local time). Equilibrium vapor pressures of the ice in those hazes would have been as high as 26 mbar, and consequently vapor abundances could have been substantial. Such fogs and low-level clouds were widespread, and yet measured vapor abundances were at their yearly minima. The reason for this discrepancy was probably masking by dust. When optical depths of dust approached unity, the underlying water vapor would have probably been nearly completely masked (D.W. Davies, personal communication) by particle backscattering at high altitude (above the vapor).

The efficiency of masking is due not only to high altitude backscattering effects, but also to absorption by dust at 1.38 μm. There is an absorption feature near 1.38 μm in the Mars reflectance spectra that is not completely accounted for by atmospheric $CO_2$. The feature appeared in spectra of bright areas and the whole disk during 1978 and we attributed it to a composite band arising from a mixture of desiccated mineral hydrate ($V_1 + V_3$) and $H_2O$ ice ($V_1 + V_3$) (Huguenin et al., 1978; McCord et al., 1978). In suspended dust, absorption bands have been shown to be stronger, due to enhanced scattering in suspended aerosol vs. a surface powder (McCord et al., 1977). The effect of these relatively broad absorptions would be to artificially reduce the apparent depth of the 1.38 μm vapor band, and hence produce artificially low vapor abundance estimates. These two effects, backscattering at high altitude and absorption, would have acted to mask vapor throughout much of the martian year. Atmospheric opacities at the Viking sites (northern

hemisphere) exceeded unity during $190 < L_s < 340$ and it was > 0.5 during most of the year. In the south opacities would have been higher.

In addition to the generalized opacities arising from global aerosol suspensions, numerous optically thick local dust plumes were observed throughout the martian year. During the dust storms the plumes were concentrated in the proposed $H_2O$ vapor source regions, and hence masking of local vapor anomalies at these sites would have been selectively enhanced.

Local condensate clouds would also have effectively masked the vapor measurements, again due primarily to backscattering by aerosols above the vapor and also to an absorption feature at 1.2 - 1.4 μm. There was substantial cloud activity throughout the martian year over large expanses of the surface, with concentrations in and around the proposed vapor source regions. The local clouds were further supplemented by a generalized condensate haze event in the southern hemisphere that started around $L_s \lesssim 135$-145 and lasted beyond the vernal equinox ($L_s = 180^o$).

Other factors that complicate interpretations of the water vapor data are albedo, topography and uncertainties in the elevation profile of vapor abundances within the column. These factors have been discussed by the MAWD team. In general, measured abundances over average dark areas would be ∿ 25 percent lower than over average bright areas for equivalent actual column abundances (Jakosky and Farmer,1981 ). Column abundances over low elevation regions are in general higher than over high elevation regions (Jakosky and Farmer, 1981), although there are significant deviations from the linear airmass relationship. These deviations may reflect variations in the $H_2O$ vapor scale height, which would complicate interpretations of surface humidity and detection of anomalies associated with possible source regions.

Even in the absence of particulate masking effects and the other complicating factors pointed out above, the detection of net annual regolith vapor sources would be questionable in light of high background vapor levels. Masking, albedo, and other effects further reduce this capability. The masking effects, particularly in the southern hemisphere, also limit the usefulness of the MAWD data for deducing models of vapor transport. The water vapor maps that have been published up to now have not been corrected for opacity, and it is possible that opacity variations may have been the dominant factor controlling apparent seasonal variatons. Previous atmospheric transport and vapor source models based on the uncorrected MAWD data, therefore, may not be valid.

Acknowledgement. This research was supported by NASA grants NSG 7397, NSG 7405, and NAGW 40 to the University of Massachusetts, and NASA grant NSG 7147 to the University of Pittsburgh.

References. Davies, D.W. (1979) Icarus 45:398; Farmer, C.B. and Doms, P.E. (1979). J. Geophys. Res. 84:2881; Huguenin, R.L., McCord, T.B., and Clark, R.J. (1978) Proc. 2nd Coll. on Planetary Water, 100; Huguenin, R.L., Clifford, S.M., Sullivan, C.A. and Miller, K.J. (1979) NASA TM 80339, 208;

Huguenin, R.L. and Clifford, S.M. (1980) NASA TM 81777, 153; Huguenin, R.L. and Clifford, S.M. (1981), preprint submitted to JGR; Jakosky, B.M. and Farmer, C.B. (1981) preprint submitted to JGR; McCord, T.B., Clark, R.N. and Huguenin, R.L. (1978) J. Geophys. Res. 83:5433, Zisk, S.H. and Mouginis-Mark, P.J. (1980) Nature 288:735.

# MARS SURFACE ATMOSPHERE EXCHANGE EXPERIMENT: ISOTHERMAL CASE

W. B. Banerdt*, F. P. Fanale**, and R. S. Saunders*, *Jet Propulsion Laboratory, California Institute of Technology, **University of Hawaii, Honolulu, HI 96822.

This report covers the initial experiments on the physical interaction between the surface and atmosphere of Mars. We are studying the effect of regolith-atmosphere $CO_2$ exchange on the pressure wave caused by the atmosphere-cap (sublimation and condensation of the seasonal polar cap). Study of regolith adsorption by Fanale and Cannon (1971, 1978) showed that a large buffering effect on the seasonal pressure would be expected if a thick regolith were involved in the seasonal $CO_2$ exchange. Dzurisin and Ingersol (1975) estimated that if the depth of penetration of the seasonal pressure wave were great, then the amplitude of the wave would be damped considerably and its phase would be shifted. Our experiments show that the effective depth of seasonal exchange is small because adsorption slows down the migration of $CO_2$.

During the past year we have conducted a study of the isothermal gas transport properties of a highly adsorbing porous medium. The experiments were carried out in the JPL Mars Surface Simulation Facility on two different soil compositions: a montmorillonite soil with a density of 0.6 $gm/cm^3$, and a 1.3 $gm/cm^3$ density soil composed of 45% montmorillonite, 45% ground basalt, and 10% iron oxide. In each test a step function in $CO_2$ pressure was applied to the top of the soil column and the pressure rise was recorded at various depths. A vapor diffusivity, D, is obtained which provides the best simultaneous analytic fit to the pressure curves at all depths. The results of one test performed at -70C are shown in Fig. 1.

One of our objectives was to test the applicability of the capillary diffusion model to Mars-like soils. This model has been successfully applied in gas chromatography (Barrer, 1967) and was recently used by Toon et al (1980) in their study of climatic change on mars. The diffusivity is given by:

$$D = \frac{4kE^2 r (2RT/\pi M)}{3 (E + \alpha)} \quad (1)$$

where k is the tortuosity, E is the porosity, r is the average pore radius, M is the molecular weight, and $\alpha$ is an adsorption parameter, defined as

$$\alpha = \frac{\partial P_{ads}}{\partial P}\Big|_T \quad (2)$$

where $P_{ads}$ is the equivalent pressure of the adsorbed gas.

Our experimental results, along with the theoretical diffusivities are shown in Table 1. The adsorption parameters were determined from the data of Fanale and Cannon (1971, 1978). The agreement between theory and experiment is quite good in the temperature region in which adsorption data is available. At the higher temperatures, where adsorption data was not available, D was calculated assuming no adsorption occurred. This is almost certainly not true, but it places an upper bound on D.

From diffusion theory, the total isothermal mass flux from the regolith over a half cycle of a sinusoidal pressure wave is given by:

$$M = \frac{2M\ (E + \alpha)}{RT} \left(\frac{D}{\omega}\right)^{1/2} \Delta P \qquad (3)$$

where $\omega$ is the angular frequency and $\Delta P$ is the amplitude of the wave. Our results indicate that this amounts to only about a 5% effect on the seasonal pressure wave. We consider this to be an upper bound, since the buffering mass flux is proportional to $(\alpha r E)^{1/2}$ (from equations (1) and (3)) and our values for these parameters are rather high ($\alpha$ = 55, r = 10 $\mu$, E = .35). Therefore we do not expect isothermal regolith buffering to be observable in the Viking meteorology data.

This still leaves open the question of thermal buffering by the regolith. We are currently undertaking an experimental program to investigate the thermal diffusive properties of our soil.

TABLE 1

| MATERIAL | TEMPERATURE | | D($cm^2$/sec) |
|---|---|---|---|
| 100% Clay | 27°C | Theory | < 4.4 |
| | | Experiment | $1.5 \times 10^{-1}$ |
| | -45°C | Theory | $7.2 \times 10^{-2}$ |
| | | Experiment | $9.2 \times 10^{-2}$ |
| 45% Clay<br>45% Basalt<br>10% Fe Oxides | 54°C | Theory | < 1.4 |
| | | Experiment | 1.2 |
| | -40°C | Theory | $2.5 \times 10^{-2}$ |
| | | Experiment | $2.7 \times 10^{-2}$ |
| | -70°C | Theory | $1.8 \times 10^{-2}$ |
| | | Experiment | $1.1 \times 10^{-2}$ |

## REFERENCES


Barrer, R. M., Surface and volume flow in porous media, in "Advances in Hydroscience", Vol. 4, V. Chow, ed., 557-609, 1967.

Dzurisin, D., and A. B. Ingersol, Icarus, 26, 437-440, 1975.

Fanale, F. P., and W. A. Cannon, Adsorption on the martian regolith, Nature, 230, 502-504, 1971.

Fanale, F. P., and W. A. Cannon, Mars: The role of the regolith in determining atmospheric pressure and response to insolation changes, JGR, 83, 2321-2325, 1978.

Toon, O. B., J. B. Pollack, W. Ward, J. A. Burns, and K. Bilski, The astronomical theory of climatic change on Mars, Icarus, 44, 552-607, 1980.



Performed under contract with NASA.


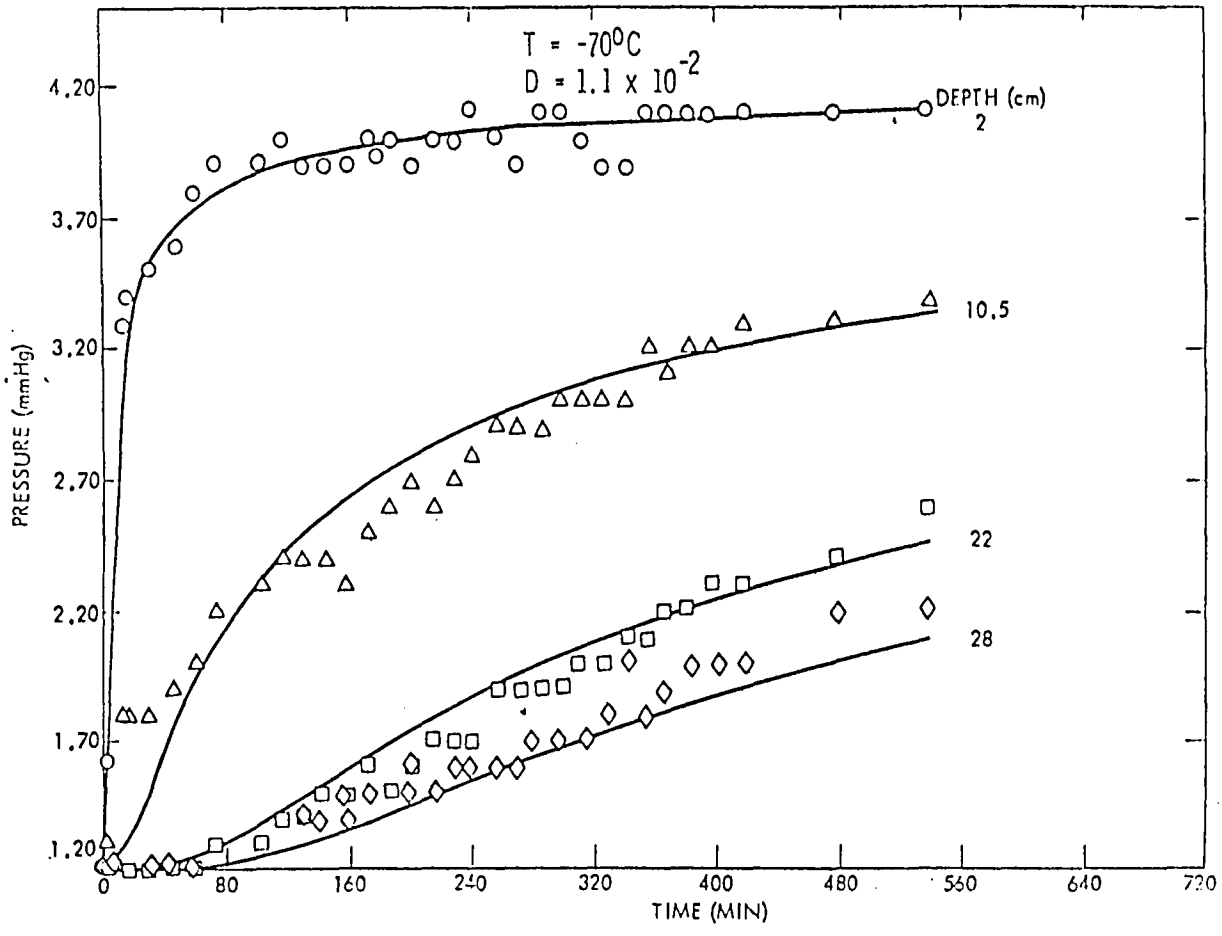


FIGURE 1

VOLATILE RELEASE FROM MARTIAN ANALOG MATERIALS

R. K. Kotra, Lockheed, 1830 NASA Road 1, Houston, TX 77058
E. K. Gibson, Jr., SN7, NASA Johnson Space Center, Houston, TX 77058
M. A. Urbancic, Chemistry Department, Univ. of Illinois, Urbana, IL 61801

The study of volatiles in surface materials of planetary bodies can potentially reveal the nature of past or present processes. The Viking XRF and GCMS data suggest that a portion of the martian regolith consists of low temperature materials such as hydrates, carbonates, and sulfates (1,2). Reflectance spectroscopy, Viking photography, infrared data, and laboratory simulations also suggest the presence of such materials (3,4,5,6). Water vapor mapping shows considerable vapor movement indicating that adsorption and desorption processes are in operation (7). Thus, the regolith may contain a significant accumulation of volatile-rich minerals.

The thermal stabilities of mineral phases and their volatile release profiles under various conditions have been extensively investigated in our laboratory by thermal methods of analysis (8). Recently, a number of martian analog materials have been studied by vacuum pyrolysis. Less than 5 mg of various hydrates, carbonates, sulfates, and clays were loaded in quartz capillaries and heated in vacuo using resistively heated platinum filament pyrolyzers. Evolved gases were analyzed by mass spectrometry. The ovens of the Viking GC-MS experiment were heated to $50^{\circ}$, $200^{\circ}$, $350^{\circ}$, or $500^{\circ}$ in 1-8 seconds, depending on T and held there for 30 seconds (1). The ramp rate of our pyroprobes was $0.1^{\circ}$ C/MS and the desired temperature could be maintained for about 15 seconds. Samples were heated three times at each interval. Therefore, the conditions of our investigation closely approximate those in the Viking GC-MS experiment.

Table 1 summarizes the volatile release data for pyrolysis experiments as well as for earlier thermogravimetric studies (TGA). It is very clear that in all cases the temperature of first release of volatiles ($T_I$) is higher in the pyrolysis experiments compared to the TGA data. The latter TGA obtained data are for a heating rate of $10^{\circ}$ C/min. The very rapid rise in temperature in the pyroprobe and the short time spent at each interval do not allow thermal equilibrium to be reached. This was also observed in the TGA investigations at rates higher than $20^{\circ}$/min. Figure 1 shows the effect of heating rates on the decomposition of siderite. The equilibrium dehydration temperature for limonite is about $170^{\circ}$. The weight loss curve is shown in Figure 2. Under the rapid heating conditions employed here, the temperature of maximum water release is $500^{\circ}$. For carbonates the partial pressure of $CO_2$ in the atmosphere also influences $T_I$. This is illustrated in Figure 3. Grain size also appears to effect the temperature of maximum volatile release (Figure 4). The finer-grained goethite releases the maximum amount of water at a temperature $100^{\circ}$ lower. These factors and others must be kept in mind in the future design of planetary probes to study the surface materials. Based on our studies, it is understandable why significant amounts of carbonate-derived $CO_2$ were not detected by the Viking GC-MS pyrolysis experiments, although it is possible that carbonate minerals may not be abundant on Mars.

Table 1. Volatile Release Temperatures of Martian Analog Materials (°C).

| Mineral | Pyrolysis * | | | Thermogravimetry ** | | |
|---|---|---|---|---|---|---|
| | $T_I$ | $T_{MAX}$ | $T_F$ | $T_I$ | $T_{MAX}$ | $T_F$ |
| Goethite | 350 | 600 | 1000 | 220-240 | 270 | 300-330 |
| Goethite (<1μ) | 350 | 500 | 1000 | - | - | - |
| Limonite (>100 mesh) | 200 | 500 | 1000 | - | - | - |
| Limonite (50-100 mesh) | 200 | 500 | 1000 | 200 | 280 | 300 |
| Brucite | 350-700 | 800 | 1000 | 300,600 | 400 | 430,720 |
| Diaspore | 350-700 | 1000 | 1000 | 400 | 530 | 600 |
| Siderite | 500-600 | 1000 | 1000 | 465 | 540 | 580 |
| Magnesite | 350-500 | 1000 | 1000 | 430 | 600 | 660 |
| Calcite | 350 | 1000 | 1000 | 660 | 820 | 880 |
| Dolomite | 350-600 | 1000 | 1000 | 630 | 800 | 830 |
| Smithsonite | 350 | 800 | 1000 | 320 | 470 | 520 |
| Rhodochrosite | 350 | 1000 | 1000 | 480 | 600 | 660 |
| $FeSO_4 \cdot 7H_2O$ - $H_2O$ | 200 | 350,700 | 1000 | 100 | 100,250 | 280 |
| $Fe_2(SO_4)_3 \cdot nH_2O$ - $H_2O$ | 200 | 500,700 | 1000 | 100 | 200 | 280 |
| $FeSO_4 \cdot 7H_2O$ - $SO_2$ | 600 | 1000 | 1000 | 600 | 625 | 700 |
| $Fe_2(SO_4)_3 \cdot nH_2O$ - $SO_2$ | 500 | 1000 | 1000 | 600 | 680 | 700 |
| $MgSO_4 \cdot 7H_2O$ - $H_2O$ | 200 | 200 | 1000 | 100 | 130 | 300 |
| $MgSO_4 \cdot 7H_2O$ - $SO_2$ | 600 | 700 | 1000 | 870 | 1000 | 1050 |
| Gypsum - $H_2O$ | 350 | 500 | 1000 | 110 | 160 | 200 |
| Selenite - $H_2O$ | 200 | 350 | 1000 | 110 | 150 | 200 |
| Dickite | 200 | 900-1000 | 1000 | 400 | - | - |
| Kaolinite | 350 | 1000 | 1000 | 440 | - | - |
| Montmorillonite | 200 | 350 | 1000 | 575 | - | - |
| Illite in Shale | 350 | 1000 | 1000 | - | - | - |

Legend: $T_I$: Temperature of initial volatile release
$T_{MAX}$: Temperature of maximum volatile release
$T_F$: Temperature of final volatile release
* Conditions: $10^{-6}$ torr vacuum
** Conditions: 1 atm. nitrogen

References:
1. Biemann et al. (1976) J. Geophys. Res. 82, 4641-4658. 2. Clark et al. (1976) Science 194, 1283-1288. 3. Adams (1968) Science 159, 1453-1455. 4. Huguenin (1974) J. Geophys. Res. 79, 3895-3903. 5. Huguenin (1976) Icarus 28, 203-212. 6. McCord et al. (1979) Second International Colloquium on Mars (abstract), 56-57. 7. Farmer et al. (1976) Science 194, 1334-1341. 8. Gibson et al. (1979) NASA Tech. Memorandum 80339, 215-217.

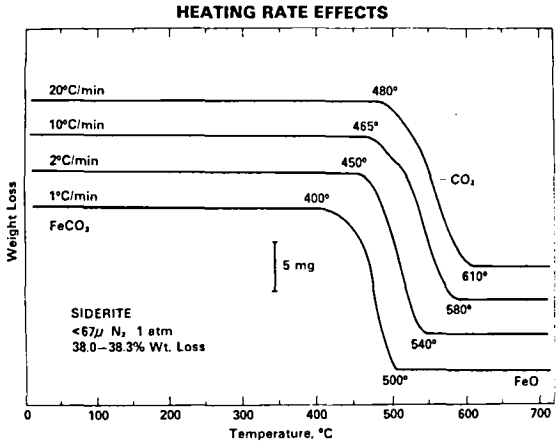


Figure 1.

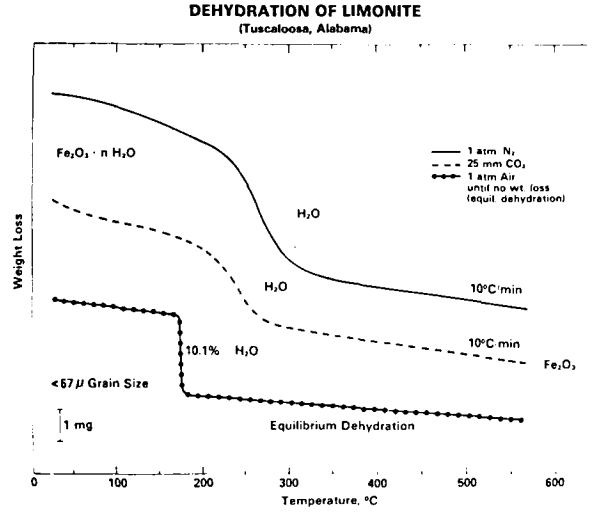


Figure 2.

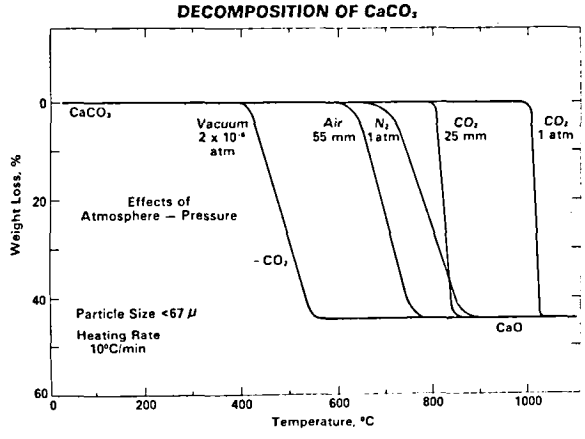


Figure 3.

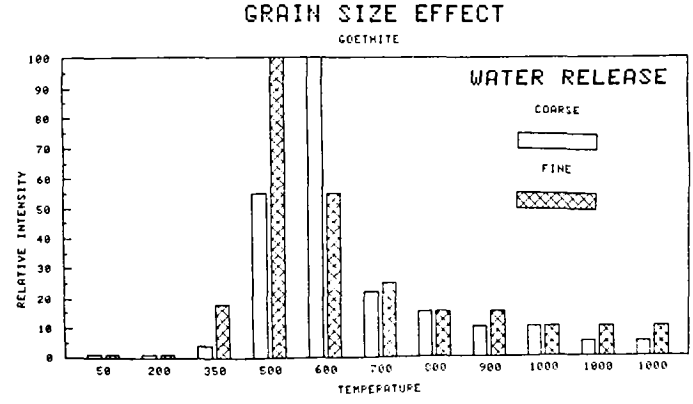


Figure 4.

Fig. 1. Decomposition of siderite as a function of heating rate.

Fig. 2. Dehydration of limonite.

Fig. 3. Decomposition of calcite as a function of pressure and atmosphere composition.

Fig. 4. Grain-size effects on dehydration of goethite.

SOLID POLYMER ELECTROLYTE HYGROMETER

James Stephens, Jet Propulsion Laboratory and Mary Yang, Planetary Geology Summer Intern from the Department of Chemistry, U.C. Berkeley.

An absolute electrolytic hygrometer measures the number of water molecules that are absorbed and electrolyzed into hydrogen and oxygen. 96,500 coulombs of electricity is required to electrolyze one gram equivalent or 9.01 grams of water. Such an instrument can detect water emitted from, or contained in, near-earth asteroids, comet nucleus or the lunar polar regions.

A solid polymer electrolyte (SPE) is used in the hygrometer developed for this task. A sulfonated fluorocarbon polymer produced and sold by DuPont called Nafion is used as the electrolyte. Its molecular structure is as follows:

$$(CF_2CF_2)m\ (CF_2CF)$$

$$\left[\begin{array}{l} O \\ CF_2 \\ FC - CF_3 \\ O \\ CF_2CF_2SO_3H \end{array}\right]_Z$$

where m and z are variables; M being as low as 5 and as high as 13.5 and z being the integers 1.2.3. ....

Since each repeating unit has a high molecular weight, its vapor pressure is close to zero. Being of a solid polymer structure, Nafion will not move under high G loads and is chemically stable. In addition, it is resistant to oxidation and reduction environments. Unlike the polyphosphoric acid film used in earlier instruments, Nafion is not affected by ammonia.

The basic design (see photograph) currently being tested incorporates the use of a glass tube which has been slit down one side. A thin layer of Au foil is laid over the tube and bent through the slit to the inside of the tube. This allows contact with the gold foil electrode to be easily made. A strip of Nafion is laid over the gold foil. The tube is then clamped tightly shut so that the edges of the slit touch together.

Three lengths of gold wire are mechanically (but not electrically) joined together. One end of the segmented wire is attached to one of the standoff pins on the tube. The segmented gold wire is then tightly wound

around the Nafion and fastened securely to standoff pins on the tube. When the clamps are released, the tube springs back and pulls on the wire thereby insuring uniform and tight electrode contact. Even during large temperature changes and high current (thus high gas evolution) operation. This configuration provides two guard electrodes on either side of the main electrode structure (the short wire sections). The guard electrodes correct for surface leakage as well as helps to prevent shorts through to the gold foil. The guard electrodes also eliminate the problem of the slow diffusion rate of water through the unelectroded Nafion at the outer edge of the structure (which greatly reduces the wet to dry response time). They also guarantee that the electric field through that part of the Nafion immediately beneath the sensor electrode is normal to the main electrode surface. This allows problems due to fringing effects to be neglected.

Four different split tube type SPE hygrometers have been constructed and operated in vacuum. A special switchboard was designed to allow independent current readings on each sensor while keeping a constant voltage across the hygrometers. The switchboard and sensors are in turn connected in series to a power supply and Hickok digital ammeter.

The preliminary vacuum operation data has been very promising. Current measurements in the one nanoamp range have been made. This corresponds to electrolysis of approximately $1.10^{-10}$ gm of water per second. When the vacuum valve was closed for short periods of time, the pressure and current readings both continued to decrease. This indicates that the SPE hygrometer was continuously pumping water out of the system. Two dummy leads in the vacuum chamber read a current of 0.1 nanoamps. This small amount of current corresponds to a leakage resistance of $10^{10}$ Ω at 10 volts. This measurement indicated that a correction for some surface leakage must be made on the SPE hygrometer when it is used in very dry environments.

Since the SPE hygrometer behaves like a battery, some polarity tests are necessary. It is vital when obtaining accurate current readings, that all the current passed through the electrolytic hygrometer be used to dissociate water. Therefore, in-depth studies of the amount of recombination, and recombination rates of hydrogen and oxygen should be made. Furthermore, the voltage breakdown of the Nafion Polymer should be determined and sensitive cryogenic as well as high temeprature calibrations need to be performed. Further in-depth study of the SPE water sensor is necessary. The work done here indicates that a SPE hygrometer could be useful in detecting water in space.

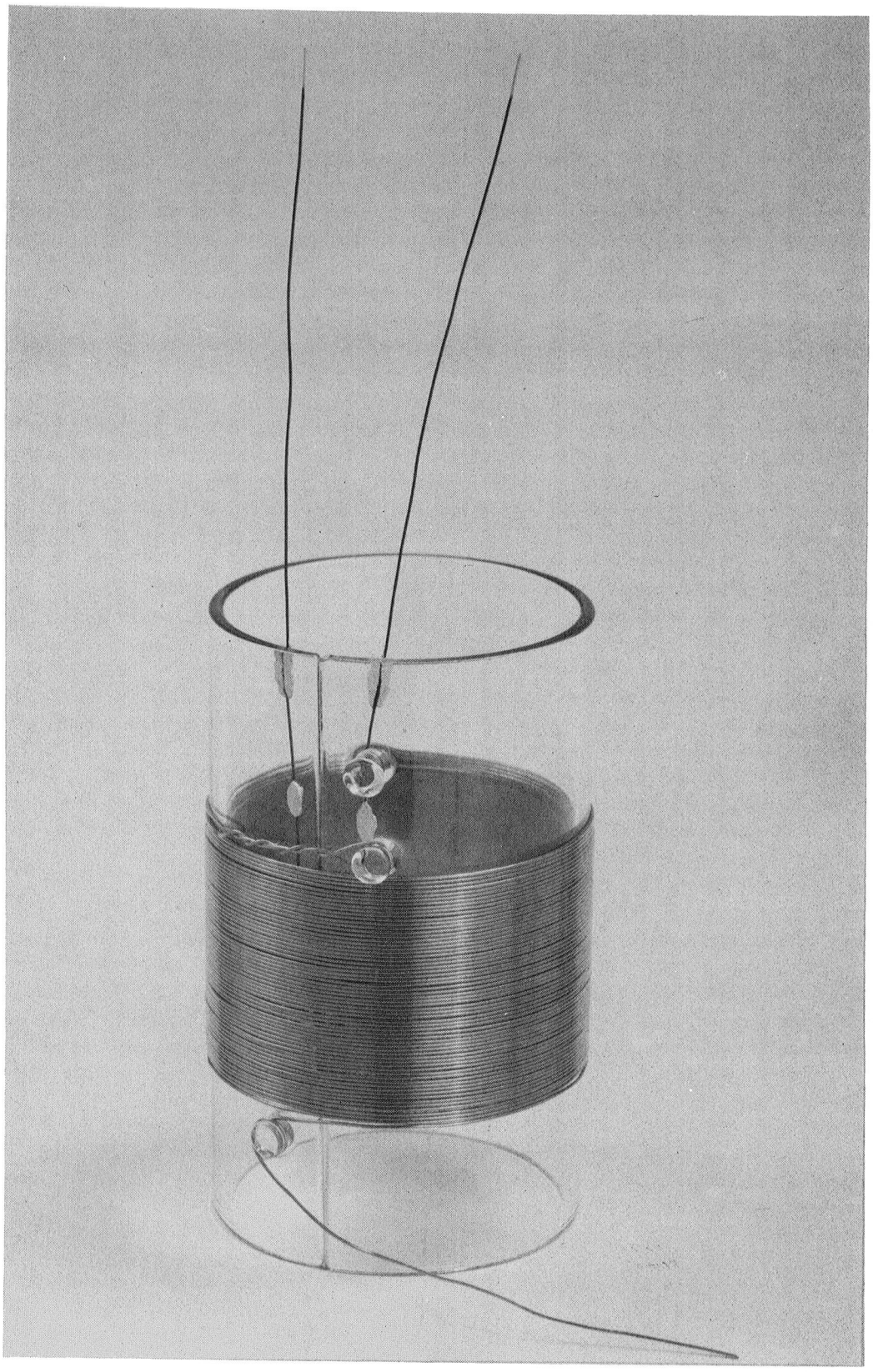

SOLID POLYMER
ELECTROLYTE HYGROMETER

Planetary Soil Water Analyzer (PSWA) Prototype.

W. Cashin (Ball Aerospace, Western Laboratories)
Dr. Duwayne M. Anderson (State University of New York, Buffalo)

A microprocessor-based differential scanning calorimeter is being designed for eventual use in planetary soil water analysis. The uniqueness of this instrument is the use of the microprocessor as an integral part of the control loops, instead of as an auxilary processor of output data.

The use of differential scanning calorimetry is advantageous in determining water content of soil samples. The basic idea is to use two matched ovens, one with a soil sample included. The average temperature of the ovens is forced to track a desired programmed temperature (normally a slow ramp) with one control loop, while a second control loop forces the oven temperatures to be equal, even during a transition. The power necessary to keep the temperatures equal is monitored, containing information as to the transition energy, and thus the water content at programmed water transition temperatures. The generalized block diagram is shown in Figure 1.

This approach uses the microprocessor to close both of the loops, taking oven sensor temperatures as an input, and providing power duty cycles as outputs. Further functions of the microprocessor include:

- Correct for sensor nonlinearities.
- Baseline subtraction (store a no-sample calibration run).
- Calibrate for temperature.
- Control scan rates and startups.
- Provide for single oven operation.
- Compensate for oven nonlinearities (oven thermal resistance).
- Compensate for heater nonlinearities (heater electrical resistance).
- Manipulate, store, and output the data obtained.
- Minimal hardware change with different oven characteristics.

The current phase of the development of the PSWA is a feasibility study and circuit design. The work was performed for the Planetary Geology Program office, NASA Headquarters. Performance goals of the final product are included in Table I. The next developmental phases include breadboarding, soft-ware design, testing, and evaluation.

In conclusion, this instrument is a significant advance in the state of the art for water measurements, and will be of great value in further planetary exploration.

1. Measurement of Exothermic Reactions by Differential Scanning Calorimetry, M.J. O'Neill.

2. Measurement of Specific Heat Functions by Differential Scanning Calorimetry, M.J. O'Neill.

3. Private phone conversations between W. Cashin and M.J. O'Neill.

TABLE I. PSWA SYSTEM GOALS

| | |
|---|---|
| • Operating temperature range (excluding oven) | 23°C ± 5°C |
| • Minimum oven ambient | -175°C, with external cooling |
| • Operating temperature range for oven | 75°C to 725°C above ambient of -175°C |
| • Temperature resolution (average loop) | ± .1°C |
| • Temperature accuracy | ± .25°C of holder temperature |
| • Differential power sensitivity | .2 mcal/sec @ 20°C/min scan rate |
| • Maximum differential power | .4 W |
| • Maximum noise (temp or diff power) | .1°C, or .22 mW |
| • Maximum transition energy without system saturation | Fusion of 200 mg of water equivalent. Vaporization of 10 mg of water equivalent at 20°C/min. |
| • Scanning rates | 20°C/min to .625°C/min |
| • Bandwidth | .1 Hz minimum |

FIGURE 1 SIMPLIFIED BLOCK DIAGRAM

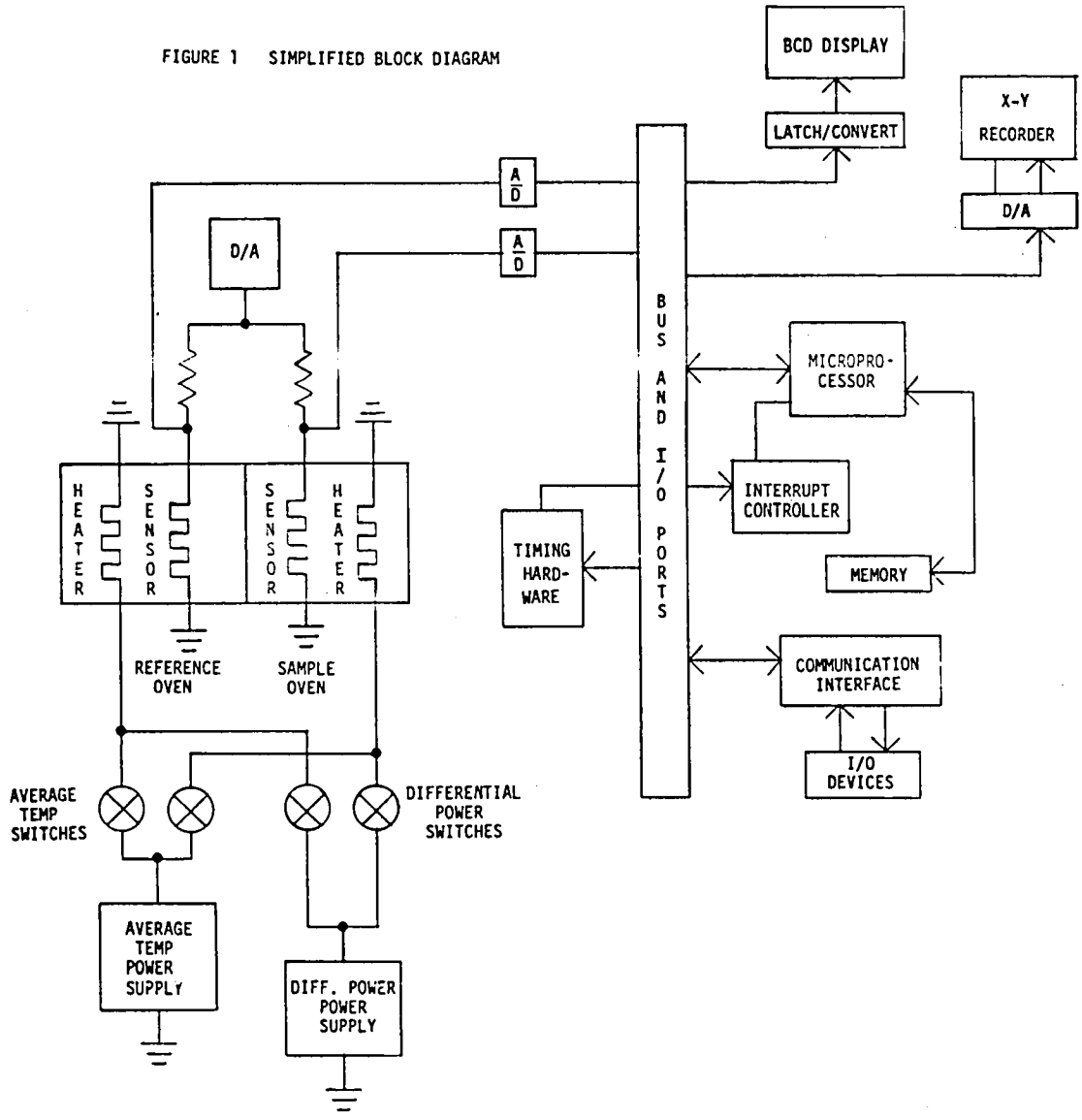

# Chapter 8

# STRUCTURE, TECTONICS AND STRATIGRAPHY

# WHAT DO HYPSOGRAMS TELL ABOUT PLANETARY TECTONICS?

Michael C. Malin, Department of Geology, Arizona State University, Tempe, AZ 85287

Among the more interesting results of the Pioneer Venus radar experiment was the production of a histogram of planetary surface area as a function of altitude--a hypsogram. The hypsogram, and topographic images with which it can be compared, have led to several papers on the style of tectonism on Venus (Masursky, et al.1980; Arvidson and Davies, 1981; Korbrick et al. 1981). Comparison with the Earth's topography has led to statements that Venus does not display comparable tectonism, in a "plate-tectonic sense".

In examining the title question, I have found less support for a topographic relationship to tectonics than for relationships to erosion, and composition and structure of the lithosphere. The bimodal terrestrial hypsogram is felt to reflect more the time-averaged level of ocean water (the "freeboard" concept proposed by Kunen, 1939, advanced by Hess, 1962 and eloquently expanded upon by our own Don Wise, 1972) than a primary result of plate tectonism, although feedback between erosion, sedimentation, and changing ocean basin geometry clearly controls sea level. Would the Earth's topography be bimodal if no oceans existed? Certainly, if they were removed, the sea-floor would only rebound a bit more than 1 km, leaving at least a 4 km difference. But would the continental mode be gaussian (as noted by Kobrick, et al.)? Computer simulations suggest a more skewed distribution (resembling a Maxwellian distribution), with the mean oceanic and mean continental height values separated by 4 km, but the mode peaks somewhat closer together.

Such a distribution is what I believe occurs on Venus: a gaussian form for the "median plains" and a "skewed" gaussian, overlapping the "median plains" by slightly less than 2 sigma (i.e. the 1/e height on the median plains is about the 1/e low on Ishtar and Aphrodite). The modes are separated by about 2 km, while the means are separated by about 2.5 km.

What does this tell us about Venus? The Venus hypsogram is "unimodal" because of the absence of an "elevated" erosional base-level, as occurs on Earth. It is also "unimodal" because there is not a lot of high standing topography, and what there is has a skewed distribution, with an even smaller area having the greatest relief. This is what the Earth resembles when freeboard and erosional transportation are taken into account. And what of isostacy? If my observation of a small, skewed mode hidden within the wings of the "median plain" gaussian mode is correct, then its small separation from the plains is consistant with either a lower density contrast between crustal components (or between crust and mantle), or perhaps as likely, a thinner lithosphere. Indeed, values of lithospheric thickness, calculated from the separation of the "modes" and assuming two dissimilar crustal densities overlying a mantle, are very much like those calculated from geophysical models based on inversion of Pioneer Venus gravity observations (e.g. Phillips et al. 1981).

References

Arvidson, R.E. and G.F. Davies (1981) Effects of lateral resolution on the identification of volcanotectonic provinces on Earth and Venus. Geophys. Res. Lett. 8, 741-744.

Heso, H.H. (1962) History of ocean basins, in Petrologic Studies (Buddington Volume), Engle, A.E.J., H.C. James and B.F. Leonard (Eds). (Geol. Soc. Am., Boulder), 599-620.

Kobrick, M., R.S. Saunders, and W.E. Brown (1981) Topography of the terrestrial planets. (submitted to Icarus)

Kunen, P.M. (1938) Quantitative estimations relating to eustatic movements. Geologic en Mijnbouw 18, 194-201.

Masursky, H., E. Eliason, P. Ford, G. McGill, G. Pettengill, G. Schaber, and G. Schubert (1980) Pioneer Venus radar results: Geology from images and altimetry. J. Geophys. Res. 85, 8232-8260.

Phillips, R.S., W. Kaula, G. McGill, and M. Malin (1981) Tectonics and evolution of Venus. Science 212, 879-887.

Wise, D.U. (1972) Freeboard of continents through time. Geo. Soc. Am. Man. 132, 87-100.

# OCEANIC RIDGES, TRANSFORMS, TRENCHES WOULD BE SEEN IN PV ALITIMETRY DATA - EVEN UNDER VENUSIAN AMBIENT CONDITIONS

R.E. Arvidson, McDonnell Center for the Space Sciences, Washington University, St. Louis, Missouri 63130

We have processed three digital topographic data sets of the Earth in a way that simulates both the lateral and vertical accuracy of the PV-Altimetry data for Venus (Arvidson and Davies, 1981; Arvidson and Guinness, 1981). The data sets are: (a) RAND/SIO global data: (b) NOAA 30 x 30 nautical mile data for the North Pacific; and (c) NOAA 1 second data for the continental United States. In addition to degrading the lateral footprint width to 100 - 150 km and reducing the vertical accuracy to no better than 100 to 200 m (Pettengill et al., 1980), we have also corrected the sea floor bathymetry by: (a) removing that part of the depth due to the load from sea water, and (b) decreased oceanic ridge heights to be consistent with the much higher ambient temperature pertinent to Venus (Arvidson and Davies, 1981). These latter two corrections reduce the relief of the sea floor by about 60%. Despite the broad footprint width and the lower relief inherent in the PV-simulated sea floor bathymetry, oceanic rises, transforms, and trenches can still be discerned. Trenches are narrow features and as such they are badly undersampled, with a relief reduction of 50% being typical. However, because of their high amplitude as compared to wavelength, they can still be discerned in the PV-simulated data. Similar features do not appear in the PV data, implying that the Venusian topography is not reflective of sea floor spreading tectonics as that concept applies to Earth. Unfortunately, PV-simulated data for regions such as the Cordillera of the western U.S., demonstrate that little can be discerned in terms of diagnostic tectonic signatures for erogenic zones. The basin and range province, the front range of the Rockies, and other features are so badly undersampled that they only appear as superimposed swells on the broad Cordillera uplift. The pattern of swells is not unlike that detected over Aphrodite Terra on Venus, although concluding that Aphrodite Terra is in detail like the Cordillera is both speculative and unwarranted by the available data.

References

Arvidson, R.E. and G. Davies, 1981, Effects of lateral resolution on the identification of volcanotectonic provinces on Earth and Venus, Geophys. Res. Lett., 8, 741-744.

Arvidson, R.E. and E.A. Guinness, 1981, Global topography of Earth, Venus, and Mars: Clues to tectonic styles, J. Geological Education, submitted.

Pettengill, G. and others, 1980, Pioneer-Venus radar results: Altimetry and surface properties, J. Geophys. Res., 85, 8261-8270.

MARTIAN CENTER OF MASS - CENTER OF FIGURE OFFSET

L.E. Roth, M. Kobrick, G.S. Downs, and R.S. Saunders, Jet Propulsion Laboratory, California Institute of Technology, Pasadena, California 91109; and G. Schubert, Department of Earth and Space Sciences, University of California, Los Angeles, California 90024

Centers of mass of those terrestrial planets for which adequate topographic information is available do not coincide with the planets' centers of figure. The two centers are usually separated by a distance of a few kilometers or less. For Mars the center of mass - center of figure (CM-CF) offset has been determined by a number of authors. Table 1 summarizes the results reported in literature. The two most recent determinations (Kobrick et al. (1981)), using the Mars Consortium global topography data and the Goldstone radar data, have in part been motivated by attempts to assign geophysical significance to the results of Bills and Ferrari (1978). Those results, as pointed out by Kobrick et al., are explainable by confusion associated with the left-handed coordinate system in use for Mars.

Because of its limited latitude coverage, radar can only yield projection onto the equatorial plane of the vector from the CM to the centroid of the ranged latitude band. This incomplete determination of the CM-CF offset serves a useful purpose, however. It provides an independent check on the results obtained by other techniques. Utilizing the Haystack 1971 data, Schubert and Lingenfelter (1973) established the projected Martion CF as being displaced by 1 km toward $100^{o}$ long. Based on the Goldstone 1971-1973 data, referenced to 6.1 mbar, Kobrick et al. found the projected offset to be ~.94 km toward ~109.2° long., in a good agreement with Schubert and Lingenfelter's results, and in a general agreement with all quoted authors except Bills and Ferrari. The agreement is all the more remarkable considering the regional discrepancies between the radar data and the other data sets (Fig. 1). In 3-d, the Martian CF is displaced by about 3 km in the approximate direction (-60° lat., 95° long.) The CM-CF line intercepts the planet's surface south of Thaumasia Fossae, close to the edge of the cratered hemisphere.

Assuming the core and mantle density to be radially symmetric, the existence of CM-CF offset is probably a manifestation of a first-order crustal asymmetry. Simplified, this asymmetry can take two forms (Lingenfelter and Schubert, 1973): (i) Crust of constant topographic relief and uniformaly varying density. CF is displaced in the direction of the density low; (ii) crust of constant density and uniformly varying relief. CF is displaced in the direction of the topographic high. For Earth, with its combination of sialic ($\rho$~2.7) and simatic ($\rho$~3.0-3.3) crusts, the CF is displaced toward 41.6°N, 34.7°E, in the direction of the Eurasian shield, and close to the center of the continental province at 46°N and 27°E (Bills and Ferrari, 1978). Because the widely accepted and evidently erroneous CM-CF offset pointing toward 272° lat. intercepted the Martian surface close to the center of the high-standing cratered hemisphere analogous claims were made for Mars (Bills and

Table 1

Martian Center of Mass - Center of Figure Offset

| Author(s) | $\bar{x}$ [km] | $\bar{y}$ [km] | $\bar{z}$ [km] | $\theta$ [deg] | $\phi$ [deg] | r [km] |
|---|---|---|---|---|---|---|
| Schubert and Lingenfelter (1973) | | | | ~ 100 | | ~ 1.0 |
| Standish (1973) | -0.12±0.25 | -1.47±0.25 | -2.89±0.20* | (94.70±..) | (-63.00±..) | (3.24±..) |
| Christensen (1975) | -0.2 | 1.4 | -2.1** | (98.1) | (-56.0) | (2.53) |
| Saunders in Mutch et al. (1976) | | | | 98 | -57 | 2.5 |
| Bills and Ferrari (1978) | | | | 272±3 | -62±3 | 2.5±0.07 |
| Sweetnam (1981) | 0.0 | -1.0 | -3.6* | 90.0 | -74.5 | 3.7 |
| Kobrick et al. (1981) | | | | 93.7 | -57.8 | 2.1 |
| Kobrick et al. (1981) | | | | 109.2 | | 0.94 |

Columns $\bar{x}$, $\bar{y}$, $\bar{z}$ : Cartesian coordinates of the Center of Figure relative to the Center of Mass
* Right-handed system; ** Left-handed system
Columns $\theta$, $\phi$, r: Spherical coordinates of the Center of Figure relative to the Center of Mass
$\theta$ : Longitude (increasing West); y: Latitude (positive North); r: magnitude of the CM-CF offset
Values in parentheses calculated from cartesian coordinates quoted in references and listed in the first three columns

Sources of Data:
Schubert and Lingenfelter (1973): Haystack radar
Standish (1973), Mariner 9 radio occultation
Christensen (1975): Mariner 9 radio occultation; Mariner 9 IR and UV spectrometry; Haystack and Goldstone radars
Saunders (1976): Same as Christensen (1975)
Bills and Ferrari (1978): Same as Christensen (1975); Mariner 9 photogrammetry
Sweetnam (1981): Viking radio occultation
Kobrick et al. (1981): USGS/Mars Consortium global topography
Kobrick et al. (1981): Goldstone radar

Ferrari 1978; Malin et al., 1978; Arvidson and Davis, 1980a, 1980b), accompanied by speculations about the possible role of the CM-CF offset in elucidating the origins of the hemispheric dichotomy. The corrected CM-CF offset even though pointing in antipodal direction does not necessarily void those speculations.

Considering any tectonic history of Mars, in which formation of the cratered highlands and resurfacing of the northern plains predates the emergence of Tharsis (e.g., Wise et al., 1979) the planet begins with a CM-CF offset vector pointing toward the presumably lower density highlands. As Tharsis grows, its contribution to the CM-CF offset causes the offset vector to gradually migrate away from the highlands and toward the emerging topographic high until the present stage is reached when the CM-CF offset intercepts the border area between the two global units. The migration of the CM-CF offset vector may have proceeded in parallel with the hypothesized poles migration (Schultz and Lutz-Garihan, 1981) but not necessarily coupled to it.

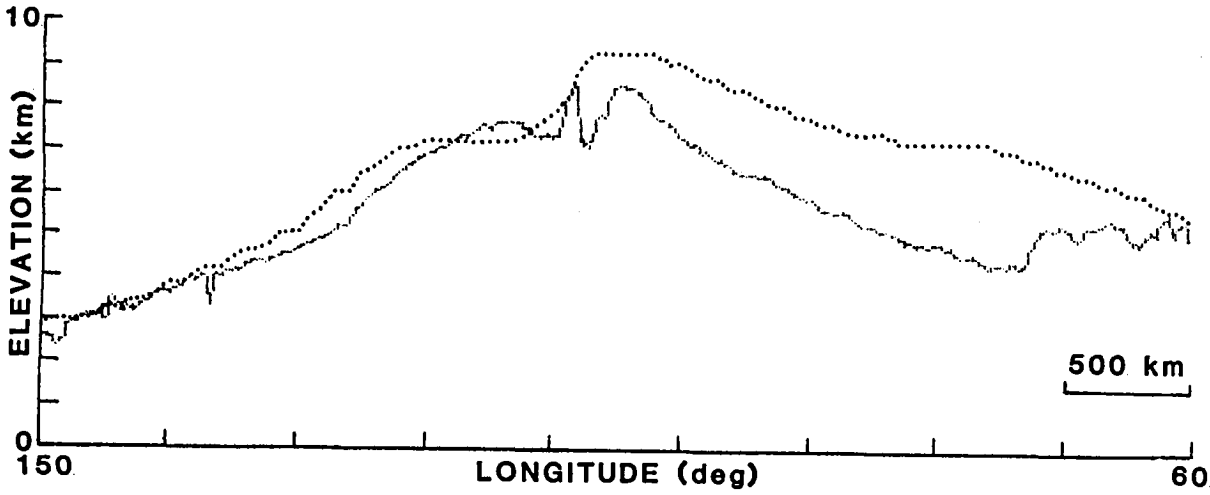


Fig. 1. Goldstone radar (full line) and Mars Consortium (dotted line) topographic profiles across South Tharsis. The radar profile is a composite of scans in the -21.30° to -21.15° latitude range. The Consortium profile runs along -21° lat. Ridge between 100° and 110° long. is Claritas Fossae.

R. E. Arvidson, G. F. Davis (1980a), EOS 61, 572. R. E. Arvidson, G. F. Davis (1980b), NASA TM 82385, 85. B. G. Bills, A. J. Ferrari (1978), JGR 83, 3497. E. J. Christensen (1975), JGR 80, 2909. M. Kobrick, L. E. Roth, G. S. Downs (1981), AGU Fall Meeting. R. E. Lingenfelter, G. Schubert (1973), Moon 7, 172. M. C. Malin, R. J. Phillips, R. S. Saunders (1978), NASA TM 79729, 83. T. A. Mutch, R. E. Arvidson, J. W. Head, K. L. Jones, R. S. Saunders (1976), Geology of Mars, 212. G. Schubert, R. E. Lingenfelter (1973), Nature 242, 251. P. H. Schultz, A. B. Lutz-Garihan (1981), 3rd Int'l Collog. on Mars. E. M. Standish, (1973), Astron. Astrophys. 26, 463. D. N. Sweetnam (1981), Personal Communication. D. U. Wise, M. P. Golombek, G. E. McGill (1979), JGR 84, 7934.

# MARS STRUCTURAL STUDIES

R. Stephen Saunders, W. Bruce Banerdt, Jet Propulsion Laboratory, California Institute of Technology, Pasadena, CA 91109, and Roger J. Phillips, Lunar and Planetary Institute, Houston, TX 77058.

Geologic models for the Tharsis region of Mars are based on the observed geomorphic features. These include the geometry of the topographic excursion, the extrusive volcanic material, the tectonic features, and relative ages of parts of the surface from crater counts. Early models argued a predominately uplift origin evidenced by the highly cratered terrain bounding the region but elevated along with the regional dome and central volcanics (Phillips et al., 1973). In this model the region, underlain by highly cratered terrain, was uplifted, fractured, and mantled by a succession of volcanic materials having a total thickness less than the total elevation.

More recently, the case for an entirely volcanic origin of the Tharsis topography has been supported by Solomon and Head (1980). They acknowledge that the youngest volcanic materials may be relatively thin, but argue that the thickness of any earlier volcanism is not well constrained.

Our current analysis of rather simple cases using low order and degree topographic and gravity models and generalized structural trends suggest that the observed structures are consistent with a response to a topographic load rather than to uplift. This would seem to support the volcanic pile model for Tharsis.

However, we have not yet modeled the time history of the load nor have we considered other than the static case in the computation of stress trajectories.

During the past year we have investigated the state of stress in the martian lithosphere induced by the Tharsis load, using the observed low-order topography and gravity field as boundary conditions in a numerical computation of the deformation of an elastic, self-gravitating sphere with a shear stress-free "core" (see Alterman, et al. 1959, Longman 1963).

Three classes of models were examined. The first was an uplift model, in which the present topography is caused by doming of the lithosphere in response to upward force (either bouyant or dynamic). The stress trajectories derived for this case show virtually no correlation with observed tectonic features. We conclude that either uplift played no major role in the history of Tharsis, or all tectonic evidence for such an episode has been obliterated.

The second class of models were "isostatic". For our purpose, we have defined isostatic to be the state of no surface displacement, i.e. the topographic load is exactly balanced by an opposite force from below. In this case the stress trajectories are a function only of the topography, independent of the mechanism of support. There is an excel-

lent correlation between tectonics and calculated stresses in the region near the Tharsis load (< 2500 km from its center), but this correspondence breaks down at greater distances.

The last case examined was a "flexure" model, in which the lithosphere was allowed to deform in response to the combined topography and gravity load. Again this model gives stress trajectories which are nearly independent of the detailed sub-surface structure. This time there is excellent agreement with the tectonics in the outlying regions, with poor correlation near Tharsis. In fact, these stress trajectories seem to be complementary to those of the "isostatic" case, in that a combination of the two (ostensibly at different times) does the best job of explaining the gross tectonic features associated with Tharsis.

One surprising feature common to both these models is that they appear to require thick crusts (~ 100 - 150 km) and lithospheres (~ 200 - 400 km). For the isostatic model, the thick crust is required in order to satisfy the gravity boundary condition with reasonable density anomalies. The thick lithosphere is not required to support the load in this case, but density anomalies must be maintained to these depths, which requires a regime in which flow is not allowed over the time scale of Tharsis. For the flexural case, the thickness of the constructional pile is determined by the thickness of the crust (through the gravity constraint) and the lithosphere, especially the latter. For a lithosphere 200 km thick, the ratio of total thickness of construction to observed relief is about 3:1, while for 100 km it is about 6:1 and 75 km it goes to > 10:1. We consider these great constructional thicknesses unreasonable, but the question remains as to how a thick lithosphere can be maintained in a thermally active province.

## REFERENCES


Alterman, Z., H. Jarosch, and C. L. Pekeris, Oscillations of the Earth, Proc. Roy. Soc. London A, 252, 80-95, 1959.

Longman, I. M., A Green's function for determining the deformation of the Earth under surface mass loads: 2. Computations and numerical results, J. Geophys. Res., 68, 485-496, 1963.

Phillips, R. J., R. S. Saunders, and J. E. Conel, Mars: Crustal structure from Bouguer gravity anomalies, J. Geophys. Res., 78, 1973.

Solomon, S. C. and Head, J, W., Tharsis Province: Uplift by anaomalous mantle, or concentration of tectonism and volcanism in a locally thin lithosphers?, Proc. Lunar Sci. Conf. XI, 1063, 1980.



Performed under contract with NASA.

TOPOGRAPHIC LINEAMENT ANALYSIS: POSSIBLE STRESS INDICATORS ON PLANETARY SURFACES. Wise, D.U., Allison, M.L., Dept. of Geol. & Geog. & Remote Sensing Center, Univ. Mass., Amherst, Ma. 01003

One major goal of structural interpretation of planetary surfaces is to find orientations of the stress field through time. New techniques of domain analysis of topographic lineaments in SW Wyoming indicate paleostress orientations can be made using remote sensing data. Thus stress analyses of imaged planetary surfaces may be possible using some of the same techniques of domain analysis.

This study is based entirely on the physical topography contained in the raised relief map of the Rock Springs, Wyo., 1 x 2 degree, 1/250,000 quadrangle. This relief map method eliminates vegetal and seasonal effects; use of the reverse or underside of the map eliminates printing, contours, and cultural clutter. This leaves the topography represented as a material of constant albedo. The photographic image of the underside is corrected by turning over the negative before printing. The problem of differing shadow illusions with different lighting angles, is suppressed by dilution through combination of results from many lighting azimuths. A recent study (1) using multiple observers on a variety of types of imagery of real topography as well as relief map images showed strong illusion effects in the enhancement of lines 30 $\pm$ 15 degrees in azimuth on either side of the lighting azimuth. There was strong suppression of lines parallel ($\pm$ 15 degrees) to the lighting azimuth.

Topographic lineaments were drawn of the quadrangle for six different lighting azimuths (30, 60, 90, 300, 330, 360 degrees) with an illumination angle from the horizontal of 8.5 degrees for all images. Approximately 300 lines were drawn for each of the six images. Gaussian curves were fitted to the various peaks on azimuth-frequency histograms. The effect is a general smoothing of the data and the ability to quantify height, width, and location of the various azimuthal peaks. The plots then are all normalized to the same height for the largest peak and plotted in both histogram (Fig. 2) and rose format (Fig. 3) for cumulative number of lines and for cumulative lengths. The rose diagram (Fig. 3) is plotted with data for cumulative numbers of lines in the upper half and cumulative lengths on the lower half.

Figure 2 illustrates azimuth-frequency histogram results of this type of lineament analysis for all six lighting directions as well as a cumulative plot for all 1860 lineaments detected. The cumulative plot enhances the recurring directions and suppresses by dilution any trends appearing only on one or two of the diagrams. Peaks from the Gaussian fits of Fig. 2 were characterized as strong, moderate, or weak and plotted at their appropriate azimuth on Fig. 4. The suppression of lines parallel to the lighting azimuth and the higher levels of illusion for lines up to 45 degrees on either side of that direction are acknowledged by the zone marked as "less reliable data." Comparisons of the peaks identified on the individual plots with those on the cumulative plot indicates that most of major elements of topographic grain were detected on most of the images having appropriate lighting azimuths. The strongest of the trends appear through the illusionary curtain of unfavorable lighting azimuths.

A total of 8 or 9 lineament trends, as indicated by letter on Fig. 3 and 4 appear to be reproducible from topography alone and to be detectable with reasonable independence of the lighting azimuth. The individual rose plots in Fig. 5 represent cumulative plots for all lighting directions for

azimuths within 35 km radius of the center of each plot location. In order of decreasing prominence the azimuth of the most strongly developed lineament swarms are: 070°, 335°, 000°, 085°, 285-295°. Weaker or more local sets occur at 318°, 029°, 042°. The trends are developed over large portions of the area suggesting an origin associated with regional-scale stress fields. Variations in lineament densities are related to the domain extents of the different stress fields. Distribution patterns and orientations of the swarms suggest that: the 000° swarm is associated with the Rock Springs uplift; the 085° set is part of the Uinta disturbance; the 070° set parallels mapped faults and may reflect the sigma-1/sigma-2 plane of late Laramide times. The extremely parallel and uniformly developed 335° swarm is interpreted as the trace of the present-day sigma-1/sigma-2 plane.

Experience with Italian lineaments (2) suggests that these sharpest peaks (narrowest width) are associated with the very youngest fracture directions. We interpret this set as an extension fracture system striking normal to the present day minimum compressive stress direction of 060° azimuth. This is in almost perfect agreement with the report (3) of minimum compression in this area. The reality and reliability of detection of the major azimuthal sets of lineament swarms is based on reproducibility of the patterns detected on variously lighted images of the same area. Different sets have differing degrees of parallelism, intensity of development and relationship in map distribution and orientation to larger tectonic elements of the area. Based on these clues and those from a similar study in Italy (2) the swarms are interpreted as subtle extensile features, mostly zones of more intense jointing, related to regional stress trajectories. They are interpreted as the outcrop of the sigma-1/sigma-2 plane for two tectonic environments: (1) broad warping as in the Rock Springs and Uinta uplifts and (2) traces of past or present maximum compressive stress trajectories during compressive events.

Among the most important but generally neglected features of lineament analysis is the map pattern of the domains over which given lineament swarms are developed. The relation of this map pattern to other structures of better known age and origin gives important clues as to the timing and the stress orientations which generated the swarms. The swarm boundaries, on the other hand, indicate the more distal limits of the region affected by that disturbance and its associated stress field (4). The present study suggests the possibility of using remote sensing to define multiple domains of paleostress orientation and related fracture swarms, to link these features to geographically datable structures, and finally to map the domain of influence and relative intensity of each of the phases. The method gives hope of detecting these effects in the important but weakly deformed distal areas of a disturbance.

1)Wise, D.U.,(1980) Repts. Plan. Geol. Prog. 1980, p 439-441; 2)Wise, D.U., Runicieillo, D.R., Parotto, M., & Salvini, F., under review Bull. AAPG; 3)Zoback, M. & Zoback, M., (1980) JGR 85, p. 6113-6156; 4) Wise, D.U.,(1976) in Proc. First Int. Conf. on New Bsmt. Tect., p.416-422.

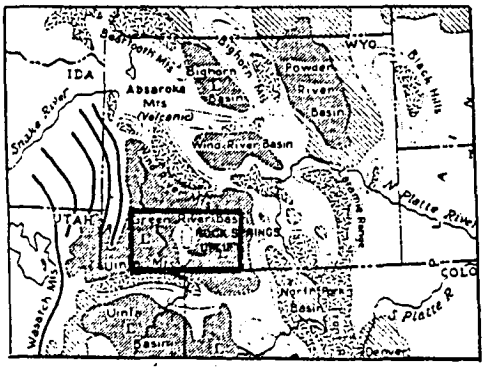


Fig. 1. Index map of the Rock Springs, Wyo., 1x2° sheet.

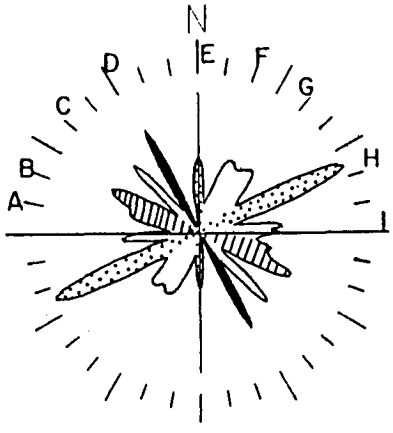


Fig. 3. Rose plot of data from all 1560 lineaments azimuths for all 6 lighting directions. Major fracture trace lineaments sets are indicated by letters. Top half of diagram represents cumulative number; lower half represents cumulative length.

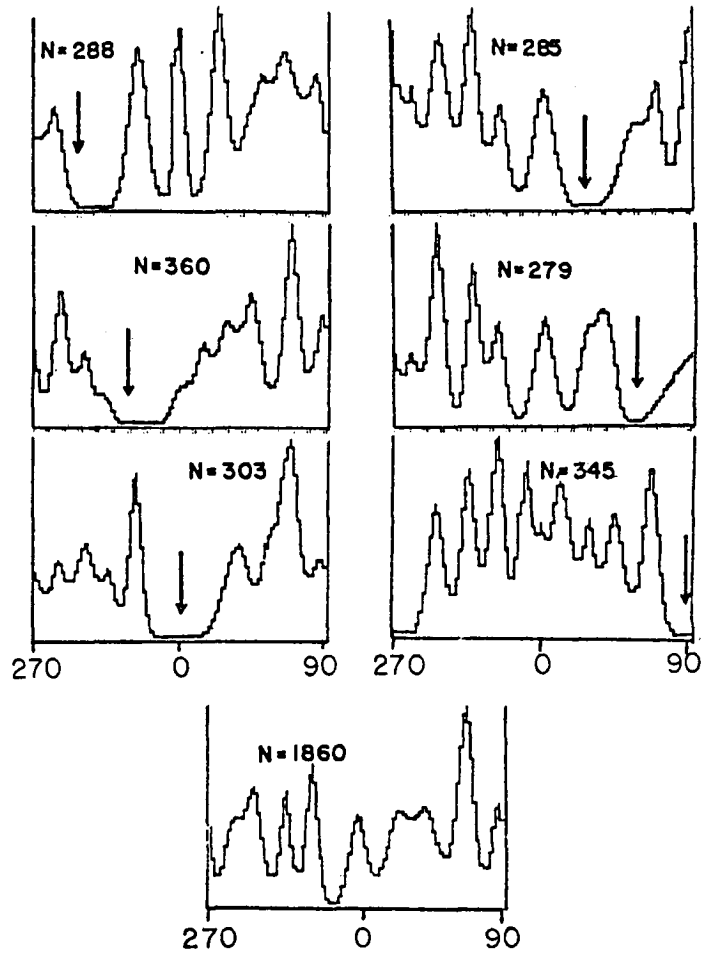


Fig. 2. Gaussian histogram for each lighting direction and for all six directions combined (bottom). Arrow indicates direction of lighting. N is the number of lineaments in each histogram. Vertical scale is normalized to the highest peak.

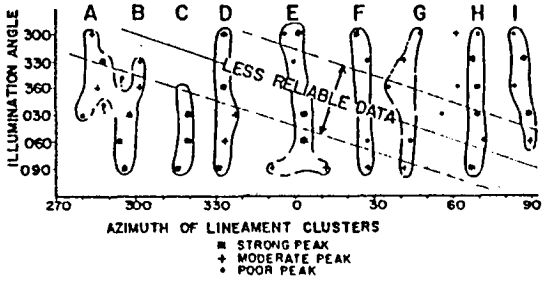


Fig. 4. Orientations of major lineament sets from each of 6 different lightings. Less reliable data are those within ±45° of the lighting azimuth. Reproducibility of a given set may be judged by whether the same set appears in many different lighting azimuths.

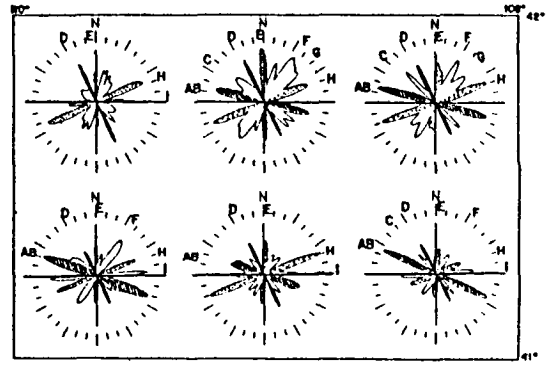

Fig. 5. Lineament azimuths for subareas of 1x2° sheet. Each plot shows lineaments from all lighting directions within a 35 km radius of the center of each rose plot. Top half of each rose is cumulative number; bottom half of each is cumulative length of lineaments.

# RIDGE ORIENTATIONS IN THE THARSIS PROVINCE OF MARS: DEVIATIONS FROM THARSIS-RELATED TRENDS.

Ted A. Maxwell and Thomas R. Watters, National Air and Space Museum, Smithsonian Institution, Washington, D. C. 20560

Local and regional structural features in the Tharsis region of Mars provide strong constraints on all models for the formation of this anomolous tectonic province. The existence of a well-developed radial fracture pattern, and wrinkle ridges that are roughly orthogonal to Tharsis have led to several models for the formation and longetivity of the bulge (1,2,3). Since the numerous ridges in this region are used as evidence for compressional stress, the isolation of those due to Tharsis from other ridges is important for geophysical modeling of the bulge. Based primarily on Mariner 9 images and maps, Wise et al. (4) used a set of 66 ridges to define a center of compression at 1° N, 122°W, but noted that ridge orientations are less symmetric about Tharsis than are fractures. When plotted on a stereographic plot, the E-W girdle of poles to ridges was attributed to elongation along a NE trend due to a crustal anistropy, perhaps related to the highland-lowland boundary in this area (4).

As part of an ongoing study of ridges on Mars, we have studied those of the Tharsis region in order to address the following question: what ridges in the Tharsis region are <u>not</u> directly related to the bulge; and may be the expression of older structure, or younger, post-Tharsis events. In order to separate Tharsis from non-Tharsis related ridges, we have compared the orientations of 1414 ridge segments in four quadrangles on either side of the center of the topographic high. Ridge segments with orientations within 20° of being normal (70° to 110°) to a projection from the ridge center of Wise et al. (4) were plotted for the Amazonis, Memnonia, Lunae Palus and Coprates quadrangles (Figs. 1A and B). The location and orientations of ridge segments outside this range is shown in Figs. 1C and D.

A significant number of ridge segments is not apparently related to a single center of the Tharsis bulge (Fig. 1). By the number of ridge segments measured, 51% are not within 20° of orthogonal. By length of ridges, those of other orientations comprise 40% of the total length measured (40,364 km). The largest number of "deviants" is in the Memnonia quadrangle, where 64% of ridges (by length) are non-orthogonal, compared to the range of 35-40% for the other three quadrangles. These non-orthogonal ridges occur at the same radial distance from the center of the bulge (1500-2000 km), due to the effect of younger non-ridged plains surrounding the Tharsis volcanoes. Rose diagrams of non-orthogonal ridges in these quadrangles indicate a predominance of generally northerly orientations. Amazonis and Memnonia display a remarkably unimodal distribution centered about North, whereas Lunae Palus and Coprates have strong peaks at NNE and

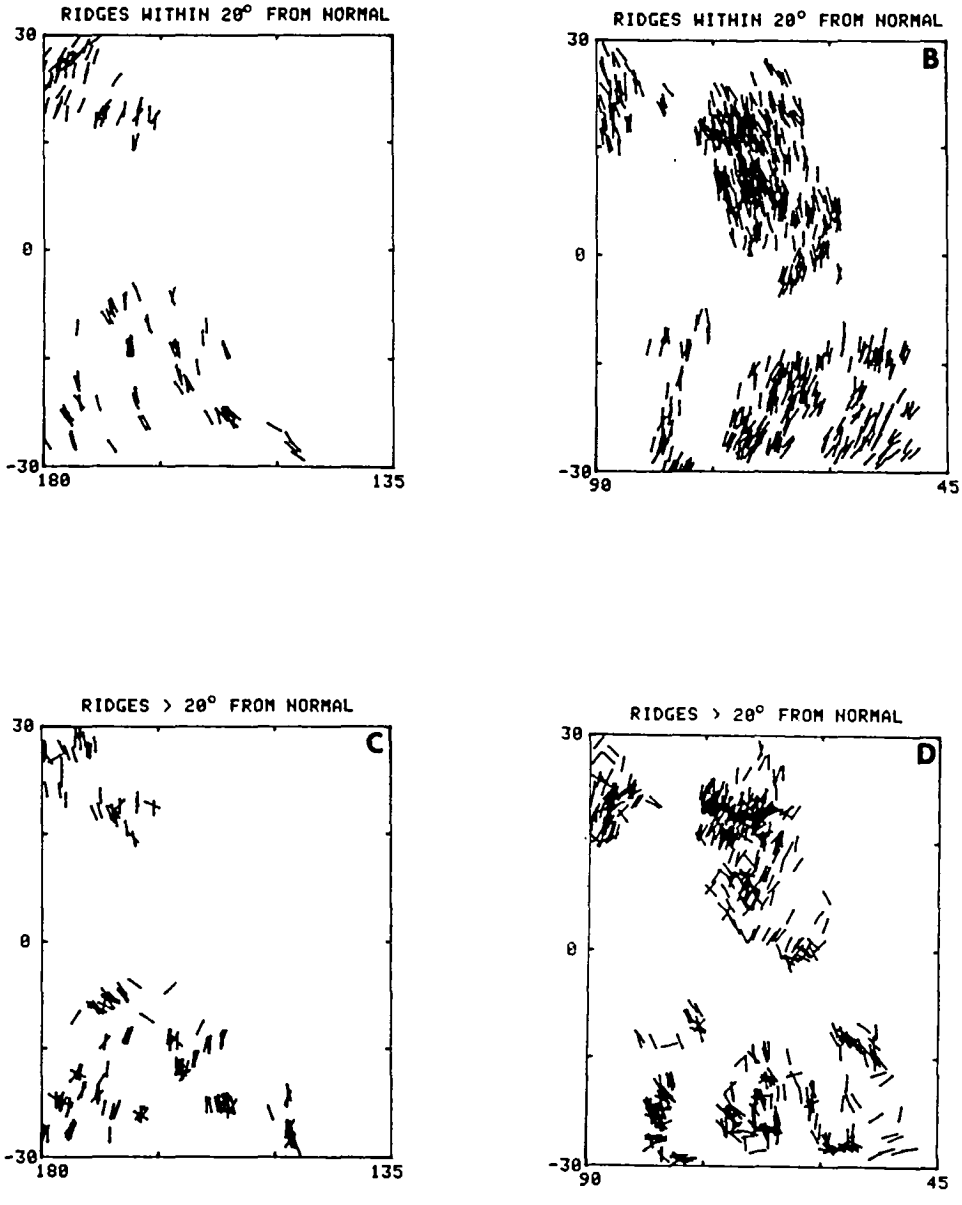


Figure 1. Ridge segments east and west of the Tharsis bulge. Length of segment is exaggerated to show orientation of ridge. Ridges within 20° of orthogonal to Tharsis shown in Amazonis and Memnonia (A), and in Lunae Palus and Coprates (B). Non-orthogonal ridges in Amazonis and Memnonia (C), and Lunae Palus and Coprates (D).

NNW respectively. In addition, secondary peaks occur at NW in Lunae Palus, and at ENE in Coprates.

The number and absolute length of ridge segment orientations indicate that not all ridges surrounding the Tharsis region can be related to a single (or possibly even several) point source for radially symmetric stress. Other causes for the formation of non-orthogonal ridges include: 1) draping and faulting over subsurface structure (5), 2) other centers of Tharsis-related stress (3), 3) reorientation of the martian lithosphere (6), and 4) a non-radially symmetric model for the loading of Tharsis. Based on the high number (and length) of non-orthogonal ridges, we believe that subsurface structure alone cannot account for these ridges. There is some support for an additional center of ridge formation in the quasi-curvilinear NW trending segments in Lunae Palus, and NNE segments in Memnonia. These ridges suggest a center at the highly fractured northern end of the Claritas Fossae (approximately 15°S, 110°W).

Based on reorientation of the martian lithosphere due to Tharsis loading, Melosh (6) predicted NNW and ENE strike-slip faults east of Tharsis, and NNE and WNW faults west of Tharsis. These predicted orientations are identical to those of of the non-orthogonal ridges in the Coprates quadrangle, but are not apparent in other areas. Additional problems also exist with this sense of movement, although strike-slip motion is supported to some extent by the en echelon appearance of some martian (and lunar) ridges. Further studies are in progress to determine the relative ages, other possible centers of symmetry, and probable origin for this significant set of martian ridges.

REFERENCES

(1) Phillips, R. J., Sleep N. H., Banerdt W. B. and Saunders R. S. (1981) Papers presented to the Third International Colloquium on Mars, p. 191-193. (2) Solomon S. C., Head J. W. and Comer R. P. (1981) Papers presented to the Third International Colloquium on Mars, p. 244-246. (3) Plescia J. B. and Saunders R. S. (1980) Proc. Lunar Planet. Sci. Conf., 11th, p. 2423-2436. (4) Wise D. U., Golombek M. P. and McGill G. E. (1979) Icarus, 38, 456-472. (5) Lucchitta B. K. and Klockenbrink J. L. (1981) The Moon and the Planets, 24, 415-429. (6) Melosh H. J. (1980) Icarus, 44, 745-751.

# RIDGE-RILLE INTERSECTIONS IN THE THARSIS PROVINCE OF MARS.

Thomas R. Watters and Ted A. Maxwell, National Air and Space Museum, Smithsonian Institution, Washington, D. C. 20560

The dominant structural features in the Tharsis region of Mars are compressional ridges, and extensional graben. In a study of the ridges in the Tharsis region, we have observed ridge rille cross-cutting relationships which suggest that in many cases, the ridges predate the formation of graben (1). As shown by Wise et al. (2), the formation of both ridges and rilles occurred very close in time, with at least some of the graben forming before the emplacement of ridged plains material. However, based on observations of ridge-rille intersections where both features occur in volcanic plains units, we believe that at least some ridge formation occurred prior to the latest episode of graben formation. Of particular importance are: 1) Can these cross-cutting relationships be used to unambiguously define a local age sequence for the formation of ridges and rilles? 2) In areas where rilles post-date ridges, are either (or both) of the features the product of Tharsis-related stress? and 3) What implications does this age relationship have for models of the evolution of Tharsis?

In order to establish a time sequence for ridge-rille intersections, we made a detailed study of 7 areas where ridges occur at the same location on both sides of a rille. Only one area has unambiguous evidence of ridge formation after fracturing. Figure 1A shows this area, located in the Coprates quadrangle where a N-S trending ridge clearly cross-cuts a roughly E-W trending degraded graben. The ridge apparently suffered little or no loss of relief crossing the graben, and may thus be used as a "type example" for a ridge forming after the graben. If all radial fractures in the Tharsis region predated ridge formation, we would expect numerous intersections of this type, particularly with graben of much less vertical and horizontal extent. In addition, this intersection provides evidence that the sides of the rille did not act as a "domain boundary," as is true for fractures in brittle material on Earth (McGill, pers. comm., 1981).

Northwest of this area, but still in the Coprates quadrangle, a generally N-S trending ridge intersects with an E-W trending fault swarm. The graben clearly cuts the ridge, and the dissected portion of the ridge has dropped into the graben (Fig. 1B). We believe that the alternative explanation, that the ridge within the graben developed on the graben floor itself, is unlikely for at least 2 reasons; 1) Within the graben, the ridge is dimensionally and morphologically similar to the ridge outside the rille walls, and 2) As shown by Fig. 1A, post-rille ridges are not greatly influenced by graben boundaries.

Figure 1C shows an area located in the Lunae Palus quadrangle, near Kasei Vallis. The N-S trending ridge intersects two fault sets

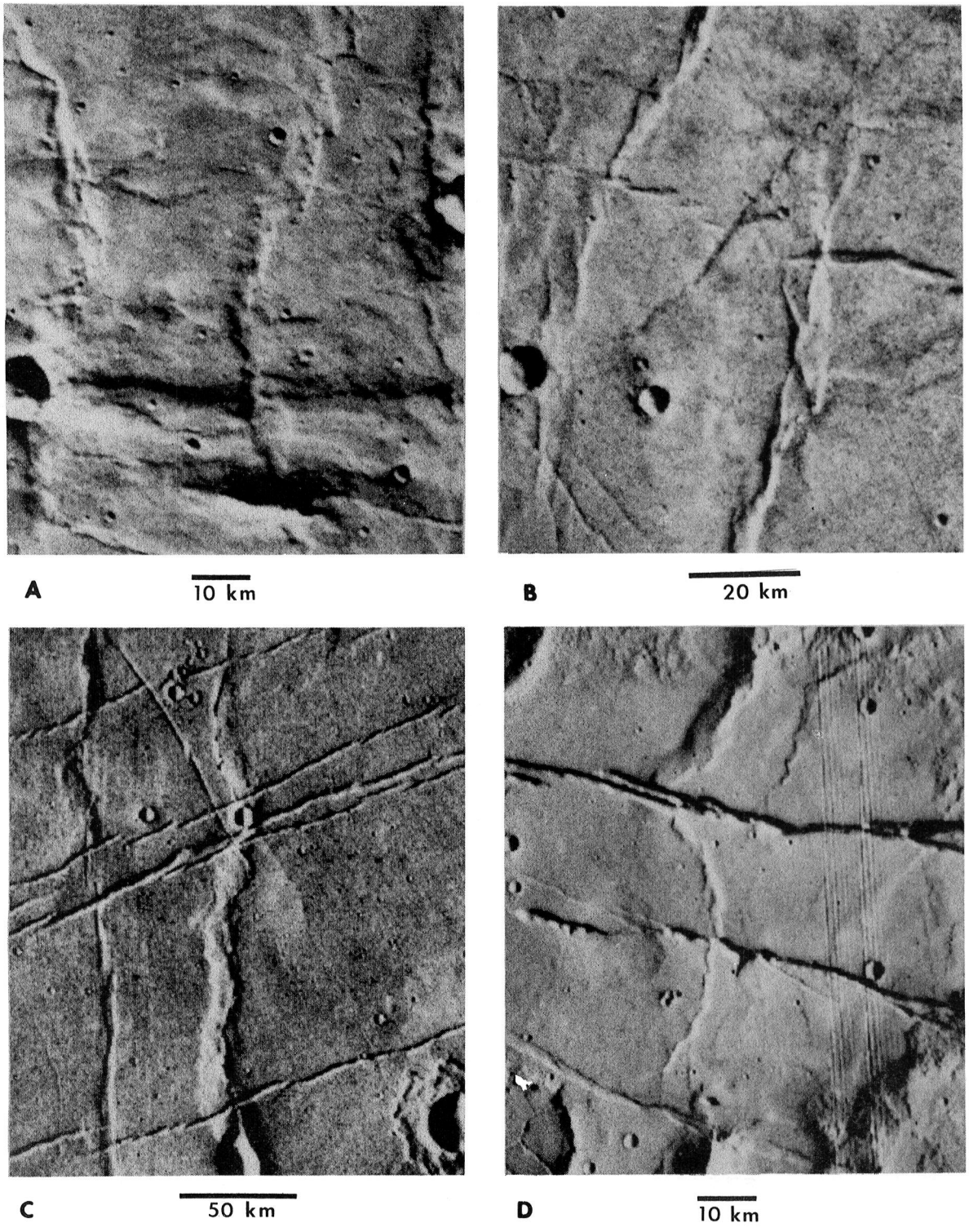


Figure 1. Ridge-rille intersections in the Tharsis region. A) Ridge post-dating graben in Coprates quadrangle. B-D) Tharsis-radial graben cross-cutting ridges in Coprates (B), Lunae Palus (C) and Memnonia (D).

which are oriented NW and NE. Based on the above criteria, both sets of graben are younger than the ridge. Some displacement on the crest of the ridge can be seen where the NW trending graben cuts the ridge.

In the Memnonia quadrangle, a roughly NW trending ridge is cut in the center, and terminated at the northern and southern ends by SE and ESE trending faults (Fig. 1D). The center of the ridge is clearly cross-cut by the SE trending fault and exhibits some degree of offset, suggestive of a strike-slip component. This ridge may have been connected to the larger N-trending ridge to the north. In any case, the ridge is at least older than the SE trending graben.

These images represent only a few examples of ridges cross-cut by graben in the Tharsis region. Graben cross-cutting ridges have also been observed in the Phaethontis, Amazonis and Arcadia quadrangles. In the Thaumasia quadrangle, E-W ridges are cross-cut by the NNW system of Tharsis radial fractures, although image resolution is not sufficient to determine whether ridge segments are present in the bottom of the graben. However, in all intersections, there is evidence for either a lineation, or a distinct offset in the crest of the ridge.

These observations indicate that ridge formation in the Tharsis region of Mars occurred before the cessation of radial fracturing. In most areas where the rilles post-date the ridges, the rilles are part of at least one of the radial fracture systems related to Tharsis (3), although locally-controlled fractures are also evident south of Valles Marineris and near Kasei Vallis. Following the relative age scheme for graben formation proposed by Plescia and Saunders (3), we suggest that ridges in the Tharsis province formed (or started to form) before the period of volcano-tectonic activity centered at Pavonis Mons, and consequently, prior to the development of Valles Marineris. Although current geophysical models (4,5) for the evolution of the Tharsis bulge do not predict the exact timing of ridge and rille formation, the relative timing indicated by ridge-rille intersections support a pulsating style of uplift and/or volcanic loading, with associated long-term crustal response.

REFERENCES

(1) Watters T. R. and Maxwell T. A. (1981) Papers presented to the Third International Colloquium on Mars, p. 270-272. (2) Wise D. U., Golombek M. P. and McGill G. E. (1979) Icarus, 38, 456-472. (3) Plescia J. B. and Saunders R. S. (1981) Papers presented to the Third International Colloquium on Mars, p. 202-204. (4) Phillips R. J., Sleep N. H., Banerdt W. B. and Saunders R. S. (1981) Papers presented to the Third International Colloquium on Mars, p. 191-193. (5) Solomon S. C., Head J. W. and Comer R. P. (1981) Papers presented to the Third International Colloquium on Mars, p. 244-246.

# STATISTICAL APPROACH TO THE FRACTURE PATTERN OF THE THARSIS REGION OF MARS

R.Salvatori, R.Bianchi, M.Coradini, M.Fulchignoni
Istituto di Astrofisica Spaziale - Reparto di Planetologia
Viale dell'Università 11 - 00185 ROMA ITALY

A new statistical approach to study the distribution of fractures surrounding th Tharsis region on Mars was taken The fracture studies were geographically limited between 170° and 40° longitude and ± 50° latitude.
The data base was obtained from the U.S.G.S. photomosaic maps at 1:2M scale. For the region without this type of the coverage we used the geological and topographic maps of the 1:5M scale series.

We attempted to take into account only extensional tectonic features; graben were considered as one single fracture. Linear features whose origin are uncertain were excluded.

The end point of the fractures were digitized, being careful to include the entire feature, especially if transected by superimposed morphologies (craters, lava flows, etc.).

The azimuths and lengths for 6723 fractures, as well

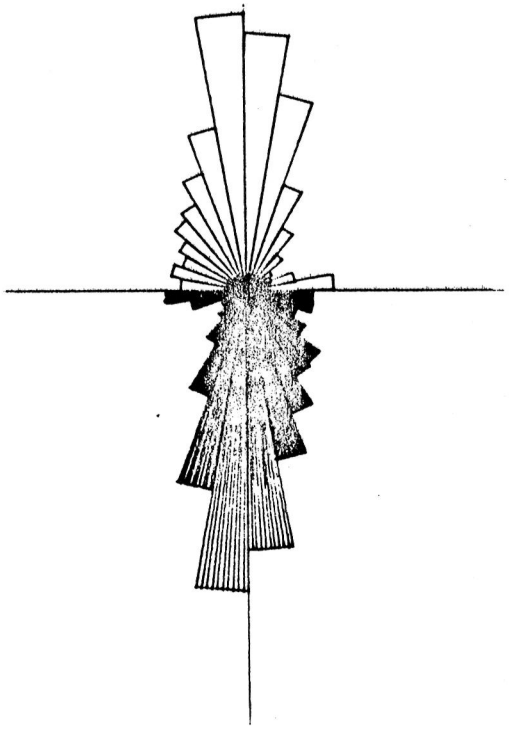

Fig. 1:
Azimuth frequency diagram of all fractures in data set.

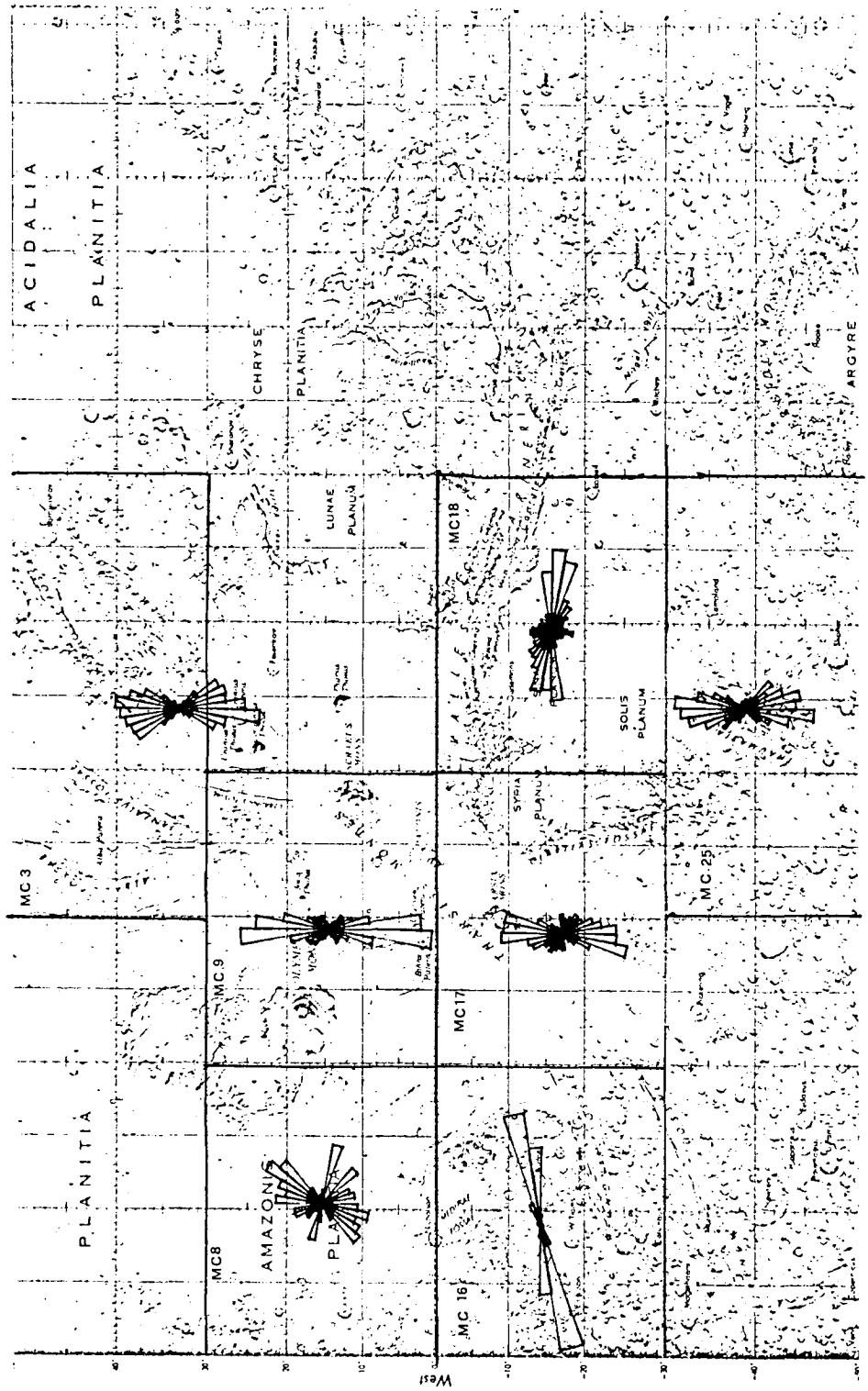


Fig. 2: Azimuth frequency diagrams for the regions around Tharsis seen on the U.S.G.S. 1:5M maps.

as the latitude and longitude of their end points, were measured. From these measurements we derived azimuth frequency diagrams that describe the general trend of all fractures in data set. The upper half of Fig. 1 shows the normalized cumulative frequency of fractures for all directions, and the lower half, the cumulative lengths. On this regional summary plot we found a major trend in a north-south direction and a secondary trend along an east-west axis. Performing the same analysis for subsets of the data within localized regions around Tharsis seen on the U.S.G.S. 1:5M map (see Fig. 2), we found the same trends. However the relative proportion of development along the two dominant directions does vary from region to region. The north-south direction is more strongly developed in the northern and southern parts of Tharsis, while the east-west direction is mainly present in Memnonia and Vallis Marineris. Only in Noctis Labyrinthus was no preferred direction of fractures observed. Instead a complex of other fracture trends are seen. Assuming that the topographic high in Syria Planum might be the center of the Tharsis bulge and the generally accepted radial fracture system, we performed the same calculations using all fractures whose trend could be projected back into a circular area of 1000 km radius centered on the same topographic high. Similar tests were performed using circles of 750, 500 and 250 km. In all four tests we found a dominance of north-south and east-west azimuths. As the test area and corresponding population of fractures decreased, an increase in the homogeneity of the distribution was observed. In conclusion we find two main directions of fractures around Tharsis. In contrast to previously reported fracture studies which seem to emphasize a radial pattern. In all probability the commonly observed radial fracture pattern is a reflexion of the longest and most prominent fractures of Tharsis. What we are seeing for the most part is a more subtle, smaller scale set of features. This could be the result of either a late stage stress field from the collapse of Tharsis or possibly very old structures which helped localize the Tharsis event into its present location.

Selected References:
Arvidson et al. 1980 Rev. of Geophys. and Space Phys. vol.18-3
Carr and Scott 1978 Geologic Map of Mars U.S.G.S.
Neukum, Wise 1976 Science vol.194 N° 4272
Wise et al. 1979 Icarus 38 456-473

THE BASAL SCARP OF OLYMPUS MONS

E. C. Morris, U.S. Geological Survey, Flagstaff, AZ 86001

The origin of the escarpment that surrounds the perimeter of the large shield volcano, Olympus Mons, has been the subject of much speculation since it was first observed in the Mariner 9 pictures. Erosional, depositional, or tectonic processes have all been proposed for its origin. The scarp is complex in its structure; though roughly concentric, it is composed of linear, concave, and convex segments (Fig. 1). Radial fractures, some extending part way up the flank of the volcano, break the scarp into its various segments. One of the radial fractures shows compressional features, i.e., several imbricate, steeply dipping blocks along its trace. The north and northwest segments of the scarp have the greatest elevation, rising 8 to 10 km above the basal plain [1]. The southeast segment is 4 to 5 km high. The southwest, east, and northeast parts of the scarp are nearly buried by young lava flows. The height of the scarps in these areas is about 2 to 4 km.

Layered material is exposed in the north, northwest and southeast segments of the scarp. This material is probably the basal unit upon which Olympus Mons was built. Blocks of this material are found along the rim of the scarp dipping toward the center of the volcano (Fig. 2). The surface of these blocks, where exposed, shows channels and grabens similar to the those on the fractured plains material [2] that lies east of Olympus Mons. A block of this material, detached from the north segment of the fault, overlies aureole material (Fig. 3).

The scarp appears to truncate some old flows that stream down the flanks of Olympus Mons; in other areas the flows are ponded behind a raised rim of the scarp. On the northeast and southwest segments, the flows cascade over and bury the scarp. These relations seem to indicate that the scarp formed late in the history of Olympus Mons during a relatively short time interval. Except where buried by young flows or modified by a few debris flows and landslides along the west segment, the scarp has changed little since its formation.

The complex nature of the basal scarp of Olympus Mons infers a tectonic origin. The scarp is interpreted to have formed by thrust faulting as a consequence of compressional forces developed in the crust during subsidence of Olympus Mons.

References

1. Wu, S. S. C. (1981) Topographic map of Olympus Mons (abs.). In Paper presented to the Third International Colloquium on Mars, LPI Contribution 441, (August 30 - September 2, 1981, Pasadena, CA.) p. 287.
2. Carr, M. H. (1975) Geologic Map of the Tharsis quadrangle of Mars (MC-9), U.S. Geol. Survey Misc. Inv. Series Map I-893.

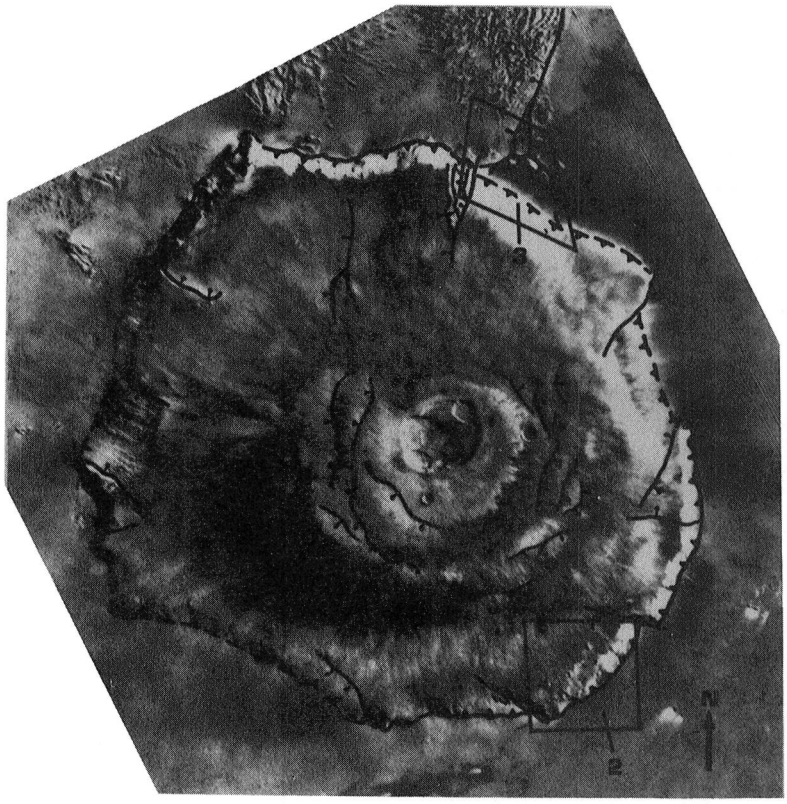


Figure 1 - Olympus Mons. Basal scarp is composed of several topographically dissimilar segments, some bounded by radial fractures. Heavy lines indicate location of faults--dashed where approximately located. Bar and ball on down/thrown side; saw teeth indicate thrust fault. Location of figures 2 and 3 are shown (Viking image 646A28).

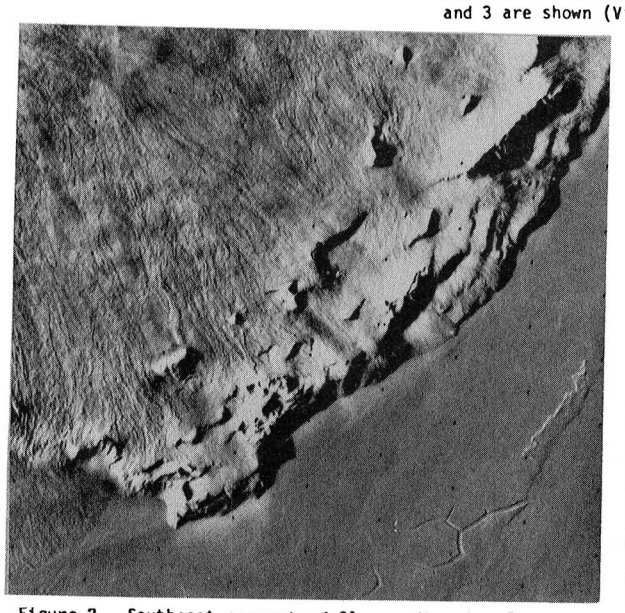

Figure 2 - Southeast segment of Olympus Mons basal scarp. Scarp consists of a number of ledges or terraces. Some blocks that form parts of the ledges dip in towards the center of the volcano. The ledges represent layered material in the scarp face or have formed from a series of imbricate thrust faults.

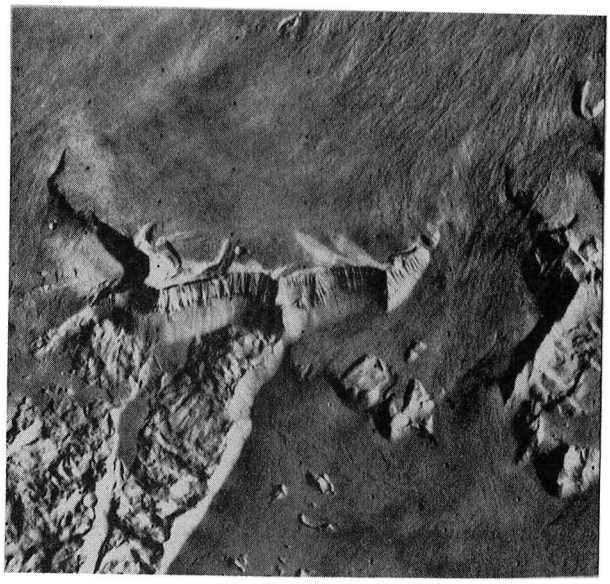

Figure 3 - Fault block overlying aureole material, north segment of the basal scarp. Upper surface of the block, where not covered by flows from Olympus Mons, shows channels and grabens similar to old plains units that lie north and east of Olympus Mons. The block probably is the basal material upon which Olympus Mons is built. The block has been thrust over the aureole material.

DEEP GRAVITATIONAL CREEP DEFORMATION: EARTH ANALOGUE OF A MARS CHAOS AREA
Baskerville, Charles A., U.S. Geological Survey, National Center, Reston, VA 22092

In the Simud Vallis of Mars at approximately 37° W, 8.5° N are two large blocks of cratered plateau material surrounded by smaller blocks of chaotic material and lineated chaotic material (Wilhelms, 1976). These chaotic materials are roughly aligned north-south, stretched out along Simud Vallis heading down channel toward the low-lying Chryse Planitia to the north (Figure 1). The slope gradient along the vallis floor at this site, according to Scott and Carr's (1978) contours is 1 meter in 2 kilometers. Mutch and others (1976) give a characteristic gradient for channels of 1 meter per kilometer.

Several theories have been advanced for the formation of the chaotic features. Wilhelms (1976) suggested that the chaotic materials were formed by erosion of collapsed material by flowing water. Wilson and others (1973) thought that the chaotic material resulted from slumping of blocks of plateau material through crustal extension along conjugate shear fractures. Sharp (1973) suggested that escarpment faces were undermined by evaporation of ground ice, and Milton (1973) suggested that ground water caused undermining of the escarpment.

This discussion proposes gravitational creep as a mechanism for the breakup of the larger mesa-like blocks in Simud Vallis and for the formation of chaotic material. This same gravitational-creep mechanism assists in the breakup and retreat of the escarpment walls along the vallis sides. One of the large mesa-like blocks shows a fracture (B in Fig. 1) in its prow that could have been caused during slow creep down the vallis.

The Earth analog of this type of slope movement does not require steep slopes. On Earth, slope movement is caused by the squeezing, or bulging, of soft rocks, such as marly shales, beneath floors of deep valleys cut into massive limestone or sandstone (Malgot, 1977; Ter-Stepanian, 1977; Zaruba and Mencl, 1976, p. 184-187). Differential loading by the massive rocks on the valley sides promotes the valley-floor bulging and deep displacement of the soft rocks beneath the valley or escarpment sides. Deformation in the substrate causes breaks along incipient fractures in the massive rocks, and the soft material beneath the resulting blocks may be squeezed up between the blocks as they move slowly, almost imperceptibly, downslope. The squeezed up soft material can tilt and rotate the broken-off blocks into an irregularly surfaced chaotic array.

The soft material in areas such as Simud Vallis could be saturated with water ice at a depth of 1 to 2 km as Sharp (1973) suggested. Translational movement in this material could be enhanced by the loading-unloading phenomenon (Flint, 1957, p. 11-22). Under a large applied force, the interstitial ice would flow plastically, facilitating movement. Figure 2 is a schematic diagram of a typical block slide of

the type suggested in this paper as a possibility for Simud Vallis and other Martian chaos areas.

Acknowledgements

This work was conducted at the U.S. Geological Survey, National Center, Reston, VA, under NASA contract W-14,730. The Mars imagery was provided by the National Space Science Data Center, Greenbelt, Md.

References

Flint, R.F., 1957, Glacial and pleistocene geology: New York, John Wiley, 553 p.

Malgot, J., 1977, Deep-seated gravitational slope deformations in neovolcanic mountain ranges of Slovakia: International Association of Engineering Geology Bulletin, no. 16, p. 106-109.

Milton, D.J., 1973, Water and processes of degradation in the Martian landscape: Journal of Geophysical Research, vol. 78, no. 20, p. 4037-4047.

Mutch, T.A., Arvidson, R.E., Head, J.W. III, Jones, K.L., and Saunders, R.S., 1976, The geology of Mars: Princeton, N.J., Princeton Univ. Press, 400 p.

Scott, D.H., and Carr, M.H., 1978, Geologic map of Mars: U.S. Geological Survey Misc. Invest. Series Map I-1083.

Sharp, R.P., 1973, Mars: Fretted and chaotic terrains: Journal of Geophysical Research, vol. 78, no. 20, p. 4073-4083.

Ter-Stepanian, G.I., 1977, Deep-reaching gravitational deformation of mountain slopes: International Association of Engineering Geology Bulletin, no. 16, p. 87-94.

Wilhelms, D.E., 1976, Geologic map of the Oxia Palus quadrangle of Mars: U.S. Geological Survey Misc. Invest. Series Map I-895.

Wilson, R.C., Harp, E.L., Picard, M.D., and Ward, S.H., 1973, Chaotic terrain: A tectonic interpretation from Mariner 6 imagery: Geological Society of America Bulletin, vol. 84, no. 3, p. 741-748.

Zaruba, Quido, and Mencl, Vojtech, 1976, Engineering geology: Amsterdam, Elsevier Scientific Pub. Co., 504 p.

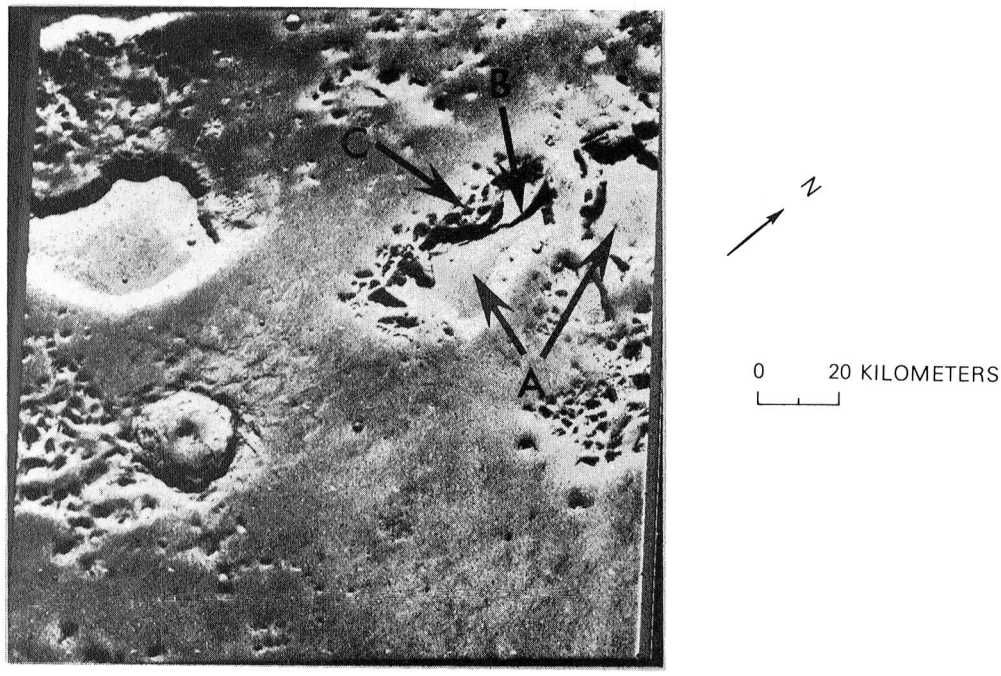


Figure 1. Mars Viking scene 897A83, centered at 7.96° N, 36.91° W in Simud Vallis. Large mesa-like blocks (A) and smaller chaotic blocks (C) are possibly the result of gravitational creep. All these blocks were originally derived from the vallis walls, a portion of which can be seen in the upper left 1/4 of the scene. Fracture in a large block (B) may have been caused by creep.

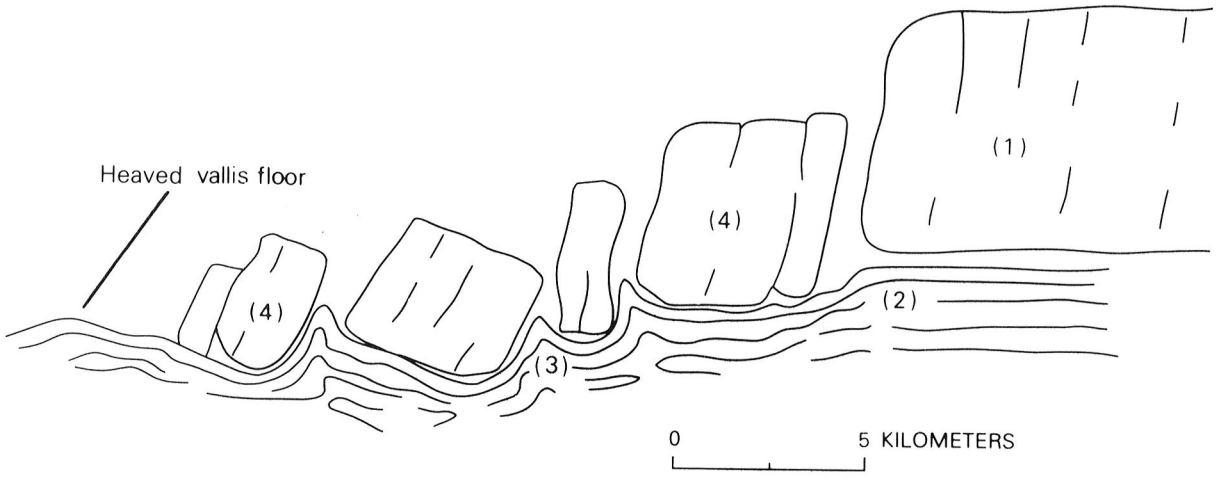


Figure 2. Sketch of typical gravitational creep deformation as suggested for the Simud Vallis on Mars: (1) massive overburden rock, (2) soft substrate, (3) squeezed up substrate, (4) chaotic blocks.

NEW YORK-PENNSYLVANIA ROCK CITIES: A MARTIAN COMPARISON

Baskerville, Charles A., U.S. Geological Survey, Reston, VA 22092

Chautauqua and Cattaraugus Counties in southwestern New York State and adjacent Warren and McKean Counties in northwestern Pennsylvania (Fig. 1) contain large areas of unusual rock exposures called "rock cities." The rock cities are scattered within a 2000-$km^2$ area, and outcrops are separated by as much as 70 km. The entire area was surveyed by reconaissance, and an area of about 620 $km^2$ was studied in some detail. The purpose of the study was to examine the idea described earlier (Baskerville, 1981) that block fields similar to terrestrial rock cities can be found along the northern plains boundary scarp of Mars.

The rock cities are composed of large blocks of grey, crossbedded quartz conglomerate. The conglomerate blocks are 15 to 30 or more meters across and 20 or more meters high. The gravel-size quartz fragments are well rounded and silica cemented. To the east, where the conglomerate is known as the Olean Conglomerate Member of the Pottsville Formation, it is coarse grained, contains fragments as long as to 3 cm, and is of Pennsylvanian age. Westward the texture becomes sandier and, in the Panama area of New York, the unit is called the Panama Conglomerate Lentil of the Cattaraugus Formation of Devonian age. The correlation of these units is moot, as they are widely separated. The underlying units are shales everywhere and are variously named the Oswayo (NY) and Conewango (PA) in the east and Chemung in the west. Smith (1953) suggested that the rock cities resulted from periglacial frost wedging.

The shale at Olean strikes N 2° W and dips 8° NE. A major joint set in the shale strikes N 15° W and dips 79° NE. The overlying conglomerate has a major joint set striking N 20° W and dipping 72° NE; thus, its attitude is not too different from that of the joint set in the shale. The conjugate joint set in the conglomerate at the Olean location strikes N 40° E and dips 70° NW. Brooks Rocks, west of Pittsfield, PA, in Warren County, have joint sets oriented N 45° W dipping vertical and N 32° E dipping 84° SE (these joints may have been tectonically generated.) Joint sets in the Panama Conglomerate Lentil strike due north and east and have nearly vertical dips. The joint sets of the various rock cities don't appear to be related to each other.

The rock cities are all located on the tops of hills or ridges. The bases of the conglomerates are at an average altitude of 700 m. Downslope from the conglomerates, the slopes are underlain by shale, whose slope generally has a gradient of 20-30 percent. On the hill tops, the conglomerate blocks are fractured into regular geometric pillars (or columns), some of which are separated by one to a few meters without much tilting. Farther down on the slopes, the separation of the blocks is 100 m or more, and the blocks are strongly tilted or toppled. Figure 2 is a view of the top surface of the blocks at the top of a ridge.

Shale overlain by massive conglomerate is an ideal combination for

sliding (Radbruch-Hall and Varnes, 1976; Radbruch-Hall, Varnes, and Savage, 1976; Pasek and Pulinowa, 1976). The movement of these blocks of conglomerate is believed to have been initiated by mechanical frost wedging under periglacial conditions (Baskerville, 1981; Pasek and Pulinowa, 1976; Smith, 1953). The Olean-Knapp Creek (Cattaraugus County, NY) rock cities were in a glacial interlobate area (Flint, 1957, p. 302-327, 355-358); therefore, no blocks were moved by glacial ice. Some large blocks of rock moved down slope intact; a few rotated backward. The areas that were glaciated, such as Panama Rocks Park and Brooks Rocks, have overturned and sheared off blocks; the result of overriding of ice or of topheavy blocks splitting along fine-grained, top- or bottom-set beds as they moved with the ice. The activity has long ceased, and presently the blocks appear to be wasting in place.

Baker and Kochel (1979) suggested that numerous periglacial activities may have been in force on Mars. They listed block fields as an indicator of ground ice and permafrost. Viking Orbiter scene 827A31 (Fig. 3) is an example of a block field that could be likened to the terrestrial rock cities except for scale differences. These blocks range from $\sim$ 6 to 25 km across, and "streets" (or separations between blocks) are 3-6 km wide. Brook (1981) suggested that ice wedging probably initiated the moving apart of the Martian blocks and created the thermokarst labyrinth topography. Gravitational sliding of a rigid, blocky, massive overlying material on an incompetent substrate containing permafrost or ground ice (Radbruch-Hall and others, 1976; Smith, 1953) probably continued the movement to its present state. Freeze-thaw of the permafrost or ground ice in the Martian substrate beneath the plateau material probably helped serve the same function as it would have served in the shale beneath the rock cities.

Acknowledgements

This work is supported by NASA Contract W-14,730. Mars imagery (Fig. 3) from National Space Science Data Center, Greenbelt, Md.

References

Baskerville, C.A., 1981, Possible "rock cities" on Mars; a preliminary observation [abs.], in Papers presented to the Third International Colloquium on Mars, Houston, Lunar and Planetary Inst., p. 22-24.

Baker, V.R., and Kochel, C.R., 1979, Martian channel morphology: Maja and Kasei Valles, Jour. Geophys. Res., vol. 84, no. B14, p. 7961-7983.

Brook, G.A., 1980, The Martian fretted terrains: examples of thermokarst labyrinth topography [abs.], in Reports of Planetary Geology Program-1980, NASA (U.S. National Aeronautics and Space Admin.) Tech. Mem., 82385, p. 369-371.

Flint, R.F., 1957, Glacial and Pleistocene geology, New York, John Wiley, 553 p.

Pasek, J., and Pulinowa, M.Z., 1976, Block movements of Cretaceous sandstones in the Stolowe Gory Mts., Poland, Bull. of the Internat. Assoc. of Engineering Geology, no. 13, p. 79-82.

Radbruch-Hall, D.H., and Varnes, D.J., 1976, Landslides-Cause and effect, Bull. of the Internat. Assoc. of Engineering Geology, no. 14, p. 205-216.

Radbruch-Hall, D.H., Varnes, D.J., and Savage, W.Z., 1976, Gravitational spreading of steep-sided ridges ("sackung") in western United States, Bull. of the Internat. Assoc. of Engineering Geology, no. 14, p. 23-35.

Smith, H.T.U., 1953, Periglacial frost wedging in the "rock cities" of southwestern New York, Geol. Soc. of America Bull., vol. 64, no. 12, p. 1474.

Wilhelms, D.E. 1976, Geologic map of the Oxia Palus quadrangle of Mars, U.S. Geological Survey Misc. Inv. Series Map I-895.

Figures

Figure 1. Location map showing the location of the four counties in New York and Pennsylvania where the Rock Cities studied can be found. A, Chautauqua County; B, Cattaraugus County; C, Warren County; D, McKean County.

Figure 2. View across the top of part of the Rock City Park blocks south of Olean, NY at latitude 40° 1′ N, longitude 78° 20′ 30" W.
Block in foreground is about 15 m across, and joints between blocks are 1-2 m wide.

Figure 3. Viking Orbiter scene 827A31 showing Hydraotes Chaos to the south (arrow in right half of scene), an example of a block field resulting from disruption of nearby plateaus (left 1/3 and lower right portion of scene) (Wilhelms, 1976). Image from National Space Science Data Center.

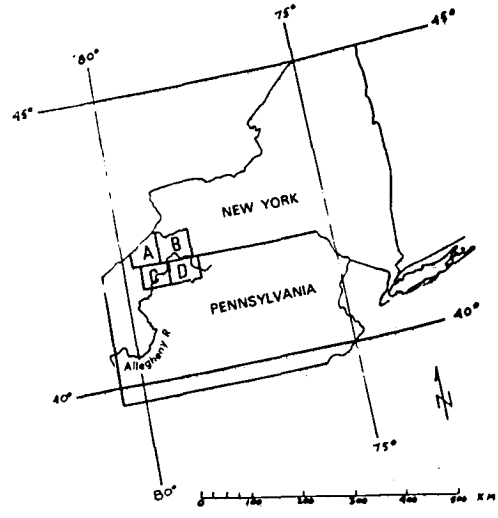


Figure 1

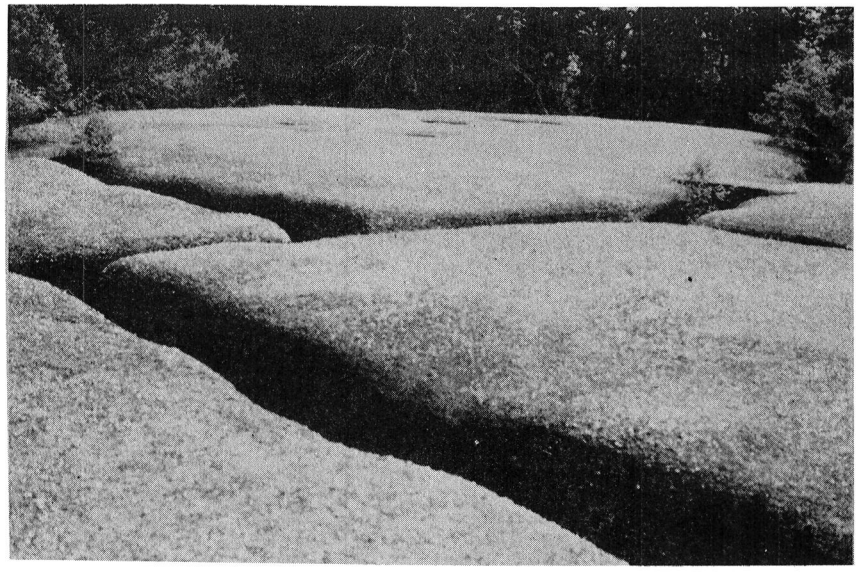

Figure 2

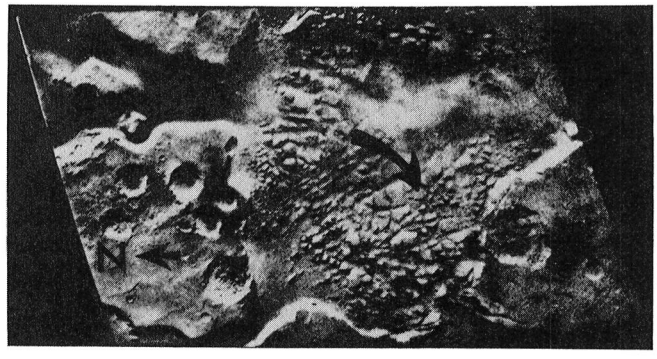


Figure 3

DEFORMED IMPACT CRATERS ON MARS.

Constance G. Andre and Farouk El-Baz, National Air and Space Museum, Smithsonian Institution, Washington, D.C. 20560.

Deformation of fairly predictable geometric forms, like fresh impact craters, provides valuable information about the nature of Martian surface and subsurface material and the forces that modify topography, such as volcanism, tectonics, impact cratering and erosion. Several types of crater deformation were observed in Viking I and II images. The initial crater shape may be disfigured by meteoroid impacts, fissures, faults, collapse, irregular slumping, differential fluid erosion, differential eolian erosion, partial exhuming by wind or water, and lava encroachment.

Crater deformation by fissures is common in the Claritas Fossae region in the southern hemisphere of Mars. Numerous subparallel fractures cross several generations of craters in these ancient uplands south of Syria Planum (Fig. 1). The tensional fractures often dissect crater floors, rims and ejecta. The most severely fractured craters are elongated perpendicular to the trend of the fractures. Despite the extreme linear segmentation, the impact structures remain. This suggests an unusually strong and cohesive crustal material.

Deformation of crater interiors on Mars may be caused by substrate processes. Figure 2 is an example of crustal conditions that cause the interior of an impact crater to be most susceptible to mechanical destruction. The floor of the crater is a disordered heap of angular blocks characteristic of the chaotic terrain, which occurs mainly in the equatorial areas of Mars between $10^{o}$ and $50^{o}$ longitude. Chaotic terrain is believed to be caused by melting of subsurface ice and the collapse of the surface layer (Sharp, 1973; Schultz and Flicken, 1979). It often forms within impact craters. The deformed crater in figure 2 shows that with the exception of a few linear extensions, the chaotic material is confined to the crater floor. If the breccia lense created below the crater during impact directly overlies a weak subsurface layer, like ice, it would destabilize the crater floor relative to the more competent surrounding lithology.

A different form of deformation occurs within craters near canyon walls. Figure 3 illustrates such a crater that is the locus of headward erosion. The crater has been partially destroyed by mass wasting and cliff retreat. Craters like this one are not uncommon in the ridged plains which resemble the flood basalts of lunar maria (McCauley, 1978). Preferential deterioration of craters like this one may be a useful indication of a less consolidated older surface surrounded by a more coherent volcanic veneer that slows erosional processes.

Effects of differential eolian erosion are evident in the dissected plateau of Acidalia Planitia (Fig. 4). The ejecta of impact craters are only visible on the high ground in the center of the image. Ejecta contours around craters on the plateau end abruptly at the edges of scarps. The importance of wind in the shaping of this landscape is indicated by white streaks in the lee of craters in the low areas (El-Baz and Maxwell, 1979). In addition, dark patches of irregular

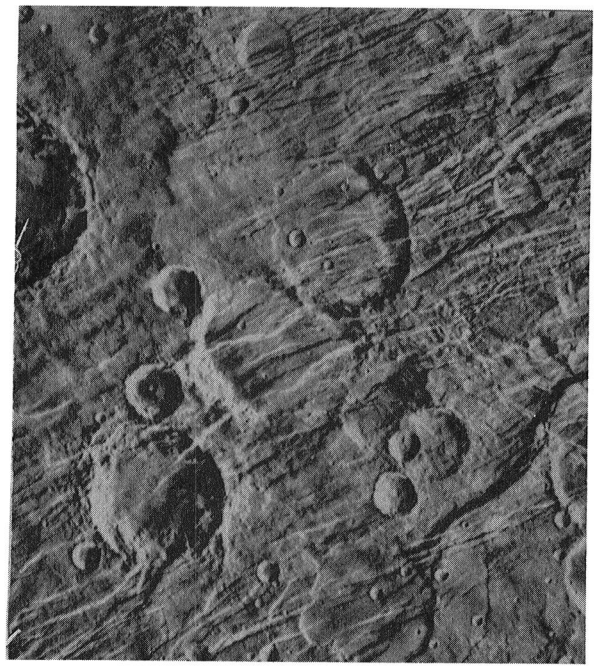

Fig. 1

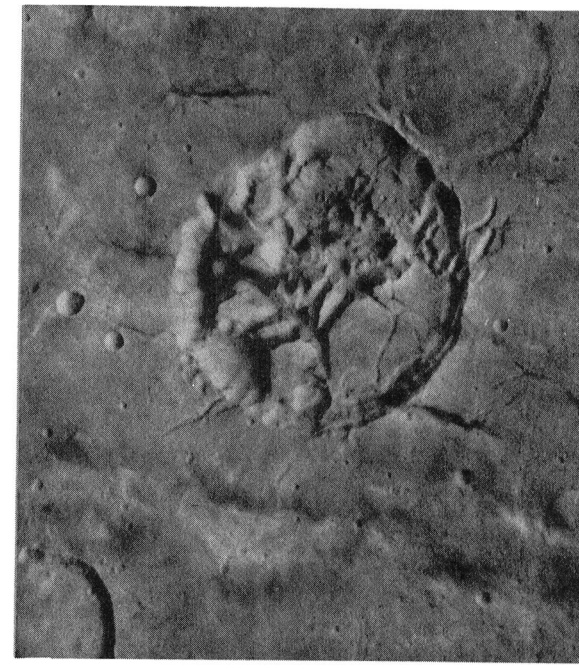

Fig. 2

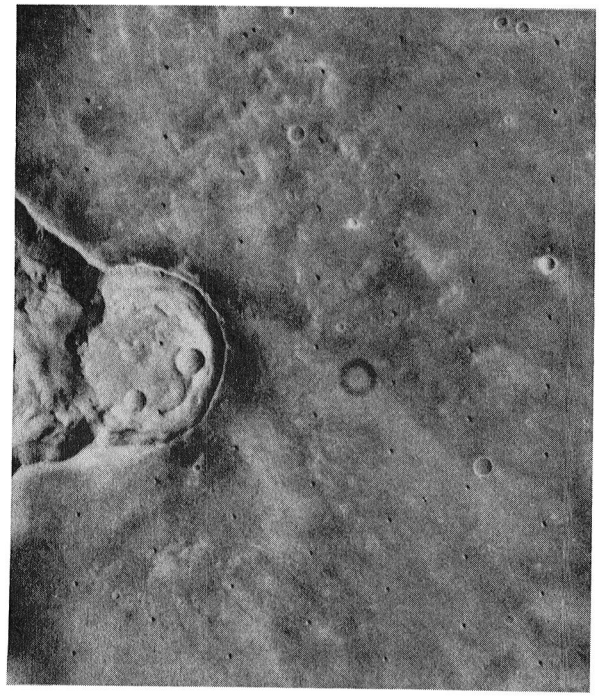

Fig. 3

Fig. 4

Impact craters on Mars deformed by: (1) fissures; (2) undermining and collapse; (3) headward erosion; (4) differential eolian erosion.

shape which are usually accumulations of dunes (Mutch et al., 1976), are confined to low-lying areas on the wind side of scarps on the floor of the largest crater. The image also illustrates that unlike the cases in figure 2 and 3, the impact craters here are particularly resistant to the forces of eolian erosion prevalent in this area.

All types of crater deformation observed on Mars are highly dependent on geographic location. None of the types discussed occur on the Moon. For this reason, distorted impact crater forms contain important information. Although impact craters are common to all terrestrial planetary bodies in the solar system, modifications to crater morphology are likely to be a function of the nature of each planet, moon or asteroid.

References

El-Baz, F. and Maxwell, T.A. (1979) Eolian streaks in southwestern Egypt and similar features in the Cerberus region of Mars. Proc. LPSC, 10th, p. 3017-3030.

McCauley, J.F. (1978) Geologic Map of the Coprates Quadrangle of Mars.

Mutch, T.A. et al. (1976) The Geology of Mars. Princeton Univ. Press.

Schultz, P.H. and Flicken, H. (1979) Impact crater and basin control of igneous processes on Mars. JGR, 84, p. 8033-8047.

Sharp, R.P. (1973) Mars: Fretted and Chaotic Terrains. JGR, 78, p. 4073-4083.

# KINEMATICS OF BASIN SUBSIDENCE, GRABENS, AND LUNAR EXPANSION

George E. McGill and Matthew P. Golombek*, Department of Geology and Geography, University of Massachusetts, Amherst, MA 01003

Although the moon is tectonically inactive relative to the earth, the presence of grabens and wrinkle ridges indicates that stresses sufficient to deform or fault surface rocks have existed for at least part of the ~3.9 by that have elapsed since the end of the heavy bombardment that characterized early lunar history. Because most of these grabens and wrinkle ridges are associated with large impact basins (Quaide, 1965), they provide an interesting opportunity to constrain long-term modifications of the lunar crust in the vicinity of large basins (e.g., Muehlberger, 1974; Melosh, 1978; Solomon and Head, 1979, 1980).

The time of formation of grabens and wrinkle ridges (Lucchita and Watkins, 1978), and the apparently greater age of grabens than wrinkle ridges are consistent with models of lunar thermal evolution that predict an early phase of lunar expansion followed by long-continued contraction (Solomon and Chaiken, 1976). As pointed out by Golombek (1979), the geometry of the grabens permits a rough quantitative check on the magnitude of the expansion phase of these models, and his results indicated that the predicted post-3.9 by radius increases of 1 km or more are quantitatively inconsistent with surface-area increases calculated from graben geometry even if all the grabens are assumed to be due to global expansion. But because most lunar grabens are associated with impact basins, it is possible that most of them are, in fact, not due to global expansion, but are caused by basin subsidence instead.

Models of basin subsidence can be developed either by 1) assuming an idealized loading geometry, calculating the resulting stresses in the lunar lithosphere, and then, by assuming values for the relevant elastic constants, comparing the calculated results with observed deformation and faulting (grabens and wrinkle ridges); or by 2) assuming an idealized subsidence geometry, calculating the resulting strains in the lunar lithosphere, and then comparing the results with observed deformation and faulting. The advantage of the second approach is that no assumptions about elastic properties are required. Even so, kinematic models of basin subsidence have not been pursued as diligently as dynamic models. Previous models (Bryan, 1973; Maxwell, 1978) either are not completely developed mathematically, or are geologically not very realistic. We are developing kinematic models of basin subsidence that are as complete as possible and that assume geologically reasonable geometry and displacements.

If the pre-subsidence basin floor is assumed to approximate a circular arc, then subsidence could occur with or without change in the radius of curvature of this circular arc, and two end-member models may be investigated: 1) subsidence entirely accomplished by an increase in radius of curvature, and 2) subsidence with no increase in radius of curvature. Any combiantion of these end members would be possible.

---

* Present address: Lunar and Planetary Institute, 3303 NASA Road 1, Houston, TX 77058

Model 1: Subsidence by increase in radius of curvature

All points on the basin floor are assumed to subside along lunar radii, hence the floor of the basin will be compressed both radially and tangentially as these points move closer together. The greatest compression occurs near the center of the basin; tangential (hoop) strain declines to 0 at the basin periphery, but radial strain declines to 0 inside the basin periphery and is slightly extensile near the periphery. Superposed on these strains is radial compression of the upper part of the lithosphere due to "unbending" fiber strains caused by the increase in radius of curvature. At the basin periphery, an anticlinal flexure is created by the subsidence. Although the extensile bending fiber strains that result from this flexure are critically dependent on its width, the total shortening implied is essentially independent of the width selected unless an unrealistically narrow and sharp flexure is assumed. The logical value to assume is the width of the circumferential graben zone. Both the unbending strain of the basin interior and the strain due to the peripheral flexure depend on the thickness of the elastic lithosphere.

Model 2: Subsidence with constant radius of curvature

As with model 1, subsidence causes radial and tangential compression of the basin floor, but the radial and hoop strains are constant throughout the basin interior, and no unbending strain exists. This model predicts both an anticlinal and a synclinal flexure at the periphery of the basin in order to maintain continuity of the lithosphere. In common with model 1, the anticlinal flexure is assumed to coincide with the zone of circumferential grabens; the synclinal flexure would be on the basinward side of the grabens.

Both models predict compression of the inner part of the basin, the first by arc shortening plus unbending, the second by arc shortening plus synclinal flexing (near the periphery only). Both also predict extension of an annulus around the basin due to anticlinal flexure. For a Humorum-sized basin (radius from basin center to inner edge of zone of grabens = 200 km, width of zone of grabens = 50 km), for an elastic lithosphere 50 km thick, and for 2 km of subsidence at the basin center some results are:

| Total radial shortening of floor of half basin | | Total radial lengthening in graben zone | | Maximum hoop shortening of half circle | |
|---|---|---|---|---|---|
| Model 1 | Model 2 | Model 1 | Model 2 | Model 1 | Model 2 |
| 615 m | 1765 m | 505 m | 485 m | 280 m | ~4075 m |

Hoop shortening is somewhat complex. Hoop strain declines from the basin center outward for model 1, but because of the increase in circle size outward, maximum total shortening actually occurs about 6/10 of the distance from the basin center to the graben zone. For model 2, hoop strain is constant so total hoop shortening increases outward until the zone of peripheral synclinal flexure is reached; beyond that, subsidence and thus hoop strain decrease rapidly. The value of hoop shortening given in the table is for a radial distance of about 150 km.

The lengthening in the zone of circumferential grabens for both models compares closely with the 470 m measured for Humorum by Golombek (1979). In addition, the predicted shortening of the basin floor seems reasonable in light of shortening in the Serenitatis basin measured by Muehlberger (1974) assuming that wrinkle ridges are structures resulting from compressive stresses. Consequently, it seems that basin subsidence is, in fact, capable of accounting for the strains implied by those grabens and wrinkle ridges associated with basins.

The thermal model developed by Solomon and co-workers provides the best explanation for the timing of graben and wrinkle-ridge formation, but it predicts changes in the lunar radius that cannot be supported by the geological data. The limited extension implied by lunar grabens, and the probability that almost all of this limited extension can be explained by basin subsidence, constrains post-3.9 by lunar expansion to essentially trivial amounts. Our results do not similarly constrain later contraction, but they do indicate that most wrinkle ridges can be explained without this global contraction.

References cited

Bryan, W.B. (1973) Proc. Lunar Sci. Conf. 4th., p. 93-106.

Golombek, M.P. (1979) J. Geophys. Res., 84 p. 4657-4666.

Lucchitta, B.K. and J.A. Watkins (1978) Proc. Lunar Planet. Sci. Conf. 9th., p. 3459-3472.

Maxwell, T.A. (1978) Proc. Lunar Planet. Sci. Conf. 9th., p. 3541-3559.

Maxwell, T.A., F. El-Baz, and S.H. Ward (1975) Bull. Geol. Soc. America, 86, p. 1273-1278.

Melosh, H.J. (1978) Proc. Lunar Planet. Sci. Conf. 9th., p. 3513-3525.

Muehlberger, W.R. (1974) Proc. Lunar Sci. Conf. 5th., p. 101-110.

Quaide, W. (1965) Icarus, 4, p. 374-389.

Solomon, S.C. and J. Chaiken (1976) Proc. Lunar Sci. Conf. 7th., p. 3229-3743.

Solomon, S.C. and J.W. Head (1979) J. Geophys. Res., 84, p. 1667-1682.

Solomon, S.C. and J.W. Head (1980) Rev. Geophys. Space Phys., 18, p. 107-141.

RELATIVE AGES OF LUNAR BASINS (II); SERENITATIS

Don E. Wilhelms, U.S. Geological Survey, Menlo Park, CA 94025

This ranking of 44 lunar ringed impact basins concludes a series of short reports on basin chronology and interpretation (Wilhelms, 1976, 1979, 1980a-d). A fuller account and supporting data are included in a book describing the geologic history of the Moon (Wilhelms, in press). Individual ranking of all known and suspected basins $\geq$300 km across is attempted, but crater densities and superposition relations do not accurately resolve many relative ages. The ranking of the 15 age groups in the table is believed valid; ranking within each group is less well established. Some age groups might be natural and not artificial. Wetherill (1975) suggests that several large impacts might cluster within a few tens of millions of years when a single large body from the outer solar system is fragmented in the inner solar system. The Imbrian, Nectarian, and pre-Nectarian basins do seem to form clusters which are more distinct than one would expect from statistical errors (Wilhelms, 1979). Smaller clusters can be inferred from similar sizes and locations of basins having similar ages. A more extreme view is that an impact "cataclysm" formed most basins within about 0.1 aeon (Tera and others, 1974).

Of particular interest is the Serenitatis basin, which may be only 40 million years older than the Imbrium basin (Jessberger and others, 1977). Serenitatis is morphologically indistinct, except for its conspicuous subcircular mare fill, and has been ranked among the older lunar basins (Stuart-Alexander and Howard, 1970). Criteria for determining its relative age are very weak. It may belong anywhere in group 4 or perhaps in an older group. However, the following observations are consistent with the young isotopic age (Jessberger and others, 1977) and eliminate the need for a "cataclysm." (1) Deep burial of western Serenitatis by Imbrium deposits contributes most of the severe degradation that makes the basin seem old, but has no absolute-age significance. (2) The apparent high crater density of the eastern Serenitatis margin is due to (a) Imbrium secondary craters (Wilhelms, 1976, 1980d) and (b) partially buried craters, which do not date Serenitatis. (3) Although Crisium is among the youngest basins of the Nectarian System, no Crisium ejecta is visible in the Taurus-Littrow (Apollo 17) region 850 km from the center of Crisium, though it extends much farther from Crisium in other directions (Wilhelms, 1980b). Therefore, either Serenitatis is the younger basin or Crisium deposits were ejected asymmetrically. (4) Serenitatis secondary craters may be superposed on Crisium ejecta northeast of Serenitatis (Wilhelms, 1976) and on the southwestern Crisium rim. (5) The large Serenitatis mascon indicates a deep mare, and a thick pre-mare fill of Imbrium ejecta also covers the basin floor. The substantial basin depth which is implied indicates little isostatic rebound since the basin formed. (6) Visual observations suggest that

| Age group | | Basin ( ) = doubtful | Diam. (km) | Lat. | Long. | Remarks |
|---|---|---|---|---|---|---|
| IMBRIAN | 1 | Orientale | 930 | 20 S | 95 W | |
| | 2 | Schrödinger | 320 | 75 S | 134 E | |
| | 3 | Imbrium | 1500 | 38 N | 19 W | Maximum diameter |
| NECTARIAN | 4 | (Sikorsky-Rittenhouse) | 310 | 69 S | 111 E | Possibly part of SP-A |
| | | Bailly | 300 | 67 S | 68 W | |
| | | Hertzsprung | 570 | 2 N | 129 W | |
| | | Serenitatis | 880 | 27 N | 19 E | Age doubtful; see text |
| | | Crisium | 1060 | 18 N | 59 E | Maximum diameter |
| | | Humorum | 820 | 24 S | 40 W | Maximum diameter |
| | | Humboldtianum | 700 | 61 N | 84 E | Double; diam. recalculated |
| | 5 | Mendeleev | 330 | 6 N | 141 E | from area as circle |
| | 6 | Mendel-Rydberg | 630 | 50 S | 94 W | |
| | | Korolev | 440 | 5 S | 157 W | |
| | | Moscoviense | 445 | 26 N | 147 E | |
| | | Nectaris | 860 | 16 S | 34 E | |
| PRE - NECTARIAN | 7 | Apollo | 505 | 36 S | 151 W | |
| | | Grimaldi | 430 | 5 S | 68 W | |
| | 8 | Freundlich-Sharonov | 600 | 19 N | 175 E | |
| | 9 | Birkhoff | 330 | 59 N | 147 W | |
| | | Planck | 325 | 58 S | 136 E | |
| | | Schiller-Zucchius | 325 | 56 S | 45 W | |
| | | (Amundsen-Ganswindt) | 355 | 81 S | 120 E | Probably part of SP-A |
| | 10 | Lorentz | 360 | 34 N | 97 W | |
| | 11 | Smythii | 840 | 2 S | 87 E | |
| | | Coulomb-Sarton | 530 | 52 N | 123 W | Diameter doubtful |
| | 12 | Keeler-Heaviside | 800 | 10 S | 162 E | Diameter doubtful |
| | | Poincaré | 340 | 58 S | 162 E | |
| | | Ingenii | 650 | 34 S | 163 E | Diameter doubtful |
| | 13 | (Lomonosov-Fleming) | 620 | 19 N | 105 E | One ring observed |
| | | (Nubium) | 690 | 21 S | 15 W | One ring probable |
| | | (Fecunditatis) | 690 | 4 S | 52 E | One ring probable; diam. ? |
| | | (Mutus-Vlacq) | 700 | 52 S | 21 E | One ring probable |
| | | (Tranquillitatis) | 775 | 7 N | 40 E | Single or double; diam. ? |
| | | Australe | 880 | 52 S | 95 E | |
| | 14 | (Al Khwarizmi-King) | 590 | 1 N | 112 E | |
| | | (Pingré-Hausen) | 300 | 56 S | 82 W | Very doubtful; diam. ? |
| | | (Werner-Airy) | 500 | 24 S | 12 E | Diameter doubtful |
| | | (Flamsteed-Billy) | 570 | 8 S | 45 W | Doubtful; diam. ? |
| | | (Marginis) | 580 | 20 N | 84 E | |
| | | (Insularum) | 600 | 9 N | 18 W | Diameter doubtful |
| | | (Grissom-White) | 600 | 40 S | 155 W | Doubtful; diam. ? |
| | | (Tsiolkovskiy-Stark) | 700 | 15 S | 128 E | Doubtful; diam. ? |
| | 15 | South Pole-Aitken | 2500 | 56 S | 180 | SP-A |
| | | (Procellarum) | 3200 | 26 N | 15 W | |

the Serenitatis massifs are much fresher than those of Crisium (Evans and El-Baz, 1973). This observation would not be conclusive even if confirmed, but weakens the equally qualitative arguments in favor of the morphologic freshness of Crisium. As few as 3 basins may be younger than Serenitatis while as many as 40 may predate it. This interpretation of the lunar stratigraphic and geochronologic data is inconsistent with a "cataclysm," but does not exclude lesser peaks in the heavy pre-mare cratering rate.

References


Evans, R.E. and Farouk El-Baz (1973) Geological observations from lunar orbit, *in* Apollo 17 Prelim. Sci. Rpt., NASA SP-330, sec. 28.

Jessberger, E.K., T. Kirsten, and Th. Staudacher (1977) One rock and many ages--Further K-Ar data on consortium breccia 73215: Proc. 8th Lunar Sci. Conf., p. 2567-2580.

Stuart-Alexander, D.E. and K.A. Howard (1970) Lunar maria and circular basins--A review: Icarus 12, p. 440-456.

Tera, F., D.A. Papanastassiou, and G.J. Wasserburg (1974) Isotopic evidence for a terminal lunar cataclysm: Earth. Planet. Sci. Let. 22, p. 1-21.

Wetherill, G.W. (1975) Late heavy bombardment of the moon and terrestrial planets: Proc. 6th Lunar Sci. Conf., p. 1539-1561.

Wilhelms, D.E. (1976) Secondary impact craters of lunar basins: Proc. 7th Lunar Sci. Conf., p. 2883-2901.

____ (1979) Relative ages of lunar basins: NASA TM 80339, p. 135-137.

____ (1980a) Irregularities of lunar basin structure: NASA TM 81776, p. 25-27.

____ (1980b) Geologic map of ringed impact basins: Conf. on Lunar Multi-ring basins, Nov. 1980, Lunar and Planet. Inst. Contrib. 414, p.115.

____ (1980c) Paleogeologic maps of the far side of the Moon: NASA TM 82385, p. 466-468.

____ (1980d) Stratigraphy of part of the lunar near side: USGS Prof. Paper 1046A, 71 p.

____ (in press) Geologic History of the Moon: to be submitted for publication as a NASA SP.

MERCURY'S HISTORY REVISITED

Leake, Martha A.*, Clark R. Chapman, Stuart J. Weidenschilling, Donald R. Davis, and Richard Greenberg, Planetary Science Institute, Tucson, AZ, 84719

Most discussion of Mercury's evolution has taken place in the context of a paradigm in which Mercury's geological record is tied approximately to the lunar cratering chronology. Thus, the Caloris Basin is interpreted to have formed late in the period of lunar basin formation, and inter-crater plains on Mercury are interpreted to have formed prior to that time (cf. Strom, 1979). During most of its later history, Mercury is thought to have been rather dormant, apart from occasional cratering.

Geophysical models for the thermal evolution of Mercury have been discussed in the same context. There are important geological constraints on Mercury's thermal evolution: (1) Core formation would have been a dramatic event on Mercury, with obvious manifestations in the geological record; (2) The scarps on Mercury are interpreted to have resulted from contraction of the mantle (and perhaps some of the core) as the interior cooled following core formation; and (3) The scarps do not show nearly the magnitude of global contraction that would be required by complete solidification of the core. The last fact is consistent with the dominant opinion that Mercury's magnetic field requires an active internal dynamo within a non-solidified core (cf. Ness, 1978). These constraints, when tied to the generally accepted crater chronology, imply that Mercury's core must have formed early (certainly within the first 0.6 aeons if not still earlier) but that planetary cooling and core solidification has still not progressed very much.

Using nominal parameters and conventional models, those studying Mercury's thermal evolution have had a difficult time meeting these constraints; Mercury's core tends to take a long time to form. If parameters are changed so that it forms rapidly, then the planet cools and solidifies too soon (cf. Solomon, 1976). There are alternative assumptions that may be made to enforce agreement with the adopted cratering chronology, such as maintaining interior warmth by imcomplete segregation of radio-actives. Indeed, the most recent models are carefully tied to the traditional cratering chronology (Toksoz et al., 1978; Solomon et al., 1981). But there is an alternative view of Mercury's chronology that may be more compatible with the straight-forward geophysical models.

There are good reasons to expect that a substantial population of bodies accreted within Mercury's orbit (Weidenschilling, 1978). For planetesimals near semi-major axis a = 0.26 AU, the characteristic time for sweep-up by Mercury would be quite long, order $10^9$ years, due to secular changes in Mercury's eccentricity. Furthermore, any such planetesimals would not contribute to the cratering records of the Moon or other planets. Thus, it may be that Mercury's cratering record has been dominated by such

*Also Lunar and Planetary Laboratory, University of Arizona, Tucson, 85721

a "vulcanoid" population -- including nearly all of the basins and craters now observed on Mercury. Several searches for populations of vulcanoids have been conducted, with negative results, but the limits established are weak ones and still permit the existence of a substantial population of vulcanoids at the present time.

Naturally, Mercury's surface must have accumulated asteroidal and cometary craters in addition to any vulcanoid cratering. But the vulcanoid source could have dominated during recent epochs, while any late heavy bombardment by the asteroidal/cometary population may have been lost in Mercury's pre-history, overwhelmed by subsequent crustal evolution and vulcanoid bombardment. It has been argued by some that the shapes of diameter-frequency distributions for craters on Mercury are similar (to greater or lesser degrees) to those on the Moon and thus that the cratering populations must be the same. While that is a good consistency argument, it may be instead that the processes that produced vulcanoids and the subsequent self-collisional evolution which must surely have modified the vulcanoid population would have yielded the same kind of evolution of sizes as occurred earlier in the populations that cratered other planets.

Much additional research, both observational and theoretical, is required to understand the probable characteristics of any vulcanoid population. More stringent observational limits can probably be established. Theoretical studies can address the original mass and size distribution, subsequent effects of gas drag on small vulcanoids, the self-collisional destruction of vulcanoids, and the time-history of their orbital evolution and impact history on Mercury. We have made a preliminary attempt, for example, to assess non-uniform longitudinal distribution of Mercurian craters predicted for a vulcanoid source (cf. Wells, 1978); unfortunately, any such effect is overwhelmed by different relative ages of surface units and by correlation of observational bias with longitude in the Mariner 10 images.

We have investigated whether the geological history of Mercury, as determined with some precision in terms of a relative chronology (Leake, 1981) can be interpreted in terms of an alternative absolute chronology dependent on a long-term history of vulcanoid impacts. First we summarize the relative chronology. Formation of intercrater plains, interpreted to be of volcanic origin, commenced while the oldest craters were being formed and proceeded until shortly before the Caloris impact. Extensive volcanism then ceased, except within isolated craters and the Caloris region, and scarp formation began, continuing perhaps until the present. There has been an extended period of global contraction, which has evidently not yet gone to completion. Core formation probably predates the oldest features, although if it could have occurred with minimal surface manifestations, the core might have been forming until shortly before scarp formation commenced. If this relative history is tied to the lunar cratering chronology so that Caloris formed about 3.9 aeons ago, then much of Mercury's geological and geophysical evolution was compressed into a short, early period. Not only would this make Mercury's period of planetary activity much shorter even than that of the Moon, but it would seem to be incompatible with the probably presence of a dynamo active in the planet today.

An alternative absolute chronology, based on vulcanoid cratering, would be more compatible with the geophysical evidence. Mercury's core could take 1 to 2 aeons to form, and we could be only part way through the planet's subsequent period of cooling and contraction. Then Mercury's surface would be surprisingly young. Perhaps the Caloris basin is only 1 or 2 aeons old, with the formation of the scarps occurring only during the last 1 to 2 aeons. This would be a radically new view of Mercury and would force a new look at other comparative planetological scenarios that have been developed in which evidence from Mercury (under the assumption of a connected cratering history) has been transferred into constraints on the cratering history of other bodies in the inner solar system. Even if it turns out that vulcanoids never existed or have not been as important as we suggest is possible, the exercise of looking at Mercury and at its implications for the inner planets with a fresh perspective, unencumbered by the lunar cratering chronology, should prove a healthy one for all of those interested in the subject of Mercury.

REFERENCES


Leake, Martha A. (1981). The Intercrater Plains of Mercury and the Moon: Their Nature, Origin, and Role in Terrestrial Planet Evolution. Ph.D. Dissertation, University of Arizona, Tucson, submitted to Advances in Planetary Geology.

Ness, Norman, F. (1978). Mercury: Magnetic Field and Interior. Space Sci. Rev. 21, 527-553.

Solomon, S.C. (1976). Some Aspects of Core Formation in Mercury. Icarus 28, 509-521.

Solomon, S.C. (1977). The Relationship Between Crustal Tectonics and Interior Evolution in the Moon and Mercury. Phys. Earth Planet. Interiors 15, 135-145.

Solomon, S.C. et al. (1981). Thermal Histories of the Terrestrial Planets. In Basaltic Volcanism on the Terrestrial Planets, Lunar and Planetary Institute, Houston, Texas, in press.

Strom, R.G. (1979). Mercury: A Post-Mariner 10 Assessment. Space Sci. Rev. 24, 3-70.

Weidenschilling, S.J. (1978). Iron/Silicate Fractionation and the Origin of Mercury. Icarus 35, 99-111.

Wells, W.C. (1978). Impacts on Mercury: There Could be Longitudinal Variations. Bull. Amer. Astron. Soc. 10 (3), pt. II, 602.

# A VIKING SOLUTION TO A MARINER STRATIGRAPHIC PROBLEM

David H. Scott, U.S. Geological Survey, Flagstaff, AZ 86001

One of the more interesting and important problems in martian geology was raised by Mariner 9 pictures of the region between Lunae Planum and Tharsis Montes. Lunae Planum appeared as a broad, nearly level plateau with a ridged surface similar to those of lunar maria. It was bordered on the west by a scarp along whose base the channel and floodplain materials of Kasei Vallis were intermittently exposed (Fig. 1). Rising westward from the channel deposits in the valley, a gently sloping surface extended towards the Tharsis Montes, some 1000 km away. Stratigraphic relations between those physiographic and geologic provinces could not be determined from Mariner 9 images. However, Milton [1], who first mapped the area, recognized some apparent flow fronts on the northeastern slopes of the Tharsis uplift, in the region west of Kasei Vallis. He proposed two alternative interpretations for the relation of this area to the Lunae Planum surface: 1) the lowland between Echus Chasma and the head of Kasei Vallis may reflect a late disruption of a continuous surface, so that materials, probably lava flows, on the Tharis slopes correlate with those of Lunae Planum; or 2) Lunae Planum and the slope materials to the west may have been structurally discontinuous from an early period.

Viking pictures have provided a solution to this problem and also have clarified some superposition relations between the alluvial materials of Kasei Vallis and lava flows originating from the Tharsis volcanoes. Answers to the stratigraphic problem, however, are somewhat more complex than the alternatives proposed by Milton [1]. New studies do confirm that, in the Echus Chasma-Kasei Vallis area, Lunae Planum and the slope materials west of the Kasei-Echus scarp have been structurally discontinuous from an early period. Here, the Tharsis slope materials generally consist of younger lava flows that were erupted after scarp formation and after emplacement of fluvial materials in Kasei Vallis; both scarp and valley formation postdate the Lunae Planum surface. This stratigraphic sequence was determined by overlap relations and substantiated by crater counts. However, the disruption between lava flows on the Tharsis slope and those on Lunae Planum is not continuous, either northward toward Tempe Terra or southward toward and beyond Valles Marineris. In these areas, where the boundary scarp between the Tharsis slope and Lunae Planum no longer exists, stratigraphic relations are more diverse. In the Tempe Terra region, a strong disconformity is clearly marked by overlap and truncation of faults and fractures in the Lunae Planum surface by younger flows emanating from volcanoes of Tharsis Montes. This boundary is nearly linear for a distance of about 400 km. In the Valles Marineris-Solis Planum region, however, the age discrepancy between earlier Tharsis flows and those of Lunae Planum is much less, and the boundary between these units is not clearly defined. It can only be determined within rather broad limits, by higher crater densities and/or a greater profusion of wrinkle-type ridges on the Lunae Planum surface.

References

1. Milton, D. J., 1975, Geologic map of the Lunae Palus quadrangle of Mars: U.S. Geol. Survey Misc. Geol. Inv. Map I-894.

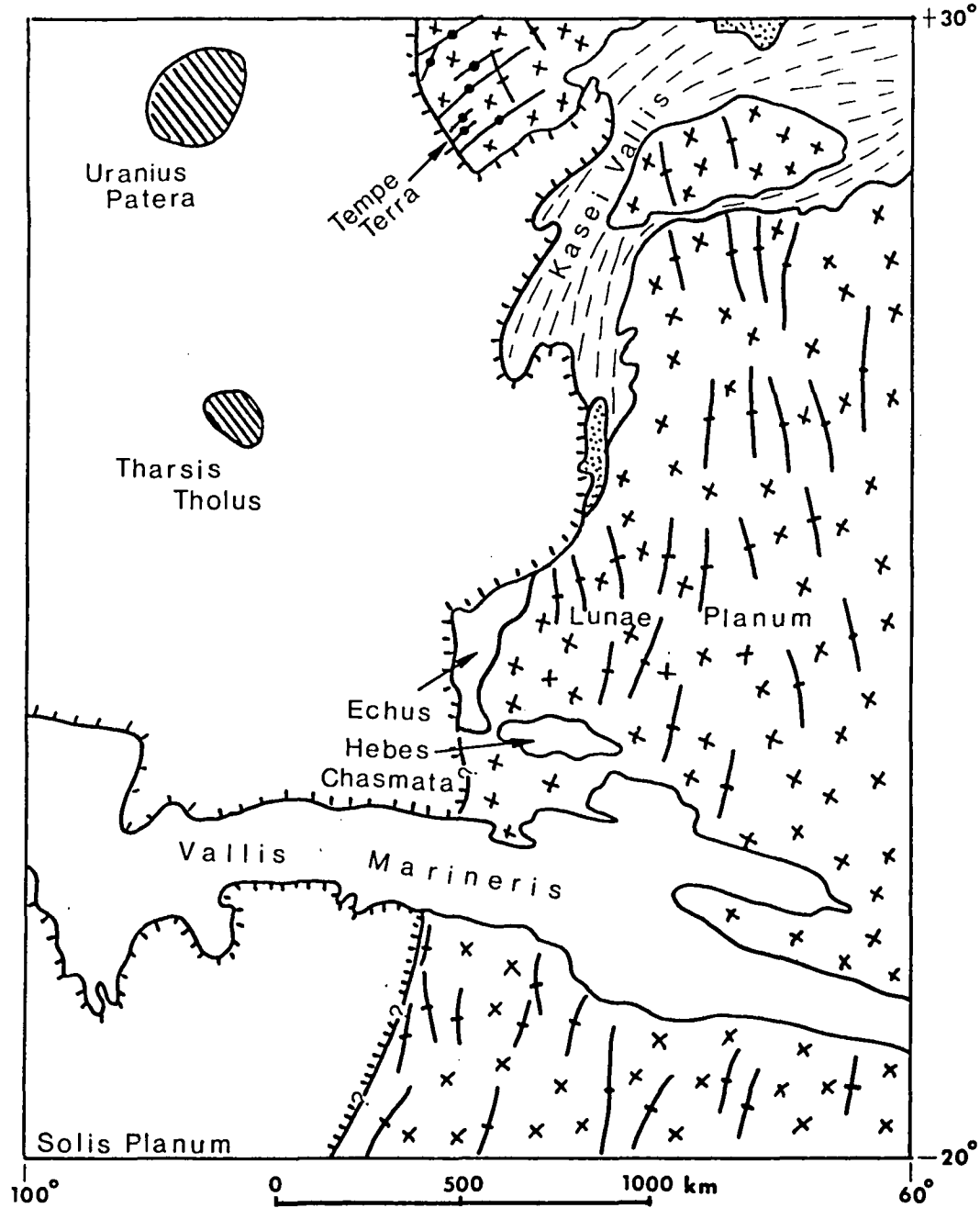
+30°
Uranius
Patera
Tempe
Terra
Kasei Valles
Tharsis
Tholus
Lunae Planum
Echus
Hebes
Chasmata
Vallis Marineris
Solis Planum
−20°
100°
0
500
1000 km
60°

Fig.1

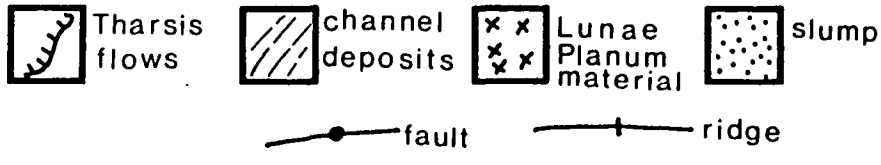
Tharsis flows
channel deposits
Lunae Planum material
slump
fault
ridge

PROGRESS REPORT: THARSIS LAVA FLOW MAP SERIES

David H. Scott, U.S. Geological Survey, Flagstaff, AZ 86001

The Tharsis lava flow map series consists of 16 geologic maps that covers the large volcanic province around Tharsis Montes and includes Olympus Mons, Alba Patera, and Syria Planum. The maps include all or parts of Mars quadrangles MC 2, 3, 8, 9, 16, 17, 24, and 25 (Fig. 1) and are compiled on quarter-quadrangle bases. Early work on the project was done by Schaber and others [1] using moderate-resolution Viking Orbiter images. Their maps showed flow materials that represent 14 distinct eruptive periods. These studies were later extended by Scott and others [2,3,4] to cover a total mapped area in excess of 15 million square kilometers. The map series shows 24 flow units made up of 7 flows of younger age (density of 1-km craters, less than 300 per million square kilometers), 7 flows of intermediate age (crater density < 2000), and 10 flows of older age (density to about 3200). The Olympus Mons aureole deposits comprise 5 of these older units. Other materials shown on the maps include slide, channel, plains, and eolian deposits and basement rocks. The primary purpose of the mapping was to describe the morphology, distribution, stratigraphic relations, and relative ages of the eruptive sequences, therefore, rock units, other than the lava flows, were not subdivided. For example, the basement-rock complex, which occurs as both rough- and smooth-fractured areas of relatively elevated terrain is mapped as one unit.

The entire series is now in press and the maps will be published during the winter of 1981-1982 in the Geological Survey's Miscellaneous Investigations Series as numbers I-1266 through I-1281.

References

1. Schaber, G. G., Horstman, K. C., and Dial, A. L., Jr., 1978, Lava flow materials in the Tharsis region of Mars: Proc. Lunar Planet. Sci. Conf. 9th, p. 3433-3458.
2. Scott, D. H. and Tanaka, K. L., 1980a, Mars Tharsis region: Volcanotectonic events in the stratigraphic record: Proc. Lunar Planet. Sci. Conf. 11th, p. 2403-2421.
3. Scott, D. H. and Tanaka, K. L., 1980b, Mars: Paleostratigraphic restoration of buried surfaces in Tharsis Montes: Icarus 45, p. 304-319.
4. Scott, D. H., Schaber, G. G., Tanaka, K. L., Horstman, K. C., and Dial, A. L., Jr., 1981-1982, Map series showing lava flow fronts in the Tharsis region of Mars: U.S. Geol. Survey Misc. Inv. Maps I-1266 to I-1280 (in press).

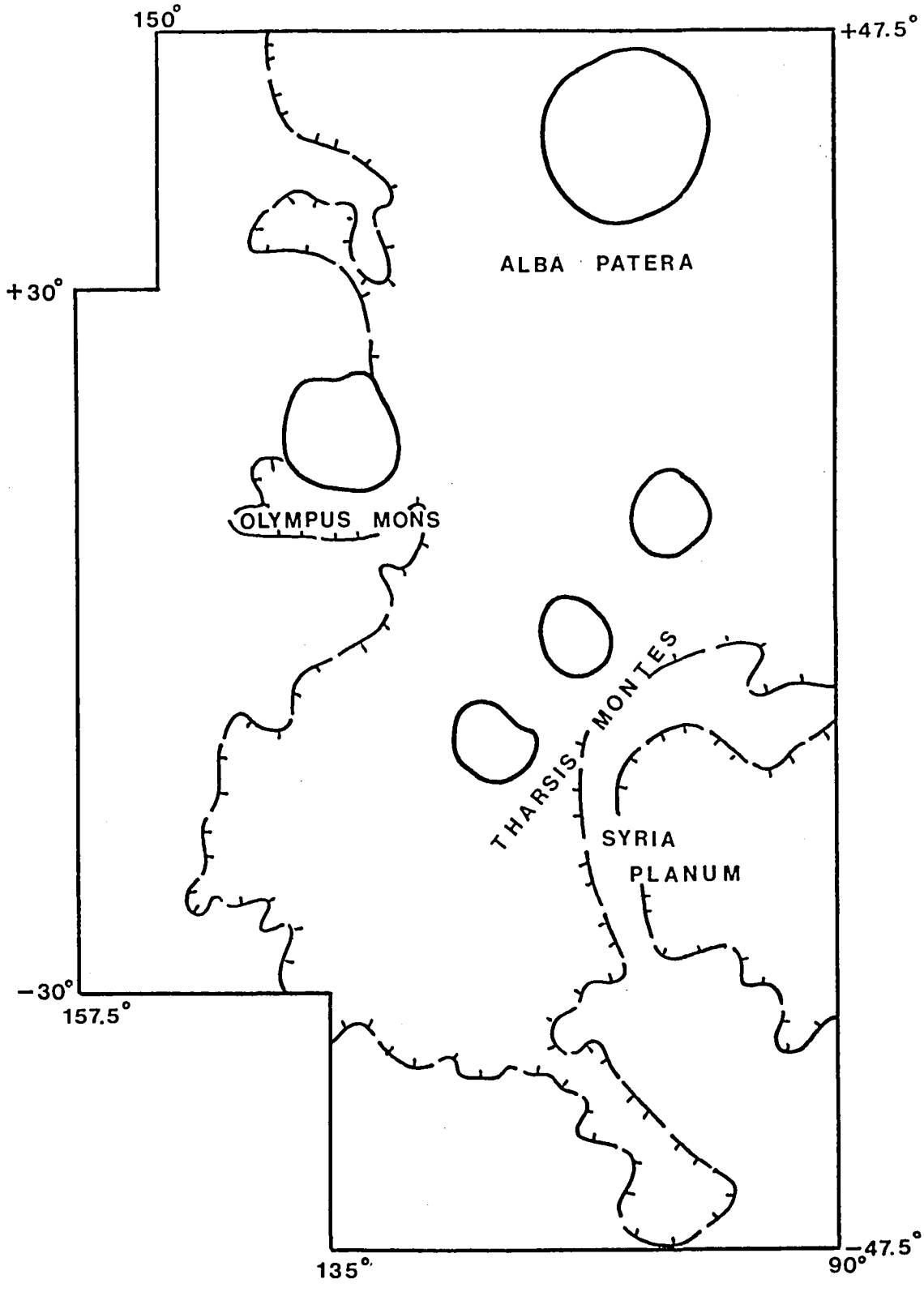
150°
+47.5°
ALBA PATERA
+30°
OLYMPUS MONS
THARSIS MONTES
SYRIA
PLANUM
-30°
157.5°
135°
90°
-47.5°

CRATER COUNTS ON OLYMPUS MONS

C. Neal, U.S. Geological Survey, Flagstaff, AZ 86001

Olympus Mons is one of the youngest volcanic structures on Mars [1]. Scarity of impact craters on its flanks, its stratigraphic relation to the surrounding terrain, and perhaps the strong associated positive gravity anomaly [2], all indicate a young age. Several workers, in an attempt to date the surface of Olympus Mons or parts of it, have used the Viking pictures to determine cratering statistics [1, 3, 4; and Arthur Dial, unpublished data]. There is considerable variance among the statistics of these workers and some are not comparable, because different methods were used to obtain the data. Factors that may have contributed to variance are varying degrees of success in recognizing and excluding from the counts a number of secondary craters from two large impact craters (9 and 13 km in diameter) near the summit and abundant volcanic features (i.e., pit craters and collapse craters) that are similar in apperance to impact craters at the resolution of the Viking pictures. A comparison of four independent crater counts of Olympus Mons is shown in Figure 1.

This study attempted to delineate distinct flow units or areas of different ages on the flanks of Olympus Mons by cratering statistics; a different technique was employed than was used previously. A mosaic was constructed of the southeast quadrant of Olympus Mons, using the moderate resolution Viking pictures. In order to define variations in crater population in both radial and concentric segments of the roughly circular Olympus Mons shield, a polar stereographic grid was centered on the central caldera and crater populations were determined for segments of the grid. Craters which obviously were of volcanic origin (e.g., chain craters) or which were of ambiguous origin were ignored. High-resolution Viking pictures were used, where available, to confirm the identification of craters made on the mosaic. Results are shown in Figure 2. Segments with the largest number of craters occur near the top of Olympus Mons, which indicates the oldest surfaces are near the summit [3]. There are some differences in crater population in a few other grid areas on the flanks; however boundaries of distinct volcanic units could not be identified morphologically within these areas to account for the differences. Very high resolution (8 to 10 m/pixel) Viking pictures of parts of the flanks of Olympus Mons show ridges of older terrain surrounded by younger flows and a surface composed of young flows overlapping older flows. If cratering statistics are to be useful in delineating or resolving various flow units on the shield there would need to be: (1) more complete coverage of the shield at very high resolution in order that craters less than 1 km in diameter could be included in the statistics, and (2) a much smaller grid spacing (100 $km^2$) to determine the crater population more precisely.

References


1. Plescia, J. B. and Saunders, R. S., 1979, The chronology of the martian volcanoes, Proc. Lunar Planet. Sci. Conf. 10th, p. 2841-2859.
2. Sjogren, W. L., 1979, Mars gravity: High-resolution results from Viking Orbiter 2, Science 203, p. 1006-1010.
3. Carr, M. H., Greeley, Ronald, Blasius, K. R., Guest, J. E., Murray, J. B., 1977, Some martian volcanic features as viewed from Viking Orbiters, Jour Geophys. Res. 82, p. 3985-4015.
4. Scott, D. H. and Tanaka, K. L., 1980, Mars Tharsis region: Volcanotectonic events in the stratigraphic record, Proc. Lunar Planet. Sci. Conf. 11th, p. 2403-2421.


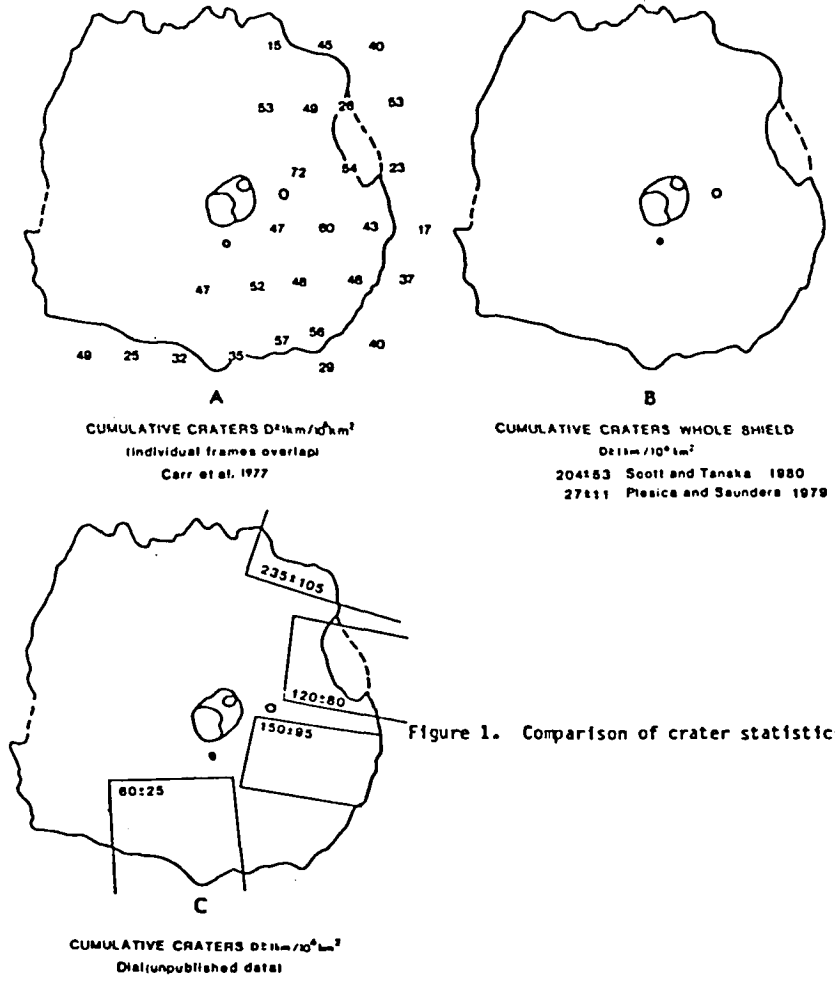


Figure 1. Comparison of crater statistics.

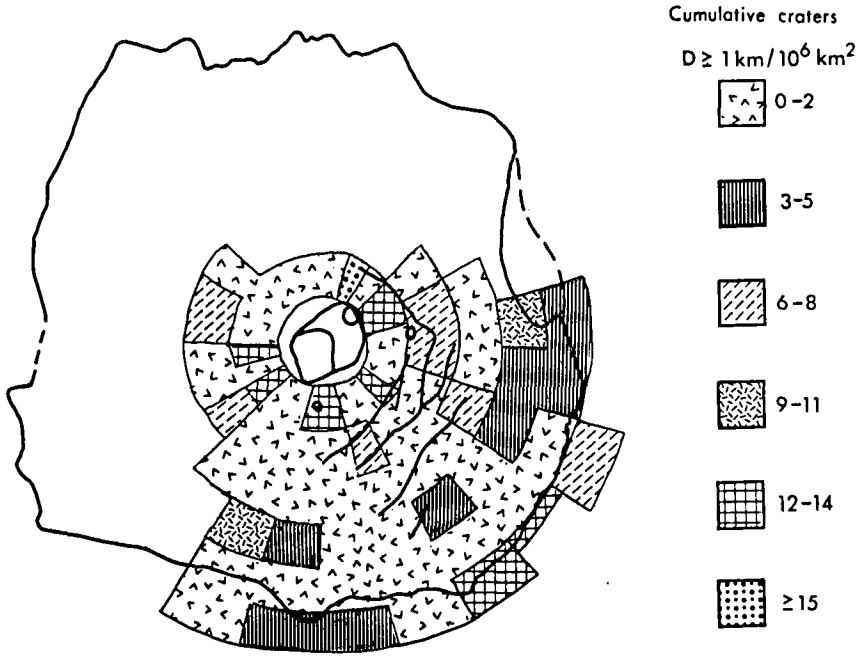


Figure 2. Crater statistics for the southeast quadrant of Olympus Mons. A polar stereographic grid centered on the caldera at the summit of the shield was used to determine crater populations for radial and concentric segments.

VALLES MARINERIS - FAULTS, VOLCANIC ROCKS, CHANNELS, BASIN BEDS

B. K. Lucchitta, U.S. Geological Survey, Flagstaff, AZ 86001.

Excellent stereographic pictures at resolutions near 100m/line pair cover parts of Ius and Tithonium, and much of Ophir, Candor, and Melas Chasmata; they were obtained late in the extended Viking mission. The pictures were studied in detail and furnished new insights into the interplay between faulting, possible volcanism, basin bed deposition, and channel erosion in the chasmata. The following is a tentative geologic summary based on the new observations.

1) The oldest geologic rocks in Valles Marineris are buried under talus in the lower trough walls; the composition of these rocks is unknown, but they apparently form unstable walls and liquefy easily, suggesting high water content. The cap rock on the walls is layered and commonly interpreted as lava of the Lunae Planum plateau [1]. This plateau is cut by many shallow grabens. Faults forming the walls of these grabens were lithified or intruded by dikes before formation of the chasmata because the faults occur as resistant spurs on the eroded trough walls or form ridge lines on eroded horsts (median ridges) in the trough interiors.

2) After plateau lava ceased to erupt (no lavas spill into the troughs) east-west trending grabens several thousand meters deep formed most of the chasmata. The graben walls were eroded vigorously into gullies, spurs, and tributary canyons. This erosional episode dates back to the period when valley networks formed on Mars, because an integrated network of valleys debouches from the Sinai Planum plateau into tributary canyons south of Ius Chasma. This observation suggests that some gullies and tributary canyons on the trough walls were eroded by runoff, in addition to sapping, which was proposed for tributary canyons by Sharp [3]. In Melas Chasma the wall retreated southward by erosion, as deduced from numerous wall rock outliers. Elsewhere the walls may have widened through successive faulting, or through repeated dislocation on the same fault, steepening spurs and gullies and promoting landslides. Old landslide scars were eroded into spurs and gullies. At least two old landslide scars later became partly buried by layered interior deposits.

3) Erosional debris from the walls apparently accumulated in the center of the troughs and formed layered basin beds. Even though some lower layers appear to be in fault contact with the trough walls, most layers were deposited against the walls and overtopped median ridges. In Ophir and Candor Chasmata, basin bed deposition stopped after surface levels reached elevations between 9000 and 10,000 meters (about 2000 m below the chasma rims) [4]. In Melas Chasma, deposits were thinner and perhaps locally absent. In the southwestern troughs, only Tithonium has some basin beds near its western and eastern ends.

4) The basin beds are stacks of layered rocks [5]. Some layers are thick, extremely bright and erode easily into steep subparallel gullies transformed by wind erosion into yardangs. Other layers are coarse and rubbly, others again are smooth, or finely gullied at various spacings. Conspicuous are interbedded dark layers that form steep-sided

caprocks supporting ledges or small mesas. The interbedded resistant, dark, and soft, very light layers resemble basin beds in Arizona and Nevada that are composed of basalts and tuffaceous sediments. The similarity suggests that martian basin beds contain volcanic materials of varying compositions. Even though no large calderas, which are the source vents of some terrestrial ignimbrites, were unambiguously identified, many small cones could be volcanic vents. Evidence for late volcanic activity in the troughs, discussed below, shows that volcanism occurred in Valles Marineris, also supporting the likelihood for earlier volcanic activity in the trough interiors. Furthermore, the volume of the interior deposits appears to be larger than the volume eroded from trough walls, most of which are steep fault line scarps, so that a contribution from elsewhere is required. As the surrounding plateau surface is little dissected, the contribution, probably, comes from the trough interior by volcanism or from the outside by wind; photogeologic considerations favor volcanism. Thus, the basin beds may be composed of interfingering fluvial deposits from the walls, volcanic flows, tuffs, and tuffaceous sediments. The level top surface suggests processes of deposition similar to those in terrestrial playas.

5) Faulting continued after the basin beds were deposited. The faults truncated wall rocks and basin beds, and rotated some horizontal beds to steep inclinations. Intensive erosion, maybe by water through new outlets in Coprates Chasma, or, more likely, by the wind, removed many of the interior deposits. At some time after basin bed deposition ended, the fluvial processes that formed the spurs and gullies also stopped. Late faults truncated spurs, left gullies as hanging valleys, and formed straight fault scarps blanketed by smooth talus.

6) Huge landslides and small debris lobes continued to fall or flow from the walls into troughs deepened by renewed faulting or erosion. Some of these deposits are in turn faulted. Large new landslides have smooth headwalls [6] probably because they postdate the episode of spur and gully formation. The landslide deposits lapped upon or spilled around basin bed remnants. Fluids emerged from their lobes and flowed into low areas in Candor Chasma, which they filled with level deposits traversed by polygonal cracks.

7) Small deposits of very dark material suggest late volcanism. The dark patches occur along faults, at the base of eroded basin beds, and in one place on top of a landslide deposit. A circular depression in one dark patch that has positive relief suggests that the patch is a cinder cone. A dark deposit with distributaries emerges from near the top of an interior mesa and extends downhill; it resembles a basaltic flow. Since most dark patches lack evidence of lava-type flows, however, the volcanism may have been largely explosive.

8) Wind erosion continued to the present. Basin beds show intense deflation. Most landslide deposits are little eroded by the wind, but some old ones have streaked textures or irregular, jagged, vaguely aligned depressions suggestive of deflation. The wall and cap rock of the troughs appears unaffected by wind erosion; apparently only selected materials are susceptible. Dark transverse and parabolic dunes overlap other deposits. Most diffuse dark wind streaks are found near dark rock

outcrops or possible volcanic vents. Dark wind deposits also tend to be concentrated near small, rugged features, suggesting preferential dropping of dark suspended materials in the turbulent air. Some interior mesas are covered by smooth deposits with vague, dune-like forms, and large areas of the chasma floors are buried by apparent wind deposits forming a gently rolling topography.

References


[1] Scott, D. H. and Carr, M. H. (1978) Geologic map of Mars, scale 1:25,000,000. U.S. Geol. Survey Misc. Inv. Map I-1083.

[2] Blasius, K. R., Cutts, J. A., Guest, J. E., and Masursky, Harold (1977) Geology of the Valles Marineris: First analysis of imaging from the Viking I Orbiter primary mission. J. Geophys. Res. 82, p. 4067-4091.

[3] Sharp, R. P. (1973) Mars troughed terrain. J. Geophys. Res. 78, p. 4063-4072.

[4] U.S. Geological Survey, Topographic map of the Coprates Northwest quadrangle of Mars, scale 1:2,000,000, unpublished map.

[5] Peterson, C. M. (1981) Hebes Chasma - A martian pyroclastic sink, in Lunar and Planetary Science XII, p. 828-829. The Lunar and Planetary Institute, Houston, Texas.

[5] Lucchitta, B. K. (1979) Landslides in Valles Marineris. J. Geophys. Res. 84, p. 8097-8113.

# PRELIMINARY OBSERVATIONS OF THE DETAILED STRATIGRAPHY ACROSS THE HIGHLAND-LOWLANDS BOUNDARY

D. Weiss, J. J. Fagan, J. Steiner, O. L. Franke
Department of Earth and Planetary Sciences
City College of CUNY, New York, N. Y. 10031

In our attempt to understand the surficial, subsurface, and tectonic factors that have led to the development and maintenance of the highland-lowland escarpment across the fretted terrain, Viking orbiter medium resolution imagery of the Ismenius Lacus, Deuteronilus Mensae and Protonilus Mensae region is being studied. The purpose of this examination is to attempt further subdivision of the major map units previously described and mapped (1, 2, 3, 4) and establish stratigraphic units which will aid in and allow a better understanding of the geology of the region. Sharp (5) first noted the abrupt escarpment between the highlands and lowlands in the vicinity of the fretted terrains and indicated that the wall materials of the escarpment itself as well as that of the outlying mesas and buttes were uniform and massive. He indicated, at the time, that the escarpment walls did not appear to have identifiable layering or structure. Greely and Guest (1) and Lucchitta (2) in their descriptive material for the Ismenius Lacus and Casius Quadrangles, respectively, implied the presence of layered material.

The existence of layered plateau and mesa terrain was reported by Guest et al. (6) for the Cydonia region. They noted that the mesas bordering the highland-lowland escarpment were remnants of the cratered plateau material of the highlands. Guest et al. (7) believed that these terrains were probably composed of flat-lying beds of eolian sediments and lava. Recently Carr (6) reported that layers are distinctly visible in canyon and channel walls cut into the intercrater plains material. The intercrater plains material which comprises the uplands plateau in our study area is described by Carr (7) as being a complex succession of bedded units.

Preliminary reconnaisance observations of the study area indicate that the upland plateau terrain, as well as the mesas and buttes of the fretted terrain, are composed of well defined layered material (Figs. 1 and 2). These units will ultimately be used in determining the stratigraphic framework and geological development of the area. As one proceeds in a northerly direction from the plateau towards the lowland plains, a series of flat lying benches and mesa/butte surfaces are observed. In this area the plateau surface itself is characterized by a moderate to bright

albedo surface (Figs. 1 and 2). Many recent and ancient craters are observed, as well as numerous subsidence depressions as described by Fagan (see this NASA TM). At this stage of the study it is assumed that the surface material is volcanic in origin. The plateau material is also seen to cap, either completely or partially, at about the same topographic level, the mesas which border the upland (Fig. 1). Proceeding across the fretted terrain, isolated topographic surfaces of lower elevation are observed. These appear to be composed of layered material which can be projected back and below the surface material of the plateau terrain. Some mesas have a step-like configuration at their edges, whereas others are bordered by uniformly steep slopes. At least three stratigraphic units have been noted. Two of these units are indicated in Fig. 1 and can be clearly mapped and correlated with others in the area based on their stratigraphic and topographic position. It is believed that unit B, in particular, can also be observed as a bench-former along the channel walls that cut the plateau terrain in the area that immediately adjoins the escarpment (Fig. 1) and further to the south (Fig. 2). In places the lower stratigraphic units appear to be covered and draped by wind blown/volcanic material and elsewhere by "flow" material (Fig. 1). In addition, "ghost-like" relicts of partially erroded and buried mesas can be observed masked by overlying lowlands material. Lower elevation mesa surfaces appear to have been buried on their plains facing sides giving the appearance of tilting in that direction.

Figure 3 is a composite diagram which illustrates our preliminary interpretation of the stratigraphic, topographic and structural relationships for the units observed in the area. Topographic and stratigraphic surfaces, in this first approximation, are assumed to be nearly horizontal and are presently assumed to be dip slopes. Photogrammetric, inclinometric, and enhancement techniques are being employed to determine: 1) actual slope angle and direction, 2) dip angles and directions, 3) units exposed along escarpment and channel walls but are obscured by deep shadows or very bright illumination. Topographic development appears to be operating in both a vertical and horizontal sense. Active processes such as sapping and slope failure are being investigated as agents responsible for vertical degradation. Intensive wind erosion may account for the planation of the horizontal surfaces. Franke (this NASA TM) is examining the maintenance of the escarpment from a slope stability standpoint. Other authors have already invoked sapping (8) or thermokarst processes (9) as the major process involved in escarpment development. Stratigraphic correlation and extension will attempt to employ the techniques of Scott and Tanaka (10) as well as those being developed by Steiner (this NASA TM) in an attempt to determine the areal extent and thickness of all observable units.

REFERENCES: 1) Greeley, R., and Guest, J.E., 1978, USGS Map I-1038. 2) Lucchitta, B.D., 1978, USGS Map I-1065. 3) Scott,D.H. and Carr, M.H., 1977, USGS Map I-1083. 4) Underwood, J. R.,Jr. and Trask, N. J., 1977, USGA Map I-1048. 5) Sharp, R.P., 1973, JGR m 78, p. 4073-4083. 6) Guest, J.E. et al., 1977, JGR, 82, p. 4111-4120. 7) Carr, M.H., 1980, Space Sci.Rev., 25, p.231-234. 8) Pieri, D.C. et al., 1980, NASA-TM 81776, p. 292-294. 9) Brook, G.A., 1980, NASA-TM 82385, p.369-372. 10) Scott,D.H., and Tanaka, K. L., 1981, Icarus, 45, p.304-319.

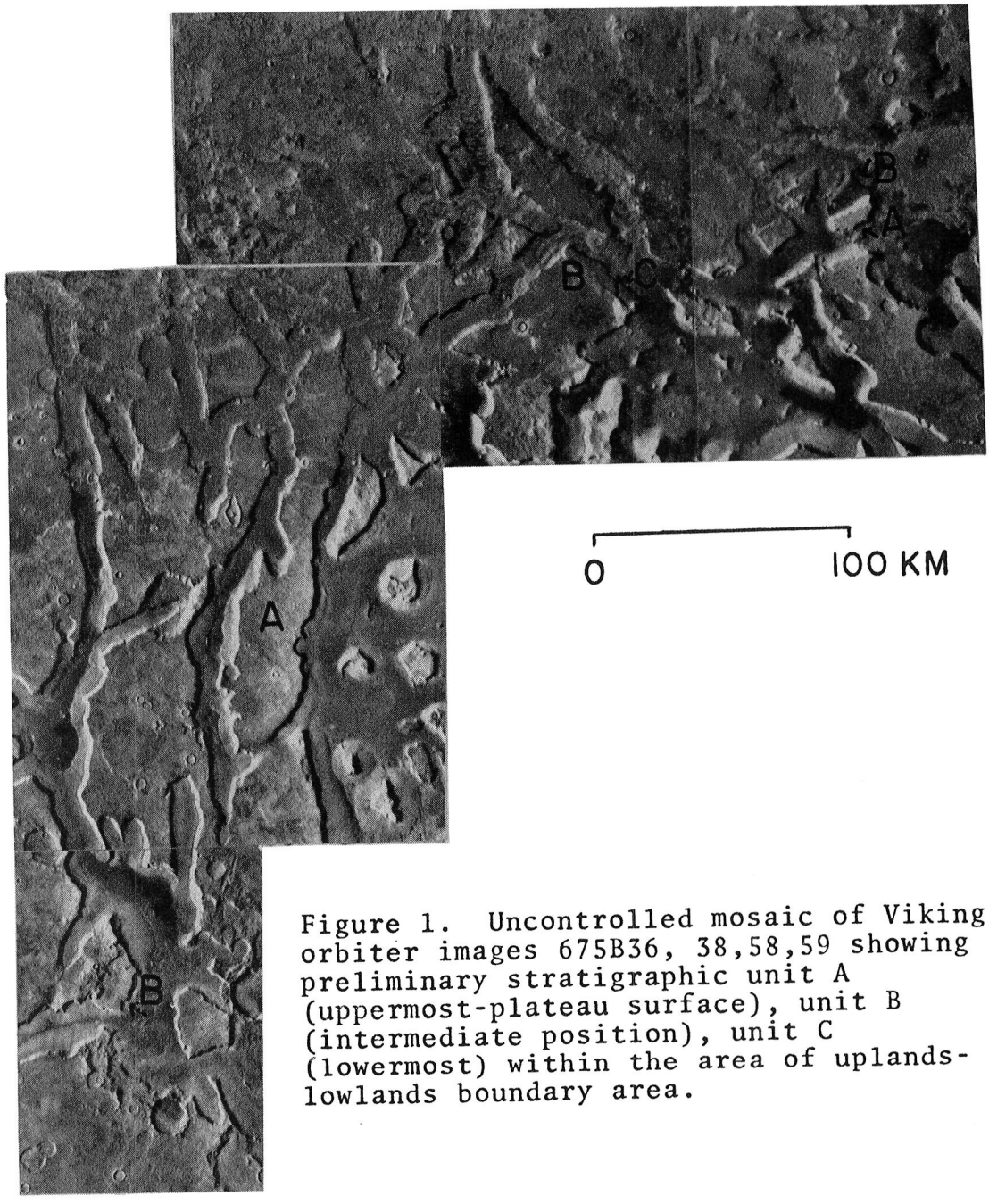


Figure 1. Uncontrolled mosaic of Viking orbiter images 675B36, 38,58,59 showing preliminary stratigraphic unit A (uppermost-plateau surface), unit B (intermediate position), unit C (lowermost) within the area of uplands-lowlands boundary area.

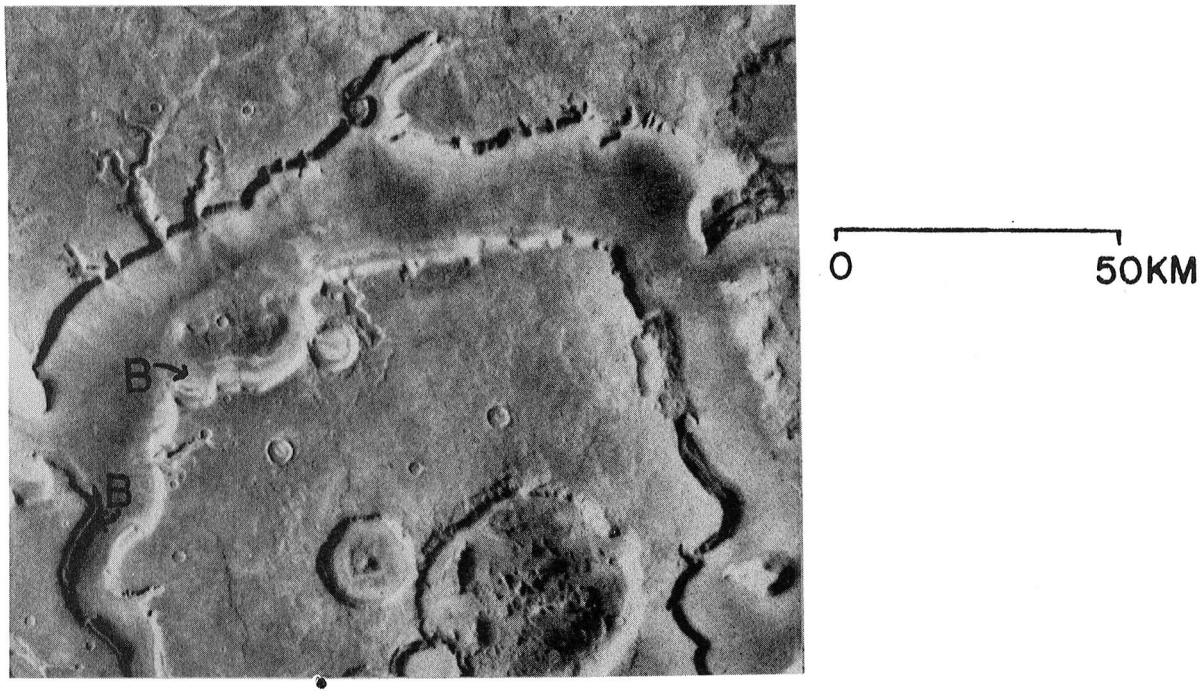


Figure 2. Viking orbiter images 567A01 at 37.17°, 343.98° showing the possible occurrence of unit B exposed in a channel wall.

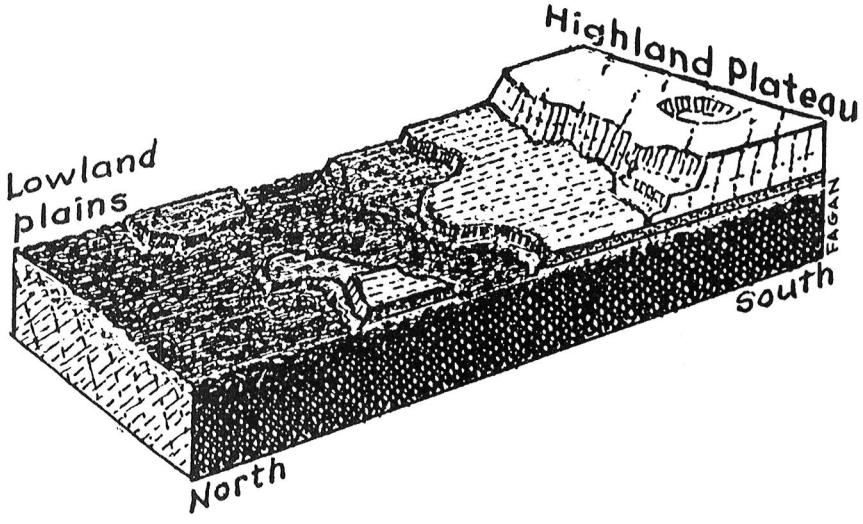


Figure 3. Idealized block diagram showing the preliminary observed relationships between topography, stratigraphy and structure. (not to scale)

# Chapter 9

# REMOTE SENSING AND REGOLITH CHEMISTRY

# THE ROUGHNESS OF THE VENUSIAN SURFACE: A PROGRESS REPORT

Gerald G. Schaber, U.S. Geological Survey, Flagstaff, AZ 86001

A significant amount of geologically important information on Venus' surface roughness is available from careful analysis of both Earth-based and Pioneer-Venus (P-V) radar observations. An investigation of surface roughness on Venus, supported by the NASA Geology Program, was initiated in FY 81. During most of FY 81 the effort was concentrated on mapping and interpreting the significance of several global-scale, linear surface disruptions recognized by this investigator during preliminary analysis of P-V altimetry, rms slope data and radar image maps. The disruption zones in question lie within lat 40° N. to 43° S. and long 60° to 300°. During FY 81, two abstracts were prepared and two oral presentations given at the Baton Rouge Planetary Geology Principal Investigator's Meeting in January 1981, and the Houston Planetary Science Conference in March 1981 [1,2]. Early in FY 82 (December 1981) an abstract was prepared, and an invited oral presentation given on global-scale rifting on Venus at the Planetary Rifting Conference at Napa Valley, CA [3].

The second phase of this study to determine Venus' surface roughness, and to assess its geologic and tectonic significance, has involved the correlation of all available Earth-based and P-V data sets, including radar brightness images (P-V and Earth-based), and P-V rms slope maps (C-factor), reflectivity (Rho-factor) maps, altimetry and gravity data. All data sets have been scaled to 1:50 million and prepared as positive prints and positive transparencies to facilitate direct comparison. Computer generated topographic profiles from both along and across P-V orbital tracks are available, in addition to isometric, 3-D graphics and complete image processing flexibility including interactive computer analysis of all Venus data sets.

When the various Venusian data sets are compared, many interesting relations are revealed but few consistent trends have appeared. The best linear correlation is between high-resolution gravity anomalies and topography; however, the currently available gravity data has not yet been corrected for mass, a necessary step for proper understanding of any gravity anomalies. Increases in rms slope values (above the Venus average) on Venus are almost always associated with changes in relief of a scale resolvable in the P-V altimetry data. The highest rms slopes are correlated with the highest terrains or the onset of the abrupt walls of the ridged-rift valleys associated with Beta and Phoebe Regios and the areas south and east of Aphrodite Terra [1,2,3].

The large shallow "planitias" on Venus are poorly defined on the Hagfors rms slope maps but are, at least in part, delineated as regions of low radar scattering (indicating few surface blocks) on the Earth-based and P-V radar brightness images. Circular and irregular areas of greatly reduced rms slope values or radar-brightness are also observed in the data. A few of these areas show reduced roughness values at both the centimeter and dekameter scale; however, most areas appear to be smooth at one or the other, but not both scales. These local differences in rms slope and radar brightness are providing important

information regarding the scale of surface roughness and possible geologic processes that are operating on the surface.

Another important P-V data set is the reflectivity or Rho-factor data. The Rho-factor, a function of reflectivity per unit area, is derived from the amplitude of the return echo. Interpretation of the reflectivity values is, however, not as simple as that of the C-factor (the shape of the radar echo) from which the rms slope data is generated. The reflectivity values are affected by surface slopes, surface scatterers, and surface electrical properties in a complex manner not well understood.

Preliminary analysis of the Rho-factor image data has, however, verified the existence of terrains with quite different Rho-factor values. In general, terrains of moderately high elevation and moderately high (5-7°) rms slopes from the C-factor analysis appear to have rather low Rho-factor values. Those terrains with the highest average rms slopes (> 10°) have very high Rho-factor values with few exceptions. Examples of terrains with low values include Tellus Regio, Alpha Regio, the foothills east and southeast of Ishtar Terra and the foothills surounding Aphrodite Terra. Examples of terrains with very high Rho-factor values include Rhea Mons (well defined in the Rho-factor map), Maxwell Montes and the three higher massifs (Ovda, Thetis, and Atla Regios) of Aphrodite Terra. It is probable that the regions of low reflectivity, or Rho-factor, have an overall lower surface density (and lower dielectric constant) than the high Rho-factor regions because of less abundant rocky debris of 2 cm to 20 cm scale. A combination of rolling 5-7° rms slopes (averaged over the 30 km altimeter footprint) and single or monotonic scattering from surface rocks may be responsible for keeping the C-factor up and the Rho-factor down in these regions. The lowest C-factor (highest rms slopes) surfaces with the highest Rho-factor values are likely characterized by extremely blocky slopes causing multiple scattering which, together with a higher overall dielectric constant (higher surface density), keeps the Rho-factor high. The ridge-and-trough complexes (Artemis, Diana and Dali Chasmata) south and east of Aphrodite Terra have a surprisingly low average Rho-factor value considering that these postulated rift valleys have the highest rms slopes on Venus and should be extremely blocky. Analysis of the P-V Rho-factor or reflectivity data will be done in concert with the other data sets; hypotheses to explain the observed relationships are presently being formulated.

An excellent high resolution (3 km radar cell size) image of Maxwell Montes, obtained by Don Campbell at Arecibo, P.R. in 1980 has recently been processed and is providing important, new geologic and tectonic information about this highly elevated feature on Venus. Both like- and cross-polarized components of the return signal were acquired for this exciting new image.

References

1. Schaber, G. G. and Masursky, Harold (1981) Ridge-and-Trench systems of Venus and global rift valleys on Earth (abs.), in Reports of Planetary Geology Program, NASA Tech. Mem. 82385, p. 82-84.

2. Schaber, G. G. and Masursky Harold (1981) Large-scale equatorial and midlatitude surface disruptions on Venus (abs.), in Lunar and Planetary Science XII, p. 929-931. The Lunar and Planetary Institute, Houston, TX.
3. Schaber, G. G. (1981) Venus: Global-scale crustal disruption, including rifting of continental rocks (expanded abs.), in Planetary Rifting Conf., Napa Valley, CA, in press. The Lunar and Planetary Institute, Houston, TX.

# CHARACTERISTICS OF MARS NORTH POLAR REGION FROM BISTATIC RADAR

Richard A. Simpson, G. Leonard Tyler, and H. Taylor Howard
Center for Radar Astronomy, Stanford University, Stanford, CA 94305

Bistatic radar observations were conducted over Mars' north polar region with Viking Orbiter 2 during 1977-1978. Unmodulated signals at wavelengths $\lambda = 13$ cm and $\lambda = 3.6$ cm were scattered by the surface and then received on earth. From the characteristics of these signals we have inferred properties of the surface, including its rms roughness $\sigma$ and dielectric constant $\varepsilon$ (Simpson and Tyler, Icarus, 46, 361-389, 1981). Here we will consider the results as they apply to geology and morphology of the polar surface.

Data were obtained along eight specular point ground tracks north of 65°N, each of which traversed a number of surface types. The limiting "footprint" in each case was determined by the intersection of the spacecraft antenna beam with the surface. However, the echo signal was dominated by scattering elements within a smaller, "effective" footprint of radius $\sigma R_p$ centered on the specular point ($R_p$ is Mars' polar radius). Within the effective footprint, only surface structure having horizontal dimensions between about $\lambda$ and $1000\lambda$ contributes to the echoes (Tyler et al., J. Geophys. Res., 76, 2790-2795, 1971). The received echo is an average response to centimeter to decameter-sized roughness, where the average is taken over the footprint (on the order of $10^5$ km$^2$).

The above guidelines apply when the surface is statistically homogeneous and isotropic. When the surface is anisotropic, as the polar dune areas must be, other considerations must be included. For periodic surfaces, scattering may resemble that from a diffraction grating, with resonances depending on $\lambda$ and the geometry. If surfaces have preferential tilts, there may be enhancements in the echo spectrum.

The first order analysis of the echo signals to obtain surface roughness did not show these special effects so we conclude that the surface structure important for the scattering is not dominated by the large-scale dune formations. Over the north polar area we found what appear to be randomly rough surfaces with a trend toward smoother surfaces at the more northern latitudes. This was particularly apparent over Vastitas Borealis, where the roughest surfaces were those that were the farthest south. Around the boundary of the permanent north polar cap, surface texture was highly variable -- with some unusually smooth surfaces detected in certain locations. The permanent cap itself appeared striking, by comparison, because of its statistical homogeneity; its roughness ranged over only $2.5^0 < \sigma < 3.0^0$.

Tsoar et al. (J. Geophys. Res., 84, 8167-8180, 1979) have mapped dune distribution and wind directions in the north polar area. In Fig. 1 we have superimposed bistatic radar ground tracks on the Tsoar et al. map with roughness estimates quantized as shown in the key. The actual tracks lie along the center of the strips; their non-zero width is intended to remind the reader of the actual footprint size -- which is usually larger than the width shown.

Although the correlation is by no means perfect, it is clear that the three quantization levels are meaningful in terms of the units identified by Tsoar et al. The large polar erg stretching from 110°W to 230°W at about 80°N latitude is uniformly rough (level C). Other, smaller dune areas (e.g., near 82°W, 77°N and near 50°W, 77°N) also fall into this category. The permanent polar cap is responsible for most of the intermediate roughness values (level B), while the plains surrounding the cap tend to be smoothest (level A). Since much of Vastita Borealis was omitted from the Tsoar et al. map, the comparisons in the plains areas are incomplete.

When the effective footprint encompasses a number of different terrain types, the echo shape is dominated by the surface at the specular point. This is particularly true when the specular point is in relatively smooth material -- a strong, narrow echo will appear from the smooth surface regardless of the contributions from the surroundings. For this reason the track which extends from about 175°W, 84°N to about 235°W, 76°N is particularly interesting. Narrow bands of plains material at 195°W and 230°W correlate with sudden decreases in radar roughness. The cap and dune formations also show up well along this track as moderately and very rough materials, respectively.

Because the roughness we are sensing appears to be independent of the quasi-periodic structure visible in images, we have not distinguished between transverse and barchan (or other) dune fields in our analysis. Barchans, however, being more sparse on a planar surface, should produce less scattering and that may be the reason we see less than 3.5° rms roughness along the track near 270°W, 77°N.

Estimates of transverse dune heights range from a few meters to a hundred meters or more. The wavelength of the transverse dunes seen in images is on the order of 1 km, so dune slopes could be less than 1° or larger than 10° depending on the model used. Since we measure an rms roughness on the order of 5° in transverse dune areas, there must be small scale structure superimposed on the visible dunes if the "low dune" model is to hold. A somewhat similar situation occurs in Chryse Planitia where the radar data imply 4-5° rms roughness at small scales (Tyler et al., Science, 193, 812-815, 1976; Simpson and Tyler, J. Geophys. Res., 85, 6610-6614, 1980) but orbital images show little or no structure (Masursky and Crabill, Science, 193, 809-813, 1976). If the "large dune" model holds, then 50 m crest-to-trough heights would be the maximum consistent with the radar results (for 1 km wavelength dunes); small scale structure, in this case, would have to be negligible.

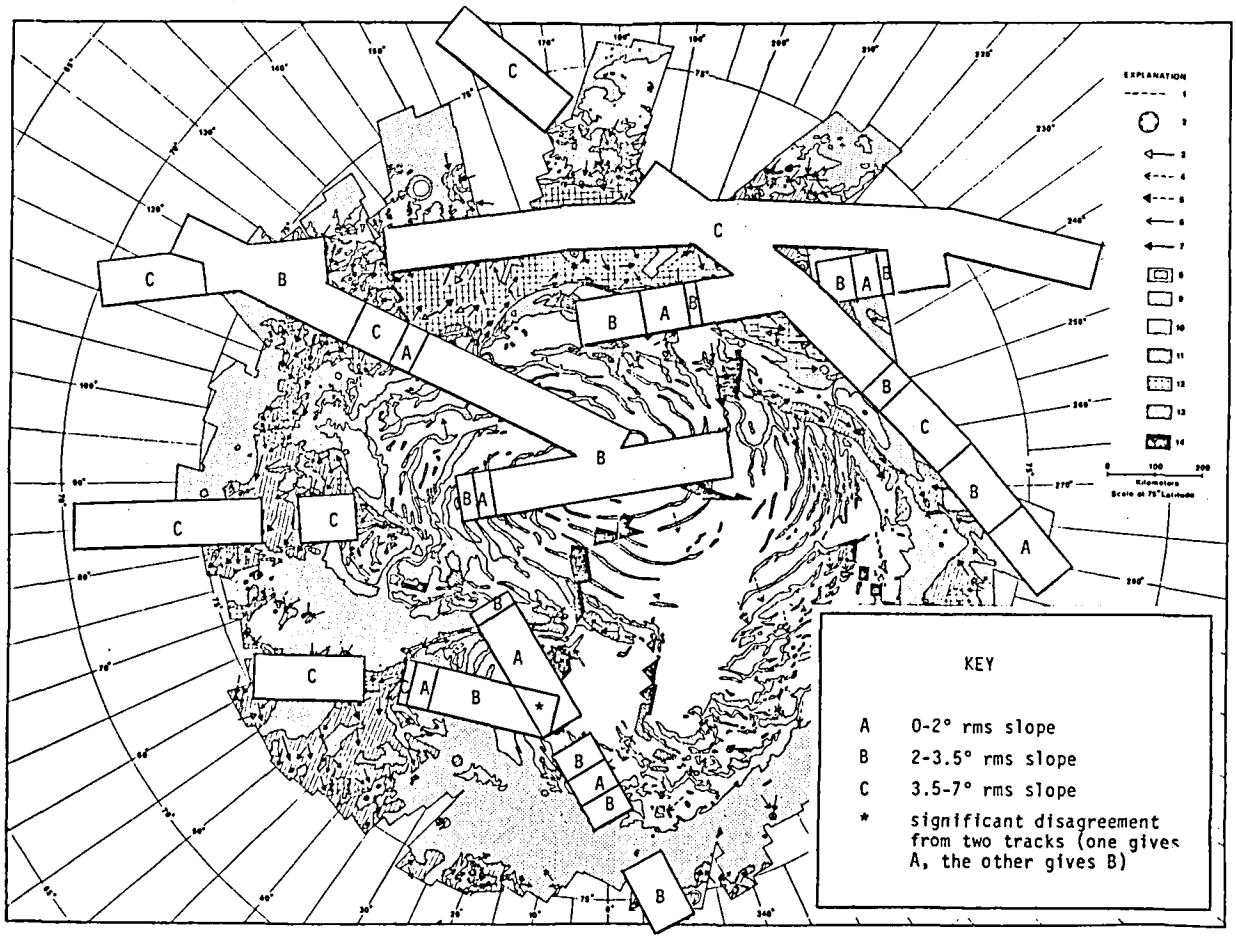


Fig. 1: Map showing dune distribution in Mars' north polar region from Tsoar et al.; overlying strips indicate ground tracks and rms surface roughness estimates from bistatic radar. Tsoar et al. units are (9) plains or layered deposits, (10) perenial ice cap, (11) possible ice dunes, (12) transverse dunes, and (13) barchan dunes; (14) denotes no coverage. Radar-derived surface roughness is greatest in dune areas (C) and least in plains (A); the permanent polar cap is intermediary (B).

# RADAR STUDIES OF THE CRATERED HEMISPHERE OF MARS

P.J.Mouginis-Mark, Dept. Geological Sciences, Brown University, Providence RI 02912; and S.H.Zisk, NEROC Haystack Observatory, Westford MA 01886

Introduction: The cratered terrains represent the most widespread physiographic unit on Mars, covering more than half of the entire planet (1). It is likely that at least some of these materials are very old (2) and, much like the lunar highlands, contain pertinent information regarding the early stages of crustal formation. While most photogeological investigations of Mars have concentrated either on the more easily interpretable northern hemisphere or on specific landforms (such as impact craters, volcanoes or channel systems), the cratered terrains within the southern hemisphere represent integral components in gaining a complete understanding of early martian geological history.

In order to obtain some insight into the surface materials present within the cratered highlands, we are persuing a number of analyses involving the interpretation of the Earth-based radar data acquired between 1971 and 1980 by Downs and coworkers at the Jet Propulsion Laboratory's Goldstone Facility. These radar measurements have generated a wealth of data which has already enabled aspects of the surface topography and scattering properties of Mars to be investigated (e.g. refs.3-5). Together with parameters not considered here, these radar measurements provide topographic information with an areal resolution of about 80-150 km in latitude and 10-25 km in longitude, with a height accuracy of about 100 meters (6,7). Data coverage is almost complete for the entire circumference of Mars between 14-22°S, while numerous groundtracks provide additional data for regions between 3-6°S, 2-4°N, 10-12°N and 21-23°N (8). Recent processing of the data from each opposition has reduced all the height estimates to the 6.1 mb reference surface for Mars (8), thereby facilitating inter-regional elevation comparisons. As a result, it is now possible to study on a near-global scale such attributes as the hypsometry of the cratered highlands and to search for individual features like eroded large impact basins and degraded erosion surfaces.

In this report, we describe two of the techniques that we are currently using in our attempts to characterize the heavily cratered areas of Mars. One particular problem we are attempting to understand for the evolution of martian ancient terrains is the degree of reworking that the original surface received toward the end of the period of intensive meteoroid bombardment. Mapping from both Mariner 9 (2) and Viking Orbiter (9) images has demonstrated that multiple surface units (probably volcanic flows) exist within the southern hemisphere, but the chronology, areal extent and diversity of the resurfacing processes remain poorly constrained. We are tackling this problem by using terrain analysis techniques (10) with the radar data and are comparing the derived relief (both the relative and absolute elevation) with surface units identified from photgeological studies. Here we illustrate these techniques with the derivation of hypsometric curves and autocorrelation functions for parts of the cratered plateau and hilly and cratered materials (2).

Hypsometry: Previous investigations of martian hypsometry (1,11) have concentrated on a global analysis using the various data sets employed to generate the USGS topographic map of Mars (12). As with the other attributes of the radar data (estimates of surface roughness and inherent reflectivity; refs. 6,7), the Goldstone altimetry measurements permit specific surface materials to be characterized solely on the basis of their radar properties. As examples of our investig-

ations of the cratered highlands, radar-derived hypsometric histograms for the cratered plateau and hilly and cratered materials are presented (Figure 1). Each histogram represents the summation of all the point estimates of surface elevation within a 5x5° latitude/longitude sample bin. Between 248-319 data points were used for each of the six samples.

While obvious differences in the shapes of the hypsometric histograms are apparent in Figure 1, their direct relationships to the regional morphology of Mars can be more readily appreciated from a concurrent investigation of the prominent surface features within each area. Craters larger than 5 km in diameter have therefore been identified for the same areas (Figure 2). Histograms with a pronounced central peak (i.e., a small range of elevations) are found to be associated with the cratered plateau material, indicating that the large (>50 km) craters are partially infilled and that the surrounding terrain is flat on a regional scale. In contrast, the histograms for the hilly and cratered material show both bi- and tri-modal height distributions, which could either represent crater floors, rims and the surrounding plains or demonstrate that true changes in regional elevation exist within the area.

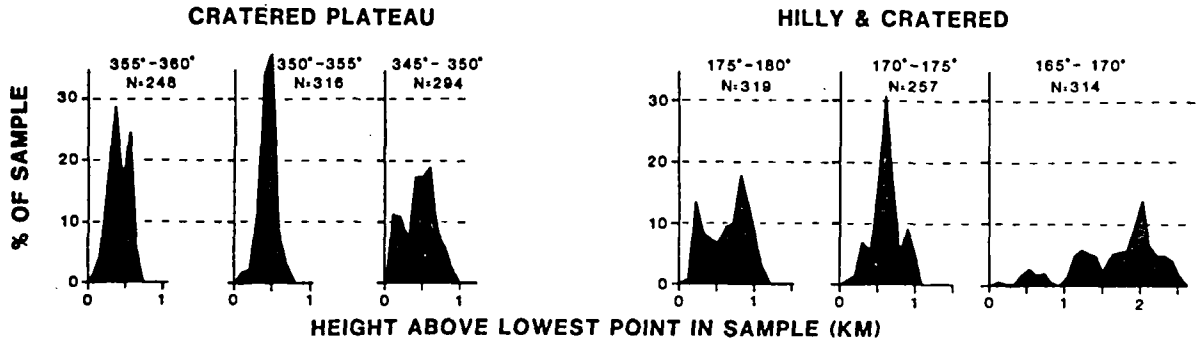


Figure 1: Radar-derived hypsometric histograms for the two main surface materials within the cratered hemisphere of Mars. Latitude range for each sample is 15-20°S. Height measurements are taken from the analysis of Downs et al. (6), here referenced to an arbitary datum set to the lowest elevation for each sample. "N" gives the size of each data sample. Bin size for the height values is 200 meters.

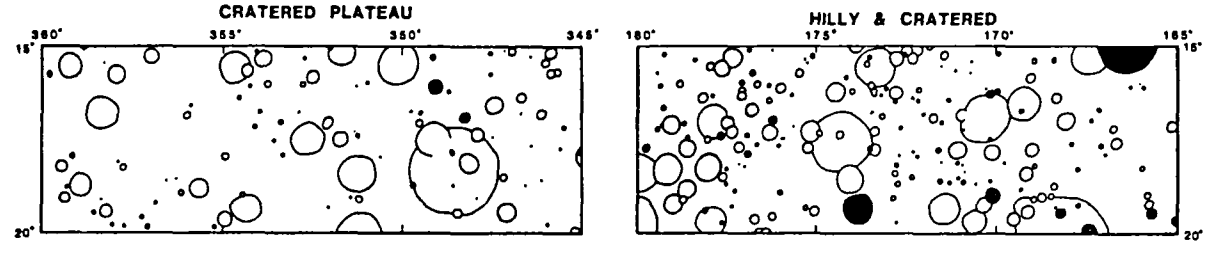


Figure 2: Distribution of all craters larger than 5 km in diameter in the two areas investigated here. Craters with solid outlines possess ejecta blankets, those craters without ejecta deposits are denoted by open outlines.

Autocorrelation: In terms of the information generated for surface units, this technique represents a different approach to the one provided by hypsometry. Because autocorrelation is unable to distinguish between flat surfaces and smooth slopes with a uniform gradient (13,14), no single numerical value can be assigned to the apparent randomness of the topography. Autocorrelation does, however, permit an assessment of the regional periodicity of a surface, thereby permitting features such as degraded lava plains to be distinguished from heavily cratered, possibly multi-origin, terrains. Here we present some preliminary results for the cratered plateau and hilly and cratered materials for surface periodicities ranging from 20 to 340 km (Figure 3).

From an inspection of the autocorrelation functions, it is clear that the cratered plateau material is much less rugged (less random relief) than that which is found in the hilly and cratered material. For lag steps (i.e., surface periodicities) in excess of 80 km, the cratered plateau material possesses changes in relief which remain within narrow (but non-quantified) bounds. This suggests that the entire surface may have been created as a coherent unit. For the hilly and cratered material, however, elevations vary wildly over distances of 100 km or more, indicating that the surface has either been extensively reworked (by cratering ?) or that the original surface(s) were not formed at the same elevation by a single geological event.

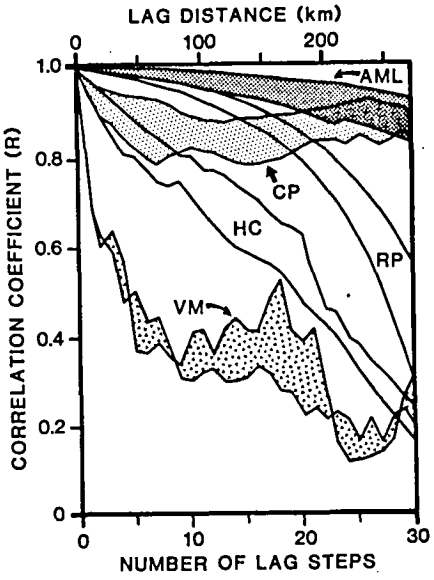


Figure 3: Autocorrelation functions for the two surface units considered in the text and equivalent data for other materials on Mars (ref.10). Data are for: Cratered Plateau (CP) at 16.20-18,25°S, 350-5°W; Hilly and Cratered (HC) at 14.90-16.07°S, 165-180°W; Arsia Mons (AML) at 19.83-21.20°S, 115-130°W; Ridged Plains (RP) at 16,30-21.19°S, 65-80°W; and Valles Marineris (VM) at 15.21-16.70°S, 42.5-52.5°W. All curves are generated with 94 data points separated at 10 km intervals, except for the Valles Marineris curves, which used 62 data points.

Conclusions: Radar altimetry data for isolated areas of the martian surface provide useful information on the distribution of local surface units. With the reduction of the entire topographic data set to the 6.1 mb Mars datum (8), additional investigations of the cratered highlands are clearly possible. In particular, we intend to carry out a comparison of the elevations at a global scale (e.g., comparing Arabia to Memnonia and Hesperia). Correlations between radar topography and other data sets (thermal inertia, color and channel distributions are also planned to search for different surface units.

References: 1) Mutch T.M. et al. (1976) The Geology of Mars, Princeton Univ.Press, N.J.,400pp. 2) Scott D.H. & Carr M.H. (1978) USGS Map I-1083. 3) Roth L.E. et al. (1980) Icarus 42, 287-316. 4) Schaber G.G. (1980) Icarus 42, 159-184. 5) Mouginis-Mark P.J. et al. (1980) PLPSC 11th., 823-838. 6) Downs G.S. et al. (1975) Icarus 26, 273-312. 7) Downs G.S. et al. (1978) Icarus 33, 441-453. 8) Downs et al. (1981) Submitted Science. 9) Greeley R. & Spudis P. (1981) Revs.Geophys.Space Phys. 19, 13-41. 10) Mouginis-Mark P.J. & Zisk S.H. (1981) Abs. 3rd Mars Colloq. 169-171. 11) Coradini M. et al. (1980) Moon & Planets 22, 201-210. 12) USGS Map I-961. 13) Pike R.J. & Rozema W.J. (1975) Ann.Assoc.Amer.Geog. 65, 499-516. 14) Craig R.G. et al. (1980) NASA-TM 82385, 319-321.

# Radar Scatterometry of Sand Dunes And Lava Flows: Results to Date

R. Blom, C. Elachi, A. Sheehan and S. Saunders

In order to quantify and understand the radar backscatter characteristics of geologic surfaces an effort has been underway to acquire and analyze scatterometer data of sand dunes and lava flows. The instruments used have been the four frequency multiple polarization scatterometers on board a NASA C-130 aircraft. These instruments are calibrated, aft looking devices which record radar backscatter in five degree increments from five through fifty degrees. Resolution of the instruments (at 1500 feet altitude) varies from 320 feet for the lowest frequency to 65 feet for the highest frequency. The four frequencies sampled are 400 MHz (P band), 1.6 GHz (L band), 4.75 GHz (C band) and 13.3 GHZ (Ku band). Simultaneous aerial photography is provided. The L band data are of particular interest as VOIR (Venus Orbiting Imaging Radar), SIR-A (Shuttle Imaging Radar) and Seasat all use this band. To date data for four sand dune fields and six volcanic fields have been received. Analysis of sand dune data are nearly complete and analysis of volcanic field data are underway. The following observations emerge from the analysis at this time.

Previous analysis of radar images of sand dunes indicated that the backscatter mechanism was primarily specular (Brown and Saunders 1978, Blom and Elachi 1980). The present analysis confirms this. Figure 1 shows a sample of backscatter data from the Kelso Dunes of California. The pronounced peak in backscatter at 30 degrees is due to specular reflection from a single dune face near the angle of repose (roughly 33 degrees). Previous modelling of dune backscatter indicated that an area 10 wavelengths on a side would produce very strong specular echos (Blom and Elachi, 1980). The observed scatterometer data conform well to that predicted by the model. The major consequence of sand dune scattering behavior is that unvegetated dunes cannot be imaged at incidence angles greater than the angle of repose. Should sand dunes exist on Venus, and should they have an angle of repose similar to terrestrial dunes, the VOIR system will not detect them at the planned incidence angle (45 degrees).

Backscatter data from lava flows at Newberry Volcano, Oregon, is presented in Figure 2. Represented are aa, pahoehoe and obsidian flows along with the surrounding forest. The data are all from the L band scatterometer (for comparison with Seasat and SIR-A data) and each line represents the mean of several independent measurements of the same lava flow. Standard deviations are less than 2 dB. In general the aa flow is the strongest scatterer and the obsidian the weakest. Considerable overlap does exist

however and in any case the differences are generally less than 3 dB. This is especially true for the two basalt flows. The fact that the backscatter from the forest canopy is nearly equal to the basalt flows bodes ill for the use of radar to map volcanic features in tropical terrains should this observation be more generally applicable. Additional data from crossed polarization images or other wavelengths can provide required discrimination (Elachi, et. al., 1980). Note also that the backscatter of the four surfaces converges at 25 degrees. An analysis of Seasat images of Newberry Volcano lava flows supports this observation (Blom and Mouginis-Mark, in preparation; the actual Seasat incidence angle is 23.2 degrees at the center of the swath when earth curvature is accounted for). The rise in backscatter from five to ten degrees for three of the surfaces is unexplained at present.

References:

Blom, R. and C. Elachi, Spaceborne and airborne imaging radar observations of sand dunes: Jour, Geophys. Res., 86, 3061-3072, 1981.

Brown, W. and S. Saunders, Radar backscatter from sand dunes: NASA Tech. Memo., 79729, 137-139, 1978.

Elachi. E., R. Blom, M. Daily, T. Farr and S. Saunders, Radar imaging of volcanic fields and sand dune fields; implications for VOIR: Proc. Radar Geology Workshop, Snowmass, Colorado, JPL Pub. 80-61, 114-150, 1980.

FIGURE 1. Scatterometer Data from Kelso Dunes, CA.

Backscatter data from a single large dune are presented. The plotted lines represent horizontally polarized transmit and receive data from all four available frequencies (except the 13.3 MHz data which are VV). The strong peak in backscatter strength at 30 degrees is due to specular reflection from the dune face. Note also the rapid decrease in backscatter at larger incidence angles.

FIGURE 2. Scatterometer Data of Lava Flows at Newberry, OR.

The plotted data are all from the 1.6 GHz (L band) scatterometer, horizontal polarization on both transmit and receive. Represented are aa, pahoehoe, obsidian, and the forest canopy. The aa has the strongest backscatter at most incidence angles and the obsidian the weakest. The forest has a very similar backscatter behaviour to the basalt flows. The rise in backscatter at low incidence angles is unexplained at present.

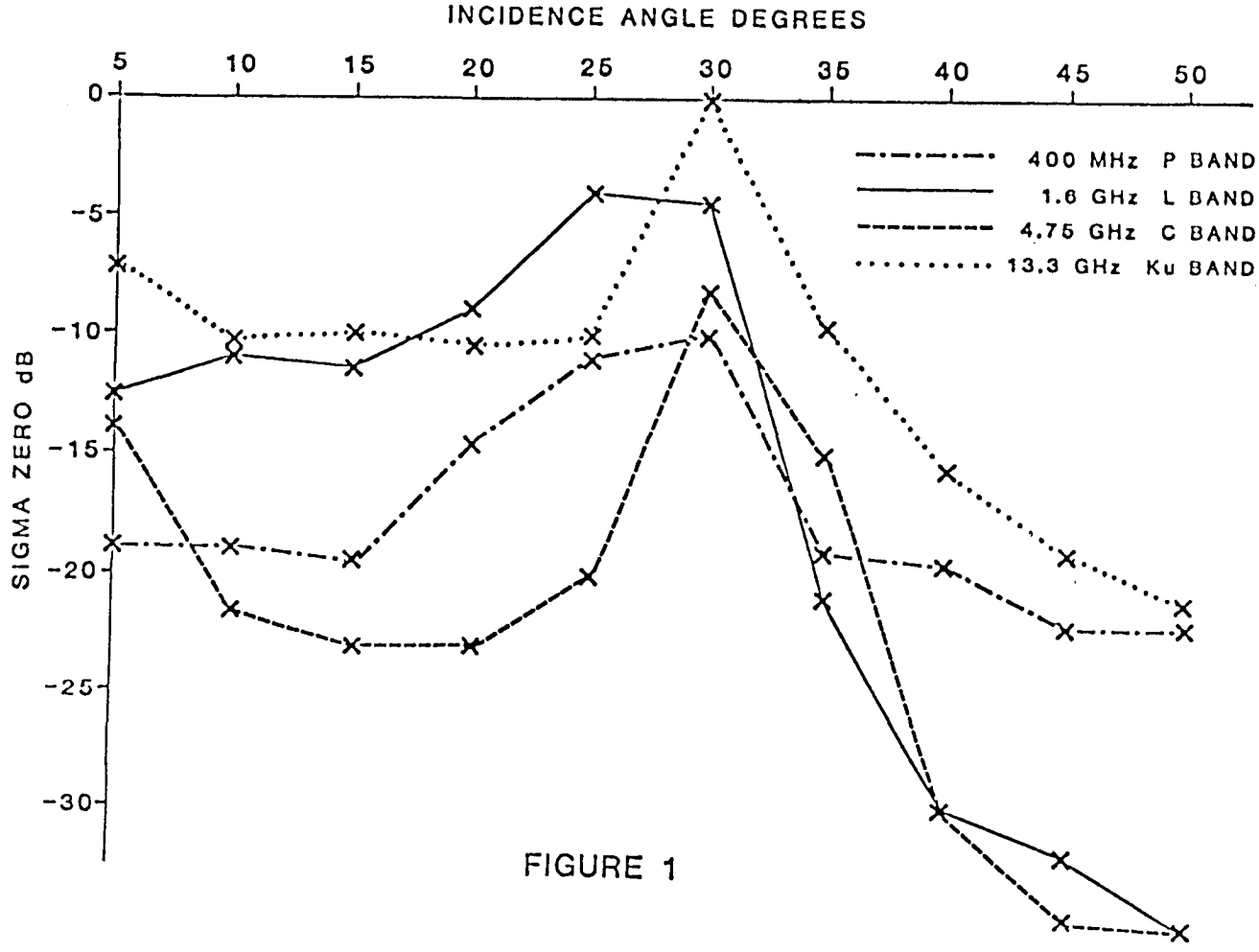


FIGURE 1

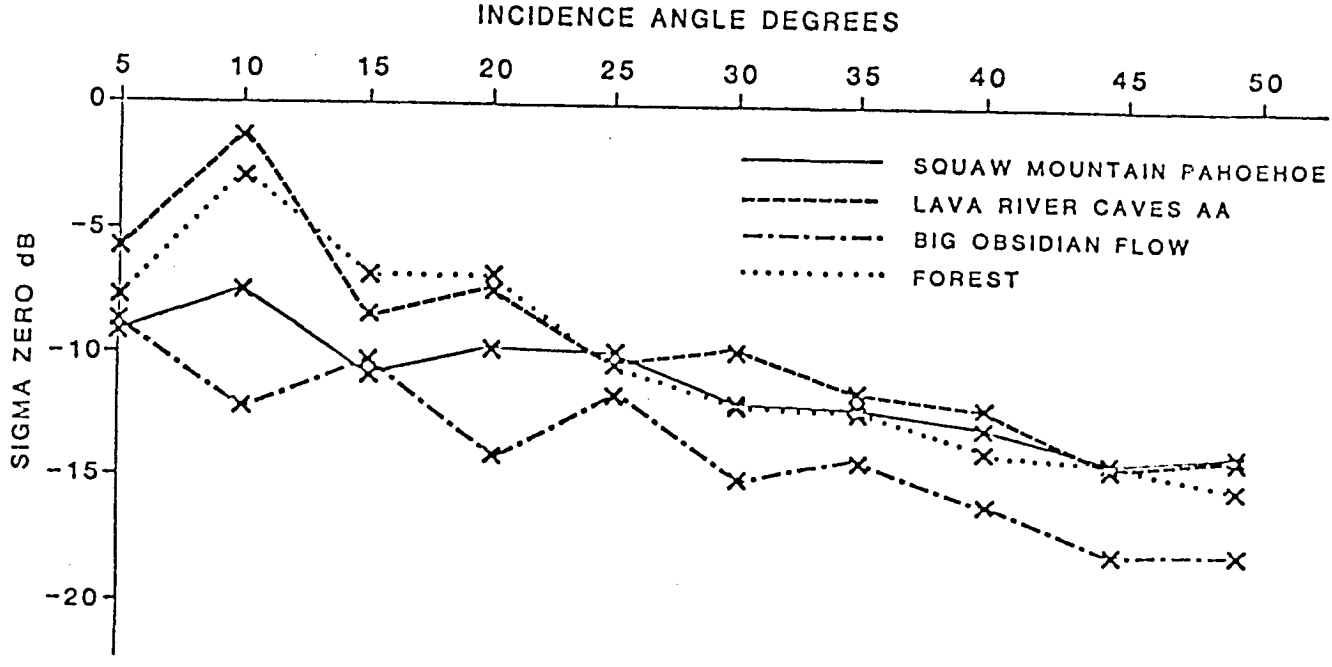


FIGURE 2

# RADAR BACKSCATTER AND IMAGE ANALYSIS RESEARCH IN NORTHERN ARIZONA: A PROGRESS REPORT

Gerald G. Schaber, U.S. Geological Survey, Flagstaff, AZ 86001

During FY 1981, a total of 221 individual strips of side-looking radar images, including many mosaics formatted for stereo viewing have been scaled to 1:250,000, mounted, and evaluated geologically. This extensive data set is unequaled in its completeness; radar images were obtained at a variety of wavelengths, polarization modes, look azimuths, look angles, stereo coverage, using various numbers of radar sensors (Table 1). These data were screened for anomalous radar signatures and field checks were initiated of the anomalous regions. Initial findings were presented during FY 1981 at a USGS radar seminar at Sioux Falls, South Dakota as part of a radar image evaluation program.

Four-frequency, multiple polarization, radar scatterometer data were obtained along 280-km flightlines across the northern Arizona test site. They were received from JSC during FY 1981, and are now being analyzed. Stereo photographs have been obtained along most of the scatterometer ground tracks to allow calibration of variance in small scale relief and surface slope with the radar spectra. Eleven-channel multispectral image data (including the 8- to 14-micron thermal band), 1:3000-scale color aerial photographs, and PRT-5 ground radiation temperature data were also acquired on the same flights as the scatterometer data.

Multiple polarization, multiple look-angle, X-band radar image data and multispectral image data were obtained by JSC in March of 1981 along 24 flightlines that cover the Northern Arizona test site. The radar image data were obtained at both HH-HV and VV-VH polarization, and were specially correlated by Goodyear Aerospace, using no gain change between the like- and cross-polarization channels, so that ratios of return power (as image density) could be made. A set of 66 individual, real-aperture, X-band image strips were purchased from MARS Inc. (Phoenix, AZ) during 1981 for the northern Arizona radar research. These excellent data have 60 percent overlap stereo and in either two or four orthogonal look-directions for the entire test site.

During FY 1982, the HH-HV and VV-VH polarization images will be evaluated to determine any significant differences between these data sets. The results of this analysis will be used to establish which polarization would be more beneficial for the nominal design of the VOIR radar system, and whether cross-polarized image data contain sufficient new information to warrant the additional cost incurred if a second receive channel were added to the current VOIR design.

TABLE I

RADAR IMAGE DATA SET FOR NORTHERN ARIZONA SITE*

| IMAGE SOURCES | WAVELENGTH | POLARIZATION/S | NUMBER OF STRIPS |
|---|---|---|---|
| Westinghouse | $K_a$ (0.86 cm) synthetic aperture | HH-HV | 33 |
| Goodyear/ U.S. Air Force | X(3 cm) synthetic aperture | HH | 17 |
| Motorola/ U.S. Army | X(3 cm) real aperture | HH | 16 |
| Environmental Research Institute of Michigan (ERIM) | X and L (simultaneous) synthetic aperture | HH-HV | 54 |
| Jet Propulsion Laboratory | L(25 cm) synthetic aperture | HH-HV<br>VV-VH | 57 |
| Johnson Space Center | X(3 cm) synthetic aperture | HH-HV<br>VV-VH | 24 |
| Mars, Inc. (Phoenix, AZ) | X(3 cm) real aperture | HH | 66 |
| Seasat | L(25 cm) synthetic aperture | HH | 2 |
| | | Total images | 221 |

* - ground resolution ranges from 3m to 20m
  - incidence angles range from $0^o$ (nadir view) to $80^o$
  - diverse look azimuths and bearings

# REMOTE SENSING OF FISSURE-FED BASALT FLOWS AND THEIR SOURCE AREAS: CRATERS OF THE MOON VOLCANIC FIELD, IDAHO

*L. Viglienzone and R. Greeley, Department of Geology, Arizona State University, Tempe, Arizona 85287*

The recognition of lava textures in remote-sensing images and the relationship of texture-type to distance from the vent are being tested on terrestrial basaltic lava flows as a means of locating fissure vents. Applying remote-sensing techniques to the problem of fissure-vent location may be appropriate for identifying source areas of extensive plains lavas on the Moon and Mars.

This study is a multisensor approach using visible-, near infrared-, and microwave-wavelength images in conjunction with field observations. The study area is the Craters of the Moon (COM) Volcanic Field in the Eastern Snake River Plain. It is one of three volcanic fields aligned along the Great Rift of Idaho (1, 2). The flows in question are those identified by Kuntz et al. (3) as the 2,000 year old to 4,000 year old basaltic pahoehoe and minor aa flows erupted chiefly from fissure vents at Vermillion Chasm and along the Great Rift (Fig. 1). Vent areas are indicated by 'X'.

The use of remote-sensing techniques to correlate fissure-fed flows with their source was first tested on the Keaiwa lava flow, Hawaii (4). The preliminary assessments, made from the comparisons between thermal infrared images and field studies, indicated that primary surface textures and weathering products influenced the TIR signatures. Based in part on these findings, special attention is being given to certain surface properties of the COM flows: 1) primary surface textures of pahoehoe and aa, 2) soil development, 3) vegetation cover, including shrubs, trees, moss, and lichen, 4) glassy crust, and 5) surface roughness as it affects specular reflection and surface scatter.

Previous remote-sensing studies of the COM Volcanic Field were successful in separating pahoehoe and aa lavas and in noting the increase in soil and vegetation on older flows, using LANDSAT data (5, 6) and the JPL, dual polarization L-band radar and L-band Seasat-A radar (7, 8). Newly acquired X-band radar (courtesy Oregon Army National Guard) is added to the list of images in this study.

Comparisons of multispectral radar, aerial photographs, and field observations of the 3,500 to 4,000 year old flow (Fig. 1) have resulted in the following preliminary assessments. First, in accordance with the studies by Swanson (9), shelly pahoehoe occurs only at the vent area, Vermillion Chasm. Forming in response to rapid degassing of the magma at the time of eruption, shelly pahoehoe is an excellent near-vent indicator. It is detected on aerial photographs as very light-toned, smooth-textured areas, and on radar images as noticeably dark areas due to the effects of specular reflection. On-site measurements confirm that it is a very smooth surface with pahoehoe rubble, 2 cm to 25 cm, commonly filling in shallow depressions. Local surface roughness rarely exceeds 1 meter and the most common vegetation, sagebrush, has an average plant height of 50 cm to 60 cm. Other vegetation includes rabbitbrush, grasses, moss, and lichen. Estimated bush cover is 40 percent of the surface, while lichen may actually cover up to 100 percent of any given 20 cm x 20 cm area of the shelly pahoehoe. Secondly, with distance away from Vermillion Chasm, the pahoehoe surface is a filamentous design of mixed-toned gray and rough texture in the aerial photographs. Radar return is a mixed-toned gray. On the ground, the pahoehoe has the Blue Dragon glassy crust and is characterized by numerous collapsed lava tubes, depressions as large as 15 meters in diameter and at least 10 meters deep, and domes up to 10 meters high. Local surface roughness ranges from 2 meters to the 10 meter cases listed above. Average plant height is again 50 cm to 60 cm; estimated bush cover is

35 percent of the surface. Lichen may obscure up to 90 percent of a typical 20 cm x 20 cm surface area of pahoehoe. Thirdly, aa lava is very dark-toned and rough textured on the aerial photographs, and is very light-toned on radar images due to the abundance of surface scatter. Blocks in an aa field range in size from 4 cm to 2 meters. Aa surfaces are devoid of vegetation except for an occasional bush or pine tree. Aa seems to occur in localized areas.

Using these preliminary assessments as a springboard, the next steps to be undertaken include 1) image processing of LANDSAT digital tapes, such as ratioing of MSS bands, to find correlations with other remote-sensing techniques, 2) determining the effects of lichen on the reflectivity of the rock surface, 3) learning the contribution to the overall surface roughness by shrubs, and 4) explaining the distribution of aa lava in terms of preflow topography, rheology of the lava, and distance from the vent area.

## REFERENCES


1. *H.T. Stearns, 1928. Idaho Bur. Mines and Geology Bull. 13, 57.*
2. *M. Prinz, 1970. Geol. Soc. of America Bull. 81, 941-947.*
3. *M.A. Kuntz, R.H. Lefebvre, D.E. Champion, L.A. McBroome, D.R. Mabey, W.D. Stanley, H.R. Covington, J. Ridenour, and R.B. Stotelmeyer, 1980. USGS Open-File Report 80-475, 42.*
4. *R. Greeley, A.R. Peterfreund, J.E. Guest, and R. Tilling, 1979. NASA TM 80339, 268-269.*
5. *R.H. Lefebvre, 1975. Int. Symp. Remote Sensing of Envir. Proc. 10, no. 2, 951-963.*
6. *R.H. Lefebvre and A. Abrams, 1977. Geol. Soc. of America Abs. with Progs. 9, no. 6, 744.*
7. *M. Daily, R. Blom, C. Elachi, and R.S. Saunders, 1980. NASA TM 80339, 362-364.*
8. *C. Elachi, R. Blom, M. Daily, T. Farr, and R.S. Saunders, 1980. Report of the Radar Geology Workshop, JPL Pub. 80-61, 114-150.*
9. *D.A. Swanson, 1973. Geol. Soc. of America Bull. 84, 615-626.*


*FIGURE 1 (following page). Location map of the basalt flows in the Craters of the Moon Volcanic Field, Idaho.*

## CRATERS OF THE MOON VOLCANIC FIELD, IDAHO

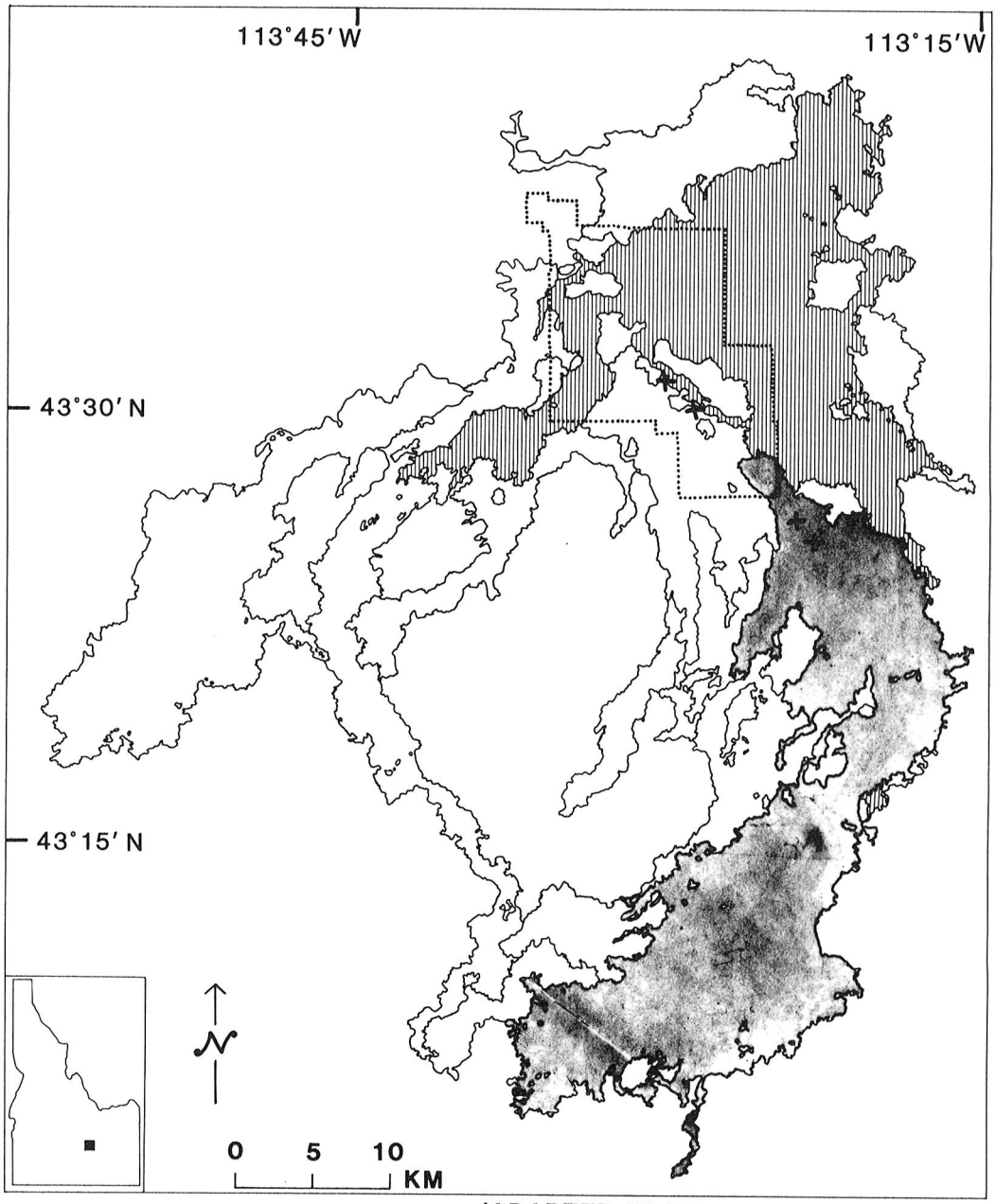


(ADAPTED FROM KUNTZ ET AL., 1980)

| | | |
|---|---|---|
| | | FLOW CONTACT |
| FLOWS: | | APPROXIMATE AGE 2,000 TO 2,500 YEARS B.P. |
| | | APPROXIMATE AGE 3,500 TO 4,000 YEARS B.P. |
| | | BOUNDARY OF COM NATIONAL MONUMENT |

# SURFACE PROPERTIES OF MARS DETERMINED FROM HIGH RESOLUTION INFRARED AND VISUAL DATA

*J. Zimbelman and R. Greeley, Department of Geology, Arizona State University, Tempe, Arizona 85287*

Surface properties have been determined for different geologic units on Mars through the combination of high resolution infrared data and photogeologic mapping of Viking images. These results can be correlated with other data sets, such as radar, to further describe the physical properties of the martian surface.

The Infrared Thermal Mappers (IRTMs) on both Viking orbiters have provided an enormous amount of data on the thermal characteristics of the surface of Mars. Mapping efforts with the IRTM data initially emphasized low spatial resolution ($\geqslant$ 2000 km$^2$) in order to determine the global characteristics of thermal inertia (1,2), predawn temperatures (1,3), and albedo (1,4). Surficial geologic units (5) were compared statistically with thermal inertia and a good correlation was observed (1). Moderate resolution (500 $\sim$ 1000 km$^2$) thermal mapping reveals that local variations in thermal inertia correlated well with dark material present within craters (6,7). High resolution ($<$ 100 km$^2$) thermal data revealed numerous localized thermal variations in regions generally more uniform in thermal properties at poorer resolution (7). High resolution infrared observations have now been combined with photogeologic mapping of the best available imaging data in order to characterize the surface properties of the geologic units.

Northern Syrtis Major (16$^o$ - 22$^o$N, 287$^o$ - 296$^o$W) was chosen for this procedure because high resolution infrared and imaging data were coincident with Earth-based radar data (8). The three data sets provide complementary information on the surface characteristics; imaging data reveal structural and morphologic information of scales greater than ~80 m, infrared data are sensitive to the size of the surface particles within the sampling areas (~13 km$^2$), and radar scattering data provide a measure of the surface roughness on the scale of 0.1 to 100 m within very large sampling areas ($>$ 10$^4$ km$^2$). The difference between surface temperatures measured at 20 $\mu$m and 11 $\mu$m also provides an estimate of the relative abundances of finer-grained soil and coarser blocks and limits the area of possible exposed bedrock to $<$ 7 km$^2$ along the groundtrack.

Three plains units are present in the Syrtis Major area of study. The stratigraphically distinct ridged plains and furrowed plains (both are volcanic plains) are observed to have very similar surface particle sizes, except for a slightly smaller block size on the older furrowed plains, while the smooth plains have a finer average particle diameter and are the least blocky of any of the geologic units examined here (9). Several km-sized craters in the smooth plains are subdued in morphology, such as results from mantling of cratered terrain (10). Crater units are relatively blockier than the plains units and have a larger average particle diameter; one 40 km crater has almost an order of magnitude variation in average particle diameter on its floor and ejecta material intermediate in surface properties between the smooth plains and the ridged and the furrowed plains units (9). The Earth-based radar data cannot resolve the individual geologic units but the northern Syrtis Major area has some of the lowest rms slopes (of reflecting surfaces) in the northern hemisphere (11). All three data sets are consistent with aeolian processes being dominant in the area.

The volcanic region including Ascraeus Mons has also been investigated with both high resolution infrared and imaging data (12). Ascraeus Mons, centered at 11$^o$N, 105$^o$W, is the northernmost of the three large shield volcanoes which comprise the Tharsis Montes (13). Viking images clearly show the sharp contact between flows of the shield and the surrounding

plains. High resolution images of the summit caldera (401B17-23) show sharp contacts between the relatively uniform caldera floors and the complexly faulted caldera walls, as well as several fresh-appearing channeled lava flows at the summit rim. Farther down the shield (401B01-10) the lava flows are less distinct.

IRTM data from revolution 543 of Viking orbiter 1 provide the best resolution available (~13 $km^2$) for Ascraeus Mons (12). The effect of decreasing gas pressure and atmospheric radiation with increasing elevation on thermal measurements (14) were removed from the data to obtain values for the average particle diameter (d) and thermal inertia (I). The entire shield is surfaced by particles with remarkably uniform properties (I ~ 4.8 x $10^{-3}$ cal $cm^{-2}$ $sec^{-1/2}$ $K^{-1}$ and d ~ 0.12 mm) and is coarser than the surrounding plains (I ~ 3.6 and d ~ 0.06 mm) (12). Low to moderate resolution thermal mapping indicates Ascraeus Mons, as well as the other large shields, are within an immense region of low thermal inertia (1,3). The sharp contact between the shield and the plains, coincident with the thermal inertia changes and break in slope, emphasizes the distinct nature of the two units. The caldera walls have the largest thermal inertias (I ~ 6.0) for the entire shield, indicating the rough surface texture visible in the images continues down to individual particles. The lowermost caldera floor and the summit areas around the caldera have similar, slightly lower thermal inertias than the shield as a whole. It is possible that some fine component has been added to these surfaces and is sufficiently thin so that summit lava flows are not masked. It is possible that the finer material at the caldera rim is ash but the lack of a systematic trend to finer material leading to the summit limits the potential distribution of ash. It is unlikely that extensive ash eruptions occurred unless they were so widely dispersed that the entire shield was covered. The apparent lack of ash is consistent with the lack of photogeologic evidence for explosive activity associated with caldera collapse (15). Dust deposition is an alternative explanation, with the rarified atmosphere at the summit not capable of remobilizing the dust.

The heavily cratered terrain in the northern equatorial and mid-latitudes (10°S to 25°N, 355° to 320°W) are being investigated as part of an effort to locate potential outcrops of ancient martian crust. Viking images reveal a variety of crater materials and morphologies as well as intercrater plains. Materials interpreted to be among the oldest extensively exposed surface on Mars (16) were included in the area studied. High resolution (~52 $km^2$) IRTM data indicate that the surface properties of numerous crater and plains materials are very uniform; most geologic contacts do not appear to alter the observed characteristics. Notable exceptions include patches of low albedo material, generally within craters, with thermal inertias (I ~ 9.0) significantly higher than their surroundings (I ~ 2.5 to 4.0). The dark patches are very similar to those mentioned earlier (6) and are presumably also of aeolian origin. It appears that the IRTM data are sampling materials that overlys the various geologic units, including portions of the ancient material, and is effectively masking the underlying units from remote sensing. Thicknesses on the order of several cm would be sufficient to produce this effect (2) so that the total thickness of material is not strongly constrained. It seems very unlikely, however, that areas larger than the resolution cell size of bedrock are exposed within the area of study. Locations east and south of the present study area may prove to be more fruitful for a bedrock search.

The combination of high resolution infrared data with high resolution Viking images, and with other data sets, provides a valuable method for determining the surface properties of individual geologic units on Mars. The high resolution IRTM data represents more than an order of magnitude improvement in spatial resolution over previously published infrared data. The application of this method of investigation to three differing geologic provinces has been

very successful in distinguishing the properties of various geologic units that previously would have been observed as a combination of the individual surface properties. Correlation with additional data sets, particularly radar scattering, would further improve the definition of martian surface properties.

## REFERENCES


1. *H.H. Kieffer et al., 1977. J. Geophys. Res. 82, 4249-4291.*
2. *F.D. Palluconi and H.H. Kieffer, 1981. Icarus 45, 415-426.*
3. *J.R. Zimbelman and H.H. Kieffer, 1979. J. Geophys. Res. 84, 8239-8251.*
4. *L.K. Pleskott and E.D. Miner, 1981. Icarus 45, 179-201.*
5. *P. Spudis and R. Greeley, 1976. NASA TM X-73, 184.*
6. *P.R. Christensen and H.H. Kieffer, 1979. J. Geophys. Res. 84, 8233-8238.*
7. *H.H. Kieffer et al., 1980. Lunar and Planet. Sci. XI, 547-548.*
8. *J.R. Zimbelman and R. Greeley, 1981. Lunar and Planet. Sci. XII, 1230-1232.*
9. *J.R. Zimbelman and R. Greeley, 1981. Proc. 12th Lunar and Planet. Sci. Conf. (in press).*
10. *J.R. Zimbelman and R. Greeley, 1981. Lunar and Planet Sci. XII, 1233-1235.*
11. *R.A. Simpson et al., 1978. Icarus 36, 153-173.*
12. *J.R. Zimbelman and R. Greeley, 1981. Third Internat. Coll. on Mars, Lunar and Planetary Institute Conf. 441, 291-293.*
13. *M.H. Carr, 1975. U.S. Geol. Surv. Map I-893.*
14. *B.J. Jakosky, 1979. J. Geophys. Res. 84, 8252-8262.*
15. *P. Mouginis-Mark, 1981. Lunar and Planet. Sci. XII, 726-728.*
16. *D.H. Scott and M.H. Carr, 1978. U.S. Geol. Surv. Map I-1083.*

MULTIVARIATE CLASSIFICATION OF SURFICIAL UNITS ON MARS FROM VIKING ORBITER COLOR AND INFRARED DATA.

E.A. Guinness, R.E. Arvidson, A. Zent, McDonnell Center for the Space Sciences, Washington Univ., St. Louis, Missouri 63130

We have utilized Viking Orbiter violet, green, and red color data, albedo data, and thermal inertia data (in Mars Consortium Format, see Kieffer, 1981) in an attempt to map surficial units on the Martian surface (Arvidson et al., 1981). The data are highly correlated making it difficult to interpret and to map clusters. The dominant trend is such that as the color ratio values increase, the albedo increases and thermal inertia decreases. A principal components rotation was performed in 5 dimension space, with the variables being R/V, G/V, R/G, albedo, and thermal inertia in an attempt to remove the dominant trend and enhance the residuals. The first component vector, which peirces through the dominant trend of the data, was found to explain about 60% of the variance inherent in the original data. This trend corresponds to "typical Mars", as can be seen by examining an image formed from this component. In order to better examine clusters within the data, contrast stretches were performed on images corresponding to each of the five component directions. In effect, the 5-dimensional data "cigar" was decorrelated by stretching the cigar into a 5-dimensional "sphere". The decorrelated sphere of data, where clusters should be more discernable, was then used in rotating back into the original variable space. Triangle diagrams for the enhanced R/V, albedo, and thermal inertia data occupy a much wider range than do the raw data, especially in darker regions, where several clusters can be discerned. A units map based on the clusters deviate significantly from the color units map of McCord et al (1981), suggesting that the addition of albedo and thermal inertia significantly increases the discriminability of surface units.

References

Arvidson, R.E., E.A. Guinness, A.P. Zent, 1981, Efficacy of aeolian processes on Mars - Present and Past, 3rd Int. Colloq. on Mars, LPI Contribution, 441, 6-8.

Kieffer, H.H., 1981, the Mars Consortium global maps, 3rd Int. Colloq. on Mars, LPI Contribution, 441, 133-135.

McCord, T.B. and others, 1981, Mars: Definition and Characterization of global surface units, with compositional emphasis, 3rd Int. Colloq. on Mars, LPI Contribution, 441, 154-155.

RECENT WEATHERING OF ROCKS AT THE VIKING LANDING SITES: EVIDENCE FROM ENHANCED IMAGES AND SPECTRAL ESTIMATE RATIOS. Edwin L. Strickland, III
Dept. Earth, Planet. Sci., Washington Univ., St. Louis, Mo. 63130

Color enhanced images of the Viking Landing sites (1) show that many of the rock surfaces have high albedo and a unique "green" color -- relative to the scene average -- not shared by any other material at the landing sites. The closest match of materials at the sites to these "green" rocks is the "green-blue" soil, present in small patches at the Viking 1 site. This unit has intermediate albedo, and a very weak "green-blue" color similar to the rocks'. The surfaces of the "green" rocks were interpreted to be a weathering coating, formed in situ from the underlying rock materials (1). The "green-blue" soil was suggested to be a thin, patchy eolian deposit, coating both "blue drift" soils and the "rocky flats" patch of duricrust. Spectral estimate ratios (2) of materials at the Viking 1 site, now show that there is a clear spectral similarity between the "green" rock surfaces and the "green--blue" soil. A recent enhancement of an image of sample trenches at "rocky flats" showed that no "orange-red" duricrust is present under the "green-blue" surface; only "rocky blue" soil is present. Thus, "green-blue" soil is present only on the surfaces of "blue" soil units. These materials belong to a well defined spectral sequence that includes many of the units at the Viking 1 site. This sequence may represent the results of recently or currently active weathering processes on Mars.

Using a modification of a technique described by Huck, et al. (3), I estimate the spectral radiance of the light entering the Lander's cameras. Useful spectral radiance estimates extend from 0.45 micrometers (blue) to 1.0 micrometers in the near IR. Despite the low -- 6 channel -- spectral resolution and spectral aliasing of the Lander camera data, these spectral estimates quantitatively characterize first order spectral differences between the martian surface materials.

Spectral radiance estimates are obtained for a few tens of pixels covering targets selected from color enhanced images. Relative spectral reflectance estimates are constructed by dividing the radiance estimate for a target by the estimate for a dust free, sunlit gray-patch on one of the Lander's test charts. Figure 1 shows the reflectance estimate obtained for the martian surface scene average in frame 12A168. To study the spectral differences between various surface units, I construct spectral estimate ratios by dividing a target's radiance estimate by the scene average's estimate. Thus, the estimate ratio for a target shows its spectral properties relative to the scene average reflectance estimate in figure 1.

Spectral estimate ratios for "blue", "green", and "yellow" rocks are shown in figure 2. These represent averages of spectra of multiple targets, except for the "yellow" rock. The "blue" rocks' spectrum slopes sharply downwards from the blue end, is concave upwards in the green region near 0.5 micrometers, and is darker than the scene average in the red and IR portions of the spectrum. The dropoff at the IR end suggests the presence of relatively strong absorption at or beyond 1.0 micrometers. This is consistent with the "blue" rocks being relatively unweathered mafic igneous rocks.

The "green" rocks' spectrum shows the appearance of strong absorption at the blue end, and a distinctive "hump" in the curve appears in the green at

0.50 to 0.525 micrometers. This is responsible for the bright "green" color of these rocks in the color enhanced images. (Note that the real color of the rocks is a moderate olive brown, compared with a scene average of moderate yellowish brown.) The "green" rocks are significantly brighter than the scene average: about 30% in the near IR. The ~1.0 micron absor tion is still present, though not as strong.

The "yellow" rock's spectrum continue the trend. Reflectance at short wavelengths drops off even stronger than the "green" rocks', while the "hump" peaks at longer wavelengths, forming a plateau around .6 micrometer. It remains high through the near IR, with the 1 micron absorption still present, but, again, weaker.

Figure 3 shows again the "yellow" rock's spectral estimate ratio, but now compares it with "orange-red" cobbles, "orange-red" soil (duricrust) and "red" soil. Absorption at short wavelengths continues to increase, but the "hump" flattens out in the "orange-red" units, the overall albedo starts to drop, and the entire spectral ratio slopes up toward the near IR. The ~1.0 micron feature is still weakly present in the "orange-red" cobbles, but is inverted in the "orange-red" soils' spectrum; it is now weaker than in the scene average. Instead, weak absorption appears at about 0.95 micrometers, corresponding to the dip in the reflectance estimate curve for the scene average.

The "red" soils' spectrum is only a poor continuation of this spectral sequence. While it continues the decline in albedo at long wavelengths, nearly paralleling the "orange-red" soils' spectrum, it doesn't bend in the visible, and crosses the "orange-red" soils' curve at the blue end. The match of the "orange-red" soil, and the poor fit to the spectral sequence of the "red" soil, both may be coincidental. Both soils appear (1) to be eolian units transported into this site, and unrelated to the rock materials there.

Figure 4 compares the "green"rocks' spectrum with that of three "green--blue" soils. The vertical scale of the soils has been expanded 3.75 times, and they have been vertically displaced for clarity. BGS-1 lies adjacent to "blue" soils, and appears to include some in its spectrum. The other "green-blue" soils strongly resemble the "green" rocks' spectrum; the center of the "green" hump is at shorter wavelengths, accounting for the weak "green-blue" color of these soils in the enhanced images. This strongly suggests that this soil is a weathering product of "blue" soils (which spectrally resemble "blue" rocks but have less spectral contrast).

In (1), I suggested that the "green-blue" soil is a thin, patchy eolian unit deposited on most other soils at this site. A new alternative is that this soil represents the *in situ* formation of the "green" weathering product on undisturbed soil. In (4, these abstracts) I present a preliminary correlation between the Viking 1 site stratigraphy and a proposed eolian unit stratigraphy for the west central equatorial region of Mars. The "blue drift" soil at the Viking 1 site may correspond to the dark "blue" Sinus Meridiani unit. Undisturbed areas of "dark blue" soil may start to accumulate "green" weathering product on grain surfaces. These areas would lighten with time, and develop a relatively high green/(violet + orange) ratio in Orbiter color images. Preliminary analysis of 3-color images of the "blue" materials at the mouth of Kasei Vallis, in the Oxia Palus region, and near

the Schiaparelli basin suggests significantly higher than average "green" ratios for some intermediate albedo portions of the Sinus Meridiani unit. This, together with incomplete coverage of the Eos unit by Sinus Meridiani materials and a dusting of recent bright storm dust, may explain the unique, patchy color/albedo pattern of the Sinus Meridiani unit.

References: (1) Strickland, E. L., III Proc. Lunar, Planet. Sci. Conf. 10th. (1979), p. 3055-3077. (2) Strickland, E. L.,III. In Reports of Planetary Geology Program, 1978-1979. NASA TM-80339 p. 71-74. (3) Huck, et al., NASA TM-72692. (4) Strickland, E. L. III, Eolian Stratigraphy of the West Central Equatorial Region of Mars: Viking Lander 1 and Orbiter Color Observations. these abstracts.

Fig. 1.

RELATIVE SPECTRAL REFLECTANCE ESTIMATE MARTIAN SURFACE SCENE AVERAGE: 12A168.

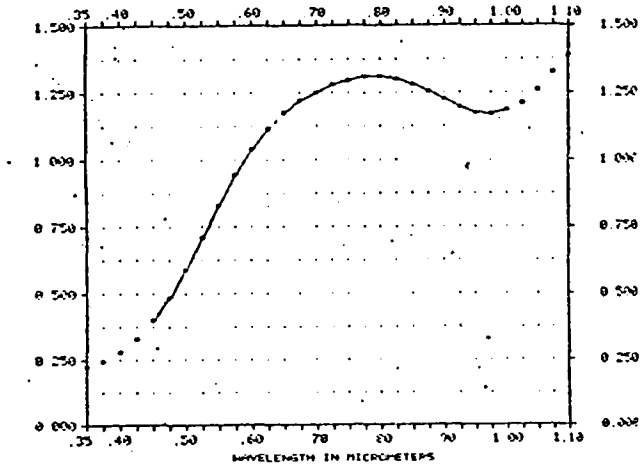

DIVIDED BY AVERAGE OF 5 GRAY PATCHES IN 12A002.

Fig. 2.

BLUE, GREEN, AND YELLOW ROCKS DIVIDED BY SCENE AVERAGE

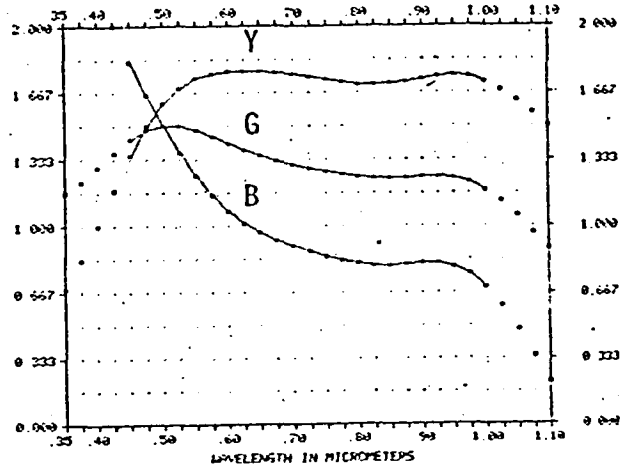


UNNORMALIZED, TO SAME SCALE.

Fig. 3.

RED, ORANGE RED SOILS AND ROCKS, AND YELLOW ROCK. DIVIDED BY SCENE AVERAGE

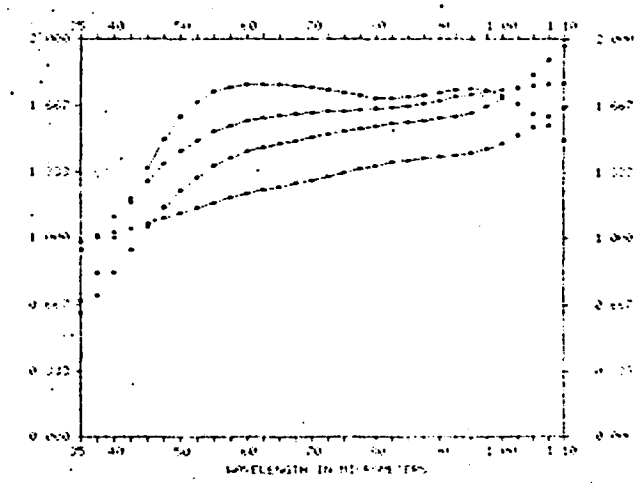

UNNORMALIZED, TO SAME SCALE. FROM TOP: 16A, 08-A2, 08-A5, A5.

Fig. 4.

GREEN ROCKS AVERAGE VS. BLUE-GREEN SOILS DIVIDED BY SCENE AVERAGE

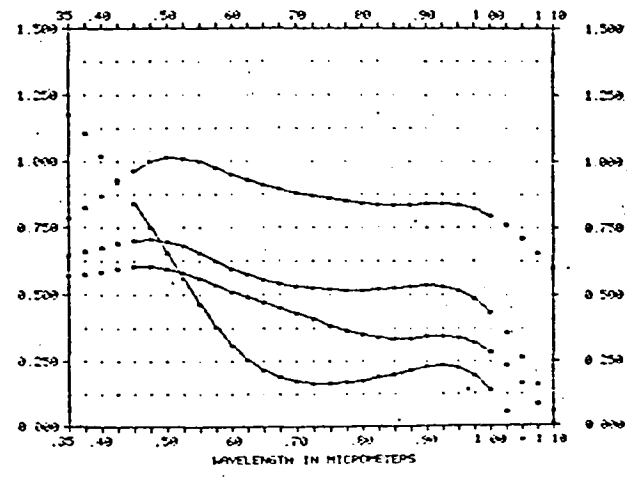

DES SCALE: X 3.75. FROM TOP: GRX AV., 365-2, 365-3, 365-1.

A TRANSPARENT ATMOSPHERE IN THE UV: RESULTS FROM DARKENING OF VIKING LANDER UV CHIPS.

Zent, A.P., E.A. Guinness, R.E. Arvidson, Dept. of Earth and Planetary Sciences, Washington University, St. Louis, Missouri 63130, C.R. Spitzer, NASA Langely Research Center, Hampton, Va. 23665.

Ultraviolet degradable patches were mounted on the Viking Lander Reference Test Charts as dosimeters to estimate the UV flux reaching the surface of Mars (1). An estimate of the UV flux is pertinent to understanding the rate of UV induced photostimulated oxidation and breakdown of rocks (2) and the rate of production of oxides and superoxides detected during Viking Lander biology experiments (3). We have estimated the UV flux incident on the surface of Mars, based on the extent of chip darkening and comparison with preliminary laboratory calibration experiments.

Each Viking Lander is equipped with three Reference Tests Charts (RTC) (4). Each RTC includes two patches that darken when exposed to ultraviolet radiation, and, in addition a blue, green, red and eleven gray patches. Each gray patch is a Lambertian scatterer with a bi-directional normal reflectance that is independent of wavelength (5). Of the approximately 500 frames covering the Lander 1 RTCs, only four proved useful for UV determinations because of problems related to saturation of the UV chips and to periods during which the atmospheric optical depth was high. Only blue channel data were utilized since preliminary analysis and consideration of calibration data indicated that the extent of darkening would be trivial in the other Lander channels.

The bi-directional reflectance of the UV patches was assumed to vary as a function of time and lighting geometry. The calibration data suggested that the patches darkened exponentially over time. Preliminary analysis of the Lander data suggested that the UV patches were not Lambertian scatterers. Thus, the Hapke-Irvine photometric function was adopted for the UV patches. Furthermore, the photometric function of the UV patches varies only as the incidence angle, since the emission angle is always zero. These assumptions lead to the following equation that describes the reflectance of the UV patches as a function of time and incidence angle:

$$\langle\rho(i,t)\rangle = 2\langle\rho_o\rangle \cos i \exp -(\beta i) \exp -(\theta t)/(\cos i+1) \quad (1)$$

where $\langle\rho(i,t)\rangle$ is the bi-directional reflectance of the patch at a given time and incidence angle, $\langle\rho_o\rangle$ is the original reflectance of the UV patch and $\beta$ and $\theta$ are coefficients which describe the decrease in brightness of the patches with incidence angle and time, respectively. Rearranging eq. (1) to define the quantity P:

$$P = (\cos i+1)\langle\rho(i,t)\rangle/2\langle\rho o\rangle = \exp -(\beta i) \exp -(\theta t) \quad (2)$$

we can write:

$$\log P = -\beta i - \theta t \quad (3)$$

The value of log P was computed from the Mars data, with $\langle\rho o\rangle$ determined from the calibration data. The parameters $\beta$ and $\theta$ were estimated from a multilinear regression analysis of the data.

The change in bi-directional normal reflectance with time can be derived by setting i equal to zero degrees in equation (3). The reflectance of the blue chip remained essentially constant throughout the period of time during which UV data was acquired. On the other hand, the reflectance of the UV2 chip has decreased from about 0.79 to about 0.60. Based on comparison of the Mars data with laboratory calibration data there is no reason to reject the hypothesis that the rate and extent of darkening of the UV chips is the same as that for the laboratory data. Since the laboratory experiments were conducted with no atmosphere, we conclude that the Martian atmosphere is essentially transparent for the wavelengths to which the UV chip is sensitive.

References

1. Shorthill, R.W., R.E. Hutton, H.J. Moore, R.R. Scott, 1972, Martian physical properties experiments: The Viking Lander., Icarus, 16, 217.

2. Huguenin, R.L., 1973, Photo-stimulated oxidation of magnetite., J. Geophys. Res., 78, 8481-8506.

3. Klein, H.P., 1977, The Viking biological investigation: General aspects., J. Geophys. Res., 82, 4677-4680.

4. Huck, F.O., D.J. Jobson, S.K. Park, S.D. Wall, R.E. Arvidson, W.R. Patterson and W.D. Benton, 1977, Spectrophotometric and color estimates of the Viking Lander sites., J. Geophys. Res., 82, 4401-4411.

5. Wall, S.D., E.E. Burcher, D.J. Jobdson, 1975, Reflectance characteristics of Viking Lander camera reference test charts., NASA Tech. Memo. 72762.

6. IITRI Calibration Tests: Inter-office memo., 1981.

ROCK AND SOIL MAPPING AND CHANGE DETECTION FROM LANDSAT MULTISPECTRAL SCANNER DATA - CLUES TO LIMITS OF INTERRETABILITY FROM VIKING ORBITER COLOR DATA

Raymond E. Arvidson and Patricia A. Jacobberger, McDonnell Center for the Space Sciences, Washington University, St. Louis, Missouri 63130; Dennis Rashka, Dept. Earth and Plant Science, University of Wisconsin-River Falls, Wisconsin, 54022.

Considerable effort is currently being expended in classifying surface units from the three channel (violet, green, red) Viking Orbiter color data and in monitoring wind-blown surface changes using temporal variations in the color and albedo of the surface. Because there are only three relatively broad channels and because of the relatively poor resolution of the data (> 1 km/pixel), considerable thought must be given to the limits of interpretability of these data. These problems can be approached from a theoretical viewpoint, e.g. simulating the spectral aliasing that arises from using only a few broadband channels (Huck et al., 1975). They also can be approached by considering terrestrial examples from an orbital perspective, examples that can also be carefully studied in the field. We chose the latter technique for this study and examined: (a) The extent to which LANDSAT multispectral scanner data can discriminate among units in a complex geologic area in Egypt (Jacobberger et al., 1981a), and (b) The kinds of information that can be derived from examination of 3 separate LANDSAT scenes acquired over SW Kansas during a period of intense drought and wind erosion in 1976 (Jacobberger, 1981b). Egypt was chosen because of a significant field mapping effort currently underway (Batiza et al., 1981), while Kansas was chosen because of its accessability and because of the extent of wind erosion (3-6 cm soil). It would be naive to draw global generalities from our studies with regard to the ability of 3 channel data to map surface units and changes on Mars. Rather, we feel that these two studies have provided important experience into possible pitfalls in interpreting these data, in addition to providing guidelines as to the most useful techniques (e.g. those techniques that provided the closest match to ground truth data) of data processing. We present results for the two cases in terms of: (a) What ground truth information would have been obtained from orbit, (b) What information would have been lost, (c) The most useful technique for processing the data, and (d) Implications for interpreting Martian data.

The Egyptian study was concentrated over the Meatiq Dome, which is abut 20 km across, and composed of a variety of granitic-granodioritic rocks together with quartzofeldspathic to mafic and ultramafic mylonites. The Dome is surrounded by greenschist-facies metamorphic terrain (Jacobberger et al., 1981). We found that principal components color enhancements provided optimum discrimination between the granitoid Dome rocks and the mylonites. In fact, our data provided the best means of accurately interpolating contact relations between field traverses. In addition, color changes between the edges and centers of wadis could be discerned, with wadi centers being brighter and redder than the edges. Alluvium samples acquired across the wadis demonstrate that particles size controls the signature, with the finer grained alluvium from the wadi centers being brighter and redder. These results are corroborated by acquiring spectral reflectance data (0.4 to 1.1 micrometers) for the samples (courtesy J. Gradie, Cornell Univ.) and degrading the data in a manner so as to allow direct comparison with the Landsat data (using

techniques developed by Evans and Adams, 1979). On the other hand, use of the Landsat data did not allow us to discriminate between the granites and the granodiorites within the Dome, e.g. soil size variations were detectable whereas subtle mineralogical variations among rock units within the Dome were not discriminable. Perhaps two lessons can be learned from this study. First, Viking Orbiter color data are typically highly correlated and consist only of 3 channels. Thus, subtle color variations, such as those between various dark regions may be difficult to discern. Therefore, incorporation of more independent data, such as thermal inertia, is very important.

From 3 to 6 cm of soil were removed from parts of southwest Kansas during the drought of 1976 (Jacobberger et al., 1981b). Analyses of three Landsat MSS frames taken over a span of 6 weeks indicate a significant reddening of dryland-farmed fields. On the other hand, circular fields, irrigated by central pivot irrigation systems, changed relatively little. We found that examination of the structure of the brightness histograms for each channel for each date provided the most informative analysis. Field studies of the area provided fundamentally new information that could not have been discerned from the Landsat data. The entire study region is underlain by interconnected dunes covered a thin veneer of immature, organic-darkened regosol. The dunes were too small into have been recognized form LANDSAT data. For Mars, bright material appears to be mobile. However, the mechanisms of entrainment are not well understood. Peterfreund (1981) recently suggested that there is a correlation between areas covered with dunes and areas in which dust storms begin on Mars. Also, we find that the higher resolution Viking Orbiter frames contain a higher areal extent of dunes. Thus, it may be possible that dust is preferentially eroded, as in Kansas, in areas with sand-sized particles. Again, incorporation of thermal inertia and radar data may help to enlighten the situation.

References


Batiza, R., N.C. Sturchio, M. Sultan, E.M. El-Shazly, A.A. Abdel-Mequid, 1980, Geology of the Maetiq Dome: A metamorphic core complex in the central eastern desert of Egypt: Geol. Soc. Amer. Abstracts with Programs, 13, 2, p. 43.

Evans, D. and J.B. Adams, 1979, Comparison of Viking Lander multispectral images and laboratory reflectance spectra of terrestrial samples, Proceedings Lunar and Planetary Science Conf. 10th, 1829-1834.

Huck, F., W. Kelly, R. Arvidson, 1975, Spectral response of the Viking Lander Camera: Preliminary Evaluation, NASA TMX-i72778, 20 p.

Jacobberger, P.A., 1981, Drought-induced wind erosion in southwestern Kansas, U.S.A. - Integration of Landsat, Seasat, and Airborne Multispectral Data, Proc. International Symposium on Remote Sensing of Environment, First Thematic Conference - Remote Sensing of Arid and Semi-Arid Lands, Nov. 3-9, 1981, in press.

Jacobberger, P.A., D.L. Rashka, R.E. Arvidson and R. Batiza, 1981, Use of Landsat Multispectral Scanner Data in Geologic Mapping of the Meatiq Dome, Central Eastern Desert, Egypt, Pro. International Symposium on Remote Sensing of Environment, First Thematic Conference: Remote Sensing of Arid and Semi-Arid Lands, Nov. 3-9, 1981, in press.

Peterfreund, A.R. and others, 1981, Sand on Mars, 3rd Int. Colloq. on Mars, LPI Contribution 441, 188-190.

CLAY MINERALS ON PLANETARY SURFACES: A CAUTIONARY NOTE REGARDING THEIR IDENTIFICATION BY VIS/NIR SPECTRAL REMOTE SENSING

J.L. Gooding*, Earth and Space Sciences Division, Jet Propulsion Laboratory, California Institute of Technology, Pasadena, CA 91109

Introduction. Clay minerals form in the presence of liquid water such that their occurrence on planetary surfaces can be used to decipher the histories of water/regolith interactions on their parent planets. Spectral remote sensing (1), through either Earth- or spacecraft-based observations, is a powerful tool for determining the minerals, including clays, which comprise planetary surfaces. For clay minerals, though, the mid-infrared (~ 3 - 15 μm) is the region of greatest diagnostic value although its use has been severely limited by the low mid-IR emissive energies of distant (from the sun) terrestrial-type bodies and by various atmospheric interferences. Consequently, spectral remote sensing of Martian and asteroid surfaces has been restricted to visible (VIS; 0.35 - 0.7 μm) and near-infrared (NIR; 0.7 - 2.5 μm) regions. Unfortunately, some poorly crystalline or amorphous weathering products of igneous rocks may possess VIS/NIR reflectance spectra which mimic those of clay minerals, thereby introducing the possibility for serious mineralogical misinterpretation of planetary surface compositions and histories. This report illustrates the problem using as examples soil materials developed by fumarolic alteration of basalts at Kilauea volcano, Hawaii.

Pseudo-clay Materials in Altered Basalts. Allophane, a category of nearly amorphous mineral alteration products (2), has long been recognized as a common component of soils developed on lavas and, especially, on vitric ashes. A related material, palagonite, forms by hydrous alteration of basaltic glass and has been advocated previously as a possible analog material for Martian surface fines (3). Comparable materials are currently forming at Kilauea volcano, Hawaii, by fumarolic alteration of tephra and glassy surfaces of pahoehoe flows. Two such materials are noteworthy for their VIS/NIR reflectance spectra which closely, but falsely, resemble those of clay minerals.

Rapid fumarolic alteration of 1971 and 1974 lava flows within Kilauea caldera has produced pale yellow-white sublimate deposits (sample K1980-2A) which overlie red-brown zones of intensely altered basalt glass (sample K1980-2B). The silt-sized (<63 - μm) fractions of both materials possess VIS/NIR reflectance spectra which are surprisingly similar to those of smectites. The spectrum of 2A closely mimics that of montmorillonite whereas, as illustrated in Fig. 1, that of 2B is quite similar to the reflectance spectrum of nontronite. The comparisons are especially striking in the NIR. However, careful analyses by x-ray diffractometry (XRD) and differential thermal analysis (DTA) show that neither 2A nor 2B contain appreciable amounts of smectites. Sample 2B, for example, is essentially amorphous with respect to XRD (Fig. 2) and possesses none of the DTA endotherms which are characteristic of smectites (Fig. 3). In fact, electron microprobe analyses of 2B show it to be a slightly quartz-normative tholeiite. Similarly, 2A possesses none of the XRD or DTA properties expected for smectites or other clay

---

*Current Address: SN2/NASA Johnson Space Center, Houston, TX 77058

minerals. However, if VIS/NIR reflectance spectra were the only analytical data available for these two materials, these soil components could easily be misidentified as smectites.

Implications for Planetary Surface Evolution. On planets such as Earth, Mars, and some asteroids, the existence of water could be conducive to the formation of clay minerals. However, if alteration of volcanic rocks is the dominant soil-forming process, the weathering products may be poorly crystalline allophane rather than clay minerals. Given VIS/NIR reflectance spectrophotmetry as the only means of assessing surface mineralogy, though, clay minerals may not be distinguishable from allophane. The resultant inability to correctly identify such potentially important soil-forming materials could lead to a totally invalid interpretation of regolith composition and history. Consequently, the limitations of VIS/NIR spectral remote sensing as a mineral identification technique argues strongly for greater reliance on data from additional sources, especially laboratory analyses of samples.

Acknowledgement. This work was performed at JPL under contract with NASA through the Planetary Geology Program.

References: (1) Goetz, A.F.H. and L.C. Rowan (1981) Geologic remote sensing. Science, 211, 781-791. (2) Birrell, K.S. and M. Fieldes (1952) Allophane in volcanic ash soils. J. Soil. Sci., 3, 156-166. (3) Allen, C.C., J.L. Gooding, M. Jercinovic, and K. Keil (1981) Altered basaltic glass: a terrestrial analog to the soil of Mars. Icarus, 45, 347-369.

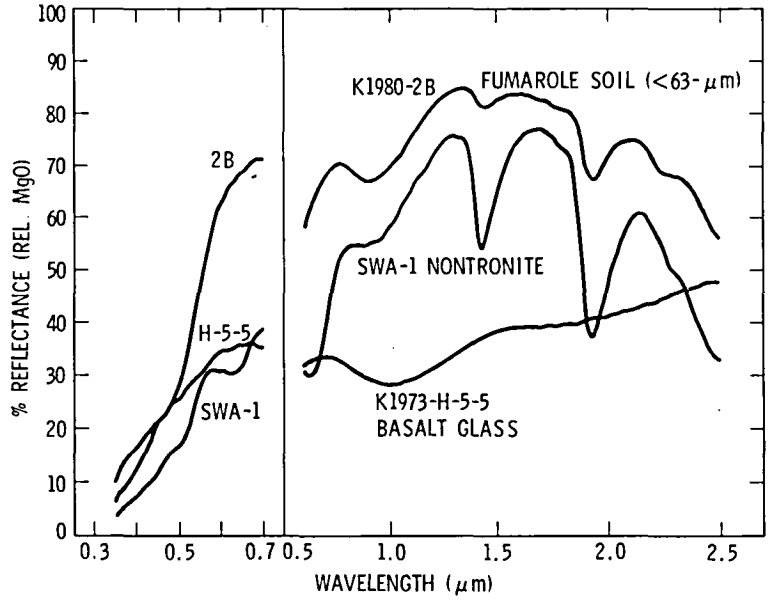


Figure 1. Visible and near-infrared reflectance spectra of a Kilauea fumarole soil compared with those of Kilauean basalt glass and a well-crystallized nontronite. Absorptions at ∿ 1.4 and 1.9 μm are attributed to water whereas those at ∿0.9-1 μm are attributed to $Fe^{2+}$ and that at ∿0.65 μm to $Fe^{3+}$. The fumarole soil spectrally mimics a ferroan smectite, especially in the NIR, although it is not a smectite.

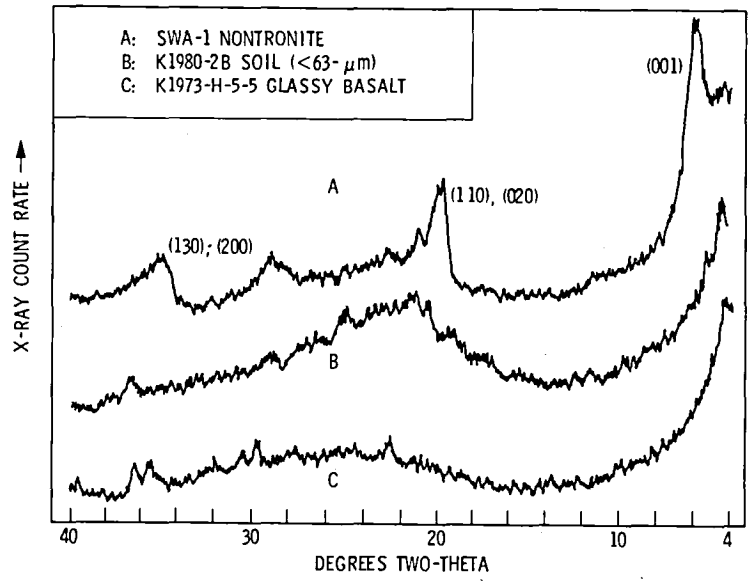


Figure 2. Selected regions of x-ray diffractometer records for the samples listed in Fig. 1. The fumarole soil is largely x-ray amorphous as is the basalt glass. Small peaks in the basalt glass record are due to olivine.

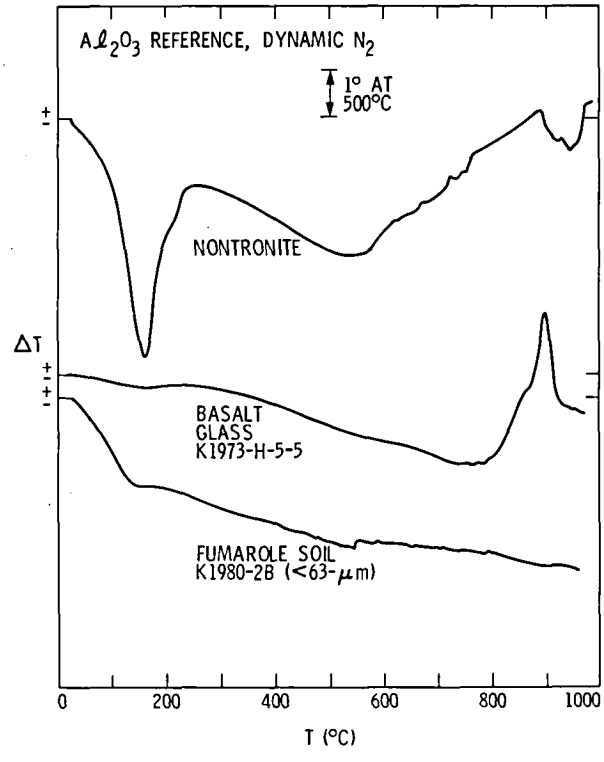


Figure 3. Differential thermal analysis curves (10° C/min heating) for the samples listed in Figs. 1 and 2. The fumarole soil exhibits neither the endotherms characteristic of smectites nor the crystallization endotherm of basalt glass. A weak endotherm at ∿ 150° C may be due to loss of loosely bound water.

# ALTERATION OF ROCKS IN HOT $CO_2$ ATMOSPHERES: PRELIMINARY EXPERIMENTAL RESULTS AND APPLICATION TO VENUS

J.L. Gooding*, Earth and Space Sciences Division, Jet Propulsion Laboratory, California Institute of Technology, Pasadena, CA 91109

INTRODUCTION. The opportunity for alteration of rocks by reaction with hot carbon dioxide gas might occur during transient heating events on volatile-rich planetary bodies but, especially, in the ambient surface environment of Venus. On Venus, mean surface conditions expose rocks to temperatures of ~ 450-475° C with an atmosphere of ~ 95 - 97 vol % $CO_2$ at a pressure of ~ 90 - 100 bars (1-3). Consequently, hot rock/$CO_2$ interactions might be important in Venusian rock weathering and soil formation and deserve experimental investigation.

EXPERIMENTAL PROCEDURE. Powdered samples of two U.S. Geological Survey standard rocks (basalt BHVO-1; andesite AGV-1) were tested. Individual aliquots (0.5 - 0.6 g) held in aluminum oxide crucibles were sealed in an externally heated stainless steel pressure bomb and, after vacuum bakeout and gas flushing of the bomb to remove atmospheric $O_2$ and $H_2O$, were heated at 350° C under a 100-bar gas load. Two series of experiments were conducted with one using $CO_2$ gas (> 99.5 % pure) and the other using $N_2$ gas as a control. Run products were "quenched" by removal of the furnace, rapid gas venting and $N_2$ gas cooling of the bomb interior. Products were analyzed by x-ray diffractometry, differential thermal analysis, and visible and near-infrared reflectance spectrophotometry for evidence of alteration.

RESULTS. The most pronounced effect of the tests on the samples was a decrease in the spectral reflectivities of the materials. The andesite was more severely darkened than the basalt although the trends in reflectivity as a function of reaction time were similar for both rocks. As shown in Fig. 1, darkening of the andesite occurred in both $N_2$ and $CO_2$ although the effect with $CO_2$ was much greater. The initial change (6 hr run) was loss of the characteristic absorption band at ~ 1.9 μm followed by steepening of the reflectance curve from ~ 0.6 to 2.0 μm and gradual loss of both total reflectivity and the absorption band at ~ 0.9 μm. In the visible range (0.35 - 0.7 μm), decreases in total reflectivity occurred both in $N_2$ and $CO_2$ although the absolute positions and shapes of the respective run product spectra were significantly different. Similar but more subtle darkening effects were observed for the basalt (Fig. 2).

The spectral darkening effects may be interpreted as either (a) artifacts of the experimental procedure or as (b) results of actual rock/gas reactions. The fact that darkening occurred both in the $N_2$ and $CO_2$ experiments might point toward (a) although the fact that the effects were most pronounced in the $CO_2$ runs tends to favor (b). Further analysis of the run products should help identify the basis of the observed effects.

Implications for Venus. Wideband photometry data from the Venera 9 and

---

* Current address: SN2/NASA Johnson Space Center, Houston, TX 77058

10 spacecraft implied a low albedo surface, possibly resembling basalt (4). Similarly, Pioneer Venus solar flux radiometer data suggested ground albedo of < 15% in the visible (5). It is noteworthy, though, that andesite experimentally darkened in hot $CO_2$ possesses a reflectance spectrum in the visible which resembles that of basalt (compare 96-hr run curves, Figs. 1b and 2). Consequently, it seems possible that andesite could exist on Venus although its spectral reflectance characteristics might have been modified by prolonged exposure to hot $CO_2$. Given the fact that Venusian surface temperatures are ~ 100 - 125° C higher than that used in these experiments, the darkening processes might be even more effective on Venus than indicated here.

Acknowledgement. This work was performed at JPL under contract with NASA through the Planetary Geology Program.

References: (1) Marov, M.Ya. (1978) Results of Venus missions. Ann. Rev. Astron. Astrophys., 16, 141-169. (2) Seiff, A. et al. (1979) Thermal contrast in the atmpshere of Venus: initial appraisal from pioneer Venus probe data. Science, 205, 46-49. (3) Oyama, V.I. et al. (1979) Venus lower atmosphere composition: analysis by gas chromatography. Science, 203, 802-805. (4) Golovin, Yu M. (1979) Optical properties of the surface of Venus: wavelength dependence of albedo. Komischeskie Issledovaniya, 17 (3), 473-476 (in Russian). (5) Tomasko, M.G. et al. (1979) Preliminary results of the solar flux radiometer experiment aboard the Pioneer Venus multiprobe mission. Science, 203, 795-797.

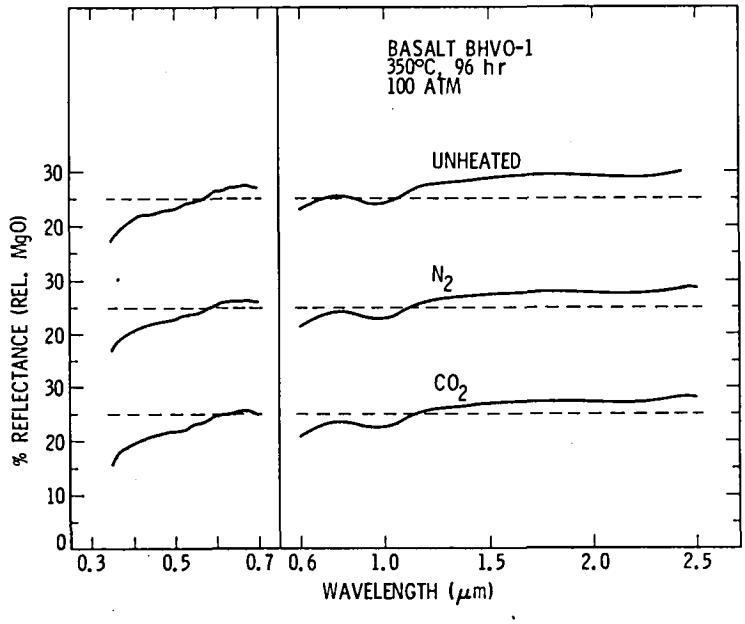


Figure 2. Visible and near-infrared reflectance spectra of samples of basalt exposed to hot, high-pressure atmospheres of nitrogen or carbon dioxide gas. Darkening is subtle both in $N_2$ and $CO_2$ but is apparently more intense in the latter.

(a)

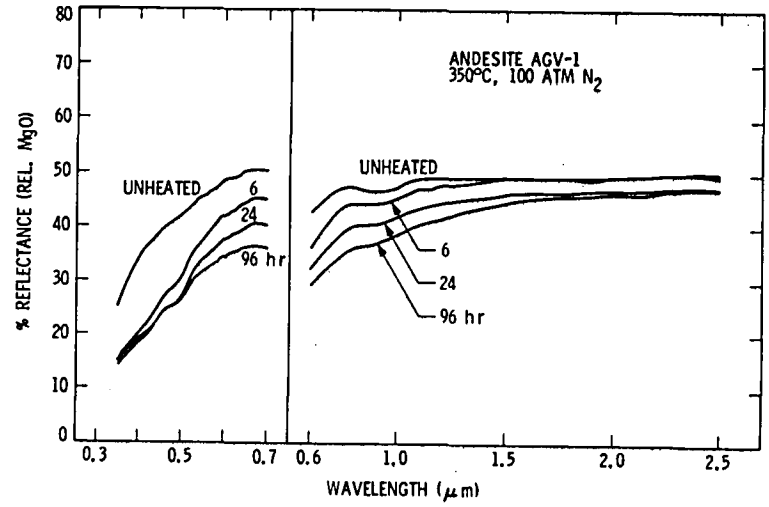


(b)

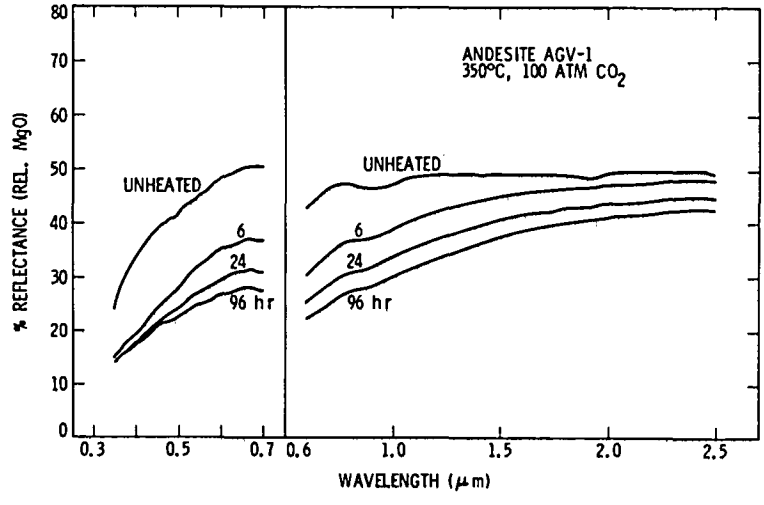


Figure 1. Visible and near-infrared reflectance spectra of samples of andesite exposed to hot, high-pressure atmospheres of (a) nitrogen gas, and (b) carbon dioxide gas. Darkening of the andesite occurs both in $N_2$ and $CO_2$ but, apparently, more intensively with the latter.

REGOLITH DEVELOPMENT IN MARS-LIKE ENVIRONMENTS

Everett K. Gibson, Jr., SN7, NASA Johnson Space Center, Houston, TX
Roberta Bustin, Chemistry Department, Arkansas College, Batesville, AR
Sue Wentworth, Lockheed, 1830 NASA Road 1, Houston, TX

Weathering of planetary regolith materials occurs from both chemical and physical interactions of the planet's surface materials with the atmosphere and, if present, the hydrosphere and biosphere along with extraplanetary objects which may produce cratering. The net result of weathering processes is to modify the original surface materials and produce secondary materials that are products of equilibrium between the atmosphere and interacting particles with the solid body. In order to adequately study weathering processes and regolith development occurring on planetary bodies, simulation studies must be carried out either in the laboratory under controlled conditions or study analog materials in the field. We have been studying as a martian analog the regolith development and weathering processes operating in the Earth's coldest and driest desert -- the Dry Valleys of Antarctica. Probably the best terrestrial analogs of the martian surface are found within the Dry Valleys (1,2,3). Surface processes operating in the Dry Valleys are similar to martian surface processes in the following respects: low temperatures (mean temperature of $-17^{\circ}C$ in Wright Valley), low absolute humidities, diurnal freeze-thaw cycles, low annual precipitation, desiccating winds, low magnetic fields, salt-rich regolith, and oxidizing environment. In the Dry Valleys, physical or mechanical weathering predominates over chemical weathering processes (4). Even though chemical alteration is a secondary weathering process in the Dry Valleys, it is still present and plays an important role in regolith development.

We collected a suite of samples from the floors and brine ponds in Wright and Taylor Dry Valleys during the 1979-1980 austral summer. The samples have been stored below $-10^{\circ}C$ since collection. The sample suite includes core samples from (1) permanent brine ponds (Don Juan Pond area) which represented mature sites, (2) brine ponds which were not as advanced in their development (Don Quixote), (3) seasonal evaporite ponds which contain standing water for only one or two months each year during the summer melting period, and (4) soils from a one-meter deep pit on Prospect Mesa Formation which represents some of the oldest soils on the Antarctic continent (5). The soil pit contained samples from above and below the permanently frozen zone.

We report here the results of a study focused on evaporite and salt forming processes. The regolith at the Viking landing sites shows evidence of evaporite-like materials. Samples were studied for their water soluble cations and anions which represented ionic transport above the permanently frozen layer. This process produces the salt enrichments found near the surface. Secondary minerals previously identified in the Dry Valley soils include halite, mirabilite, bloedite, gypsum, calcite, aragonite, monohydrocalcite, soda niter, thenardite, antarcticite, bishovite, sylvite, trona, and limonite (6,7). Comparisons of the total sulfur and chlorine contents of the Dry Valley soils along with their major element compositions with those at the Viking 1 and 2 sites on Mars (3,8,9) indicate the weathering processes operating inn the Dry Valleys produce enrichments in S and Cl identical to those found on Mars (Figure 1).

Comparisons of the differences in Cl contents with evaporite pond maturity is shown in Figure 2. Samples from the center of Don Juan Pond (DJ 2074) contain Cl abundances approximately twice those found at the edge of the pond (DJ 33). The tope of core DJ 33 shows depletion of Cl content (upper 2-3 cm) reflecting the dilution of the salt abundances with wind blown material from the valley floor and valley walls. Samples from the Don Quixote Pond (DQ 35) also show the surface enrichment as compared to the seasonal evaporite pond (WV 52).

From the investigations of the soils and cores from the Dry Valleys, an idealized soil profile for the regolith (8) has been developed which is very applicable to the martian regolith (Figure 3). The soil profile is composed of five basic zones: an aeolian zone, a salt formation zone, an active zone, a seasonally frozen zone, and a permanently frozen zone. The four zones above the permanently frozen zone are the regions where the majority of the chemical and physical weathering occur. The aeolian zone (upper 1-2 cm) represents the region where daily activity is occurring. Effects of the surface winds, temperature fluctuation, moisture deposition, and radiation environment are recorded within this regolith zone. The salt formation zone represents the area where salts are forming and deposited. Salts are associated with the duricrust and their presence has recently been reviewed (9). The salt zone is located within 1 cm to 5 cm of the surface. The active zone represents the region of transition between the salt zone and the frozen zones where the abundances of surface deposited salts decrease as a function of depth and daily temperature fluctuations and are damped as compared to the upper zones. The seasonally frozen zone represents the region of the regolith which undergoes melting-thawing and freezing, depending upon the season. The permanently frozen zone remains at a temperature below the frost point throughout the martian year. In such a region ice is stable on a yearly basis. The observed condensates in the Solis Lacus and Noachis-Hellespontus regions (10) could easily be accounted for by this model. The movement of moisture through the regolith with subsequent loss to the atmosphere would leave behind those anions and cations which favor salt formation. The seasonal cycling of moisture from the regolith would result in salt-rich deposits near the surface similar to those observed at the Viking sites.

References:


1. Horowitz, N.H. et al. (1972) Science 176, 242-245.
2. Morris, E.C. et al. (1972) U.S.G.S. Interagency Report: Astrogeology 52, 156 pages.
3. Gibson, E.K., Jr. (1981) Third International Colloquium on Mars (abstract), p. 90-92.
4. Harris, H. (1981) Ph.D. Dissertation, University of Illinois, and Ugoline, F.C. (1963) Ph.D. Dissertation, Rutgers University.
5. Bockheim, J. (1979) Personal communication.
6. McKay, D.S. and Prestell, D. (1980) NASA Tech. Memo. 82385, 496-498.
7. Watanuki, K. et al. (1979) Memoirs of National Institute of Polar Research, Special Issue No. 14, 52-56.
8. Gibson, E.K., Jr., and Ransom, B. (1981) In Lunar and Planetary Science XII, 342-344.
9. Clark, B. and Van Hart, D.C. (1981) Icarus 45, 370-378.
10. Zisk, S.H. and Mouginis-Mark, P.J. (1980) Nature 288, 735-738.

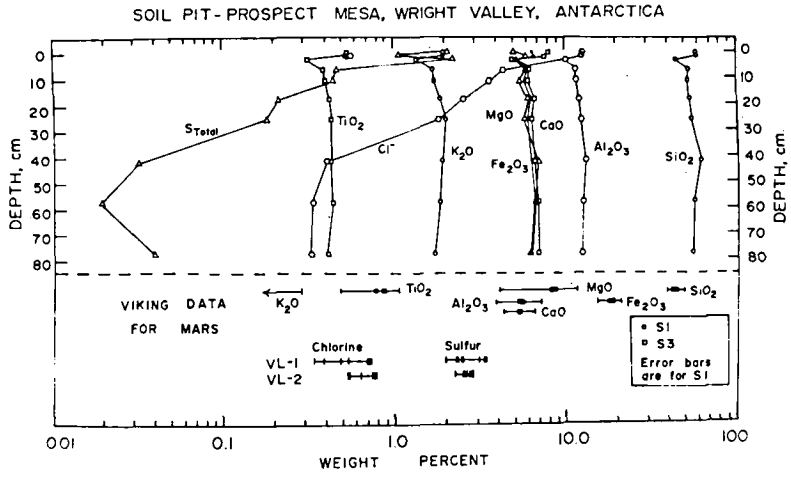


Figure 1. Comparison of the compositional data from Dry Valley soil pit with the Viking 1 site on Mars. Viking data is from Clark (1981, personal communication)

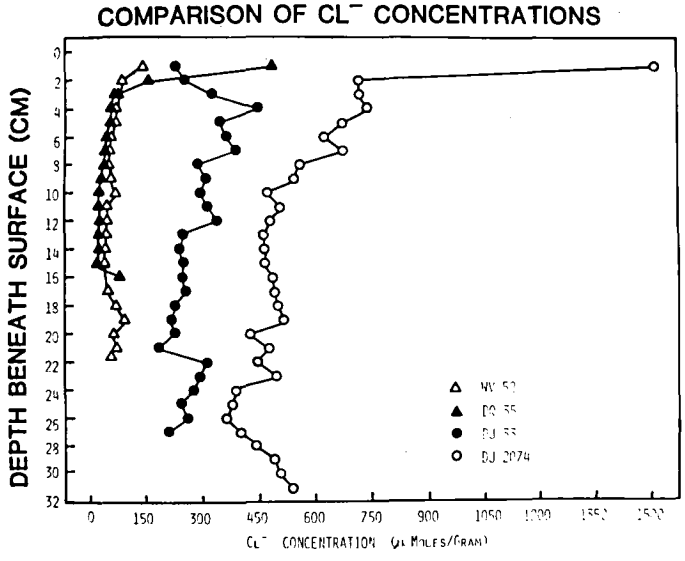


Figure 2. Chlorine concentrations at four sites with different maturity. Maturity scale: DJ 2074 > DJ 33 > DQ 35 > WV 52.

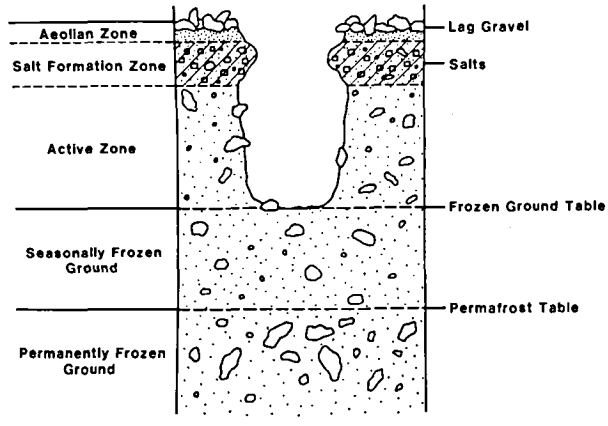


Figure 3. Idealized soil profile for the Martian regolith. Most of the chemical alterations and secondary mineral formation occur within or above the active zone.

CHEMICAL WEATHERING AND DIAGENESIS IN A SOIL PROFILE IN ANTARCTICA: IMPLICATIONS FOR THE MARTIAN REGOLITH.

David S. McKay, SN6-NASA Johnson Space Center, Houston, TX 77058
Susan Wentworth, Lockheed, 1830 NASA Rd. 1, Houston, TX 77058
Richard Morris, SN7-NASA Johnson Space Center, Houston, TX 77058

Introduction: The Martian regolith consists of unconsolidated fragmental debris and fine-grained material overlying more competent rock units at depth. Considerable evidence exists that this regolith contains extensive ice or permafrost and may even contain an active ground water system beneath a frozen zone (Clifford, 1981). Such a regolith would almost certainly be the site of chemical weathering and diagenesis. The Dry Valleys of Antarctica are probably the best available terrestrial analog to the surface of Mars (Gibson, 1980, 1981). As part of a broader study of the Dry Valleys as Martian analogs started by E. Gibson of JSC, we have been investigating some of the features associated with chemical weathering and diagenesis in Wright Valley. In this abstract we report some of the results of our studies of a sequence of 10 soil samples from a soil pit at Prospect Mesa in Wright Valley. The general description and chemical data on soluble cations for these samples are reported in Gibson et al. (this volume).

Geologic Setting: The soils at Prospect Mesa were apparently deposited during the most recent axial glaciation of eastern Wright Valley which occurred about 4 m.y. ago (Harris, 1981). The soils in eastern Wright Valley are probably the oldest soils in Antarctica (Gibson, 1981). Harris (1981) summarizes the local geology. Source rocks include gneisses, granitic intrusives, granodiorites, sandstones, shales, conglomerates, and dolerites. The Prospect Mesa soil pit penetrates a well-developed lag surface covered by abundant cobbles and pebbles (Gibson and Ransom, 1981). Beneath this surface the soil consists primarily of fine to medium sand-size material with a few larger fragments. The pit penetrates a salt-rich horizon at 2 cm, cuts through an active zone which is subject to freeze-thaw cycling, and then penetrates a permanently frozen zone at about 40 cm. Total depth sampled by the pit is approximately 80 cm.

Description of Soil Samples: We have studied soil samples from the pit by optical petrography and SEM. In the coarser fraction, the soil is predominately composed of lithic fragments, including bedrock fragments and microbreccias; mineral grains are the main constituent in the finer fraction. Relative abundances of silicate minerals are 45% plagioclase, 20% clinopyroxene, 15% amphibole, 10% quartz, 10% K-feldspar, and minor biotite and iron oxides. The finest grain size (<20 micrometers) consists of fragments of the major silicate minerals and fine-grained alteration products, mostly clay minerals. Nearly all of the plagioclase and pyroxene grains show some alteration in thin section, consisting mainly of incipient formation of fine-grained clay minerals. In some cases, only relic grains remain; the original grain is completely altered. SEM photographs of feldspars show examples of crystallographically controlled etch pits (Fig. 1), which are characteristic of dissolution during weathering in temperate climates (Wilson, 1975). Many pyroxenes show differential weathering along exsolution lamellae (Fig. 2). Most mineral grains show partial coatings of clay mineral sand authigenic salt minerals, as previously noted for quartz (McKay and Prestel, 1980). Some microbreccias from the permanently frozen zone are slightly porous and we have observed secondary authigenic minerals associated with the pores (Fig. 3). Electron microprobe analyses of two of the typical secondary minerals correspond to zeo-

lite compositions with the formulas $Na_{1.07}\ K_{.34}\ Mg_{.24}\ Ca_{.06}\ Al_2Si_4O_{12}\cdot\eta H_2O$ and $Na_{.72}\ K_{.27}\ Mg_{.29}\ Ca_{.15}\ (Fe_{.06})\ Al_2Si_4O_{12}\cdot\eta H_2O$. Because of the relatively low abundance of these minerals we do not have x-ray diffraction data; however, they may be mixed compositions related to the analcime-wairakite or chabazite-gmelinite series.

While it is clear that soil in this pit has been subjected to considerable weathering and diagenesis, it is not really clear how much of this activity took place in situ. The presence of pore space containing secondary minerals at least suggests that these processes are possibly now active in the lower soil horizons. Wentworth and McKay (this volume) discuss more fully the time scale of chemical weathering in Antarctica.

The presence of zeolites in these samples, if fully confirmed by further analysis, may have implications for the Martian regolith. On Earth, zeolites are often found in soils in arid climates where evaporation is important; soils rich in zeolites are typically reddish-brown (Hay, 1977). Zeolites are also often found in soils formed from volcanic glass. We know of no reason why zeolites could not form in the Martian regolith. The absorption and exchange properties of zeolites are well known; an appreciable abundance of zeolites in the Martian regolith might strongly influence atmosphere-regolith interactions; zeolites might serve as a reservoir for $CO_2$.

Diffuse Reflectance Spectra: Reflectance spectra of Mars obtained from Earth-based telescopes have provided information about the mineralogical state of the Martian surface (e.g., Singer et al., 1979). One goal of this study is to evaluate the extent to which secondary minerals produced by weathering processes dominate the primary minerals in the reflectance spectra of the Dry Valley soils. In doing so, we gain insight into how well the reflectance spectra of Mars may represent the primary Martian rock-forming minerals.

The diffuse reflectance spectra of the four Wright Valley soils were recorded on a Cary-14 spectrophotometer configured with a 9-inch integrating sphere. All the spectra have bands located near 1.4 and 0.98 μm and a strong adsorption edge extending from ~0.56 μm into the UV. The 1.4 μm band arises from O-H perhaps from water or the clay minerals present in the soils. The remaining features in the spectra are suggestive of ferrous iron in clinopyroxene (e.g., Hunt and Salisbury, 1970). This is entirely compatible with the mineralogy state of the soils as discussed above; clinopyroxene is the dominant iron-bearing mineral.

The reflectance spectra of Wright Valley soils are distinctly different from that of the Martian bright regions. In the former case, ferrous iron dominates the spectra while in the latter (e.g., Singer et al., 1979) ferric iron does. Thus, the initial mineralogical state of the two regions is very different or weathering processes on Mars must be more pervasive than for the Antarctic soils in order to effectively mask (in an optical sense) any ferrous silicates given comparable periods for weathering. As discussed in Wentworth and McKay (this volume), the Antarctic soil profile may represent weathering over a period of 4 m.y. or so.

References: Clifford, S. M. (1981) In: Third Int. Mars Colloquium, p. 44-45. Gibson, E. K. (1980) NASA TM 82385, p. 199-201. Gibson, E. K. (1981) In: Lunar and Planet. Sci. XII, p. 339-341. Gibson, E. and Ransom, B. (1981) In: Lunar and Planet. Sci. XII, p. 342-344. Harris, H. (1981) Ph.D. Dissertation, Univ. of Illinois. Hay, R. L. (1977) In: M.S.A. Short Course: Min. and Geol. of Nat. Zeolites, F. Mumpton, ed; p. 53-63. Hunt, G. R. and Salisbury, J. W. (1970) Mod. Geo., v. 1, p. 283. McKay, D. and Prestel, D. (1980) NASA TM 82385, p. 496-498. Singer, R. B. et al. (1979) J. Geophys. Res., v. 84, p. 8415. Wilson, M. J. (1975) Soil Science, v. 119, p. 349-355.

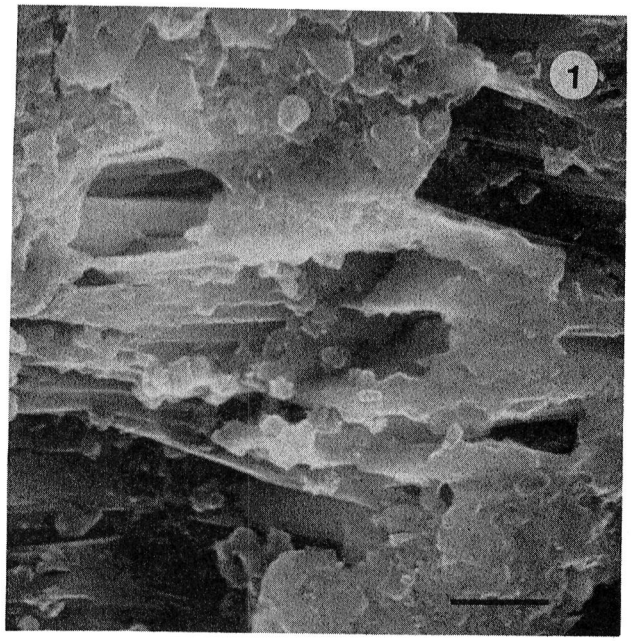



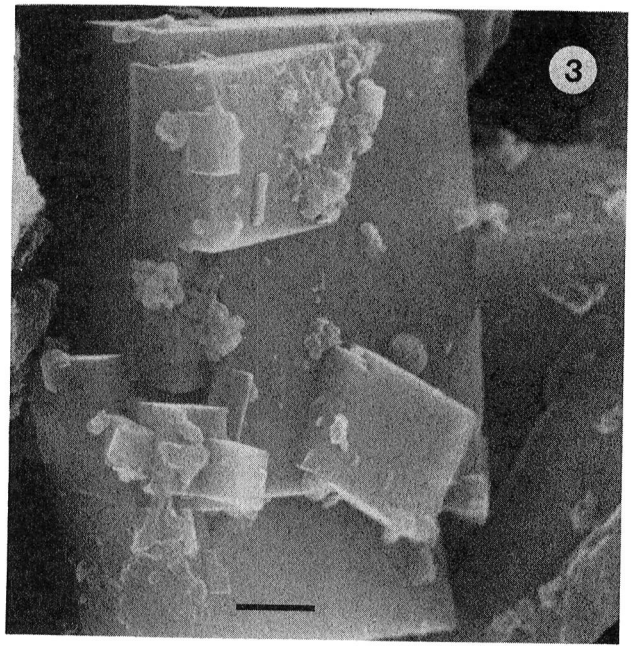


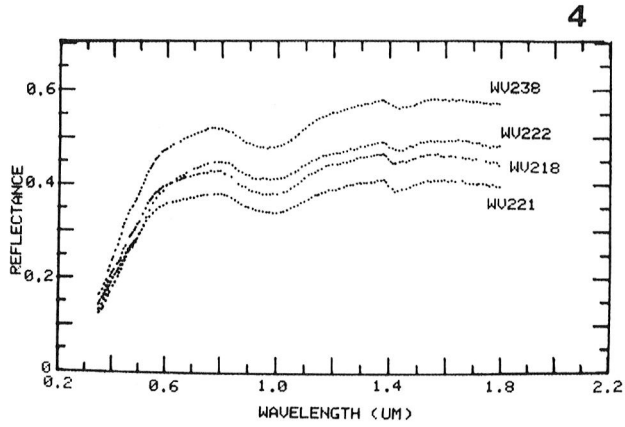


Fig. 1: Dissolution pits in plagioclase; grain surface partly covered by clay minerals. Scale bar 2 micrometers (WV 221).
Fig. 2: Differential weathering along exsolution lamellae in clinopyroxene. Scale bar 2 micrometers (WV 221).
Fig. 3: Secondary authigenic mineral, apparently zeolite. Scale bar 2 micrometers (WV 221).
Fig. 4: Diffuse reflectance spectra of four samples from soil pit. Depths are: WV 222, 0-1 cm; WV 238, 2-4 cm; WV 218, 24-28 cm; WV 221, 75-80 cm.

# WEATHERING OF SILICATE MINERALS IN ANTARCTIC DRY VALLEYS: IMPLICATIONS FOR VOLATILE-REGOLITH INTERACTIONS ON MARS

S. J. WENTWORTH, Lockheed, 1830 NASA Rd. 1, Houston, TX 77058
D. S. McKay, SN6-NASA Johnson Space Center, Houston, TX 77058

## Introduction

The Dry Valleys of Antarctica, an ice-free region characterized by extremely cold temperatures, low precipitation rates, high evaporation rates, and negligible organic matter, are considered by many workers to be the best terrestrial analog of the surface of Mars (Horowitz et al., 1972). Soils from the Dry Valleys exhibit features similar to those observed by Viking, including high sulfur and chlorine abundances, a cemented horizon just beneath the surface, and a permanently frozen zone (e.g., Gibson and Ransom, 1981).

There is now considerable evidence that processes of chemical weathering and secondary mineral formation are currently active in the Dry Valleys, even in frozen soils. A reasonable argument can be made that frozen water and possibly a fluid ground water system may exist beneath much of the Martian surface (Clifford, 1981). Consequently, we believe that it is likely that similar chemical weathering processes may be occurring in the Martian regolith. Workers at JSC are now studying soil samples from the Dry Valleys in order to determine the causes and effects of chemical weathering in cold, dry environments.

## Evidence for Chemical Weathering in Antarctica

In the Antarctic, physical weathering occurs at a relatively fast rate and includes comminution by freezing and thawing, wind abrasion, and glacial action. Chemical weathering also occurs, but at a very slow relative rate. Earlier workers (e.g., Kelly and Zumberge, 1961) concluded that chemical weathering is negligible in present-day Antarctica. More recent studies, however, have shown conclusively that chemical weathering processes have been active in Antarctica. For example, soil weathering profiles are common in the Dry Valleys. The percentage of oxidized iron increases with increasing soil age and within individual soil profiles in Wright Valley, oxidized iron generally increases towards the surface (Ugolini, 1963). The ratio of $SiO_2$/ $Al_2O_3$+$Fe_2O_3$decreases in older soils, a reflection of the alkaline weathering environment (Ugolini and Jackson, 1977).

In addition to soil alteration profiles, the presence of soluble salts rand the formation of evaporite mineral concentrations are a characteristic feature of the Dry Valley soils. Evaporite sequences formed in soil profiles are also characteristics of arid regions from other parts of the world. Salt abundances increase with soil age in Dry Valley soils (Pastor and Bockheim, 1980), but the source of the water-soluble ions that form the salts is not well understood. A large portion (notably Na and Cl) probably originated as marine aerosols, but some were probably derived by rock weathering (Claridge, 1965). Claridge and Campbell (1976) determined that most $Ca^{2+}$ and $Mg^{2+}$ were derived from pyroxenes and amphiboles in diabasic country rocks and from biotite in granitic rocks. Muscovite and, to a small extent, potash feldspar, contributed most of the $K^{+}$. Claridge and Campbell also noted that calcite encrustations were only found in areas containing carbonate source rocks, indicating leaching and redeposition of calcium carbonate. The major chemical weathering effect on pyroxenes and amphiboles is the alteration of iron to hydrous oxides. Micas alter to clay minerals by means of hydration. Feldspars alter to amorphous material or to micas and, eventually, to clay minerals (Bockheim, 1979). Authigenic clays, including vermiculite, montmorillonite, and illite, are common soil constituents. They are not abundant, however: the mineralogy of the clay-size fraction is dominated by primary rock-forming minerals even in the oldest soils (Bockheim, 1979). We should

note that the oldest Antarctic in situ soil is about 4 m.y. old, an age that would be considered extremely young in a Martian context.

While most of the Antarctic source rocks are intermediate or felsic, the weathering of basic and ultrabasic rocks in Antartica is also documented. Nearly all of the hundreds of meteorites collected in Antartica and returned to JSC have shown some evidence of chemical weathering, usually in the form of reddish-brown stains, presumably caused by the oxidation of iron (Score et al., 1981). Some of these meteorites are pervasively weathered throughout their entire volume.

## Time Scale of Chemical Weathering

While many authors (e.g., Ugolini and Jackson, 1977) believe that much of the chemical weathering in the Dry Valleys was probably produced in the past during periods of warmer, wetter climatic conditions, there is also considerable evidence that weathering is presently occurring, although it is proceeding at a relatively slow rate. For example, all of the soil weathering profiles in Wright Valley are younger than about 4 m.y. Is weathering occurring at the present time in these soil profiles, even in the permanently frozen zones? There are some indications that it is. Of major importance to this question is the work of Ugolini and Anderson (1973) which showed that ionic migration occurs in frozen soils by means of liquid films on individual soil particles. The formation of evaporite minerals at or near the surface of the soils is clearly taking place under current conditions (Gibson, 1981).

## Alteration in Prospect Mesa Soil Pit

We are currently studying alteration features of mineral grains from the Prospect Mesa soil pit in Wright Valley. The geologic setting, general soil description, and optical reflectance features of the soil samples from this pit are described more fully in McKay et al. (this volume). One objective of this study is to document the weathering and alteration features present in these soils and to relate these features to present-day weathering processes. We have selected individual feldspar and pyroxene grains from samples in the permanently frozen zone and active layer (which undergoes several freeze-thaw cycles during the austral summer). Preliminary results of scanning electron microscopy (SEM) show that minerals in both the active and the permanently frozen zones are in various stages of alteration, and that nearly all mineral grains are altered to at least some degree. Many mineral grains in these samples show small-scale dissolution features, as described by McKay et al. (this volume). This alteration is also confirmed in thin sections from the soil pit (McKay et al., this volume). We have not yet determined whether the observed alteration effects, especially for the minerals in the permanently frozen zone, are the products of present-day chemical weathering. However, the presence, in the permanently frozen zone, of the very fresh-appearing authigenic zeolites on the surfaces of plagioclase minerals undergoing obvious dissolution (McKay et al., this volume) is highly suggestive of chemical reactions within this zone. It is unlikely that these features, many of which are very delicate, would have survived transportation without the formation of abrasion features and fracturing. Although not conclusive, the presence of delicate dissolution features on minerals and authigenic secondary minerals is at least highly suggestive that chemical water-ice-soil interactions are taking place under present-day conditions, possibly within the permanently frozen zone in these Dry Valley soils.

## The Martian Connection

If it can be conclusively shown that chemical alterations are occurring under present-day conditions in the Antarctic regolith by water-ice-soil interactions, then it is nearly certain that analogous reactions are occurring on Mars. The difference in atmospheres between the two planets may make no

fundamental difference in the weathering process. The main requirements are the presence of reactive minerals, and of ice or water. In fact, rock-forming minerals on Mars are probably more reactive than those in the Dry Valley soils because Martian rocks are likely to be rich in mafic minerals, which are more susceptible to ordinary weathering processes than quartz and feldspar. We conclude, therefore, that chemical weathering on Mars may have many similarities to chemical weathering in the Dry Valleys. We concur with Allen et al. (1981) that it is time to re-evaluate simple models for the mineralogy of the Martian regolith. We suggest, based on our Antarctic studies, that even starting with a relatively simple suite of rock forming minerals, the weathering process on Mars is likely to create an exceedingly complex mixture of secondary minerals, evaporite minerals, and partly-weathered primary minerals in all grain sizes (including the finest clay size which may comprise windblown dust). A better understanding of the nature of this mixture and how it might form can best be obtained by continuing detailed studies of Antarctic soils coupled with appropriate laboratory experiments.

References

Allen, C. C., Gooding, J. Jercinovic, M. J. and Keil, K. (1981) Third Intr. Colloq. on Mars. p. 1-3.

Bockheim, J. G. (1979) Soil Science, v. 128, p. 142-152.

Claridge, G. G. C. (1965) N. Z. Jour. Geol. and Geophys., v. 8, p. 186-220.

Clifford, S. M. (1981) Third International Colloquium on Mars, Abstract, p. 44-45.

Claridge, G. G. C. and Campbell, I. B. (1977) Soil Science, v. 123, p. 377-384.

Gibson, E. (1981) in Lunar and Planetary Science XII, p. 339-341.

Gibson, E. and Ransom, B. (1981) in Lunar and Planetary Science XII, p. 342-344.

Horowitz, N. H., Cameron, R. E., and Hubbard, J. S. (1972) Science, v. 156, p. 242.

Kelly, W. C. and Zumberge, J. H. (1961) Jour. Geol., v. 69, p. 433-446.

Pastor, J. and Bockheim, J. G. (1980) Soil Sci. Am. J., v. 44, preprint.

Score, R., Schwartz, C., King, T., Mason, B., Bogard, D. and. Gabel, E. (1981) Antarctic Meteorite Descriptions. Curatorial Branch Pub. 54, NASA JSC, 144pp.

Ugolini, F. C. (1963) Ph.D. Dissertation, Rutgers, Univ.

Ugolini, F. C. and Anderson, D. M. (1973) Soil Science, v. 115, p. 461-470.

Ugolini, F. C. and Jackson, M. L. (1977) Third Symp. Antarctic Geol. and Geophys.

# REFLECTANCE SPECTROSCOPY OF STRUCTURAL CHANGES EFFECTED BY THE DEHYDRATION OF GOETHITE (α-FeOOH) AND LEPIDOCROCITE (γ-FeOOH)

Richard V. Morris, Code SN7, NASA Johnson Space Center, Houston, TX 77058
Howard V. Lauer, Jr., Lockheed, 1830 NASA Road 1, Houston, TX 77058

## Introduction

X-ray powder diffraction studies have shown that a sequence of changes in crystal structure occurs during the thermal dehydration of goethite (α-FeOOH) and lepidocrocite (γ-FeOOH) to anhydrous forms (e.g., Francombe and Rooksby, 1959; Bernal et al., 1957). For example, Francombe and Rooksby (1959) found in the X-ray powder diffraction patterns of samples of heat-treated geothite certain line-broadening effects. They concluded that in the dehydration process the oxide ions ordered to the hematite structure before the ferric ions did. These structural changes should also be manifest in other types of data which are structure sensitive.

In this study, we are concerned with the reflectance spectroscopy of the structural changes effected by the thermal dehydration of goethite and lepidocrocite. To establish the structural state of the heat-treated samples, we will employ X-ray powder diffraction techniques. The results are pertinent to the interpretation of the reflectance spectra where FeOOH/$Fe_2O_3$ assemblages have been inferred (e.g., Singer et al., 1979).

## Experimental Procedures

The goethite (GTS3) and lepidocrocite (LPS2) used were synthetically-prepared powders having sub-micron mean grain sizes. Their chemical and physical properties are given by Morris and Lauer (1981). Individual samples of these powders were heated in air at selected temperatures for $\sim$ 300 hours. After heat treatment, the X-ray diffraction patterns and the diffuse reflectance spectra were obtained at room temperature. The diffuse reflectance spectra were recorded on a Cary 14 configured with a nine inch diameter integrating sphere; the sphere was coated with Halon and all the reflectance spectra reported here are relative to a Halon standard.

## Results and Discussion

### Goethite

The diffuse reflectance spectra of samples of goethite GTS3 heat treated at nine temperatures between 117 and 440°C are shown in Figure 1. The position of the $^6A_{1g} \rightarrow {}^4T_{1g}$ is plotted as a function of the temperature of the heat treatment in Figure 2. Also indicated are the phases observed in the X-ray diffraction patterns. For the samples heated at $\leq$ 200°C, the only phase observed in the X-ray data was goethite. The position of the $^6A_{1g} \rightarrow {}^4T_{1g}$ band is unchanged from that of the unheated GTS3. The $^6A_{1g} \rightarrow {}^4T_{2g}$ band, however, becomes progressively less well defined until it does not show a minimum in the 200°C sample. Presumably this results from some combination of a small shift to longer wavelength and broadening of the UV absorption edge and a shift to shorter wavelength of the $^6A_{1g} \rightarrow {}^4T_{2g}$ band

from 0.65 μm. Apparently, some structural changes occurred which were not evident in our X-ray data.

By 245°C, the X-ray data and reflectance spectra have markedly changed. The diffuse nature of some of the X-ray lines indicate a disordered hematite structure (Francombe and Rooksby, 1959) for the 245 and 280°C samples; the samples at still higher temperatures have the ordered hematite structure. The transition from disordered to ordered hematite seems to be accompanied by a more pronounced shoulder at ∿ 0.62 μm, an increase in the depth of the $^6A_{1g} \rightarrow {}^4T_{1g}$ band, and a higher reflectivity in the near-IR. More data is needed in the 160-245°C temperature interval to better determine the relationship between the band positions and the UV adsorption edge.

## Lepidocrocite

The diffuse reflectance spectra of samples of lepidocrocite heat treated at six temperatures between 145 and 280°C are shown in Figure 3. The position of the $^6A_{1g} \rightarrow {}^4T_{1g}$ band and the phases indicated in the X-ray diffraction patterns are shown as a function of temperature in Figure 4. The behavior of lepidocrocite is more complex than that of goethite because the former decomposes to maghemite ($\gamma$-$Fe_2O_3$) in route to hematite. The only phase observed in the 145 and 163°C samples was lepidocrocite; the position of the $^6A_{1g} \rightarrow {}^4T_{1g}$ band is the same as that for LPS2. The $^6A_{1g} \rightarrow {}^4T_{2g}$ band and UV adsorption edge behave in a manner similar to that discussed above for goethite; at 163°C, the band is apparent only as a shoulder near 0.63 μm.

The X-ray patterns of the 197 and 223°C samples indicate a disordered maghemite phase, and indeed these samples are strongly magnetic. The reflectance spectra of these two samples approximates that for well-crystalized maghemite (e.g., Morris and Neely, 1981). The X-ray patterns of the 252 and 280°C samples indicate the presence of disordered maghemite and disordered hematite. For these four samples, the UV adsorption edge is nearly the same but is shifted to longer wavelength relative to the 163°C sample but is still at a shorther wavelength relative to that for ordered hematite in Figure 1. The position of the $^6A_{1g} \rightarrow {}^4T_{1g}$ band varies from 0.91 to 0.87 μm as the structure approaches hematite.

## Application to Mars

The reflectance spectra of the bright regions of Mars are characterized by a weak absorption bandnear 0.87 μm and a shallow absorption edge extending from ∿ 0.75 μm to 0.40 μm. Although additional samples are required, the results so far indicate that it is difficult to account for these features with any of the structural forms above. This is the case because the forms which have the appropriate band near 0.87 μm have the adsorption edge at too long a wavelength.

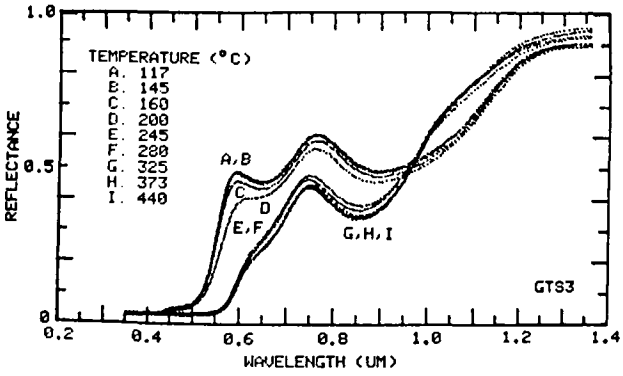


Fig. 1. Diffuse reflectance spectra of goethite GTS3 heated in air at various temperatures for ∿ 300 hours.

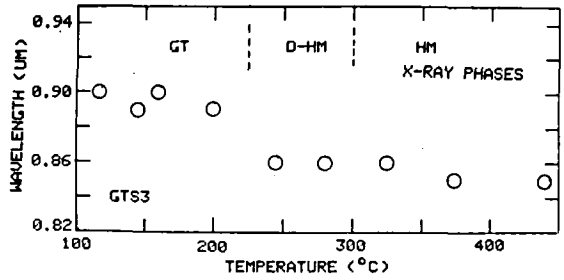


Fig. 2. Position of the $^6A_{1g} \rightarrow {}^4T_{1g}$ band as a function of the temperature of the heat treatment for GTS3. Also shown are the phases observed in the X-ray diffraction patterns. (GT = goethite; D-HM = disordered hematite; HM = hematite)

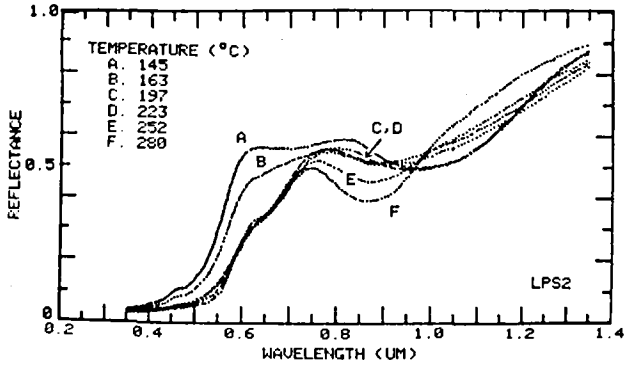


Fig. 3. Diffuse reflectance spectra of lepidocrocite LPS2 heated in air at various temperatures for ∿ 300 hours.

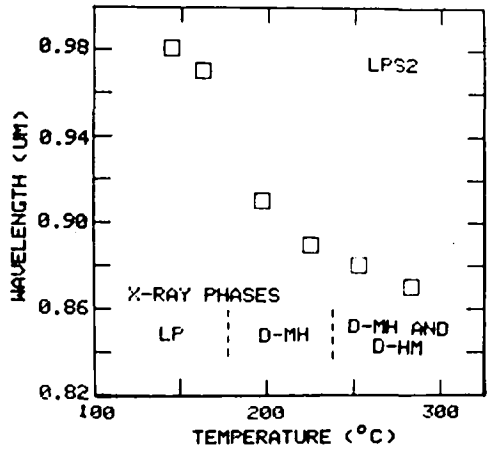


Fig. 4. Position of the $^6A_{1g} \rightarrow {}^4T_{1g}$ band as a function of the temperature of the heat treatment for LPS2. Also shown are the phases observed in the X-ray diffraction patterns. (LP = lepidocrocite; D-MH = disordered maghemite; D-HM = disordered hematite)

REFERENCES:
Bernal J.D., Dasgupta D.R., and MacKay A.L. (1957) Nature 180, 645.
Francombe M.H. and Rooksby H.P. (1959) Clay Min. Bull. 4, 1.
Morris R.V. and Lauer H.V., Jr. (1981) J. Geophys. Res., in press.
Morris R.V. and Neely S.C. (1980) Reports of Planetary Geology Program - 1980, 445.
Singer R.B., McCord T.B., Clark R.N., Adams J.B., and Huguenin R.L. (1979) J. Geophys. Res. 84, 8415.

BIDIRECTIONAL REFLECTANCE SPECTROSCOPY. III. CORRECTION FOR MACROSCOPIC ROUGHNESS.

Bruce Hapke, University of Pittsburgh, Pittsburgh, PA 15260.

A mathematically rigorous formalism is derived by which an arbitrary photometric function for the bidirectional reflectance of a smooth surface may be corrected to include first-order effects of general macroscopic roughness. Using physically reasonable assumptions and mathematical approximations the correction expression is evaluated analytically. The resulting expression allows for the first time the realistic prediction of the brightness profile across the surface of a planet. The correction involves only one arbitrary parameter, the mean slope angle, and is applicable to surfaces of any albedo. To illustrate the effects of roughness the correction is applied to the new bidirectional reflectance function of Hapke (1981). Brightness profiles on hypothetical smooth and rough planets of low and high albedo are calculated and shown. The theory is also compared with Mariner 10 observations of Mercury and is shown to account for the apparent polar darkening and lack of limb brightness surge on the planet. The corrected rough-surfaced bidirectional reflectance function is sufficiently simple that it can be conveniently evaluated on a programmable hand calculator.

THE STRENGTH OF ABSORPTION BANDS IN REFLECTANCE SPECTROSCOPY.
Bruce Hapke, University of Pittsburgh, Pittsburgh, PA 15260.

A series of relfectance spectra were computed for a particulate medium having solid state absorption bands of varying strengths using the new reflectance theory of Hapke (1981). The relation between reflectance r and absorption coefficient $\alpha$ is shown to be highly non-linear. When $\alpha$ is small ($\alpha << \lambda^{-1}$) an increase in $\alpha$ causes r to decrease, but when $\alpha$ is large ($\alpha >> \lambda^{-1}$) an increase in $\alpha$ causes r to increase. The concept of a transition minimum in reflectance spectroscopy is introduced. This type of minimum results from a transition between the weak and strong $\alpha$ cases. Without additional knowledge it is not possible to distinguish between a transition minimum and the naive interpretation of a minimum due to an absorption band. The occurance of transition minima in an actual substance of interest on a planetary surface is illustrated using the UV and IR reflectance spectra of $H_2O$ frost.

# Chapter 10

# CARTOGRAPHY, GEODESY AND GEOLOGIC MAPPING

# GLOBES OF THE PLANETS

R. M. Batson and J. L. Inge, U. S. Geological Survey, Flagstaff, Arizona 86001

Globes have been manufactured or are being prepared for planets and satellites investigated under the Planetary Geology Program. Those of Mercury, Venus, Earth, Moon and Mars have been manufactured by Replogle Globes, Inc. of Chicago, and distributed to PGPIs during FY81. Globes of the Galilean satellites of Jupiter are in preparation, and may be produced in FY83. All of these globes are at nominal scales of 1:32,000,000. At this scale, Earth and Venus are approximately 16 inches in diameter. The moon, Io, and Europa are approximately 4.5 inches in diameter, and Mercury, Ganymede, and Callisto are approximately 6 inches in diameter. Mars is approximately 8.5 inches in diameter. To avoid the costly manufacture of globes of slightly different sizes, the same size globe is used for bodies that are nearly the same size. The diameters of the Io, Europa, Ganymede, Callisto, Mercury and Venus globes are therefore approximate.

Globes of Mercury, the Moon and Mars are airbrush shaded relief renditions (Inge and Bridges, 1976) drawn by J. L. Inge, that are based on spacecraft pictures, or on maps made from them. No albedo variation is shown in these portrayals. The globe of the Earth is also a shaded relief portrayal by Inge; it is intended to show the Earth in the same style as that used to portray the planets to facilitate geologic comparisons. The source materials used for the globe of the Earth include maps of the sea floors by T. E. Chase (1975), Heezen and Tharp (1977), and comments by and discussions with various marine geologists. Information for land areas came primarily from global navigation charts produced by the Defense Mapping Agencies. The globe of the Earth is intended to show the rocky surface, unobscured by ice or ocean. In many areas the source materials are far from adequate for this purpose, and the portrayal must be considered highly speculative.

A brownish color is used for the globes of the Moon and Mercury, whereas a reddish color, approximating the color of Mars, is used for that planet. The ocean covered areas on the Earth globe are shown in blue, and the land in tan. The colors are not intended to represent the actual colors of the planets.

Entirely different techniques were used to portray the surface of Venus. Although at a similar scale, the Venus globe is not actually a part of the series described above. Radar soundings from the Venus Pioneer spacecraft were used to model the surface at 1/8 degree increments of latitude and longitude (Masursky and others, 1980). The portrayal used on the globe is a color sliced elevation map designed by Harold Masursky, E. M. Eliason and J. L. Inge. This elevation map was superposed on a computer generated shaded relief image (Batson and others, 1975) of the elevation model.

Planetwide maps, and then globes will be made for the Galilean satellites. Current plans require that they be made in colors that approximate the colors of the respective satellites. The style of surface portrayal on these globes will not match that used for the other terrestrial planets because high resolution relief data of uniform quality are not available. The globes will therefore show albedo as well as relief information.

We anticipate making globes of the Saturnian satellites eventually, although the 1:32,000,000 scale will not be feasible because these objects are so small. Scales and other specifications have not yet been decided.

References

Batson, R. M., Edwards, K. B. and Eliason, E. M., 1975, Computer generated shaded relief images: Journal of Research of the U. S. Geological Survey, v.3, no.4, p 401-408.

Chase, T. E., 1975, Topography of the Oceans (Map, Scale 1:47,520,000): IMR Technical Report Series TR57, University of California.

Heezen, Bruce, and Tharp, Marie, 1977, The world ocean floor (Map, scale 1:23,230,000): U. S. Navy, Offices of Naval Research.

Inge, J. L. and Bridges, P. M., 1976, Applied photointerpretation for airbrush cartography: Photogrammetric Engineering and Remote Sensing, v.42, no.6, p 749-760.

Masursky, Harold, Eliason, Eric, Ford, P. G., McGill, G. E., Pettengill, G. H., Schaber, G. G. and Schubert, Gerald, 1980, Pioneer Venus radar results: geology from images and altimetry: Journal of Geophysical Research, v.85, no.A13, p 8232-8260.

# THE CONTROL NETWORKS OF THE SATELLITES OF JUPITER AND SATURN

Davies, Merton E., The Rand Corporation, Santa Monica, California 90406

Geodetic control networks are being computed for the large satellites of Jupiter and many of the satellites of Saturn using pictures from the Voyager 1 and 2 encounters. Points have been identified on the satellites and their coordinates computed by single-block analytical triangulations. The status of the control nets is summarized in the following tables:

| Satellites | Points | Pictures | Measurements | Normal Equations | Overdetermminations | σ(μm) |
|---|---|---|---|---|---|---|
| *Jupiter* | | | | | | |
| Io | 596 | 234 | 9570 | 1894 | 5.05 | 21.04 |
| Europa | 174 | 120 | 3704 | 708 | 5.23 | 14.62 |
| Ganymede | 1668 | 295 | 17192 | 4237 | 4.07 | 23.51 |
| Callisto | 578 | 207 | 8740 | 1771 | 4.92 | 18.31 |
| *Saturn* | | | | | | |
| Mimas | 109 | 32 | 1374 | 314 | 4.38 | 18.60 |
| Enceladus | 34 | 9 | 242 | 95 | 2.55 | 21.35 |
| Tethys | 25 | 9 | 144 | 77 | 1.87 | 39.64 |
| Dione | 97 | 20 | 1020 | 254 | 4.02 | 12.95 |
| Rhea | 301 | 57 | 702 | 73 | 3.50 | 21.44 |
| Iapetus | 17 | 5 | 146 | 49 | 2.98 | 17.90 |

The coordinate systems have been established assuming that all of the satellites are in synchronous rotation and that their spin axes are normal to their orbital planes. These assumptions have been confirmed for the satellites of Jupiter (Davies and Katayama, 1980) and as of September 1981 appear to be true for the satellites of Saturn with the possible exception of Hyperion.

In the convention of the IAU (Davies et al., 1980), the ephemeris position of the prime meridian of each body is given by the angle W, where W is measured along the satellite's equator in an easterly direction from the ascending node of the satellite's equator on the 1950.0 Earth's standard equator to the point where the prime meridian crosses the satellite's equator. The equations for W currently in use are

Io $W = 262.^{\circ}7+203.^{\circ}4889538d-0.^{\circ}085 \sin J_1-0.^{\circ}022 \sin J_2$

Europa $W = 158.^{\circ}3+101.^{\circ}3747234d-0.^{\circ}980 \sin J_2-0.^{\circ}054 \sin J_3-0.^{\circ}014 \sin J_4-0.^{\circ}008 \sin J_5$

Ganymede $W = 196.^{\circ}8+50.^{\circ}317\ 6081d+0.^{\circ}033 \sin J_2-0.^{\circ}389 \sin J_3-0.^{\circ}082 \sin J_4$

Callisto $W = 157.^{\circ}5+21.^{\circ}5710715d+0.^{\circ}061 \sin J_3-0.^{\circ}533 \sin J_4-0.^{\circ}009 \sin J_6$

where $J_1 = 19.^{\circ}2+4850.^{\circ}7T$
$J_2 = 120.^{\circ}8+1191.^{\circ}3T$
$J_3 = 349.^{\circ}5+262.^{\circ}1T$
$J_4 = 198.^{\circ}3+64.^{\circ}3T$
$J_5 = 241.^{\circ}6+2382.^{\circ}6T$
$J_6 = 317.^{\circ}7+6070.^{\circ}0T$

d = interval in ephemeris days from JED 2433282.5

T = interval in ephemeris centuries of 36525 days from JED 2433282.5

THE CONTROL NETWORKS OF THE SATELLITES OF JUPITER AND SATURN
Davies, Merton E.

| | |
|---|---|
| Mimas | $W = 246.^{\circ}9+381.^{\circ}9945550d-13.^{\circ}0 \sin S_1-43.^{\circ}4 \sin S_6$ |
| Enceladus | $W = 301.^{\circ}8+262.^{\circ}7318996d$ |
| Tethys | $W = 31.^{\circ}7+190.^{\circ}6979085d-9.^{\circ}3 \sin S_2+2.^{\circ}2 \sin S_6$ |
| Dione | $W = 121.^{\circ}6+131.^{\circ}5349316d$ |
| Rhea | $W = 14.^{\circ}1+79.^{\circ}6900478d-3.^{\circ}0 \sin S_3$ |
| Iapetus | $W = 275.^{\circ}5+4.^{\circ}537\ 9571d$ |

where $S_1 = 68.^{\circ}6-36505.^{\circ}5T$
$S_2 = 314.^{\circ}5-7225.^{\circ}9T$
$S_3 = 134.^{\circ}9-1016.^{\circ}3T$
$S_6 = 64.^{\circ}9+506.^{\circ}2T$

The W equation for Hyperion is not included because of uncertainty in its rotational parameters at this time. The systems of longitude for Europa, Ganymede, and Callisto are defined by surface features (Davies and Katayama, 1980). In the future the systems of longitude for most of the Saturnian satellites will be defined by surface features which will modify the $W_o$ terms in the W equations.

The author is indebted to Tom Duxbury, Jay Lieske, and Andrew Sinclair for the higher order terms in these expressions.

References

Davies, M. E., V. K. Abalakin, C. A. Cross, R. L. Duncombe, H. Masursky, B. Morando, T. C. Owen, P. K. Seidelmann, A. T. Sinclair, G. A. Wilkins, and Y. S. Tjuflin, "Report of the IAU Working Group on Cartographic Coordinates and Rotational Elements of the Planets and Satellites," *Celestial Mechanics*, Vol. 22, 1980, pp. 205-230.

Davies, M. E., and F. Y. Katayama, *Coordinates of Features on the Galilean Satellites*, The Rand Corporation, N-1617-JPL/NASA, November 1980; to be published in *J. Geophys. Res.*

# THE CONTROL NETWORK OF MARS: SEPTEMBER 1981

Davies, Merton E., The Rand Corporation, Santa Monica, California 90406

The planetwide control net of Mars has been strengthened by adding strips of Viking mapping frames to the existing data set. These high resolution strips lie between the Viking 1 lander site and Airy-0, north along the prime meridian to 60° latitude, and then south and west to the Viking 1 lander site. Within the strips the accuracy of the coordinates of the control points is improved; the errors in latitude and longitude vary from point to point and lie between 40 m and 3 km (see Davies and Dole, 1980).

The horizontal coordinates of the control points on Mars have been updated with a single-block planetwide analytical triangulation computed in September 1981. The computation contained 45,114 measurements of 6457 points on 1701 pictures. These were divided into 1054 Mariner 9 frames and 647 Viking frames; 18,017 normal equations were solved. The overdetermination factor was 2.50 and the standard error of measurement was 19.17 μm. The longitude of the Viking 1 lander site was 47°.964. The last published control net (Davies et al., 1978) contained coordinates of 4138 control points and was based on 27,582 measurements on 1213 pictures. At that time the longitude of the Viking 1 lander site was given as 47°.968.

## References

Davies, M. E., F. Y. Katayama, and J. A. Roth, Control Net of Mars: February 1978, The Rand Corporation, R-2309-NASA, February 1978.

Davies, M. E., and S. H. Dole, Improved Coordinates of Features in the Vicinity of the Viking 1 Lander Site on Mars, The Rand Corporation, R-2600-NASA, March 1980.

VOYAGER CARTOGRAPHY

R. M. Batson, P. M. Bridges and K. F. Mullins, U. S. Geological Survey, Flagstaff, Arizona 86001

Maps of the Jovian and Saturnian satellites are being made at several scales from Voyager 1 and 2 data. Details of the Galilean satellite mapping program are given by Batson and others (1980). The proposed Saturnian satellite mapping plan can be summarized as follows:

| SATELLITE | SCALE | NO. SHEETS | FORMAT |
|---|---|---|---|
| Mimas | 1:2M+1:5M | 1+1 | same as I-1391[a] |
| Enceladus | 1:2M+1:5M | 1+1 | like I-1390[b] |
| Tethys | 1:2M | 3 | like Lunar 1:5M |
| | 1:5M | 1 | same as I-1389 |
| Dione | 1:5M | 1 | same as I-1389 |
| Rhea | 1:5M | 3 | like Lunar 1:5M |
| Hyperion | 1:5M | 1 | TBD |
| Iapetus | 1:5M(?) | 3(?) | like I-1390(?) |
| Total no. sheets: | | 16 | |

[a]USGS, 1981a
[b]USGS, 1981b

The steps in preparing each Voyager cartographic project are:

1. First level image processing. Includes radiometric processing of all images that will be used in the mapping, along with reseau removal and general cosmetics, excluding filtering and stretching
2. Second level image processing. Includes sun-angle (photometric) correction and geometric transformation of images to appropriate map projections. High-pass filtering and contrast stretching are done on film images of the processing, but not on the image data bases.
3. Compilation of controlled photomosaics.
4. Airbrush compilations.

Copies of the processed images are distributed to NSSDC and to the Regional Planetary Image Facilities. These products include negatives, 8x10 reference prints, and, for facilities that can use them, magnetic tapes.

Summary of progress on the Galilean satellite cartography:

| | |
|---|---|
| Frames processed through Level 1: | 361 |
| Frames processed through level 2: | 82 |
| Mosaics completed: | 5 |
| Map sheets in press: | 2[a,b] |

Summary of progress on the Saturnian satellite cartography:

| | |
|---|---|
| No. Frames processed through Level 1: | 58 |
| No. Frames processed through Level 2: | 5 |
| No. Mosaics complete: | --[b] |
| No. Map sheets in press: | --[b] |

[a]Io, Ji02; Europa, Je03
[b]Does not include preliminary versions

References

Batson, R. M., Bridges, P. M., Inge, J. L., Isbell, C. E., Masursky, Harold, Strobell, M. E., and Tyner, R. L., 1980, Mapping the Galilean Satellites of Jupiter with Voyager data: Photogrammetric Engineering and Remote Sensing, v. 46, no. 10, p 1303-1312.

U. S. Geological Survey, 1981(a) Preliminary pictorial map of Tethys, I-1390: U. S. Geological Survey, Reston, VA.

U. S. Geological Survey, 1981(b), Preliminary pictorial map of Dione, I-1389: U. S. Geological Survey, Reston, VA.

MARS ATLASES

R. M. Batson and R. L. Tyner, U. S. Geological Survey, Flagstaff, Arizona 86001

The catalog of Viking Orbiter pictures processed prior to December, 1978 is in press. This catalog consists of 198 "subquad" mosaics (originally compiled at a scale of 1:1,250,000) their attendant cutline indexes, and lists of all frames that lie within the mosaic area, whether included in the mosaic or not. The catalog is authored by R. L. Tyner and R. D. Carroll, and 20 associate authors, and is planned for publication as a NASA contractor's report. A final volume that will show locations of all Viking frames will be published when all of the pictures have been processed.

A revision of the Atlas of Mars (Batson and others, 1979) will include all 1:5,000,000 scale revisions, all 1:2,000,000 photomosaics, all color maps, and all special maps of Mars, as well as an updated Gazeteer. Because much of this work has yet to be done, this atlas will not be published for several years. An interim atlas is being prepared that will contain color pictures and maps, and other special products is in progress; it may be submitted for publication during FY82.

Reference

Batson, R. M., Bridges, P. M. and Inge, J. L., 1979, Atlas of Mars: The 1:5,000,000 map series: National Aeronautics and Space Administration Special Publication SP 438, 146p

# 1:2,000,000 SCALE CONTROLLED PHOTOMOSAICS OF MARS

R. M. Batson and R. L. Tyner, U. S. Geological Survey, Flagstaff, Arizona 86001

Compilation of a series of 140 controlled photomosaics of Mars is continuing. The mosaic scale is 1:2,000,000. They are based on the control net defined by Davies and others (1978). Progress on the series, and the relation of the mosaics to the 1:5,000,000 Mars map series is shown in figrure 1. To date, a total of 71 mosaics have been published, 29 mosaics are in press, and 18 mosaics are in preparation.

The mosaics are carefully controlled so that at least two thirds of all control images lie within 0.5mm of their correct location as defined by the control net. Relatively little effort is expended, however, on the cosmetic appearance of the mosaics. Some variation in tones between contiguous frames is tolerated, and frame edges are not feathered. On some mosaics, particularly those prepared early in the program, gaps in coverage comprising as much as five percent of the mosaic area was allowed, because it was uncertain whether coverage would become available in time for the complete mosaic to be useful to planetary geologists.

Figure 1 shows that most of the mosaics are either complete or in progress. The most difficult part of the program is yet to come, however; pictures in the polar regions, where illumination angles, surface frost conditions, and cloud cover vary widely, will give these mosaics a patchy appearance, and, in many cases, a dynamic range that cannot be accommodated by the printing process. Investigators may find them somewhat difficult to use. Airbrush versions of the maps in these regions will provide more coherent portrayal of surface detail. The airbrush maps are considered "special maps" and are discussed elsewhere by Batson (1981).

## References

Batson, R. M., 1982, Special purpose Mars mapping: in Reports of the Planetary Geology Program, 1981-1982, NASA TM (this volume).

Davies, M. E., Katayama, F. Y. and Roth, J. A., 1978, Control net of Mars; February, 1978: The Rand Corporation, R-2309-NASA, 91p

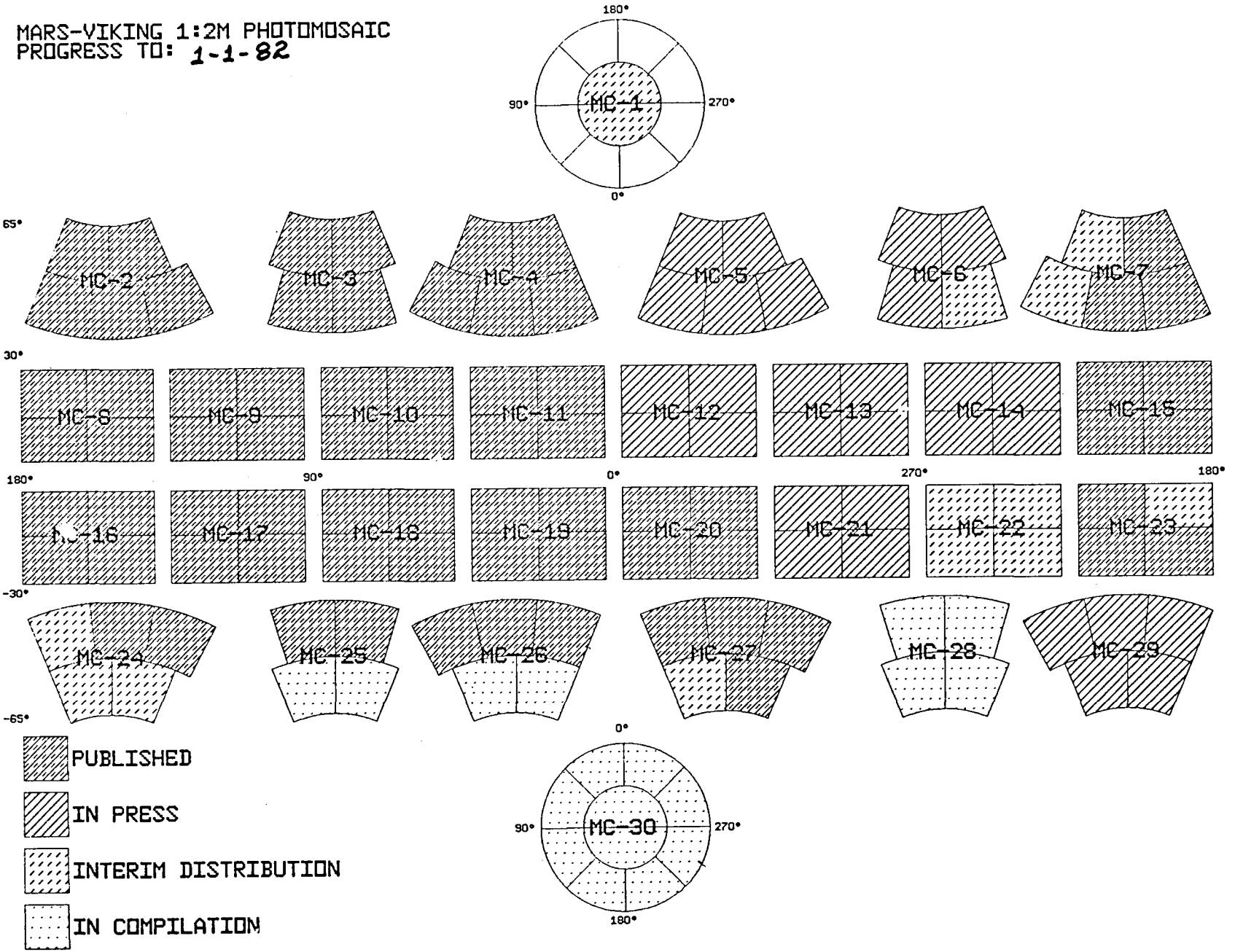


Figure 1. Status of compilation of 1:2,000,000 controlled photomosaics.

MARS 1:2 MILLION CONTOUR MAPPING PROBLEMS WITH VIKING ORBITER PHOTOGRAPHS

Sherman S. C. Wu, Raymond Jordan, and Francis J. Schafer; U.S. Geological Survey, Flagstaff, AZ 86001

Specially developed photogrammetric techniques [1,2] are being used to compile topographic maps of Mars at various scales Viking Orbiter photographs of various resolutions are used for the compilations [3,4]. Factors that limit the accuracy of the compilations include low resolution (many of the pictures were taken from slant-ranges as great as 37,000 km), the very narrow field-of-view of the Viking cameras, weak photogrammetric geometry (i.e., small base-to-height ratios) and the presence of haze and mist in the Martian atmosphere. Figure 1 is an example of a recently compiled 1:2 million Mars map MC-9NW. Dashed contour lines at the northeast corner of the map are interpolated from surrounding compilations because clouds and dust obscure the surface in pictures of that area. A depression of about 2 km deep is shown at the central part of the map. This area was compiled from 4 adjacent stereo models, all of which indicated the depression. However, a radar profile from Goldstone Observatory shows an elevation of about 2 km in this area [5]. Evidence that could settle the question may be contained in Viking pictures, as yet unlocated, taken through the red filter or through a clearer atmosphere.

Another puzzling phenomenon in photogrammetric compilation with Viking Orbiter photographs is the fact that contours compiled from high-resolution (low altitude) photographs tend to indicate smooth terrain, while contours of the same feature compiled with low resolution (high altitude) photographs tend to indicate a rougher or more undulating surface. For example, the contours of the slopes of Olympus Mons on the 1:2 million map (Fig. 1) indicate a rough surface, whereas the slopes appear smoother on a larger scale map compiled with high-resolution pictures [6]. One possible explanation may be that albedo variations have more of an effect on stereo compilation with high altitude photographs than with low altitude, high resolution pictures. Differences in the direction of illumination may also be a factor.

References

[1] Wu, S. S. C. (1980) Photogram. Appl. to Planet. Mapping. NASA Tech. Memo. 81766, p. 354-357.

[2] Wu, S. S. C., Elassal, A. A., Jordan, Raymond, and Schafer, F. J. (1981) Photogram. Appl. of Viking Obital Photog. Planetary and Space Sci. (in press).

[3] Wu, S. S. C. (1979) Mars Photogram. NASA Tech. Memo. 80339, p. 432-435.

[4] Wu, S. S. C., Schafer, F. J., and Jordan, Raymond (1980) Topog. Mapping of Mars: 1:2 million contour series. NASA Tech. Memo. 82385, p. 458-461.

[5] Ruth, L. E., Downs, G. S., and Saunders, R. S. (1980) Radar Altimetry of South Tharsis Mars. Icarus 42(3), p. 287-316.

[6] Wu, S. S. C., Garcia, P. A., Jordan, Raymond, and Schafer, F. J. (1981) Topog. Map of Olympus Mons. 3rd Intl. Colloquium on Mars, LPI Contr. 441, p. 287-289.

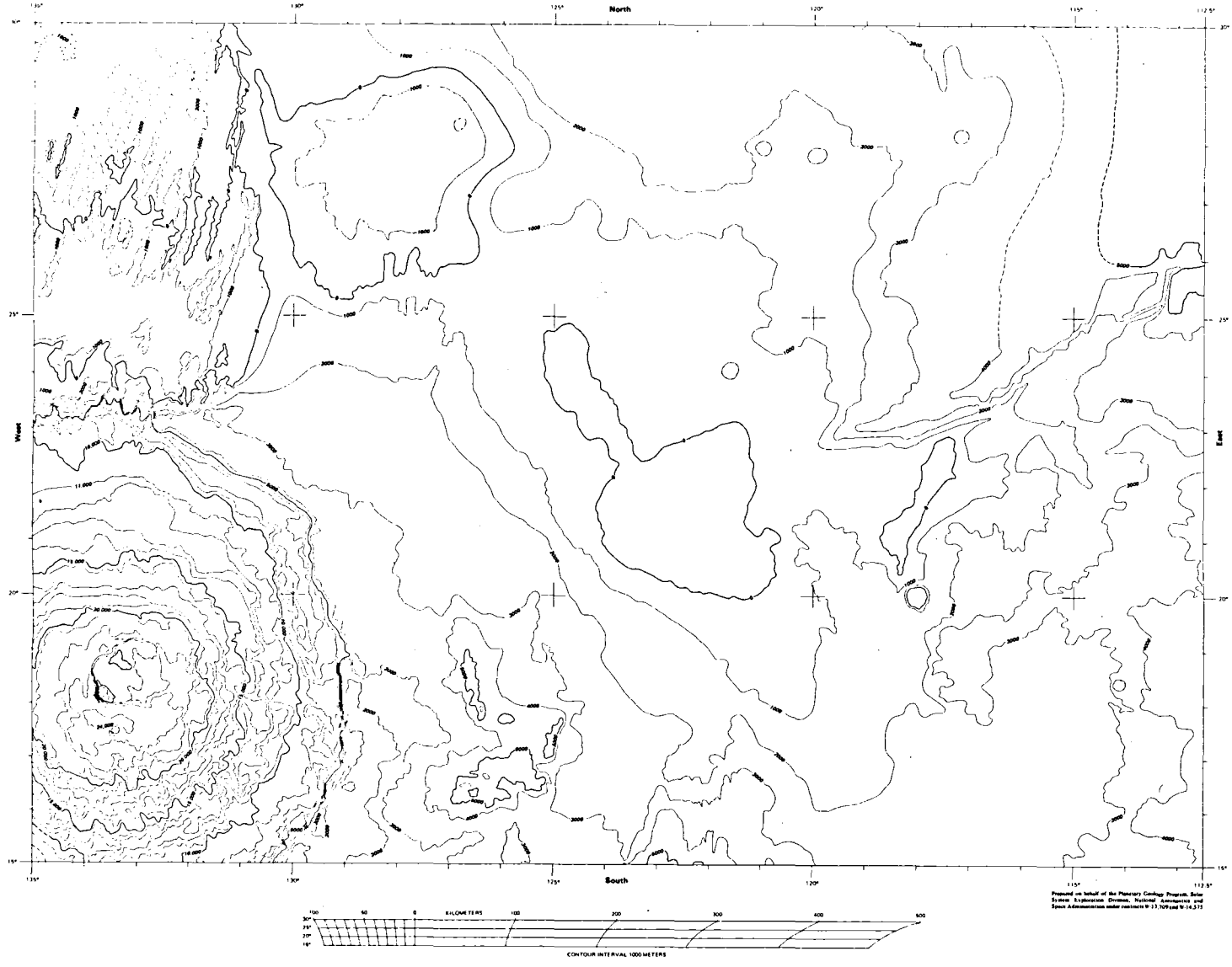


Figure 1. Topographic map of northwest quadrange of Mars, MC-9NW. This is an example of the Mars 1:2 million topographic map series, at reduced scale.

# SPECIAL PURPOSE MARS MAPPING

R. M. Batson, U. S. Geological Survey, Flagstaff, Arizona 86001

Four special Mars maps were completed and either published or submitted for publication during FY 81. These are: 1) Shaded Relief Map of the Chryse Planitia region of Mars, 2) Orthophotomosaic of the Arsia Mons region of Mars, 3) Controlled photomosaic of the Olympus Mons region of Mars, and 4) Shaded relief map of the Coprates NW quadrangle of Mars.

The Shaded relief map of the Chryse Planitia was drawn by Patricia M. Bridges using conventional airbrush techniques (Inge and Bridges, 1975). The map was made on an oblique stereographic projection centered on lat $15^{o}$ N., $40^{o}$ W., and covers an area of about 14 million square kilometers. The average radius from the center of the map is 2100 kilometers. The center of the projection is offset from the center of the map because a large area on the western border was added after map compilation was well underway. The map is irregularly pentagonal in outline because the boundaries were selected based on the extent of natural drainage features, rather than by arbitrary positions of latitude or longitude. The photomosaic base (compiled by Holly M. Ferguson, under the supervision of R. L. Tyner) contains approximately 500 Viking Orbiter frames. Approximately 300 additional Viking frames were examined in making the shaded relief portrayal.

The Arsia Mons orthophotomosaic was made using techniques similar to those described by Batson and others (1979). Batson and others (1982) discuss this product in more detail elsewhere in this volume.

The controlled mosaic of the Olympus Mons region was made by Patty Thomas and Cynthia Phelan under the supervision of R. L. Tyner. Frame edges were feathered and more effort was made to match tones between contiguous frames than is attempted for the 1:2,000,000 controlled photomosaics series of Mars. Approximately 140 Viking pictures are contained in the mosaic. Most of these frames are scaled versions of the JPL MTIS orthographic projections of the Viking pictures; six frames covering the area on the north west flank of Olympus Mons were specially processed and high-pass filtered by Lynda Sowers to bring out detail that is usually obscured by saturated highlights or shadow. The map is printed on a transverse Mercator projection with the central meridian at long $137.5^{o}$W. The scale at the central meridian is 1:2,016,000; the average scale for the entire map area is 1:2,000,000. The map neatline is rectangular, rather than longitudinal and latitudinal. It extends roughly 1300 kilometers north, 840 kilometers south, 320 kilometers east, and 1020 kilometers west of the Olympus Mons caldera.

The Coprates NW quadrangle was compiled using conventional airbrush techniques, by Susan L. Davis; base material was the 1:2,000,000 controlled photomosaic of the same area. The quadrangle was selected for shaded relief treatment because extensive haze and cloud cover over parts of most of the Viking Orbiter pictures of the area precluded coherent portrayal of landforms from Viking pictures alone. Unexpectedly large relief parallax was discovered in the images after the airbrushing was complete, when an attempt was made to overlay a newly compiled contour map (Wu, 1980) over the shaded relief rendition. After an unsuccessful attempt was made to correct these

distortions on a digitized version of the airbrush map, the decision was made to publish the shaded relief map separately from the contour map. Future shaded relief maps at this scale will be compiled after the the contour maps (if such are planned for the area) so that they can be corrected for relief parallax during compilation. At least one version of each of these maps will be printed with a contour overprint.

Work on two additional 1:2,000,000 shaded relief maps has been suspended pending resolution of various kinds of control problems. The airbrushing on the Mare Boreum "A" and Mare Boreum "B" quads is complete, but was tied to base mosaics with severe control anomalies, caused by the scarcity of control points in the northern hemisphere of Mars, and by difficulties in identifying accurately the few control points that exist. Until these difficulties are resolved and corrected, these two maps will not be published.

An airbrush version of the Phoenicis Lacus NE 1:2,000,000 quadrangle was begun by J. L. Inge, but work was suspended pending completion of the contour map of the area. Patricia Hagerty is currently working on the airbrushed version of Phoenicis Lacus NW. This sheet will be published with a contour overprint that is already available (Wu, 1980).

References

Batson, R. M., Hall, D. G., and Edwards, Kathleen, 1979, An orthophoto mosaic of Tithonium Chasma: in Reports of the Planetary Geology Program, 1978-1979, NASA TM 80339, p. 415.

Batson, R. M., Edwards, Kathleen, and Skiff, B. A., 1982, Orthophoto mosaics and three dimensional transformations of Viking Orbiter pictures: in Reports of the Planetary Geology Program, 1981-1982, NASA TM (this volume).

Inge, J. L., and Bridges, P. M., 1976, Applied photointerpretation for airbrush cartography: Photogrammetric Engineering and Remote Sensing, v.42, no. 6, p. 749-760.

Wu, S. S. C., Schafer, F. J. and Jordan, Raymond, 1980, Topographic mapping of Mars: the 1:2,000,000 contour map series, in Reports of the Planetary Geology Program, 1980, NASA TM 82385, p.458-459.

# ORTHOPHOTO MOSAICS AND THREE DIMENSIONAL TRANSFORMATIONS OF VIKING ORBITER PICTURES

R. M. Batson, Kathleen Edwards and B. A. Skiff, U. S. Geological Survey, Flagstaff, Arizona 86001

Techniques for merging image data with elevation data have been previously described by Batson and others (1976, 1979). These techniques have now been sufficiently refined to allow their routine use in compiling orthophoto mosaics and in making three-dimensional transformations for special purpose illustrations. They have been applied to Viking Orbiter pictures of the Arsia Mons region, to make an orthophotomosaic (figure 1), a single monoscopic oblique presentation of the mountain (figure 2), and a stereogram of an oblique presentation of the mountain (figure 3).

The Arsia Mons products are based on a contour map (Wu, 1981) and on four Viking Orbiter pictures. A digital terrain model was made from the contour map by interpolating elevations between contour lines on an array of rows and columns, to create a raster of values the same size as the desired data base. The terrain model was then rotated so that its surface presented the same viewing orientation as a picture in the mosaic. The picture was then superposed digitally on the model so that each pixel in the image could be identified with a specific elevation value in the terrain model. The procedure was repeated for each picture in the mosaic. Each of the pictures was then transformed as a three-dimensional array to an orthographic view, and a mosaic was made. The resulting mosaic has no relief parallax, because each pixel was shifted as a function of its elevation during the transformation.

In effect, the data base from which figure 1 was made constitutes a three dimensional model of Arsia Mons that can be oriented by computer to any desired perspective for optimum viewing, just as a solid plaster model could be physically rotated to any desired orientation. The view of figure 2 is from 15 degrees above the horizon along an azimuth of 225 degrees. The view of figure 3 is from 25 degrees above the horizon along an azimuth of 225 degrees for the right-hand member of the pair, and along an azimuth of 230 degrees for the left member, to create the stereoscopic effect. In figures 2 and 3, the digital terrain model was exaggerated by a factor of 5 to more clearly delineate the vertical dimension.

## References

Batson, R. M., Edwards, Kathleen and Eliason, E. M., 1976, Synthetic stereo and LANDSAT pictures: Photogrammetric Engineering and Remote Sensing, v.42, no.10, p 1279-1284.

Batson, R. M., Hall, D. G. and Edwards, Kathleen, 1979, An orthophoto mosaic of Tithonium Chasma: in Reports of the Planetary Geology Program, 1978-1979, NASA TM 80339, p 415.

Wu, S. S. C., 1981, Contour map of Arsia Mons: written communication

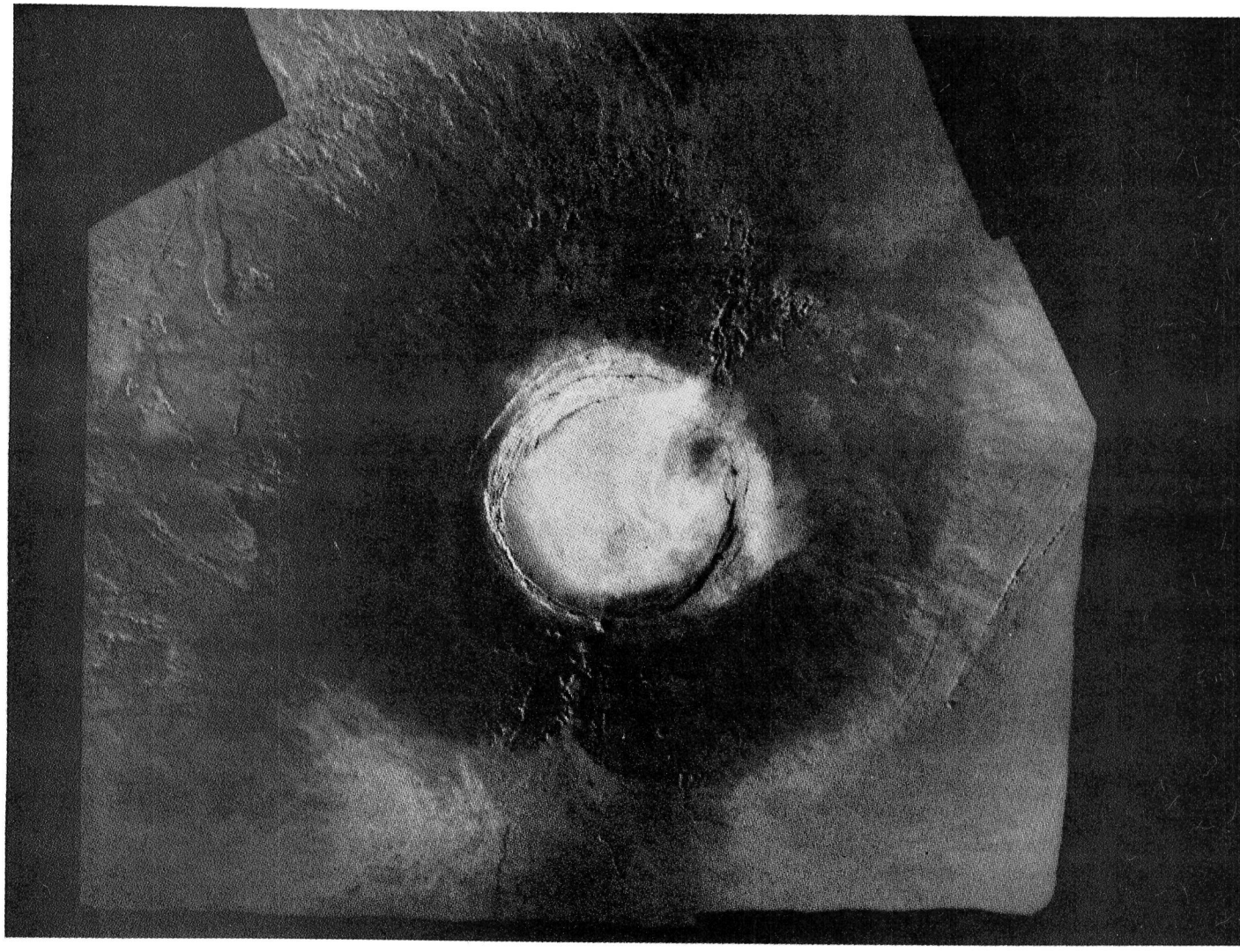

Figure 1. Orthophotomosaic of the Arsia Mons area of Mars

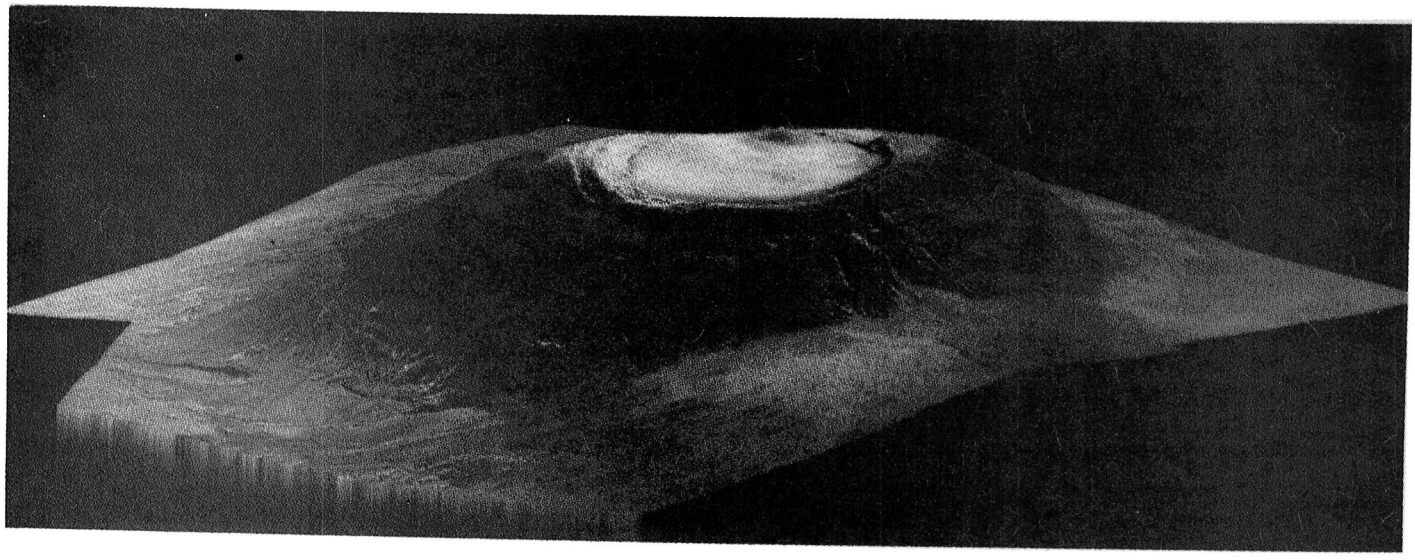

Figure 2. Oblique view of the Arsia Mons orthophotomosaic. The vertical dimension is exaggerated five times. The view is from 15 degrees above the southwestern horizon.

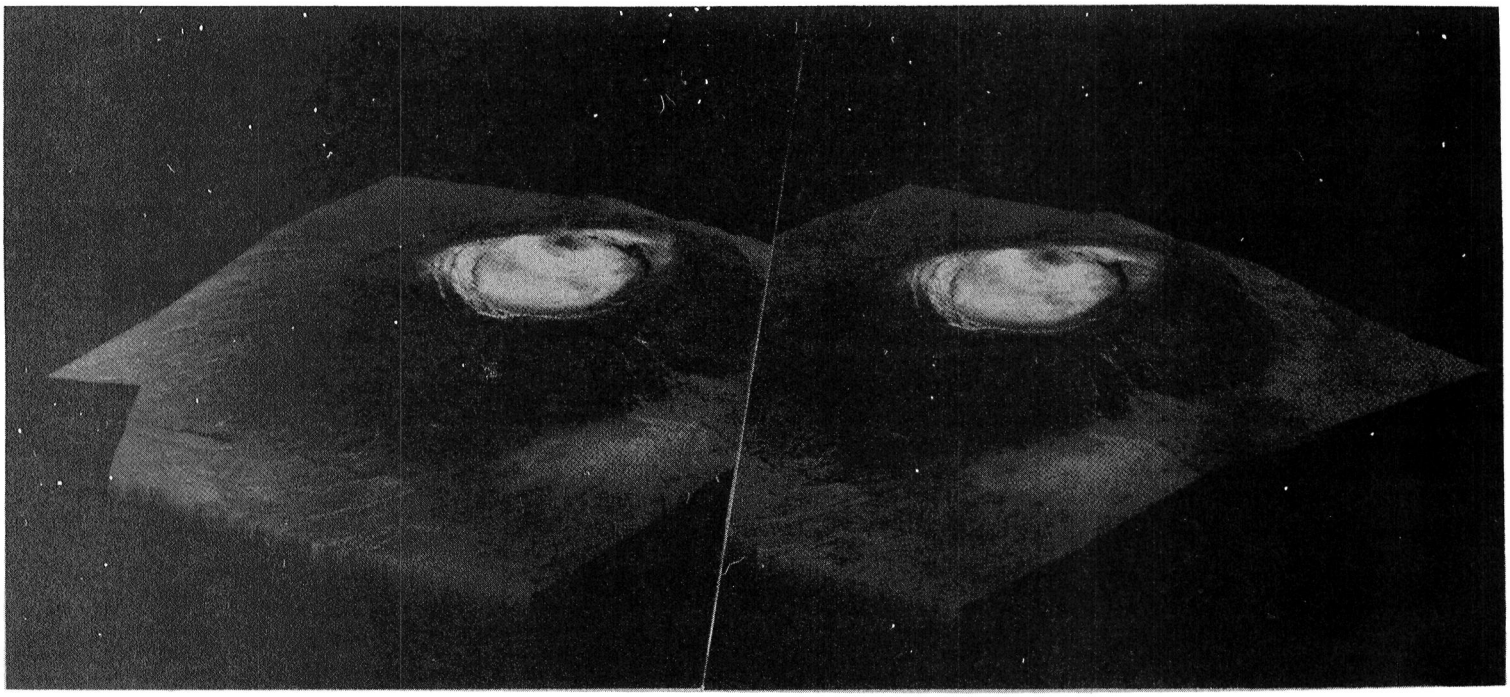

Figure 3 Oblique stereogram of Arsia Mons orthophotomosaic. The vertical dimension is exaggerated five times. The view is from 25 degrees above the southwestern horizon. Stereoscopic convergence is five degrees.

# REVISIONS OF 1:5,000,000 SCALE MARS MAPS

R.M. Batson and P. M. Bridges, U. S. Geological Survey, Flagstaff, Arizona 86001

Several of the 1:5,000,000 maps of Mars originally compliled from Mariner 9 pictures are being upgraded by adding detail from Viking Orbiter pictures to the original airbrush drawings. No attempt is being made to reposition features according to new control data; the maps remain tied to the Mariner 9 datum (Davies 1973). The maps in the northern hemisphere of Mars are particularly improved by these revisions, because the resolution of Mariner 9 pictures was so poor in that region. Mariner 9 pictures taken near perieapsis, in the martian equatrial region, are often degraded by cloud or haze cover, however. The maps are therefore improved considerably by the addition of information from the Viking Orbiter pictures. The status of these revisions is as follows:

| | |
|---|---|
| Quadrangles published or in press: | 5 |
| Quadrangles in revision process: | 4 |
| Quadrangles yet to be done | 17-21 |

## Reference

Davies, M. E., 1973, Mariner 9: primary control net: Photogrammetric Engineering, v.39, no.12, p 1297-1302.

PHOTOGRAMMETRIC COMPILATION OF THE GLOBAL MAP OF THE MOON,

Sherman S. C. Wu, U.S. Geological Survey, Flagstaff, AZ 86001

A global topographic map of the Moon is being compiled at a scale of 1:5,000,000 with a contour interval of 500 m (1). An intermediate product is the topographic contour map of the Eastern region of the Moon compiled using 340 stereo pairs of metric photographs from the Apollo 15, 16, and 17 missions on the AP/C analytical plotter (Fig. 1). The map was compiled using the same format as the existing NASA Lunar Planning Chart and covers the same area as LOC-3 (2), but is 10° shorter in the north and south boundaries because of the available coverage of near vertical photographs from the Apollo metric cameras.

This intermediate map was compiled at a scale of 1:2,750,000 with a contour interval of 500 m. However the scale of 1:2,750,000 is true only at the equator since a Mercator projection is used. Contour lines and elevations are referred to a new topographic datum of the Moon, which is defined by using a gravity field described in terms of spherical harmonics of fifth-degree and fifth-order with the sixth-degree sectorial terms combined with a mean radius of 1738 km (3,4). Control nets derived by Schmit-Doyle (5) and by the Defense Mapping Agency from Apollo photographs were used. The same coordinate system adopted for the lunar control network is used for the map compilation. For the computation of the map projection, a spherical figure with radius of 1738 km of the Moon is used.

Photogrammetric compilation is being continued for areas covered by LOC-1, LOC-2, and LOC-4. The entire global topographic map of the Moon will then be completed by synthesis of existing available topographic information from various data sources (1,4).

References

(1) Wu, S. S. C. (1979) NASA Technical Memorandum 80339, Report of Planetary Geology Program, 1978-1979, p. 429 - 431.

(2) NASA Lunar Planning Chart LOC-3 1st edition,

(3) Wu, S. S. C. (1981) International Review, Annales de Geophysique Central National de la Recherche Scientifique, p. 147-160.

(4) Wu, S. S. C. (1981) Lunar and Planetary Science XII, p. 1217-1218.

(5) Doyle, F. J., Elaissal, A. A., and Lacas, J. R. (1977) NOAA Technical Report NOS7 NGS5, 53 p.

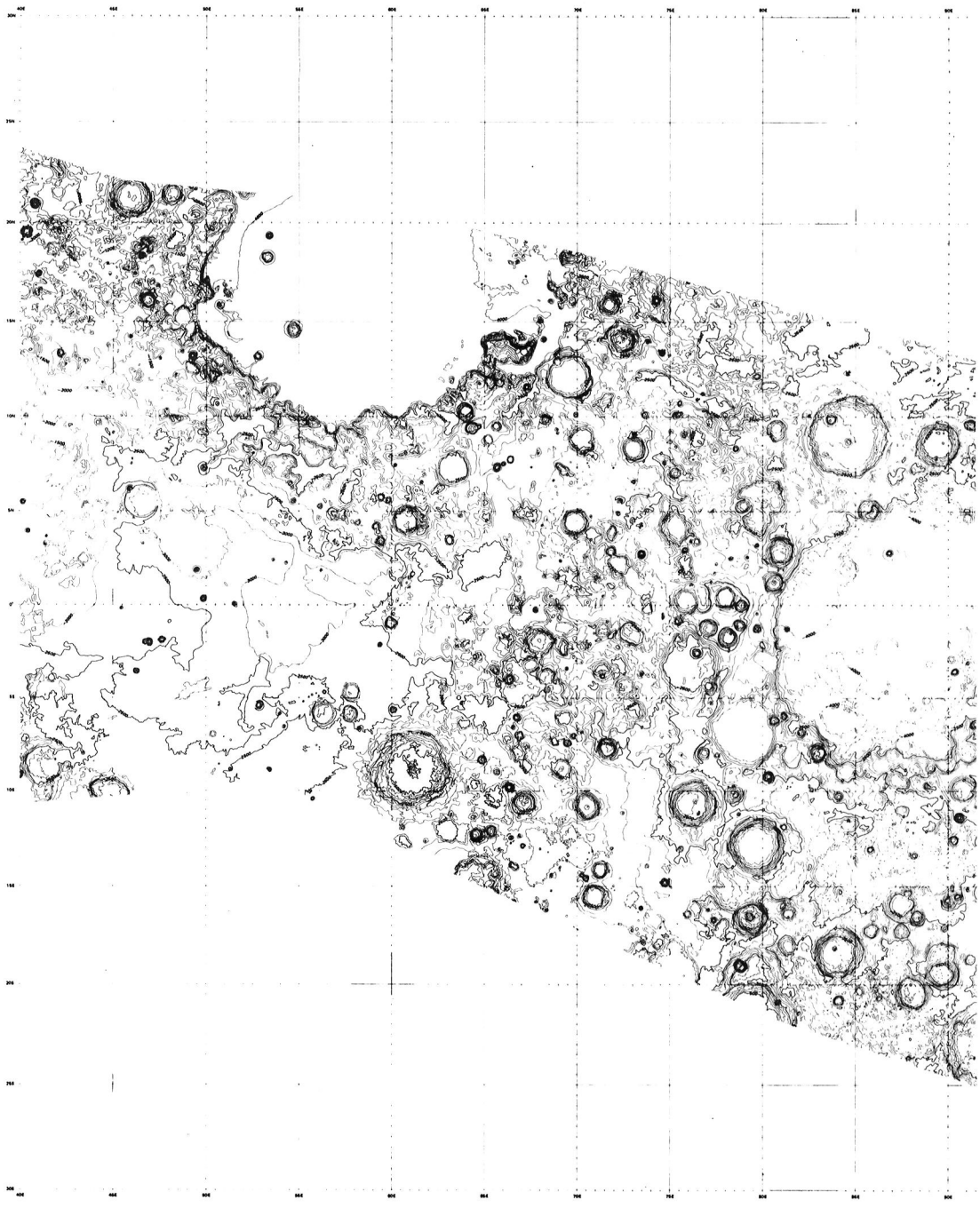

Figure 1. Topographic map of the Moon (Eastern Region - LOC-3). The map was compiled at a scale of 1:2,750,000. The reduced map scale in this figure is 1:11,000,000. Vertical reliability is about 100 to 200 meters.

(a) Coverage of 40°E to 90°E of longitude.

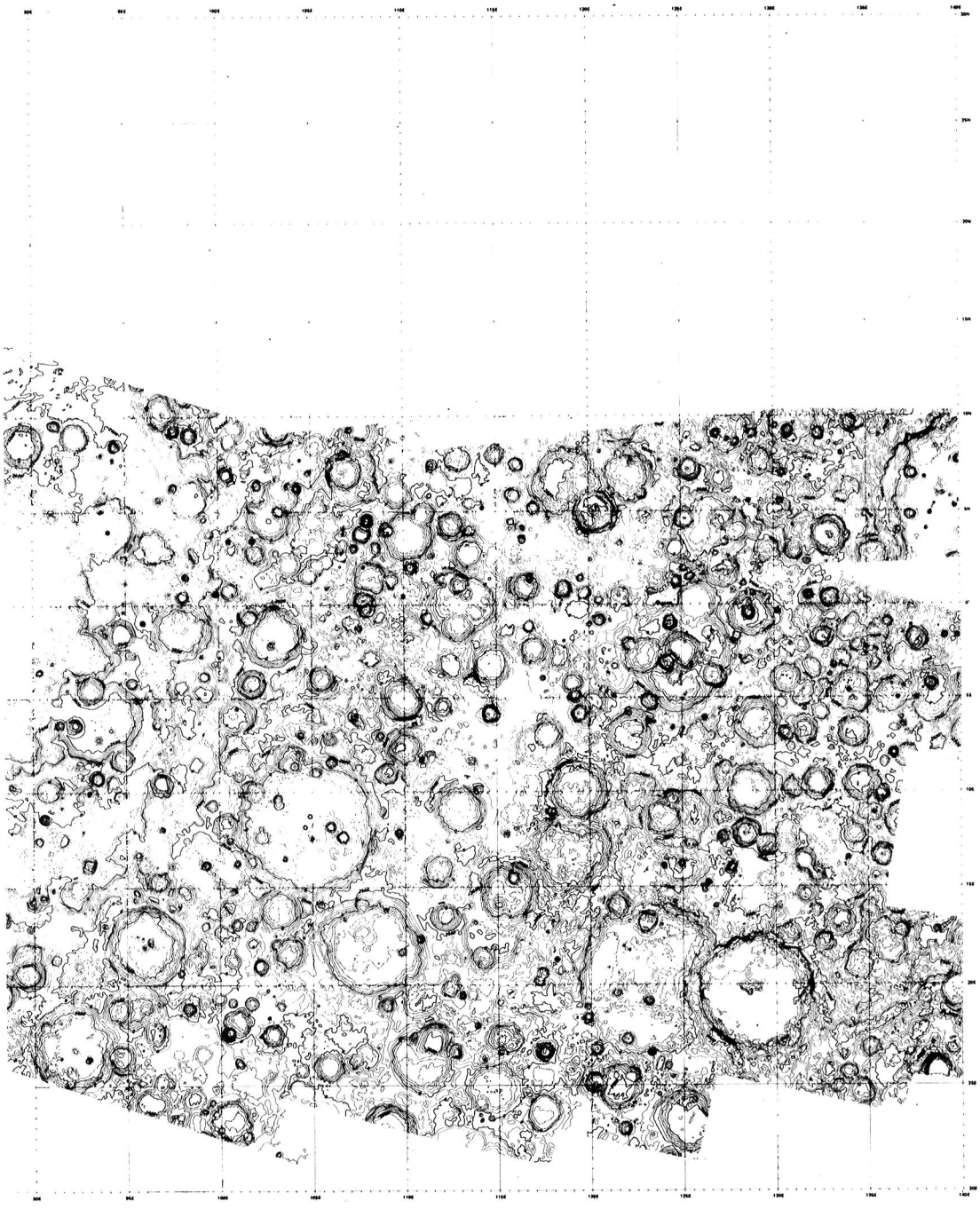

Figure 1. Topographic map of the Moon (Eastern Region - LOC-3). The map was compiled at a scale of 1:2,750,000. The reduced map scale in this figure is 1:11,000,000. Vertical reliability is about 100 to 200 meters.

(b) Coverage of 90°E to 140°E of longitude.

# REVIEW AND HIGHLIGHTS OF MARS GEOLOGIC MAPPING - WESTERN HEMISPHERE

David H. Scott, U.S. Geological Survey, Flagstaff, AZ 86001

Geologic mapping of Mars' western hemisphere at 1:15 million scale from Viking images has revealed several new areas of interest, particularly for volcanologists and stratigraphers. For example, the number of volcanoes found in this region has been increased three to four times over those mapped from the Mariner 9 pictures. Most of the new features, provisionally mapped as volcanoes or volcano-tectonic structures, occur in the southern highland region [1] where Mariner resolution and picture quality was poor. They are moderate to large in size and lie 1000 km or more south and southwest of Tharsis Montes. They are not alined with the giant shield volcanoes, however, and appear to be considerably older morphologically; this relation is substantiated in places by the stratigraphic sequence. Lava flows from the Tharsis volcanoes have flooded large areas of this southern terrain and have overlapped or embayed many of the volcanic constructs. Calderas and summit craters are not uncommon; generally they are highly degraded by infilling and dissection that resulted from faulting and channeling. In this structurally complex region many of the volcanoes and vents appear to follow older tectonic trends.

Another interesting discovery was made in the Tempe Terra area (lat 40° N., long 70° W.) where several large (250-km diameter) circular structures were found. They are not associated with impact craters or basins, have no visible relief, and are ringed by concentric fractures resembling those around Alba Patera and other volcanoes in Tharsis Montes. One of the structures encircles a caldera-like depression and small prominent dome; lava flows extend for distances greater than 100 km from its central area. The flows bury faults in places but are transected by them in others. They probably have been extruded episodically during a long period of tectonic activity. The occurrence of these and other known ring-fracture systems on Mars suggests a continuum between structural evolution and volcanism. The circular structures show different stages of development whose progression appears to culminate in volcanic mountain building.

Additional studies of postulated ignimbrite units [2] in the Amazonis, Memnonia, and Aeolis quadrangles of Mars show that they probably cover more than 2 million $km^2$. They overlie parts of the western and southern aureole deposits of Olympus Mons but are embayed in places by the lava plains of Amazonis Planitia. Stratigraphic relations between the lava flows of Tharsis Montes and the ignimbrites are not clearly defined; crater counts indicate that younger ignimbrites postdate the flows.

## REFERENCES

1. Scott, D. H., and Tanaka, K. L., 1982, Mars: A large highland volcanic province revealed by Viking images: Proc. Lunar Planet. Sci. Conf. 12th, in press.
2. Scott, D. H. and Tanaka, K. L., 1980, Martian ignimbrites (abs.), *in* Reports of Planetary Geology Program, 1980, NASA TM 82385, p. 255-257.

# GEOLOGIC MAPPING OF MANGALA VALLIS FROM VIKING ORBITER SURVEY MISSION DATA

Ellen Stofan, College of William and Mary, Williamsburg, VA; David Pieri and R. Stephen Saunders, Jet Propulsion Laboratory, California Institute of Technology, Pasadena, CA 91109.

The major channel systems of Mars occupy the heavily cratered terrains. The largest systems such as Tiu and adjacent valleys and Kasei and related channels converge on the low plains of Chryse. Some other smaller systems, for example, Ma'adim and the subject of this study, Mangala, were formed by material flowing into the low region associated with Amazonis.

Thus, in the regional setting these channel systems were created by the flow of material into the basins that flank the Tharsis bulge. It has been argued that the Tharsis topography and the flanking basin are genetically related (Phillips and Saunders, 1975). If this is the case, we would expect that the channel floors are approximately the same age in the Chryse and Amazonis systems and that some Tharsis related surfaces are also contemporaneous with the channels. We are currently studying these temporal relationships. The study to date has emphasized the local sequence of events within the Mangala Valles.

The Mangala Valles lie within the Memnonia Quadrangle (MC-16). It is a 750 km long north-south trending system that occupies the boundary region between cratered terrain and northern plains. The geology was mapped by Mutch and Morris (1979). They support the model proposed by Sharp and Malin (1975) who proposed a catastrophic flood origin for the channels. Accordingly, Mutch and Morris (1979) suggest that the channel floors may include mud flow material.

The region studied was imaged by the Viking Survey Mission at a scale of 45 m/pixel. The coverage occupies a 200,000 $km^2$ region covering the central two-thirds of the valley system. Detailed geologic mapping of this region reveals a series of related flow events and much a more complex sequence than had previously been seen. Lobes of channel material in some parts of the system support the idea that mud flow material is present locally.

Within the region are major structural trends in the form of ridges that apparently acted as temporary barriers to the flood. We propose that flood material, probably in the form of a viscous mud flow, ponded behind these dams, partially dewatered, and upon breaking through created the complex of terraces and channels. In at least one instance, a distributory channel cut to the northwest was subsequently recaptured by the main north-trending flow. Some viscous material flowed a short distance southward from a local crater pond following that capture. Counts of crater density on various parts of the channel do not show any age differences.

## REFERENCES

Mutch, T. A., and Morris, E. C., 1979, Geologic map of the Memnonia Quadrangle of Mars: U. S. Geol. Survey Misc. Inv. Map. I-1137.

Phillips, R. J., and Saunders, R. S., 1975, The isostatic state of martian topography: Jour. Geophys. Research, v. 80, p. 2893-2898.

Sharp, R. F., and Malin, M. C., 1975, Channels on Mars: Geol. Soc. America Bull., v. 86, p. 593-609.

Geologic Mapping of Martian Valley Systems I: Nirgal Vallis and Vicinity

D.C. Pieri, Jet Propulsion Laboratory, Pasadena, CA 91109 and T. Parker, ERTECH Corporation, Long Beach, CA

As part of a program of detailed geologic mapping of martian valley systems, we have completed a preliminary version of a detailed geologic map of the region between the northeast rim of Argyre Basin and the central part of Margaritifer Sinus, including Nirgal Vallis, and The Uzboi-Ladon-Holden Valles complex from Viking Orbiter medium and high-resolution images. Preliminary interpretations include (a) the subdivision of the nearby Lunae Planum cratered plains into several units with an apparent range of ages, including exposures of relatively old substrate possessing well-oriented lineament and valley systems, (b) the assertion that both upper and lower Nirgal Vallis is expressed in a lineated somewhat younger, and specific cratered plains unit. and (c) that strong structural controls provided by a little recognized, old 600 km diameter basin in Margaritifer Sinus dictate at least part of the alignment of Uzboi-Ladon-Holden Valles.

The mapping of Nirgal itself from high resolution (20 m/pixel) reprocessed Viking Orbiter images is underway and findings include the expression of wrinkle-ridge structure in valley walls, structured debris deposits on the valley floor, possible thalweg features in some valley reaches, and a small chaotic debris deposit associated with the mouth of Nirgal at its debouchment into Holden Vallis. Further analysis and detailed crater counts on various map units are underway.

Pieri, D. and T. Parker, 1981, The Geologic Setting of Nirgal Vallis and Vicinity, in preparation.

The research described in this abstract was carried out by the Jet Propulsion Laboratory, California Institute of Technology, under contract with the National Aeronautics and Space Administration.

# GEOLOGIC MAPPING OF PLAINS MATERIAL IN MARE ACIDALIUM QUADRANGLE (MC-4), MARS

Witbeck, N.E. and James R. Underwood, Jr., Department of Geology, Kansas State University, Manhattan, KS 66506

Geologic studies based on poor quality Mariner 9 images resulted in the subdivision of the lowland plains of Mare Acidalium (MC-4) into three basic geologic units: mottled plains material, plains material, and plains and dissected plateau material, undivided. The mottled plains which occur in the northern region of the quadrangle, are characterized by high-albedo zones surrounding numerous craters. There is a distinct NW-SE erosional grain, and the mottled plains material was interpreted as "plains lowered by wind erosion" (Underwood and Trask, 1978). The plains materials in the eastern and southern part of MC-4, are relatively smooth and featureless, with very few craters, and were interpreted as "eolian sediment or, especially to southwest, alluvium and eolian sediment." The plains and dissected plateau material, undivided, occupy the southern part of the quadrangle and form a relatively smooth surface with scattered craters. This material was thought to represent "plains of lava mantled by eolian debris of varied thickness" (Underwood and Trask, 1978).

The higher resolution Viking Orbiter images have revealed a variety of surface textures and features that have enabled workers to recognize additional geologic units and to subdivide further previously mapped units (Underwood and Witbeck, 1980). Preliminary geologic mapping (Figure 1) has indicated that eight geologic subdivisions can be recognized within these lowland plains where previously, on the basis of Mariner 9 data, only three were identified.

The mottled plains material, believed to be the oldest of the plains units in this region, has been subdivided into mottled plains-undivided (pm), mottled plains-hummocky (pmh), mottled plains-patterned (pmp), and mottled plains-subdued and patterned (pmsp). The undivided mottled plains materials are characterized by high-albedo zones that extend out from impact craters 3-4 crater diameters. Crater floors are commonly filled or partially filled with light material, and there is a distinct NW-SE eolian grain. This unit is believed to have undergone several episodes of erosion and deposition. A gradational boundary exists between the mottled plains material-undivided and the hummocky mottled plains material. This hummocky terrain is characterized by an abundance of small, dark crested hills or knobs with lighter bases. These dark knobs, which may be volcanic material, also occur on the floor of Lomonosov, the 130-km crater in the NE corner of the quadrangle, indicating that their formation is post impact. The patterned and subdued patterned plains occupy the region south of the mottled and hummocky plains materials. These plains are characterized by a polygonal pattern of troughs superimposed on low albedo plains material. Several origins have been proposed for the formation of this polygonal pattern (Helfenstein and Mouginis-Mark, 1980). The eolian grain is not

present, and there are numerous small features that have been interpreted by Frey (1981) to be small pseudo-volcanic cones. Pedestal craters are common. Boundaries between the patterned and subdued patterned mottled plains are gradational, and the subdued patterned mottled plains are believed to be patterned mottled plains blanketed with a mantle of varied thickness.

A small area of fractured plains (pf) occurs to the south of the patterned mottled plains. The fractured plains are characterized by much larger troughs that lack rims and have flat floors. Pechmann (1980) reported offset in some of these troughs and argued for the tectonic origin of these features.

Similar in age and origin to the mottled plains material, the knobby plains material (pk) exhibits characteristics similar to the hummocky mottled plains material, except that the knobby plains material has much higher albedo. This higher albedo may be the result of the presence of a slightly thicker eolian mantle.

The youngest of the plains units are the smooth (ps) and patterned smooth plains (psp) which occupy the southern region of MC-4. These are vast, sparsely cratered, featureless plains with varied albedo. A subdued pattern occurs on the smooth plains adjacent to the patterned mottled plains, possibly representing another gradational boundary between units in which smooth plains material partially covers the patterned mottled plains. Knobby material occurs in patches throughout the smooth plains unit and may represent either remnants of the underlying, more heavily cratered surface, or erosional remnants of the previously overlying cratered plateau. Many streamline features and channels indicate the presence of water much farther north than previously reported (Scott, 1980). This area contains materials that represent a complex sequence of depositional and erosional events including, but not limited to, emplacement of lava flows, alluvial and eolian sediments, and erosion by wind and by water.

References

Frey, H., and Jarosewich, M., 1981, Small cones on Mars: distribution and properties: Third Int. Colloquium on Mars, Lunar and Planetary Institute Contrib. 441, p. 84-86.

Helfenstein, P., and Mouginis-Mark, P.J., , 1980, Morphology and distribution of fractured terrain on Mars: Lunar and Planetary Science XI, p. 429-431.

Pechmann, J.C., 1980, The origin of polygonal troughs on the northern plains of Mars: Icarus, v. 42, p. 185-210.

Scott, D.H., and Tanaka, K.L., 1980, Mars stratigraphy: Lowland plains and Valles Marineris: NASA Tech. Memo 82385, p. 104-106.

Underwood, J.R., Jr., and Trask, N.J., 1978, Geologic map of the Mare Acidalium quadrangle of Mars: U.S. Geol. Survey, Misc. Geol. Inv. Map I-1048.

Underwood, J.R., Jr., and Witbeck, N.E., 1980, Mottled plains of Mars: a review: NASA Tech. Memo 82385, p. 101-103.

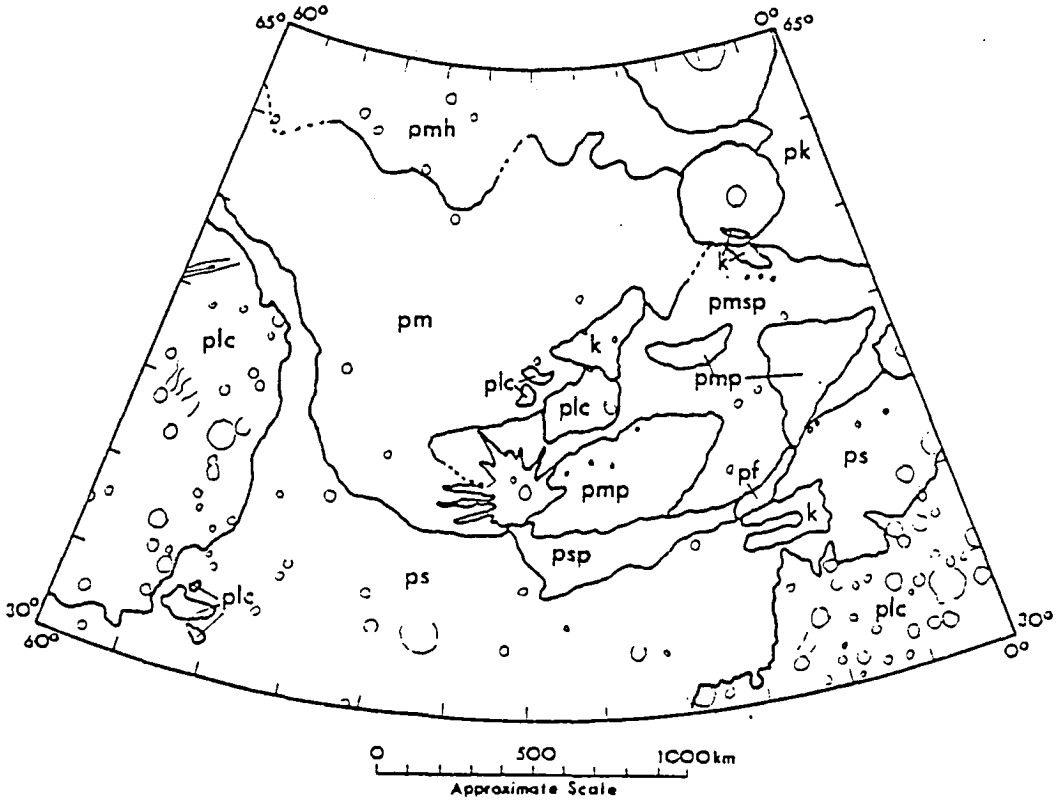


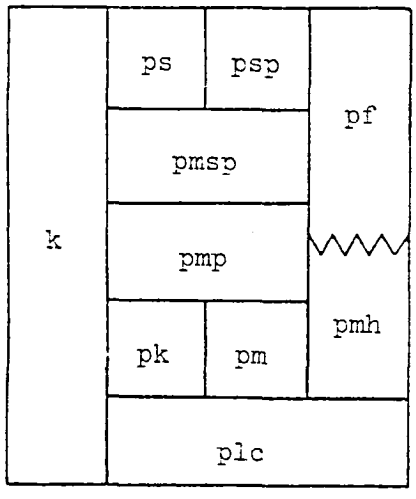


EXPLANATION

| | |
|---|---|
| ps | Smooth plains material |
| psp | Patterned smooth plains material |
| pf | Fractured plains material |
| pmsp | Mottled subdued patterned plains material |
| pmp | Mottled patterned plains material |
| pmh | Mottled hummocky plains material |
| pm | Mottled plains material undivided |
| pk | Knobby plains material |
| k | Knobby material |
| plc | Cratered plateau material |

Figure 1. Generalized geologic map of Mare Acidalium Quadrangle

# THE GALILEAN SATELLITE GEOLOGICAL MAPPING PROGRAM

B. K. Lucchitta, U.S. Geological Survey, Flagstaff, AZ 86001

The Galilean Satellite Geological Mapping Program was established in order to illuminate detailed geologic relations on these satellites. The maps will furnish insights into the history of the individual satellites, thereby contributing to our understanding of the solar system. The mapping program involves about 40 investigators from various universities, research institutes, and government offices in the U.S.A., England, Germany and Italy. Each quadrangle will have several authors because many members of the scientific community have expressed interest in the project. Twenty-four researchers have been assigned to map 10 quadrangles on Ganymede, 15 to map 6 quadrangles on Io, and 4 to map 2 quadrangles on Europa. No mapping assignments have been made on Callisto because processing of base materials is not yet scheduled. All maps are at scale 1:5 million except three maps of Io, where high-resolution pictures permit compilation of selected maps at larger scales. On Ganymede, some maps include small parts of adjacent quadrangles where high-resolution coverage was too restricted to justify compilation of separate maps.

The production of geologic maps involves the following steps. After airbrush base maps are prepared by the planetary cartography section in Flagstaff, under the direction of R. Batson, data packages are mailed to the investigators. Each package includes stable-base brown-line cronaflex and cronapaque photocopies of albedo- and shaded-relief airbrush maps, a photocopy of the controlled photomosaic, a footprint chart of the photomosaic, and copies of all pictures in the map area. One year after receipt of the mapping materials, the authors are requested to return to the mapping coordinator a first draft of the geologic map, including an explanation and text. During the second year of the program the maps are scheduled to complete the review cycle required by the Geological Survey. The maps will be published as U.S. Geological Survey Miscellaneous Investigation Maps.

Map assignments, schedules and geologic mapping principles were discussed at a mappers' meeting convened in January 1981, in Baton Rouge, LA. Unforeseen circumstances delayed the production of base maps beyond the originally scheduled date; the revised schedule calls for completion of five base maps during calendar year 1981, and six base maps during the calendar year 1982. Data packages containing all good-quality high-resolution pictures of Io and Europa have been mailed to mappers of these satellites, and images of Ganymede will be mailed early in FY 1982. These materials will enable the researchers to gain an overview of the geology of the planet and give them an opportunity to establish a preliminary definition of geologic units before they concentrate on detailed geologic interpretation of individual quadrangles. Geologic mappers of the Galilean satellites will discuss preliminary findings at a meeting convened in January 1982 at Pasadena, CA.

# A GEOLOGIC MAP OF EUROPA

B. K. Lucchitta and L. A. Soderblom, U.S. Geological Survey, Flagstaff, AZ 86001

Enhanced high-resolution multispectral images acquired by the Voyager 2 imaging system were used to prepare a geologic map covering the area between lat 60° to 90° S., long 130° to 211° [1]. The geologic units were subdivided chiefly on the basis of color and albedo; several sets of structural features were distinguished. The photoanalysis and mapping lead to the following conclusions:

1) Unlike the surfaces of the terrestrial planets and other Galilean satellites, Europa lacks evidence of a horizontally stratified crust. Rather, Europa's geology appears characterized by disruptions of the crust and intrusions of ice-rock breccia [2] or icy slurries into an icy shell.

2) The surface of Europa consists of two general types of terrain units: plains and mottled terrain. The plains units are oldest; all other terrain units appear to have developed through disruption and replacement of plains material. Of the mottled terrain units, the gray unit is older than the brown; stripes and bands cross the gray unit, but are disrupted in the brown, which may have formed through lodgement of old plains units on a subsurface high in the silicate sphere. Dark-gray and brown spots and patches, and dark material in stripes and bands, were emplaced throughout much of the history of Europa's present crust. Emplacement of gray materials may have preceded that of brown materials, or brown materials may have become gray with age. Light stripes running along the center of many dark bands may be late intrusions of clean ice [2].

3) Numerous straight and curved lineations, streaks, stripes, and bands cross Europa's surface on a global and local scale [2,4]. Most lineations appear related to fractures in Europa's crust [5]. Straight fractures tend to dominate the northern and east-central regions of the area covered by Voyager 2 images, while curvilinear fractures dominate the west-central and southern regions. This difference in pattern appears fairly old, and associated fractures appear rejuvenated by later structural activity. This activity appears to have resulted in four distinct structural sets that have different origins. Gray curvilinear bands are centered on a point near lat 65° S., long 110°, and are probably old. Sharply delimited dark bands look young and appear to be fractures opened by translational and rotational movement of slabs of crust [6]. Ridges are thought to be the youngest of all lineations [7], because they cross most others. They may form small circles centered on the antijovian point [5], although lighting conditions may artificially enhance this pattern. Global bands, consisting mostly of dark bands flanking central light stripes, form great circles and apparently have developed throughout the existence of Europa's present crust. Trend diagrams suggest that Europa's tidal deformation influenced many structural patterns [8,9].

4) Five fresh craters in the 10- to 30-km-diameter range are visible; one appears to divert ridges that radiate from it. A large

circular brown spot of little relief could be a crater palimpsest similar to palimpsests on Ganymede. Global bands appear tangential to this spot. On low-resolution global images, other brown spots also appear to control radiating dark bands, suggesting that impact-induced fracturing has controlled the location of some structural features.

5) The apparent low density of craters superposed on Europa's surface suggests that the surface is $\sim 10^8$ yr old [10]. This young age may be due to resurfacing or regeneration of the crust within the last $10^8$ yr, or to the collapse of topographic features by cold flow and by annealing of the ice within this time period. The resolution of Voyager 2 images is inadequate to make a choice between these hypotheses.

6) The dark spots, stripes, and bands that appear to have replaced sections of Europa's crust along structures and in the mottled terrain suggest that material was transported to the surface from the subjacent silicate lithosphere. Depth to the silicate subcrust is probably no more than a few tens of kilometers because dense ice and mud slurries would have difficulty reaching the surface through a thicker crust of lighter ice. On the other hand, the evidence for rafting and rotation of the crust and collapse of large craters suggests that the ice shell must have been thick enough to permit local decoupling at some depth of ice slabs near the surface from the silicate subcrust.

7) The geologic evidence permits an appraisal of the two major crustal models of Europa; the thick-ice model of Fanale et al. [11] and Cassen et al. [12] in which about 100 km of ice overlies an essentially dry silicate lithosphere, and the thin-ice model of Ransford et al. [13] and Finnerty et al. [2], in which only about 25 km of ice overlies a hydrated lithosphere. The geologic map of Europa and accompanying interpretations are more consistent with the thin-ice hypothesis.

References


1. Lucchitta, B. K. and Soderblom, L. A. (1981) The geology of Europa. In Satellites of Jupiter, Univ. Arizona Press, Tucson, Ariz., in press.
2. Finnerty, A. A., Ransford, G. A., Pieri, D. C., and Collerson, K. D. (1980) Is Europa's surface cracking due to thermal evolution? Nature 289, 24-27.
3. Smith, B. A. and the Voyager Imaging Team (1979a) The Jupiter system through the eyes of Voyager I. Science 204, 951-972.
4. Smith, B. A. and the Voyager Imaging Team (1979b) The Galilean satellites and Jupiter: Voyager 2 imaging science results. Science 206, 927-950.
5. Pieri, D. C. (1980) Lineament and polygon patterns on Europa. Nature 289, 17-21.
6. Schenk, P. M. and Seyfert, C. K. (1980) Fault offsets and proposed plate motions for Europa (abstract). EOS 61, 286.
7. Malin, M. C. (1980) Morphology of lineaments on Europa. In The Satellites of Jupiter, IAU Colloq., no. 57, May 13-16, 1980, Kailua-Kona, Hawaii. Session 7-2.

8. Helfenstein, P. and Parmentier, E. M. (1980) Fractures on Europa: Possible response of an ice crust to tidal deformation. Proc. Lunar Planet. Sci. Conf. 11, 1987-1998.
9. Lucchitta, B. K., Soderblom, L. A., and Ferguson, H. M. (1981) Structures on Europa. Proc. Lunar Planet. Sci. Conf. 12th, in press.
10. Shoemaker, E. M., and Wolfe, R. F. (1981) Cratering timescales for the Galilean satellites. In Satellites of Jupiter, Univ. Arizona Press, Tucson, Ariz., in press.
11. Fanale, F. P., Johnson, T. V., and Matson, D. L. (1977) Io's surface and the histories of the Galilean satellites. In Planetary Satellites, (J. A. Burns, ed.), Univ. Arizona Press, Tucson, AZ, 379-405.
12. Cassen, P., Peale, S. J., and Reynolds, R. T. (1980) Tidal dissipation in Europa. A correction. Geophys. Res. Lett. 7, 963-970.
13. Ransford, G. A., Finnerty, A. A., and Collerson, K. D. (1980) Europa's petrological thermal history. Nature 289, 21-24.

Geologic Mapping of Europa

David Pieri, Jet Propulsion Laboratory, Pasadena, CA 91109, USA and Konrad Hiller, Ludwig-Maximillians, Universitat, Muenchen, FRG

As part of the Galilean Satellite Mapping Program, we have begun the geological reconnaissance of the Je-3 quadrangle on Europa. Of interest is the differentiation of terrain units by morphology and spectral type and detailed understanding of lineament generation sequence, morphology and color systematics.

Previous work has suggested a lineament classification scheme and demonstrated differences in lineament network style as a function of position with regard to the anti-jove point (Pieri, 1981). Also, Luccitta and Soderblom (1981) have suggested differentiation of terrain units based on color differences as seen in Voyager broad-band spectral data. Both suggestions are under detailed study. Principal component analysis will be applied to Voyager color data (e.g. Guinness, 1981).

Guinness, E.A., 1981, Spectral properties (.4 to .7 microns) of soils exposed at the Viking 1 landing site, Journ. Geophys. Res., in press.

Pieri, D.C., 1981, Lineament and Polygon Patterns on Europa, Nature, 289, p. 17 - 21.

The research described in this abstract was carried out by the Jet Propulsion Laboratory, California Institute of Technology, under contract with the National Aeronautics and Space Administration.

# Chapter 11

# SPECIAL PROGRAMS

# THE THIRD MARS YEAR OF IMAGING AT THE MUTCH MEMORIAL STATION

S. D. Wall, Jet Propulsion Laboratory
D. C. Pieri, Jet Propulsion Laboratory

The Viking Lander Monitor Mission continues to return imaging and meteorology data from the Viking I Lander (renamed the Thomas Mutch Memorial Station), now in its third Mars year of operation. In the past year there have been substantial delays in image processing as the data routing was changed to exclude JPL's Mission Control Center, but the new data route is now operational and images are being received by investigators 50-100 sols after they are taken. This number is expected to improve as Voyager priorities decline.

Five images are taken by the lander every 37 sols. Two of these are always the images shown in Figs. 1 and 2. The other three alternate among other images which either monitor areas such as drifts, piles, annd test charts or which can be mosaicked into larger panoramas. The images in Figs. 1 and 2 are taken every 37 sols and the rest are taken once per Mars year.

Figures 1 and 2 show images of the "Big Joe" area and the rocks/drift region in front of the lander, taken with the blue diode over a recent span of about 300 sols. There is clear indication of variation in insolation by a factor of 2 and suggestions of redistribution of fine materials, implying dust-storm type activity. Meteorology data taken during this same period show diurnal ambient pressure variations comparable to those during global dust storms, but semi-diurnal pressure variations which are small. The large diurnal tides indicate atmospheric heating which is localized both in latitude and in height, but semi-diurnal tides are not large enough to allow global activity[1]. Previously observed global dust storms have occurred at $200 < L_s < 280$ [2]. The preliminary conclusion is that there has been some localized dust storm activity at the VL-1 site.

## References

1. C. Leovy, Personal Communication
2. Ryan, J. A. and Sharmon, R. D., J. Geophys. Res. 86, C4, p. 3247-3254.

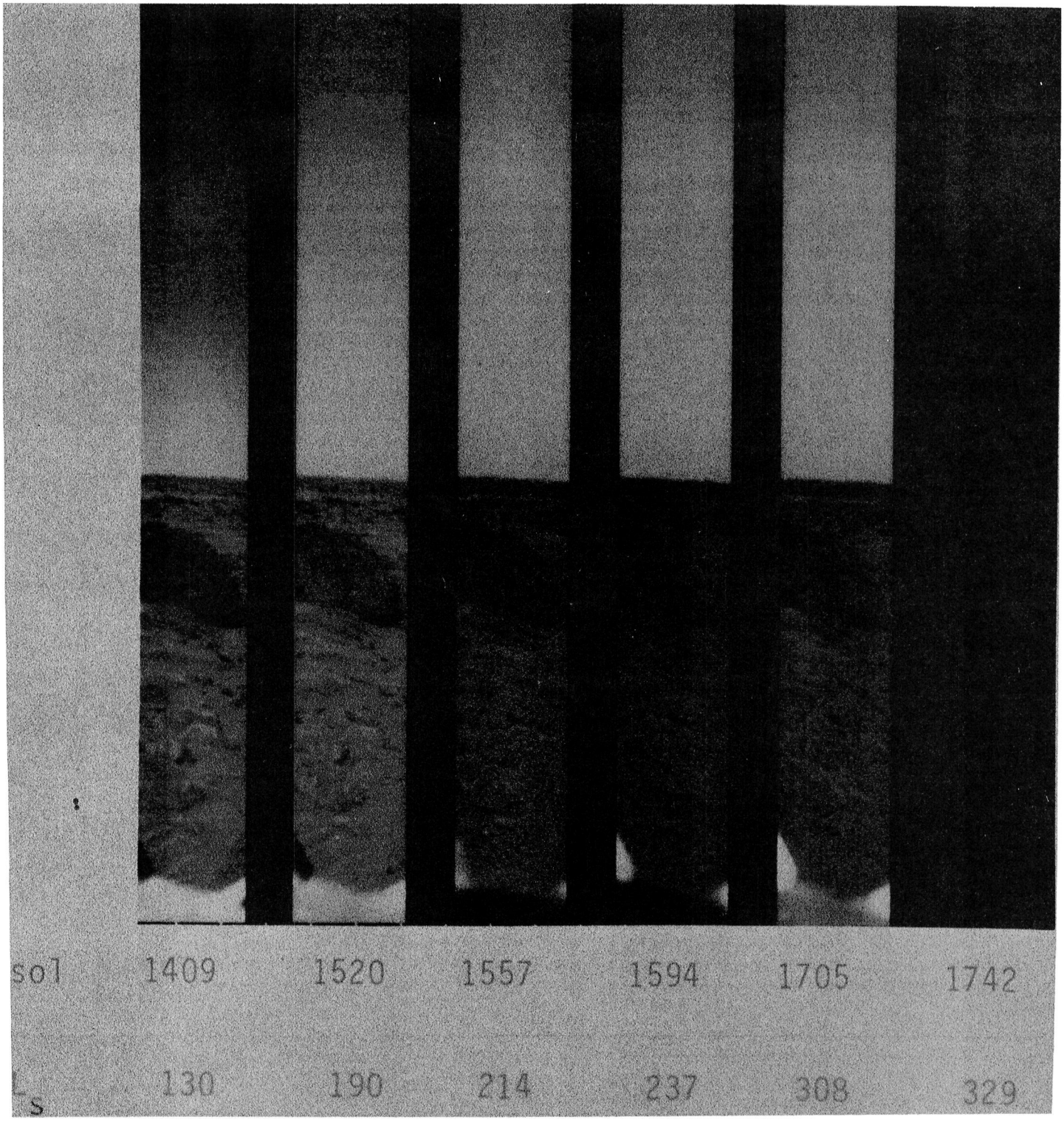


Figure 1. - "Big Joe" area imagery during the sol 1409 - 1742 period. $L_s$, aerocentric longitude, is shown in degrees.

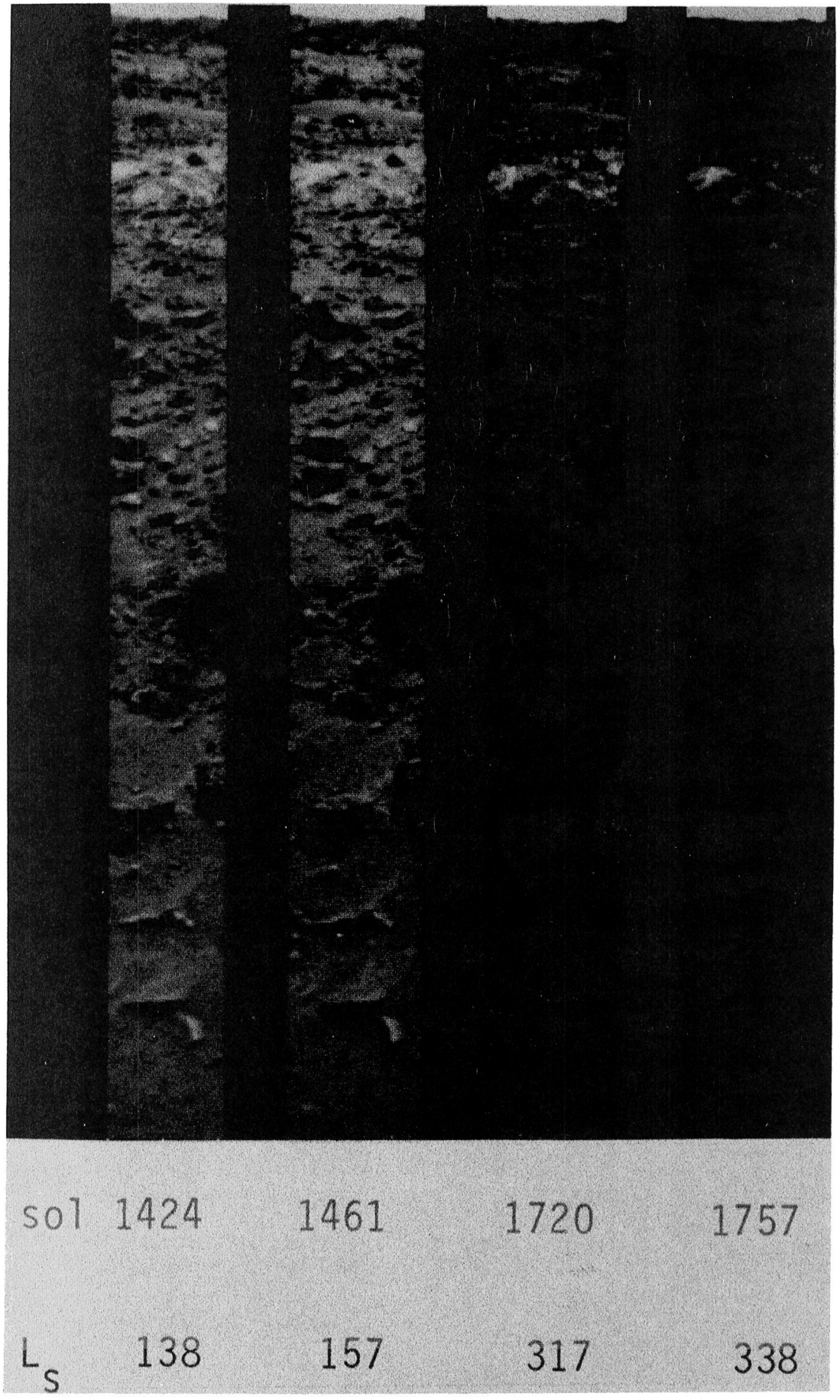


Figure 2. - Imagery of the area in front of the lander from sol 1424 - 1757. $L_s$, aerocentric longitude, is shown in degrees.

VIKING LANDER IMAGING EXPERIMENT - UPDATE AND NEW OBSERVATIONS, II

K.L. Jones and S.K, LaVoie, Jet Propulsion Laboratory, Pasadena, CA 91109

As of the most recently received image (11J136, sol 1809), both cameras on the Viking I Mars Lander continue to operate normally. Since the start of the Lander Monitor Mission (sol 935, Ls=243), 57 camera events (out of a possible 119) had been received. Missing camera events are generally due to non-availability of a tracking station.

The imaging sequence is planned so that during each Mars-year, the same camera events are repeated (within a 2 sol tolerance) so that solar lighting angles are as close as possible. This allows computer picture difference techniques to enhance year-to-year changes between such "repro" pairs. The imaging sequence has completed its first 90 camera events and, beginning with 12J108, (sol 1601) began a second cycle of images. However, although the imaging sequences now overlap by 29 camera events, only a single pair of "Repro" images (11J046 and 11J136) have been received. The number of "Repro" images should increase dramatically during 1982.

## Data Reduction and Distribution

As of September 1, 1980, Experiment Data Record (EDR) tapes containing VL-1 camera events through 11J130 (sol 1765) had been distributed. Photoproducts are in various stages of completion - EDR distribution planned for October, 1981, and TDR distribution for November, 1981.

## VL-1 Imaging Observations - Third Winter Duststorm

During the entire first imaging cycle of the Lander Monitor Mission, the Chryse site remained notably static. There had been an apparent absence of any significant duststorm activity during the previous winter and, correspondingly, only a minimal surface change - a thin accumulation of bright dust (7).

Late in the third winter season, the cameras documented what apparently is duststorm acitvity over the Lander site. A first darkening of images is observed in camera event 12J124 (sol 1720 becomes a maximum in 11J127 (sol 1742), and apparently clears by 11J136 (sol 1809). A late update of the effects of this dust event is in preparation for the January, 1982 PGPI meeting.

## References

1) Jones, K.L., M. Henshaw, C. McMenomy, A. Robles, P.C. Scribner, S.D. Wall, J.W. Wilson, Viking Lander Imaging Investigation, Picture Catalog of Extended Mission and Continuation Mission Experiment Data Record, 2 vols., NASA Reference Publication, in press.
2) Tucker, Robert B., Viking Lander Imaging Investigation Picture Catalog of Primary Mission Experiment Data Record, NASA Reference Publication 1007.
3) Jones, K.L. and S.K. LaVoie, Two Mars Years - Viking Lander Imaging Observations, abstract in NASA TM-81776, Jan. 1980, Reports of Planetary Geology Program, 1979-1980.

References Con't.

4) Jones, K.L., R.E. Arvidson, E.A. Guinness, S.L. Bragg, S.D. Wall, C.E. Carlston and D.G. Pidek, One Mars Year: Viking Lander Imaging Observations, Science, 204, pp. 799-806, 25 May 1979.
5) Guinness, E.A., R.E. Arvidson, D.C. Gehret and L.K. Bolef, Color Changes at the Viking Landing Sites Over the Course of a Mars Year, J. Geophys. Res., 84, 1979.
6) Wall, S.D. Analysis of Condensates Formed at the Viking 2 Lander Site: The First Winter, submitted to Icarus.
7) Jones, K.L. and S.K. LaVoie, Viking Lander Imaging Experiment - Update and New Observations, abstract in NASA TM 82385, Dec. 1980, Reports of Planetary Geology Program - 1980.

SOME OBSERVATIONS OF CHANGES - VIKING LANDERS 1 AND 2.

H. J. Moore, U.S. Geological Survey, Menlo Park, CA 94025, R. E. Hutton, 1501 Palos Verdes Dr., Harbor City, CA 90710, C. R. Spitzer, NASA Langley Research Center, Hampton, VA 23665.

Situations for which changes might occur were created intentionally, inadvertently, naturally, and by the presence of the spacecraft: (a) conical piles of surface materials were constructed to detect changes induced by martian winds or other processes; (b) debris and dust were deposited in the footpads by engine exhaust gases, by the surface samplers, and from the atmosphere; (c) trenches with steep walls and tailings were excavated and fresh materials exposed; (d) natural materials containing planes of weakness on steep slopes may change because of natural processes; (e) chips with ultraviolet (UV) sensitive paints were placed on the landers to measure the intensity of UV radiation at the surface; (f) seasonal variations in the atmosphere could result in changes of materials at the surface; and (g) the landed spacecraft itself might be unstable. Most changes at the landing sites can be detected by direct, uncomplicated observations, as chiefly reported here; other changes require careful and sophisticated reduction of photographic data.

Conical piles of surface materials constructed by the surface samplers in open areas, among rocks, and on top of rocks have retained their form and relief for at least 635 sols (Lander 1) and 787 sols (Lander 2). Analyses of engine-exhaust erosion [1,2], gas adsorption [3] and sample trenches as well as wind-gust speeds [4] indicate that the piles should be stable. Diffuse halos around the piles disappeared with time because of sedimentation of fines generated by surface sampler activities, from the lander, and from the atmosphere. Sedimentation of fines during surface sampler activities could be considerable because only about 20 $cm^3$ of fines is needed to produce a 1-μm layer of dust in the sample field; sedimentation from the sky produces a 1-μm layer during a year [5,6]. The conical pile on the grid of Lander 1 changed rapidly in response to lander vibrations and swirling winds.

Materials deposited in the footpads have changed in dramatic ways [7], undramatic ways, and hardly at all. Slumping and collapse of the surface has occurred above the buried rim of footpad 2 of Lander 1. Materials in footpad 3 of Lander 1 have moved in response to wind eddies, accumulated with time, and slid down the footpad walls. Materials in footpads 2 and 3 of Lander 2 appear to have been unaffected by winds; but, material has been added to footpad 2 as a result of surface sampler activities on Sols 522, 523, 535, and 545.

The miniature "landslide" in footpad 3 of Lander 1 constrains the coefficient of friction between the metal and surface materials to less than 0.87 ($< \tan 41°$), or adhesion to less than 9 Pa; best estimates are 0.36 ($\tan 20°$) and 5 Pa. For Lander 2, adhesion is greater than 16 Pa when the coefficient of friction is 0.36.

Generally, the walls and tailings of trenches are stable. Little or no modification of the walls has occurred except shortly after excavation when disrupted units collapsed, fell toward the floor, and formed small talus cones. Sedimentation of fines introduced into the atmosphere as a result of surface sampler activities and from the sky [5,6] caused initially dark appearing trenches to become lighter with time.

Changes in the natural scene also have occurred. Patches on a dune in front of Lander 1 have changed from light to dark with time [5]. Two small landslides of drift material have occurred on natural slopes [7], for unknown but natural reasons, in late summer ($L_S \simeq 148$) during periods of reduced atmospheric pressure [8], higher average surface and air temperatures [4,9], and large differences in maximum and minimum daily temperatures [4,9]. Both slides were on the leeward sides of large blocks; hourly average wind speeds were only 4-8 m/s. The slides, which appear to have occurred along local planes of weakness, may be triggered by positive pore pressures in the surface materials generated by desorption of gas, such as $CO_2$ [10], when several environmental factors act in concert.

Sophisticated reduction of photographic data indicates that the chips coated with UV-sensitive paints on the Reference Test Charts of Lander 1 have darkened with time at a rate indicating that the atmosphere is essentially transparent to UV radiation [11].

Deposits of condensate observed on the surface of the Lander 2 site during the wintertime were interpreted to be at least partly water ice [7]. Temperatures measured throughout diurnal cycles by the surface-sampler-collector-head sensor, inserted about 0.05 m into the surface materials in the winter ($L_S = 289$) and spring ($L_S = 355$), support this interpretation [12]. On Sols 957-958, winter temperatures reached 182° and 171°K; they exceeded 158°K for about 11 hours and 152°K for about 15 hours; air temperatures never dropped below 152°K. Color pictures show that surface condensate was present near the inserted collector head as well as on illuminated surfaces beyond the shadow of the lander. In the spring, diurnal temperatures measured by the collector head sensor always exceeded 171°K and local patches of condensate were still present on the surface.

Lander 2 has moved slightly; analyses of pictures up to Sol 518 indicate that the lander had rotated counterclockwise about 0.3°, possibly because Lander 2 is perched on rocks. Although of doubtful significance to the dynamics of martian processes, such a rotation may seriously affect stereometric and photogrammetric measurements. If the lander moved between the two times of acquisition of a stereopair, the calculated spacecraft coordinates of objects derived from picture coordinates will be seriously in error. Calculated spacecraft coordinates are acceptable only when no movement has occurred between the times of acquisition of pictures, so that corrections are straightforward.

References:


1. Moore, H. J. and others, 1979, Sample fields of the Viking landers, physical properties, and aeolian processes: J.G.R., v. 84, no. B-14, p. 8365-8377.

2. Hutton, R. E. and others, 1980, Surface erosion caused on Mars from Viking descent engine plume: The Moon and Planets, v. 23, p. 293-305.

3. Ballou, E. V. and others, 1978, Chemical interpretation of Viking Lander 1 life detection experiment: Nature, v. 2871, p. 644-645.

4. Ryan, J. A. and Henry, R. M., 1979, Mars atmospheric phenomena during major dust storms, as measured at surface: J.G.R., v. 84, no. B-6, p. 2821-2829.

5. Guinness, E. A. and others, 1979, Color changes at the Viking landing sites over the course of a Mars year: J.G.R., v. 84, no. B-14, p. 8355-8364.

6. Pollack, J. B. and others, 1979, Properties and effects of dust particles suspended in the martian atmosphere: J.G.R., v. 84, no. B-6, p. 2929-2945.

7. Jones, Kenneth L. and others, 1979, One Mars year: Viking Lander imaging observations: Science, v. 204, no. 4395, p. 799-806.

8. Hess, S. L. and others, 1980, The annual cycle of pressure on Mars measured by Viking Landers 1 and 2: Geophys. Res. Lttrs., v. 7, p. 197-200.

9. Kieffer, H. H., 1976, Soil and surface temperatures at the Viking landing sites: Science, v. 194, p. 1344-1346.

10. Fanale, F. P. and Cannon, W. A., 1979, Mars: $CO_2$ adsorption and capillary condensation on clays - significance for volatile storage and atmospheric history: J.G.R., v. 84, no. B-14, p. 8404-8414.

11. Zent, A. P. and others, 1982, this NASA Technical Memorandum.

12. Moore, H. J. and others, 1980, Viking surface sampler diurnal temperatures: Rpts. Planet. Geol. Prog., 1979-1980, NASA TM 81776, p. 166-168.

# VIKING ORBITER STEREO IMAGING CATALOG: SECOND EDITION

K.R. Blasius, A.V. Vetrone, Planetary Science Institute, Science Applications, Inc., 283 S. Lake Ave., Suite 218, Pasadena, CA 91101; and M.D. Martin, Jet Propulsion Laboratory, Pasadena, CA 91109

In order to simplify qualitative and quantitative assessment of topography of Martian surface features, the compilation of an index of useful orbital stereo imaging coverage was undertaken in 1978. Here we describe the second edition of this index now ready for publication.

During the missions of the Viking orbiters, over 52,000 images were acquired. The majority of these show features of the solid surface of Mars rather than cloud fields, star fields, or Martian satellites. Because many areas of Mars have been photographed several times from different perspectives, there is considerable stereo imaging data. Stereo viewing of surface features and quantitative determinations of topography by photogrammetric techniques can be extremely valuable interpretive aids.

Unfortunately, useful stereo imaging cannot be easily located simply by going through the Viking Project index which lists pictures by geographical location (1,NSSDC ID-75-075A-011). Images suitable for viewing under a stereoscope or for compilation into topographic maps must, aside from being targeted to the same location, be somewhat similar in atmospheric clarity conditions, lighting conditions, spatial resolution, and contrast of surface features. Thus as part of the cataloging task, we have eliminated from consideration large blocks of images showing dense cloud cover, images for which less than 70% of data was received, images for which the central emission angle is greater than $65^{o}$, and images for which the central solar incidence angle is greater than $85^{o}$. Candidate overlapping images were then grouped according to spatial resolution so as to allow pairing of images with others differing up to 50% in resolution. These images were further screened to eliminate pairs for which solar azimuth differs by greater than $45^{o}$, solar incidence differs by greater than $30^{o}$, or for which differences in the distribution of surface (polar) ice which make the scene appearances very dissimilar.

Except for evaluation of cloud or polar ice cover comparisons of images were made through reference to the Project SEDR record (NSSDC ID-75-075A-01E, etc.). These engineering data are admittedly imperfect, but experience indicates the specific data being used to compile the stereo catalog are usefully precise over 95% of the time. Where systematic large errors are known to occur (as in the location of certain very high resolution images acquired late in the mission) the user is forwarned.

Having passed evaluation by the above criteria, sets of stereo images are cataloged by compiling maps and indexed tables of data organized by $10^{o}$ latitude x $10^{o}$ longitude regions on Mars.

The first edition of this catalog (2) was published by NASA and distributed in 1980 before the end of the Viking Orbiter 1 Mission. The second edition, now compiled, encompasses the complete Viking Orbiter 1 data set including the Survey Missions.

This project was supported by NASA Contract NASW-3208.

REFERENCES: (1) Vostreys, R.W. (ed.), 1978, Catalog of Viking Mission Data, Nat'l. Space Science Data Center, Greenbelt, Maryland. (2) Blasius, K.R., Vetrone, A.V., and Martin, M.D., 1980, NASA Contractor Report 3277.

# ARCHIVAL STORAGE OF DIGITAL DATA ON VIDEOTAPES AND VIDEODISKS

R.E. Arvidson, L.K. Bolef, and R. Lewis,, McDonnell Center for the Space Sciences, Washington University, St. Louis, Missouri 63130.

Severe problems exist within NASA in regard to efficient, economic distribution of digital image data (Bernstein et al., 1981). Projected solutions for archival systems being considered by the NEEDS (NASA End to End Data System) include use of optical disk systems (Holcomb, pers. comm.). In addition, the possibility exists for use of 6250 BPI tape drives in the future. We have been working on an alternative system utilizing encoded digital data stored on videodisks (Bolef et al., 1981). We plan to transfer about 10**10 bytes of data from magnetic disk, through a pulse code modulation encoder, to videotape. This videotape would then be used to master a videodisk at SONY. We then plan to read data from the videodisk through a PCM decoder and store the data on magnetic disk. Our intent is to demonstrate the technology with a test disk. As such, calibration signals will be included to determine the bit error rate. The most expensive hardware in this system is the encoding/decoding device, which is a SONY PCM-1600 encoding system on loan to us. For general use it is quite possible that an encoding system being built for real time storage of Meteosat data on videotape, with a projected cost of a 1600 BPI tape drive, may be nearly ideal (Hunt, G.E., pers. comm.). We project the overall cost of the videodisk player, decoding system, and interface to be a factor of two below the cost of a 6250 BPI drive and perhaps an order of magnitude cheaper than the projected cost of the write-once optical disk systems under development by several companies. The 50,000 frame Viking Orbiter digital image data would fit on approximately 40 videodisks, rather than on the approximately 2000 tapes that now exist in the JPL Data Library.

References

Bernstein, R. and others, 1981, A new approach to data management for space science and applications research, National Academy Sciences, Nat. Res. Council, in press.

Bolef, L.A. and R.E. Arvidson, 1980, Frequency-encoded storage of digital image data on videodisks, NASA TM-82385, p. 478.

## Planetary Data at the National Space Science Data

Robert W. Vostreys, National Space Science Data Center
Goddard Space Flight Center, Greenbelt, Maryland

The National Space Science Data Center/World Data Center A for Rockets and Satellites (NSSDC/WCA-A-R&S) is the repository for reduced data from planetary mission investigations. These data are available for additional studies beyond those conducted by the investigators and teams involved with each mission. Data are available to researchers throughout the world.

Venus data from the Pioneer-Venus orbiter and probes are being actively archived. Although a complete data set is not available at this time, specific data requests can be responded to by NSSDC.

Virtually all the expected data from the Viking missions are available to interested investigators. Orbiter imagery from late in the mission is still being processed and indexes for this portion of the mission are not currently available. However, requests for specific frame numbers can, in many cases, be satisfied. The USGS photomosaics with accompaning footprints of individual frames are proving useful to many researchers in their studies.

Recent acquisitions include data from the Pioneer 10 Jupiter encounter and from the Pioneer 11 Jupiter and Saturn encounters.

Data from all the Voyager Jupiter encounter investigations are now available for distribution to interested investigators. Saturn encounter data from these missions are starting to become available. Due to the limited amount of data and lack of indexes and catalogs, please contact NSSDC directly for information on specific data products.

For information on the availability of specific data sets from any of the lunar and planetary missions, please consult the NSSDC Planetary Data Listing. It contains the spacecraft, experiment, and data set names. Included are the time period covered, form of the data, and quantity. This Data Listing will be available at the meeting. NSSDC should be contacted directly for further information concerning data from these or any other space science missions. An order form is included in the Data Listing for your convenience.

## PLANETARY GEOLOGY SPEAKERS BUREAU

*R. Greeley and R. D'Alli, Department of Geology, Arizona State University, Tempe, Arizona 85287*

A Planetary Geology Speakers Bureau was established in the Spring, 1981 to present to universities and other institutions the latest results of solar system exploration and to present colloquia on topics of current interest. Fifteen Planetary Geology Principal Investigators from across the United States comprise the speakers bureau, and are capable of addressing a wide range of topics. Posters for the program were sent to all earth science departments in the United States and announcements were published in EOS and Geotimes.

Arizona State University coordinates the Bureau by serving as the initial point of contact for the host institution, and in scheduling potential speakers. The host institution is expected to pay reasonable and customary expenses associated with the speakers travel.

For additional information, contact R. Greeley, Department of Geology, Arizona State University, Tempe, Arizona 85287.

# The Planetary Geology Undergraduate Research Program

John S. King, State University of New York at Buffalo

The Planetary Geology Undergraduate Research Program (PGUR) was started in 1977 as a follow-up to the overwhelmingly successful Viking Intern Program. The objective of this program is to bring highly qualified undergraduate students majoring in geology or related sciences into a research participation arrangement with selected Principal Investigators of the Planetary Geology Program of NASA. Often traditional training in the geological sciences spurs an interest in extraterrestrial applications but opportunities for further development are rare. Thus there exists a three-fold aim in this program:

1) to provide incentive for the development of future planetary geologists
2) to broaden the base of participation in planetary geology
3) to introduce traditional terrestrial geologists to planetary studies

Students who are selected are assigned to hosts who have requested interns and every effort is made to match the interests and/or aptitudes of the intern with the focus and requirements of the research. Each selected Undergraduate Research Partipipant is provided allowances for travel and per diem as well as a weekly stipend during their assignment. Assignments generally extend over a six to eight week period during the summer months. The assignments are defined to involve interns in research tasks which contribute significantly to the Principal Investigator's project in a meaningful and constructive way and which will stimulate the intern's interests and motivation. Most such tasks are those which can be completed during the intern's residency. Thus each intern can derive a sense of satisfaction of the work completed as well as the contribution made to the project.

The project has been very successful since its inception. Comments by both hosts and interns have been laudatory and expressive of the success of the goals of the program.

Twelve interns were selected for participation in 1981 as follows:

1) Carlos Atallah (University of California, Davis) worked with Eleanor Helin (CalTech) on the planet crossing asteroid survey.
2) Maureen Kilcoyne (University of Massachusetts) worked with David Scott (USGS, Flagstaff) studying morphology and structural associations of martian volcanoes.
3) David B. Ouellette (Beloit College) worked with Robert Strom and Alex Woronow (Univ. Arizona) on impact crater morphologies and statistics on both Galilean and Saturnian satellites.
4) Dennis Rashka (University of Wisconsin) worked with Ray Arvidson (Washington Univ) on stratigraphic mapping of the northern plains of Mars.
5) Lynn Reding (James Madison University) worked with Ron Greeley (Ariz. State Univ) on an experiment to determine the effect of carbon dioxide frost on particle motion (NASA Ames Research Center).
6) Henry Schuver (Western Washington University) worked with Charles Wood (Johnson Space Center) on statistical studies of volcano morphology.
7) Ellen Stofan (College of William and Mary) worked with Steve Saunders (JPL) on mapping valley systems on Mars.

8) Ellen Sugarman (University of Rochester) worked with James Head (Brown) on martian albedo variations.
9) Alejo Verdes (Hunter College) worked on a quantitative approach to craters and cratering phenomena with Elliott Morris (USGS, Flagstaff).
10) Steven Heckendorn (Wittenberg University) worked with water/ice interactions as applied to terrestrial planets and their satellites with Duwayne Anderson (State University of New York at Buffalo).
11) Stephen Wetzel (Franklin and Marshall) worked on ejecta distribution around small lunar craters with James Head (Brown).
12) Mary Mei-ling Yang (University of California, Berkeley) worked with Eric Laue (Planetary Surfaces Research Laboratory-JPL) on water on planetary surfaces.

Outer Solar System Nomenclature

Owen, Tobias, Earth and Space Sciences, State University of New York, Stony Brook, NY 11794

The IAU Task Group on Outer Solar System Nomenclature had only one formal meeting in 1981. But several members met informally in association with the Voyager 1 Saturn encounter. The formal meeting was held in conjunction with the IAU Colloquium on Uranus in Bath, England, April 1981. Participating U.S. scientists supported by this grant were M. E. Davies, H. Masursky, T. Owen, and B. A. Smith. Other attending members were K. Aksnes (Norway), A. Brahic (France), and V. G. Teifel' (USSR). N. P. Erpylev (USSR) and M. Bobrov (USSR) were unfortunately unable to attend. The following resolutions were passed at this meeting:

**OSSTG RESOLUTIONS**

**Bath, England**

**13 April 1981**

1. Names of Surface Features on Saturn's Satellites:

   A) In general, names shall be assigned to features on the following satellites from the listed sources:

| | | |
|---|---|---|
| B) MIMAS | The Legend of King Arthur: | (31 names) |
| C) TETHYS | The Odyssey<br>Largest Crater: Odysseus | (5 names + Ithaca) |
| D) DIONE | The Aenead: | (29 names) |
| E) RHEA | Creation Myths - Asian Emphasis: | (46 names) |

   Lists of the names with preliminary coordinates determined from the maps (and identified by the dates of those maps) are hereby submitted to the WGPSN for approval.

   Names for surface features on other satellites will be deferred until after the Voyager II Encounter in August 1981.

   F) Names of satellite discoverers will be commemorated on one of the satellites they discovered.

2. Names for New Satellites

   A) Jupiter

   We accepted the proposals of the discoverers, E. Danielson and D. Jewett for 1979 J1 and S. Synott for 1979 J2 and 1979 J3, as follows:

| | | |
|---|---|---|
| 1979 J1 | Adrastea | XIV |
| 1979 J2 | Thebe | XV |
| 1979 J3 | Metis | XVI |

B) Saturn

We deferred assignment of all names until our next meeting in April 1982.

C) Pluto

1978 P1 - We have accepted the name Charon proposed by the discoverer J. Christy but we defer assignment until the orbit has been better characterized and the uniqueness of the satellite has been fully established. This may not occur until 1985-1986.

3. Saturn Rings

The existing nomenclature of the A B C D E F G rings will be retained (see SCIENCE 10 April 1981). Fine structure within these rings will be designated by radial distance in km from the center of the planet and/or units of Saturn radii.

The Encke and Cassini divisions are retained, but no additional names for divisions or gaps are accepted.

4. We propose the initial notation for newly discovered rings be as follows:

UR1-81 (for the first Uranus ring discovered in 1981), NR10-81 for the tenth Neptune ring discovered in 1981, etc. We suggest that this temporary notation be replaced by numbers in order of discovery when the reality of the rings is confirmed. When the full system is defined for a given planet, a system of letters can be imposed.

Future Work: We are planning to meet informally during the Voyager 2 Saturn encounter to continue this effort. The satellites Iapetus and Enceladus should be viewed with sufficient detail to require the assignment of names to surface features. We must also consider nomenclature schemes for the small satellites found in the Lagrangian points of larger bodies in this system. Finally, we must seek appropriate names for the ring-shepherding satellites and the co-orbital satellites. We hope to have proposals in all of these areas for our 1982 meetings.

# GEOLOGY OF SMALL BODIES: PROSPECTUS FOR THE PLANETARY GEOLOGY PROGRAM WORKSHOP

Clark R. Chapman, Planetary Science Institute, Tucson, AZ, 85719

Until the past decade, the small planetary satellites, asteroids, and comets were objects for astronomical observation far beyond the realm of geology. Mariner 9 and, later, Viking took pictures of Phobos and Deimos which revealed topography and surface morphology on bodies much smaller than had ever been available for geological study before. More recently, Voyager has provided imagery of Amalthea as well as a host of Saturnian satellites and moonlets. Meanwhile, a variety of astronomical observations, meteoritical studies, and theoretical research has dealt with geological and geophysical processes affecting the surfaces of bodies yet "unseen": asteroids and cometary nuclei.

The time is ripe for considering the geology of these small bodies, generally less than 1000 kilometers in diameter, as a subdiscipline of planetology. The pictures have proven that these bodies are not all just small versions of our Moon, as was once imagined. Rather, they are a diverse group of bodies, rarely identical in appearance to the Moon, made of materials as divergent as solid metal alloy and virtually rock-free ices. All of these bodies have one trait in common, which separates them from much larger moons and planets: they are so small and have such low surface gravity that they lose material to space. In fact, their gravitational binding energy is so low that they all have been subjected to the threat of being catastrophically disrupted and destroyed by impacts with other small bodies. Many of these bodies may, in fact, be fragments themselves.

The degree to which asteroids and small satellites have been battered by cratering bombardment can be studied by careful analysis of crater populations on their surfaces and other morphological evidence of particularly severe collisions. Depending on the location of the small bodies (in heliocentric orbits in either the inner or outer solar system or in planetocentric orbits), they will have been subjected to different fluxes of impacting bodies. In general, there will have been a different mix of asteroidal meteoroids, small comets, planetary ring particles, and other planetary satellites impacting each body.

The proximity of small planetary satellites to their primaries can be decisive in terms of the major geological features visible on their surfaces. First, conditions of formation may have varied as a function of distance from the primary, both in terms of composition and subsequent thermal evolution. Second, tidal stresses may manifest themselves on satellite surfaces, especially on those satellites close to their primaries like Phobos. Third, ejecta from small satellites may be trapped in orbit around the planet and may re-impact or re-accumulate onto the satellite or onto a neighboring satellite. Gravitational focusing effects of the primary planet may augment the flux of cometary or asteroidal impacts onto a satellite.

Comets, and possibly some satellites and asteroids (especially those located in resonances far from the main belt), may be fairly pristine samples of planetesimals from which planets accreted. If so, craters and faults may expose stratigraphy that reflects the formative processes of planetesimal accretion: these would be the earliest geologic structures that can still be studied in the solar system.

Although we normally think of bodies smaller than 1000 km diameter as being necessarily dormant throughout most of solar system history, because of their inability to accumulate radioactive heat, there is reason to expect that many of them may exhibit a much longer phase of geological activity; indeed, some may still be geologically active today. Some of the differentiated meteorites have properties that suggest the interiors of their parent bodies were warm for hundreds of millions of years or longer. A few meteorites seem to indicate that their parent has been active until quite recently (possibly such meteorites come from Mars, but the conventional view is that they must come from an asteroidal parent body).

Bodies of primitive, hydrated composition may be susceptible to aqueous processes throughout solar system history, perhaps triggered by large impacts. Icy bodies are even more susceptible to exhibiting geological activity, given some source of heating, because ices melt at much lower temperatures than rocks. Extreme examples of geologically active small bodies are cometary nuclei. Although no such nuclei have been studied so far, theoretical models suggest complex surface processes resulting from solar heating of near-surface layers of the presumed ice/dust conglomerates.

The geology of small bodies is particularly fascinating for all of the above reasons. Not only do the surfaces record the history of each body's interactions with impacting populations of projectiles and dust, but they manifest a variety of subterranean geological and geophysical processes relating to body dynamics, thermal evolution, and physico-chemical modifications. We have the potential opportunity for studying processes important for larger planets in regimes where gravity is much diminished. Because of the large number of small bodies distributed throughout the solar system, we can sample the geological manifestations of processes dependent on location. Finally, we can attempt to understnad the complex array of data derived from meteoritical samples of many of these bodies.

Phobos and Deimos have been studied in greater detail than other small bodies because we have had data from them for the longest time, and some of the pictures have very high resolution. These studies have fostered a tremendous amount of creative research about processes that had hardly been imagined before. The most startling observations to be explained were the grooves on Phobos and the great differences in appearance between the two satellites. In fact, a final consensus has not yet been reached on these questions. One important goal of the workshop will be to summarize research on the Martian satellites and to develop a consensus about what we have learned and what questions remain to be solved. An important

question to be addressed is the degree to which the characteristics of Phobos and Deimos are generalizable to other small, rocky bodies (e.g., the asteroids) compared with the degree to which their characteristics are uniquely shaped by their location in Mars' orbit. In other words, are Phobos and Deimos good asteroidal analogs?

Another broad topic is the question of what can be learned with confidence about Amalthea, the smaller satellites of Saturn (the co-orbitals, trojans, and sheparding satellites), and other small bodies for which image resolution is within a couple orders of magnitude of the dimensions of the body, or poorer. Such considerations will prove useful for determining what kind of resolution will be necessary in future spacecraft missions to asteroids and comets in order to elucidate the primary geological questions.

Much theoretical effort has recently gone toward understanding regolith processes on asteroids. The models are currently constrained somewhat by meteorite data but very little by observations of the bodies themselves. Some scientists believe that many asteroids are large rubble piles of megaregolith, while others still consider asteroidal surfaces in terms of more conventional surficial regoliths. A related question concerns theoretical calculations of what it takes to catastrophically fragment an asteroid or planetary satellite. Large craters on Phobos and Mimas provide a lower limit to the size of impact required to split a body apart; are there more restrictive limits? And what are the outcomes of such destructive events? Would double or multiple bodies result? What morphological evidence is there for believing that any of the small Saturnian satellites in the same orbits are pieces of a precursor body?

In this period of diminished expectations about what kind of planetary missions may be launched during the next two decades, there have been recent suggestions that reconnaissance missions to asteroids and comets may be both realizable and economical. What kind of scientific questions can be addressed by simple missions of these types? This will be another question to be addressed at the workshop.

Finally, what is the relationship of small-body geology to the whole field of planetary geology? To what degree are broader comparative planetological questions addressed by studies of bodies at the small end of the size spectrum? What can geological studies of asteroids, satellites, comets, and meteorite parent bodies tell us about larger questions concerning the origin and evolution of the planetary system? Should more or less attention be devoted to these bodies in the future, given the extreme fiscal constraints confronting planetary science? The essence of the workshop will be the reporting and synthesis of scientific research, not programmatic issues. Yet, we hope that all participants will be cognizant of programmatic questions about future directions -- both in terms of data analysis and theoretical research and in terms of potential future spacecraft missions. The time and locatin of the workshop will be announced at the P.G.P.I. meeting.

# LATE ABSTRACTS

A COMPARISON OF SOME EXPLOSIVE VOLCANIC ERUPTION PROCESSES ON THE EARTH, MOON, MARS, VENUS AND IO. L. Wilson, Lunar & Planetary Unit, Dept. of Environmental Sciences, Univ. of Lancaster, Lancaster LA1 4YQ, U.K. and J. W. Head, Dept. of Geol. Sci., Brown Univ., Providence, RI 02912, U.S.A.

While there are many similarities between the styles of volcanic activity which occur, or can be seen to have occurred, on the Earth, Moon, Mars and Io, there are also significant differences. Eruption style is controlled by a combination of factors such as magma composition (which controls magma rheology), magma volatile content (which tends to dominate eruption velocity in the vent) tectonic setting (which influences the depth from which magma erupts) and external environment (e.g. atmospheric pressure, gravity). Furthermore, these several factors are interrelated in various ways (Wilson and Head, 1981a) and detailed consideration of the relationships allows some predictions to be made about possible eruption styles on Venus. On the basis of numerical treatment of many of these factors in the references listed below we have reached the following conclusions:

Moon

1) The high mass eruption rates implied by the lengths of some lunar lava flows and sinuous rilles (Hulme and Fielder, 1977) require that lunar tectonic regimes produced fissure systems up to about 10 m wide.
2) Although lunar magma volatile contents were very low by terrestrial standards, the absence of atmosphere should have ensured that magma disruption into pyroclasts was a common event.
3) High effusion rate eruptions should have produced optically thick eruption clouds from which pyroclasts landed hot and coalesced to form lava flows. The landing zone could have been up to 4 km wide along elongate fissures and up to 6 km in diameter around central vents. The lava pool marking such a landing zone will have produced a thermally eroded depression feeding a sinuous rille if the eruption rate was greater than about $10^7$ kg/s. (Head and Wilson, 1981).
4) Low effusion rate eruptions could have produced cinder/spatter ridges up to 1 km wide along fissure sources. Central vents could have produced dome- or cone-like cinder deposits with diameters up to 5 km.
5) Very widespread, thin deposits (up to 200 km in diameter) of sub-millimeter pyroclastic droplets will have been formed for a wide range of mass eruption rates in events where the bulk of the erupted material was retained near the vent in lava flows or cinder cones.

Mars

1) The low atmospheric pressure on Mars means that magma disruption into pyroclasts is much more likely to occur there than on Earth.
2) The eruption velocities of gas and small pyroclasts on Mars will be higher than on Earth for the same volatile content by a factor of about 1.5.
3) Martian eruption clouds will rise to heights greater than those on Earth by a factor of about 5 for the same mass eruption rate and pyroclasts will be much more widespread than on Earth, though relatively finer grained.
4) Pyroclastic flow formation will be significantly more common on Mars than on Earth for similar ranges of eruption rate.

Io

1) The currently observed eruption clouds must contain large proportions (up to 15 wt%) of volaties (apparently sulphur or $SO_2$) and may be the equivalent of terrestrial phreatomagmatic eruptions.
2) If the mean size of particles in the clouds is of order 100 microns or more then the particle motions must be largely ballistic. Cloud brightness

modelling shows that parts of the clouds are optically thick which implies that eruption rates are greater than $10^7$ kg/s and that up to 40% of the entire heat flux from Io's interior may emerge through its active volcanoes.

Venus

1) The atmospheric pressure in the Venus lowlands is so great that magma cannot be disrupted at all by gas bubble growth unless the exsolved magma volatile content exceeds 2 wt% $H_2O$ or 5 wt% $CO_2$. The corresponding figures for the Venus highlands are 1 and 3 wt%, respectively. Such high volatile contents of relatively insoluble gases like $CO_2$ can only be obtained if the magma source region is at a depth greater than about 40 km. Thus, if magmas on Venus are very deficient in volatiles with high solubilities like that of $H_2O$, pyroclastic eruptions may never occur there.
2) If pyroclastic eruptions do occur, eruption velocities will be smaller by a factor of 2 to 4 than those on Earth for the same volatile contents.
3) Eruption cloud heights will be about 3 times lower than on Earth for the same mass eruption rate and pyroclasts will be much less widely dispersed.
4) If magma disruption can occur, pyroclastic flow formation will be much more likely than on Earth if the likely ranges of mass eruption rate are similar.

References

Blake, S. (1981) Volcanism and the dynamics of open magma chambers: Nature 289, 783-785.

Head, J. W. and Wilson, L. (1981) Lunar sinuous rille formation by thermal erosion: eruption conditions, rates and durations: Lunar and Planet. Sci. XII, 427-429.

Hulme, G. and Fielder, G. (1977) Effusion rates and rheology of lunar lavas: Phil. Trans. R. Soc. Lond. A285, 227-234.

Sparks, R. S. J. (1978) The dynamics of bubble formation and growth in magmas: a review and analysis: J. Volcanol. Geotherm. Res. 3, 1-37.

Sparks, R. S. J., Wilson, L. and Hulme, G. (1978) Theoretical modelling of the generation, movement and emplacement of pyroclastic flows by column collapse: J. Geophys. Res. 83, 1727-1739.

Wilson, L. (1980) Relationships between pressure, volatile content and ejecta velocity in three types of volcanic explosion: J. Volcanol. Geotherm. Res. 8, 297-313.

Wilson, L. and Head, J. W. (1981a) Ascent and eruption of basaltic magma on the Earth and Moon: J. Geophys. Res. 86, 2971-3001.

Wilson, L. and Head, J. W. (1981b) Volcanic eruption mechanisms on Mars: some theoretical constraints: Lunar and Planet. Sci. XII, 1194-1196.

Wilson, L. and Head, J. W. (1981c) Io volcanic eruptions: mass eruption rate estimates: Lunar and Planet. Sci. XII, 1191-1193.

Wilson, L., Sparks, R. S. J., Huang, T. C. and Watkins, N. D. (1978) The control of volcanic column heights by eruption energetics and dynamics: J. Geophys. Res. 83, 1829-1836.

Wilson, L., Sparks, R. S. J. and Walker, G. P. L. (1980) Explosive volcanic eruptions IV; The control of magma properties and conduit geometry on eruption column behavior: Geophys. J. R. Astr. Soc. 63, 117-148.

# CRATER FREQUENCY DISTRIBUTIONS ON GANYMEDE

Sam S. Mims, Institute for Astronomical Research, P.O. Box 15854, Baton Rouge, LA 70895
Dag Nummedal, Dept. of Geology, Louisiana State University, Baton Rouge, LA 70803

Crater frequency distributions were compiled for a total of twenty different regions on the leading hemisphere of Ganymede. The areas counted represent the old cratered (dark), reticulate, grooved, and smooth terrains. The counts were made within small, structurally uniform regions (cells).

Several problems are inherent in crater counting on Ganymede. Many craters have indistinct rims preventing assignment of a precise diameter. Smaller craters are nearly invisible in the dark terrain due to lack of albedo contrast. In the bright grooved terrain, some very crisp craters might be buried by ice; measured crater densities, therefore, may record the age of some intermediate stage of the formation of the grooved lane. Finally, there is the inevitable problem of secondaries. Several large recent craters show very high densities of surrounding secondaries. Although the areas chosen for counting are far removed from obvious fields of secondaries, the possibility of contamination of the data set is present. In counting on the cratered terrain, all old crater palimpsests were excluded.

The dark terrain is the most densely cratered unit on Ganymede. This supports earlier crater counts and stratigraphic relationships (Shoemaker, et al., 1981). Actual crater densities measured in this study, however, exceed those reported by Shoemaker, et al. The range of crater densities is great. The cumulative number of $>$10km craters per $10^6$ km$^2$ ranges from about 200 to 2000 (fig. 1).

Densities of $>$10km craters for grooved and reticulate terrain are less than 200 per $10^6$ km$^2$ (figs. 2 and 3). The cumulative crater frequency curves for grooved terrain have gentler slopes than those for cratered terrain. For crater sizes less than 10km, therefore, the two clusters of curves are widely separated. This probably reflects preferential flooding and obscuration of smaller craters during groove formation.

The initial phase of grooved terrain formation appears to be the opening of a major continuous fissure. This fissure commonly transects any type of boundary or terrain. Bright deposits, probably ice-flows, commonly overlie the cratered terrain adjacent to the fissure. Offsets of many craters cut by fissures demonstrate that both lateral widening and strike-slip motion generally were part of the initial fissure formation (see also: Lucchitta, 1980).

Following fissure-opening, grooves generally form parallel to the original fissure. The continued deposition of surface water-ice appears to be an integral part of groove formation. However, the lateral extent of flooding appears to decrease with widening of the grooved sulci. Very few flows overlie cratered terrain adjacent to wide sulci. Large craters are generally visible underneath the flows of the grooved terrain. Some of these are craters split by the initial fissure, suggesting that stoping is not a very significant process in the formation of grooved sulci.

REFERENCES

Lucchitta, B.K., Grooved terrain on Ganymede, Icarus, 44, 481-501.
Shoemaker, E.M., B.K. Lucchitta, J.B. Plescia, S.W. Squyres, and D.E. Wilhelms, Geology of Ganymede, in The Satellites of Jupiter, D. Morrison (ed.), (in press).

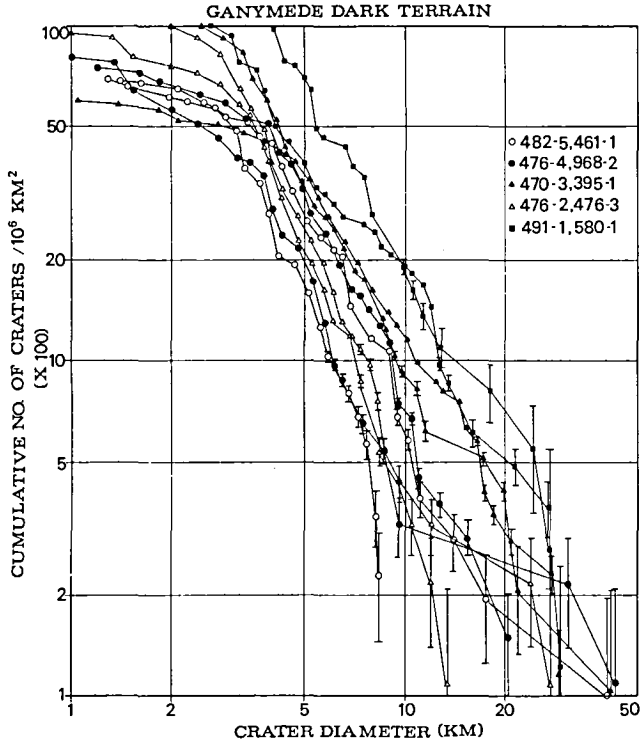


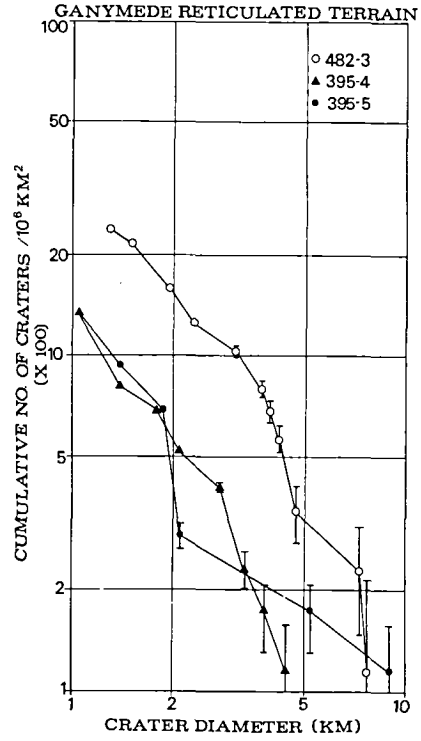


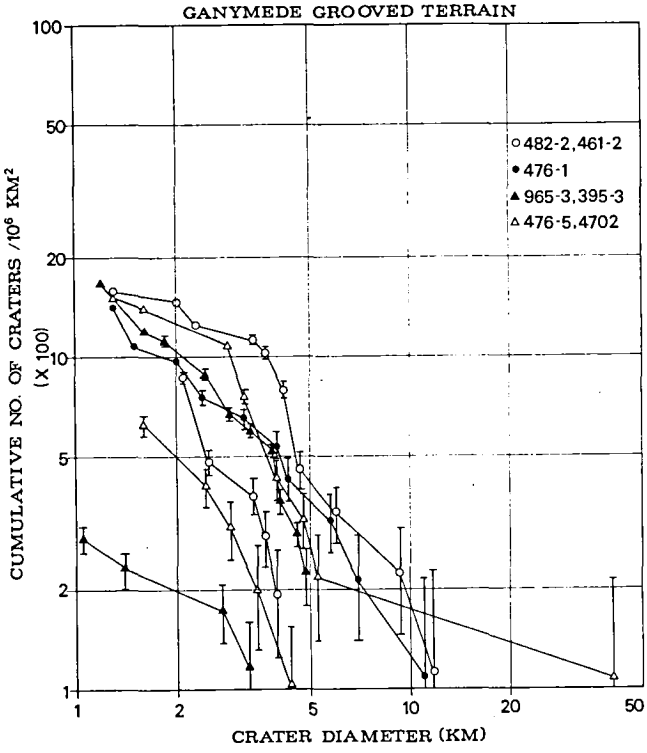


Cumulative crater frequency distributions for the major terrain types on Ganymede.

Fig. 1 (upper left): Cratered (dark) terrain.

Fig. 2 (upper right): Reticulate terrain.

Fig. 3 (lower left): Grooved terrain.

WHAT DETERMINES A VOLCANO'S FORM? C. A. Wood and H. J. Schuver*, SN6/NASA Johnson Space Center, Houston, TX 77058. *NASA Planetary Geology Intern, Summer 1981.

The shape of a volcano depends on many factors which interact in complex ways throughout the lifetime of the mountain. The importance of eruption style has long been recognized (e.g., Lacroix, 1908, p. 74), and the common association of particular styles with certain magma compositions led to a general acceptance that volcano morphology is controlled by chemistry (e.g., Ollier, 1969, p. 1). More recently, volcanoes of the "wrong" composition (e.g., basic stratovolcanoes and felsic shields, e.g., Wood, 1978a) have been recognized, leading to a renewed emphasis on eruption mechanism or style. A third factor - mass wasting - has yet to receive serious consideration as an influence on volcano morphology, although evidence suggests it can be an important process even during the active lifetime of a volcano. In this note we discuss the importance of magma composition, eruption style, and mass wasting in the formation and modification of volcanoes concentrating on the composite cone or stratovolcano.

Magma Composition

Although exceptions exist, there are generally consistent patterns in volcano morphology and magma chemistry: most shield volcanoes are basaltic, most composite cones are andesitic or some other felsic material, and most domes are rhyolitic or dacitic. If sufficient data were available a diagram like Figure 1 would probably result.

The volcanological literature contains very few studies specifically designed to define the influence of magma composition on volcano morphology, however, some relations have been documented.

(1) Smith (1970) discussed various element abundance ratios (e.g., (Si+Al)/O; Total $FeO/Al_2O_3$; Na/K; Fe/(Si+Al)) that influence magma viscosity, and he pointed out that in the cases studied these ratios indicated a relatively high viscosity for volcanic domes and a lower viscosity for associated flows of nearly the same composition.

(2) Volcanic domes extruded on flat surfaces are not constrained by crater walls or distorted by downslope flow. In a study of Quaternary volcanic domes in Japan, Moriya (1978) found that the diameter/height ratio of such domes varied according to composition, from ~7 for 75% $SiO_2$ to ~18 for 50% $SiO_2$. Thus, as expectable, felsic domes are relatively tall and squat, whereas more mafic domes are low and flat. this relation needs to be confirmed for domes in other volcanic regions.

(3) In detailed studies of basaltic landforms in southern Iceland Jakobsson (1979) found systematic relations between magma composition and resulting volcanic landforms. Nearly all of the small shields are olivine tholeiites (ave. $K_2O$ <0.1%); tholeiites and transitional basalts ($K_2O$~0.2%) produce more explosive vent structures such as spatter and cinder cone rows, and the most explosive, lava-free fissures formed from transitional and alkalic basalts ($K_2O$ ~0.7-0.8%). Jakobsson interprets the increase in explosivity as evidence for a morphologically significant increase in water and other volatiles with increasing $K_2O$ content. Potassium abundance also correlates with smaller scale morphology: The smoothest (and presumably most fluid) lavas Jakobsson studied are those of the pahoehoe lava shields composed of low $K_2O$ olivine tholeiites, while the roughest aa lavas occur in association with high $K_2O$ transitional basalts that form cinder cone rows. Are there similar subtle chemical controls of aa and pahoehoe flows in Hawaii?

To search for a more explicit understanding of how magma chemical composition influences the morphology of volcanoes we compared the mean silica content (compiled from data in various volumes of the Catalog of Active Volcanoes of the World) and average flank slope (computed from Pike's (1978) data) for 45 morphologically youthful composite cones (Fig. 2). A few shield volcanoes were included to increase the range of slopes. Although there are various types of uncertainties and inadequacies in both data sets the result is unambiguous - in this sample $SiO_2$ content does not correlate with slope. Comparisons of other indicies of magma composition (e.g., alkali ratio, serial index, iron ratio) and morphology (e.g., cone height and volume) are equally at odds with expectations. Thus, we conclude that, whereas magma composition tends to

correlate with landform type, other processes must be more important in controlling cone morphology.

Eruption Style

The classification of eruptions into various types, such as Strombolian, Vulcanian, Plinian, Peleean, and Hawaiian, denotes the existence of characteristic styles and products of eruptions. Most volcanoes exhibit a range of eruption styles throughout their lifetimes (and often during a single eruption sequence), but usually at any volcano a few styles dominate and a volcano approaches classical shield or composite cone or dome morphology. Virtually no statistical data have been compiled on eruption style and volcano morphology. As an index of effusion rate (Walker, 1973), a major factor in eruption style, we have compared the average lengths of lava flows (measured on various maps and photographs) and average slope for 17 composite and shield volcanoes (Fig. 3). This correlation is reasonably good, especially considering the number of processes other than lava flow emplacement that contribute to cone morphology. Short, stubby flows, building up the vent region, contribute to the steep slopes of composite cones, whereas long, thin flows, often erupted from flank fissures (Wood, 1981), yield low-angle shield volcanoes. Transforming these product observations to process deductions we conclude (confirming Walker's (1973) suggestion) that low effusion rate lava flow eruptions yield composite volcanoes, whereas high effusion rate eruptions produce shield volcanoes.

Mass-Wasting

All volcanoes erode through time in a slow Huttonian fashion, evolving through fairly regular degradational stages (e.g., Kear, 1957; Wood, 1980). Less well known are nearly instantaneous erosional modifications caused by eruptions. In the extreme case of caldera or amphitheater formation, due to lateral blasts (e.g., Mt. St. Helens), the summit and flanks of a cone may be drastically reduced in height. Smaller scale eruptions often cause increased erosion: Ash fall and flow deposits from the 1979 eruption of La Soufriere in St. Vincent were quickly eroded from the volcano's flank, providing fresh abrasives to carve channels in underlying deposits. The net morphological result of the eruption was destructional. Flank ash deposits on composite cones often are washed downslope as lahars initiated by heavy rainfall. Ash tends to accumulate at the base of composite cones through mass wasting processes and as primary deposits of pyroclastic flows. Indeed, Hazlett (1977, Fig. 8) indicates that laharic and alluvial deposits comprise the low angle skirt of material at the base of San Cristobal volcano in Nicaragua. Lava flows erupted from the summit or flank vents spread laterally as slope decreases and thus also contribute to lower flanks of volcanoes.

Conclusions

Although simple models have been proposed to explain the shapes of composite volcanoes as the result of single factors (Milne, 1878; Steinberg and Solov'yev, 1976; Lacey et al., 1981), it is clear that multiple factors and processes are important. A felsic chemical composition of erupting magma is in itself not sufficient to yield a composite cone (Fig. 2), although the necessary conditions most commonly appear to be met in the eruption of such magmas (Fig. 1). The large height to diameter ratio of composite cones (compared to shields) results from eruptions of short stubby lava flows (Fig. 3) and presumably little-dispersed ash falls from a central vent. As composite cones increase in basal diameter (= age) their average slopes exponentially decrease from ~35° to 15° (Wood, 1978b). Examination of composite volcano cross sections suggests that this decrease in slope is due to growth of an increasingly broad and high apron with a much lower slope than the original volcano. We propose that the characteristic decreasing slope from summit to base of composite cones is the result of the accumulation of ash fall and flow deposits, lava flows, and especially talus. Composite cones do not owe their shapes to one process but rather to various processes that are important at different positions on a volcano and at different times during its evolution.

References:
Hazlett, R. W. (1977) Geology and hazards of the San Cristobal volcanic complex, Nicaragua. M. Sc. Thesis, Dartmouth College, Hannover, NH; p. 212.
Jakobsson, S. P. (1979) Petrology of recent basalts of the Eastern Volcanic Zone, Iceland. Acta Naturalia Islandica #26; p. 102.
Kear, D. (1957) Erosional stages of volcanic cones as indicators of age. New Zealand J. Sci. Tech. 38B, 671-682.
Lacey, A., Ockendon, J. R. and Turcotte, D. L. (1981) On the geometrical form of volcanoes. Earth Planet. Sci. Lett. 54, 139-143.
Lacroix, A. (1908) La Montagne Pelee apres ses eruptions... Paris, Masson.
Milne, J. (1978) On the form of volcanoes. Geol. Mag. 5. 337-345.
Moriya, I (1978) Topography of lava domes. Bull. Dept. Geogr., Komazawa Univ., Japan 14, 55-69 (in Japanese). See also Volcano News #1, p. 5.
Ollier, C. (1969) Volcanoes. Cambridge, MIT Press, p. 177.
Pike, R. J. (1978) Volcanoes on the inner planets: some preliminary comparisons of gross topography. Proc. Lunar Planet. Conf. 9th, 3239-3273.
Smith, E. I. (1970) A comparison of selected terrestrial and lunar volcanic domes. Ph.D. dissertation, Univ. New Mex., Albuquerque, p. 200
Steinberg, G. S. and Solov'yev, Ts. V. (1976) The shape of volcanoes and the position of subordinate vents. Izv. Earth Phys. #5, 83-84.
Walker, G.P.L. (1973) Lengths of lava flows. Phil. Trnas. Roy. Soc. London 274, 107-118.
Wood, C. A. (1978a) Non-basaltic shield volcanoes. Abstracts Planet. Geol. Field Conf. Snake River Plain, Idaho, NASA TM 78-436, 34-39.
Wood, C. A. (1978b) Morphometric evolution of composite volcanoes. Geophys. Res. Lett. 5, 437-439.
Wood, C. A. (1980) Morphometric analysis of cinder cone degradation. J. Volc. Geothermal Res. 8, 137-160.
Wood, C. A. (1981) On the geometric form of volcanoes: Comment. Earth Planet. Sci. Lett. (in press).

FIG. 1: SCHEMATIC RELATION BETWEEN MAGMA CHEMISTRY AND VOLCANO MORPHOLOGY

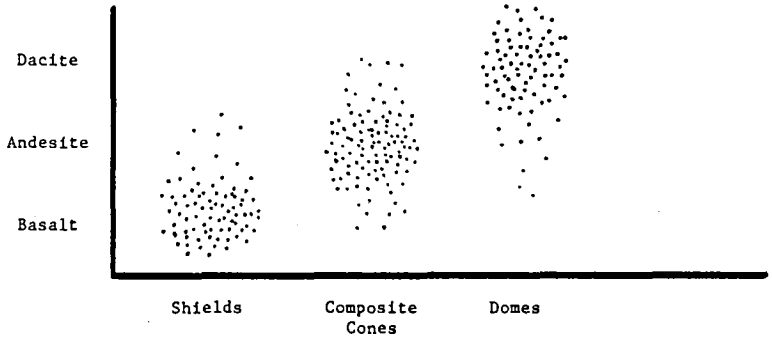


Fig. 2

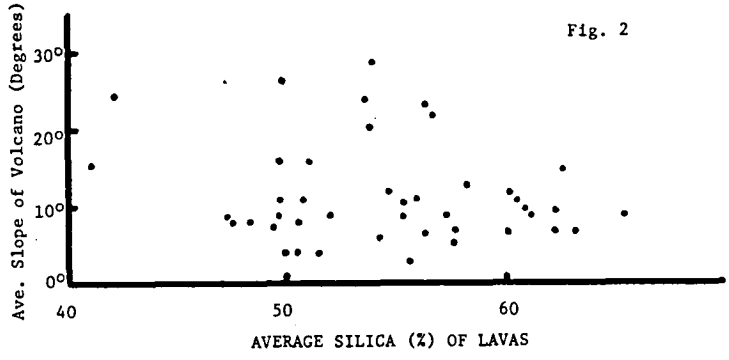


Fig. 3

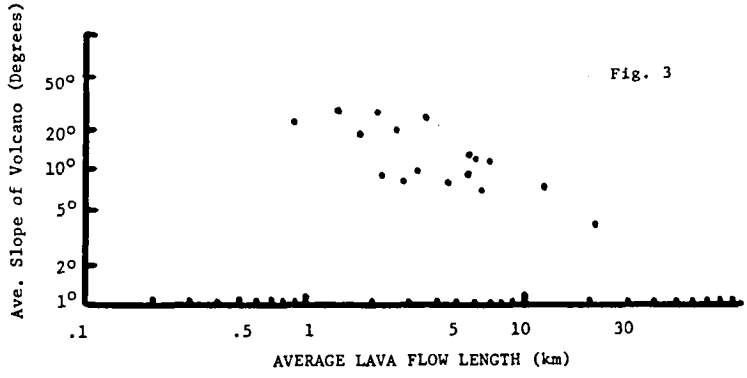

# SEAFLOOR INSTABILITIES ON CONTINENTAL SLOPES AND MARS ANALOGS

Dag Nummedal, Department of Geology,
Louisiana State University, Baton Rouge, LA, 70803

Previous studies on submarine seafloor instabilities have found that the morphology of failure scars in shallow water on the Mississippi delta front are strikingly similar to many of the chaos-channel systems in the Chryse region on Mars (Nummedal and Prior, 1981). It has been inferred that the mechanics of substrate failure, flow slide retrogression, loading-induced collapse and debris flowage, which operate on the Mississippi delta front, might also have been responsible for the generation of chaos and outflow channels on Mars. As with so many mechanisms proposed for geological phenomena on Mars, a major unresolved problem has been the disparity of scale.

Within the last year, side-scan sonar precision mapping and associated geophysical surveys have been extended into much deeper water on the upper continental slope off the active Mississippi delta. Here it is found that progradation of the shelf edge deposits generally is accompanied by oversteepening which results in large-scale instability on the upper shelf-edge slopes. Deep-seated rotational slides move large volumes of sediment and deposit them on the adjacent slope and upper continental rise. Near the shelf edge, extensive contemporaneous faults (growth faults) commonly form and extend several hundred meters into the subsurface.

Massive retrogressive, arcuate-shaped landslide scars and canyons, or trenches, also form at the shelf edge due to slumping and other mass-movement processes. These instabilities can attain widths of 10-20km, depths of 800m and lengths of 80-100km. The features are associated with the transport of large volumes of shallow water sediments into the adjacent deepwater basins where they grade into massive submarine fans. One such mapped fan off the delta covers 18,700km$^2$.

Subsequent infilling of such failure scars by deltaic progradation is rapid. The low yield strength of the rapidly infilled underconsolidated sediments causes downslope creep or reactivation of failure mechanisms, resulting in multiple episodes of canyon-head filling and evacuation with attendant canyon flow. The morphological detail of the distal canyon and associated fan has not yet been mapped.

Mapping of continental slope instabilities by means of side scan sonar and other geophysical techniques is currently underway in a multitude of settings. A recent cruise with the RRS DISCOVERY along the Norwegian continental slope, equipped with Gloria II, geological long range inclined asdic, revealed numerous massive slide and slump features. The largest, the Storegga slide, has a vertical relief of 1600m, a distance from head scarp to toe of at least 160km and extends along the shelf edge for a distance of about 200km. The average slope where the slide occurred is only 1.6° (Continental Shelf Institute, 1981).

Massive slides and slumps have also been recorded in Pleistocene and Holocene continental slope deposits in the Gulf of Alaska and the northwestern Gulf of Mexico.

It is becoming increasingly apparent that the largest slides on earth occur beneath the sea. This fact is in part due to the propensity for rapid sediment deposition, hence, underconsolidation and low yield strengths in selected marine regions. Moreover, the greatly reduced effective gravity acting on submarine sediments because of buoyancy will aid in reducing compaction. The greatly reduced acceleration of gravity on Mars as compared to earth could contribute to the widespread occurrence of large failures on that planet. It is, therefore, to be expected that submarine features on earth will provide the best ensemble of analogs to Mars. As increasingly more side-scan data are obtained from the earth's ocean floor, the Martian landscape may begin to assume the appearance of the familiar.

REFERENCES

Continental Shelf Institute (of Norway), Stability of the Norwegian continental slope, NEWS, 2, 1981.

D. Nummedal and D.B. Prior, Generation of Martian chaos and channels by debris flows, Icarus, 45, 77-86, 1981.

# IMPACT EXPERIMENTS AND REGOLITH BUILDUP

William K. Hartmann, Planetary Science Institute, Tucson, Az, 85719

A new planetary geology program has recently been begun to understand the extent of buildup of regolith and megaregolith depth as a function of total accumulated cratering on different planets and satellites, using a methodology described by Hartmann (1980). The methodology allows calculation of regolith or megaregolith depth even when a surface is super-saturated with craters, if the total number and diameter distribution of craters is specified.

No results directly from the new theoretical program are yet available, but interesting supporting results have been obtained from a parallel experimental program of impacts into regolith-like powders. This program measured masses of ejecta blankets from small craters. Ejecta masses were measured in annuli at different distances from the craters. Impact velocities varied from 5 to 2320 m/s; impact energies varied from 0.06 to 256 joules; crater diameters varied from 4 to 18 cm. The goal of the program was to measure velocity distributions of ejecta powders; but the measurement of mass distribution as a function of distance from crater center allowed comparative studies of scaling of ejecta blanket morphology.

Early data reduction has stressed the search for simple algorithms and plots that summarize the results of all experiments. It was found that cumulative fractional mass of ejecta blanket beyond radius R, plotted versus relative distance from crater center, in terms of crater radii ($R/R_c$), gave remarkably consistent plots for all experimental impacts into single target material. This is shown in Figure 1.

Figure 1 also shows the interesting result that a different mass/radius distribution was found for a fine pumice powder target than for a slightly coarser basalt powder target. (The two types of target appeared to bracket the coarseness of actual lunar regolith.)

The results suggest, in other words, that ejecta blankets in a specified target may scale homologously with a single relation of fractional mass versus $R/R_c$, as the crater size increases. This is born out by a striking visual resemblance between the diameter-scale ejecta blankets observed in the experiments and the multi-kilometer-scale ejecta blankets seen on planetary worlds. It is hoped that these results may lead to better understanding of crater ejecta blanket scaling and their effects on megaregolith evolution.

## REFERENCES

Hartmann, W.K. (1980). Dropping Stones in Magma Oceans: Effects of Early Lunar Cratering. In Proc. Conf. Lunar Highlands Crst. (J. Papike and R. Merrill, Eds.), pp. 155-171, Pergamon Press, N.Y.

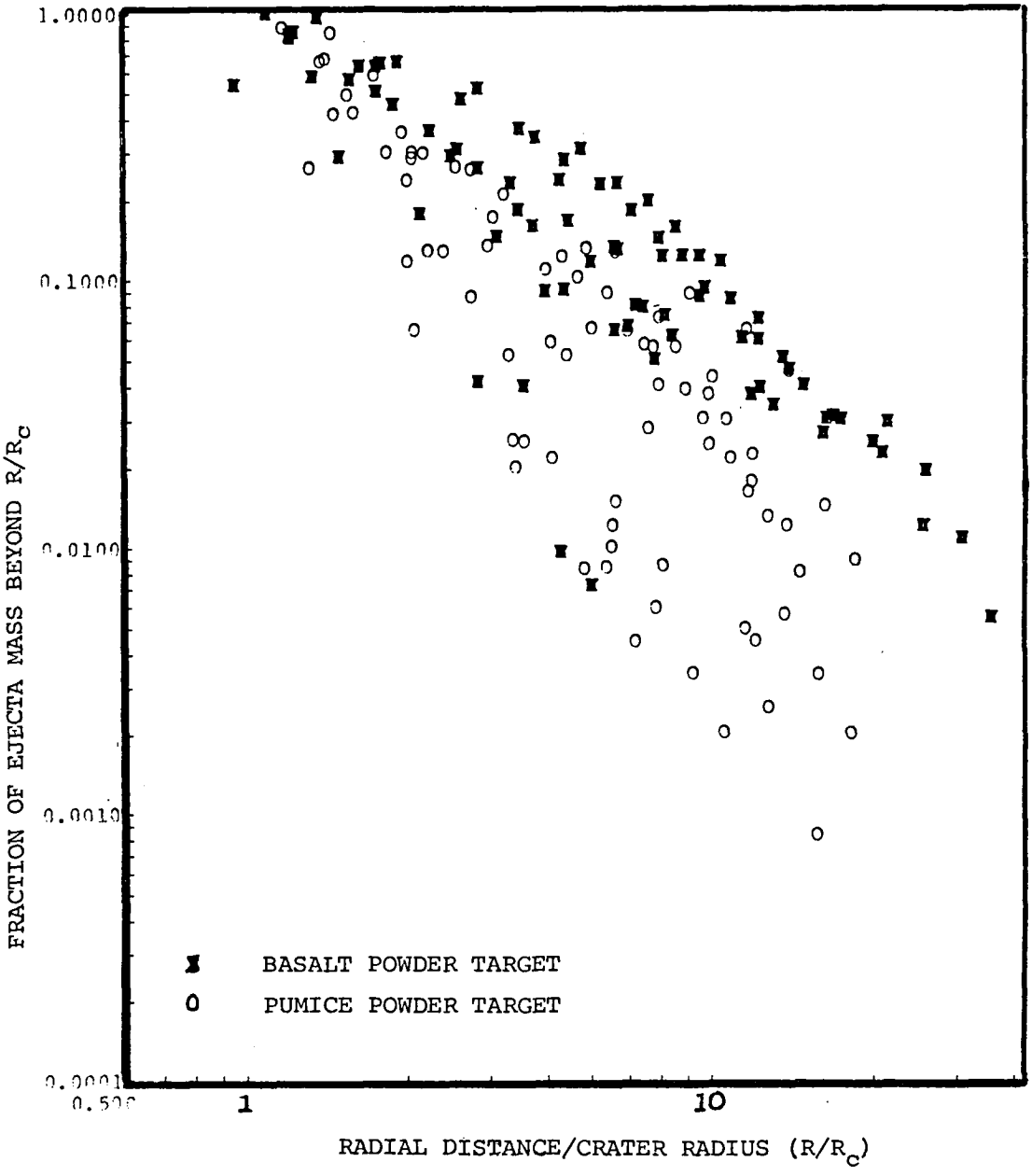


Figure 1: Crater ejecta morphology in dimensionless terms, plotted for a variety of experimental craters with impact energy ranging over 3½ orders of magnitude. The graph plots cumulative amount of ejecta mass beyond distance R. expressed in terms of crater radii ($R/R_{crater}$). Data suggest a fairly narrowly defined relation for each target material.

GEOCHEMICAL ANOMALIES ON THE LUNAR SURFACE: IMPLICATIONS FOR EARLY VOLCANISM AND THE ORIGIN OF LIGHT PLAINS.

B. Ray Hawke, Hawaii Inst. of Geophysics, Univ. of Hawaii, Honolulu, HI 96822; P.D. Spudis, Dept. of Geology, Ariz. State Univ., Tempe, AZ 85281; and P.E. Clark, Jet Propulsion Lab., Cal. Tech., Pasadena, CA 91103

Introduction: Analyses of the orbital geochemistry data sets have shown that some lunar regions have unusual abundances of certain elements relative to surrounding or adjacent areas, or have a surface chemistry unlike that which would be anticipated from the examination of local geologic relationships. Investigation of the formation of geochemical anomalies can provide important clues to understanding impact and volcanic processes operative during the early phases of lunar evolution as well as the lateral and vertical composition of the highlands crust[1,2,3,4].

The purposes of the present study include the following: 1) to locate and determine the extent of geochemical anomalies in selected lunar regions, 2) to determine the compositions of anomalous regions, 3) to correlate the anomalies with specific geologic units or surface features, and 5) to determine the origin of the anomalies and associated surface features.

Method: Digital versions of the various orbital chemistry data sets were obtained and utilized in this study. The Aℓ/Si values utilized were the newly revised data described by Clark and Hawke[5]. The digital Fe and Ti data used were those presented by Davis[6]. The Th abundances are those presented by Metzger et al.[7]. In addition, images showing Fe and Ti abundances as determined by Metzger and co-workers[8,9] were kindly provided by Dr. A. Metzger. The digital data were analyzed using a variety of image processing techniques including a units mapping technique described by McCord et al.[10].

Selected Geochemical Anomalies: 1) Terrain northeast of Mare Smythii--A number of major geochemical anomalies have been identified immediately northeast of Mare Smythii. The Aℓ/Si intensity map shows that an area of relatively low Aℓ/Si values (∿1.00-.70) extends along the Apollo 16 groundtrack between 92°E and 99°E. Considerably higher Aℓ/Si values predominate in other highland areas to the east and southeast of Smythii. Previous workers[2,11] noted that relatively high Mg/Si values (MgO%≅8%) were associated with the plains material inside Babcock crater which is within the anomalous region. The deconvolution studies by Haines et al.[12] indicated that at least the northern half of Babcock exhibited enhanced Th abundances (3.4ppm). The region also exhibits enhanced Fe and Ti values.

The geochemically anomalous region closely corresponds to a geologic province characterized by relatively young light plains mapped by Wilhelms and El-Baz[13]. The province is dominated by Imbrian plains (Ip), middle Imbrian to late Nectarian plains (INp) and Imbrian-age terra mantling material (It). It is significant that areas which exhibit low Aℓ/Si values can be correlated with specific deposits of light plains or terra mantling material. In addition, Schultz and Spudis[2] mapped a high density of dark-haloed impact craters in this region. There appears to be a clear association of geochemical anomalies with light plains deposits which exhibit a high concentration of dark-haloed impact craters.

In general, the present surface composition of the anomalous region is intermediate between mare basalts and highland material. While it is con-

ceivable that these plains could be the products of an episode of volcanic activity which emplaced material of intermediate composition, another explanation seems more likely based on the results of studies in other lunar regions[1,2,3,4]. The region probably experienced an episode of mare volcanism early in lunar history. The surfaces of these basalts were subsequently contaminated by highlands material contributed by a variety of subsequent impact events.

2) Region near Langemak crater--A major farside geochemical anomaly is located in the general vicinity of Langemak crater. Hubbard et al.[14] first pointed out the rather striking variations in Mg/Si and Aℓ/Si intensity ratios which occur near Langemak. Schultz and Spudis[2] correlated the highest Mg/Si intensity ratios with two dark-haloed impact craters and suggested that the region had been the site of an early episode of basaltic volcansim. Relatively high Fe and Ti values are associated with the Langemak region[1,6]. No Th or radioactivity anomaly has been identified in the region[1].

Examination of the most recent Aℓ/Si maps[5] showed that the lowest Aℓ/Si intensity values (.99-.70) are centered on the two dark-haloed craters described by Schultz and Spudis[2]. Only slightly higher values are associated with the relatively dark Langemak ejecta blanket and Nectarian light plains. Similar patterns are seen in other versions of the orbital X-ray data sets (Andre and Adler[15], Hubbard et al.[16], Bielefeld et al.[17]). Another small Aℓ/Si anomaly (.99-.70) is located in the southern part of the Langemak region (15°-16°S, 113°-115°E) and appears to correlate with a small deposit of light plains material.

3) The Pasteur crater region--Aℓ/Si intensity ratios in portions of the Nectarian plains in the northern floor of Pasteur (10°-12.5°S, 105°-108°E) range from 1.0 to 0.84. Similar Aℓ/Si values occur in the floor of Backlund crater on the south rim of Pasteur and correlate with a light plains unit (INp). No Ti or Th anomaly was identified but relatively high (up to 7.4%) Fe values occur on the northeast rim of Pasteur and extend into the northeastern portion of the crater floor. Relatively low Aℓ/Si values were also found to be correlated with light plains units northwest of Pasteur[15,17] (∿9°S, 98°E). To date, no dark-haloed impact craters have been identified in the Pasteur region.

4) Region NW of Milne basin--An area of anomously high (2.4-3.5%) Ti values occurs northwest of Milne basin. The high values are seen on both the Ti distribution maps of Davis[6] and Metzger. Fe values in the high Ti area are variable but increase systematically from the northeast to the southwest. The region contains a variety of highland units as well as a very small amount of mare material in the northernmost extension of Lacus Solitudinis. At least four dark-haloed impact craters have been identified around Lacus Solitudinis and their presence suggests that mare volcanism was more widespread in this region than is currently recognized. Two of these dark-halo craters occur within the high Ti area. The Ti anomaly may be in part due to the small amount of mare material in the region and to dectector response to the larger expanse of mare material to the south in Lacus Solitudinis. Still, the extent and magnitude of the anomaly suggests that the above factors alone cannot account for the feature. The presence of early mare basalt, thinly covered by and mixed with highland material may also be partly responsible for the anomaly.

5) Eastern Mendeleev region--Relatively high Fe abundances (5.6-7.4%)

occur on the northeast rim of Mendeleev basin[6]. Slightly lower values (4.4-5.6% Fe) occur in the eastern portion of the floor of Mendeleev and extend to the east of the basin. An area of high Ti values (~3.2%) can be seen on the northeastern floor and rim of Mendeleev on Metzger's unpublished Ti distribution map. The Fe anomaly is centered on a concentration of Imbrian light plains. No dark-haloed craters have been identified in the region. It seems unlikely that the high gamma-ray values are caused by detector response to mare material north of the groundtrack because the nearest significant expanse of basalt occurs over 400 km to the north on the interior of Moscoviense basin.

6) Terrain north and northeast of Korolev basin (6°-10°N, 202°-214°E)--This region is characterized by relatively high Fe abundances (5.6-7.4%) and very low (~0.3%) Ti abundances. No Th anomaly has been identified in the region and no X-ray data exist. The region contains a variety of highland units including Imbrian light plains. While light plains are abundant in the anomalous region, they are equally abundant in adjacent areas outside the anomaly. No dark-haloed craters have been located in the vicinity.

Conclusions: 1) These anomalies are commonly, though not always, associated with light plains deposits which exhibit a high density of dark-haloed impact craters. 2) In light of recent results of spectral reflectance studies of dark-haloed impact craters[3,4], it seems likely that the chemical anomalies associated with light plains which exhibit abundant dark-haloed impact craters are due to the presence of basaltic units thinly covered by highlands material. The subjacent basaltic material could have been incorporated in the surface material either by local mixing during emplacement of the highlands material or by later vertical mixing. 3) In those instances where geochemical anomalies correlate with light plains without identified dark-haloed impact craters, the origin of the anomalies remains uncertain. The thinly buried basalt hypothesis is still viable but other explanations (such as highland volcanism and the impact excavation of anomalous material) must be considered. 4) The burial of pre-existing volcanic surfaces by varying thicknesses of highland material appears to have been an important process in the formation of lunar light plains. 5) Basaltic volcanism on the lunar surface was more extensive in both space and time than has previously been suggested.

References: 1) B. Hawke and P. Spudis (1980) Proc. Conf. Lunar Highlands Crust, 467. 2) P. Schultz and P. Spudis (1979) PLPSC 10, 2899. 3) B. Hawke and J. Bell (1981) PLPSC 12, in press. 4) B. Hawke and J. Bell (1981) this volume. 5) P. Clark and B. Hawke (1981) PLPSC 12, in press. 6) P. Davis (1980) JGR 85, 3209. 7) A. Metzger et al. (1977) PLSC 8, 949. 8) A. Metzger and R. Parker (1979) EPSL 45, 155. 9) E. Haines and A. Metzger (1980) PLPSC 11, 689. 10) T. McCord et al. (1980) LPS XI, 679. 11) C. Andre et al. (1979) PLPSC 10, 1739. 12) E. Haines et al. (1978) PLPSC 9, 2985. 13) D. Wilhelms and F. El-Baz (1977) USGS Map I-948. 14) N. Hubbard et al. (1978) In Mare Crisium: The View from Luna 24, 13. 15) C. Andre and I. Adler (1980) Frontispiece, PCLHC. 16) N. Hubbard et al. (1978) Frontispiece, PLPSC 9. 17) M. Bielefeld et al. (1977) Frontispiece, PLSC 8.

Global Inventory of Martian Impact Craters: Status Report

D. J. Roddy, A. S. McEwen, A. Wasserman, C. L. Mardock, H. O. Webb, P. A. Davis, and L. A. Soderblom
U.S. Geological Survey, Flagstaff, AZ 86001

The Viking Orbiter images have shown that martian impact craters and their ejecta blankets have a wide range in morphological types, suggesting that the martian crust was highly variable in both type and space. This has led a number of workers to prepare various types of inventories of martian craters. The work described here presents an impact crater inventory that incorporates detailed qualitative information and quanitative data, as well as planimetric information, in formats identical to the large data sets available for terrestrial impact and explosion craters. This new inventory of martian impact craters and ejecta blankets has been partly completed and includes positional, dimensional, and morphological data for all craters one kilometer in diameter and larger. The objective is to determine the global distribution of the different types of martian impact craters and examine their interactions with various martian crustal materials. Data acquisition has been completed or is now being completed for the area from 30° N to 30° S latitudes and from 57.5° W to 180° W longitudes (U.S.G.S. Quadrangles MC-8, MC-9, MC-10, MC-11, MC-16, MC-17, MC-18). The 1:2 million controlled photomosaics derived from Viking Orbiter images are being used for this study; and the resolution is about 130 to 300 m/picture element with an average sun angle of about 20°.

The methods of data collection and transformation include: (a) tracing or point-locating each crater element, such as rim crests or central peaks, on a high-resolution digitizer board, (b) storing all digitized positional data on computer tape in x,y (vector) map coordinates, (c) processing and decoding the data into Calcomp plotter format, (d) processing each crater data base to determine surface areas of closed-line data and directional information on both closed-line lengths and direction of minimum and maximum radius of crater and ejecta boundaries, and (e) printing selected results in tabular and map formats for editing and statistical assemblages. The vector data sets being collected include: closed-line data, open-line data, point data, and crater/ejecta visual characterization data. The closed-line data include information on rim crests, bases of central peaks, central pit boundaries, ejecta blanket boundaries, and bases of crater walls. The open-line data include information on crater terrace positions, secondary crater chains, and other linear features. The point data include information on centers of central peaks, central pits, and secondary impact clusters. The x,y position of each crater, its maximum and minimum diameters, ejecta blanket radii, and a large number of other dimensions can be extracted from the computer tapes. In addition, each of the craters and ejecta blankets has a series of morphological statements added to the computer data. These include over 40 different descriptive characterizations, such as, bowl-shaped, flat-floored, central uplift, hummocky ejecta, grooved ejecta, and flow ejecta, as well as a number of other descriptive statements.

We are currently extending this collection of data between the longitudes of 57.5° W to 180° W to as far north and south as the photography permits. The final phase of this study will be to use the large body of digital-tape data to (a) study the different types of craters as a function of their visual characteristics, the distributions of physical dimensions, the associated ejecta types, and the geographical and geological positions, and to (b) manipulate this data statistically to study the interactions of the impact cratering events with the martian crustal materials.

Martian Impact Crater Forming Processes and Crater Physical Dimensions

D.J. Roddy, D.A. Arthur, P.A. Davis, and L.A. Soderblom,
U.S. Geological Survey Flagstaff, AZ 86001

A study of martian impact craters has been in progress to collect quantitative data on the major types of craters and ejecta blankets. The goals of this work are: (a) to try to better understand martian crater-forming processes, and (b) to examine how large impact events interact with different types of martian crustal materials. One of our specific objectives has been to collect detailed dimensional data which is representative for each of the different types of martian craters. These data include rim crest diameters and depths, apparent diameters and depths (values derived from extrapolation of pre-impact target surface), rim crest heights, crater rim crest volumes, apparent volumes, ejecta thicknesses, ejecta volumes, and a variety of other cratering data. The types of data collected are similar to the larger data sets given in Roddy (1977, 1979) for impact and explosion craters, and are designed to permit direct comparison with the terrestrial data bases.

The crater dimensions were derived from Viking Orbiter 1 photography by two different photoclinometric techniques. One method used solar-shadow positions and is described by Arthur (1974). Accurate depths, heights, and certain lateral dimensions can be determined when this method is applied to craters whose rim crests cast sharp shadows on both the crater floor and ejecta blanket. The values obtained by this method, however, are restricted to specific locations in a crater and on its ejecta surface. The second photoclinometric method involved automated computer techniques which are described in Davis et al. (1981), and were used to directly determine topographic profiles of the craters and their ejecta blankets. The same craters were used in both photoclinometric methods in order to check the accuracy of the crater dimensions. Over three hundred Viking frames representing each of the major martian crater types were initially examined, and detailed data on dimensions have been determined now for twenty of these craters by the methods described above. Representative craters are shown in Figures 1 and 2 and their dimensional values are given in Table 1.

The shadow method has been shown by previous workers to provide accurate values for crater depths and rim heights for specific locations when shadows are well-defined. Topographic profiles derived by computer-photoclinometric methods are equally necessary to calculate volumes of craters and ejecta blankets. In addition, slope profiles give critical information on the true shape of the crater and the ejecta distribution. An additional advantage of the computer method is that it can be used to determine profiles of craters that do not have well-defined solar shadows on the Viking images.

Preliminary comparisons between the crater and ejecta data and terrestrial impact and large-scale explosion crater data show a number of similarities and differences. As seen in Table 1, average diameter/depth ratios (rim crest values) of martian craters are comparable to those of terrestrial average values for impact and explosion craters of the same morphological type. Mass balance

calculations of cratered mass versus ejecta mass appear to present a problem in that only about one-third of the cratered mass can be accounted for in the ejecta blanket (using our shadow-measured thicknesses and assuming density contrast of 50 percent). Generalization of this relationship , however, requires further substantation. An additional 50 craters are being included in our final Mars data base on crater and ejecta dimensions, and these detailed numerical and observational data will be tabulated and used to compare with existing terrestrial impact and explosion data bases to study martian cratering effects.

References


Arthur, D. W. G., 1974, Lunar Crater Depths from Orbiter IV Lunar Crater Depths from Orbiter IV Long-Focus Photographs, Icarus 23, 116-131.

Davis, P. A., et al. (1981) 3rd Int. Colloq. Mars, 56-58

Roddy, D. J., Pepin, R. O., and Merrill, R. B., 1977, Impact and Explosion Cratering, Pergamon Press (New York), p. 185-246.

Roddy, D. J., 1978, Proc. Lunar Planet. Sci. Conf. 9th, p. 3891-3930.


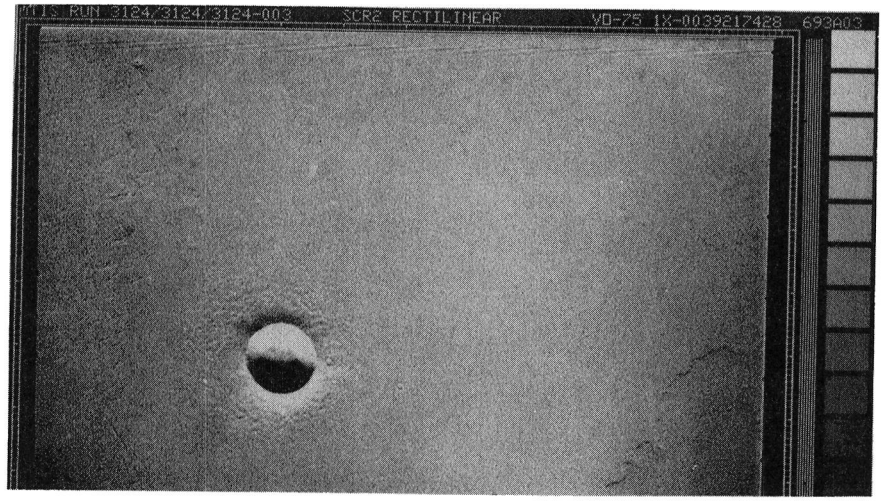


Figure 1. Viking Orbiter image 693A03 showing a bowl-shaped impact crater and ejecta blanket


Figure 2. Viking Orbiter image 467A10 showing a flat-floored impact crater and ejecta blanket

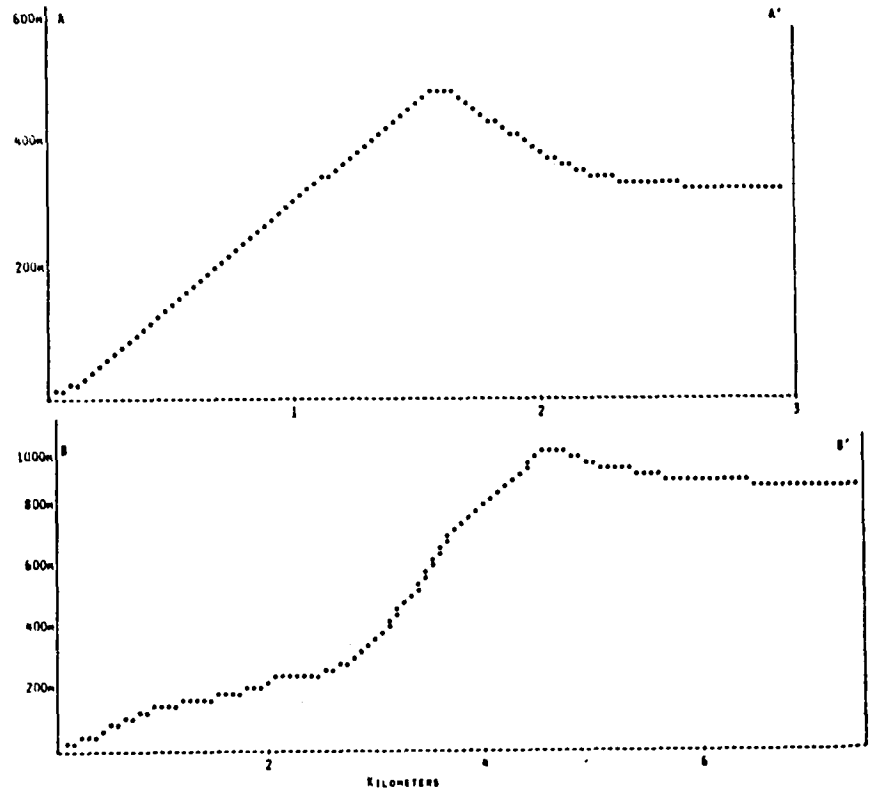


Figure 3. Computer-generated topographic profiles of a bowl-shaped impact crater (693A03, profile A-A') and a flat-floored impact crater (467A10, profile B-B') (See Figs. 1 & 2).

Table 1. Representative diameters and depths measured at the rim crests and determined by sun-shadow and automated computer methods. The shadow depths and rim crest heights are maximum values, whereas the computer depths and heights are averaged values for those areas. The terrestrial impact and explosion average rim crest values are from field measurements by Roddy (1977, 1979). The D/d ratios use averages of the shadow and computer values.

| Viking Image | Crater Type | Shadow Diameter | Computer Diameter | Shadow Depth | Computer Depth | Shadow Rim Crest Height | Computer Rim Crest Height | D/d | Terrestrial Impact D/d | Explosion D/d |
|---|---|---|---|---|---|---|---|---|---|---|
| 693A03 | Bowl-shaped | 3.3 km | 3.2 km | 520 m | 475 m | ~130 m | ~150 m | 6.6 | ~5 to 7 | ~4 to 6 |
| 467A10 | Flat-floored | 9.4 km | 9.3 km | 850 m | 710 m | ~160 m | ~100 m | 12.0 | ~15 to 25 | ~8 to 18 |

# AUTHOR INDEX

# AUTHOR INDEX

*U.S. GOVERNMENT PRINTING OFFICE: 1981 539-007/15 1-3

| 1. Report No. | 2. Government Accession No. | 3. Recipient's Catalog No. |
|---|---|---|
| NASA TM-84211 | | |

| 4. Title and Subtitle | 5. Report Date |
|---|---|
| Reports of Planetary Geology Program - 1981 | December 1981 |
| | 6. Performing Organization Code |

| 7. Author(s) | 8. Performing Organization Report No. |
|---|---|
| Compiled by Henry E. Holt | |
| | 10. Work Unit No. |

| 9. Performing Organization Name and Address | 11. Contract or Grant No. |
|---|---|
| Planetary Geology Program<br>Office of Space Science<br>Solar System Exploration Division | |

| 12. Sponsoring Agency Name and Address | 13. Type of Report and Period Covered |
|---|---|
| National Aeronautics and Space Administration<br>Washington, D.C. 20546 | Technical Memorandum |
| | 14. Sponsoring Agency Code |

15. Supplementary Notes

16. Abstract

This is a compilation of abstracts of reports from Principal Investigators of NASA's Planetary Geology Program, Office of Space Science.

The purpose is to provide a document which succinctly summarizes work conducted in this program. Each report reflects significant accomplishments within the area of the author's funded grant or contract.

No attempt has been made to introduce editorial or stylistic uniformity; on the contrary, the style of each report is that of the Principal Investigator and may best portray his research. Bibliography information will be included in a separately published document.

Full reports of selected abstracts will be presented to the annual meeting of Planetary Geology Principal Investigators at Jet Propulsion Laboratory (JPL), Pasadena, California, January 12-14, 1982.

| 17. Key Words (Suggested by Author(s)) | 18. Distribution Statement |
|---|---|
| Planetary Geology<br>Solar System Evolution<br>Planetary Geologic Processes | Unclassified - Unlimited<br><br>Subject Category 91 |

| 19. Security Classif. (of this report) | 20. Security Classif. (of this page) | 21. No. of Pages | 22. Price* |
|---|---|---|---|
| Unclassified | Unclassified | 582 | A25 |

N-305

For sale by the National Technical Information Service, Springfield, Virginia 22161

National Aeronautics and
Space Administration

Washington, D.C.
20546

Official Business
Penalty for Private Use, $300

SPECIAL FOURTH CLASS MAIL
BOOK

Postage and Fees Paid
National Aeronautics and
Space Administration
NASA-451


NASA

POSTMASTER: If Undeliverable (Section 158
Postal Manual) Do Not Return